

NASA Technical Memorandum 88784

NASA-TM-88784-VOL-2
19860018570

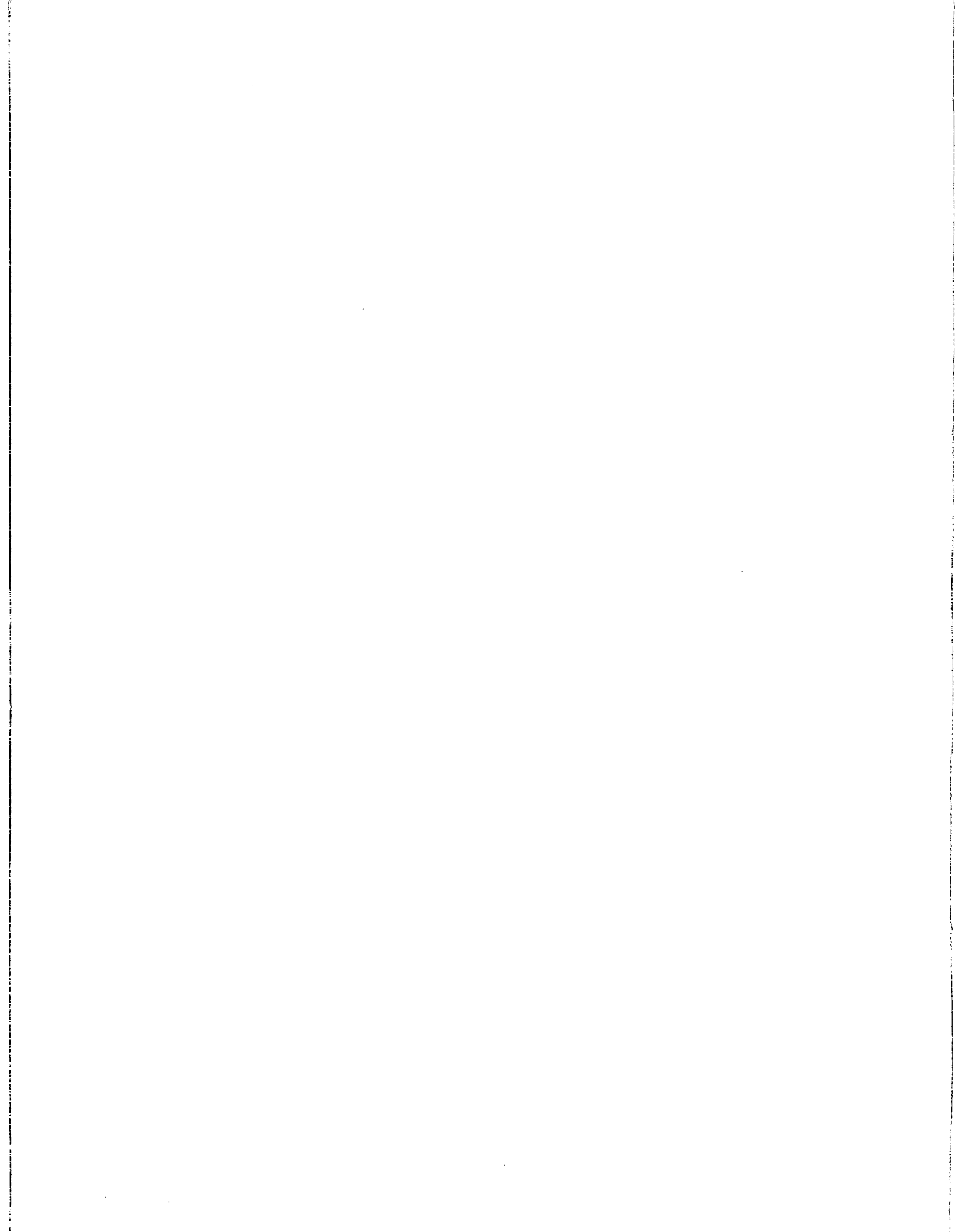
Advances in Planetary Geology

Volume 2

JULY 1986

LIBRARY COPY

LANGLEY RESEARCH CENTER
LIBRARY, NASA
HAMPTON, VIRGINIA



NASA Technical Memorandum 88784

Advances in Planetary Geology

Volume 2

*NASA Office of Space Science and Applications
Washington, D.C.*



National Aeronautics
and Space Administration

Scientific and Technical
Information Branch

1986

FOREWORD

This document is a compilation of reports from Principal Investigators and their Associates of NASA's Office of Space Science and Applications, Solar System Exploration Division, Planetary Geology and Geophysics Program. The reports present research that adds to our knowledge of the origin and evolution of the solar system and to our understanding of the earth as a planet. Advances in Planetary Geology was established as a complement to the abstract document "Reports of the Planetary Geology and Geophysics Program" and to professional journals. This document provides a method of publishing research results which are in a form that would not normally be published elsewhere. The research reports may be in the form of lengthy research reports, progress reports, Ph.D. dissertations, or master's theses.

Joseph M. Boyce
Discipline Scientist
Planetary Geosciences Program
Office of Space Science and Applications

To Contributors:

A wider variety of manuscripts can be accommodated by Advances in Planetary Geology than by most journals. Particularly appropriate are completed theses, dissertations, and research reports reliant on extensive presentations of supporting data. All contributions must be of direct interest to planetary geologists and must be of high scientific quality. Manuscripts must be typed, preferably single spaced, in a camera-ready format. Inquiries concerning contributions as well as submissions of contributions should be made to:

Dr. Alex Woronow
Geosciences Department
University of Houston, University Park
Houston, TX 77004

CONTENTS

Multispectral and Geomorphic Investigations of the Surface of Europa.....	1
Thomas Allan Meier	
Reports of the 1983 Intern Program	
Structural Control of Valley Networks on Mars.....	361
Virginia Gulick	
Flux, Ripples, and Dunes on Venus.....	364
S. J. Bougan	
Morphological Features of Terrestrial and Martian Landslides.....	368
E. Ann Kirkpatrick	
Localized Measurements of Geothermally Enhanced Heat Flow Through Remote Infrared Imaging.....	375
Mark S. Marley	
New Techniques in Morphometric Analysis of Craters.....	380
Irene Llewellyn Meglis	
Survey for Bright Mars-Crossing Asteroids.....	389
Suzanne Smrekar	
Properties of Residues from Sublimed Dirty Ice.....	393
Stephen Sutton	
The Classification of Martian Rampart Craters.....	398
Mary Norris	
The Gravity Response of Impact Craters and Volcanic Constructs on Mars.....	402
Teresa F. McDonald	
Reports of the 1984 Intern Program	
Origin of the Moon: Constraints from Volatile Elements.....	411
Melanie E. Kreutzberger	
Inquiries into the Nature of the Martian Highlands- Lowlands Boundary.....	412
Jeffrey D. Corrigan	

CONTENTS (Continued)

Spectral Reflectance of Carbon-Sulfur Mixtures.....	419
April Clare and Jonathan Gradie	
Lab Experiments on UV Spectra of Gaseous and Adsorbed Sulfur Dioxide and Applications to Io.....	438
Julianne I. Moses	
Topographic Slope of Lunar Maria and Highlands.....	452
Bruce A. Minturn	
Evaporation of Volatile Ices During Icy Satellite Accretion.....	463
Zoran Spasojevic	

MULTISPECTRAL AND GEOMORPHIC INVESTIGATIONS
OF THE SURFACE OF EUROPA

MULTISPECTRAL AND GEOMORPHIC INVESTIGATIONS
OF THE SURFACE OF EUROPA

A Thesis
Presented to
the Faculty of the Department of Geosciences
University of Houston

In Partial Fulfillment
of the Requirements for the Degree
Master of Science

By
Thomas Allan Meier
May, 1985

ACKNOWLEDGEMENTS

This thesis is dedicated to the creator of Europa (no, not Arthur C. Clarke), with gratitude that I was allowed to finish it before 2010. Many others are due thanks for their kind assistance and support. At the USGS Branch of Astrogeology in Flagstaff, Arizona, thanks to Larry Soderblom for guiding me into choosing Europa as a topic and allowing me to work with him two summers; Elliot Morris and Barb Lucchitta for technical support and advice; and Eric Eliason, Kevin Mullins, Brian Skiff, and the rest of the image processing staff for assistance and advice in computer processing the Voyager images. At the Lunar and Planetary Institute in Houston, Texas, thanks to Pete Schultz for serving as LPI advisor and offering useful data reduction suggestions, Ron Weber for photo support, and very special thanks to Rebecca McAllister for innumerable acts of image processing assistance and encouragement. Equally special thanks must go to Cathy Meier for typing the monster, acting as project anchor, and remaining my wife. At the University of Houston, thanks to Elbert King for serving as thesis committee chairman and graduate advisor, John Casey and William Sheldon for serving as thesis committee members, and John Butler for helping arrange departmental support and a grant that made possible travel to the USGS in Flagstaff.

ABSTRACT

Voyager 2 high-resolution imagery of two areas on the surface of Europa were subjected to intensive multispectral and geomorphic investigations. The first, an area between 220° and 180° Longitude and -24° and -2° Latitude, was chosen for its high density of dark lineations. Features studied included 193 dark lineation segments and their surrounding plains. The second area, between 220° and 178° Longitude and -44° and -41.5° Latitude, studied the white line Agenor Linea, its flanking dark patches, and surrounding plains. Objectives were to characterize these features, model their origin and evolution, and apply the findings to the surface of Europa as a whole. Brightness values (DN's) at violet, blue, and orange wavelengths were normalized and plotted on ternary diagrams for all features studied. Characteristic classifications based on orange relative spectral reflectance, local brightness, area of ternary diagram plots, density of points in ternary diagram plots, degree of dispersion of points in ternary diagram plots, and feature orientation were made for the dark lineations; many of these classifications were made for the other features studied. Agenor Linea was additionally mapped for its lengthwise compositional variation based on the spectral position of each pixel in the feature's multispectral ternary diagram.

The dark lineation characteristic classes were correlated with each

other to find significant pairs of characteristics present. The major discovery made was that as the albedo of a dark lineation increases, its orange relative reflectance decreases. Specifically, as a dark lineation becomes fainter as compared to its surrounding plains, it becomes spectrally more similar to the plains as well. This finding is best modeled as plains unit resurfacing of dark lineations via water vapor/frost particle plumes. In addition to studying the dark lineation suite as a whole, specific dark lineations were cited based on unusual spectral and ternary diagram properties. Agenor Linea was found to contain intermittent bright spots, causing a slightly pinched appearance. These bright spots were interpreted to be sites of liquid water "lava" eruption, with water lava flows coalescing to form the continuous white line Agenor Linea. Flanking dark patches are believed to be remnants of a dark lineation that initially formed a triple band structure with Agenor Linea. No major lengthwise sequences of a single composition or gradational compositions were found in Agenor Linea.

The two resurfacing mechanisms, water vapor/frost plumes and liquid water volcanism, lead to a model of the life cycle of a European fracture/dark lineation. Fracture rejuvenation and degradative processes (ion erosion, micrometeoroid gardening, and ice sublimation) can make lineation resurfacing reversible. Plume resurfacing is favored as the dominant mechanism of large-scale resurfacing of Europa because of the per site area covered compared to water volcanism. The European plains were found to display zoning in enhanced color ratio composite imagery.

It is presently unclear whether this zoning is a genuine manifestation of diminishing concentrations of Io-derived sulfur in Europa's surface ice or an artifact of computerized image processing.

TABLE OF CONTENTS

<u>Section</u>	<u>Page</u>
LIST OF FIGURES	11
LIST OF TABLES	12
LIST OF APPENDICES	13
I. INTRODUCTION	14
A. Early Research	14
B. Radiometry	17
C. Theoretical Studies	20
1. Viscous Relaxation	23
2. Ion Erosion	24
D. Mutual Occultations	25
E. Imagery and Ensuing Studies	26
F. Laboratory Analogs	30
G. Spectrophotometric Studies Since 1965	31
II. STATEMENT OF OBJECTIVES	37
III. DESCRIPTION OF DATA AND DATA PROCESSING	39
A. History of Voyager Imagery	39
B. Sources of Error and Compensation Techniques	40
C. Image Processing at LPI	49
D. Corrections Applied After Image Processing	51
E. Plotting the Data	54
F. Study of <u>Agenor Linea</u>	67
IV. RESULTS AND DISCUSSION: DARK LINEATION AREA	70
A. Description of Dark Lineation Area	70
B. Dark Lineation Ternary Diagram Plots	73
C. Dark Lineation Characteristics Evaluated	75
D. Plains Surrounding Dark Lineations	99
E. Interpretation of Results	99
F. Other Dark Lineations Properties	109
G. Individual Dark Lineations of Merit	125
H. Color Ratio/Classifier Images of the Study Area	142
V. RESULTS AND DISCUSSION: <u>AGENOR LINEA</u> AND ENVIRONS	151
A. Description of <u>Agenor Linea</u> Area	151
B. Ternary Diagram Plots and Characteristics of the CDF's	152
C. Lengthwise Compositional Variation Map of <u>Agenor Linea</u>	160
D. Bright Spots in <u>Agenor Linea</u>	171

<u>Section</u>	<u>Page</u>
VI. A SATELLITE-WIDE SURFACE MODEL FOR EUROPA	182
A. Overview	182
B. Aspects of Water Plumes and Water Volcanism	183
1. Identifying Eruption Sites	183
2. Origin of Mottled Terrain	184
a. Lack of Craters/Palimpsests	184
b. Role of Water Volcanism	186
c. Effect of Degradative Mechanisms	187
C. Life Cycle of a Dark Lineation	189
D. Large-Scale Resurfacing	191
E. Availability of Liquid Water	195
VII. SUMMARY AND CONCLUSIONS	198
REFERENCES	205
APPENDICES	217

LIST OF FIGURES

<u>Figure</u>	<u>Page</u>
1. Spectral Response Curves for Voyager TV Cameras	42
2. Color Ratio Images of Europa's Southern Hemisphere	46
3. The Reference Ternary Diagram	59
4. Methodology for Constructing a CDF Polygon	60
5. Base Map of the Dark Lineation Study Area	71
6. Rel% Cumulative Point Count Ternary Diagram	76
7. Weak Cluster Within the Rel% Cumulative Point Count Ternary Diagram	77
8. Dark Lineation Spectral Classification Map	95
9. Dark Lineation Local Brightness Classification Map	96
10. Dark Lineation CDF Area Classification Map	97
11. Dark Lineation Degree-of-Data-Point-Dispersion-in-CDF Classi- fication Map	98
12. Data Point Sampling Locations for Plains in the Dark Linea- tion Study Area	100
13. CDF Polygon Daisy-Chain Diagrams	102
14. Map of DL121 and Intersecting Dark Lineations	135
15. Map of DL77/DL78 and Surrounding Dark Lineations	140
16. Color Ratio Composite Image of Europa's Southern Hemisphere .	144
17. Color Ratio Composite Image of the Dark Lineation Study Area.	145
18. Map of <u>Agenor Linea</u> and Surrounding Features	154
19. Data Point Sampling Locations for Plains in the <u>Agenor Linea</u> Study Area	155
20. Lengthwise Compositional Variation Map of <u>Agenor Linea</u> . . .	161
21. Keys to the Lengthwise Compositional Variation Map of <u>Agenor</u> <u>Linea</u>	168
22. Pixel Maps of the Bright Spots in <u>Agenor Linea</u>	173
23. Life Cycle of a Dark Lineation	190
24. Short Dark Lineation Map	193

LIST OF TABLES

<u>Table</u>	<u>Page</u>
1. Key to Dark Lineation Characteristic Classifications	80
2. Dark Lineation Characteristic Classifications	81
3. Physical Meaning of Dark Lineation Characteristics	91
4. Relationship Matrix for Dark Lineation Characteristic Pairs	93
5. Averaged Relationship Matrix for Dark Lineation Characteristic Pairs	94
6. The Average Dark Lineation	110
7. Positive and Negative Relationships for Dark Lineation Characteristic Pairs	113
8. Averaged Relationship Matrices for Dark Lineation Data Point Number, CDF Area, and CDF Point Density	115
9. Positive and Negative Pair Relationships for Dark Lineation Data Point Number, CDF Area, and CDF Point Density	116/117
10. Dark Lineations of Special Interest	126
11. <u>Agenor Linea</u> , FDP, AL Plains, and DL Plains Characteristic Classifications	157

LIST OF APPENDICES

<u>Appendix</u>	<u>Page</u>
A. Multispectral Ternary Diagram Plots for Dark Lineation Segments .	217
B. Color Distribution Field (CDF) Polygons for Plotted Dark Lineation Segments	315
C. Multispectral Ternary Diagram Plots for Plains in the Dark Lineation and <u>Agenor Linea</u> Study Areas	350
D. Multispectral Ternary Diagram Plots for Segments of <u>Agenor Linea</u> .	352
E. Multispectral Ternary Diagram Plots for Flanking Dark Patches (FDP's) of <u>Agenor Linea</u>	355

INTRODUCTION

EARLY RESEARCH

Europa, along with Io, Ganymede, and Callisto, was discovered by the Italian scientist Galileo in 1610 in one of the first applications of the telescope. For this reason, they are commonly referred to as the Galilean satellites of Jupiter. These satellites remained visible only as pinpoints of light through even the most powerful telescopes for hundreds of years; indeed, only disc-integrated measurements could be made until the 1970's. Research on the Galilean satellites for the first three centuries following their discovery was restricted to refining descriptions of the orbital characteristics of each body.

Europa is the smallest of the Galilean satellites, with the most recent estimate placing its diameter at 3130 ± 30 kilometers (Smith et al., 1979a). Its bulk density is believed to be approximately 3.03 g/cm^3 . The four Galilean satellites were generally studied as a group in Earth-based research, so that the properties of each could be compared to the others.

The first significant research on the characteristics of the Galilean satellites themselves was published by Stebbins (1927) and Stebbins and Jacobsen (1928); these works were refined and added to by Harris (1961). Their efforts concentrated on photometric measurements of each satellite's magnitude as a function of solar phase angle (i.e., the Sun-satellite-Earth angle) and orbital phase angle (i.e., particular longitudinal area of the satellite visible from Earth). The dis-

coveries reported in these works were that the Galilean satellites: (1) are in synchronous rotation about Jupiter (i.e., the periods of the satellites' lightcurves and their revolutions about Jupiter are identical); (2) all show spectral variations with orbital phase; and (3) all possess low reflectances in blue and ultraviolet wavelengths, particularly Io. The synchronous rotations about Jupiter mean that the Galilean satellites are tidally coupled to Jupiter in their orbits; this is the lowest energy state a satellite can possess.

The near-infrared part of the spectrum ($\approx 1.0\text{-}2.5\mu\text{m}$) is most useful for identifying specific minerals and ices composing satellite surfaces. An excellent overview of the physical principles underlying such spectrophotometry and a history of efforts through the mid-1970's are found in Johnson and Pilcher (1977). Two types of transitions occurring in materials are responsible for spectral absorptions. Crystal field transitions, the most useful for specific identifications, are characteristic of materials containing Fe^{2+} and Ti^{3+} . This allows for the identification of feldspar, pyroxene, and olivine, all of which produce absorption features near $1.0\mu\text{m}$. Charge transfer transitions are not quite as useful as crystal field transitions, but still produce absorption features in the blue and ultraviolet due to silicate minerals. Additionally, ices and frosts produce multiple narrow absorption features in the near-infrared that are generally easier to identify than those of silicate minerals.

Early studies of Europa and the other Galilean satellites fell

mainly into the categories of photometry and spectrophotometry. Research conducted in the 1950's and early 1960's suffered from low spectral resolution and low signal-to-noise ratios in the data. This prevented the positive identification of any specific surface materials on the bodies. Among the first near-infrared studies of the Galilean satellites were those by Kuiper (1957), Owen (1965), and Moroz (1965). These were in general agreement that the overall shape of the spectral reflectance curves and the spectral albedos supported the contention that the surfaces of Europa and Ganymede were covered with water snow or ice.

Beginning in the 1960's, detector technology was sufficiently developed to permit the Galilean satellites to be studied via the techniques of infrared radiometry and optical polarimetry. The first serious attempts to model the internal and surface properties of these bodies also were undertaken at this time. In the early 1970's, studies of laboratory analogs of potential surface materials of the Galilean satellites were begun. Observations of occultations of Europa by Io were first carried out in the early 1970's. By the mid-1970's, radar technology became advanced enough to send radar signals to the Galilean satellites and receive the reflections back on Earth. The first spacecraft flybys of the Jovian system by Pioneers 10 and 11 in the mid-1970's returned very low-resolution images of the Galilean satellites, but truly spectacular and important images of Europa and the other Galilean satellites were returned by the Voyager 1 and 2 spacecraft

during their Jupiter flybys in 1979. Each of these fields of study will be briefly reviewed before presenting a more detailed account of the history of spectrophotometric and Voyager image-studies of Europa, which are the areas of study most closely related to this thesis.

RADIOMETRY

Radiometry measures solar energy that is absorbed by the surface of a body such as Europa and reradiated at longer wavelengths. Thermal infrared wavelengths have received the most attention in radiometric studies of the Galilean satellites, with microwave wavelengths having gotten somewhat less attention. The first radiometric measurement of Europa was at $10\mu\text{m}$ by Low (1965), however, his and other very early research suffered from large uncertainties in radiometric flux calibrations and estimates of satellite radii which are needed to calculate radiometric brightness temperatures. Determining the brightness temperature of Europa indicates some things about the thermal properties of the surface material, such as composition, porosity, etc. In addition to direct measurements of disc-integrated radiometric brightness temperatures of Europa (e.g., Gillet et al., 1970; Morrison et al., 1972; Hansen, 1976), useful information has been obtained by measuring how fast temperatures increase after Europa emerges from Jupiter's eclipse shadow (e.g., Hansen, 1973; and Morrison and Cruikshank, 1973). An excellent overview of radiometry of the Galilean satellites and other solar system bodies is found in Morrison (1977).

Optical polarimetry of a solid body with a negligible atmosphere (which each of the Galilean satellites is) measures the type of polarization (i.e., negative or positive) of scattered, reflected sunlight from the body's surface and the amount of partial linear polarization of that reflected sunlight. The terminology and principles of polarimetry, as well as a summary of research conducted on the Galilean satellites and other bodies through the mid-1970's is contained in a review paper by Veverka (1977). Polarization measurements can be used to derive information on surface texture and opacity of surface materials, but not specific compositional identifications. Results of polarization studies in unfiltered white light by Veverka (1971), at $0.55\mu\text{m}$ by Gradie and Zellner (1973), and at $0.5\mu\text{m}$ by Dolfus (1975) have led to the belief that the surfaces of Europa and Ganymede are covered by a low opacity material or materials, probably consisting dominantly of water frost. Also, Europa shows little variation in the amount of polarization with orbital phase (i.e., longitude).

Radar studies consist of the impressive feat of striking Europa and the other Galilean satellites with radar signals transmitted from Earth and receiving the reflected waves with radio telescopes. The first successful radar observations of the icy Galilean satellites (i.e., Europa, Ganymede, and Callisto) made at 12.6 cm made the startling discovery that the reflected waves were circularly polarized in the same sense as the transmitted signal (Campbell et al., 1978). This is exactly the opposite of the sense of polarization of radio waves

reflected from the terrestrial planets. It was also found that the icy Galilean satellites have very large radar geometric albedos, with Europa possessing the largest. These unusual properties are partially due to the presence of water ice and/or frost on the surfaces of these objects, but the problem of the circular polarization inversion in the reflected waves remains. Ostro and Pettengill (1978) suggested that if the reflections are surface reflections, the circular polarization inversion could best be explained by the presence of nearly perfectly hemispherical, smooth-walled craters on the surface, a highly unlikely situation. Later models that seem more reasonable were based on the assumption of reflections from subsurface satellite regions. Goldstein and Green (1980) modeled the circular polarization inversion employing a regolith model wherein the upper few meters of each icy satellite surface is composed of an array of randomly oriented, faceted icy boulders. More recent radar observations at 12.6 cm (Ostro et al., 1980) and at 70 cm (DePater et al., 1984) have shown that Europa possesses a much lower radar albedo at 70 cm than at 12.6 cm. This has led to a regolith model for Europa of a regolith containing flat, randomly oriented veins about 10 cm thick of a slightly lower refractive index than the surrounding regolithic material (see Ostro (1982) for a more detailed explanation of this model and a review of the history of radar studies of the icy Galilean satellites).

THEORETICAL STUDIES

Efforts to develop theories and successful models of Europa and the other icy Galilean satellites have paralleled and complemented the various types of observations that have been made. Theoretical work can be divided into several categories. Early research, at a time when very little reliable data was available for the Galilean satellites, focused on potential satellite surface compositions, particularly volatiles. Significant work in this area was performed by Miller (1961), Watson *et al.* (1963), and Lebofsky (1975). Although water ice was positively identified by Pilcher *et al.* (1972) and remains the only known volatile on the surface of the Galilean satellites, it has been pointed out that the strong absorption bands of water ice could mask the presence of smaller amounts of other volatiles such as CH₄ and NH₃ ices in infrared spectra (Gehrels, 1977). Smythe (1975) also reported that CH₄ and CO₂ gas hydrates could be stable as solids in the temperature regime of the outer solar system and have spectra similar to H₂O frost, thus making their identification by remote sensing difficult. Some effort has gone into the prediction and search for atmospheres on Europa and Ganymede, as by Gross (1974), but the Voyager flybys of 1979 have proven that atmospheres around these bodies are nonexistent or negligible.

A considerable amount of work has been done on structural/thermal history models of the interior of Europa. Work by Lewis (1971), and Consolmagno and Lewis (1976,1977,1978) modeled Europa and the other icy

Galilean satellites as having accreted from the solar nebula in the vicinity of Jupiter, being composed of a mixture of volatiles (assumed to be primarily water) and silicates. Radioactive elements then began heating each body as they decayed, leading to each satellite differentiating into a body with a dense core containing the radioactive elements, a possibly liquid water mantle, and a relatively pure water ice crust. Fanale et al. (1977) modeled Europa as having formed a core with a 1450 km radius, a liquid mantle 75 to 100 kilometers thick, and a crust 40 kilometers thick. The question of whether Europa's mantle is presently composed of liquid water or ice is of paramount importance in light of current speculation that Europa's surface has been continually resurfaced. This speculation is based on the extreme lack of craters on Europa's surface (Smith et al., 1979b). Research has looked at solid-state convection, liquid convection, and conduction as modes of heat transport from the core outwards. Cassen et al., (1979) and their later revision in Cassen et al., (1980) evaluated heating produced by Jovian tidal force dissipation in addition to internal heat transport and found that even under these circumstances, it is not likely that Europa's mantle is still liquid water. There is enough uncertainty in the assumed values of the parameters involved, however, to say that the present state of the mantle is still an open question.

Ransford et al. (1981) and Finnerty et al. (1981) took a different approach in modeling Europa's thermal history. Assuming that Europa formed from a mixture of water and chondritic material, the petro-

logical sequence arising from its thermal evolution could have formed hydrated silicates (especially chlorite and/or serpentine, and brucite) that would have locked up nearly all of Europa's water. This would have prevented formation of either a liquid or ice mantle, and would have limited Europa's water ice crust to perhaps only a few kilometers. Knowing Europa's bulk density to be approximately 3.03g/cm^3 gives confidence to the estimated thinness of the ice crust after the formation of hydrated silicates, if the other assumptions of the hypothesis are correct.

The hydrated silicate model also provides for a hypothesis of the origin of the network of dark lineations on Europa that are believed to be fractures. Finnerty et al. (1981) proposed that dehydration of hydrated silicates deep within Europa created significant positive volume changes which relayed stress to the overlying crust, ultimately causing fracturing on the surface. The fractures were then filled with xenolith-laden fluid (the water having come from the hydrated silicate dehydration) from depth via a mechanism analogous to CO_2 -driven kimberlite eruptions on Earth. As the xenolithic material would have been darker than the surrounding plains material on Europa's surface, dark lineations would result. The bright medial stripe seen in some dark lineations (forming so-called triple bands) is modeled by Finnerty et al. (1981) as having originated by a second episode of eruption of purer water in the center of the dark lineation.

An alternative model for the origin of dark lineations on Europa

is that of fracturing in response to tidal distortion arising from interactions with Jupiter's massive gravitational field (Helfenstein and Parmentier, 1980,1983; Helfenstein, 1982, 1983). Such interactions could have resulted from orbital recession and orbital eccentricity of Europa, as well as planetary volume changes (not necessarily due to dehydration of hydrated silicates). Helfenstein and Parmentier (1983) presented an extensive study of orientations and distribution of dark lineations, triple bands, and cusped ridges on Europa and compared them to those predicted by theory for tidal distortion. Their results showed good agreement, and the tidal distortion model is generally favored over the hydrated silicate model of Finnerty et al. (1981).

Viscous Relaxation

Viscous relaxation of surface topography on icy bodies has been theoretically studied in earnest since the early 1970's, with work done by Johnson and McGetchin (1973) being an important early example. Viscous relaxation could be an important mechanism on the surface of Europa and could help explain the lack of topographic relief there. The main acting mechanism in viscous relaxation of ice is creep deformation. This action will cause ice topography to become level in a geologically brief period of time. Johnson and McGetchin (1973) found that viscous relaxation of an essentially pure ice surface will rapidly reduce topography if the scale of the topographic feature is less than the thickness of the ice layer the feature is embedded in. Complete

relaxation could take place in as few as 10^6 years, or even less.

Ion Erosion

All of the Galilean satellites are within Jupiter's very intense magnetosphere. Europa is exposed to the most intense fluxes of ions and electrons of the icy Galilean satellites. Great interest developed in the interaction of Jovian magnetospheric ions with Europa's surface after laboratory experiments revealed that MeV light ions impacting thin ice films caused many times more molecules to be ejected than corresponding ions impacting metal surfaces (Brown et al., 1978, 1980). This ice sputtering or ion erosion was immediately recognized as a potentially major surficial modification process on Europa (Haff and Watson, 1979; Johnson et al., 1981), because laboratory results implied that ion erosion of satellite surface ice would occur at a rate many times greater than that for silicate minerals. Calculations by Johnson et al. (1981) determined that if there has been no significant atmosphere or magnetic field around Europa in the past, ion erosion could have removed up to 100 meters of ice per billion years from the surface of Europa. The discovery of active volcanoes on Io by Voyager 1 (Morabito et al., 1979) and the discovery of SO_2 on the surface of Europa (Lane et al., 1981) led to a theoretical evaluation of the effects of Io ejecta (i.e., sulfur ions) on the surface of Europa by Eviatar et al. (1981). Their work showed that, in order for SO_2 to be present in sufficient quantities on the surface of Europa to be spectroscopically detected as it

was, the capture and residence times of implanted sulfur ions must have been such that only two meters of ice could have been eroded on Europa's surface over its entire 4.5 billion year history, in direct contradiction to the results of Johnson et al. (1981).

In addition to the works cited above, a thorough paper by Wolff and Mendis (1983) combined a review of previous Galilean satellite research with new evaluations of the effects of possible Galilean satellite atmospheres and magnetic fields on ion erosion, as well as comparing ion erosion with competing candidates for surface modification of these bodies.

MUTUAL OCCULTATIONS

When the orbital planes of the Galilean satellites intersect the Earth, it is possible to observe the satellites occult each other. In 1973, many scientists made telescopic observations of multiple occultations of Europa by Io (Murphy and Aksnes, 1973; Blanco and Catalano, 1974; Aksnes and Franklin, 1975a; and Greene et al., 1975). Each of these works reported finding a bright north polar cap on Europa, with less evidence for a bright south polar cap. A later re-evaluation of theoretical considerations by Aksnes and Franklin (1975b), however, nullified the claims of bright polar caps. The change of interpretation was based on a decision to favor de Sitter's theory of the orbital motions of the Galilean satellites over the theory of Sampson which had been used earlier. Changes in the relative positions of, and distances

between, Io and Europa resulted. The conclusion reached was that, at best, Europa possessed poles slightly brighter than the rest of its surface. Slightly bright poles were in fact confirmed by images of Europa returned by the Voyager 1 spacecraft (Smith et al., 1979a).

IMAGERY AND ENSUING STUDIES

Even today, the Galilean satellites can be seen from the Earth only as points of light except through the best telescopes under ideal viewing conditions. Some efforts have been made to create maps of surface features (i.e., albedo markings) of Europa from Earth-based telescopes (Murray, 1975; Greene et al., 1975), but resolution has been on the order of hundreds of kilometers. The Pioneer 10 and 11 spacecraft returned images of Europa with slightly better resolution in the early 1970's.

A truly quantum leap in quality and resolution of Europa imaging was achieved with the flybys of the Voyager 1 and 2 spacecraft in 1979 (Smith et al., 1979a,b). Detailed descriptions of the Voyager television cameras (one wide-angle and one narrow-angle camera) and their color filter suites are found in Smith et al. (1977) (see also the section of this thesis entitled Description of Data and Data Processing), while Danielson et al. (1981) described the actual calibration data for the cameras plus summaries of their photometric and radiometric performance in flight.

Voyager 1 returned digital images of Europa with a best resolution

of about 33 km per pair of image lines, while Voyager 2 returned images of some portions of Europa with a resolution of 4 km per line pair (Smith et al., 1979b). The high resolution images show that at least part of Europa is covered with a network of dark lineations embedded in a brighter plains unit, with large areas of mottled terrain that appear to be similar in color to the dark lineations. The plains unit and darker mottled terrain unit are the two major terrain units recognized on Europa, yet the degree of contrast between them is quite small. The dark lineations have two known structural variations -- those that are uniformly dark throughout and those that possess a medial white stripe (forming so-called triple band structures). In addition to the features described above, Voyager images revealed bright ridges on Europa, some of which are quasi-linear and some of which have taken on a strange repeating cusped form.

Perhaps the most notable revelation about the surface of Europa made by Voyager was the finding of an extreme lack of craters. Lucchitta and Soderblom (1982) positively identified only five sharp-rimmed, bowl-shaped craters, with a handful of other candidates for more subdued craters and palimpsests (non-topographic remnants of craters after complete viscous relaxation, visible as bright or dark discolorations of the surface). Such a lack of craters on Europa is not consistent with the cratering records of Ganymede and Callisto. The most reasonable explanation of this discrepancy is that Europa's surface has been resurfaced until at least several hundred million years ago, and this is

possibly still an active process today. Viscous relaxation is an alternate possibility, but the number of expected palimpsests is missing. Ion erosion also is a possibility for elimination of craters, but the rate of erosion over geologic time is the subject of controversy (see page 11). Resurfacing on Europa, if it exists, is believed to be in the form of water volcanism, which could be expressed as frost-vapor eruption plumes analogous to the spectacular sulfur eruption plumes on Io. Helfenstein and Cook (1984) studied a transient bright feature on two Voyager 2 images and concluded that, although less bright and less well defined than eruptive plumes on Io, it fit the characteristics of a water vapor-frost plume better than the characteristics of icy materials under differing photometric conditions.

The dark lineations on Europa have received more attention than any other type of feature on the satellite. It should be pointed out that the dark lineations are essentially albedo markings, with little or no topographic relief (Smith et al., 1979b). Many of the major dark lineations also form great circles or small circles on the body. Several distinct types of lineations are present. Pieri (1981) devised a classification system with eight classes of lineations based on morphology, brightness, and orientation. His study also examined the properties of polygons formed by the intersection of lineations and compared them with polygons of intersecting lineations formed by different geologic processes on Earth. Lucchitta et al. (1981) adopted a simpler lineation classification system with four divisions based on

morphology and spectral properties. Rose diagrams were also employed to analyze lineation trends in a search for structural patterns diagnostic of specific geologic processes. Results of their work agreed with the basic premise of Helfenstein and Parmentier (1980) that lineation patterns around the anti-Jovian point on Europa support an origin of fracturing due to tidal deformation, but added that variations of structural forms may well be due to internal forces.

Evidence of both extension and compression on Europa is present in the dark lineations and quasi-linear/cuspate ridges, respectively (Malin, 1980). Schenk and Seyfert (1980) pointed out a lateral displacement, associated with a dark lineation, and a white line (bright lineation) at a location consistent with the area comprising an icy plate that has undergone a limited amount of plate tectonic activity. This is supported by the belief that white lines are icy ridges under lighting conditions that do not allow shadow formation. If so, the white line icy ridge would be the compressional counterpart of the extensional feature present at the lateral displacement location. It should be noted that there are very few examples of this type of displacement on Europa (although it should also be noted that a relatively small percentage of Europa's surface was imaged at a sufficient resolution to show displacements along dark lineations). Present evidence indicates that there has been very little plate tectonic activity on Europa, both in terms of numbers of locations of motion and amount of motion, if indeed there has been any plate motion at all.

LABORATORY ANALOGS

In order for spectrophotometric curves of Europa and other solar system objects to be interpretable, it is necessary to have laboratory measurements taken under similar physical and photometric conditions in order to identify mineral constituents present on satellite surfaces. This is an exceedingly difficult task. Not only are there problems with developing infrared detectors with sufficient sensitivity to find narrow absorption features of some minerals, but very opaque substances like carbonaceous material (a very common solar system material) can suppress absorption features (Johnson and Fanale, 1973), as can vitrification.

Most laboratory spectral measurements made directly for the purpose of comparison with spectra of the icy Galilean satellites have been made of candidate ices and frosts. Water ice and frost have received the most attention (Kieffer and Smythe, 1974; Fink and Larson, 1975; Clark, 1981b). Temperature dependence of water ice reflection spectra was reported by Fink and Larson (1975), particularly important being a significant intensity change at $1.65\mu\text{m}$. This wavelength was thus believed to be useful for determining ice temperatures on Europa and other icy bodies. Later work by Clark (1981b) showed that the $1.65\mu\text{m}$ feature is in fact ice grain-size dependent and not a good tool for temperature determination. Another study of interest was of reflectance spectra of CH_4 and CO_2 gas hydrates from 1 to $6\mu\text{m}$ by Smythe (1975). The significant finding was that clathrates and gas hydrates can have

spectra similar to water frost, making their detection on solar system objects by remote sensing very difficult.

Many studies of mineral reflectance spectra have been carried out in investigations not directly intended for application to icy solar system bodies. Some of this work has been useful for comparisons with outer solar system spectra. More useful are reflectance spectra of mixtures of water ice and mineral grains, which are believed to more closely approximate the actual surface composition of the icy Galilean satellites. The best published results of this type of laboratory work is by Clark (1981a), where reflectance spectra were presented in the 0.325-2.5 μ m wavelength region for bound water, water-mineral mixtures, mineral grains on frost, and frost on minerals at low temperatures. Minerals used were montmorillonite, kaolinite, beryl, Mauna Kea red cinder, and black charcoal.

SPECTROPHOTOMETRIC STUDIES SINCE 1965

By the late 1960's, visible and infrared detectors had become sensitive enough to permit the first detailed spectral reflectance curves of Europa and the other Galilean satellites. Johnson and McCord (1970, 1971) investigated Galilean satellite brightness dependence on orbital and solar phase angle and their spectral geometric albedos at wavelengths ranging from 0.30-2.5 μ m. Similar studies were conducted by Johnson (1971), Wamsteker (1972), and Lee (1972). As much as the quality and resolution of spectral reflectance measurements had improved by

this time, uncertainties in the diameters of the icy Galilean satellites made determinations of their geometric albedos similarly uncertain. Still, these investigations clearly showed spectral differences between all of the Galilean satellites, variations of each satellite's spectral reflectivity with orbital phase angle and variation of each satellite's spectral reflectivity with wavelength.

A major step forward in the remote sensing of the Galilean satellites was the positive identification of water frost in infrared spectra of Europa, Ganymede, and Calisto, first reported by Pilcher et al. (1972) and later confirmed by Fink et al. (1973). Europa showed the deepest frost absorptions and was interpreted to have 50 to 100 percent of its surface covered by water frost, much more than Ganymede or Calisto. It was also found that the non-frost materials on the icy Galilean satellites display increases of albedo with increasing wavelength, consistent with a silicate composition.

In this same general period of time, additional photometric and spectrophotometric Galilean satellite work was carried out by Owen and Lazor (1973), Morrison et al. (1974), Hansen (1975), and Millis and Thompson (1975). Results tended to confirm previous works while supplementing them with additional measurements of rotation curves and albedos at various wavelengths. It was also found that the leading hemisphere (i.e., the side of a satellite facing forward relative to its direction of orbital motion) and trailing hemisphere (the exact opposite of the leading hemisphere) of Europa and each of the other Galilean

satellites display different albedo and spectral properties. The leading hemisphere of Europa was found to be brighter than its trailing hemisphere. Caldwell (1975) presented ultraviolet observation data from an Earth-orbiting spacecraft showing that the trend of decreasing spectral reflectivity with decreasing wavelength that Europa displays beginning at about $0.55\mu\text{m}$ continues to at least $0.21\mu\text{m}$.

Spectrophotometric studies of the Galilean satellites of yet higher spectral resolution were conducted by Nelson and Hapke (1978), Pollack et al. (1978), Clark and McCord (1980), and McFadden et al. (1981). The increased spectral resolution is evident by considering that the spectral survey of Johnson and McCord (1971) had a resolution of $0.05\mu\text{m}$, while the measurements of Nelson and Hapke (1978) had a resolution of $0.004\mu\text{m}$, an improvement of more than an order of magnitude. With the improvement in resolution came several new discoveries. Pollack et al. (1978) pointed out that strong spectral absorption bands on the trailing side of Europa may be broadened by the effects of magnetospheric particle bombardment of the surface there, and that this mechanism may explain the difference in spectral appearance of the two sides of Europa. Clark and McCord (1980) were the first to report absorption features at 1.25, 1.06, 0.90, and $0.81\mu\text{m}$ in spectra of Europa. They also determined that water ice absorptions for Europa, Ganymede, and Callisto are caused by free water and not bound water or water absorbed onto minerals. Areal coverage of water frost was reported to be at or near 100% for the trailing side of Europa, while Pollack et al. (1978)

reported frost coverage of greater than or equal to 85% for Europa's leading side.

Clark (1980) performed a detailed analysis of the high resolution IR reflectance spectra of McFadden et al. (1981) and Clark and McCord (1980), comparing them with laboratory spectral work that later appeared in Clark (1981a,b). Conclusions of important relevance to Europa were: (1) spectra indicate Europa's surface is covered with ice blocks or ice crystals larger than or equal to one centimeter, or frost on ice; (2) non-water materials on Europa are not in spectrally isolated patches but apparently occur as mineral grains intimately mixed with water; and (3) the non-water grains (which only constitute a few percent of Europa's surface material) appear to be composed of minerals containing Fe^{3+} , possibly carbonaceous chondrite material. A new, unknown absorption feature at $1.15\mu m$ was tentatively identified in Europa's spectra.

After the remarkable image and data return on the Galilean satellites and Jupiter from the Voyager 1 and 2 spacecraft in 1979, emphasis shifted from Earth-based telescopic studies to multispectral processing of global and high resolution Voyager images of Europa, and comparisons of telescopic data with Europa images. One important discovery reported by Lane et al. (1981) was made by the Earth-orbiting International Ultraviolet Explorer (IUE) spacecraft. The IUE found a spectral absorption feature in the ultraviolet at $0.28\mu m$ which was due to SO_2 on the surface of Europa. The greatest concentration of this SO_2 was determined to occur on Europa's trailing hemisphere (central longitude

270°). The favored explanation of this was that sulfur originally present in Io eruption plumes became ionized and was incorporated into the Jovian magnetosphere, from whence it impacted Europa's surface and became injected into surficial ice, forming SO₂.

Global multispectral images of Europa, Ganymede, and Callisto, from Voyager 1 and 2 have been computer-processed (in a manner similar to that described on page 31 of this thesis) in order to extract spectrophotometric data from them. Images used were taken at wavelengths of 0.35μm (UV), 0.41μm (violet), 0.48μm (blue), and 0.59μm (orange). The global multispectral mosaic constructed for Europa was computer-processed in a variety of ways, the most important being the generation of color ratio images (see page 31 for definition). Results, first reported by McCord et al. (1982), defined four distinct color/albedo units on Europa. Two of these spectral units were found to be on the leading hemisphere and two on the trailing hemisphere. Data was consistent with the conclusion that the two spectral units (light and dark) on the trailing side were the analogs of the two units on the leading side except for the presence of additional ultraviolet-absorbing material on the trailing side. This was a very important conclusion because it supported the contention of Lane et al. (1981) that sulfur ions from Io ejecta were implanted in the ice of Europa's trailing side. Johnson et al. (1983) published global multispectral mosaics of all three icy Galilean satellites that were processed identically so that they could be directly compared to one another. The findings of McCord et al.

(1982) were verified. The additional finding was presented that the brightest spectral unit on all of the icy Galilean satellites is the plains unit on Europa (bright craters on Ganymede are of about equal brightness), consistent with high albedo measurements of Europa made from Earth.

Burrati and Veverka (1983) used Voyager images with phase angles ranging from 3° to 143° to derive photometric data on Europa. They found that Europa's plains unit photometrically displays more homogeneity than the other major terrain unit, the darker mottled terrain. The scattering properties of the units could not be reasonably described by a lunar-like photometric law, but it was found that a lunar-like law with the addition of a Lambert component provided a much better, albeit still simplistic, photometric law for Europa.

Further information on the history and principles of Galilean satellite spectrophotometry and photometry can be found in comprehensive review papers by Morrison and Morrison (1977) for photometry, and Johnson and Pilcher (1977) and Sill and Clark (1982) for spectrophotometry.

STATEMENT OF OBJECTIVES

The objectives of this thesis entail multispectral and geomorphic studies of Voyager 2 images of Europa in order to describe and classify surface features, and, hopefully, draw some conclusions about surface processes on Europa and the evolution of the satellite. Specific goals are assigned to two areas on Europa covered by high resolution Voyager 2 images: (1) a 200 pixel by 225 pixel block covering an area from approximately 220° to 180° Longitude and -24° to -2° Latitude, and containing among the highest density of dark lineations on the satellite; and (2) the major white line feature Agenor Linea, covering an area ranging from approximately 220° to 178° Longitude and -44° to -41.5° Latitude, and its immediate surroundings. The primary objective for the dark lineation region is to develop classification systems for the dark lineations based on the characteristics of dark lineation relative spectral reflectance (defined on page 42); local brightness; area covered by plotting data points of relative spectral reflectance, and the associated density of data points in the spectral plot areas; the degree of dispersion/clustering of data points in the spectral plots; and the orientations of the dark lineations on Europa. A further objective for the dark lineations is to correlate the aforementioned characteristic classes with each other in order to identify significant combinations of characteristics present in the dark lineation suite. A third goal is a comparison of the spectral properties of the plains unit

surrounding the dark lineations with the dark lineations and their characteristics. It is hoped that this latter effort will reveal information about the interaction of the plains unit and the dark lineations, and any possible surface processes that may have taken place there.

The objectives for Agenor Linea and its environs include determining the relative spectral reflectance properties of Agenor Linea, its flanking dark spots, and the plains surrounding it. An additional objective for Agenor Linea but not for the dark lineation area is an investigation of the change in relative spectral reflectance/composition along the length of the white line feature. Combining the results of all of these investigations, coupled with a geomorphic evaluation of the Agenor Linea area, has the goal of providing insight into the origins of Agenor Linea (and hence white line features on Europa in general) and any surface processes that may have modified it.

Finally, is the objective of a comparison of the spectral characteristics of the plains in the dark lineation area with the plains surrounding Agenor Linea, for the purpose of partially defining any changes in spectral properties/composition of the plains unit with latitude that may exist on Europa. Comparing the characteristics of the dark lineations with those of Agenor Linea has a similar objective of better defining the similarities and differences between the two types of features. Synthesizing all results obtained for Europa will be attempted in order to draw conclusions about the surface evolution of the satellite as a whole.

DESCRIPTION OF DATA AND DATA PROCESSING

HISTORY OF VOYAGER IMAGERY

The data set used in this study was obtained by the Voyager 2 spacecraft during its flyby of Jupiter and its satellite system in 1979. Voyager 2 flew by Europa at a distance of approximately 204,000 km at its closest approach, allowing for a best resolution of 4.5 km per pair of digital scan lines comprising the image. The camera system consisted of one wide angle and one narrow angle slow scan selenium-sulfur vidicon camera, described in detail in Smith *et al.* (1977). Each camera possessed a suite of color filters, six for the narrow angle and eight for the wide angle. Images were transmitted digitally, each in an 800 x 800 picture element (pixel) format. Each pixel was binary encoded with 8 bits, resulting in a data number (DN) ranging in value from 0 to 255 according to pixel brightness.

The image set actually used in this thesis is Voyager 2 images 1195J2-001 (violet filter), 1198J2-001 (blue filter), 1201J2-001 (orange filter), and 1204J2-001 (ultraviolet filter). These images each cover roughly the same area on Europa, and are among the highest resolution images obtained of Europa. Raw images sent by the spacecraft were digitally recorded on magnetic tape at the Jet Propulsion Laboratory (JPL) in Pasadena, California. From there the tapes were processed at the U.S. Geological Survey's (USGS's) Branch of Astrogeology in Flagstaff, Arizona. The first image processing steps, known as level 1

processing, started with computer removal of reseaus (circular calibration marks etched onto the vidicon faceplate, thus appearing on every image) and replacement of reseau areas with averages of DN's of the surrounding pixels. It was the reseau removal program that failed during image processing at the USGS, necessitating very time-consuming manual correction techniques during the course of this thesis. Other level 1 computer-generated processing steps included corrections for sun angle differences across each image. For the image set studied, a significant portion of the distance from Europa's limb to terminator is covered by each image, so that making a correction wherein each pixel appears as if it were illuminated by the same sun angle becomes very important.

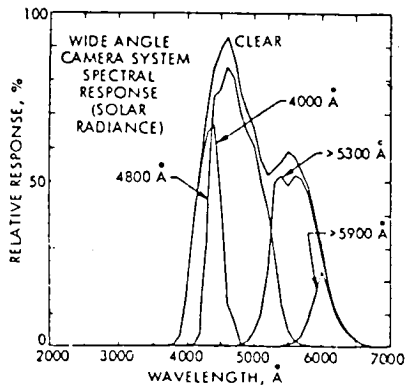
SOURCES OF ERROR AND COMPENSATION TECHNIQUES

In addition to sun angle corrections, several types of geometric corrections were applied to the images studied. Distortion corrections were made to compensate for imperfections inherent in the TV camera design. To derive multispectral data for specific areas on Europa, control points were taken of identical locations on each of the four images of interest and used to create a geometric transformation ("stretch") of three of the images to the perspective of the fourth image. This process, known as image registration, would ideally produce a set of images that could be superimposed on each other so perfectly that specifying the same pixel coordinates in each image would provide four DN values of

the same area on Europa. Unfortunately, the difficulty of taking a sufficient number of control points with uniform distribution over each image and with perfect precision between all four images is, for all practical purposes, impossible. Though the Europa image set was fairly well registered, it was not such that usable multispectral data could be obtained by simply sampling the same pixel coordinates in each image. Manual techniques were developed to provide improved multispectral data extraction from the registered images. These are described later in this section.

The image processing methods described above improved the scientific utility of the Voyager Europa images; however, some errors existed in Voyager imagery for which corrections either were not possible or were not in a sufficient state of development at the time processing was performed at Flagstaff (1980 and 1981) to be used. A fundamental problem that could not be compensated for was the spectral response of the vidicon cameras in the imaging subsystem. Figure 1, from Smith et al. (1977), shows the spectral response curves for each of the two vidicon cameras. Note that camera response in the red portion of the spectrum falls off sharply. This, coupled with the fact that no combination of three of the color filters used in imaging corresponded to the three primary colors, meant that it was not possible to construct a true color composite from the Voyager Europa images. A color composite was constructed substituting the orange-filtered image (1201J2-001) for a red one, the blue-filtered image (1198J2-001) for a green one, and the

(A)



(B)

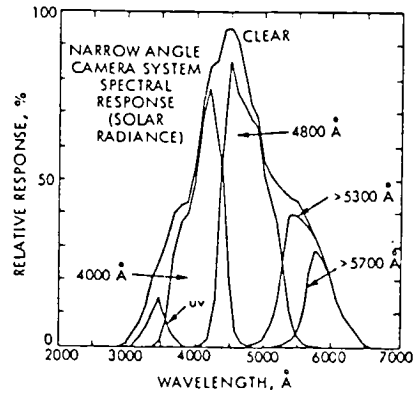


FIGURE 1. Spectral response curves for (A) the Voyager spacecraft wide-angle TV camera and five of its color filters, and (B) the Voyager spacecraft narrow-angle TV camera and six of its color filters. Diagrams are from Smith et al. (1977).

violet-filtered image (1195J2-001) for a blue one. Thus, the colors seen in the composite image do not represent the true colors of Europa, but are fair approximations of them.

A second source of error in Voyager imagery that could not be corrected at the time of Flagstaff processing was the so-called "dark current." Dark current, as it occurred in Europa imaging, was residual or spontaneous charging of Voyager imaging subsystem vidicons that did not represent pictorial data, and was generated by the effects of charged particles in the Jovian magnetosphere in the vicinity of the spacecraft. This charging alters the DN's in the image data, though by relatively minor amounts. Such false data can be most easily seen in color composites as brightly colored intricate patterns where black should be for deep space off the satellite's limb. Although dark current correction factors have subsequently been developed and applied to Voyager imagery (McEwen, personal communication), none were available at the time of USGS image processing in Flagstaff.

Another property of the image data for which no correction factor was available was the photometric function for Europa. Briefly, the photometric function describes how light is scattered by a body's surface, the scattering being a function of phase angle (incident angle plus emission angle of sunlight hitting the surface), properties of the sunlight hitting the surface, and properties of surface texture and composition. The terminology and fundamentals of astronomical photometry are described in detail by Harris (1961) and Veverka (1977). The prob-

blem caused by the photometric effect arises from the fact that the phase angle varies greatly from the limb of the body to its terminator. If not corrected, the photometric effect will cause highly inaccurate brightness measurements across any image that covers a significant portion of the distance from limb to terminator, which the Voyager Europa images used in this study did. A correction factor could have been applied to the images if the photometric function could have been mathematically modeled. Unfortunately, this is no simple task. No photometric correction was applied to this project's images, although at a later time a simple Minnaert law correction was used by Johnson et al. (1983) as a first generation approximation of Europa's photometric function.

The problem of Europa's photometric function was nearly completely circumvented, however, by two conceptually similar techniques. The more standard technique was the construction of color ratio images from the registered images. In this method, one image is divided by another image through the process of dividing each pixel's DN in one image by each corresponding pixel's DN in the second image, creating a third image. The resultant quotients are then each multiplied by a constant to re-establish the dynamic range in the new image. For the registered images of Europa, the following formula was followed:

$$\frac{(\text{UV, VI, or BL})}{\text{OR}} \times 100$$

This produced UV/OR, VI/OR, and BL/OR color ratio images, which are

shown in Figure 2. These images were then combined to produce a color ratio composite image where features appeared in false color perspective. The advantages of generating color ratio images are: (1) the photometric function is virtually eliminated, because the photometric function of the first filtered image is divided by the photometric function of the second filtered image during ratioing; and (2) subtle color variations of the surface are brought out by color ratioing since for any change in gray level to occur from pixel to pixel in the ratio image, there must be an accompanying difference in the relative spectral reflectances between the two filter colors at those points. Concerning the elimination of the photometric function, there could still be a small photometric effect present in the ratio image if the photometric function is wavelength dependent. Detailed modeling of Europa's photometric scattering properties by Buratti and Veverka (1983) did find a wavelength dependence for the albedo of the dark material unit on Europa. The implications of this for multispectral data interpretation are discussed in this thesis in the section beginning on page 129.

The second technique for eliminating Europa's photometric function is the plotting of relative spectral reflectances of three colors on a ternary diagram. As with color ratioing, this method would not eliminate any part of the photometric function that is wavelength dependent. The ternary diagram plotting technique is described in a later section along with the linear feature profiling technique.

(A)

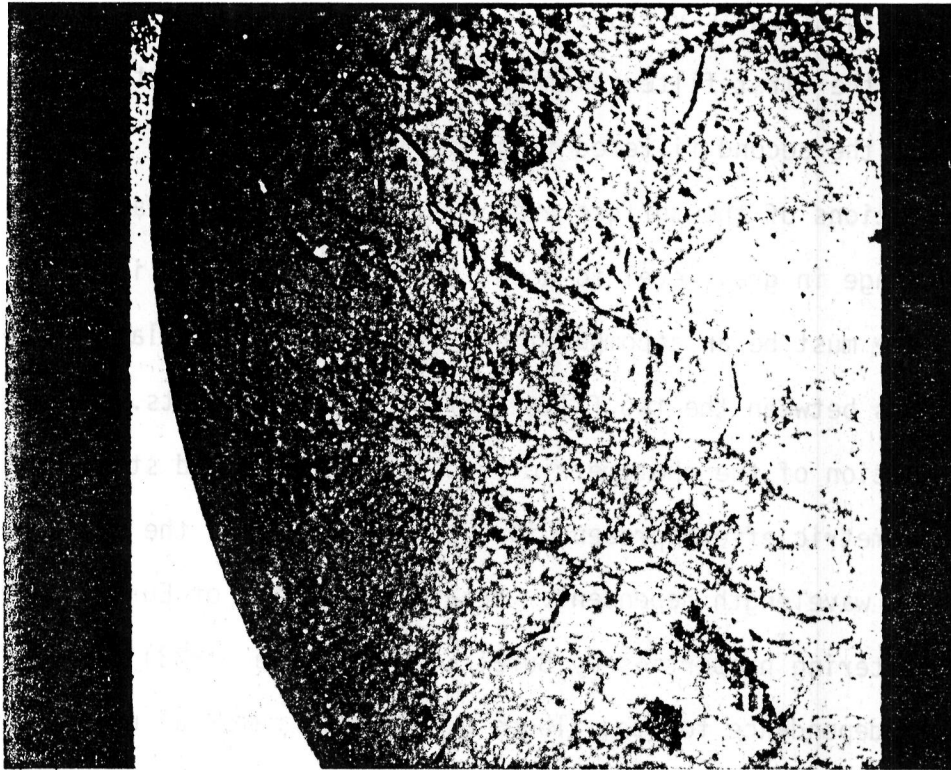


FIGURE 2. Color ratio images of a portion of the southern hemisphere of Europa which includes the dark lineation study area (upper part of each image) and part of the Agenor Linea study area (extreme southern part of each image). Images shown are: (A) ultraviolet/orange ratio image, (B) violet/orange ratio image, and (C) blue/orange ratio image. The image set used to generate the ratio images consists of registered Voyager 2 images 1195J2-001 (violet filter), 1198J2-001 (blue filter), 1201J2-001 (orange filter), and 1204J2-001 (ultraviolet filter).

(B)

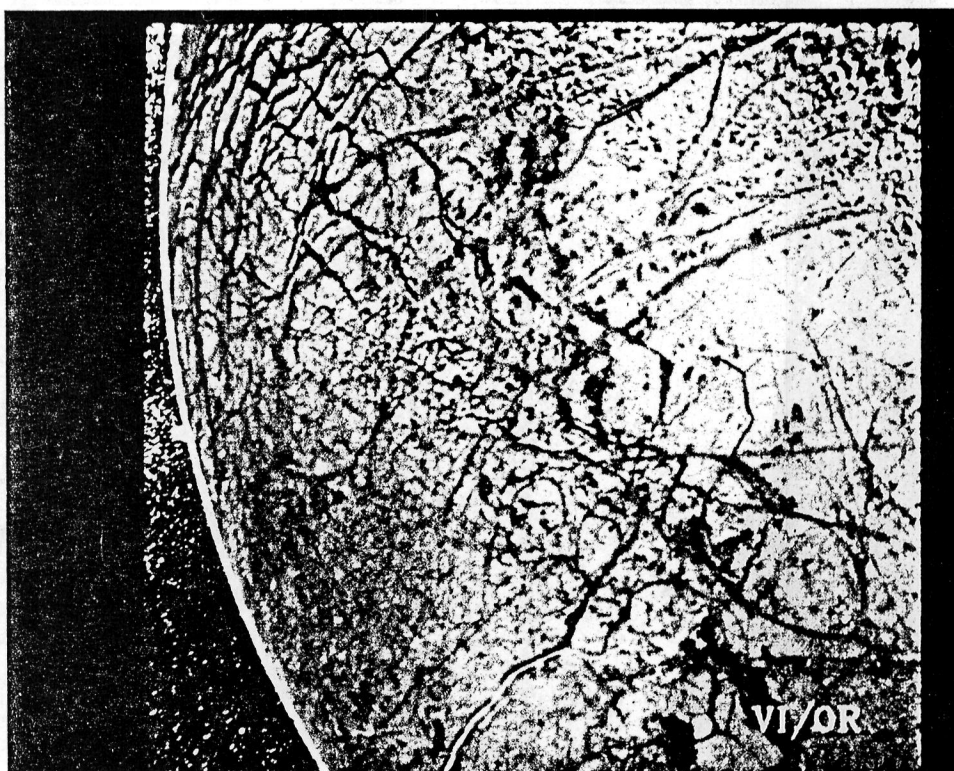


FIGURE 2. (Continued)

(C)

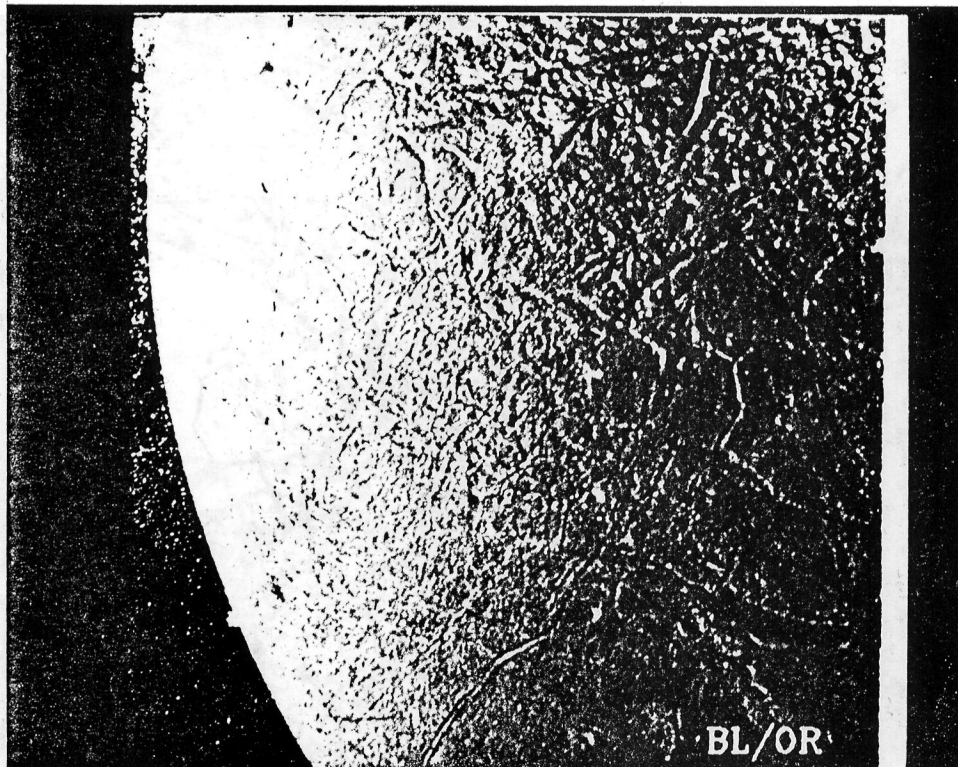


FIGURE 2. (Continued)

IMAGE PROCESSING AT LPI

After completing color ratio constructions at the USGS in Flagstaff, the remainder of Europa image processing was performed at the Lunar and Planetary Institute (LPI) in Houston, Texas. The system used at LPI consisted of a Gould/DeAnza IP8500 Image Processing System interfaced to a DEC VAX 11/780 computer. The system included a video monitor, joystick, controller, hard copy unit, and the LIPS image processing software package.

In addition to the normal color composite and color ratio composite images created at the USGS, computer processing at LPI generated contrast enhanced images, density-sliced images, and parallelepiped classified images. Contrast enhancements enabled sharper differentiation between surface features on Europa, both in individual images and color composites. In density-sliced images, colors are assigned to user-chosen sequences of DN's. The resulting false color image depicts areas of equal brightness as the same color. This method was not found suitable to use on normal images because of the large photometric effect near Europa's limb, where this study concentrated. Density slicing was found useful for better delineating spectral features in color ratio images, however. The parallelepiped classifier is a means for classifying areas of distinct spectral properties by defining DN ranges in each of three colors for three registered images. These three ranges form a solid rectangular box, or parallelepiped, when plotted on a coordinate system of three mutually perpendicular axes. The method

employs the use of training areas, wherein the image composite is displayed on a CRT and a training area is defined, via a joystick. All areas on the image that fall within the same spectral parallelepiped as the training area are then assigned the same color, along with the training area. The classifier program used at LPI, called LSCLAS, is capable of defining up to six training areas, which may or may not replace the entire image with a classified false color image.

Contrast enhancements can be performed without creating erroneous data, as can density slicing, on individual images. When the parallelepiped classifier is performed, however, the final product is misleading. Considering that the classifier is applied to a composite image, it becomes clear that imperfectly registered areas are being classified. For dark lineations on Europa, for example, a problem arises because a strip of misregistered pixels is formed bordering each lineation. Each strip will have a spectral character not representative of dark lineations nor the plains material in which the lineations are embedded. Provided that these areas are ignored, the interiors of the lineations and the plains beyond the misregistered strips should be accurately assigned even though each point is misregistered by a pixel or two. This is based on the assumption that lineation material and plains material do not vary significantly in composition over the distance covered by one or two pixels.

Following the completion of computerized image processing of Voyager Europa images 1195J2-001, 1198J2-001, 1201J2-001, and 1204J2-001, a

portion of the image set was chosen on which to focus studies. The primary area of study chosen was a 200 pixel-by-225 pixel block in the upper left area of the registered images (see Figure 19 and 20). This area corresponds to the approximate coordinates of 220° to 180° Longitude and -24° to -2° Latitude on Europa. The main reason for choosing this area was because it contains one of the highest concentrations of dark lineations per unit pixel area anywhere on the high resolution-imaged portion of Europa. A secondary area of study was the major white line feature on Europa, Agenor Linea, spanning an area from approximately 220° to 178° Longitude and ranging from -44° to -41.5° Latitude.

CORRECTIONS APPLIED AFTER IMAGE PROCESSING

The areas chosen for intensive study were small enough to allow paper printouts to be obtained of pixel DN's for the whole block. Thus, DN listings for the entire 200 pixel-by-225 pixel block were made for the violet-filter image (1195J2-001), the blue-filter image (1198J2-001), and the orange-filter image (1201J2-001). Only three images could be accommodated by the ternary diagram method used later. The ultraviolet-filter image (1204J2-001) was eliminated for this part of the study because surface features on Europa were poorly defined in the ultraviolet (i.e., the range of DN's in the ultraviolet image was much smaller than for the violet, blue, or orange images).

The pixel printouts were photoreduced and mosaicked for the violet, blue, and orange images for the 200 pixel-by-225 pixel block. After

being put into this more manageable form, the pixel mosaics could be used for making detailed surface feature maps. The blue-filter pixel mosaic was used to map Europa's dark lineations because it possessed maximum feature discriminability. Lineations were defined on the basis of sharp contrasts in the pixel DN's marking the boundaries between dark lineations and the relatively bright plains unit surrounding them. Both bold dark lineations and faint dark lineations (i.e., dark lineations differing in pixel brightness from the surrounding plains less than more boldly dark lineations) were mapped, however, no attempt was made to completely map the faint dark lineations. The blue-filter image was frequently referred to as an aid for determining where a specific point on the pixel mosaic was located, but the mapping on the pixel mosaic was done independent of the image. The resulting pixel mosaic map therefore did not perfectly match what was visible in any given print of the image because the extent to which dark lineations are visible in a print depends on the particular contrast enhancement the image underwent before a print was made.

Once the dark lineations were mapped on the blue-filter image pixel mosaic, the map was precisely traced onto the orange-filter and violet-filter pixel mosaics. This preserved the feature misregistration on the orange and violet mosaics, creating slightly inaccurate maps on them. It was therefore not possible to compare DN's of the same location in three colors simply by accessing the same pixel coordinates on each mosaic. Two correction techniques were employed to allow sampling of

multispectral data. The primary technique is ideally suited for use on thin, linear features, which is essentially what Europa's dark lineations are. This consists of taking a series of parallel profiles of a dark lineation, each perpendicular to the trend of the lineation at that location. The DN's are examined along each profile of the dark lineation to identify the darkest DN. (In the case of a bright lineation, such as a white line (e.g., Agenor Linea), each profile is examined to identify the brightest DN.) By identifying the darkest DN in a dark lineation profile, the highest probability is secured of having identified pure dark lineation material, since the darkest DN almost invariably is found at the center of the dark lineation in each profile. Profiles were spaced one pixel apart in order to generate the maximum number of data points. The result was a series of points forming a one-dimensional representation of the lineation. Dark lineations were profiled on all three pixel mosaics so that when the darkest DN of a lineation profile in, say, blue was compared with the darkest DN's from corresponding profiles in violet and orange, it was reasonable to conclude that the three DN values came from the same location on Europa, or at least from very similar material from locations very close to each other.

This profiling method was adequate if the direction of misregistration of the lineation was perpendicular to the trend of the profile. Where this was not the case, an additional correction was applied to compensate for whatever the direction of misregistration was at that location. In this technique, the necessary shifting of pixels is enacted

after the profiling is done, such that all that is needed is to shift the column of recorded darkest DN's appropriately for one color relative to another color. Through the careful application of the two methods of correction just described, the best possible approximation of a perfect registration of features was achieved.

All told, 193 dark lineation segments within the 200 pixel-by-225 pixel block were mapped, profiled, compensated where needed, and recorded in terms of darkest DN's. While this was not all of the dark lineations present in the area by any means, it was a large percentage of them and did provide a good representation of both the bold and faint dark lineations.

PLOTTING THE DATA

At this stage, dark lineation multispectral data had been acquired and listed in the form of DN's that represented spectral reflectance values at violet, blue, and orange wavelengths. It should be remembered that these DN's could not be directly compared to each other in a useful way from one part of the study area to another because they contained large photometric effects, particularly near Europa's limb. The photometric effect expressed itself as brightness differences across the area, with similar features near the limb being much brighter than their counterparts closer to the terminator. To obtain useful data, pixel printouts could have been acquired from color ratio images. Indeed, two-axis plots of color ratio data have been constructed for Europa

by McCord et al. (1982), for Io by Clancy and Danielson (1981), and for the surface of Mars by Guinness (1981), to give just a few examples.

For this thesis, however, a new application was developed of the ternary diagram method of plotting three variables against each other simultaneously. Ternary diagrams have traditionally been used in geology, particularly petrology, and metallurgy, but very little in multispectral studies. The main benefit of using a ternary diagram plot versus the commonly used two-variable plot in multispectral research is the ability to evaluate three variables (colors) simultaneously instead of the two variables (colors) in the rectangular plot. The addition of the third variable, or color, in the ternary diagram enhances spectral discriminability significantly, and its importance should not be underestimated.

The DN's recorded in violet, blue, and orange from profiled dark lineations contained photometric effects, as mentioned previously, and so could not be converted to accurate spectral reflectance values without applying correction factors based on detailed modeling of Europa's photometric function. This problem can be circumvented by plotting relative spectral reflectances rather than the spectral reflectances themselves. To accomplish this, the violet, blue, and orange DN's of each point that was recorded are added. The data is then normalized by dividing each color's DN by the sum of the DN's. Each resulting relative spectral reflectance percentage (abbreviated as rel% throughout this thesis) can not only be plotted on a ternary diagram, but also have

removed all or nearly all of the photometric effect because when a DN is divided by the sum of the DN's, the photometric function effect in the DN is divided by the photometric function effect in the DN sum. A hypothetical example will illustrate this. Say that a point in a dark lineation produced DN values of 120 in orange, 90 in blue, and 70 in violet. Normalizing the orange DN yields: $120/(120 + 90 + 70) = 42.86\%$ relative spectral reflectance. Blue yields 32.14% relative spectral reflectance and violet yields 25.00% relative spectral reflectance. Note that the relative spectral reflectances will always add up to 100%. Now, if photometric effects are responsible for, say, 25% of the DN value for each color, the value for the orange spectral reflectance after removing the photometric contributions becomes: $90/(90 + 67.5 + 52.5) = 42.86\%$. Similarly, blue again yields 32.14% and violet again yields 25.00% relative spectral reflectance. Using other values for the DN's produces the same results, namely, that normalizing the three colors removes the photometric effects present in the data. This method is as effective as the color ratio method described previously. Like the color ratio technique, producing relative spectral reflectances will not remove any wavelength dependent photometric effects, but, as stated previously, these are expected to be minor.

Relative spectral reflectances do not represent, and cannot be converted to, albedo values, but are nonetheless highly useful for identifying spectral differences between features plotted on ternary diagrams. As with color ratio imagery, relative spectral reflectances

plotted on ternary diagrams are most useful for showing differences in reflectivity between different colors (i.e., filtered images) and changes in spectral reflectivity differences. The plotting of purely spectral data on a ternary diagram has probably been done for the first time in this thesis, however, in a study of geological units on Mars by Arvidson et al. (1982), a technique for plotting red/violet ratio, albedo, and thermal inertia data on a ternary diagram was developed independently of the multispectral ternary diagram method first reported by Meier (1981). The inclusion of thermal inertia data in Arvidson's ternary diagram provided a distinct advantage in identifying compositional units over the use of multispectral end members only. Unfortunately, it was not possible to use infrared data in this study because of the very poor resolution of the Voyager infrared interferometer spectrometer at Europa (Hanel et al., 1979).

The relative spectral reflectance values for Europa's dark lineations were plotted on ternary diagrams, each lineation segment being plotted on a separate ternary diagram. The data points in each ternary diagram are the three-variable equivalent of two-variable scatter diagrams that have been used in previous multispectral studies of Europa by McCord et al. (1982) and of Io by Clancy and Danielson (1981), for example. All data points for features studied in this thesis plotted within a very small portion of the orange/blue/violet ternary diagram. For this reason, a small part of the ternary diagram is used for all figures in this work. This is called the reference ternary diagram, and

is defined and illustrated in Figure 3.

New techniques were developed at this stage of the thesis to derive the maximum amount of data from the ternary diagrams. The ternary diagram-plotted points for each lineation segment define what will be called the color distribution field (CDF) of the dark lineation (or whatever surface feature is plotted). Each color distribution field was polygonalized by connecting the outermost points of the CDF with straight line segments such that: (1) any three CDF points serving as a continuous series of vertices of the polygon form an angle θ where $0^\circ < \theta < 180^\circ$, (2) that a straight line segment connecting any two vertices of the CDF polygon will not go outside of the polygon, and (3) that no data points of the CDF fall outside of the CDF polygon. Figure 4 illustrates the formation of a CDF polygon. It should be noted that nearly every CDF will form an irregular polygon.

Several dark lineation properties and statistical characteristics were evaluated for the 193 dark lineation segments, many using the ternary diagram CDF plots and CDF polygons. These were: (1) spectral position of the CDF within the ternary diagram, (2) number of data points in the CDF, area of the CDF, and density of data points within the CDF, (3) a simple indication of the degree of dispersion of data points within the CDF, (4) the local brightness of each dark lineation segment, and (5) orientation of each dark lineation segment on the surface of Europa. Each of these will now be discussed in more detail.

The spectral position of a dark lineation segment's color distribu-

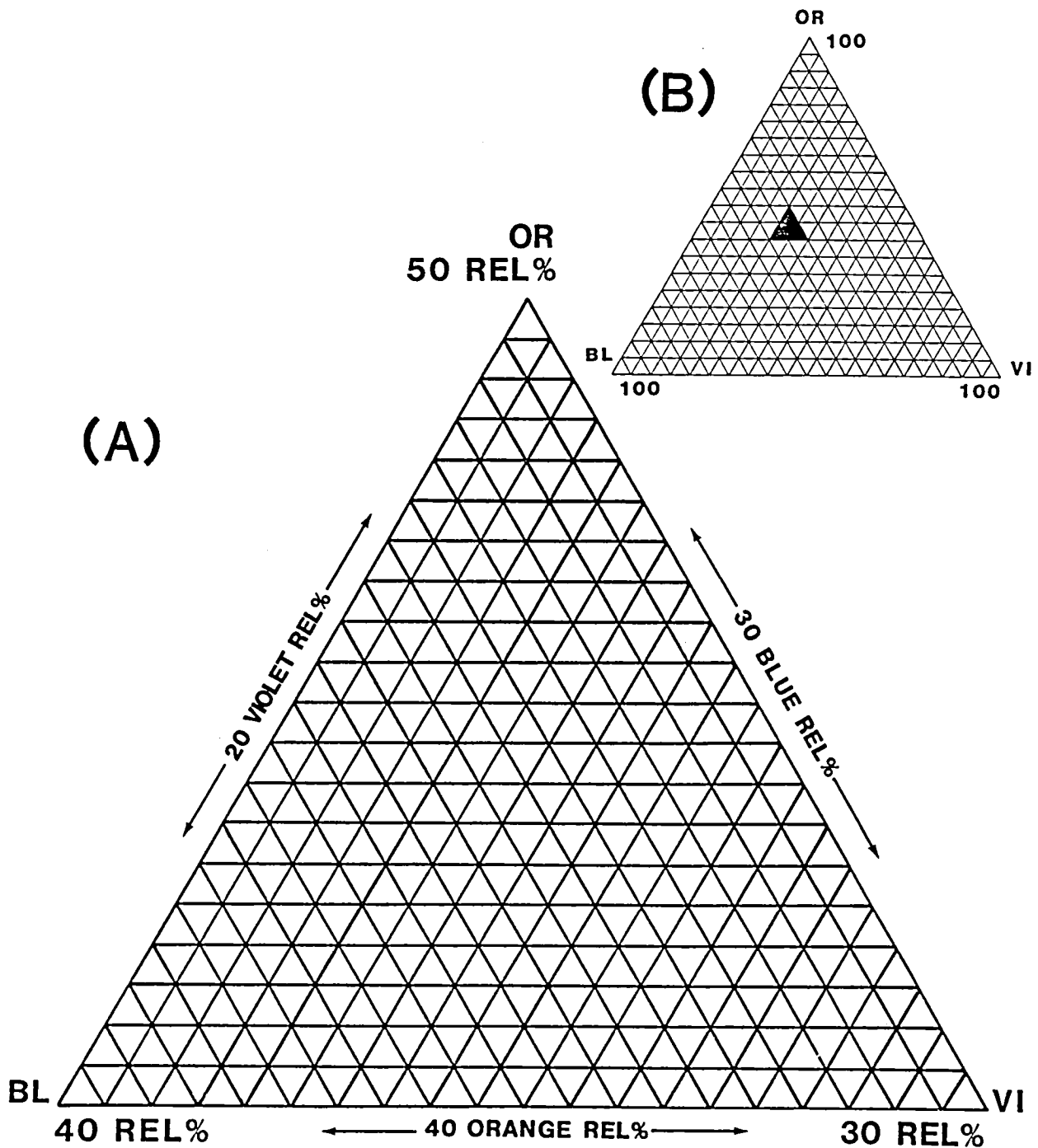


FIGURE 3. (A) The reference ternary diagram used to plot relative spectral reflectances (rel%'s) for all European features studied in this thesis. (B) The entire ternary diagram with orange, violet, and blue rel% end members. The location of the reference ternary diagram is shown as the darkened portion of the entire ternary diagram.

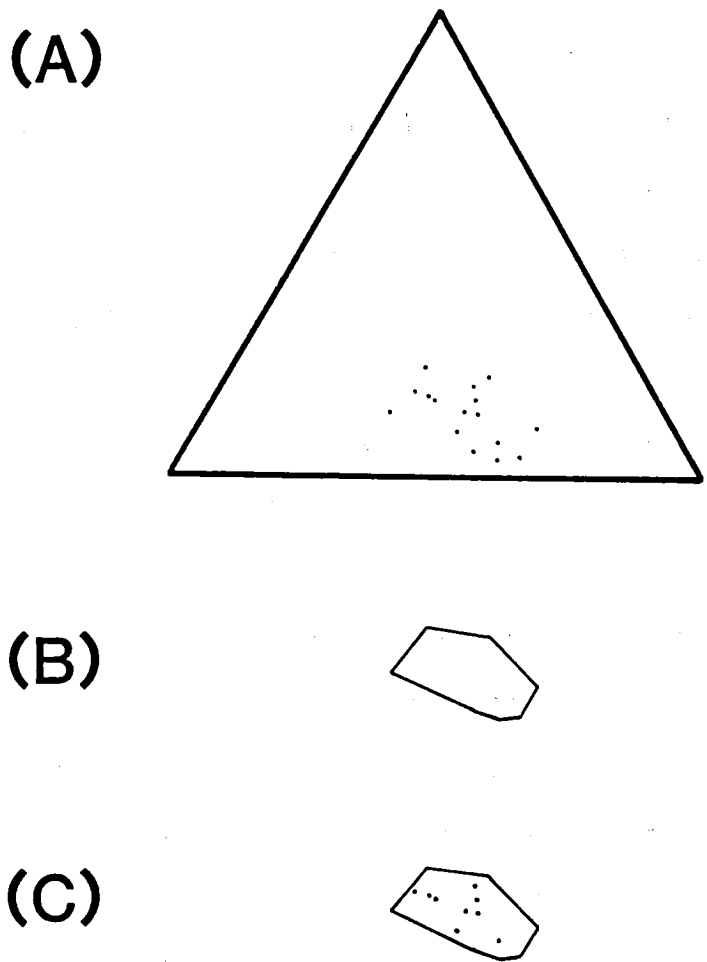


FIGURE 4. Methodology for constructing a CDF polygon, using the actual ternary diagram plot for DL182. (A) Field of rel% data comprising the color distribution field (CDF) within the ternary diagram. (B) Polygon constructed from the outermost data points of the CDF. Note that all angles are between 0° and 180° when measured facing the interior of the CDF polygon. (C) CDF polygon showing that no data points fall outside the polygon boundary. Interior data points are not shown in the CDF polygons presented in Appendix B.

tion field in a ternary diagram is the simplest and most fundamental basis for constructing a spectral classification system for Europa's dark lineations. Through the comparison of CDF polygon positions of all 193 dark lineation segments, a three-level spectral classification was established. Classification was based on differences in the position of CDF's along the orange relative spectral reflectance axis because orange displayed the greatest amount of variation in CDF position. CDF position changes between different dark lineation segments are directly attributable to changes in relative spectral reflectances, and therefore changes in surface composition.

The number of data points comprising a color distribution field, the area of the CDF polygon, and the density of data points within the CDF polygon are all directly related to each other. The area of a CDF polygon is a measure of the degree of variation in the relative spectral reflectances. The area is thus a measure of spectral homogeneity, hence compositional homogeneity, of the dark lineation plotted in the ternary diagram. This type of evaluation is of particular interest to help determine if Europa's dark lineations are of uniform composition along their length, or if some variation exists that could help explain their history.

Correlating the number of data points in a CDF with the area of the CDF provides a good test of how representative the data is of the true spectral nature of the surface features being studied. Consider that most of the dark lineations look spectrally similar in a color image of the study area on Europa. Rank the dark lineation segments according to

the number of data points in each. If, as the number of data points increases progressing through the dark lineation segments, the areas of the associated CDF's stay roughly the same size or change in size in a random pattern, then it can be said that the area of a CDF is independent of the number of data points comprising it. This is desirable because it indicates that the CDF areas are giving accurate representation of true amounts of relative spectral reflectance variations regardless of the number of data points taken for a given dark lineation segment. If, on the other hand, as the number of data points progressively increases, the areas of the associated CDF's also progressively increase, then it can be said that CDF area is dependent on the number of data points. This would damage the utility of CDF areas for making any conclusions about relative spectral reflectance variability because it would indicate that CDF's constructed from fewer data points did not provide an adequate sampling of all the spectral variability present in the dark lineation segments.

Dispersion of data points within a CDF polygon and its converse, cluster analysis, provide insight into the relative distribution of specific spectral/compositional variations within the total spectral/compositional range defined for a dark lineation segment by its CDF polygon. Since each data point represents an approximately equal area within a dark lineation (except very near the limb), knowing the number of data points comprising a cluster within a CDF polygon helps assess what percentage of the dark lineation segment has that more specific

compositional range defined by the cluster as opposed to the entire CDF polygon. If two or more multispectral clusters can be recognized within a CDF polygon, then the feature being studied will be known to possess multiple compositional units. Conversely, if data points within a CDF polygon are more-or-less uniformly dispersed (i.e., no clusters can be recognized), then the dark lineation segment being studied can be said to have an approximately uniform variation in composition along its length, with no specific compositions being favored.

In the remote sensing study of Mars by Arvidson et al. (1982), cluster analysis software was used on a ternary diagram of a large area of the Martian surface to define 6 compositional units. Unfortunately, no cluster analysis software for ternary diagrams was readily available for this project. Simplified techniques were developed to provide indications of the degree of dispersion/clustering of data points in each CDF. The geometric mean and the statistical mean of the data points of each CDF were plotted within each CDF polygon. The geometric mean is defined as the average of the high and low coordinates for the maximum and minimum points of each CDF for each of the three ternary diagram colors (i.e., violet, blue, and orange). Because most CDF polygons are irregular and non-symmetrical in shape, the geometric mean will usually not be a point but rather an equilateral triangle. The size of the equilateral triangle will depend on differences in the size of max-min separations between the three axes. The geometric mean also may not appear to be at the center of the CDF polygon because of the ir-

regular shape of some. The statistical mean is defined as the average of all CDF data points by averaging each color's coordinates separately.

It is the distance between the geometric mean and statistical mean that is of interest in estimating the degree of dispersion in each CDF. Ideally, if the geometric and statistical means are coincident, it means that the data points are uniformly dispersed throughout the CDF polygon. Conversely, the greater the separation between the geometric and statistical means, the less the dispersion and greater the degree of clustering in the data, ideally speaking. If a cluster, itself containing a uniform distribution of data points, is perfectly centered at the geometric mean, however, the statistical mean will be coincident with the geometric mean even though clustering is present. If two or more clusters of equal size and dispersion are symmetrically arranged around the geometric mean, the statistical and geometric means will again be coincident. Based on these considerations, the assessment of the degree of CDF dispersion was accomplished by a combination of plotting the statistical mean and geometric mean and visually inspecting the distribution of points using the two means as reference points. This technique was sufficient to construct a three-tiered classification of CDF dispersion.

A simple method that served as a cluster analysis of sorts was developed and applied to the entire set of data points for all 193 dark lineation segments. In this method, a cumulative count was made of all CDF data points in each unit area of the ternary diagram measuring 0.5 rel% x 0.5 rel% x 0.5 rel% where data points were present. The cumula-

tive point counts were then recorded in each unit area of the ternary diagram. By visual inspection of this cumulative point count diagram, it was then possible to draw certain conclusions about overall clustering trends in the dark lineation set.

In addition to the just-described statistical evaluations of color distribution fields in ternary diagrams, two other characteristics of dark lineations in the study area were assessed. One characteristic was the local brightness of each dark lineation. This evaluation was implemented by comparing the brightnesses of the DN's of a dark lineation with the brightnesses of DN's of dark lineations in the same longitudinal strip, on the blue pixel mosaic. Photometric effects will be displayed primarily on features that cover large amounts of latitude, but little over the amount of longitude covered by dark lineations in the study area. By evaluating dark lineation segments on a local basis, it was possible to accurately use the same brightness classification system over the entire study area in spite of the photometric brightening present.

The second characteristic ascertained was the orientation of each dark lineation segment on the surface of Europa. Because the study area pixel printouts came from Voyager images that had not undergone any projection changes, the apparent orientations of the dark lineations were distorted along the east-west component. Linear features that appear to be nearly north-south in orientation near Europa's limb in Voyager images are actually much closer to northeast-southwest in

Mercator-projection maps. The difficulty in translating the apparent orientations of dark lineations in Voyager images to true orientations resulted in the adoption of only a two-level orientation classification system, where dark lineations were assigned based on their possessing either a northeast-southwest character or a northwest-southeast character.

Following the classification of the dark lineation segments according to the appropriate division of each statistical property and physical characteristic, a pairing matrix was generated to search for relationships among these factors. Frequency counts were made in each class of each property or characteristic. Each of these numbers served as the denominator across the matrix row for that property/characteristic class. The numerator was supplied by the number of matches between the two classes at each row/column position in the pairing matrix. It should be noted that because the class frequencies were all different, the pairing coefficient between any two classes always had two values. This was due to the fact that although the number of matches (i.e. numerator) was the same at both matrix positions for a given property/characteristic class pair, the class frequency (i.e. denominator) was different at each matrix position. The pairing matrix thus was not mirror-symmetrical about its diagonal. It should be noted that no class of a characteristic/property was paired with itself or any other classes of the same characteristic/property; this defined the diagonal swath of NA's (not applicables). After computing the entire

pairing matrix, each property/characteristic class pair in the upper half of the matrix was averaged with its counterpart on the other side of the matrix diagonal. The average pairing coefficient was then recorded in a new matrix that had only its upper half filled in with pairing averages. Note that this is not a true correlation matrix because it does not follow the statistical procedure for correlating and does not generate any negative coefficients. The calculation of the number of matches between pairs of classes does, however, help define the significant physical property combinations present in the dark lineation segments (e.g., if most bold dark lineations are compositionally homogeneous, if most bright dark lineations have a NE-SW orientation, etc.).

STUDY OF AGENOR LINEA

The preceding sections of this chapter have included descriptions of processing and data analysis techniques applied to the dark lineations in the primary study area on Europa. These same techniques were also applied to the secondary area of study, Agenor Linea, the largest white line structure imaged on Europa. This feature stretches from 220° to 178° Longitude and varies from -44° to -41.5° Latitude. While this feature displayed a curvilinear trend in Voyager images, its thinness (five or less pixels wide in most places) still made it ideal for the pixel profiling method previously described. In addition to the dark lineation analysis techniques, one additional technique was devel-

oped and applied to Agenor Linea. In this technique, a color distribution field with its geometric mean plotted is divided into six equal-sized relative spectral reflectance bins (the bins will not be equal-sized if the edge of the CDF polygon is considered to be the edge of each bin), with the geometric mean serving as the center of the bins. Each bin can be considered to be a spectral subunit of the spectral field defined by the entire CDF. Figure 21 depicts the specific spectral properties of each bin. Each spectral subunit, or bin, can then be used to make a map of the lengthwise spectral/compositional variation of the feature under study. This is accomplished by assigning a color or symbol code to each bin and using that code on all of the data points in that bin. By tagging each data point, it becomes possible to accurately map each profiled location along the linear or curvilinear feature. This technique was first described and its results for Agenor Linea first presented in Meier (1983a).

The mapping of the lengthwise compositional variation of a curvilinear feature is important because it enables the identification of sequences of pixels representing the same composition, sequences with gradational compositional changes, and sequences of random changes in composition. This information, in turn, can be used to help construct models of the origin and evolution of the features being studied.

The spectral bin technique, as with most of the techniques developed for the dark lineation segments, was implemented manually and was thus, of course, very time-consuming. Time limitations prevented the

use of the spectral bin technique on the dark lineation segments, although it was well suited for those features.

RESULTS AND DISCUSSION: DARK LINEATION AREA

DESCRIPTION OF DARK LINEATION AREA

The 200 pixel-by-225 pixel registered Voyager image block used for studying Europa's dark lineation features occupies, as noted previously, a region spanning the approximate coordinates 220° to 180° Longitude, -24° to -2° Latitude. Remembering that a strong UV-absorption feature of a probable SO₂ composition covers Europa's trailing hemisphere (Lane et al. 1981), centered at 270° Longitude, it can be seen that the dark lineation study area falls within the SO₂-covered hemisphere. If SO₂-imbedded ice actually covers the entire trailing hemisphere, then one of its boundaries will be located at 180° Longitude. Thus, the entire dark lineation study area should be part of the easternmost portion of the SO₂-covered hemisphere, and their easternmost margins should approximately correspond. The SO₂-imbedded materials may best be spectrally observable in Europa's plains unit because its composition is thought to be closer to pure ice than the dark lineation material, and ice would have best allowed sulfur ion implantation from Io ejecta. The plains in the dark lineation study area may therefore contain important spectral information on the nature of the margin of the SO₂-imbedded trailing hemisphere of Europa.

A map of the dark lineation study area of Europa and the 193 lineation segments that were evaluated are shown in Figure 5. The lineations in the study area are of several different geomorphic types, the exact

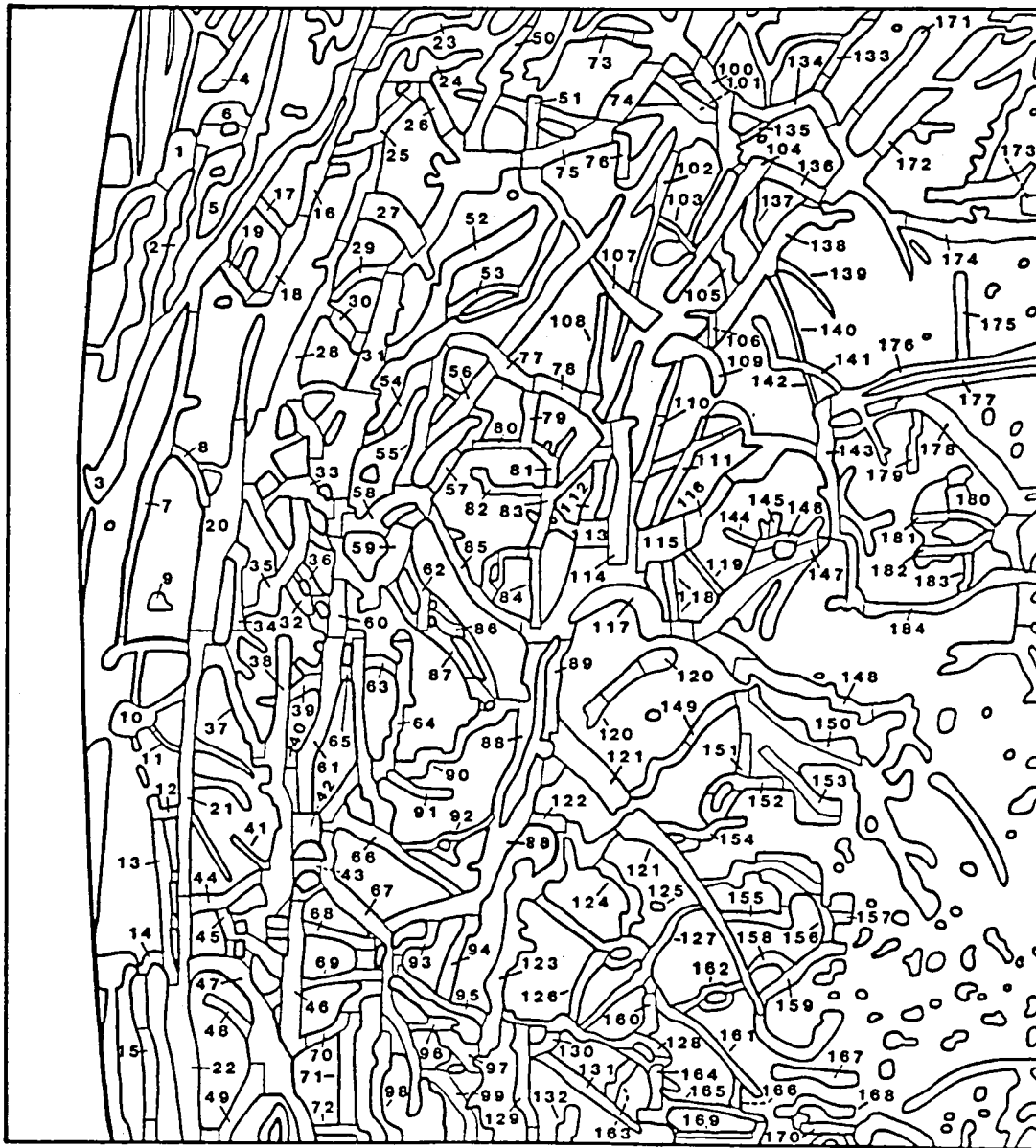


FIGURE 5. Map of the dark lineation (DL) study area derived from Voyager 2 frame 1198J2-001 (blue filter). All major bolder and most of the minor, brighter DL's present in the area are shown, with the DL segments that were profiled and plotted on ternary diagrams outlined and labeled. Note that a thin north-south strip of the DL study area (equal to approximately one-fifth the width of the area shown) was inadvertently not mapped. This strip contains DL's 185-193 and portions of DL's 173, 174, 176-178, and 184.

number of which depends on which classification system is used. In the eight-level lineation classification system of Pieri (1981), three types of lineations are definitely present. Lineation type 1 (long, regularly-spaced, ENE-trending, some with central white lines), type 2 (very dark, short and wedge-shaped, most trending NW-SE), and type 5 (very short, subdividing polygons formed by the intersection of type 1 and type 2 lineations) are present, while the other five lineation types apparently are not. According to the four-level lineation classification system of Lucchitta et al. (1981), two lineation types are present in the study area: dark, wedge-shaped bands and triple bands. Neither Pieri's nor Lucchitta's classification maps show any bright (i.e., probably near-pure ice) ridges in the dark lineation study area, but their identification was possible only near the terminator, where visible shadows were cast by the ridges. Bright ridges may be present in the study area, but are unable to be identified because of a lack of shadows near Europa's limb (where the study area is situated) and a lack of contrast with the plains material in which they are located.

At the extreme eastern side of the dark lineation study area, the dark lineations and plains units begin to give way to a mottled terrain unit, specifically, the gray mottled terrain (Lucchitta and Soderblom, 1982). All of the 193 lineation segments evaluated in the study area are dark lineations, although some in the eastern portion appear to be transitional with dark spots and patches comprising the gray mottled terrain. Some dark spots are aligned with dark lineations in a manner

consistent with their being remnants of portions of the lineations that have either been disrupted by plains material or were never fully emplaced with dark lineation material.

DARK LINEATION TERNARY DIAGRAM PLOTS

The ternary diagrams for the 193 dark lineation segments that were profiled in orange, blue, and violet, and plotted as relative spectral reflectances on a lengthwise pixel-by-pixel basis, are shown in Appendix A. The associated color distribution fields (CDF's) for each dark lineation (DL) are shown in their polygonalized form in Appendix B. In these figures, each CDF has a point representing the statistical mean of the CDF and an equilateral triangle representing the geometric mean of the CDF. The size of the triangle is directly proportional to the degree to which the CDF polygon is non-symmetrical; in cases where the CDF polygon is very close to symmetrical in shape, the geometric mean will be represented by a point because the size of the equilateral triangle is too small to be plotted.

It can be clearly seen from Appendix A and Appendix B that there are distinct differences in relative spectral reflectance properties among the dark lineation segments evaluated. Many different pairs of dark lineation ternary diagrams can be chosen in which the respective CDF's are completely non-overlapping (eg., DL39 and DL42, DL63 and DL153, DL133 and DL145). In some cases, CDF's are completely isolated from each other by several relative reflectance percentage points along

the orange axis (eg., DL27 and DL183, DL125 and DL150, DL65 and DL151). This illustrates that there are definite compositional differences between dark lineations in the study area. This is in itself a significant finding, since color (and therefore compositional) differences between dark lineations in this area are not readily apparent when viewing Voyager color composite images. The wavelength dependence of Europa's photometric function, while certainly imparting some influence on the position of data points in the ternary diagrams plots, cannot be responsible for the distinct CDF groups of non-overlapping high and low orange relative spectral reflectance dark lineations. This is because several dark lineations from different spectral position groups are found in both the western and eastern portions of the study area; multispectral photometric differences would be expected to cause the distribution of DL spectral groups to be more-or-less polarized along an east-west line.

Comparisons between dark lineation ternary diagrams can be made more meaningful if the spectral properties of the dark lineation suite as a whole are plotted in a similar fashion. This also enables the spectral properties of the dark lineation terrain unit to be compared to those of other terrain units on Europa. For these reasons, a ternary diagram plot of the cumulative point count of all 193 dark lineation segments was made using the same relative spectral reflectance percentage (hereafter abbreviated as rel%) ranges as for individual dark lineations. The resultant ternary diagram is depicted in Figure 6, with

cumulative point counts shown for each 0.5 rel% X 0.5 rel% X 0.5 rel% area. In addition to being useful as a reference for comparing with individual dark lineation ternary diagrams and other European terrain units' spectral ternary diagrams, the cumulative point count ternary diagram is useful for a very simple type of cluster analysis of the relative spectral reflectance data. If any strong clustering is evident in the data, it would indicate the presence of significant compositional unit(s) on Europa. A weak cluster was found by simple visual inspection of the cumulative point counts, using all frequencies above fifty per unit area to define the cluster. The area occupied by the cluster is indicated in Figure 7. Note that there are no truly sharp contrasts in the size of point count frequencies between unit areas within the cluster and unit areas surrounding the cluster. The physical interpretation of this can best be made when the cumulative point count ternary diagram data is combined with that for other characteristics of the dark lineations, and so will be presented after describing the results for the other characteristics.

DARK LINEATION CHARACTERISTICS EVALUATED

A major goal of this thesis has been to construct classification maps of the dark lineations in the study area based on important characteristics of the lineations. The properties chosen to be evaluated were dark lineation spectral position within the reference ternary diagram, area of each lineation's color distribution field (CDF), density of data

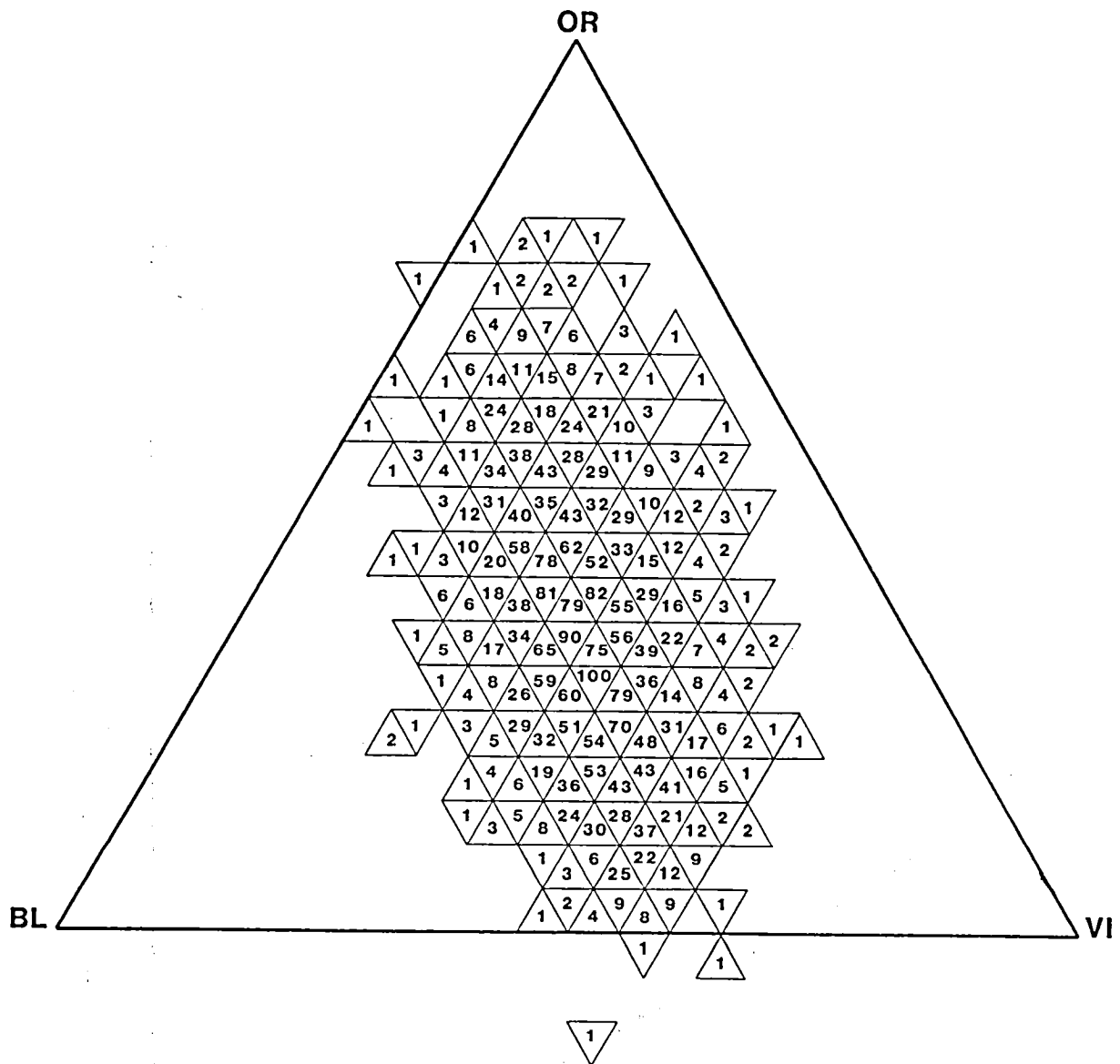


FIGURE 6. Cumulative point count ternary diagram for all 193 dark lineation segments, plotted on the reference ternary diagram. Each small triangle displays the cumulative frequency for a region of 0.5 orange rel% X 0.5 blue rel% X 0.5 violet rel%.

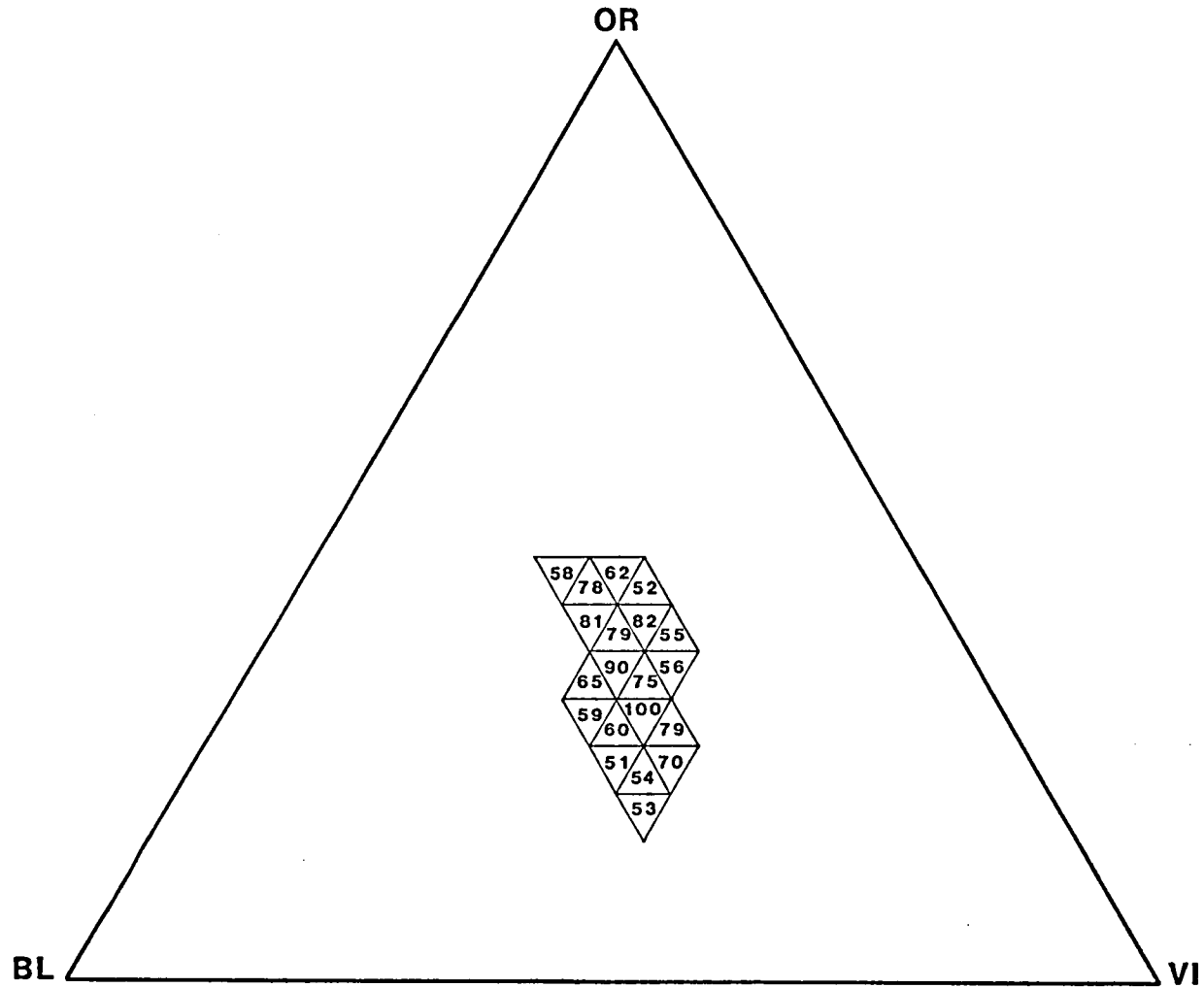


FIGURE 7. Weak cluster of relative spectral reflectance data points within the cumulative point count ternary diagram shown in Figure 6.

points in each CDF, degree of dispersion/clustering of data points within each CDF, local brightness of each dark lineation (relative to other dark lineations in that immediate area), and general orientation of each dark lineation (whether each lineation's trend is closer to NE-SW or NW-SE). Each characteristic evaluated was divided into three classes (except dark lineation orientation) based on the limits found for each in the dark lineation suite. The ranges of the classes for each characteristic are listed in Table I. Defining the ranges for CDF area and CDF point density was an exercise in balance between splitting the total range for each characteristic into three classes of equal range and setting up three classes of equal frequency. Having classes of approximately equal frequency with all other class sizes for all other characteristics would be ideal for tabulating matches between classes when comparing two different dark lineation properties. A fair compromise was arrived at for CDF area and point density that allowed class sizes to be closer to each than otherwise would be possible, by making the two lowest classes for CDF area and point density equal in the size of range and leaving the range of the highest class open-ended in such a way as to increase its frequency to a level approaching that of the other classes.

Even with characteristic class sizes set as close to each other as could be reasonably done, there were still large numerical differences between some of them. Table II lists the characteristic classifications for all 193 dark lineation segments for all six lineation properties.

From these results, a series of dark lineation classification maps were made of the study area, one for each property evaluated except lineation orientation. These are presented in Figures 8 through 11. These maps are quite useful for studying the distributions of dark lineations possessing specific properties. To achieve useful interpretations about the nature of Europa's dark lineations, however, it is necessary to know the physical interpretation of each characteristic assessed. Such information is outlined in Table III. More useful than individual properties for characterizing the nature of the dark lineations is to find pairs of characteristics that have strong affinities for appearing together in the same dark lineations because this reveals something about what types of dark lineations do and do not exist on this part of Europa. Finding the important pairs of characteristics was accomplished by constructing a characteristic pair matching matrix, hereafter referred to as a relationship matrix because it seeks to find the relationships between various dark lineation properties. Table IV gives the results of the percentages of matches for all possible two-property combinations of lineation characteristics. Two values are shown, each one reflecting the number of matches divided by the number of dark lineations in one of the two characteristic classes in that pair. For greater ease in interpretation, the average value of each characteristic pair's matching percentage is presented in Table V.

TABLE I. Key to dark lineation (DL) characteristic classifications in Table II.

OR REL% CLASSIFICATION

SCA = A: $\geq 50\%$ of data points ≥ 44 orange rel%
 SCB = B: $> 50\%$ of data points > 42 and < 44 orange rel %
 SCC = C: $\geq 50\%$ of data points ≤ 42 orange rel%

.....

LOCAL BRIGHTNESS CLASSIFICATION

BCA = A: Very dark to dark as compared to other DL's in the area
 BCB = B: Average darkness as compared to other DL's in the area
 BCC = C: Bright to very bright as compared to other DL's in area

.....

NUMBER OF DATA POINTS CLASSIFICATION

PCA = A: 1-15
 PCB = B: 16-30
 PCC = C: > 30

.....

AREA OF CDF CLASSIFICATION

ACA = A: 1-300 area units
 ACB = B: 301-600 area units
 ACC = C: > 600 area units

.....

DENSITY OF DATA POINTS IN CDF CLASSIFICATION

DCA = A: 0-3.000 data points/100 area units
 DCB = B: 3.001-6.000 data points/100 area units
 DCC = C: > 6.000 data points/100 area units

.....

DEGREE OF DISPERSION OF DATA POINTS IN CDF CLASSIFICATION

DSCA = A: well dispersed
 DSCB = B: slightly clustered
 DSCC = C: well clustered

.....

ORIENTATION OF DARK LINEATION CLASSIFICATION

OCA = A: NW - SE
 OCB = B: NE - SW

TABLE II. Classifications of all 193 dark lineation (DL) segments in the DL study area according to all characteristics evaluated. Acronyms and classes are defined in Table I.

DL NUMBER	SPECTRAL CLASS (OR REL%)	LOCAL BRIGHTNESS CLASS	NUMBER OF DATA POINTS/ CLASS	AREA OF CDF/ CLASS	DENSITY OF DATA POINTS IN CDF/ CLASS	DEGREE OF DISPERSION CLASS	ORIENTATION CLASS
DL1	B	C	10 A	255 A	3.922 B	B	B
DL2	B	B	29 B	570 B	5.088 B	B	B
DL3	A	A	57 C	1430 C	3.986 B	C	B
DL4	B	C	10 A	235 A	4.255 B	A	B
DL5	B	B	33 C	640 C	5.156 B	C	B
DL6	A	A	7 A	240 A	2.917 A	A	B
DL7	B	C	56 C	1710 C	3.275 B	C	B
DL8	B	B	12 A	440 B	2.727 A	A	A
DL9	A	B	5 A	440 B	1.136 A	A	A
DL10	A	B	19 B	375 B	5.067 B	C	B
DL11	B	B	4 A	60 A	6.667 C	A	A
DL12	B	B	7 A	110 A	6.364 C	B	A
DL13	A	C	38 C	620 C	6.129 C	B	B
DL14	A	B	9 A	470 B	1.915 A	A	A
DL15	B	B	16 B	330 B	4.848 B	C	B
DL16	B	B	12 A	200 A	6.000 B	C	B
DL17	A	C	5 A	305 B	1.639 A	C	A
DL18	A	B	15 A	450 B	3.333 B	C	B
DL19	B	C	7 A	270 A	2.593 A	B	A
DL20	B	A	37 C	750 C	4.933 B	C	B

TABLE II. (Continued)

DL NUMBER	SPECTRAL CLASS (OR REL%)	LOCAL BRIGHTNESS CLASS	NUMBER OF DATA POINTS/ CLASS	AREA OF CDF/ CLASS	DENSITY OF DATA POINTS IN CDF/ CLASS	DEGREE OF DISPERSION CLASS	ORIENTATION CLASS
DL21	A	A	50 C	670 C	7.463 C	C	B
DL22	A	A	50 C	490 B	10.204 C	C	B
DL23	B	A	5 A	75 A	6.667 C	A	B
DL24	B	B	18 B	345 B	5.217 B	A	B
DL25	B	B	14 A	400 B	3.500 B	A	B
DL26	B	A	8 A	175 A	4.571 B	A	A
DL27	A	A	12 A	290 A	4.138 B	B	A
DL28	B	B	18 B	440 B	4.091 B	A	B
DL29	B	C	9 A	225 A	4.000 B	A	B
DL30	C	C	7 A	130 A	5.385 B	A	A
DL31	A	A	17 B	1220 C	1.393 A	A	B
DL32	B	B	21 B	570 B	3.684 B	C	A
DL33	A	B	13 A	340 A	3.824 B	A	A
DL34	B	B	20 B	720 C	2.778 A	C	B
DL35	A	A	19 B	890 C	2.135 A	B	B
DL36	B	B	4 A	185 A	2.162 A	A	A
DL37	A	A	13 A	410 B	3.171 B	A	A
DL38	B	B	42 C	640 C	6.563 C	B	B
DL39	A	A	8 A	150 A	5.333 B	A	B
DL40	A	A	4 A	65 A	6.154 C	A	A

TABLE II. (Continued)

DL NUMBER	SPECTRAL CLASS (OR REL%)	LOCAL BRIGHTNESS CLASS	NUMBER OF DATA POINTS/CLASS	AREA OF CDF/CLASS	DENSITY OF DATA POINTS IN CDF/CLASS	DEGREE OF DISPERSION CLASS	ORIENTATION CLASS
DL41	B	C	9 A	245 A	3.673 B	A	A
DL42	A	A	4 A	40 A	10.000 C	A	A
DL43	B	B	7 A	80 A	8.750 C	B	A
DL44	B	C	15 A	340 B	4.412 B	B	B
DL45	B	C	11 A	480 B	2.292 A	B	A
DL46	A	B	35 C	560 B	6.250 C	A	B
DL47	A	A	45 C	590 B	7.627 C	C	A
DL48	B	C	9 A	370 B	2.432 A	A	A
DL49	B	C	15 A	125 A	12.000 C	C	B
DL50	A	A	26 B	1080 C	2.407 A	A	B
DL51	C	C	11 A	270 A	4.074 B	B	B
DL52	A	A	32 C	570 B	5.614 B	B	B
DL53	C	C	14 A	370 B	3.784 B	A	B
DL54	B	C	10 A	510 B	1.961 A	A	B
DL55	B	B	24 B	440 B	5.455 B	B	B
DL56	B	B	11 A	430 B	2.558 A	A	B
DL57	B	C	6 A	115 A	5.217 B	A	B
DL58	A	B	16 B	820 C	1.951 A	A	B
DL59	B	B	26 B	1130 C	2.301 A	B	$\frac{1}{2}$ A & $\frac{1}{2}$ B
DL60	A	B	16 B	510 B	3.137 B	B	B

TABLE II. (Continued)

DL NUMBER	SPECTRAL CLASS (OR REL%)	LOCAL BRIGHTNESS CLASS	NUMBER OF DATA POINTS/CLASS	AREA OF CDF/CLASS	DENSITY OF DATA POINTS IN CDF/CLASS	DEGREE OF DISPERSION CLASS	ORIENTATION CLASS
DL61	A	A	38 C	570 B	6.667 C	C	B
DL62	B	B	18 B	590 B	3.051 B	A	A
DL63	B	B	6 A	100 A	6.000 B	B	A
DL64	B	B	27 B	490 B	5.510 B	A	B
DL65	A	A	3 A	20 A	15.000 C	A	A
DL66	A	A	13 A	670 C	1.940 A	A	A
DL67	A	A	37 C	1000 C	3.700 B	B	A
DL68	B	B	12 A	530 B	2.264 A	A	A
DL69	B	C	13 A	390 B	3.333 B	A	A
DL70	B	B	9 A	145 A	6.207 C	C	B
DL71	B	C	21 B	790 C	2.658 A	B	B
DL72	B	C	16 B	500 B	3.200 B	A	A
DL73	B	C	11 A	490 B	2.245 A	B	A
DL74	A	A	10 A	335 B	2.985 A	B	B
DL75	A	B	12 A	400 B	3.000 A	B	B
DL76	B	B	11 A	315 B	3.492 B	B	B
DL77	A	A	17 B	400 B	4.250 B	C	A
DL78	B	A	13 A	560 B	2.321 A	A	A
DL79	B	B	12 A	920 C	1.304 A	B	B
DL80	C	C	10 A	530 B	1.887 A	B	A

TABLE II. (Continued)

DL NUMBER	SPECTRAL CLASS (OR REL%)	LOCAL BRIGHTNESS CLASS	NUMBER OF DATA POINTS/ CLASS	AREA OF CDF/ CLASS	DENSITY OF DATA POINTS IN CDF/ CLASS	DEGREE OF DISPERSION CLASS	ORIENTATION CLASS
DL81	B	B	9 A	650 C	1.385 A	A	A
DL82	B	C	15 A	640 C	2.344 A	B	A
DL83	B	B	13 A	540 B	2.407 A	A	B
DL84	C	C	9 A	175 A	5.143 B	B	B
DL85	A	B	27 B	1170 C	2.308 A	B	A
DL86	B	C	9 A	370 B	2.432 A	B	A
DL87	B	C	16 B	540 B	2.963 A	A	A
DL88	B	B	38 C	620 C	6.129 C	C	B
DL89	A	A	47 C	1350 C	3.481 B	A	B
DL90	B	C	28 B	520 B	5.385 B	C	B
DL91	B	B	12 A	380 B	3.158 B	A	A
DL92	B	C	17 B	275 A	6.182 C	C	B
DL93	B	A	9 A	430 B	2.093 A	A	B
DL94	B	C	13 A	325 B	4.000 B	B	B
DL95	B	B	17 B	810 C	2.099 A	B	A
DL96	A	B	8 A	450 B	1.778 A	B	A
DL97	A	B	11 A	430 B	2.558 A	A	A
DL98	B	C	21 B	255 A	8.235 C	A	B
DL99	A	A	16 B	680 C	2.353 A	A	A
DL100	B	B	22 B	670 C	3.284 B	A	A

TABLE II. (Continued)

DL NUMBER	SPECTRAL CLASS (OR REL%)	LOCAL BRIGHTNESS CLASS	NUMBER OF DATA POINTS/ CLASS	AREA OF CDF/ CLASS	DENSITY OF DATA POINTS IN CDF/ CLASS	DEGREE OF DISPERSION CLASS	ORIENTATION CLASS
DL101	B	B	11 A	100 A	11.000 C	A	A
DL102	C	C	22 B	355 B	6.197 C	C	B
DL103	A	A	9 A	640 C	1.406 A	B	A
DL104	B	B	45 C	1250 C	3.600 B	B	B
DL105	C	C	10 A	125 A	8.000 C	A	A
DL106	B	C	6 A	75 A	8.000 C	A	B
DL107	A	A	18 B	600 B	3.000 A	B	A
DL108	C	C	18 B	210 A	8.571 C	C	B
DL109	A	A	20 B	820 C	2.439 A	C	A
DL110	B	B	10 A	305 B	3.279 B	A	B
DL111	C	C	20 B	560 B	3.571 B	B	B
DL112	B	B	13 A	310 B	4.194 B	A	B
DL113	A	A	13 A	610 C	2.131 A	B	A
DL114	A	A	31 C	1230 C	2.520 A	C	B
DL115	A	A	8 A	670 C	1.194 A	A	B
DL116	B	B	8 A	80 A	10.000 C	C	B
DL117	A	A	19 B	1280 C	1.484 A	A	A
DL118	B	B	12 A	270 A	4.444 B	B	A
DL119	C	C	9 A	265 A	3.396 B	A	A
DL120	B	B	16 B	165 A	9.697 C	B	B

TABLE II. (Continued)

DL NUMBER	SPECTRAL CLASS (OR REL%)	LOCAL BRIGHTNESS CLASS	NUMBER OF DATA POINTS/ CLASS	AREA OF CDF/ CLASS	DENSITY OF DATA POINTS IN CDF/ CLASS	DEGREE OF DISPERSION CLASS	ORIENTATION CLASS
DL121	A	A	42 C	1980 C	2.121 A	C	A
DL122	C	C	10 A	820 C	1.220 A	C	A
DL123	B	A	33 C	780 C	4.231 B	C	B
DL124	C	C	17 B	820 C	2.073 A	C	A
DL125	C	C	4 A	90 A	4.444 B	A	A
DL126	B	C	13 A	410 B	3.170 B	A	B
DL127	C	C	25 B	1030 C	2.427 A	C	B
DL128	B	B	34 C	950 C	3.579 B	A	A
DL129	A	B	20 B	640 C	3.125 B	A	B
DL130	B	B	5 A	275 A	1.818 A	A	B
DL131	C	C	18 B	470 B	3.830 B	B	A
DL132	B	C	11 A	490 B	2.245 A	A	B
DL133	C	C	9 A	105 A	8.571 C	C	B
DL134	B	B	20 B	1540 C	1.299 A	B	B
DL135	C	C	6 A	90 A	6.667 C	A	B
DL136	B	C	13 A	245 A	5.306 B	A	A
DL137	B	B	10 A	105 A	9.524 C	B	A
DL138	B	B	20 B	490 B	4.082 B	C	B
DL139	C	C	11 A	255 A	4.314 B	C	A
DL140	C	C	16 B	325 B	4.923 B	B	A

TABLE II. (Continued)

DL NUMBER	SPECTRAL CLASS (OR REL%)	LOCAL BRIGHTNESS CLASS	NUMBER OF DATA POINTS/CLASS	AREA OF CDF/CLASS	DENSITY OF DATA POINTS IN CDF/CLASS	DEGREE OF DISPERSION CLASS	ORIENTATION CLASS
DL141	B	A	18 B	350 B	5.143 B	A	A
DL142	C	C	7 A	160 A	4.375 B	B	A
DL143	A	A	43 C	1260 C	3.413 B	A	A
DL144	C	C	7 A	110 A	6.364 C	B	A
DL145	B	B	5 A	40 A	12.500 C	B	B
DL146	B	B	8 A	310 B	2.581 A	A	B
DL147	B	B	23 B	790 C	2.911 A	C	B
DL148	A	A	23 B	1560 C	1.474 A	A	A
DL149	B	B	10 A	120 A	8.333 C	B	B
DL150	A	A	18 B	430 B	4.186 B	A	A
DL151	C	C	10 A	220 A	4.545 B	A	B
DL152	B	C	12 A	640 C	1.875 A	A	A
DL153	A	B	4 A	165 A	2.424 A	A	A
DL154	B	C	12 A	580 B	2.069 A	B	A
DL155	B	B	11 A	175 A	6.286 C	B	A
DL156	B	B	8 A	730 C	1.096 A	A	A
DL157	A	A	4 A	45 A	8.889 C	A	A
DL158	B	A	8 A	740 C	1.081 A	A	B
DL159	B	B	15 A	680 C	2.206 A	C	B
DL160	B	C	8 A	290 A	2.759 A	B	B

TABLE II. (Continued)

DL NUMBER	SPECTRAL CLASS (OR REL%)	LOCAL BRIGHTNESS CLASS	NUMBER OF DATA POINTS/ CLASS	AREA OF CDF/ CLASS	DENSITY OF DATA POINTS IN CDF/ CLASS	DEGREE OF DISPERSION CLASS	ORIENTATION CLASS
DL161	B	B	42 C	1350 C	3.111 B	B	A
DL162	B	C	12 A	490 B	2.449 A	B	B
DL163	C	C	8 A	165 A	4.848 B	A	B
DL164	B	B	8 A	500 A	1.600 A	A	B
DL165	B	C	22 B	1190 C	1.849 A	B	A
DL166	C	C	7 A	145 A	4.828 B	A	B
DL167	B	B	13 A	550 B	2.364 A	A	A
DL168	B	B	14 A	620 C	2.258 A	A	A
DL169	B	B	15 A	480 B	3.125 B	A	A
DL170	B	B	8 A	150 A	5.333 B	A	A
DL171	C	C	20 B	260 A	7.692 C	B	B
DL172	A	A	12 A	250 A	4.800 B	B	B
DL173	C	B	19 B	510 B	3.725 B	C	B
DL174	B	B	8 A	150 A	5.333 B	B	A
DL175	B	C	17 B	590 B	2.881 A	B	B
DL176	B	B	35 C	660 C	5.303 B	A	A
DL177	B	B	22 B	730 C	3.014 B	B	A
DL178	A	A	30 B	1500 C	2.000 A	B	A
DL179	C	C	12 A	160 A	7.500 C	C	B
DL180	B	C	4 A	125 A	3.200 B	C	B

TABLE II. (Continued)

DL NUMBER	SPECTRAL CLASS (OR REL%)	LOCAL BRIGHTNESS CLASS	NUMBER OF DATA POINTS/CLASS	AREA OF CDF/CLASS	DENSITY OF DATA POINTS IN CDF/CLASS	DEGREE OF DISPERSION CLASS	ORIENTATION CLASS
DL181	C	C	7 A	30 A	23.333 C	A	A
DL182	C	C	16 B	630 C	2.540 A	A	A
DL183	C	C	6 A	80 A	7.500 C	B	B
DL184	C	B	26 B	1130 C	2.301 A	C	A
DL185	C	C	13 A	230 A	5.652 B	C	B
DL186	C	C	18 B	320 B	5.625 B	C	B
DL187	C	B	16 B	560 B	2.857 A	C	B
DL188	A	A	10 A	740 C	1.351 A	B	A
DL189	C	C	10 A	155 A	6.452 C	C	A
DL190	A	A	23 B	590 B	3.898 B	B	A
DL191	C	C	9 A	180 A	5.000 B	B	A
DL192	A	A	6 A	470 B	1.277 A	A	B
DL193	B	A	9 A	280 A	3.214 B	B	A

TABLE III. Physical meaning of each dark lineation characteristic that was used to classify dark lineations in Table II.

<u>CHARACTERISTIC</u>	<u>PHYSICAL MEANING</u>
1) ORANGE REL%	Specific orange relative spectral reflectances (hence also specific blue and violet relative spectral reflectances) correspond to specific surface compositions, though those compositions are unknown.
2) LOCAL BRIGHTNESS	Indicates albedo of surface material, which in turn is a function of surface composition and texture. Brighter surface areas on Europa are believed to be composed of a higher percentage of water ice than darker areas.
3) [a] AREA OF CDF	Indicates amount of spectral/compositional variation within a dark lineation or other surface feature (i.e., the larger the CDF AREA, the greater the amount of compositional variation).
[b] NUMBER OF DATA POINTS/ DENSITY OF DATA POINTS IN CDF	<p>These dark lineation characteristics provide a measure of the validity of using CDF area to assess compositional variation, as follows:</p> <p>(1) if, as NUMBER OF DATA POINTS increases, CDF AREA increases and CDF POINT DENSITY does not significantly change, then CDF AREA is dependent on the NUMBER OF DATA POINTS, which means that the true amount of compositional variation is not reflected by CDF AREA for dark lineations with a small NUMBER OF DATA POINTS.</p> <p>(2) if, as NUMBER OF DATA POINTS increases, CDF AREA does not significantly change and CDF POINT DENSITY increases, then, CDF AREA is independent of the NUMBER OF DATA POINTS and CDF AREA accurately represents the amount of compositional variation for all dark lineations.</p> <p>(3) if, as NUMBER OF DATA POINTS increases, CDF AREA increases and CDF POINT DENSITY increases, then, the situation is somewhere between (1) and (2) above (i.e., CDF AREA is weakly dependent on the NUMBER OF DATA POINTS).</p>

TABLE III. (Continued)

<u>CHARACTERISTIC</u>	<u>PHYSICAL MEANING</u>
4) DEGREE OF * DISPERSION	<p>(1) Good dispersion/poor clustering of data points within a CDF means that there is roughly an equal frequency of each of the spectral/compositional subunits in the dark lineation (if the CDF is designated as the whole unit). Thus, no specific subcomposition can be said to constitute a major portion of the dark lineation. This does not necessarily mean that the subunits are uniformly distributed along the length of the lineation.</p> <p>(2) Poor dispersion/good clustering of data points within a CDF means that at least one cluster is present. The presence of a cluster indicates that a significant part of the corresponding dark lineation is composed of a specific subunit, which could be either a specific pure composition or, more likely, the same proportion of two or more surface materials. The presence of a cluster does not necessarily mean that the parts of the dark lineation composed of the same subunit are contiguous.</p>
5) DARK LINEATION ORIENTATION	<p>Identifying sets of dark lineations with the same orientation indicates the presence of structural sets that may correspond to discrete episodes of fracturing in Europa's history.</p>

*See also subunit discussions and map pursuant to Agenor Linea on page 55 and Figures 20 and 21.

TABLE IV. Relationship matrix for pairs of dark lineation characteristics defined in Table I. Explanation of the procedure used to arrive at the matching values shown is provided in the text. NA stands for "not applicable", since a characteristic class cannot be matched with itself or other classes of the same characteristic.

	SCA	SCB	SCC	BCA	BCB	BCC	ACA	ACB	ACC	DCA	DCB	DCC	DSCA	DSCB	DSCC	OCA	OCB
SCA	NA	NA	NA	.7091	.2545	.0364	.1818	.3818	.4364	.5091	.3091	.1818	.4727	.3091	.2182	.5636	.4364
SCB	NA	NA	NA	.0882	.5784	.3333	.3431	.3922	.2647	.3725	.4510	.1765	.4706	.3529	.1765	.4466	.5534
SCC	NA	NA	NA	.0000	.0833	.9167	.6111	.2500	.1389	.1944	.5000	.3056	.3056	.3056	.3889	.4722	.5278
BCA	.8125	.1875	.0000	NA	NA	NA	.2292	.2917	.4792	.4583	.3542	.1875	.5000	.2708	.2292	.5625	.4375
BCB	.1842	.7763	.0395	NA	NA	NA	.2763	.4211	.3026	.3816	.4342	.1842	.4605	.3289	.2105	.4675	.5325
BCC	.0290	.4928	.4783	NA	NA	NA	.5072	.3478	.1449	.3188	.4493	.2319	.3768	.3768	.2464	.4638	.5362
ACA	.1493	.5224	.3284	.1642	.3134	.5224	NA	NA	NA	.1045	.4478	.4478	.4776	.3433	.1791	.4925	.5075
ACB	.3000	.5714	.1286	.2000	.4571	.3429	NA	NA	NA	.4143	.5143	.0714	.4714	.3143	.2143	.4429	.5571
ACC	.4286	.4821	.0893	.4107	.4107	.1786	NA	NA	NA	.6607	.2679	.0714	.3571	.3393	.3036	.5263	.4737
DCA	.3836	.5205	.0959	.3014	.3973	.3014	.0959	.3973	.5068	NA	NA	NA	.4795	.3562	.1644	.5811	.4189
DCB	.2099	.5679	.2222	.2099	.4074	.3827	.3704	.4444	.1852	NA	NA	NA	.4568	.3210	.2222	.4444	.5556
DCC	.2564	.4615	.2821	.2308	.3590	.4103	.7692	.1282	.1026	NA	NA	NA	.3333	.3077	.3590	.3846	.6154
DSCA	.3059	.5647	.1294	.2824	.4118	.3059	.3765	.3882	.2353	.4118	.4353	.1529	NA	NA	NA	.5647	.4353
DSCB	.2656	.5625	.1719	.2031	.3906	.4063	.3594	.3438	.2969	.4063	.4063	.1875	NA	NA	NA	.5385	.4615
DSCC	.2727	.4091	.3182	.2500	.3636	.3864	.2727	.3409	.3864	.2727	.4091	.3182	NA	NA	NA	.2500	.7500
OCA	.3298	.4894	.1809	.2872	.3830	.3404	.3511	.3298	.3191	.4574	.3830	.1596	.5106	.3723	.1170	NA	NA
OCB	.2400	.5700	.1900	.2100	.4100	.3700	.3400	.3900	.2700	.3100	.4500	.2400	.3700	.3000	.3300	NA	NA

TABLE V. Averaged relationship matrix for pairs of dark lineation characteristics. In this table, the two matching values for each characteristic pair in Table IV (on opposing sides of the unsymmetrical matrix) have been averaged to obtain the most reliable single matching value.

	SCA	SCB	SCC	BCA	BCB	BCC	ACA	ACB	ACC	DCA	DCB	DCC	DSCA	DSCB	DSCC	OCA	OCB
SCA	NA	NA	NA	.7608	.2194	.0327	.1656	.3409	.4325	.4464	.2595	.2191	.3893	.2874	.2455	.4467	.3382
SCB	NA	NA	NA	.1379	.6774	.4131	.4328	.4818	.3734	.4465	.5095	.3190	.5177	.4577	.2928	.4680	.5617
SCC	NA	NA	NA	.0000	.0614	.6975	.4698	.1893	.1141	.1452	.3611	.2939	.2175	.2388	.3536	.3266	.3589
BCA				NA	NA	NA	.1967	.2459	.4450	.3799	.2821	.2092	.3912	.2370	.2396	.4249	.3238
BCB				NA	NA	NA	.2949	.4391	.3567	.3895	.4208	.2716	.4362	.3598	.2871	.4253	.4713
BCC				NA	NA	NA	.5148	.3454	.1618	.3101	.4160	.3211	.3414	.3916	.3164	.4021	.4531
ACA							NA	NA	NA	.1002	.4091	.6085	.4271	.3514	.2259	.4218	.4238
ACB							NA	NA	NA	.4058	.4798	.0998	.4298	.3291	.2776	.3864	.4736
ACC							NA	NA	NA	.5838	.2266	.0870	.2962	.3181	.3450	.4228	.3719
DCA										NA	NA	NA	.4457	.3813	.2186	.5193	.3645
DCB										NA	NA	NA	.4461	.3637	.3157	.4137	.5028
DCC										NA	NA	NA	.2431	.2476	.3386	.2721	.4277
DSCA													NA	NA	NA	.5377	.4027
DSCB													NA	NA	NA	.4554	.3808
DSCC													NA	NA	NA	.1835	.5400
OCA																NA	NA
OCB																NA	NA

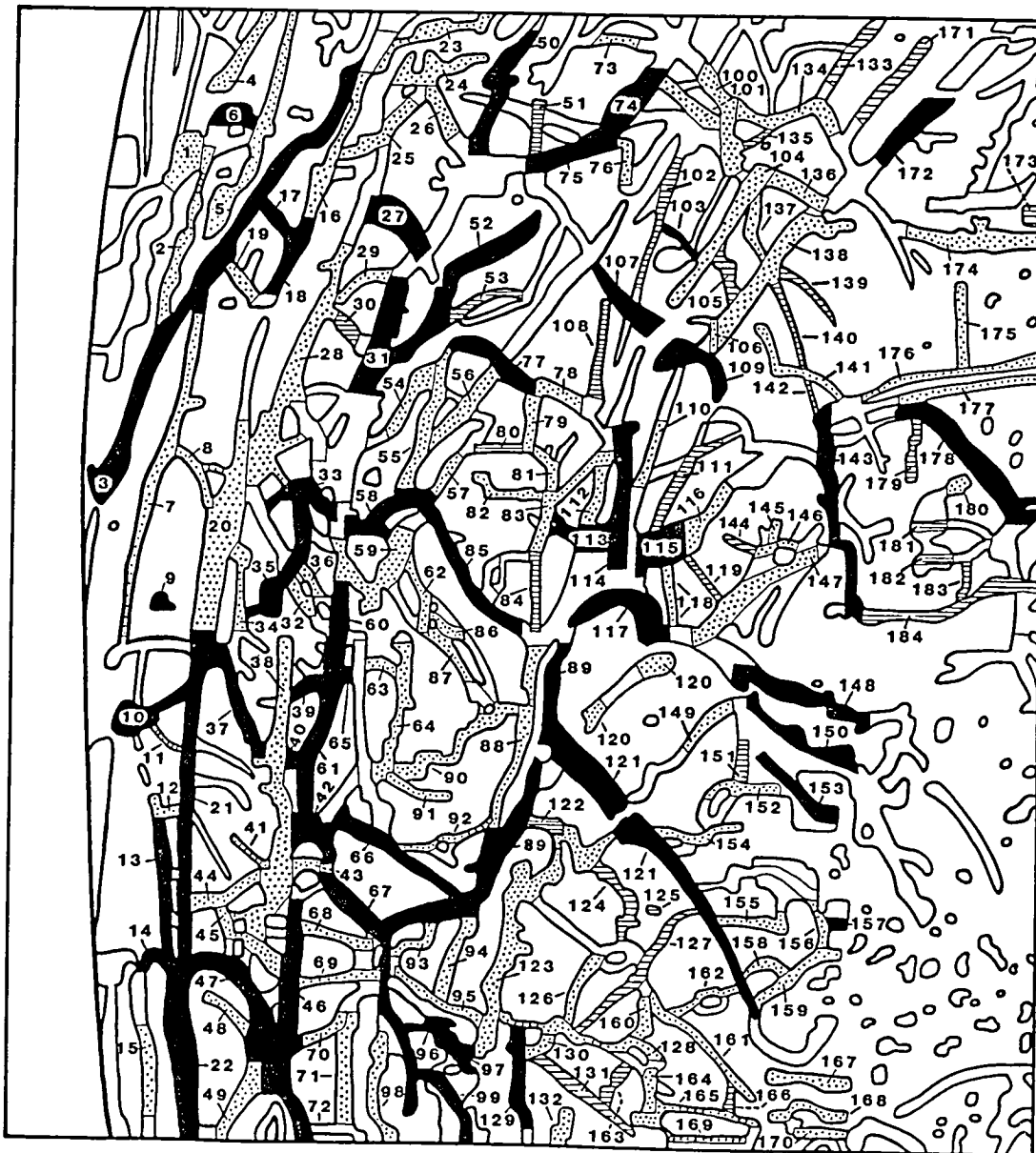


FIGURE 8. Spectral classification map and associated key for 184 of the 193 dark lineation (DL) segments in the DL study area. The spectral classes are defined by the amount of orange relative spectral reflectance (as compared to blue and violet rel%'s) of DL segments, and are the same as those used in Table II; solid black DL's are in spectral class A, stippled DL's are in class B, and striped DL's are in class C.

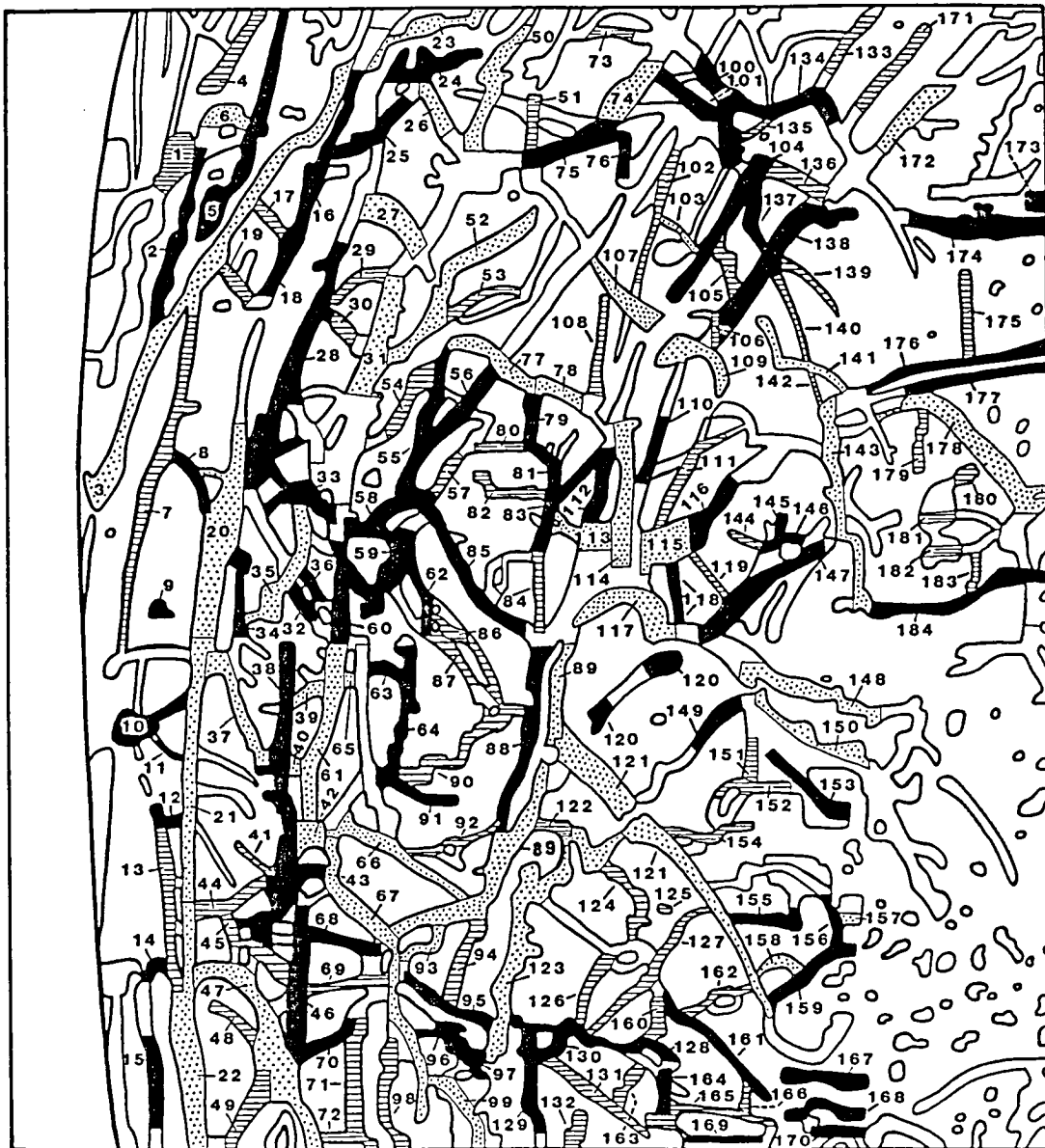


FIGURE 9. Local brightness classification map and associated key for 184 of the 193 dark lineation (DL) segments in the DL study area. The local brightness classification of a DL segment is made relative to other DL segments in the area, not the surrounding plains. Stippled DL's are in local brightness class A, solid black DL's are in class B, and striped DL's are in class C; classifications assigned are the same as those presented in Table II.

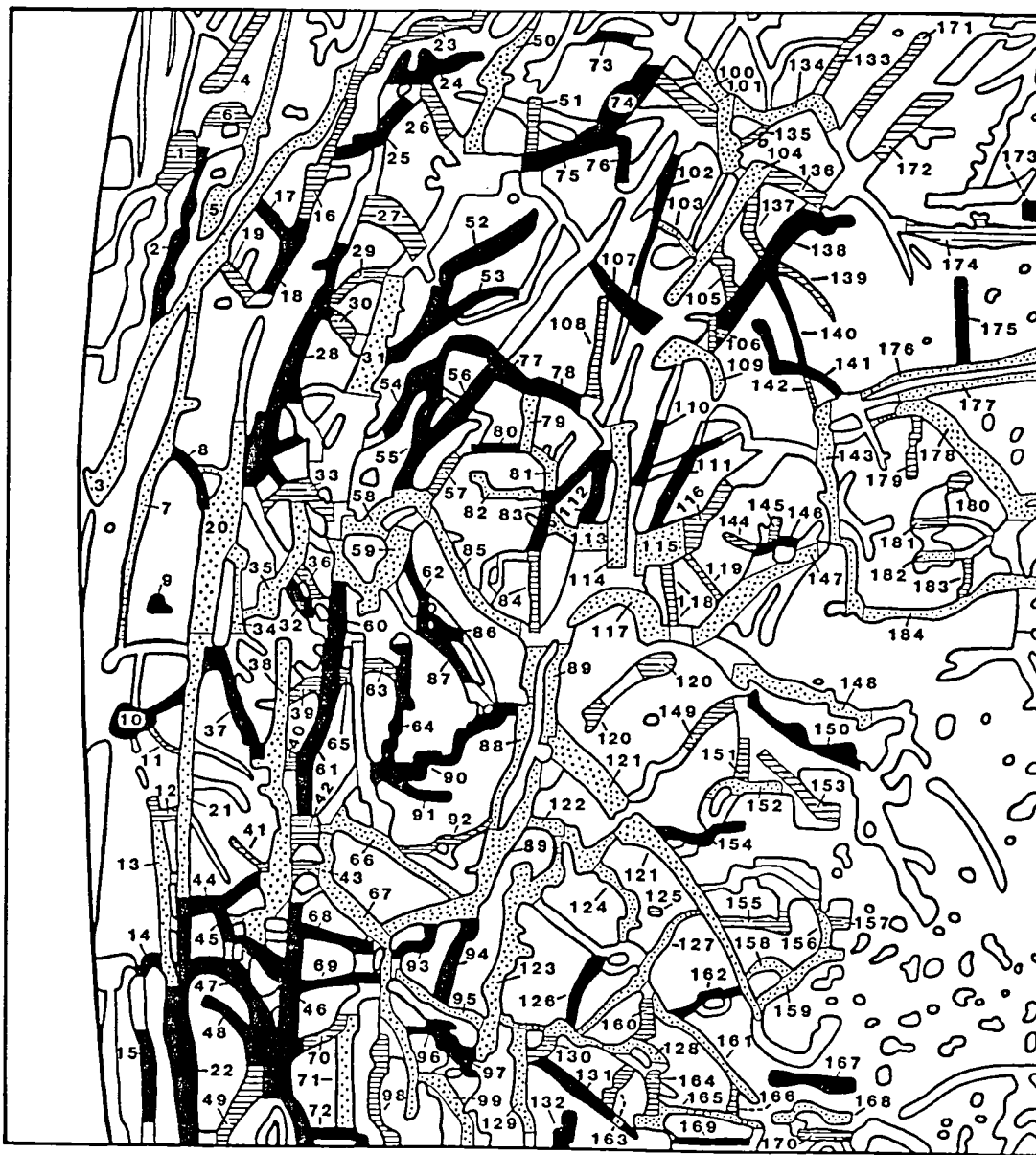


FIGURE 10. CDF area (i.e., degree of compositional variation) classification map and associated key for 184 of the 193 dark lineation (DL) segments in the DL study area. Striped DL's are in CDF area class A, solid black DL's are in class B, and stippled DL's are in class C; classifications assigned are the same as those presented in Table II.

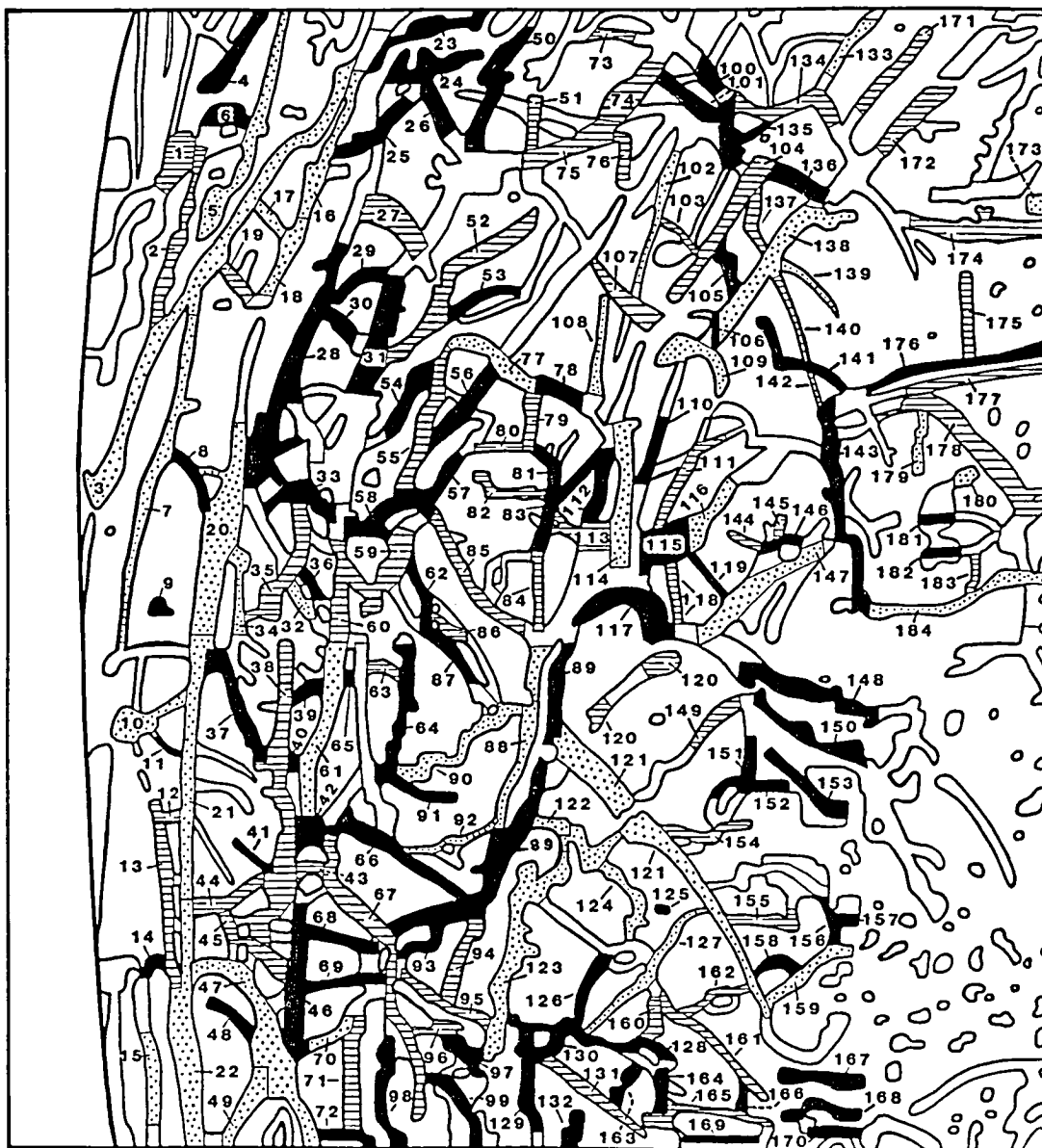


FIGURE 11. Classification map and associated key for 184 of the 193 dark lineation (DL) segments in the DL study area based on the degree of dispersion of data points in DL CDF's. The degree of data point dispersion classification is related to the frequency of compositional subunits in a DL segment, which is explained in Table III. Solid black DL's are in dispersion class A, striped DL's are in class B, and stippled DL's are in class C; classifications assigned are the same as those presented in Table II.

PLAINS SURROUNDING DARK LINEATIONS

Valuable information about the history of the dark lineation study area can be obtained by defining the spectral properties of both the dark lineations and the encompassing plains. Thirty-five data points were taken of the plains unit, dispersed over the northern half of the lineation study area, in orange, blue, and violet. The criterion used for selecting plains data points was to find the locally brightest DN's within several inter-lineation plains areas. This was assumed to represent the purest plains material, and also allowed compensation for image misregistration. The sampling locations for the plains data points are shown in Figure 12. From these multispectral data points a ternary diagram plot of relative spectral reflectance was generated, which is depicted in Appendix C. By plotting on the same reference ternary diagram it is possible to directly compare the spectral characteristics of the plains unit with the dark lineation unit, including the spectral variations amongst the 193 dark lineation segments. This will be presented in the section of this thesis immediately following.

INTERPRETATION OF RESULTS

Having presented all results for the dark lineations and encompassing plains, it is now possible to make interpretations of them in an integrated manner. The most obvious new finding is a gradational change in relative spectral reflectance properties between individual dark lineations within the dark lineation suite. This is indicated in part



FIGURE 12. Map depicting locations of data points used in plotting relative spectral reflectances of the plains in the dark lineation (DL) study area. Rel%'s are plotted in the reference ternary diagram in Appendix C. Note that four of the thirty-five data points are not shown in the map above; these are in the small part of the DL study area that falls to the right (east) of the area displayed.

by the definition of only a weak cluster of data points in the cumulative point count ternary diagram. A better indication that dark lineations differ slightly in their compositions but with no dark lineations having a composition distinctly different from all other dark lineations is found in the CDF's. It is possible to plot dark lineation CDF polygons in such a way that overlapping polygons stretch from very near the maximum orange rel% for all DL's to at or very near the minimum orange rel% with no gaps. Two of these "daisy chain" ternary diagrams are shown in Figure 13.

Coupled with the finding of gradational changes in dark lineation relative spectral reflectances are two other new discoveries. The first is that some of these dark lineations have relative spectral reflectances very similar to those of the plains unit within the dark lineation study area. The composition of these lineations and the plains must be very similar. The second discovery is actually a series of findings about the relationship between dark lineation spectral class and brightness. Referring back to Table V, it is noted that the three highest averaged percentages of matchings between pairs of characteristics for dark lineations occurs for: (1) high orange rel%/darkest dark lineations, (2) intermediate orange rel%/intermediate darkness lineations, and (3) low orange rel%/brightest dark lineations (i.e., bright as compared to the other dark lineations; these could also be thought of as faint dark lineations when compared to the surrounding plains). There is clearly a trend for the brightness of a dark lineation to in-

(A)

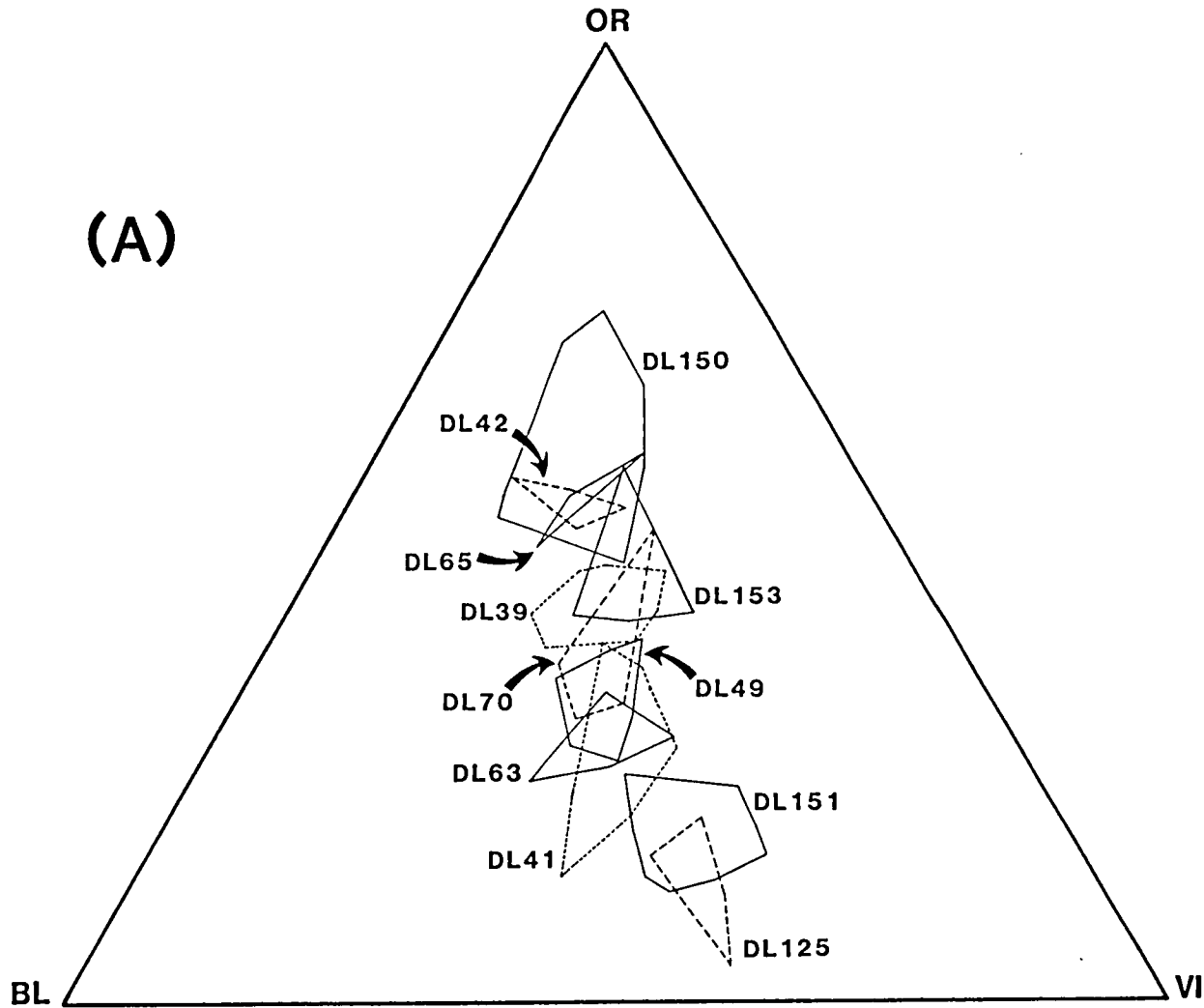


FIGURE 13. (A) and (B) each depict a "daisy-chain" diagram of linked dark lineation CDF's. Plots are within the reference ternary diagram; dashed lines of different lengths are used to provide an aid in delineation of individual CDF polygons.

(B)

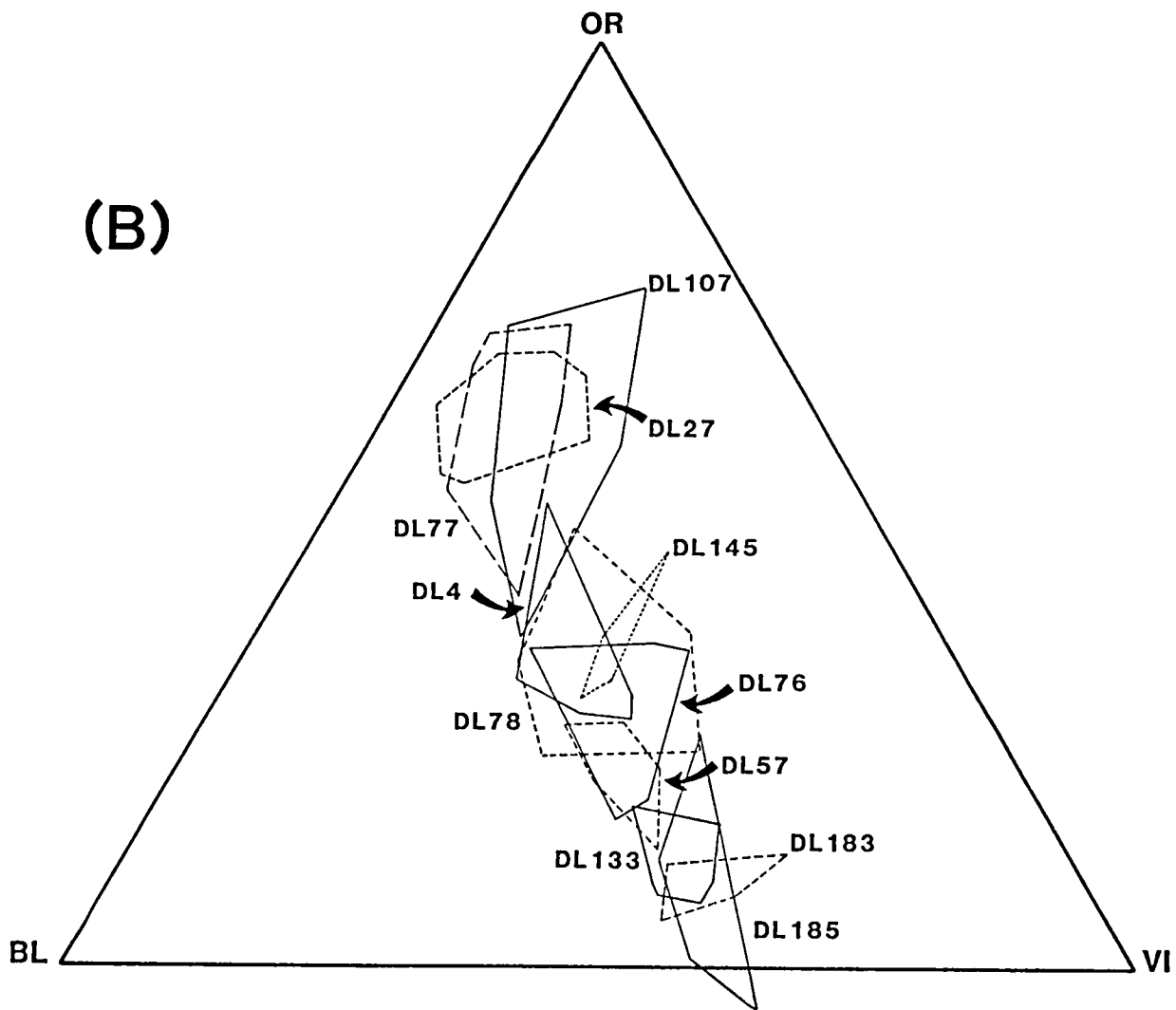


FIGURE 13. (Continued)

crease as the relative spectral reflectance in orange decreases. Thus, the albedo changes as the composition changes. Taken together with the cumulative point count ternary diagram data, the evidence points to the existence of only two fundamental spectral/compositional units in the dark lineation study area. One is the dark lineation unit, with relative spectral reflectance values of roughly 47 rel% orange, 32 rel% blue, and 21 rel% violet. The second fundamental unit is the plains unit, with relative spectral reflectance values of roughly 40 rel% orange, 34.5 rel% blue, and 25.5 rel% violet. All dark lineations with CDF's that fall between these extremes (which is nearly all of the dark lineations) are interpreted as having compositions of mixtures of dark lineation material and plains material. This invokes a linear mixing model wherein the position of a dark lineation's CDF on the reference ternary diagram is directly proportional to the ratio of dark lineation material to plains material in the lineation. The fact that the greatest number of dark lineations are clustered (albeit weakly) in the cumulative point count ternary diagram so far from both compositional end members simply reflects the fact that this particular proportion of dark lineation material to plains material is the most common composition of lineations in the study area.

The most logical and straightforward conclusion derived from these spectral/compositional findings is that plains material is progressively replacing dark lineation material in the lineations, causing them to become progressively brighter and shifting their relative spectral

reflectances to a lower orange, slightly higher blue, and higher violet area on the reference ternary diagram as the plains material replacement progresses. This is exciting because such material activity would be a resurfacing mechanism for Europa, something that has been searched for since the finding of an extreme lack of craters on Europa (Smith et al., 1979b). The gradational variation in relative spectral reflectances among the dark lineations and the relationship between lineation brightness and CDF spectral position in the reference ternary diagrams provide clues as to the nature of the resurfacing mechanism, especially when evaluated in conjunction with a possible European water vapor/frost eruption plume studied in Voyager imagery by Cook et al. (1982) and Helfenstein and Cook (1984). The very smooth gradation of point counts in the dark lineation cumulative point count ternary diagram is indicative of a mode of plains material emplacement in which very thin and relatively uniform layers of plains material are laid over the dark lineation material. This would gradually shift the spectral position of a dark lineation's CDF from the dark lineation material location in the upper region of the reference ternary diagram to the plains material location in the lower region. Plotting dark lineations in various stages of plains material burial would result in CDF's scattered along the entire path between the two compositional end members, generating the cumulative data point distribution seen.

The thin layer plains resurfacing model is consistent with a water vapor/frost plume mechanism for spreading thin layers of plains material

over large areas of Europa's surface. An examination of dark lineation DN's in pixel printouts disclosed that lineations which are faint compared to the surrounding plains are faint along their entire length, with the ends of some of them being ill-defined due to a gradually decreasing contrast between lineation and plains over the distance covered by a few pixels. Similarly, boldly dark lineations tend to be very dark along their entire length, with some lessening of contrast with the surrounding plains occurring at the ends of some of these lineations. In no class of dark lineations are there significant examples of lineations possessing a geomorphology of alternating patches of faint and bold dark lineation material (not included in this definition are chains of widely-spaced patches of mottled terrain in which patches appear to be separated by pure plains material). These facts argue against resurfacing via numerous small extrusion sites where liquid water (or liquid water containing a small amount of silicate material) erupts in a manner analogous to lava. The facts do support a resurfacing model in which a relatively small number of extrusion sites spread water or water plus minor silicate material via eruption plumes consisting of water vapor and/or frost particles. The number of water extrusion sites that could exist in this area of Europa is unclear, but relatively few are necessary compared to the requirements of a liquid water lava model. This conclusion is based on the spectral uniformity of faint dark lineations along their length, which infers that plume material has been deposited uniformly over an entire lineation. This

uniformity could best be attributed to deposition from a single water vapor/frost plume, whereas several liquid water eruption sites would be necessary to give an entire dark lineation a fainter appearance. The observation that many lineations become progressively fainter towards one or both ends could be due to the original fracturing mechanism, where a dark lineation-generating fracture was open and clear in the center, which allowed dark lineation material to freely intrude, but was ill-developed at an end allowing less dark material to intrude and giving that part of the lineation a fainter appearance. A single plume would probably resurface a large area containing several dark lineations, and thus an eruption site would not have to exist in every dark lineation. A plume site would not have to be within a dark lineation at all, but lineations are obvious choices because, if they are formed by fracturing as most researchers believe (e.g., Smith et al., 1979b; Helfenstein and Parmentier, 1980; Pieri, 1981), they may very well be the points of greatest weakness in Europa's present crust. Indeed, Lucchitta et al. (1981) proposed that older fracture/strain pattern reactivation is evidenced in lineation patterns currently seen on Europa, including the dark lineations in this project's study area.

The possible water vapor/frost plume that has been found on a Voyager image of Europa and studied by Cook, et al. (1982) and Helfenstein and Cook (1984) fits very well the requirements for a resurfacing mechanism imposed by the spectral and albedo discoveries previously described for the dark lineations. Although its position (approx-

mately -31 Lat., 335 Long.) is nowhere near the study area, its association with an anomalously bright region on Europa agrees with the dark lineation brightening model advanced in this section. The transient nature of the proposed plume lends support to the concept that active plume sites could exist in the study area but would not have to have been erupting at the time the Voyager spacecraft imaged that portion of Europa. Of course, plume sites would not have to be presently active in the study area if the degree of resurfacing observed had taken place in the past.

There are several conditions which must be met in order for the plume resurfacing proposal to be plausible. The material being spread via the plumes must match plains material in both spectral and brightness properties. The discovery that a large percentage of Europa's surface is covered by water frost or ice (Pilcher et al., 1972) plus the knowledge that the plains unit is the brightest geologic unit on Europa supports a model wherein water containing very little or no silicate contamination is driven from a subsurface source to the surface, where it forms a vapor/frost particle plume. The existence of liquid water in Europa is highly uncertain and is in fact not favored by Cassen et al. (1980) in their evaluation of tidal heating plus internal heat transport. Finnerty et al. (1981), however, proposed that a region of convecting upwelling may have been responsible for causing the fracturing that became the dark lineations at the present anti-Jovian point (0° Latitude, 180° Longitude). Such an upwelling, possibly in the form

of a mantle plume, would concentrate more heat than average in this section of Europa and, because the anti-Jovian point is extremely close to the northeast corner of the dark lineation study area, could provide a source of liquid water for resurfacing in the study area that may not exist for other places on Europa's surface. An alternative source of liquid water could be a mechanism analogous to partial melting processes that generate magmas in the Earth's crust.

OTHER DARK LINEATION PROPERTIES

The pixel mappings and ternary diagrams of the 193 dark lineation segments plus surrounding plains contain a wealth of information about them. Besides the relative spectral reflectance CDF positions in the reference ternary diagram and their daisy-chain gradational distribution, and the spectral/brightness relationships used to develop the plains resurfacing model, all of the other dark lineation characteristics assessed provided useful new information on Europa's dark lineations. A convenient standard which can be utilized to compare with individual dark lineations is the concept of the average dark lineation. This imaginary lineation was derived by averaging each property by all 193 lineations, creating the set of characteristics displayed in Table VI.

The finding for the degree of dispersion is interesting and revelatory when combined with an examination of the profiled dark lineations on the pixel printout maps. The fact that the average lineation possesses a slight clustering of data points in its ternary diagram CDF is

TABLE VI. The Average Dark Lineation.

1) Number of Points:	16.363
2) CDF Area:	495.466 Area Units
3) CDF Point Density:	3.303 Points/100 Area Units (Using Above Two Statistics)
	4.305 Points/100 Area Units (Mean of all 193 DL CDF Point Densities)
4) Spectral Class:	(B) Intermediate OR Re1%
5) Brightness Class:	(B) Intermediate Darkness
6) Degree of Dispersion:	Slightly Clustered (Not Perfectly Dispersed)

due to the continued sampling of lineation DN's when the feature begins to lose contrast with the surrounding plains. These fainter DN's produce significant spectral/compositional shifts from the darker parts of the lineation. Thus, the dark portion of the lineation appears to form a CDF cluster while the data points of the fainter portion almost appear to be statistical outliers. Certainly, some highly displaced data points could be legitimate outliers due to inaccurate DN values caused by Voyager vidicon dark current, dropouts/image processing artifacts, etc., but most displaced points represent actual major compositional shifts. Some of these appear to be a consequence of incomplete dark lineation material intrusion or incomplete plains material replacement in dark lineations. This manifestation is important because it affects not only dispersion classifications but also CDF areas and CDF point densities for dark lineations.

The characteristic pair matching matrix that sought to find relationships between all possible pairings of dark lineation properties provides a great deal of insight into the nature of the lineations. If lineations are uniformly distributed in all three classes of each characteristic (two classes for lineation orientation), the percentage of matches for each characteristic pair would be expected to be 0.3333 (0.500 for each pair containing a lineation orientation class). Based on these expectations, any characteristic pairs with matching percentages significantly above 0.3333 (0.500 for pairs with an orientation class) indicate a significant positive relationship between the prop-

erties and anything significantly below the expectations are indicative of a significant negative relationship. Average matching values of 0.500 (0.7500 for orientation class pairs) were chosen as the lower threshold for defining positive relationships and 0.1667 (0.2500 for orientation class pairs) as the upper threshold for defining negative relationships. Table VII lists and ranks the characteristic pairs found to be related both positively and negatively in the pair matching matrix. Not only do the large positive relationships for SCA/BCA (.7608), SCB/BCB (.6774), and SCC/BCC (.6975) provide some of the evidence for progressive plains unit material replacement of dark lineation material, but the very low negative relationships for SCC/BCA (.0000), SCA/BCC (.0327), and SCC/BCB (.0614), and the somewhat low negative relationship for SCB/BCA (.1379) further support the validity of plains material resurfacing of dark lineations. This is because the characteristic pairs for which very low matching values were found would have upset or even disproven the progressive resurfacing model if they had been found to possess high matching values. Finding negative relationships for pairs of properties is important because it indicates what the dark lineations definitely are not, just as positive relationships reveal what they definitely are.

The relationship between the number of data points comprising a dark lineation segment and its CDF area and between number of data points and CDF point density were treated as special cases because whether or not significant positive or negative relationships were found

TABLE VII. (A) Positive relationships (in descending order) and (B) negative relationships (in ascending order) found for dark lamination characteristic pairs, taken from averaged matching values listed in Table V. The meanings of most of these relationships are discussed in the text. Acronyms are defined in Table I.

(A)	<u>CHARACTERISTIC PAIR</u>	<u>AVERAGED MATCHING VALUE</u>
1)	SCA/BCA	.7608
2)	SCC/BCC	.6975
3)	SCB/BCB	.6774
4)	ACA/DCC	.6085
5)	ACC/DCA	.5838
6)	SCB/DSCA	.5177
7)	BCC/ACA	.5148
8)	SCB/DCB	.5095

(B)	<u>CHARACTERISTIC PAIR</u>	<u>AVERAGED MATCHING VALUE</u>
1)	SCC/BCA	.0000
2)	SCA/BCC	.0327
3)	SCC/BCB	.0614
4)	ACC/DCC	.0870
5)	ACB/DCC	.0998
6)	ACA/DCA	.1002
7)	SCC/ACC	.1141
8)	SCB/BCA	.1379
9)	SCC/DCA	.1452
10)	BCC/ACC	.1618
11)	SCA/ACA	.1656
12)	DSCC/OCA	.1835

would indicate if a sufficient number of data points were taken for each lineation to accurately assess the compositional variation of the feature. Individual pair matching matrices for these characteristics are presented in Table VIII and a summary of the matrix results are listed in Table IX. The results show clearly that dark lineations with a small number of data points tend to plot with small CDF areas and high point densities, and almost never plot with large CDF areas and/or low point densities. As the number of data points per lineation grows, there is a strong preference for the CDF area to grow proportionately and for a corresponding decrease in CDF point density to accompany it. Therefore, most of the dark lineations with a large number of data points plot with a large CDF area and low CDF point density. Although it is possible that the short dark lineations (most of which are of Type 5 in the lineation classification system of Pieri, 1981) could possess different spectral properties than the longer dark lineations, it is more likely that the small numbers of data points for short lineations are inadequate to sample the full range of spectral/compositional variation present in the features. It is not precisely clear if the CDF areas of dark lineations with large numbers of data points have captured all of the spectral variation present in the lineations, but it appears that they have. It is curious as to exactly why the shortest dark lineations possess the highest CDF point densities, but it may be that in some cases composition changes as a function of dark lineation length.

The net result of these findings is that short dark lineation seg-

TABLE VIII. Averaged matching values between (a) number of data points per dark lineation and area per corresponding CDF, and (b) number of data points per dark lineation and density of data points per corresponding CDF. Class acronyms and ranges follow those defined in Table I.

(a)	ACA	ACB	ACC
PCA	.7347	.4381	.1864
PCB	.0820	.4339	.4286
PCC	.0000	.1444	.5520

(b)	DCA	DCB	DCC
PCA	.5168	.4541	.4302
PCB	.3945	.3775	.1305
PCC	.0572	.3629	.2765

TABLE IXa. Positive characteristic pair relationships amongst DL number of data points, CDF area, and CDF point density. Acronyms follow those defined in Table I.

POSITIVE RELATIONSHIPS (In Descending Order)

Characteristic Pair	Pair Matching Value	Literal Meaning DL's with a:
1) PCA/ACA	.7347	small number of data points have small CDF areas.
2) ACA/DCC	.6085	small CDF areas have high CDF point densities.
3) ACC/DCA	.5838	large CDF areas have low CDF point densities.
4) PCC/ACC	.5520	large number of data points have large CDF areas.
5) PCA/DCA	.5168	small number of data points have low CDF point densities.*

*The finding that DL's with a small number of data points have low CDF point densities is in apparent contradiction to numbers 1 and 2 of the positive relationships. It is probable that positive relationship number 5 is not as correct as 1 and 2, since its matching value of .5168 is very near the lower cutoff value of .5000 for positive relationships; also, there are relatively large matching values between PCA and all three of the CDF point density classes (i.e., DCA, DCB, DCC) -- refer to Table V to confirm this.

TABLE IXb. Negative characteristic pair relationships amongst DL number of data points, CDF area, and CDF point density. Acronyms follow those defined in Table I.

NEGATIVE RELATIONSHIPS (In Ascending Order)

Characteristic Pair	Pair Matching Value	Literal Meaning DL's With a:
1) PCC/ACA	.0000	large number of data points never have small CDF areas.
2) PCC/DCA	.0572	large number of data points do not have low CDF point densities.
3) PCB/ACA	.0820	intermediate number of data points do not have small CDF areas.
4) ACC/DCC	.0870	large CDF areas do not have high CDF point densities.
5) ACB/DCC	.0998	intermediate CDF areas do not have high CDF point densities.
6) ACA/DCA	.1002	small CDF areas do not have low CDF point densities.
7) PCB/DCC	.1305	intermediate number of data points do not have high CDF point densities.
8) PCC/ACB	.1444	large number of data points do not have intermediate CDF areas.

ments (i.e., those composed of 15 or less data points) should be regarded as suspicious and probably inaccurate in terms of CDF area and CDF point density, although still accurate with regard to spectral, brightness, degree of dispersion, and orientation classifications. Dark lineation segments with an intermediate number of data points (i.e., 16-30) should be considered to have possibly suspect CDF areas and point densities, with those characteristics becoming more reliable in the upper part of the data point number range. Lineation segments of more than 30 data points can basically be regarded as accurate in terms of CDF areas and point densities, with perhaps some slight suspicion for lineations in the lower portion of the data point number range.

The remaining positive and negative relationships in Table VII provide information on the nature of the material that constitutes dark lineations in the study area and how the proposed water vapor/frost plumes may be modifying it. Some of these significant characteristic pairings contain classes of CDF areas and point densities and thus the reliability of these relationships is uncertain. Still, the fact that three different pair matching values involving two different lineation properties coupled with CDF area and point density classes point to the same conclusion about dark lineation material lends some degree of credibility to data obtained from the smallest CDF area class. These pairings, which were found to have negative relationships, and their matching values are SCC/ACC (.1141), SCC/DCA (.1452), and BCC/ACC (.1618). The fact that spectral class C and brightness class C were

found to correlate with each other very strongly in the dark lineations (matching value of .6975) leads to the conclusion that they describe the same compositional unit. The negative relationship between SCC and ACC literally means that dark lineations composed of low orange relative spectral reflectance material do not possess the largest-area CDF's. The interpretation of this is that low orange rel% material is not the most impure material observed in dark lineations in the study area. Similarly, the negative relationship between SCC and DCA promotes the same interpretation because the low CDF point densities represented by the DCA class also would have meant the most impure material. The negative relationship between BCC and ACC falls into the same category, except that this time it says that the brightest dark lineation material is not the most impure dark lineation material. This latter conclusion gives still further support to the proposal that the brightest dark lineation material is predominantly transported plains material, because the plains in the study area show much more spectral/compositional purity than the dark lineation suite as a whole.

There is additionally a positive relationship that can be used in conjunction with the negative relationships just cited. The percentage of matches between BCC and ACA was found to be 0.5148. This shows that the brightest dark lineations (faintest compared to the surrounding plains) possess the smallest variation in composition along their length. Coordinating this finding with those from the negative relationships just detailed, the discovery is made that not only is the high

albedo, low orange rel% material that comprises bright dark lineations not the most impure class of dark lineation material, it is in fact the purest material found in dark lineations in the study area. Contrasting with this is the low matching value between SCA and ACA (.1656), which reveals that high-orange rel% dark lineations do not possess the smallest amount of compositional variation, hence high-orange rel% dark lineation material is comparatively impure. Also, the positive relationship matching value of 0.5095 between SCB and DCB indicates that intermediate-orange rel% dark lineations have an intermediate density of data points in their CDF's. The exact interpretation for this characteristic pair is not as clear as for others cited, but it may be that lineations composed of intermediate-orange rel% dark material have an intermediate degree of compositional purity.

Taken together, these relationships amongst the properties of dark lineations in the study area allow for the construction of a detailed model of water plume modification/resurfacing of these features. First of all, although water could initially be ejected from a plume vent in the form of liquid or vapor, the sharp temperature drop would cause the water in the plume to return to the surface in the form of frost particles in a manner somewhat like that of falling snow. The original dark lineation material, as it is when first emplaced by intrusion, is in its darkest state. It either possesses a much higher degree of compositional variation than the surrounding plains material or even the most unaltered dark lineations in the study area have some small amount

of plains material contamination. Plume material spectrally identical to plains material is dispersed over a large area of Europa's surface per plume in the form of frost particles. Each plume would lay down fresh plains material in a circular pattern perhaps several hundred kilometers across. Frost particles, possibly containing small amounts of silicate or other contamination, are deposited in a thin, uniform layer over the entire area of plume influence, including dark lineations. As the frost layer builds up, it changes the characteristics of dark lineations slowly and gradationally. A dark lineation will become both progressively brighter and spectrally more similar to plains material, most noticeably by a progressive decrease in its orange relative spectral reflectance, as the deposition continues. It is interesting to note that a resurfacing mechanism in which frost particles are deposited on the surface is compatible with the conclusion from Earth-based studies by Clark (1980) that Europa's surface could consist of frost on ice.

The high matching percentage between SCB and DSCA (0.5177) indicates that there is a real connection between these properties in dark lineations in the study area. The literal interpretation is that dark lineations with an intermediate orange relative spectral reflectance have the best dispersion of data points in their CDF's. What this corresponds to in terms of dark lineation formation/evolution seems to be related more with the proposed resurfacing process than the actual formation of the lineation. Assuming that all dark lineations origin-

ally form with high-orange re% material, then by approximately midway through the resurfacing process the lineation has attained the highest degree of compositional diversity between its compositional extremes. This does not necessarily mean that composition changes uniformly in a contiguous sequence along the length of the lineation, but it does mean that there is a well-dispersed range of compositions throughout the lineation as a whole. Such compositional diversity may be related to the fact that different parts of a dark lineation are different distances from a water frost plume source, thus receiving plains material frost at slightly different rates. Different parts of the lineation then might be resurfaced at slightly different rates, resulting in a spectrum of slightly different compositions until such time as resurfacing material thicknesses became sufficient over the entire lineation to mask the spectral properties of the original dark lineation material.

If the water vapor/frost plume resurfacing model is correct, there are several important consequences arising from it. Taken to its logical extreme, frost particle deposition would eventually completely bury a dark lineation, making its location indistinguishable from the surrounding plains. A depositional layer would not need to be very deep to completely mask the albedo and spectral signatures of the original dark lineation material; certainly less than a meter, and perhaps only a few centimeters or millimeters, would be sufficient provided all exposures of dark lineation material were covered. In fact, it is very difficult to imagine water plumes creating thick frost deposits on the order of

hundreds of meters or kilometers, especially when considering that compaction and annealing of frost particles will reduce frost layer thickness as deposits build up. Because of this, it is highly unlikely that plume resurfacing could be sufficient to bury large craters on Europa. This mechanism, then, fails to account for the extreme lack of craters on this satellite. The remaining viable possibilities for crater disappearance are viscous relaxation of the icy surface (a strong candidate) and liquid water "magma" eruption (see Results and Discussion, Agenor Linea and Environs).

The gradational, apparently uniform, rate of water frost plume resurfacing of dark lineations makes it tempting to try to establish an age classification system for the lineations in the study area. Efforts to do so, however, are complicated by several factors that tend to defeat the intent of the classification system. If an age classification system could be constructed, it would basically correspond to the spectral classification map shown in Figure 8, with the high-orange rel% (generally lowest albedo) lineations being the youngest (i.e., least resurfaced) and the low-orange rel% (generally highest albedo) lineations being the oldest (i.e., most resurfaced yet still recognizable as lineations). Several considerations complicate this. (1) The system would be based on the assumption that dark lineation material of the same composition and albedo was emplaced in all of the lineations at the time of their origin. This assumption may not be far from the truth in light of the overall homogeneity of the light and dark materials on Europa's

surface. (2) The age classification system assumes that resurfacing has been uniform over the entire study area in terms of amount of plains material deposited, composition of deposits, and length of time of deposition. This becomes difficult when more than one water vapor/frost plume is present, although in fairness only a few plumes would be needed to cover the study area and if a localized convection upwelling was responsible for the plumes, it probably would have activated them all simultaneously. (3) Frost particle deposition must be balanced against ion erosion/sulfur implantation. While this would tend to preserve relative ages in an area as small as the study area, it makes absolute age determination impossible at this stage of our understanding. There is also the possibility that some other method of dark lineation rejuvenation, such as fracture reactivation, could have preferentially overcome resurfacing for some lineations but not for others.

In spite of these complications, a modification of an age classification system can be constructed in an acceptable fashion. Rather than saying that the spectral classification system shown in visual form in Figure 8 is also an age classification system, it is more accurate to say that it is also an age-of-most-recent-exposure classification system. In this system, the same spectral class-to-age (of exposure) conversions apply as cited earlier. Such a system is still of use for determining relative age relationships between dark lineations in a localized area.

INDIVIDUAL DARK LINEATIONS OF MERIT

Having treated the study area dark lineations as a whole and as a collection of large groups, it is now worthwhile to look at individual lineations whose uniqueness merits special attention. Caution does need to be taken in the examination and interpretation of any surface feature on Europa in Voyager imagery which has spectral properties that differs significantly from all other similar features on Europa. The reason for this is because of the many sources of noise and false data in Voyager Europa imagery, including vidicon dark current, multispectral photometric effects, and computer processing artifacts (including improperly removed reseau marks in the images used in this thesis). Fortunately, these effects are all localized to some extent in Voyager imagery, so it is possible to test for their influence by searching for patterns or clumps of spectrally odd dark lineations. These are not apparent and, even though some aberrations in the spectral data certainly exist, the identification of spectrally unusual dark lineations is considered to be sound.

Table X lists the dark lineations of special interest and the categories to which they belong. The physical interpretation of each of these categories and their influences on/contributions to the models of Europa's surface developed thus far will be presented here. Categories 1 through 5 concern dark lineations whose range of relative spectral reflectance in one color is unusually narrow or wide compared to the ranges in the other two colors. This disproportionality is most easily

TABLE X. Dark lineations of special interest; OR = orange, BL = blue, VI = violet. Units for DL PROPERTIES mini-tables are the same as those defined in Table I.

<u>CATEGORY</u>	<u>DESCRIPTION/SUBDIVISION</u>	<u>DARK LINEATIONS IN CATEGORY/SUBDIVISION</u>
ATYPICAL COMPOSITION	1A) Unusually wide range of VI rel% compared to BL and OR rel%'s	(1) DL7 (2) DL157 (3) DL187
	1B) Unusually narrow range of VI rel% compared to BL and OR rel%'s	(1) DL45 (2) DL145 (3) DL173
	1C) Unusually narrow range of BL rel% compared to VI and OR rel%'s	(1) DL18 (2) DL20 (3) DL79 (4) DL83 (5) DL103 (6) DL179 (7) DL187
	1D) Large BL rel%'s, yet narrow range of BL rel%'s	(1) DL17
	1E) Unusually narrow range of OR rel% compared to BL and VI rel%'s	(1) DL157 (2) DL73

TABLE X. (Continued)

<u>CATEGORY</u>	<u>DESCRIPTION</u>	<u>DARK LINEATIONS/DL PROPERTIES (WHERE APPLICABLE)</u>			
			<u>AREA</u>	<u># PTS</u>	
HOMOGENOUS (NEAR-)PURE DL UNIT COMPOSITION	2) Large OR rel%'s with small CDF area	(1) DL27	290	12	
		(2) DL37	410	13	
NEAR-PURE PLAINS UNIT COMPOSITION	3) Minimum OR rel% signifi- cantly <40%	(1) DL173			
		(2) DL185			
VERY HOMOGENEOUS COMPOSITION	4) >5 points, small CDF area/ high point density	(1) DL49	125	15 B	12.000
		(2) DL101	100	11 B	11.000
		(3) DL105	125	10 C	8.000
		(4) DL116	80	8 B	10.000
		(5) DL120	165	16 B	9.697
		(6) DL133	105	9 C	8.571
		(7) DL137	105	10 B	9.524
		(8) DL149	120	10 B	8.333
		(9) DL181	30	7 C	23.333
WIDE COMPOSI- TIONAL RANGE	5) Very large CDF area	(1) DL7	1710		
		(2) DL121	1980		
		(3) DL134	1540		
		(4) DL148	1560		
		(5) DL178	1500		

TABLE X. (Continued)

<u>CATEGORY</u>	<u>DESCRIPTION</u>	<u>DARK LINEATIONS/DL PROPERTIES (WHERE APPLICABLE)</u>		
			<u>AREA</u>	<u># PTS</u>
UNIFORM PARTITIONING OF COMPOSITIONAL VARIATIONS	6) Very uniformly dispersed points within CDF	(1) DL50	1080	26
		(2) DL143	1260	43
DISTINCT COMPOSITIONAL SUBUNITS(?)	7) Very well-developed clusters of points within CDF's	(1) DL104		
		(2) DL108		
		(3) DL116		
		(4) DL147		
		(5) DL155		
		(6) DL184		
POSSIBLE FRACTURE REACTIVATION	8) Apparently a single DL with a sudden shift in DL width and DL spectral properties/composition	(1) DL77/DL78		

evident by comparing the shapes of the CDF's of these lineations to the typical shapes of CDF's for the rest of the dark lineation suite. The concept of what form the average CDF shape takes is based on the dark lineations in the study area only and may not exactly apply to all of Europa. The tendency for a dark lineation CDF to owe its shape to a large rel% range in orange compared to the rel%'s for blue and violet is so overwhelming that it is strongly believed to be valid for all of Europa's dark lineations. Divergence from this standard relationship between multispectral relative spectral reflectances corresponds to anomalous compositions and anomalous distributions of composition in dark lineations. Categories 1 through 5 in Table X show that anomalous dark lineation compositions fall into distinct groups, supporting the validity of their existence. Not much can be said about the actual meaning of individual anomalous CDF's. Specific minerals and ices cannot be determined from low-resolution Voyager multispectral and infrared data. Dark lineations possessing anomalous CDF's may have only a small fraction of their length composed of anomalous materials because only a few data points are necessary to drastically alter a CDF shape. Anomalous dark lineation areas may represent intrusion of subsurface material from different depths in Europa's crust than normal dark lineation material, or may simply be indicative of non-homogeneity of dark source material in Europa's outer crust. Alternatively, anomalies could be created by contamination from extraterrestrial sources (e.g., unusual micrometeoroid bombardment, atypical Io ejecta), but it is difficult to

conceptualize why such sources would contaminate some areas of lineations but not others.

It should be pointed out that the dark lineation classification system and the associated progressive plains resurfacing model is based on changes in orange relative spectral reflectance compared to blue rel% and violet rel%. This is a simplistic model and the actual changes in relative spectral properties that define different classes of dark lineations could be much more complex. If this is so, the definition of anomalous dark lineations would also change. The systems as defined in this thesis do work, however, and should be considered successful first-order approximations of Europa's dark lineation spectral hierarchy.

Other categories of unique dark lineations in Table X reveal still more facets of the form these features on Europa can take. Category 6 lists dark lineations owning CDF's with relatively small areas and having all of each CDF at high orange rel%'s. DL27 and DL37 are also very dark compared to the entire dark lineation suite. This combination of properties leads to the interpretation that DL27 and DL37 are composed of material that is both very pure dark lineation material and very homogeneous material. As such, they appear to represent the youngest, most unaltered exposures of dark lineation material. Being the "youngest" dark lineations could mean either that they represent the most recent original emplacements of dark lineation material within the study area on Europa or the most recent lineation rejuvenations in the area. Alternatively, it is possible that DL27 and DL37 are located in

areas that have experienced no resurfacing, but this is believed to be unlikely because none of the dark lineations around these show similar properties.

Category 7 shows dark lineations at the other spectral extreme, with DL173 and DL185 both having CDF's that dip below 40 orange rel%. DL173 falls within the intermediate brightness dark lineation class and DL185 is in the brightest class. These two lineations are thought to contain areas of the purest plains replacement material, though the whole lineations are not particularly homogeneous in their compositions.

In category 8 are listed dark lineations with more than five data points that have very small areas and therefore very high CDF point densities. This may not constitute a legitimate set of properties because, as was reported earlier, the relationship between number of data points and CDF area is suspicious, especially at low data point numbers. Still, it is not easy to explain why, as in the case of DL49, a dark lineation with 15 data points can have a CDF density of 12.000 points/100 area units unless its composition is very homogeneous. Another interesting factor that was previously pointed out in a different manner in the section on the relationship matrix is that all of the very small-area CDF's are in the intermediate-orange rel% and low-orange rel% spectral classes. No dark lineations are in the high-orange rel% class, which means that very dark lineation material is not as compositionally homogeneous as higher-albedo dark lineation material. This translates to a belief that the darkest lineations possess a small

amount of contamination from plains materials, but in a non-homogeneous pattern along the length of the lineation. Opposite this is the conclusion that brighter dark lineations sometimes are composed of a mixture of dark material and brighter plains resurfacing material in a very homogeneous fashion, which could be due to the thin layers of frost deposition from water plumes.

Category 9 counterpoints category 8 by listing dark lineations with extremely large CDF areas. Large areas are generated by large compositional variations along the length of the lineations, which, for the most part, can be related to large albedo changes within lineations. The relationship between albedo and orange relative spectral reflectance for points within individual lineations generally parallels that for the lineation suite as a whole. Large fractions of CDF areas can be attributed to contiguous sequences of five or more pixels corresponding to a particular brightness class for that part of the lineation. This seems to be saying that large sections of dark lineations have undergone either highly different mechanisms of origin or highly different modification processes since origin. More discussion of what possibilities could fit these constraints are found in a later section of this chapter that deals with DL121, the lineation with the largest CDF area of the 193 dark lineation segments in the suite.

In category 10 is listed dark lineations whose CDF's contain particularly well-dispersed data points. Dispersion of data points corresponds to uniformity of compositional variation. All dark lineations

show compositional variations (otherwise, their CDF's would each consist of a single point), but highly dispersed data points infer that no two pixels making up the lineation have the same composition. Such heterogeneity leads to the conclusion that some dynamic process has been associated with dark lineation formation, having caused disruption of dark material through mixing, either at depth before surficial emplacement or actually during emplacement. Mixing of dark material with extant plains material during lineation formation appears to be the most attractive hypothesis for generating the observed data point dispersion in ternary diagram plots. Less likely candidates are unusual variations in dark lineation resurfacing or some other post-formation modification process.

The counterpart of category 10 is category 11, which shows dark lineations which have very well-developed clusters of data points in their CDF's. The presence of a cluster is dependent on having some data points in the CDF being highly displaced from the others. This has been previously discussed in this chapter when the results of the relationship matrix were presented. A further point that should be added is that the presence of a CDF point cluster infers that a specific composition, with minor variations, makes up a large percentage of a dark lineation. If that composition made up the entire dark lineation, it would not plot in a CDF as a cluster but as a very small-area CDF as was presented in category 8. It is probable that some of the small-area CDF's in category 8 would have been classified as CDF's with well-

developed clusters in category 11 if their lineations had been profiled beyond their ends to a point where they had much less contrast with the surrounding plains.

Three dark lineations are sufficiently unique and clear-cut in their properties to warrant individual attention. DL121 is very prominent in both its geomorphic and spectral properties. This is the most classic wedge-shaped dark lineation evident in Voyager 2 imagery. DL121 is classified as a Type 5 lineament by Pieri (1981) and as a dark, wedge-shaped band by Lucchitta et al. (1981). In its northern, wider section, DL121 contains some of the lowest-albedo material observed on the entire surface of Europa. The nearly perfect wedge shape suggests that some limited sort of icy plate tectonic activity may have taken place there, involving rifting and associated plate rotation (Schenk and Seyfert, 1980; Lucchitta et al., 1981). Emplacement of dark lineation material appears to have occurred in the same style as for other types of dark lineations, except that wedge-shaped lineations (e.g., DL27, DL107, DL109, DL117) are darker than other types.

Figure 14 depicts a portion of the profiled DN's of DL121 from the Voyager 2 blue filter image (1198J2-001). Note that the profiled DN's of DL121 maintain generally the same brightness levels except where white lines and dark lineations of different albedoes intersect it. This situation changes at point A, where a general trend of increasing brightness of DL121 begins. Point B shows an increase in DN brightness where DL121 intersects a white line associated with DL149. If the

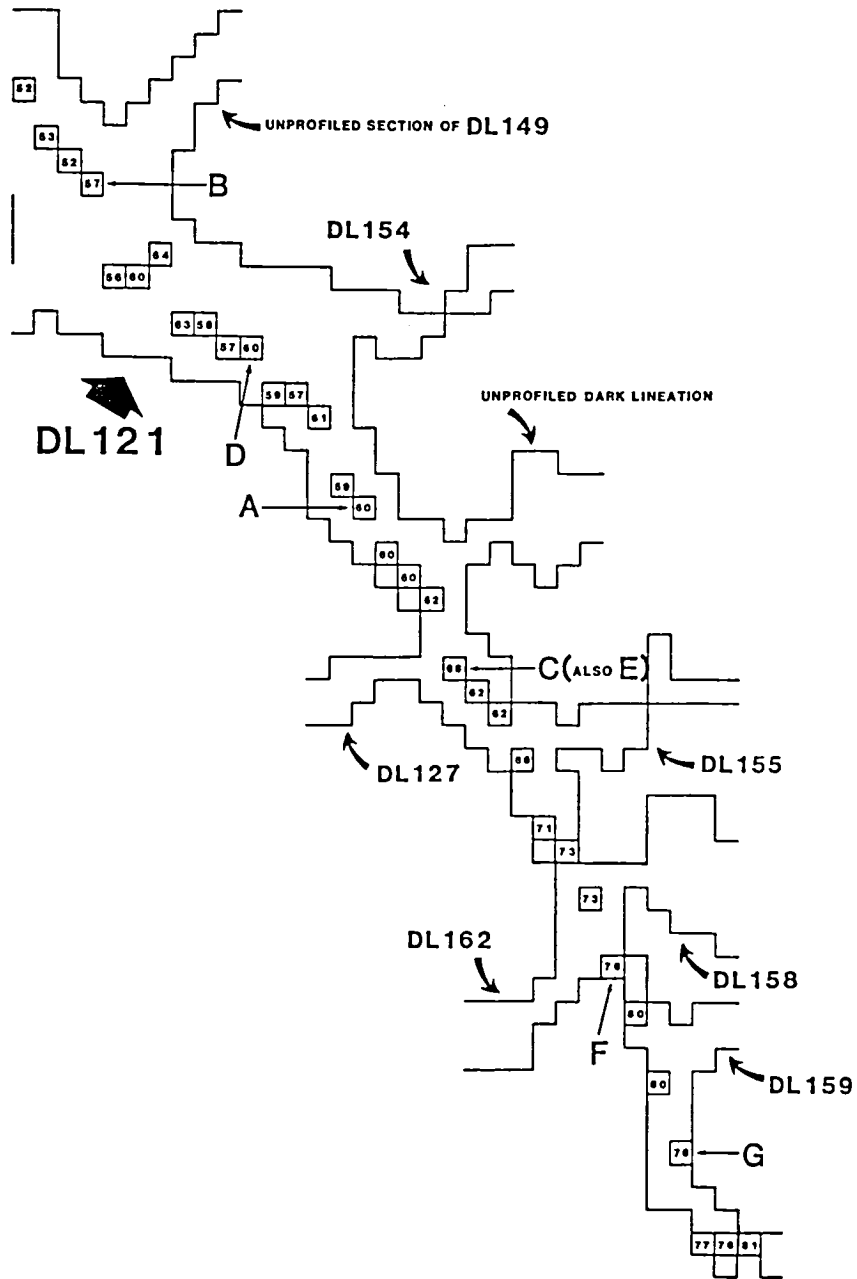


FIGURE 14. Map of the southern three-quarters of DL121. The edge of DL121 is outlined at single-pixel resolution, broken where other DL's intersect it. Outlined numbers in the interior of DL121 are profiled darkest pixels from the blue filter Voyager 2 image (1198J2-001) shown in their correct positions. Labeled pixels are points of interest that are explained in the text.

intersection area is considered to belong to both DL121 and the white line, it can be said that DL121 becomes brighter and the white line becomes darker there. At point C, a large permanent increase in brightness occurs. Other brighter dark lineations intersect DL121 at point D (DL154), point E (DL155), and point F (DL158). At all of these locations, the intersecting brighter dark lineations become darker while DL121 becomes brighter. DL121 changes in brightness less than the dark lineations intersecting it, however. Finally, at point G, the DN brightness trend begins to fluctuate as DL121 loses some of its contrast with the surrounding plains.

These observations add much to previous models of wedge-shaped dark lineations. Lucchitta et al. (1981) and Lucchitta and Soderblom (1982) suggested that the dark, wedge-shaped lineations (including DL121) are a very young class of dark lineations as seen in high-resolution Voyager imagery of Europa. They based this on the sharply defined edges of these features and their dominance when intersecting other features. The results of this thesis support the contention that DL121 (and other wedge-shaped dark lineations) are among the youngest dark lineations in the study area and probably all of Europa. In addition to the observations by Lucchitta and Soderblom (1982), this is based on the presence of very dark material in the northern part of DL121 which, according to models developed in this thesis, has probably undergone little or no plains material resurfacing. Also, detailed examination of pixel printouts shows that DL121 does not really truncate other dark lineations it

intersects, but interacts with them in a more complex way. As shown at points D, E, and F in Figure 14, brighter dark lineations are still identifiable where they intersect DL121, but their brightness is considerably reduced. This supports a model of material mixing between DL121 and the brighter dark lineations, because DL121 becomes brighter at intersection regions where the area can be considered to belong to both lineations. This complicates the establishment of age relationships between DL121 and the dark lineations intersecting it, so the relative age of DL121 is better indicated by other factors such as material darkness.

The sudden, large increase in brightness of DL121 shown at point C in Figure 14 is of great geomorphic significance. The region of higher albedo constitutes the tapered end of DL121, while the widest portion of the lineation's wedge shape holds the darkest material. There is a corresponding difference in relative spectral reflectance properties between the two sides of the lineation. Thus, the very dark material in the northern, wider part of DL121 is responsible for much of the higher orange rel%'s in its CDF and the brighter dark lineation material in the southern, tapered portion of DL121 has caused most of its data points to plot in the lowest orange rel% part of its CDF. This dichotomous albedo distribution is the reason why DL121 has the largest CDF area of any of the 193 profiled dark lineation segments. Its CDF covers 1980 area units with only 42 data points. This is impressive, since the dark lineation with the largest number of data points (DL3) has 57 points but

an area of only 1430 units and DL7, the lineation with the second-largest CDF area, has a CDF covering only 1710 area units.

Based on these observations, it can be said that the southern, brighter portion of DL121 differs from the northern portion in geomorphic, albedo, and spectral/compositional properties, and that the change between the two areas is abrupt. If the water vapor/frost plume resurfacing previously outlined is applied, certain problems arise. Any plume or plumes would have to have been sufficiently localized that they would have partially resurfaced the southern part of DL121, but left the northern part virtually untouched. This scale of plume resurfacing seems to be much smaller than that believed to be responsible for the spectral and albedo characteristics of other dark lineations in the study area. The sharp brightness division between the two parts of DL121 also seems inconsistent with a water frost plume origin. A more logical model for DL121 is that its tapered end represents a propagating fracture with the direction of tapering corresponding to the direction of fracture propagation. Under this model, the northern, wider portion of DL121 was the site of original fracturing. As the fracture propagated to the southeast, it grew wider at the top (northern) end, possibly by some limited form of icy plate rotation (Schenk and Seyfert, 1980). Intrusion of dark lineation material accompanied this phase of fracturing. Eventually, fracture propagation stopped. Fracturing was apparently reactivated at some later time, however, exploiting the crustal weakening created by the first phase of fracturing. It was

during this second phase that intrusion of somewhat brighter material occurred as fracture propagation continued toward the southeast. This model is similar in some respects to the two-phase hypothesis for formation of dark lineations with bright medial stripes (i.e., triple band structures) formulated by Finnerty et al. (1981). Both models are contingent on purer water being intruded/extruded during later episodes of fracturing than the dark material-entrained fluid believed to have formed the dark lineation network on Europa during earlier fracturing. In this model for DL121, however, the later fluid intrusion has to be only slightly higher in water content than the first. Both models also require reactivation of lineations' fractures, which represent zones of crustal weakness. The fulfillment of this latter requirement is supported by observations that entire sets of similarly-trending dark lineations appear to be reactivations of older lineations and stress patterns (Lucchitta et al., 1981; Lucchitta and Soderblom, 1982).

The other two dark lineation segments that merit individual attention (DL77 and DL78) appear to be one continuous lineation in Voyager 2 imagery. Figure 15 shows a portion of the dark lineation classification map that contains DL77 and DL78. There are several intriguing facets to this pair of features. They were first profiled and plotted on the orange/blue/violet ternary diagram as a single dark lineation. It was then noticed that the CDF could be split into two completely non-overlapping CDF's if the first 17 data points were assumed to constitute one dark lineation and points 18 through 30 to constitute a second dark

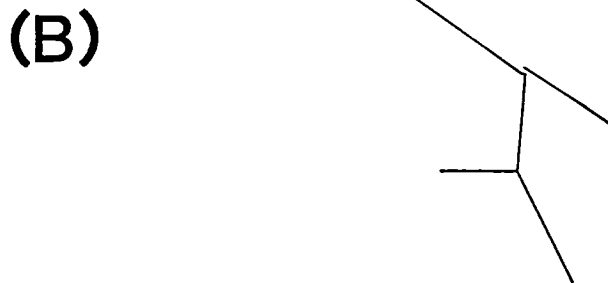
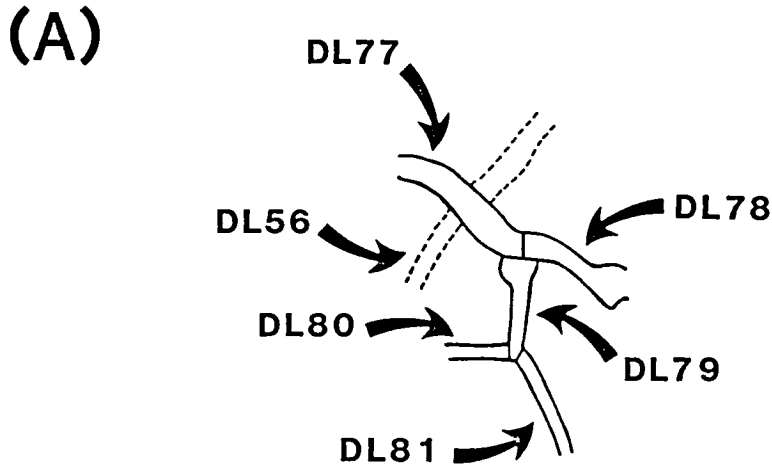


FIGURE 15. (A) Map of dark lineations DL77, DL78 and those immediately surrounding them. (B) Generalized trends of DL's 77, 78, 79, 80, and 81. Note that DL77 and DL78 are essentially parallel, with only a slight offset between them. Also, note that DL79, DL80, and DL81 form a triple junction. DL81 appears slightly different than it does in Figures 5, 8 - 11 because it was mapped from a different contrast enhancement in this figure than in the others.

lineation.

Going back to the pixel printouts on which these features were mapped, a significant brightness change was found to correspond exactly to the point of division identified by the two CDF's. As would be expected from the results of the relationship matrix, the darker of the two lineations (i.e., DL77) plots with significantly higher orange relative spectral reflectances than the brighter lineation (i.e., DL78). Thus, DL77 falls into spectral class A and DL78 into spectral class B of the dark lineations.

The truly intriguing aspect of these lineations is that the division between DL77 and DL78 corresponds exactly to the intersection point of a third dark lineation, namely DL79. DL79 lies within the intermediate-orange rel% dark lineation class (i.e., spectral class B), along with DL78. One end of DL79 terminates at the intersection with DL77 and DL78. The other end of DL79 intersects DL80 and DL81, and these dark lineation segments together form a slightly imperfect triple junction. Numerous triple junction features have been identified on Europa (Pieri, 1981), but their mechanism of origin is not known with certainty. It appears as though DL79 did play an important role in the evolution of DL77 and DL78 as two spectrally/compositionally distinct dark lineations. The different compositions and albedos of DL77 and DL78 imply that they did not form at the same time or that one of the lineations formed as a continuation of the other in a nonstop process. A reasonable model seems to be that DL78 began forming as a propagating fracture

at roughly the same time as DL79 began forming in the same manner. DL78 is favored over DL77 because DL78 has a spectral signature closer to that of DL79. DL79 began propagating northward as DL78 began propagating towards the point where it would eventually intersect DL79. When the intersection actually happened, it terminated the propagation of both DL78 and DL79. From this stage onward, the development model is similar to that formulated for DL121. Fracture reactivation at some later point created DL77 along the same general trend as DL78, but because of the time elapsed between fracturing episodes, brighter dark lineation material of a different composition could have intruded into DL77. Alternatively, and perhaps preferably, the higher orange relative spectral reflectance of DL77 over DL78 and DL79 may simply reflect the younger exposure age of DL77 and, hence, its lower degree of resurfacing over DL78 and DL79.

Many other dark lineations in the study area and over the entire surface of Europa may have undergone histories similar to those proposed for DL121 and DL77/DL78. The low-resolution nature of Voyager Europa imagery makes studies of individual lineations difficult, however. These examples were given to show that spectral ternary diagrams and albedo data can partially compensate for the lack of imaging detail in developing evolutionary models of dark lineations.

COLOR RATIO/CLASSIFIER IMAGES OF THE STUDY AREA

The main purpose of generating color ratio, color ratio composite,

and classifier images of the dark lineation study area was to provide more classical methods with which to construct lineation classification systems. This would have been useful for verifying the classification system derived from the relative spectral reflectance ternary diagram plotting method. Unfortunately, as mentioned on page 37, the imperfect registration of the orange, blue, violet, and ultraviolet Voyager 2 images makes the ratio and classifier images of little use.

The most useful aspect of the specially processed images is the zoning evident in the plains unit across the study area and, in fact, across the entire image composite from which the study area was excised (i.e., 1195J2-001, 1198J2-001, 1201J2-001; and 1204J2-001 for the color ratio composite). Figure 16 shows the color ratio composite for a 512 line by 512 sample area of the color ratio composite, while Figure 17 shows a parallelepiped-classified image of the dark lineation study area. Four zones of Europa's plains are seen in the larger-area color ratio composite. In the study area, two plains unit color ratio zones cover the majority of the area, with a gradational transition between them. The second spectral zone from the limb begins to grade into the third zone in the extreme eastern portion of the study area. The parallelepiped classifier image confirms these zones, except that it does not show the diffuse third zone. A disturbing quality of the zonation is that the zones take the form of almost exactly vertical strips on the Voyager composite image. This does correspond roughly to lines of longitude on Europa, especially farther from the limb, but the

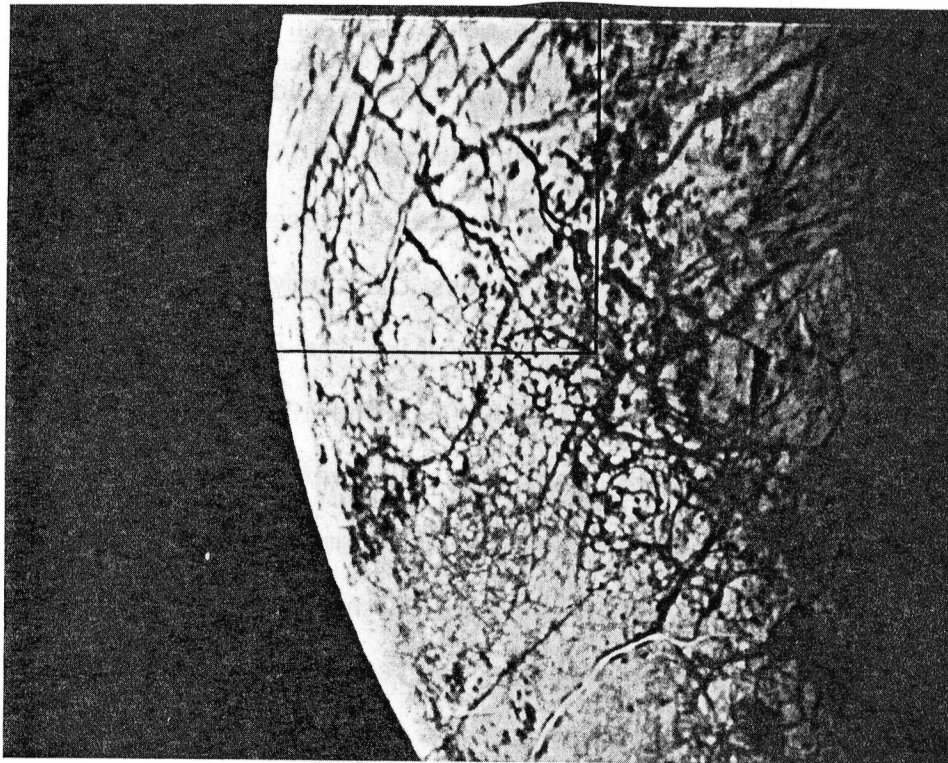


FIGURE 16. 512 x 512 pixel portion of a full 800 x 800 pixel color ratio composite image of a portion of the southern hemisphere of Europa generated from Voyager 2 images. The false color composite was created by substituting the ultraviolet/orange, violet/orange, and blue/orange ratio images from Figure 3 for a normal color image's blue, green, and red components, respectively. The dark lineation study area is shown outlined by the black box.

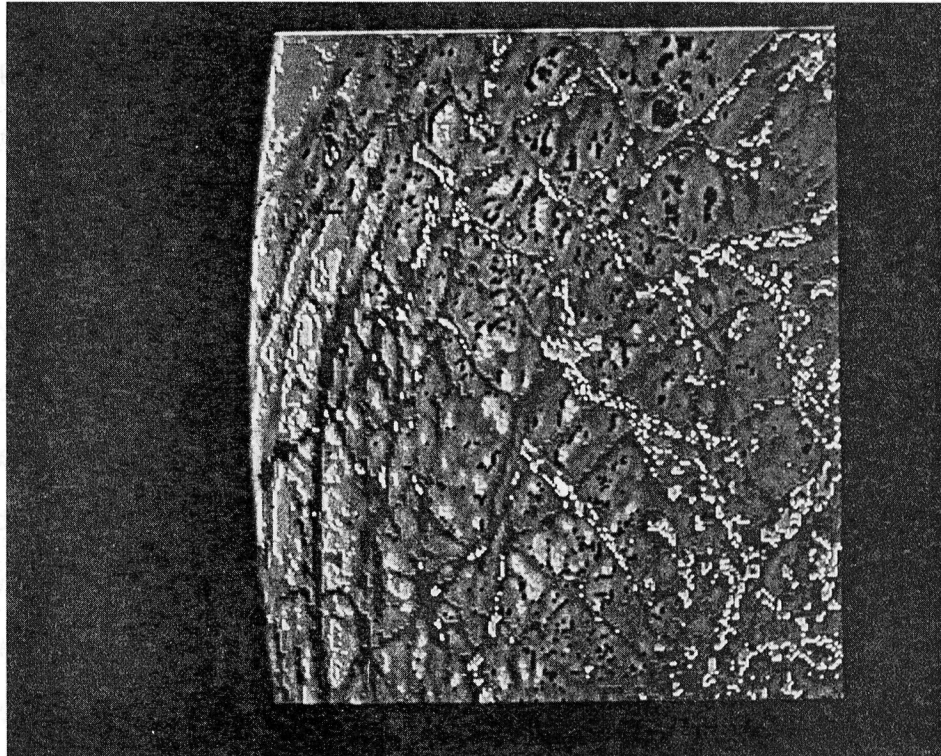


FIGURE 17. False color, parallelepiped-classified image of the dark lination study area (200 x 225 pixels).

linear, vertical trend in all parts of the composite looks suspiciously artificial. This zonation may be a computer-processing artifact related to the multispectral photometric effect for Europa reported by Buratti and Veverka (1983) from a study of Voyager imagery of that body. Alternatively, the zones could be an expression of the decreasing concentrations of sulfur ions implanted in European surface ice (Lane et al., 1981) associated with the margin of the trailing hemisphere. The boundary between the trailing and leading hemispheres of Europa passes through 180° Longitude, which is roughly marked by the boundary between the second and third plains zones. This is intriguing, because it is that zone boundary that marks the line of greatest spectral change in the plains unit. Plains zones 1 and 2 (i.e., those belonging to the presumed sulfur-implanted trailing hemisphere) appear in an enhanced version of the color ratio composite as shades of orange and tan, respectively. Conversely, zones 3 and 4 of the plains unit (i.e., zones belonging to the presumed non-sulfur-implanted leading hemisphere) appear in false color as shades of light blue. This supports the interpretation that spectral zones in the plains are due to varying amounts of implanted sulfur. This is certainly plausible, especially when considering that the division between Europa's hemispheres follows lines of longitude, as do divisions between plains zones. The unresolved problem is why the concentrations of sulfur ions implanted in surficial ice would take the form of fairly distinct zones, rather than a continuously gradational sequence from west to east. The definitive

test between the processing artifact model and sulfur-in ice concentration model is to see if the spectral zones are present in Voyager image color ratio composites in which detailed photometric corrections have been applied. Unfortunately, that was not possible in this thesis, but hopefully future work by other researchers will cover this issue.

Regardless of whether or not the plains zoning is due to the wavelength dependence of Europa's photometric function (Buratti and Veverka, 1983), the dependence still affects the dark lineation relative spectral reflectance ternary plots and the derivative spectral classification system. Buratti and Veverka (1983) showed that as the phase angle of Europa increases from 32° to 103° the average ratio of orange DN to violet DN for dark mottled terrain (spectrally very similar to dark lineation material) increases from 1.59 to 1.91 on Europa. This clearly creates problems for the spectral classification system of the dark lineations, but the constraints imposed on this thesis made it impossible for wavelength dependence to be removed from the Voyager data. Several arguments support the ternary diagram spectral plotting/classification system for the dark lineations as the best possible system to use with the wavelength dependence still in the multispectral data. Primary photometric effects are removed because of the calculation of relative spectral reflectances. Re1% errors occur as the phase angle changes, so that errors will be largest for lineations near the limb, and will fall off sharply for lineations farther from the limb. Wavelength dependence effects for the Voyager images used are generally a

function of longitude and not latitude, so that dark lineations can be compared with each other in north-south strips with a good amount of confidence. No dark lineation covered so much longitude that inconsistent relative spectral reflectance data would be generated by opposing ends, leading to a spectral misclassification of the feature. While it is true that dark lineation classifications at the extreme east and west ends of the study area should not be compared with each other, dark lineations in close proximity can always be compared. The dark lineations closest to the limb have the greatest possibility of being spectrally misclassified; note that there are no low-orange rel% dark lineations near the limb in Figure 8. Offsetting this, however, was the purposeful establishment of only three levels of spectral classification, each occupying several percentage points of orange relative spectral reflectance and requiring only 50% of a dark lineation's points to fall in its range in order to receive its classification. This set up buffer zones in the spectral classification system that could accept a good deal of inaccurate data and still put a dark lineation in its correct spectral class. This also meant that the relationships of CDF's to each other for dark lineations close to each other on Europa should be correct even if the spectral positions of the CDF's in the ternary diagram were not correct (in terms of orange rel%). Finally, the fact that all three spectral classes of dark lineations are dispersed throughout the entire portion of the study area east of DL30 is good evidence that this entire sub-area is probably correctly classified.

One small, distinctive group of dark lineations in the study area allows use of the color ratio composite and parallelepiped classifier images to confirm the validity of the orange rel% classification system. Several very dark, NW-SE trending lineations that are classified as dark, wedge-shaped bands by Lucchitta et al. (1981) and as Type 5 lineations by Pieri (1981). Of this group, DL27, DL77, DL107, DL109, and DL121 all appear deep orange in the color ratio composite. Only a few other dark lineations in the study area have this spectral appearance. The five listed dark lineations all fall into the high-orange rel% classification via multispectral ternary plotting. Comparisons with the parallelepiped classifier image are more difficult because the ternary diagram method assigns one spectral classification to an entire dark lineation while the parallelepiped method classifies each registered pixel into one of six spectral classes. A rare spectral unit in the parallelepiped classified image makes up the majority of DL27 and DL107, and constitutes portions of DL77, DL109, and DL121. These agreements not only give credence to the ternary diagram/orange rel% classification system, but they also show that a group of dark lineations with unique morphologic and albedo properties share a relatively unusual spectral/compositional unit as well. This entire lineation set appears to have formed at a different time than other dark lineations in the area (Lucchitta et al., 1981), and evidence indicates that they may be the youngest, not only because of their cross-cutting relationships with other lineations, but also because of where their very dark material

fits in the water vapor/frost plume resurfacing model developed in this thesis.

RESULTS AND DISCUSSION: AGENOR LINEA AND ENVIRONS

DESCRIPTION OF AGENOR LINEA AREA

Agenor Linea is the largest white line feature positively identified in Voyager 2 high resolution imagery of Europa. A white line is defined in this thesis as a quasi-linear, high-albedo feature whose dimensions of width are much smaller than its length. Topographic determinations for white lines are not possible because of their high lighting angles in Voyager imagery; however, white lines are probably the same as bright ridges that are seen near Europa's terminator in Voyager imagery. The bright ridges are known to possess some height based on the presence of shadows near the terminator, and are believed to be no more than a few hundred meters high. Agenor Linea appears to be much wider than other white lines on Europa. It is flanked along its length by a series of dark patches on both sides in its southern portion. In its northern portion it is flanked on both sides by a continuous dark linear feature, giving the appearance of a triple band in this area. The white line and dark flanking material bifurcate at a point where the trend of Agenor Linea changes markedly from NE-SW to nearly due east-west. The dark material takes the form of a dark lineation beyond the point of bifurcation.

Agenor Linea covers an area extending from approximately 220° to 178° Longitude and -44° to -41.5° Latitude. If the believed sulfur-implanted-in-ice region on Europa (Lane et al., 1981) fully occupies

the satellite's trailing hemisphere, then Agenor Linea is surrounded by sulfur-embedded plains. It should be noted, however, that part of Agenor Linea is located at the extreme eastern edge of the trailing hemisphere, which is also true for the dark lineation study area. Considering that part of the boundary of the trailing hemisphere is marked by 180° Longitude, two degrees of longitude containing Agenor Linea falls outside the trailing hemisphere. The boundary of sulfur ion implantation probably does not correspond exactly to the boundary of the trailing hemisphere, so it is uncertain how much of Agenor Linea is located in sulfur-embedded plains. Luchitta and Soderblom (1982) classified the plains surrounding Agenor Linea as the fractured plains unit, based on the presence of a dense network of small-scale darkish lineations in the plains. This is opposed to the classification of the plains in the dark lineation study area as the bright plains unit by Lucchitta and Soderblom (1982).

There is another major white line, located near Agenor Linea, which is centered at 224° Longitude, -39° Latitude. This is a short, relatively wide white line that appears similar to Agenor Linea in its albedo and color. Other than this, the area surrounding Agenor Linea appears to be devoid of white lines and also lacks dark lineations of the sizes found in the dark lineation study area.

TERNARY DIAGRAM PLOTS AND CHARACTERISTICS OF THE CDF'S

Ternary diagram plots were constructed for Agenor Linea (pro-

filed), 10 flanking dark patches (profiled), and 35 widely-spaced points in the plains near Agenor Linea. Agenor Linea's 162 data points were plotted on four separate ternary diagrams. The reason for this is that this white line covers so much longitude (48°) that multi-spectral photometric effects will be exhibited across the feature. By partitioning the data into four ternary diagrams, inaccurate interpretations due to multispectral effects dependent on phase angle will be minimized. Inaccurate plotting of data points because of multi-spectral photometric effects cannot be avoided, but because contiguous segments are isolated from each other, the larger spectral inaccuracies between points at opposite ends of Agenor Linea will not be plotted together while the data points that are plotted together should have very small relative spectral reflectance errors. Segments of Agenor Linea were not made the same size. Proceeding from west (i.e., nearest Europa's limb in the Voyager 2 images used) to east (i.e., farthest from the limb), segments were established of 20, 30, 56, and 56 profiled data points. The smaller segment sizes closer to Europa's limb were chosen because features are longitudinally compressed in images taken near the limb.

A sketch map showing where all the features are located is depicted in Figure 18, and the sampling locations for multispectral data points in the plains surrounding Agenor Linea are shown in Figure 19. The relative spectral reflectance ternary diagram plots for Agenor Linea are shown in Appendix D, for the flanking dark patches in

AGENOR LINEA

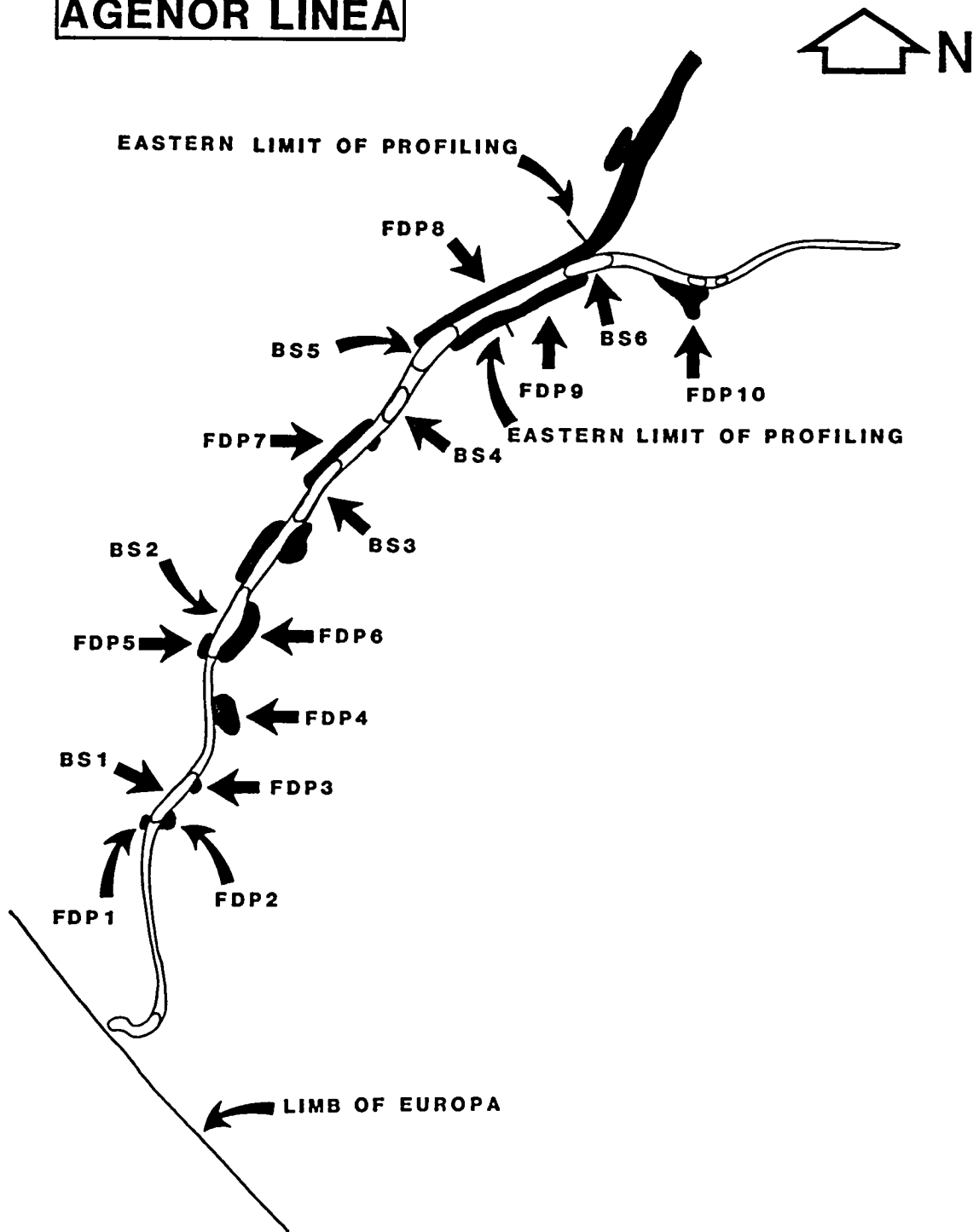


FIGURE 18. Map of Agenor Linea (the long curvilinear white feature), its internal bright spots (BS's), and flanking dark patches (FDP's). This map was traced from unrectified Voyager 2 frame 1198J2-001.

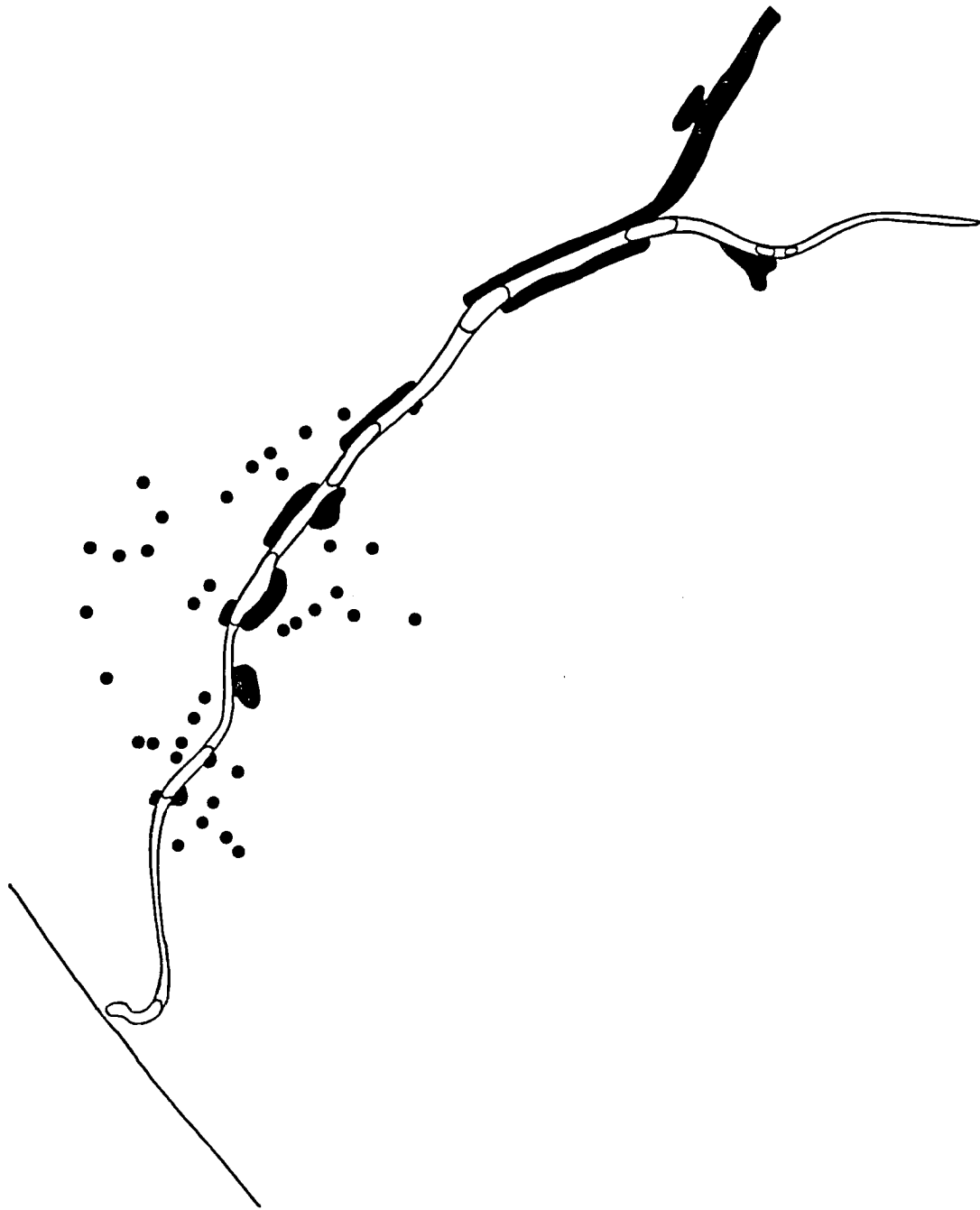


FIGURE 19. Map depicting locations of data points used in plotting relative spectral reflectances of the plains immediately surrounding Aenor Linea. Rel%'s are plotted in the reference ternary diagram in Appendix C.

Appendix E, and for the plains surrounding Agenor Linea in Appendix C. By making all of these plots on the same reference ternary diagram as was utilized for the 193 dark lineation segments and the plains engulfing the dark lineation segments, direct comparisons of the spectral characteristics of members of this diverse set of European features can be made. Most of the other characteristics of the CDF's that were evaluated for the dark lineations (i.e., CDF area, data point density, and data point dispersion) were also evaluated for Agenor Linea, its flanking dark patches, and the surrounding plains. These results are tabulated and presented in Table XI. Local brightness classifications were not assigned to these features because there were so few similar features in the area with which to compare them.

The ternary diagram spectral reflectance plots for the segments of Agenor Linea do not bear as strong a resemblance to the plots for the plains surrounding it as they do the plots for the plains in the dark lineation study area, insofar as the CDF positions along the orange rel% axis are concerned. The plains surrounding Agenor Linea are higher in orange rel% in many areas than the white line feature, enough so that the surrounding plains qualify for spectral class B (i.e., intermediate-orange rel%) while all segments of Agenor Linea belong to spectral class C (i.e., low-orange rel%). It should be noted that Agenor Linea is significantly brighter than its encompassing plains, and is in fact one of the brightest known features on Europa. The brightness of Agenor Linea appears to be closer to the

TABLE XI. Classifications of Agenor Linea (AL) segments, flanking dark patches (FDP's), the plains immediately surrounding Agenor Linea, and the plains in the dark lineation (DL) study area, using many of the same characteristics, classes, and class ranges that were used for the dark lineations in Table II.

	DL SPECTRAL CLASSIFICATION (OR REL%)	NUMBER OF DATA POINTS	CDF AREA	CDF POINT DENSITY	DEGREE OF DISPERSION CLASSIFICATION
AL1	C	20	460	4.348	B
AL2	C	30	1000	3.000	C
AL3	C	56	460	12.174	B
AL4	C	56	510	10.980	B
FDP1	B	3	110	2.727	A
FDP2	A	4	65	6.154	A
FDP3	A	3	50	6.000	A
FDP4	A	4	185	2.162	B
FDP5	B	5	160	3.125	A
FDP6	A	9	1260	0.714	A
FDP7	A	9	590	1.525	B
FDP8	A	40	2790	1.434	C
FDP9	A	12	190	6.316	B
FDP10	A	5	195	2.564	B
AL PLAINS	B	35	690	5.072	B
DL PLAINS	C	35	305	11.475	B

brightness of the plains in the dark lineation study area, although photometric effects make such comparisons difficult. Remembering the two-component spectral/compositional unit model (i.e., dark lineation unit and plains unit) and simple linear mixing model from page 91, it seems reasonable to conclude that Agenor Linea is composed of a more pure "plains" unit composition than its surrounding plains are. The spectral properties of the plains could be due to the presence of the fine, dense network of darkish lineations (i.e., the "fractures" of the fractured plains) that could extend to below the limit of resolution of Voyager 2 imagery.

CDF areas and point densities for Agenor Linea segments show mixed similarities to those for the plains surrounding it and the plains in the dark lineation study area, although for segments with more data points (i.e., more statistical confidence) they tend to bear a closer resemblance to those for the dark lineation study area plains. The degree of dispersion of data points within each CDF is basically the same for Agenor Linea, the plains engulfing it, and the dark lineation study area plains. Each of these shows a slight clustering of data points, probably because one or a few points at the extreme ends of each profile sampled a different compositional proportion of the two basic spectral units (as also occurred with several dark lineations). Slight clustering for the two plains locations is somewhat more difficult to explain, because the plains were not profiled. Multispectral data was obtained by sampling the locally bright-

est pixels at different locations, so any clustering present in the CDF's are probably the result of one particular plains composition being present at the brightest sites over much of each plains location, with variations of that composition constituting the brightest sites over a lesser fraction of each plains location.

Based on color and albedo data garnered from a simple visual inspection of Voyager 2 imagery, the flanking dark patches (FDP's) of Agenor Linea would be expected to emulate the dark lineations in the study area to the north in their spectral and other CDF properties. This turns out to be only partially true. Each flanking dark patch CDF generally corresponds to some group of dark lineations in the properties of spectral class, CDF area, CDF point density, and degree of dispersion of data points. Two exceptions to this are the extremely low CDF point density of 0.714 for FDP6 and the extremely high orange rel%'s for FDP8 (some of which have >50% orange relative spectral reflectance). The very low point density for FDP6, plus low densities for FDP7 and FDP8, indicates that a wide range of compositions exists in each of these dark spots, probably owing to some disruptive process associated with Agenor Linea that resulted in different mixtures of dark material and bright material units being created throughout the patches. The extremely high orange rel%'s found in the ternary diagram plot for FDP8 make it not only the most orange feature studied in this thesis, but also are partly responsible for it possessing the largest-area CDF of any feature examined in this

thesis. FDP8 happens to be the long, continuous strip of dark material bordering Agenor Linea that eventually veers away from the white line as a dark lineation. The extremely large CDF area, along with the low CDF point density, shows that a great diversity of compositions exists in FDP8, as for FDP6 and probably for the same reason. The very orange material is related to the presence of a bright spot in Agenor Linea that will be discussed later in this section beginning on page 158.

LENGTHWISE COMPOSITIONAL VARIATION MAP OF AGENOR LINEA

The technique of dividing each CDF of an Agenor Linea segment into six equal-area relative spectral reflectance bins in order to map spectral subunit distribution was used in a search for sequences of profiled pixels containing non-random compositional distributions. Results are very sensitive to contributions to multispectral DN values from distortion-producing effects such as vidicon dark current and multispectral photometric effects. These distortions were partially offset by creating a separate spectral/compositional variation map for each segment of Agenor Linea based on the slightly different CDF of each. Thus, although the same map symbols are used for corresponding subunits from each segment's CDF and Agenor Linea's subunit distribution is presented as one continuous map in Figure 20, there are really four separate maps covering data point numbers 1-20 (-43 to -41 Lat, 202 to 200 Long), 21-50 (-41 to -40.5 Lat., 200 to 197 Long.), 51-106 (-40.5 to -40 Lat., 197 to 190 Long.), and 107-162 (-40 to -39

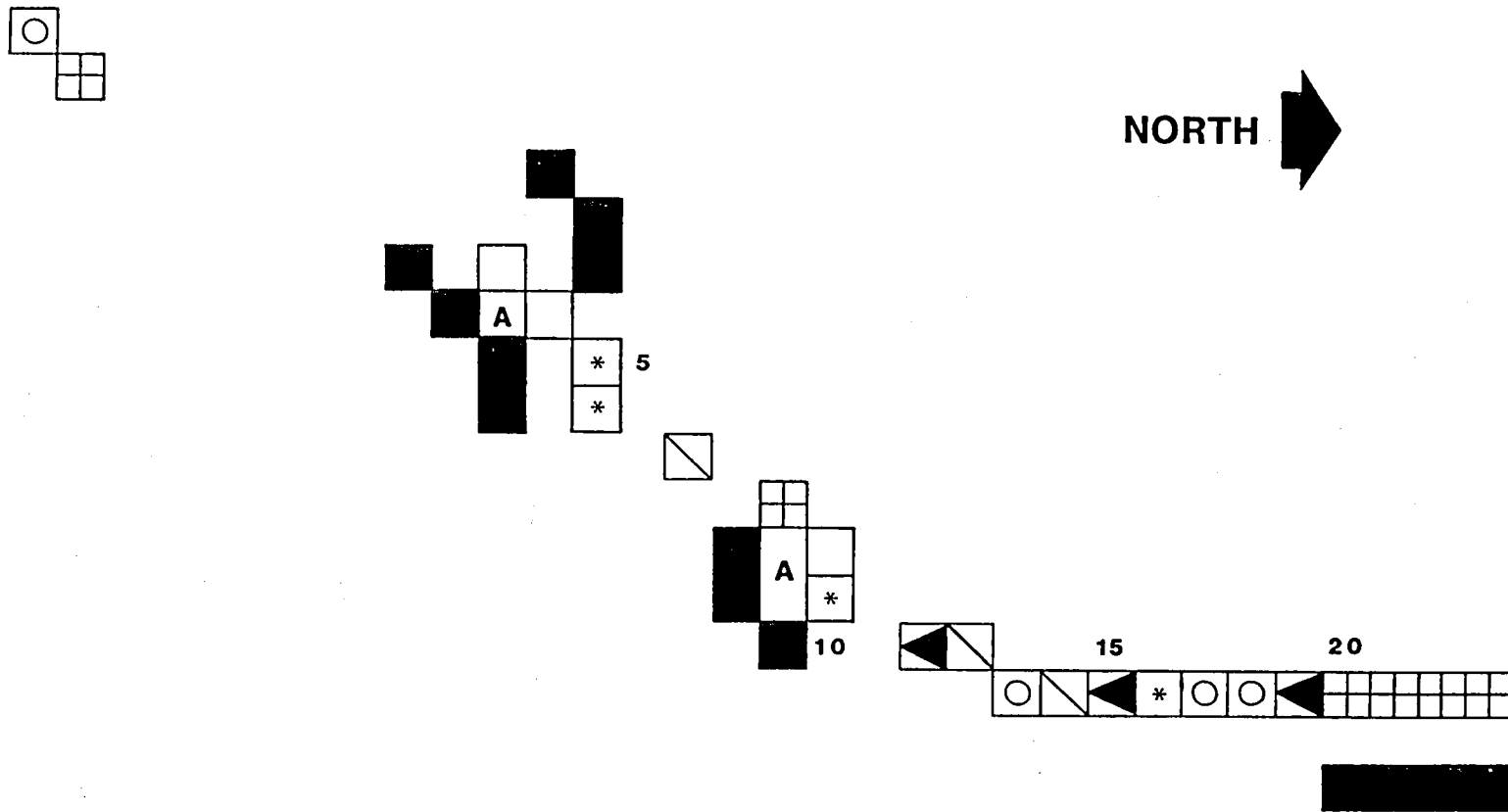


FIGURE 20. Lengthwise compositional variation map for Ageron Linea, plus a mapping of the locations of the major flanking dark patches (FDP's) which were profiled (dark squares). The accompanying subunit key for this map is found in Figure 21. Numbers on the map are of the individual profiled pixels.

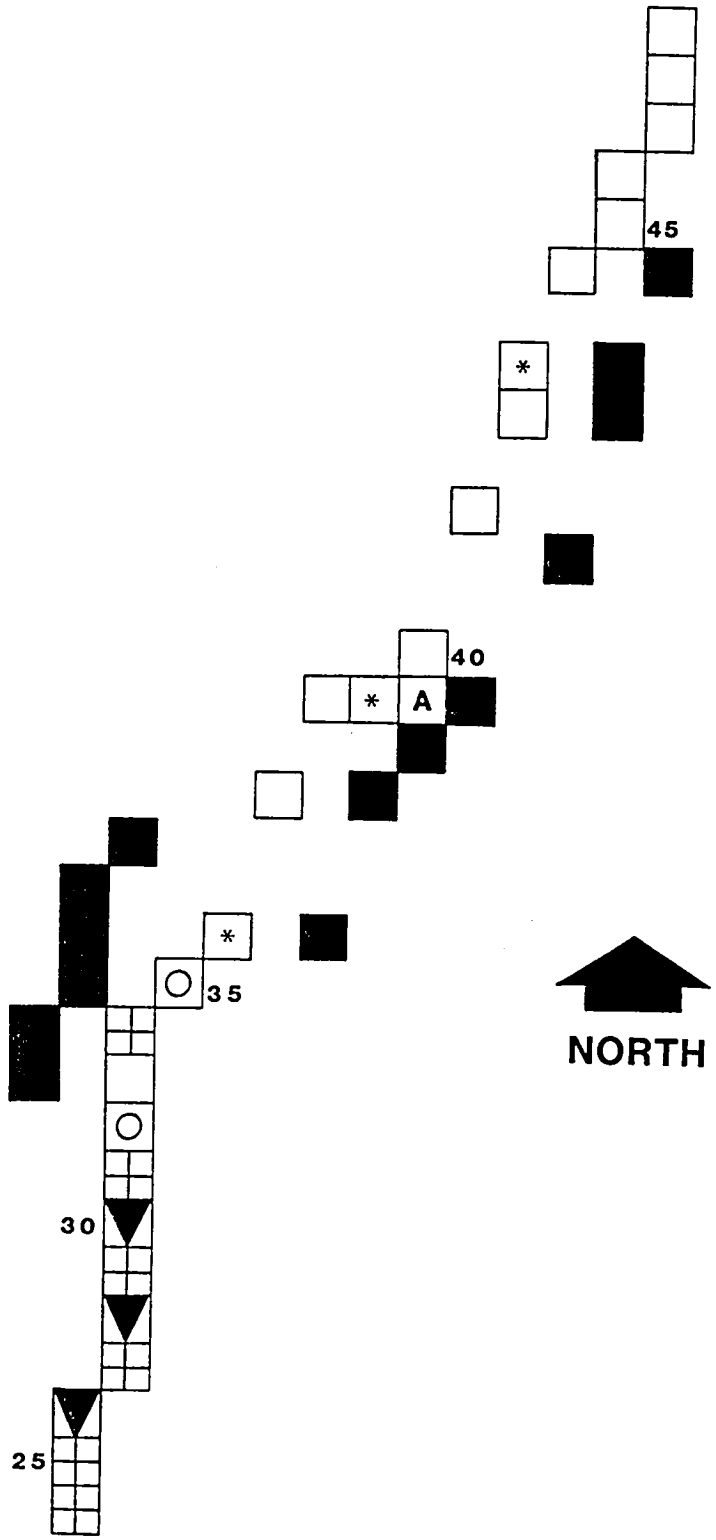


Figure 20. (Continued)

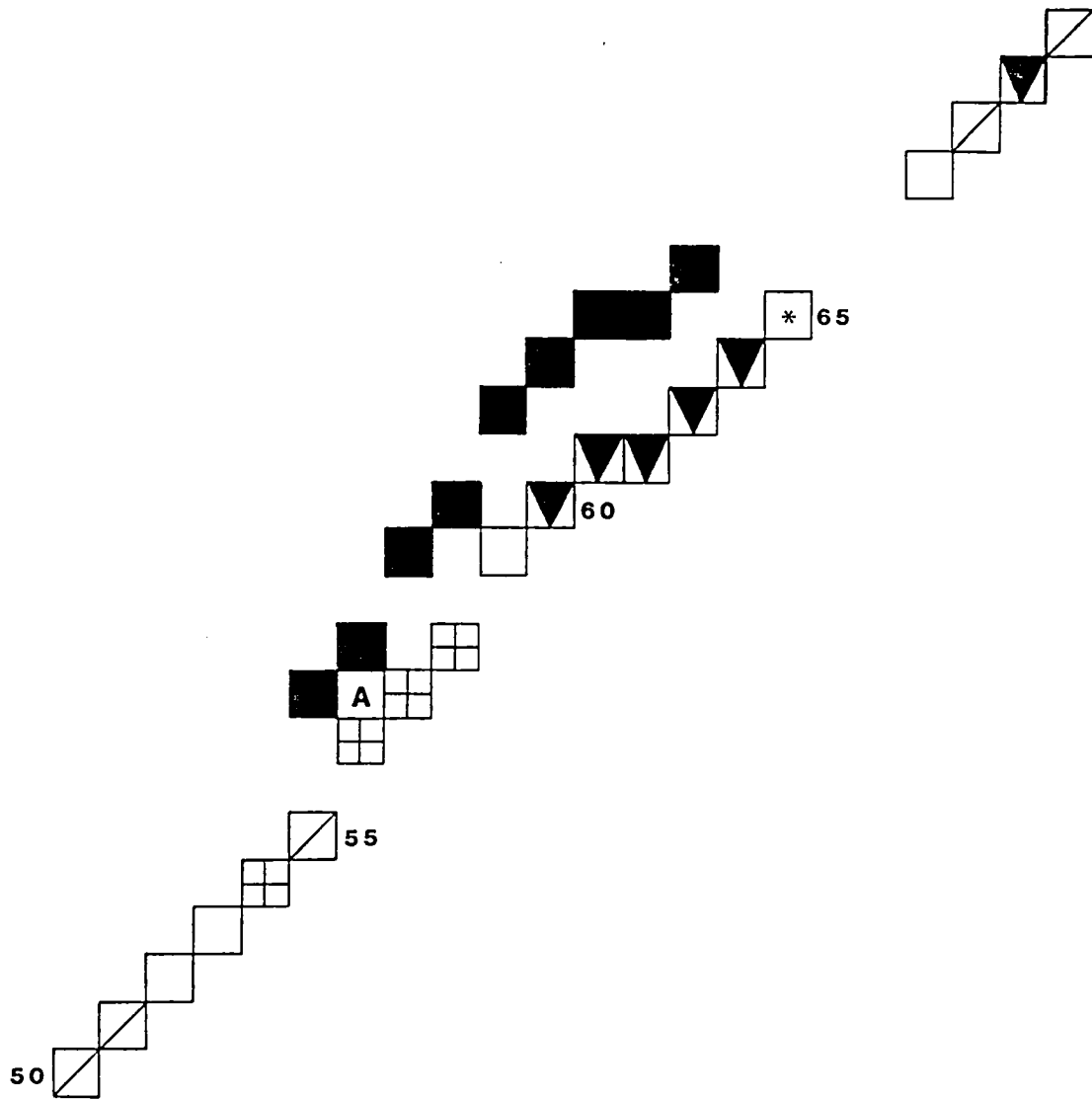


Figure 20. (Continued)

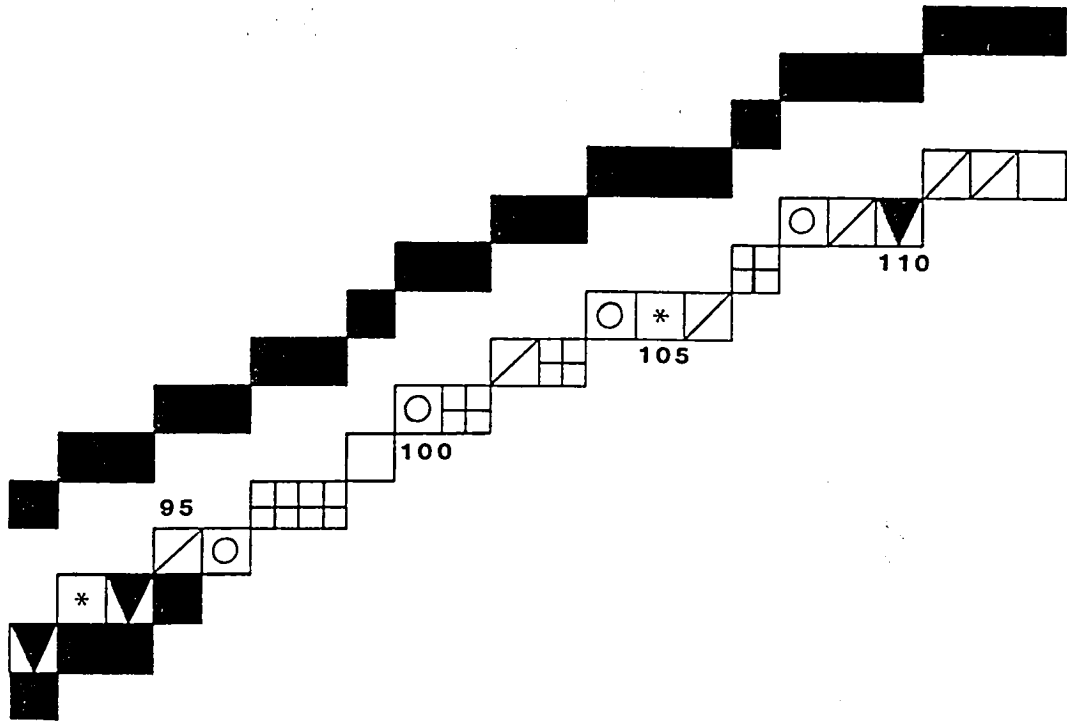


Figure 20. (Continued)

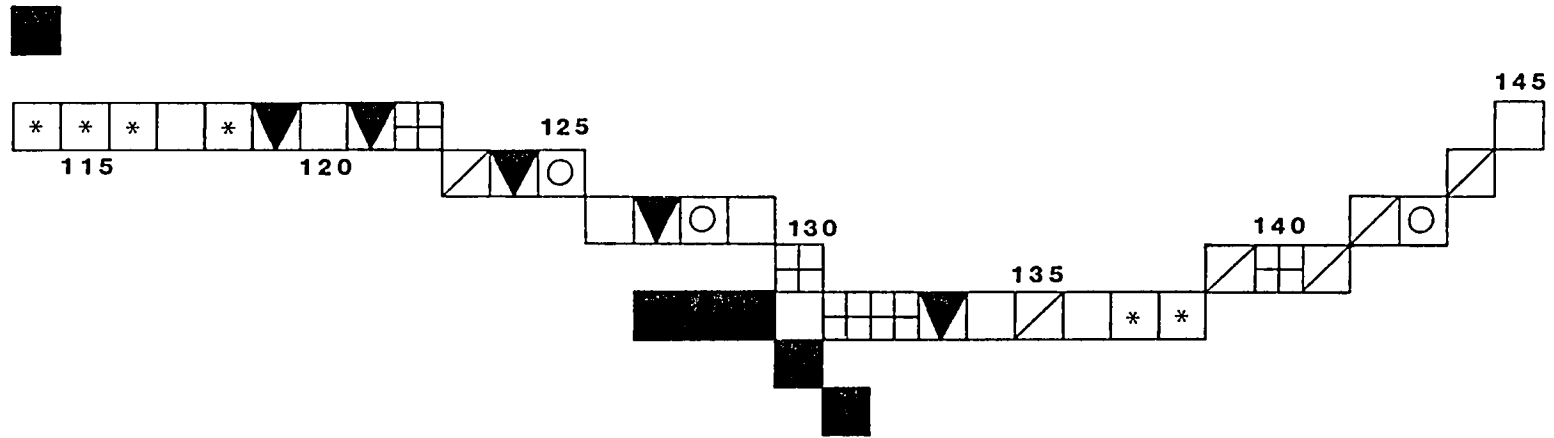


Figure 20. (Continued)

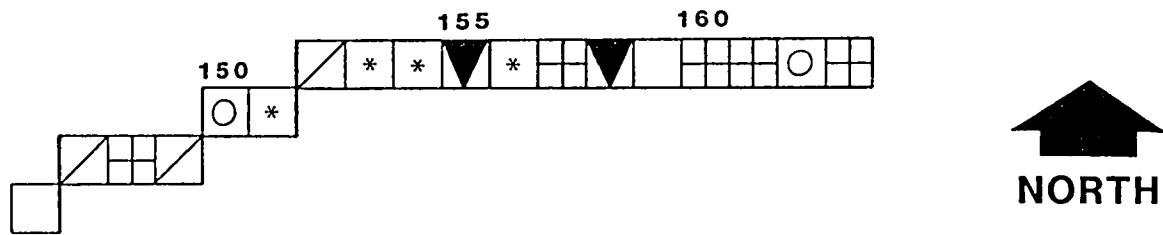
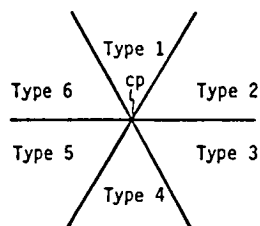


Figure 20. (Continued)

(A)



str = strong in terms of relative spectral reflectance within CDF
wk = weak in terms of relative spectral reflectance within CDF
dom = dominant color (of vi, bl, or) with respect to CDF
cp = central point of CDF

Type 1 = str or, wk bl, wk vi (OR DOM)
Type 2 = str or, wk bl, str vi
Type 3 = wk or, wk bl, str vi (VI DOM)
Type 4 = wk or, str bl, str vi
Type 5 = wk or, str bl, wk vi (BL DOM)
Type 6 = str or, str bl, wk vi

(B)

-  Orange-dominant spectral subunit Type 1.
-  No-color-dominant spectral subunit Type 2.
-  Violet-dominant spectral subunit Type 3.
-  No-color-dominant spectral subunit Type 4.
-  Blue-dominant spectral subunit Type 5.
-  No-color-dominant spectral subunit Type 6.
-  Flanking dark patch material.
-  Area not a part of Agenor Linea or a flanking dark patch.

FIGURE 21. Keys to the lengthwise compositional variation map of Agenor Linea presented in Figure 20. (A) Depiction of the division of a CDF into equal-area subunit bins and explanation of the relative spectral characteristics of each bin (taken from Meier, 1983a). (B) Symbols for the Agenor Linea map and explanation of each, including those utilizing the CDF subunits in (A).

Lat., 190 to 182 Long.). Each map can be considered comparable to the other maps for the purpose of assessing the overall lengthwise compositional changes in the white line feature. The map shown in Figure 20 correctly depicts the positional relationship of each profiled pixel of Agenor Linea to the next one, and the correct positional relationship of each profiled pixel of each flanking dark patch to the next profiled pixel. Each flanking dark patch profiled pixel is correctly shown in relation to the profiled pixel of Agenor Linea it corresponds to, but no attempt has been made to correctly represent the distance of the flanking dark patch pixels to their corresponding Agenor Linea pixels.

The resulting lengthwise compositional variation map, which were first reported in Meier (1983a), are shown in Figure 20, while Figure 21 provides a key to the meaning of each spectral subunit.

To call Agenor Linea a white line feature is somewhat of a misnomer since its mean spectral reflectances are 40.43% OR, 34.12% BL, 25.45% VI. If its composition was very homogeneous, two results would be expected -- 1) There would be an equal number of pixels of each of the six spectral types, and 2) the sequence of spectral types of adjacent pixels would be totally random (i.e., two adjacent pixels would be expected to be of the same spectral type only one of every six times, etc.). What was found for pixel frequencies compared to the expectation was: type 1: +28.83%, type 2: -0.61%, Type 3: -7.98%, Type 4: +17.79%, type 5: -4.30%, type 6: -33.74%. The findings for frequencies of numbers of sets of adjacent pixels (AP) of the same spectral type were: two AP

only (14 sets), three AP only (5 sets), five AP only (1 set), 6 AP only (2 sets). In addition to finding the contiguous areas of uniform composition, sequences of pixels were discovered that indicate gradational compositional changes along the length of Agenor Linea. Nine such gradational areas were found that possessed at least three spectral types each. One was even found that transitioned through all six spectral types. These can all be found by examining the lengthwise compositional variation map of Agenor Linea in Figure 20. Although not all of the flanking dark patches of Agenor Linea were mapped and profiled, all of the major, darkest ones were. There are no particularly strong patterns evident in the spectral subunit distribution of Agenor Linea where the major dark patches flank the white line. The four pixels of FDP4 do correlate with a sequence of pixels in Agenor Linea that are all of the orange-dominant subunit (i.e., Type 1) and some other flanking dark spots do correlate to sequences of two or three orange-dominated subunit pixels in Agenor Linea (i.e., FDP7, FDP8, FDP10).

Sequences of two pixels of the same spectral subunit may not be reliable in light of the factors contributing errors to the multispectral data, but longer sequences probably have some physical meaning. The fact that there are both sequences of pixels of the same spectral subunit and of gradational changes of subunits implies that different processes have dominated different parts of Agenor Linea. Sequences of the same spectral subunit correspond to areas of highly homogeneous, pure composition implying either a smooth, non-interrupted emplacement

of high-albedo Agenor Linea material or, less likely, some sort of uniform post-emplacement modification process. Gradational sequences of pixels where each adjacent pixel is one subunit different from the previous pixel's subunit represents areas where the composition of white line material changes gradually but in a continuous manner. This could be related to some dynamic but slowly developing process involved in white line material emplacement or, less likely, post-emplacement modification. Random sequences of spectral subunits suggest material emplacement was relatively dynamic, mixing materials of slightly different compositions but not homogenizing them. It should be borne in mind that the mapping was performed on only the brightest (i.e., most pure white line material) pixel in each profiled slice of Agenor Linea. This is the best way to map the lengthwise compositional variation, but it may not be representative of the composition across each profile, which measured four or more pixels in many areas of Agenor Linea.

BRIGHT SPOTS IN AGENOR LINEA

A discovery made late in the execution of the thesis yet obvious in even a cursory examination of Voyager 2 color composite imagery was the finding that several portions of Agenor Linea appear brighter than the neighboring portions. This gives Agenor Linea somewhat of a pinched appearance at several points along its length. Examining multispectral pixel printouts of Agenor Linea identified six major bright spots (i.e., continuous bright regions consisting of at least

six pixels in at least two of the three colors orange, blue, and violet) and several minor ones. Although their size and shape do not exactly correspond in the three colors in which they were imaged, there is in every case enough overlap to make their identification a certainty. Figure 22 shows the size, shape, and contrast with surrounding areas of Agenor Linea of each major bright spot (abbreviated as BS) in orange, blue, and violet. The elevated brightness levels compared to surrounding white line material and the continuity of each bright spot confirm that Agenor Linea possesses significant heterogeneity in its albedo properties.

The bright spots within Agenor Linea show no correlation with any non-random sequences of pixels mapped by spectral subunits. Many bright spots within the white line have corresponding flanking dark patches outside Agenor Linea (see Figure 18), but this is believed to be only coincidental, with one exception. That is the relationship between BS6 and FDP8. Data points 36, 39, and 40 at the end of FDP8 definitely correlate with three points at the beginning of BS6. All of FDP8 is in the high tier of orange relative spectral reflectance, but some data points possess extremely high orange rel%'s, the highest plotted in a ternary diagram in this thesis. Of the three pixels of FDP8 that line up with bright pixels in BS6, points 36 and 39 fall into the extremely-high orange rel% range.

The spectral and geomorphic evidence points to a causal relationship between BS6 and the orange enhancement in rel% at the end of FDP8,

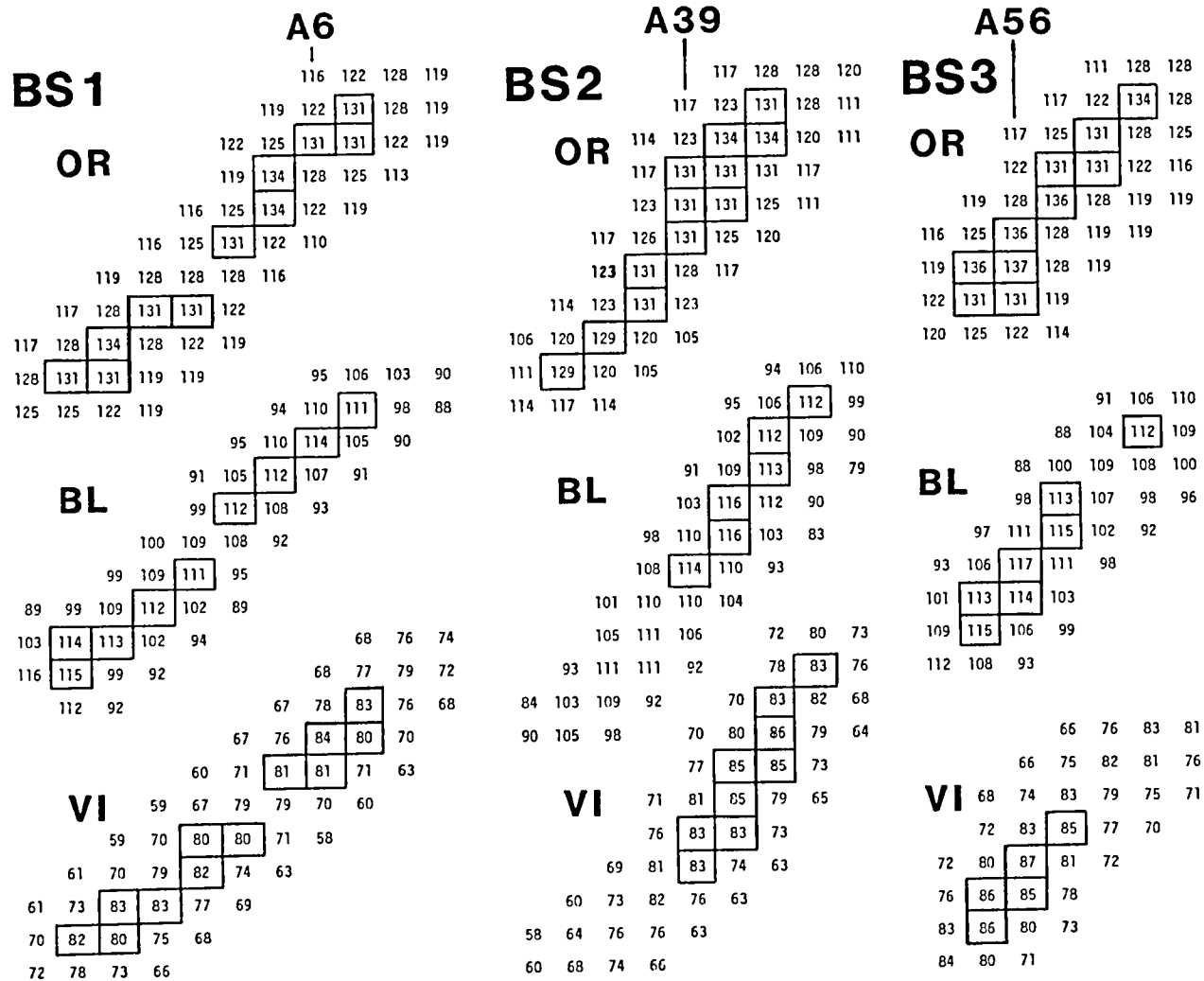


FIGURE 22. Pixel DN maps of major bright spots (BS's) in Aqenor Linea in orange (OR), blue (BL), and violet (VI) Voyager 2 Europa imagery. A vertical line through any part of a pixel map will access the same sample (column) coordinate in all three filter images, showing that each bright spot is defined in orange, blue, and violet. Larger numbers prefixed by an "A" refer to pixel locations in the lengthwise compositional variation map of Aqenor Linea in Figure 20. The locations of the bright spots relative to each other are shown in Figure 18.

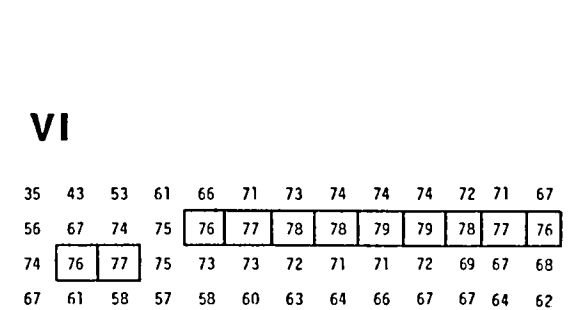
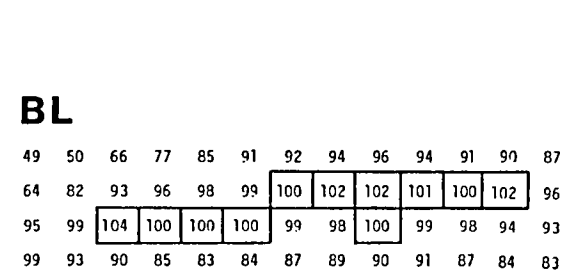
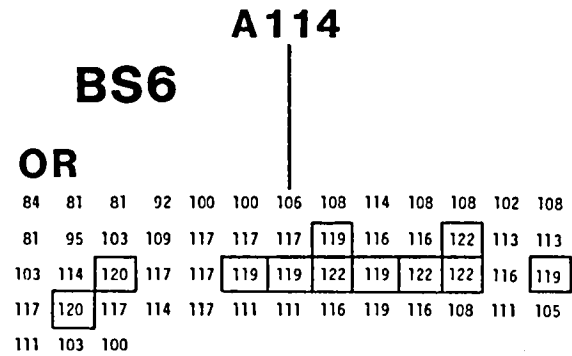
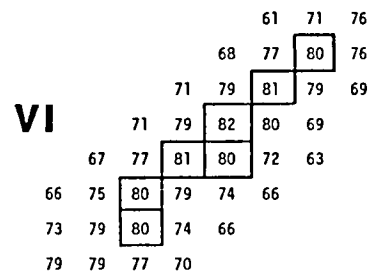
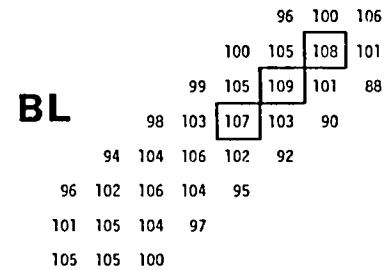
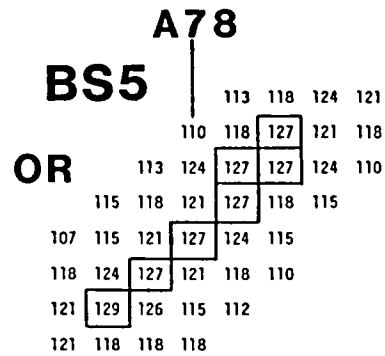
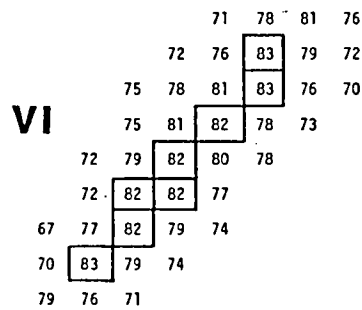
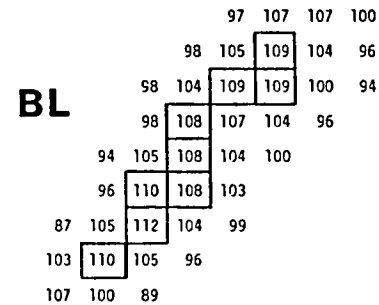
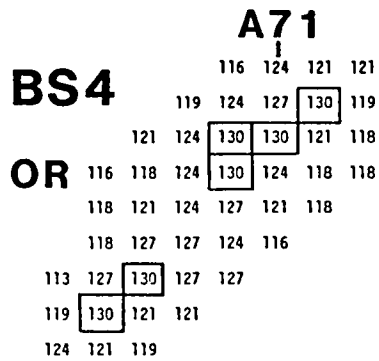


FIGURE 22. (Continued)

but before discussing that it is necessary to model the bright spots in Agenor Linea. The spacing of bright spots and their morphologic appearance in Agenor Linea lead to the conclusion that they are eruption sites for water in some form. The evidence strongly indicates that the mode of eruption is liquid water in a sort of "lava" rather than water vapor/frost plumes as are believed to exist in the dark lineation study area. This conclusion is based on the limited dimensions of bright spots and their confinement to the general shape of Agenor Linea. If the eruption mechanism were a water vapor/frost plume, it would be expected to spread bright material over a much larger area and in a more-or-less circular pattern as opposed to the narrow elongated patterns that bright spots actually make.

Implicit in the model of Agenor Linea bright spots is the assumption that the flanking dark patches are the remnants of a dark lineation and that Agenor Linea is the central bright stripe that formed a triple band structure with the dark lineation. The flanking dark patches fit the model of a dark lineation very well, considering that their outer margins are all approximately equidistant from Agenor Linea, so that they would form a continuous thin strip of dark material with the dimensions of a European dark lineation if they were all connected. Also, remembering that FDP8 along the northern portion of Agenor Linea is a long dark strip that veers away from the white line as a dark lineation, it is easy to perceive FDP8 as a relatively unaltered segment of the dark lineation that at one time engulfed all of Agenor Linea. In this

model, Agenor Linea represents an especially fat medial stripe, somewhere between being easily recognized as part of a triple band structure and completely burying its surrounding dark lineation, perhaps becoming indistinguishable from the surrounding plains.

If the proposition that Agenor Linea is located within a dark lineation is accepted, it becomes easier to model the history of the feature. Even though photogrammetric studies of Voyager 2 imagery has provided no evidence that dark lineations possess any topography, it is thought that they could well possess some depth which would be below the resolution of Voyager imagery. This could still result in a depth of as much as several tens of meters, which would be consistent with dark lineations being fractures filled with intruded dark materials. Such a depth is important in modeling the formation and evolution of Agenor Linea's bright spots, since the dark lineation "valleys" would constrain the shape of water "lava" flows. Bright spots would thus be forced to mimic the shape of the parent dark lineation.

The complete model for the evolution of Agenor Linea develops as follows: Initially came the formation of the dark lineation in the same manner as other dark lineations on Europa. The first stage in the formation of Agenor Linea was probably similar in some respects to the model of formation of central bright stripes in dark lineations proposed by Finnerty et al. (1981). The parent dark lineation remained a zone of weakness in Europa's crust even after dark material intruded and solidified. At some later time a second episode of fracturing occurred

lengthwise through the center of the dark lineation, allowing extrusion of subsurface material, this time much purer and brighter than the dark lineation material. This second material emplacement episode creates the bright medial stripe of the resultant triple band feature, probably in the form of a low icy ridge. The model for Agenor Linea departs from that of Finnerty et al. (1981) in the details of the bright material extrusion. Rather than creating a long, continuous, uninterrupted fissure during the second episode of fracture, it is believed that fracturing is non-continuous and poorly developed, probably because of a chaotic arrangement of subsurface blocks where the fracturing is taking place. (The intermittent fissure development may or may not have occurred at the initial fracturing stage that created the dark lineation.) Incomplete fracture development would have manifested itself during bright material extrusion by forming discrete extrusion (i.e., eruption) sites. The initial surface expression of these probably liquid water eruption sites would be a series of irregularly-spaced yet isolated bright spots along the parent dark lineation of Agenor Linea. As liquid water lava continued to erupt, the bright spots would grow, physically assuming a morphology similar to that of very low, wide shield domes on the Earth and Mars where basalt lavas with extremely low viscosities erupt. Superficially, it would seem that erupting liquid water, because of its rheology, would quickly cover the entire channel surface of the parent dark lineation with a thin, uniform layer of water which would become ice. It must be remembered, however, that as the liquid water

spreads and thins as it recedes from the eruption site, it becomes highly susceptible to freezing because of Europa's extremely low surface temperatures. The balance between rheology and surface temperature should limit the extent to which any water lavas can propagate from their sources. Low, bright shield domes should result as water eruptions continue to build up sequences of thin ice layers. The long-term evolution of these eruptions should be for the ice shields to converge with each other, if not by water lavas physically merging with each other, then by icy layered deposits (i.e., frozen lava flows) merging because of downslope creep (i.e., viscous relaxation). The merging of icy flow deposits from different bright spot eruption sites would eventually create the continuous white line feature currently recognized as Agenor Linea. The eruption sites would still appear brighter than the inter-site areas because the eruption sites could well be covered with a thin layer of water frost, associated with water eruption phenomena, that would only affect the immediate area around each eruption site. Such a frost deposit would act as a specular reflecting surface, brightening that area in comparison to other parts of Agenor Linea. This is similar to a proposal by Lucchitta and Soderblom (1982) for thin frost deposits enhancing the brightness of Minos Linea, a prominent orange-hued dark lineation found north of the dark lineation study area on Europa. Their same work also proposed frost enhancement for the very orange appearance of what this thesis calls FDP8, the dark strip along Agenor Linea with the highest orange rel%'s measured in this

thesis. The problem with this proposal is the question of why should a frost coating raise the orange rel%. If the frost is plains-like material from Agenor Linea or an eruption plume, it could increase the albedo of FDP8, but the plains-like composition of the frost should actually decrease the orange rel% of the dark material in FDP8.

The last major facet of the Agenor Linea model of this thesis explains the present appearance of the flanking dark patches and strips along the white line. The formation of bright spot water eruption sites and their subsequent coalescence would cover most of the pre-existing dark lineation material. How much dark material would be buried would basically be a function of the growth of the bright spots and their icy lava flows. Since the sites of second episode fracturing are located along the central lengthwise line in the parent dark lineation (Finnerty et al., 1981), the last portions of the dark lineation to be covered by bright material would be the outermost edges of the dark lineation. The growth of Agenor Linea either stopped before reaching these outermost edges or the white line is still growing and has not yet reached the edges. In either case, irregularities in the shape of the parent dark lineation, its believed channel, and the bright spots/icy lava flows would cause some areas of dark lineation outer edge to be covered, resulting in a series of flanking spots and patches of dark material, and some outermost edges to remain uncovered, leaving the long dark strip that is FDP8.

The location of the very orange material at one end of FDP8 cor-

relates with the location of a bright spot in Agenor Linea, but because the two materials are spectrally incompatible, the orange enhancement cannot be from material derived from the bright spot. The positional correlation can be explained, however, by remembering that the bright spot eruption site marks a structurally weak point in Europa's crust. It is possible that a larger crustal weak zone exists in that immediate area, such that it would allow eruption of both fresh FDP8 material and bright spot water lavas. There is some difficulty in constructing a model for a weak zone that would allow extrusion of such divergent materials, but it is possible. FDP8 material would not have had to have been extruded at the same time as the water lavas, so that, for example, the dark material of FDP8 could have intruded from a greater depth and at an earlier time than the more pure water composition of BS6 material, which could have been extruded from a relatively shallow depth as the fracture annealed towards the surface.

Alternatively, it is possible that FDP8 is not related in origin to BS6 at all, but that FDP8 simply tapped a subsurface pocket of xenolithic dark material when it formed. The extremely high orange rel%'s in FDP8 are not terribly difficult to understand when considering the very low albedo of some of its pixels. The extremely low rel%'s in blue (10 of 40 data points are less than 30 rel% blue) are more difficult to comprehend because they do not fall on the reference ternary diagram trend line of increasing orange rel%, relatively uniform blue rel%, and decreasing violet rel% as dark lineation albedo decreases. The dis-

crepancy is relatively minor, however. It seems fair to say that the composition of FDP8 represents more of a variation of the fundamental dark lineation compositional unit than a new compositional unit for Europa. Such a statement may not hold true for all non-plains spectral features on Europa, but all of the features studied in this thesis can be assigned to either the dark lineation spectral/compositional unit, the plains spectral/compositional unit, some variation of one of these units, or a linear mixing of these two units.

A SATELLITE-WIDE SURFACE MODEL FOR EUROPA

OVERVIEW

Most research of Europa after the Voyager flybys of 1979 has concentrated on identifying and studying the origin and development of fracture sets on Europa (e.g., Helfenstein and Parmentier, 1980; Lucchitta et al., 1981; Lucchitta and Soderblom, 1982). Part of the reason for this is that the lower resolution of Voyager imagery of Europa compared to that for the other Galilean satellites has discouraged detailed modeling of Europa's surface features and processes. The intention of this thesis has been to not compete with topics of research for Europa that are being intensively pursued by others, but rather to search for new insights into Europa's history through the study of aspects of Europa that have received little attention. The detailed evaluations of the multispectral and geomorphic properties of an area of the surface containing a high density of dark lineations, plus a major white line feature and its surroundings located several hundred kilometers from the lineation study area, has produced a data base of many of the major types of surface features on Europa. The aggregate data from several types of dark lineations (including some transitional to mottled terrain), a white line, dark patches, and two widely separated areas of plains is sufficient to attempt a comprehensive model of Europa's surface processes and (at least the most recent phase of) surficial evolution.

ASPECTS OF WATER PLUMES AND WATER VOLCANISM

Identifying Eruption Sites

Spectral and geomorphic evidence for two types of resurfacing mechanisms, water vapor/frost particle plumes and liquid water lava eruptions, have been found in this thesis. In the case of frost particle plumes, it has not been possible to identify specific eruption sites in this thesis, although Cook et al., (1982) and Helfenstein and Cook (1984) analyzed Voyager imagery of a proposed water vapor/frost eruption plume and traced it to its probable source location. Candidate water lava eruption sites can sometimes be identified, though identification is probably more the exception than the rule. The elicitation of eruption sites in Agenor Linea was a fortuitous combination of the exceptionally large size of this particular white line and its being present in the highest resolution Voyager 2 images. Many liquid water eruption sites on Europa are probably undetectable because their visible features fall below the limit of resolution in Voyager images or they present insufficient contrast with surrounding plains to be observable. There is, however, a class of European features that may show many sites of previous water lava eruption. These are dark lineations that terminate in plains material but have chains of dark spots continuing their trends beyond their terminations. No examples of this type of dark lineation are in the lineation study area; those known are found to the north and east of the study area. These chains of dark spots could represent old dark lineations that have been broken up by extrusion of

liquid water magmas at intermittent locations along the lineation. Such a disruption would be essentially identical to the mechanism constructed for Agenor Linea on page 163. Conversely, the chains of dark spots could mark sites where dark material intruded/extruded into plains material along the same line of crustal weakness that produced the dark lineation, but subsurface obstructions prevented extrusion along the entire weak zone. This latter hypothesis is essentially the one proposed by Lucchitta and Soderblom (1982) in their review of Europa's surface features. Both the water eruption and dark material intrusion models are similar, requiring some subsurface blockage of material intrusion. If the liquid water eruption model is correct, it provides hard evidence of resurfacing over a much larger area on Europa than the dark lineation and Agenor Linea study areas previously proposed in this thesis. Even if the water lava model is not correct for the chains of dark spots, it does not cripple this work's resurfacing model for Europa as a whole. The identification of subtle resurfacing, as well as validation or denial of other models proposed in this thesis, should be achieved with the Galileo Jupiter orbiter/probe spacecraft later in this decade.

Origin of Mottled Terrain

Lack of Craters/Palimpsests

The two resurfacing mechanisms proposed for Europa can be extrapolated from the study areas to the entire satellite. This does not

necessarily mean that every area of Europa's surface has continually been resurfaced throughout its history. Examination of Voyager global imagery shows large regions of relatively dark, non-plains material, covering the surface in non-continuous patterns. These constitute the mottled terrain unit. These areas in particular may represent parts of Europa that have not experienced significant resurfacing and hence could be the oldest areas on Europa. Mottled terrain regions, however, do not reveal a higher density of craters than other areas on Europa at the resolution of Voyager imagery (which varies from about 3 to 4 kilometers to several tens of kilometers). This superficially implies that the mottled terrain unit has not been exposed at Europa's surface any longer than other geomorphic units, including the brighter plains. The most likely explanation for this apparent discrepancy between expected age and apparent age of the mottled terrain is that resurfacing is not the primary mechanism that eradicates large European craters, but that viscous relaxation of the icy surface layer is instead the cause. The believed relatively high purity of the ice on the surface of Europa (Pilcher et al., 1972; Clark, 1980) makes this plausible, but then the question arises as to why more palimpsests are not seen on Europa. In the case of Ganymede, palimpsests appear as non-topographic, higher-albedo circular or elliptical surface markings (Smith et al., 1979b; Shoemaker et al., 1982). On Europa, such markings would probably possess insufficient contrast with their surroundings to be detectable in the brighter plains units. Photogeologic evidence, however, indi-

cates that some palimpsests on Europa may take the form of relatively dark surface markings, based on the identification of circular/elliptical features in the plains and elsewhere on the satellite (Lucchitta and Soderblom, 1982; Meier, 1983b). If this is the case, it may well be that dark European palimpsests would not provide sufficient contrast to be detectable in the mottled terrain. Europa may therefore possess a great number of both dark and bright palimpsests that are not observable in Voyager imagery because of limitations in its camera system's dynamic range and signal-to-noise ratio. Assuming that a greater density of palimpsests exists in the mottled terrain than the plains (i.e., that the mottled terrain has an older surface exposure age than the plains), the logical conclusion is that resurfacing processes have not been active in the mottled terrain areas. This leads to a view of Europa as consisting of rocky, "continent-like" areas (i.e., the mottled terrain) that may not overlie easily accessible reservoirs of liquid water, and purer-ice "ocean-like" plains that probably do have ready access to large supplies of crustal or sub-crustal liquid water. Such a model, if correct, indicates that Europa's crust is poorly differentiated, with a significantly thicker crust under mottled areas as opposed to plains areas.

Role of Water Volcanism

White line (i.e., ice ridge) continuous-along-length water lava eruptions and Agenor Linea-style intermittent water lava eruptions could

be responsible for the dissected appearance of dark material in some areas of mottled terrain. In areas where dark patches constituting mottled terrain are in close proximity, with minor amounts of plains material in between, the plains material may have been emplaced by the eruption of water lava through a network of fractures in the mottled terrain. Long-term or prolific eruptions would have overflowed the fracture walls (i.e., water lava channels), flooding areas of surrounding terrain many times wider than the parent fracture. Consequently, the distance between mottled terrain dark patches would increase as the patches themselves decreased in size. This model is probably not suitable for areas of mottled terrain characterized by widely-separated dark spots and patches that do not form chain-like patterns. Here it appears that dark areas represent either sites of dark material intrusion or impacts that have penetrated the bright surface layer to expose underlying dark material (Lucchitta and Soderblom, 1982).

Effect of Degradative Mechanisms

The subject arises concerning why mottled terrain areas may show evidence of water lava eruptions but not water frost particle plume eruptions. Plumes should be possible in most areas where liquid water lavas are possible on Europa, although because of subsurface structural considerations the converse is not thought to be true. The answer to the question of which resurfacing processes have left observable evidence in mottled regions is that plume depositional products, being much

thinner than those of water lava, probably have been removed by degradative processes if the rate of frost particle deposition is less than the rate of ion erosion plus other degradative surface processes on Europa (e.g., micrometeoroid gardening and ice sublimation). This is plausible if plume eruptions are intermittent, with significant periods of dormancy between eruptive episodes. Laboratory results indicate that the rate of ion erosion for water ice is several orders of magnitude higher than for the silicate minerals that probably compose the dark materials on Europa's surface (Brown et al., 1978). Similarly, gardening and sublimation processes preferentially remove surface ice, leaving rocky material relatively undisturbed. Given enough time without resurfacing, the net effect is to leave a surface "armor" of silicate material that resists further erosion (Shoemaker et al., 1982). Water vapor/frost particle plume resurfacing effects could thus be completely negated in mottled terrain areas if, for example, greater crustal thickness in mottled areas has inhibited continuous plume eruptions.

Since the spectral and albedo properties of the mottled terrain were not studied in this thesis, the degree to which any plume effects may have been offset by degradative mechanisms cannot be determined. If plume effects have been removed and water lava flow deposits remain in the mottled terrain, however, it provides evidence that the mottled terrain unit is older than the dark lineation study area where plume effects survive. This conjecture is highly speculative, of course,

because times and frequencies of water frost plume eruptions could have fluctuated between different provinces of Europa, but the implications of the conjecture are important enough to the historical model of the satellite to warrant consideration.

LIFE CYCLE OF A DARK LINEATION

The observations in the dark lineation and Agenor Linea study areas, plus the models of two resurfacing mechanisms that were developed, allow for the synthesis of a model of the birth, life, death, and reincarnation of a dark lineation on Europa. This model is shown in the form of a flow diagram in Figure 23. Basic to this model is the development of two styles of surface fractures -- uninterrupted fractures (i.e., open fissures with no subsurface obstructions to intrusion/extrusion) and interrupted fractures (i.e., incompletely-developed fractures that are obstructed in the subsurface such that intrusion/extrusion is possible only at certain points along the length of the fracture). Individual steps in the dark lineation life cycle have been previously discussed at various points in this thesis and will not be repeated here. What is important to note about this flow diagram is that the evolution of a dark lineation can cease at any point in the diagram after the intrusion/extrusion of dark lineation material into a surface fracture. Steps involving water vapor/frost plume resurfacing must also be considered reversible because their slow deposition rates could be nullified by the effects of ion erosion and micrometeoroid

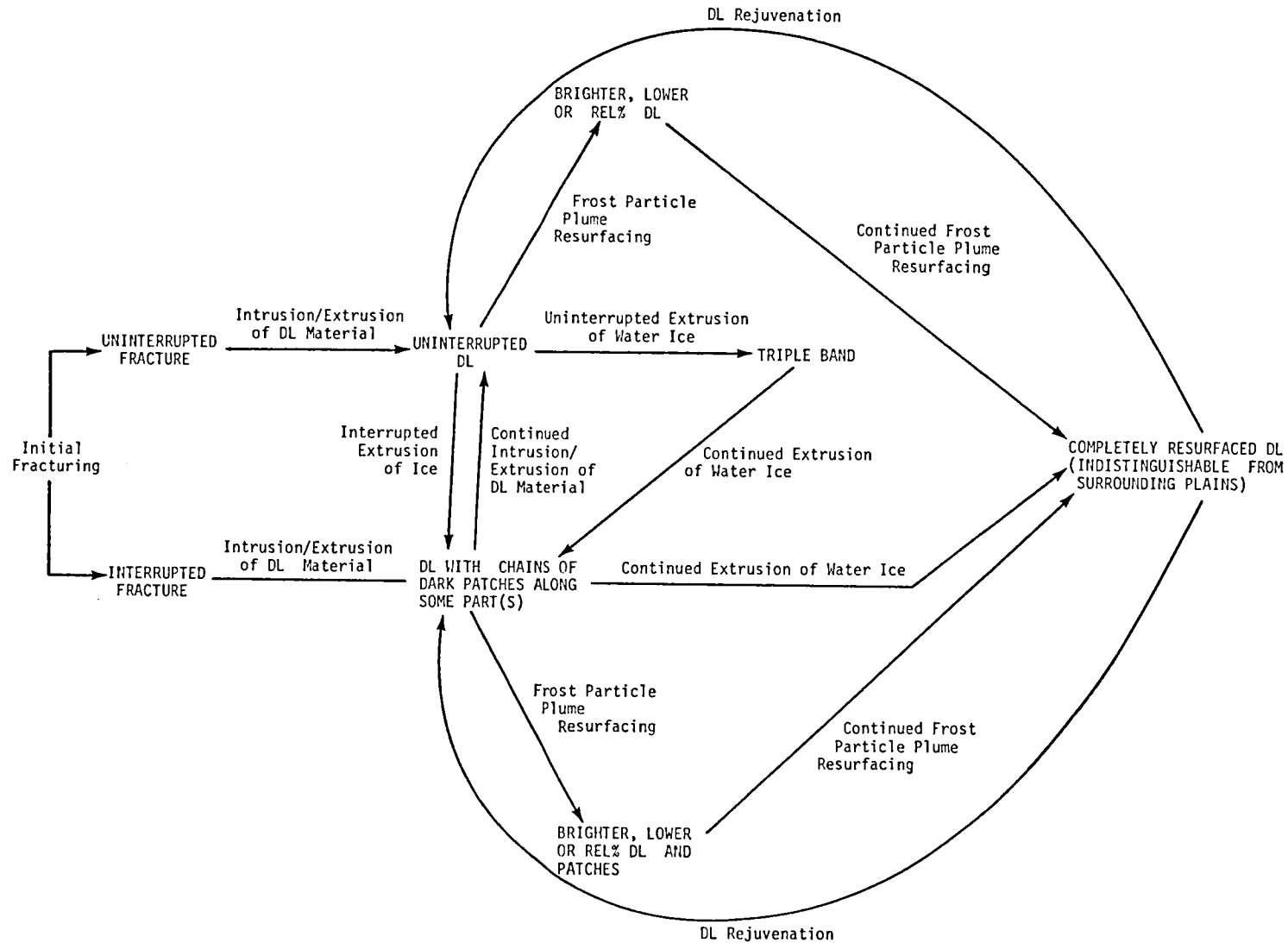


FIGURE 23. Life cycle of a dark lineation. Processes are italicized and the resulting states of the dark lineation are shown in upper case letters.

gardening processes (Haff and Watson, 1979; Johnson et al., 1981; Wolff and Mendis, 1983) and ice sublimation (see Squyres, 1980, for an analogous discussion of sublimation on Ganymede and Callisto). The life cycle of a dark lineation thus can be more complicated than is indicated in Figure 23.

LARGE-SCALE RESURFACING

The large-scale picture of Europa that emerges from the findings of this thesis is of a satellite which has recently undergone or is currently undergoing highly variable rates of resurfacing over different areas. Water vapor/frost particle plumes cover relatively large areas (circular regions probably up to a few hundred kilometers in diameter) but leave very thin deposits that can take several thousand years or more to completely resurface a dark lineation. If plume activity is intermittent, destructive processes such as ion erosion, micrometeoroid gardening, and ice sublimation can negate much of their depositions. Liquid water lava eruptions provide thicker, more permanent resurfacing deposits in relatively short lengths of time, but their extent is highly localized (probably limited to a few tens of kilometers or less).

Liquid water eruption sites constitute the most attractive method of achieving complete resurfacing if the requirement for a very large number of eruption sites can be satisfied. This requirement may be met in some areas of Europa. A close examination of the highest resolution Voyager 2 images, especially blue filter images, shows that darkish

lineations exist at all scales from the largest dark lineation observed down to the limit of resolution, both in size and contrast with the surrounding plains. Figure 24 depicts the location of the shortest, faintest lineations in the areas covered by high resolution imagery. Note the concentration of these features in the area comprising the fractured plains unit in the geomorphic surface map of Lucchitta and Soderblom (1982). Ubiquitous fracture distributions such as in the fractured plains area probably cover a much larger percentage of Europa's surface than is indicated by Figure 24, but may not have been visible under the lighting conditions in which Voyager 2 imagery was made. The concentrations of dark lineations/fractures are sufficient in the areas imaged for those entire regions to be resurfaced by coalescing liquid water lava flows erupting from the fractures. Also, because darkish lineations exist down to the observable limit of resolution, it is probable that they exist below the limit of resolution as well. This translates to lineations of less than Voyager 2's approximately 8 to 10 kilometer length limit of recognition, which would of course result in an even greater density of dark lineations on Europa's surface. The faintness (as compared to the surrounding plains) of many of the short dark lineations indicates that water vapor/frost particle plumes may be an important resurfacing mechanism for them, and possibly the major agent of resurfacing. It must be remembered that, although liquid water eruption is the most attractive model for complete resurfacing, spectral and albedo evidence for plume resurfacing was found at many more sites

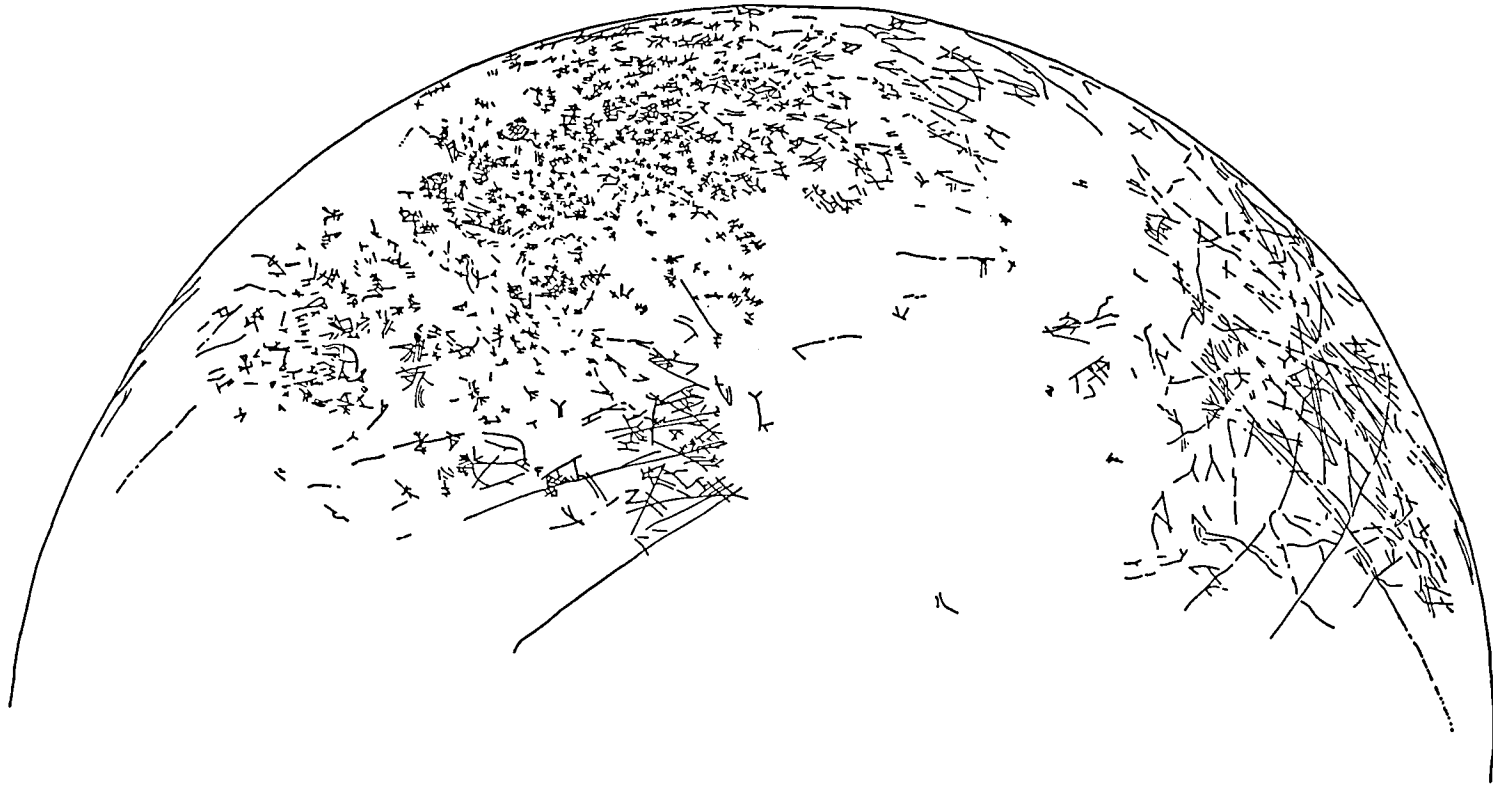


FIGURE 24. Map of short dark lineations (DL's) on a portion of Europa's surface, made from a mosaic of high-resolution blue filter Voyager 2 images. Most of these are classified as Type 5 lineations in the lineation classification system of Pieri (1981). Nearly all longer DL's have been eliminated from this map. The short DL's are generally brighter (i.e., fainter when contrasted with the surrounding plains) than longer DL's. Note the high concentration of short DL's in the area at the top center, which has been termed fractured plains by Lucchitta and Soderblom (1982).

over a much larger area (i.e., the dark lineation study area) than the one example of possible liquid water resurfacing found at Agenor Linea. Eruption of water via plumes could also completely resurface areas of dense, small-scale dark lineations, especially when considering that high densities of plumes in such areas would multiply the deposition rates because of significant plume overlap.

Objectively, then, evidence favors plume resurfacing over liquid water lava resurfacing as the primary means of burying surface features over the portion of Europa imaged at high resolution. In fairness, it should be noted that the resolution of Voyager imagery prevents an equal comparison of both processes, since many liquid water eruption features could exist below the spatial limit of resolution. Agenor Linea is an exceptional case, being larger by far than most white lines on Europa (which often appear as features only one pixel wide in Voyager images). As such, it may be the only white line feature on Europa for which Voyager 2 was able to provide evidence of liquid water eruption. Even if other white lines and triple bands are sites of liquid water magma/lava eruption, however, the amount of surface they could bury even by overflowing their quasi-linear channels or other constraining features is very limited. Water eruption sites other than lineations and white lines are possible, but some mechanism or phenomenon is necessary to penetrate Europa's crust and reach a source of liquid water. Cratering impacts are a possibility, but most probably lack sufficient kinetic energy to generate fractures that would penetrate the crust

deeply enough to tap liquid water sources. Some craters on Europa have radial fractures associated with them (Lucchitta and Soderblom, 1982), so some liquid water resurfacing could be related to impacts. The overwhelming advantage of water frost particle plumes for large-scale resurfacing is the much larger surface area covered yet relatively uniform layer deposited as contrasted with liquid water resurfacing. The favored model for Europa that combines all plausible resurfacing mechanisms is for water vapor/frost plumes to be the dominant process of burying surface features under relatively clean ice deposits, working slowly but progressively over large areas. Water lava eruptions are an important adjunct to frost plumes, allowing areas to be absolutely resurfaced relatively quickly, but limited in the areas they can completely cover to regions of dense fractures/lineations that can be reactivated to allow water intrusion/extrusion. Large impacts may serve as an important exogenic component of water lava resurfacing if the solid portion of Europa's crust is thin enough at the impact site and the impact possesses sufficient kinetic energy to generate fractures that can penetrate the crust and reach a source of liquid water. Impact-induced resurfacing probably has been quite limited in the recent geologic past due to the expected low frequency of large impacts and the observational lack of bright palimpsests on Europa.

AVAILABILITY OF LIQUID WATER

The whole topic of resurfacing on Europa hinges on the question of

whether or not the satellite possesses a liquid water mantle or some other form of liquid water reservoir. Mechanisms to transport liquid water to Europa's surface are not difficult to conceive, as has been previously suggested in the form of tidally- and impact-induced fractures. A considerable degree of controversy has arisen as to Europa's capacity to supply enough heat to maintain a liquid water mantle, however. Cassen et al. (1979) at first concluded that Europa probably does possess a liquid water mantle, then decided that it probably does not (Cassen et al., 1980) when they found that they had made heat dissipation calculations more appropriate for a silicate body than one with an outer shell of ice in their original paper. Their research has been adamant in stating that if Europa's mantle ever froze, radiogenic heating would be insufficient to ever remelt it. It is not a goal of this thesis to add to the quantitative theoretical work that has been done on Europa's thermal history. It should be pointed out, however, that such modeling tends, by necessity, to greatly simplify the entire set of factors contributing to the thermal evolution of a body, and that the results are very sensitive to the initial conditions chosen and the values selected for them. These latter characteristics are very difficult to define with great accuracy. Consequently, the results of even the best thermal modeling could easily be in error on the matter of the state of Europa's mantle. Several studies have pointed to evidence of the products of liquid water resurfacing: the very high albedo and identification of water ice on Europa's surface (Pilcher et al., 1972; Fink

et al., 1973); the lack of craters at all observable scales on the surface (Smith et al., 1979b; Lucchitta and Soderblom, 1982); the observation of a possible water vapor/frost plume and an associated bright spot on Europa's surface (Helfenstein and Cook, 1984); and the strong relationship between the albedo of a dark lineation and its spectral resemblance to the surrounding plains (this thesis). These factors alone almost obligate Europa to have an accessible supply of subsurface liquid water. Though there is a danger of becoming model-dependent, theoretical work should continue to search for reasonable conditions under which Europa could have evolved with and preserved a liquid water mantle or subsurface reservoir of some type.

SUMMARY AND CONCLUSIONS

The surface of Europa does not possess the degree of multispectral and albedo variation that the other Galilean satellites do, yet a detailed examination of these properties reveals a remarkable diversity amongst European surface features. Developing and utilizing new ternary diagram techniques for displaying multispectral relative reflectance data has led to the discovery of many new facts and relationships between dark lineations, white lines, dark patches, and plains units on Europa. Most significant is the finding of a strong correlation between the spectral class of a dark lineation and its local brightness (i.e., brightness compared to other dark lineations in the area immediately surrounding it) in an area of Europa between 220° and 180° Longitude and -24° and -2° Latitude. The relationship found is that the albedo of a dark lineation increases as the relative spectral reflectance of the feature decreases at the Voyager TV subsystem's orange wavelength (as compared to violet and blue relative spectral reflectances). Coupled with this finding is the discovery that the dark lineations with the lowest orange relative spectral reflectance (which are also the highest albedo dark lineations) bear a strong spectral resemblance to the surrounding brighter plains unit in ternary diagram plots. Taken together, these findings strongly indicate that the plains unit is replacing the dark material unit in the dark lineations. Considering the gradational spectral sequence of

dark lineations that was found within the 193 dark lineation segment suite investigated, the material replacement process is believed to be gradual and relatively uniform. The gradational spectral sequences of lineation relative spectral reflectances within the dark lineation suite leads to a model of two fundamental compositional surface units, the dark lineation material unit and the plains unit. Spectral diversity within the dark lineation suite can be explained in terms of a simple linear mixing model between the two compositional units. The most likely mechanism for enacting the material replacement process is water vapor/frost particle plumes of a type similar to that which may have been found in Voyager imagery by Cook et al. (1982). These spectral/albedo discoveries are among the first hard evidence of the long-suspected resurfacing of Europa proposed by many researchers based on the lack of observable craters on the satellite.

Agenor Linea, a prominent white line feature found between 220° and 178° Longitude and -44° and -41.5° Latitude, provides support for the existence of a second style of resurfacing on Europa, namely liquid water lava eruptions. The evidence for this was found in the form of distinctly brighter regions within the already high-albedo white line. The presence of at least six major bright spots spaced intermittently along Agenor Linea is taken as evidence of discrete liquid water lava eruption sites. The enhanced albedoes at these sites is interpreted as the consequence of the emplacement of a thin layer of specularly-reflecting frost on the depositional sequences of

water ice forming the low-relief eruption cones. This frost would not be present in the inter-site areas.

No evidence was found for major contiguous lengthwise areas of the same spectral/compositional subunit or gradational subunit sequences in Agenor Linea, although short sequences of each were found. Similarly, no strong spectral relationships were found between the bright material of Agenor Linea and its flanking dark patches. The plains immediately surrounding Agenor Linea are higher in orange relative spectral reflectance than the plains in the dark lineation study area to the north. Agenor Linea itself more closely resembles the dark lineation study area plains than its surrounding plains, in a spectral sense. The plains surrounding Agenor Linea are probably possessed of a less pure plains composition than the plains to the north, because plains near Agenor Linea may contain a network of darkish lineations below the resolution of Voyager 2 imagery. This would be consistent with the pattern of darkish lineations in the fractured plains present in this area, but at a smaller scale. Consequently, the composition of Agenor Linea appears to be of a relatively pure plains unit composition compared to its own encompassing plains.

The findings for dark lineations and Agenor Linea lead to a model for the life cycle of a fracture on Europa. Two basic types of fractures are indicated, one with subsurface obstructions allowing only intermittent intrusion/extrusion along its length and the other al-

lowing uninterrupted intrusion/extrusion along its entire length. From these, all types of linear features observed on Europa can be generated. A model for Agenor Linea based on this life cycle consists of initial fracturing; dark lineation material intrusion; bright material emplacement during a second intrusive/extrusive episode in which liquid water volcanism occurred at intermittent sites along the length of the dark lineation, forming a chain of bright spots; continued extrusion of liquid water lava, causing bright spots to merge into a white line feature and creating a poorly-defined triple band structure in the process (the dark lineation being dissected into a chain of irregularly-spaced dark patches on either side of the white line). Water vapor/frost particle plume resurfacing is not included in the model of Agenor Linea, but is believed to be a significant surface modification process in the dark lineation study area.

The relative balance between liquid water volcanism and water vapor/frost plume resurfacing is uncertain, but plume resurfacing is favored for large-scale surface modification because of the much larger area a single site can affect. Liquid water lava resurfacing is quicker to bury features and more resistant to degradative mechanisms such as ion erosion and micrometeoroid gardening because of the thickness of water lava deposits. Degradative effects could negate plume resurfacing if plume eruption episodes are highly intermittent or cease in a geologically short period of time; such effects therefore complicate the life cycle flow diagram of European fractures.

These effects, plus fracture reactivation, mean that buried dark lineations could be rejuvenated. Liquid water lava eruptions through networks of fractures, with flooding of surrounding terrain beyond fracture walls, is a possible explanation for the dissected appearance of mottled terrain in areas where the dark patches are closely spaced.

Besides the strong relationship between a dark lineation's spectral class and local brightness, other relationships were found between dark lineation properties of spectral class, local brightness, number of data points per lineation, color distribution field (CDF) area in the lineation's ternary diagram plot, CDF point density, degree of point dispersion in the CDF, and the dark lineation's orientation. None of the other relationships found are as strong as that between the spectral and brightness classes. Some are negative relationships (i.e., the number of matchings found between two properties' classes is much lower than expected from a normal distribution). Some of the very short dark lineation segments (i.e., those composed of 15 or less data points) show signs that they are not composed of enough data points to accurately reveal the amount of spectral/compositional variation they possess.

The suite of 193 dark lineation segments was large enough to permit identification of unique dark lineations. Some dark lineations are unique in their spectral/compositional properties because some of their data points plot with unusual blue or violet relative spectral reflectances. Other dark lineations are compositionally unique

because they possess an extremely large or extremely small amount of compositional variation along their length. A few dark lineations are unusual in several respects. DL121 is a large wedge-shape dark lineation that not only shows morphological evidence of rifting and limited icy plate rotation, but also shows a distinct compositional and albedo division between the wider, northern portion and the narrower, southern portion. The brighter, narrow portion shows evidence of plume resurfacing while the darker, wider portion does not. A plausible model of DL121 shows that the narrower, southern portion may be a product of fracture reactivation that occurred at a later time than the northern portion of the dark lineation was formed. Two other dark lineation segments, DL77 and DL78, actually appear to be sections of one continuous feature that show distinctly different spectral properties. A third dark lineation, DL79, intersects DL77 and DL78 at exactly the point where the spectral division occurs. This fact, plus the difference in spectral properties, may be evidence that different fracturing episodes took place in a small area.

Zoning was found in the plains in color ratio composite images of Europa. It is uncertain from the structure of the zones if they are a genuine manifestation of decreasing concentrations of implanted Io-derived sulfur ions in surficial ice, or an artifact of computer image processing.

The results taken in total show that the ternary diagram multi-spectral plotting techniques developed for this thesis work very well

and should be applicable to a wide variety of other multispectral studies. Particularly encouraging was the finding that a much greater diversity of multispectral classifications can be made (i.e., much more subtle spectral variations can be detected) with ternary diagram plots than with color ratio images or parallelepiped classifiers. The techniques used in this thesis may have been better than the quality of the data could accommodate. Noise or error due to dark current in Voyager TV camera vidicons, photometric and multispectral photometric effects across Voyager Europa images, and improperly registered images or improperly/inappropriately profiled linear features could have been processed along with the valid data. The data processed is the only data of its kind available, however, and was processed in the best manner possible at the time it was done. Until the Galileo Jupiter orbiter/probe spacecraft arrives at Jupiter later in this decade, these results should be considered to be as valid as is possible to achieve.

REFERENCES

- 1) Aksnes, K., and Franklin, F.A. (1975a). Mutual phenomena of the Galilean satellites in 1973. I. Total and near-total occultations of Europa by Io. *Astron. J.* 80, 56-63.
- 2) Aksnes, K., and Franklin, F. (1975b). DeSitter's theory "melts" Europa's polar cap. *Nature* 258, 503-505.
- 3) Arvidson, R.E., Guinness, E.A., and Zent, A.P. (1982). Classification of surface units in the equatorial region of Mars based on Viking Orbiter color, albedo, and thermal data. *J. Geophys. Res.* 87, 10,149-10,157.
- 4) Blanco, C., and Catalano, S. (1974). Mutual eclipses of Jupiter's satellites. *Astron. Astrophys.* 33, 303-309.
- 5) Brown, W.L., Augustyniak, W.M., Lanzerotti, L.J., Johnson, R.E., and Evatt, R. (1980). Linear and nonlinear processes in the erosion of H₂O Ice by fast light ions. *Phys. Rev. Lett.* 45, 1632-1635.
- 6) Brown, W.L., Lanzerotti, L.J., Poate, J.M., and Augustyniak, W.M. (1978). "Sputtering" of ice by MeV light ions. *Phys. Rev. Lett.* 40, 1027-1030.
- 7) Buratti, B., and Veverka, J. (1983). Voyager photometry of Europa. *Icarus* 55, 93-110.
- 8) Caldwell, J. (1975). Ultraviolet observations of small bodies in the solar system by OAO-2. Presented at IAU Colloq. No. 28. *Icarus*

- 25, 384-396.
- 9) Campbell, D.B., Chandler, J.F., Ostro, S.J., Pettengill, G.H., and Shapiro, I.I. (1978). Galilean satellites: 1976 radar results. *Icarus* 34, 254-267.
 - 10) Cassen, P., Peale, S.J., and Reynolds, R.T. (1980). Tidal dissipation in Europa: A correction. *Geophys. Res. Lett.* 7, 963-970.
 - 11) Cassen, P., Reynolds, R.T., and Peale, S.J. (1979). Is there liquid water on Europa? *Geophys. Res. Lett.* 6, 731-734.
 - 12) Clancy, R.T., and Danielson, G.E. (1981). High resolution albedo measurements on Io from Voyager 1. *J. Geophys. Res.* 86, 8627-8634.
 - 13) Clark, R.N. (1980). Ganymede, Europa, Callisto, and Saturn's rings: Compositional analysis from reflectance spectroscopy. *Icarus* 44, 388-409.
 - 14) Clark, R.N. (1981a). The spectral reflectance of water-mineral mixtures at low temperatures. *J. Geophys. Res.* 86, 3074-3086.
 - 15) Clark, R.N. (1981b). Water frost and ice: The near-infrared reflectance 0.65-2.5 μm . *J. Geophys. Res.* 86, 3087-3096.
 - 16) Clark, R.N., and McCord, T.B. (1980). The Galilean satellites: New near-infrared reflectance measurements (0.65-2.5 μm) and a 0.325-5 μm summary. *Icarus* 41, 323-339.
 - 17) Consolmagno, G.J., and Lewis, J.S. (1976). Structural and thermal models of icy Galilean satellites. In *Jupiter* (T. Gehrels, Ed.), pp. 1035-1051. Univ. of Arizona Press, Tucson.
 - 18) Consolmagno, G.J., and Lewis, J.S. (1977). Preliminary thermal

- history models of icy satellites. In *Planetary Satellites* (J.A. Burns, Ed.), pp. 492-500. Univ. of Arizona Press, Tucson.
- 19) Consolmagno, G.J., and Lewis, J.S. (1978). The evolution of icy satellite interiors and surfaces. *Icarus* 34, 280-293.
 - 20) Cook, A.F., Shoemaker, E.M., Soderblom, L.A., Mullins, K.F., and Fiedler, R. (1982). Volcanism in ice on Europa. *Bull. Amer. Astron. Soc.* 14, 736-737.
 - 21) Danielson, G.E., Kupferman, P.N., Johnson, T.V., and Soderblom, L.A. (1981). Radiometric performance of the Voyager cameras. *J. Geophys. Res.* 86, 8683-8689.
 - 22) DePater, I., Brown, R.A., and Dickel, J.R. (1984). VLA observations of the Galilean satellites. *Icarus* 57, 93-101.
 - 23) Dollfus, A. (1975). Optical polarimetry of the Galilean satellites of Jupiter. *Icarus* 25, 416-431.
 - 24) Eviatar, A., Siscoe, G.L., Johnson, T.V., and Matson, D.L. (1981). Effects of Io ejecta on Europa. *Icarus* 47, 75-83.
 - 25) Fanale, F.P., Johnson, T.V., and Matson, D.L. (1977). Io's surface and the histories of the Galilean satellites. In *Planetary Satellites* (J.A. Burns, Ed.), pp. 379-405. Univ. of Arizona Press, Tucson.
 - 26) Fink, U., Dekkers, N.H., and Larson, H.P. (1973). Infrared spectra of the Galilean satellites of Jupiter. *Astrophys. J.* 179, L155-L159.
 - 27) Fink, U., and Larson, H.P. (1975). Temperature dependence of the water ice spectrum between 1 and 4 microns: Application to Europa,

- Ganymede and Saturn's rings. *Icarus* 24, 411-420.
- 28) Finnerty, A.A., Ransford, G.A., Pieri, D.C., and Collerson, K.D. (1981). Is Europa's surface cracking due to thermal evolution? *Nature* 289, 24-27.
- 29) Gehrels, T. (1977). Picture of Ganymede. In *Planetary Satellites* (J.A. Burns, Ed.), pp. 406-411. Univ. of Arizona Press, Tucson.
- 30) Gillet, F.C., Merrill, K.M., and Stein, W.A. (1970). Albedo and thermal emission of Jovian satellites I-IV. *Astrophys. Lett.* 6, 247-249.
- 31) Goldstein, R.M., and Green, R.R. (1980). Ganymede: Radar surface characteristics. *Science* 207, 179-180.
- 32) Gradie, J., and Zellner, B. (1973). A polarimetric survey of the Galilean satellites. *Bull. Amer. Astron. Soc.* 5, 404.
- 33) Greene, T.F., Vermilion, J.R., Shorthill, R.W., and Clark, R.N. (1975). The spectral reflectivity of selected areas of Europa. *Icarus* 25, 405-415.
- 34) Gross, S.H. (1974). The atmospheres of Titan and the Galilean satellites. *J. Atmos. Sci.* 31, 1413-1420.
- 35) Guinness, E.A. (1981). Spectral properties (0.40 to 0.75 microns) of soils exposed at the Viking 1 landing site. *J. Geophys. Res.* 86, 7983-7992.
- 36) Haff, P.K., and Watson, C.C. (1979). Ion erosion on the Galilean satellites of Jupiter. *Proc. 10th Lunar Planet. Sci. Conf.*, pp. 1987-1998.

- 37) Hanel, R., Conrath, B., Flasar, M., Herath, L., Kunde, V., Lowman, P., Maguire, W., Pearl, J., Pirraglia, J., Samuelson, R., Gautier, D., Gierasch, P., Horn, L., Kumar, S., and Ponnampereuma, C. (1979). Infrared observations of the Jovian system from Voyager 2. *Science* 206, 952-956.
- 38) Hansen, O.L. (1973). Ten micron eclipse observations of Io, Europa, and Ganymede. *Icarus* 18, 237-246.
- 39) Hansen, O.L. (1975). Infrared albedos and rotation curves of the Galilean satellites. *Icarus* 26, 24-29.
- 40) Hansen, O.L. (1976). Thermal emission spectra of 24 asteroids and the Galilean satellites. *Icarus* 27, 463-471.
- 41) Harris, D.L. (1961). Photometry and colorimetry of planets and satellites. In *Planets and Satellites* (G.P. Kuiper and B.M. Middlehurst, Eds.), pp. 272-343. Univ. Chicago Press, Chicago.
- 42) Helfenstein, P. (1982). Tidal origin of Europa's fractures: A refined analysis. In *Lunar Planet Sci. XIII, Abstracts*, pp. 314-315. Lunar and Planetary Institute, Houston.
- 43) Helfenstein, P. (1983). Geomorphic structures on Europa: A new method for the recognition of features near the limit of resolution. In *Lunar Planet. Sci. XIV, Abstracts*, pp. 295-296. Lunar and Planetary Institute, Houston.
- 44) Helfenstein, P., and Cook, A.F. (1984). Active venting on Europa?: Analysis of a transient bright surface feature. In *Lunar Planet. Sci. XV, Abstracts*, pp. 354-355. Lunar and Planetary Institute,

- Houston.
- 45) Helfenstein, P., and Parmentier, E.M. (1980). Fractures on Europa: Possible response of an ice crust to tidal deformation. *Proc. 11th Lunar Planet. Sci. Conf.*, pp. 1987-1998.
 - 46) Helfenstein, P., and Parmentier, E.M. (1983). Patterns of fracture and tidal stresses on Europa. *Icarus* 53, 415-430.
 - 47) Johnson, R.E., Lanzerotti, L.J., Brown, W.L., and Armstrong, T.P. (1981). Erosion of Galilean satellite surfaces by Jovian magnetospheric particles. *Science* 212, 1027-1030.
 - 48) Johnson, T.V. (1971). Galilean satellites: Narrowband photometry 0.30 to 1.10 microns. *Icarus* 14, 94-111.
 - 49) Johnson, T.V., and Fanale, F.P. (1973). Optical properties of carbonaceous chondrites and their relationship to asteroids. *J. Geophys. Res.* 78, 8507-8518.
 - 50) Johnson, T.V., and McCord, T.B. (1970). Galilean satellites: The spectral reflectivity 0.30-1.10 microns. *Icarus* 13, 37-42.
 - 51) Johnson, T.V., and McCord, T.B. (1971). Spectral geometric albedo of the Galilean satellites, 0.3 to 2.5 microns. *Astrophys. J.* 169, 589-594.
 - 52) Johnson, T.V., and McGetchin, T.R. (1973). Topography on satellite surfaces and the shape of asteroids. *Icarus* 18, 612-620.
 - 53) Johnson, T.V., and Pilcher, C.B. (1977). Satellite spectrophotometry and surface compositions. In *Planetary Satellites* (J.A. Burns, Ed.), pp. 232-268. Univ. of Arizona Press, Tucson.

- 54) Johnson, T.V., Soderblom, L.A., Mosher, J.A., Danielson, G.E., Cook, A.F., and Kupferman, P. (1983). Global multispectral mosaics of the icy Galilean satellites. *J. Geophys. Res.* 88, 5789-5805.
- 55) Kieffer, H.H., and Smythe, W.D. (1974). Frost spectra: Comparison with Jupiter's satellites. *Icarus* 21, 506-512.
- 56) Kuiper, G.P. (1957). Infrared observations of planets and satellites. *Astron. J.* 62, 245.
- 57) Lane, A.L., Nelson, R.M., and Matson, D.L. (1981). Europa's UV absorption band: Evidence for sulfur implantation? *Nature* 292, 38-39.
- 58) Lebofsky, L.A. (1975). Stability of frosts in the solar system. *Icarus* 25, 205-217.
- 59) Lee, T. (1972). Spectral albedos of the Galilean satellites. *Comm. Lunar. Planet. Lab.* 9, 179-180.
- 60) Lewis, J.S. (1971). Satellites of the outer planets: Thermal models. *Science* 172, 1127-1128.
- 61) Low, F.J. (1965). Planetary radiation at infrared and millimeter wavelengths. *Bull. Lowell Obs.* 5, 184-187.
- 62) Lucchitta, B.K., and Soderblom, L.A. (1982). The geology of Europa. In *Satellites of Jupiter* (D. Morrison, Ed.), pp. 521-555. Univ. of Arizona Press, Tucson.
- 63) Lucchitta, B.K., Soderblom, L.A., and Ferguson, H.M. (1981). Structures on Europa. *Proc. 12th Lunar Planet. Sci. Conf.*, pp. 1555-1567.

- 64) McCord, T.B., Clark, R.N., Meloy, A., Nelson, M., Johnson, T.V., Matson, D., and Mosher, J.A. (1982). Spectral unit maps of Europa. In *Lunar Planet. Sci. XIII, Abstracts*, pp. 485-486. Lunar and Planetary Institute, Houston.
- 65) McFadden, L.A., Bell, J., and McCord, T.B. (1981). Visible spectral reflectance measurements 0.3-11 μm of the Galilean satellites at many orbital phase angles 1977-1978. *Icarus* 44, 410-430.
- 66) Malin, M.C. (1980). Morphology of lineaments on Europa. IAU Colloq. No. 57: *The Satellites of Jupiter*, abstract 7-2.
- 67) Meier, T.A. (1981). Color distribution fields of geomorphic features on Europa: Initial results from a new technique. In *Reports of Planetary Geology Program-1981*, NASA TM 84211, pp. 47-49.
- 68) Meier, T.A. (1983a). A detailed spectral study of *Agenor Linea*, Europa. In *Lunar Planet. Sci. XIV, Abstracts*, pp. 495-496. Lunar and Planetary Institute, Houston.
- 69) Meier, T.A. (1983b). Possible fossil craters on Europa. In *Lunar Planet. Sci. XIV, Abstracts*, pp. 497-498. Lunar and Planetary Institute, Houston.
- 70) Miller, S.L. (1961). The occurrence of gas hydrates in the solar system. *Proc. Nat'l. Acad. Sci.* 47, 1798-1808.
- 71) Millis, R.L., and Thompson, D.T. (1975). UVB photometry of the Galilean satellites. *Icarus* 26, 408-419.
- 72) Morabito, L.A., Synnott, S.P., Kupferman, P.N., and Collins, S.A. (1979). Discovery of currently active extraterrestrial volcanism.

- Science* 204, 972.
- 73) Moroz, V.I. (1965). IR spectrophotometry of satellites: The Moon and the Galilean satellites of Jupiter. Translation in *Soviet Astron.* 9, 999-1006.
- 74) Morrison, D. (1977). Radiometry of satellites and of the rings of Saturn. In *Planetary Satellites* (J.A. Burns, Ed.), pp. 269-301. Univ. of Arizona Press, Tucson.
- 75) Morrison, D., and Cruikshank, D.P. (1973). Thermal properties of the Galilean satellites. *Icarus* 18, 224-236.
- 76) Morrison, D., Cruikshank, D.P., and Murphy, R.E. (1972). Temperatures of Titan and the Galilean satellites at 20 μ . *Astrophys. J.* 173, L143-L146.
- 77) Morrison, D., and Morrison, N.D. (1977). Galilean satellite photometry. In *Planetary Satellites* (J.A. Burns, Ed.), pp. 363-378. Univ. of Arizona Press, Tucson.
- 78) Morrison, D., Morrison, N.D., and Lazarewicz, A. (1974). Four-color photometry of the Galilean satellites. *Icarus* 23, 399-416.
- 79) Murphy, R.E., and Aksnes, K. (1973). Polar cap on Europa. *Nature* 244, 559-560.
- 80) Murray, J.B. (1975). New observations of surface markings on Jupiter's satellites. *Icarus* 25, 397-404.
- 81) Nelson, R.M., and Hapke, B.W. (1978). Spectral reflectivities of the Galilean satellites and Titan, 0.32 to 0.86 micrometers. *Icarus* 36, 304-329.

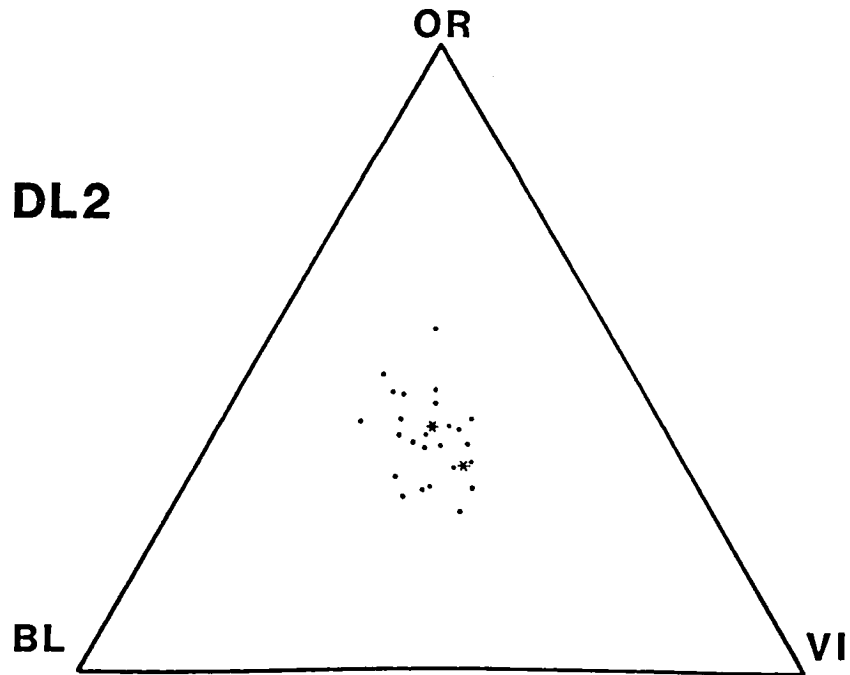
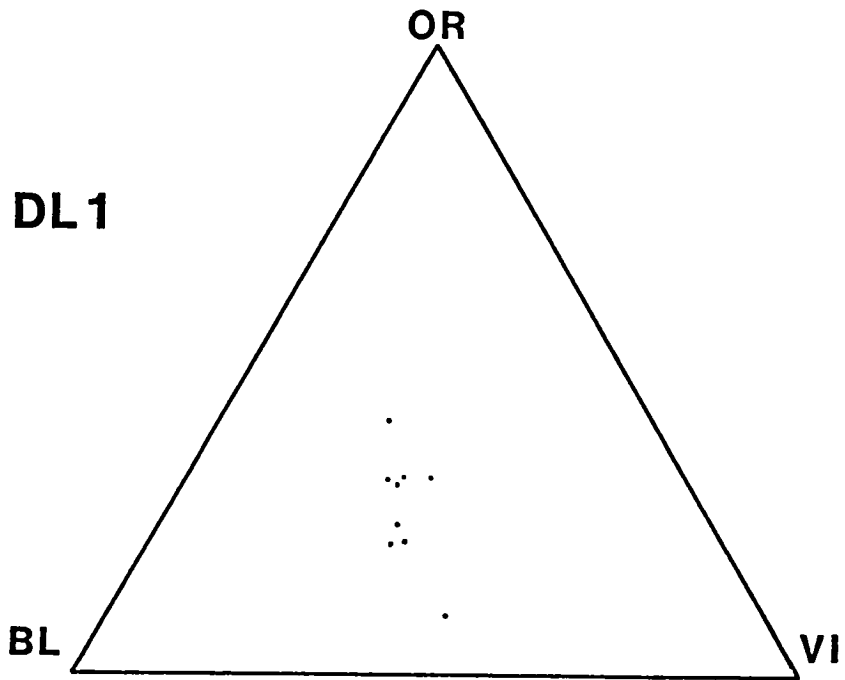
- 82) Ostro, S.J. (1982). Radar properties of Europa, Ganymede, and Callisto. In *Satellites of Jupiter* (D. Morrison, Ed.), pp. 213-236. Univ. of Arizona Press, Tucson.
- 83) Ostro, S.J., Campbell, D.B., Pettengill, G.H., and Shapiro, I.I. (1980). Radar observations of the icy Galilean satellites. *Icarus* 44, 431-440.
- 84) Ostro, S.J., and Pettengill, G.H. (1978). Icy craters on the Galilean satellites? *Icarus* 34, 268-279.
- 85) Owen, F.N., and Lazor, F.J. (1973). Surface color variations of the Galilean satellites. *Icarus* 19, 30-33.
- 86) Owen, T.C. (1965). Saturn's rings and the satellites of Jupiter: Interpretation of the infrared spectrum. *Science* 149, 974-975.
- 87) Pieri, D.C. (1981). Lineament and polygon patterns on Europa. *Nature* 289, 17-21.
- 88) Pilcher, C.B., Ridgway, S.T., and McCord, T.B. (1972). Galilean satellites: Identification of water frost. *Science* 178, 1087-1089.
- 89) Pollack, J.B., Witteborn, F.C., Edwin, F.E., Strecker, D.W., Baldwin, J.B., and Bunch, B.E. (1978). Near-infrared spectra of the Galilean satellites: Observations and implications. *Icarus* 36, 271-303.
- 90) Ransford, G.A., Finnerty, A.A., and Collerson, K.D. (1981). Europa's petrological thermal history. *Nature* 289, 21-24.
- 91) Schenk, P.M., and Seyfert, C.K. (1980). Fault offsets and proposed

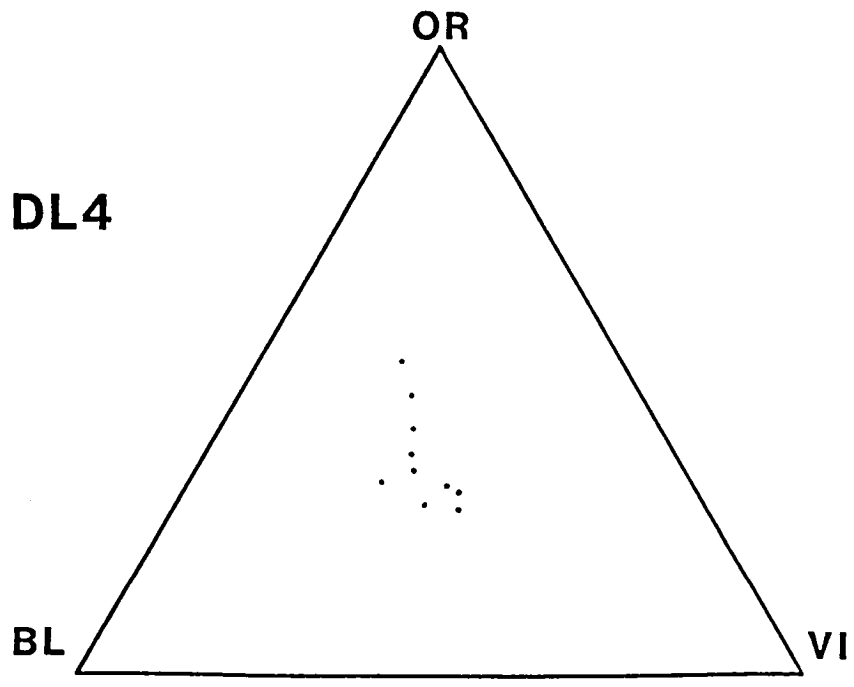
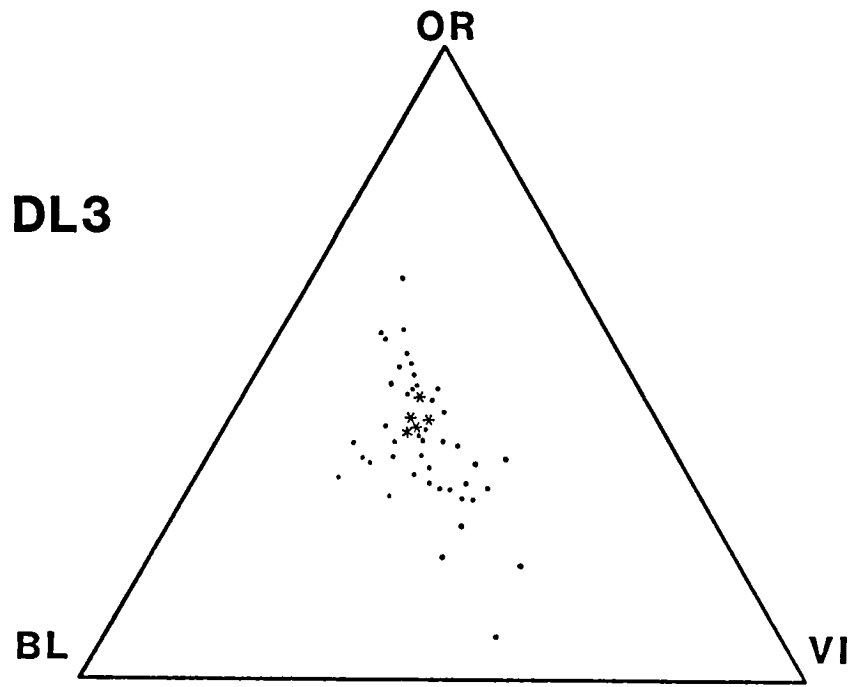
- plate motions for Europa. *EOS* 61, 286.
- 92) Shoemaker, E.M., Lucchitta, B.K., Plescia, J.B., Squyres, S.W., and Wilhelms, D.E. (1982). The geology of Ganymede. In *Satellites of Jupiter* (D. Morrison, Ed.), pp. 435-520. Univ. of Arizona Press, Tucson.
- 93) Sill, G.T., and Clark, R.N. (1982). Composition of the surfaces of the Galilean satellites. In *Satellites of Jupiter* (D. Morrison, Ed.), pp. 174-212. Univ. of Arizona Press, Tucson.
- 94) Smith, B.A., Briggs, G.A., Cook, A.F., Danielson, G.E., Davies, M.E., Hunt, G.E., Masursky, H., Owen, T., Sagan, C., Soderblom, L.A., and Suomi, V.E. (1977). The Voyager imaging experiment. *Space Sci. Rev.* 21, 103-117.
- 95) Smith, B.A., and the Voyager Imaging Team (1979a). The Jupiter system through the eyes of Voyager. *Science* 204, 951-972.
- 96) Smith, B.A., and the Voyager Imaging Team (1979b). The Galilean satellites and Jupiter: Voyager 2 imaging science results. *Science* 206, 927-950.
- 97) Smythe, W.D. (1975). Spectra of hydrate frosts: Their application to the outer solar system. *Icarus* 24, 421-427.
- 98) Squyres, S.W. (1980). Surface temperatures and retention of H₂O frost on Ganymede and Callisto. *Icarus* 44, 502-510.
- 99) Stebbins, J. (1927). The light-variations of the satellites of Jupiter and their application to measures of the solar constant. *Lick Obs. Bull.* 13, 1-11.

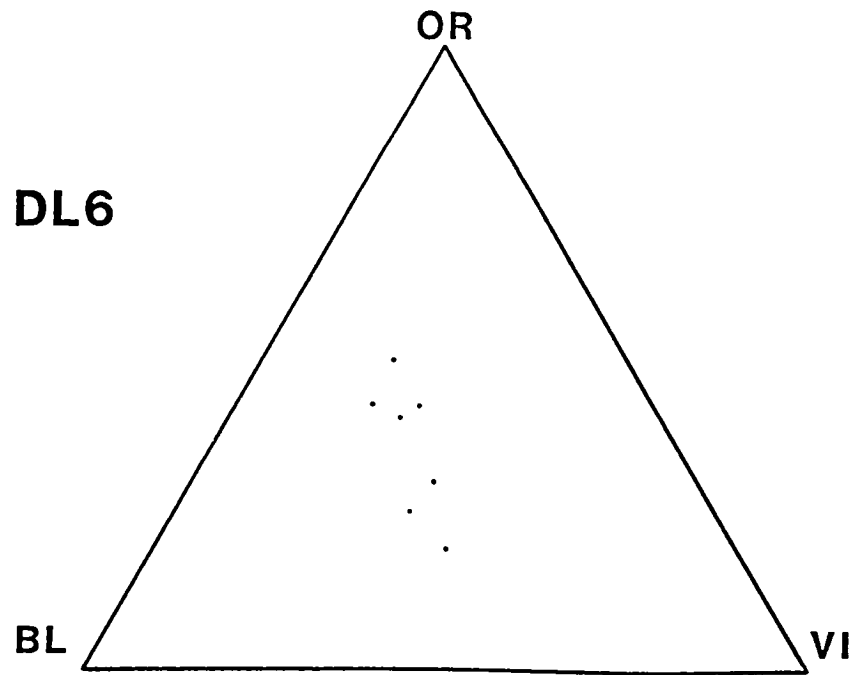
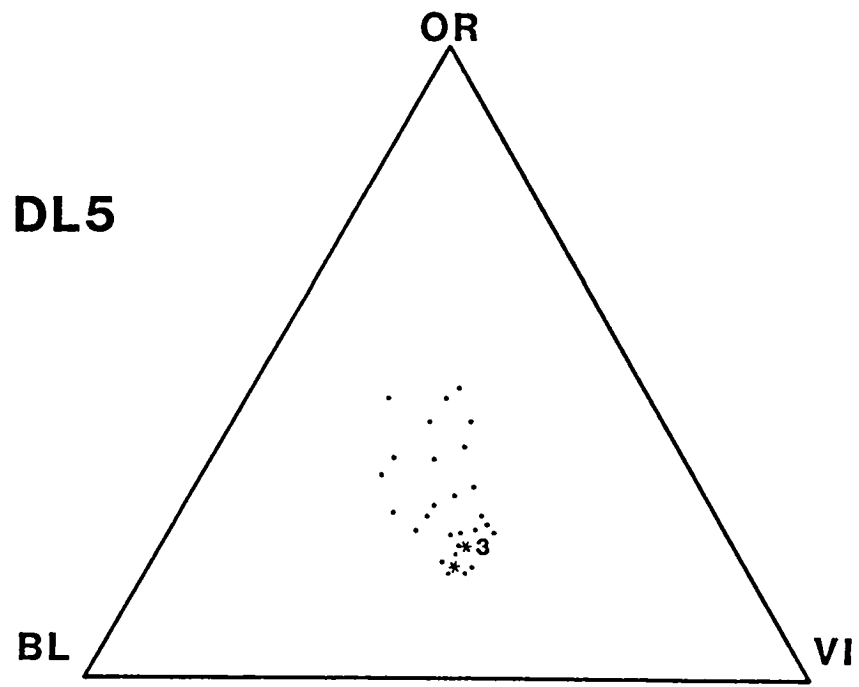
- 100) Stebbins, J., and Jacobsen, T.S. (1928). Further photometric measures of Jupiter's satellites and Uranus, with tests for the solar constant. *Lick Obs. Bull.* 13, 180-195.
- 101) Veverka, J. (1971). Polarization measurements of the Galilean satellites of Jupiter. *Icarus* 14, 355-359.
- 102) Veverka, J. (1977). Photometry of satellite surfaces. In *Planetary Satellites* (J.A. Burns, Ed.), pp. 171-209. Univ. of Arizona Press, Tucson.
- 103) Wamsteker, W. (1972). Narrow-band photometry of the Galilean satellites. *Comm. Lunar Planet. Lab.* 9, 171-177 and 10, 70.
- 104) Watson, K., Murray, B.C., and Brown, H. (1963). The stability of volatiles in the solar system. *Icarus* 26, 361-366.
- 105) Wolff, R.S., and Mendis, D.A. (1983). On the nature of the interaction of the Jovian magnetosphere with the icy Galilean satellites. *J. Geophys. Res.* 88, 4749-4769.

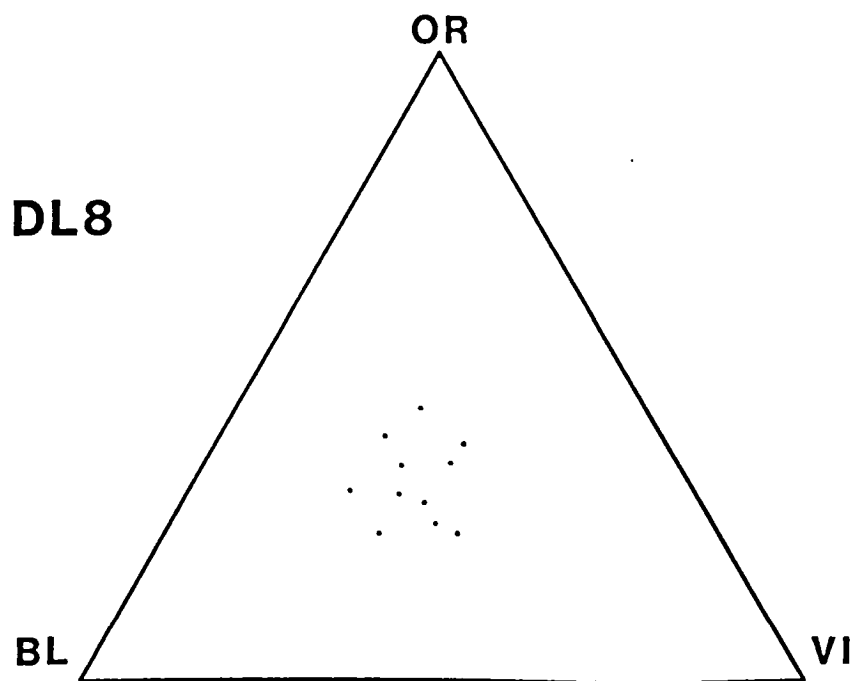
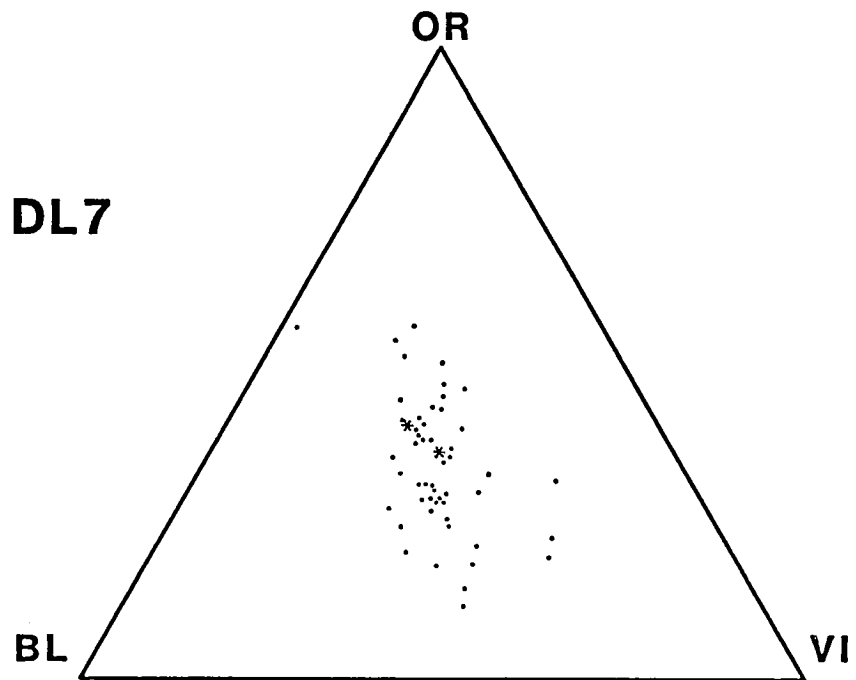
A P P E N D I X A

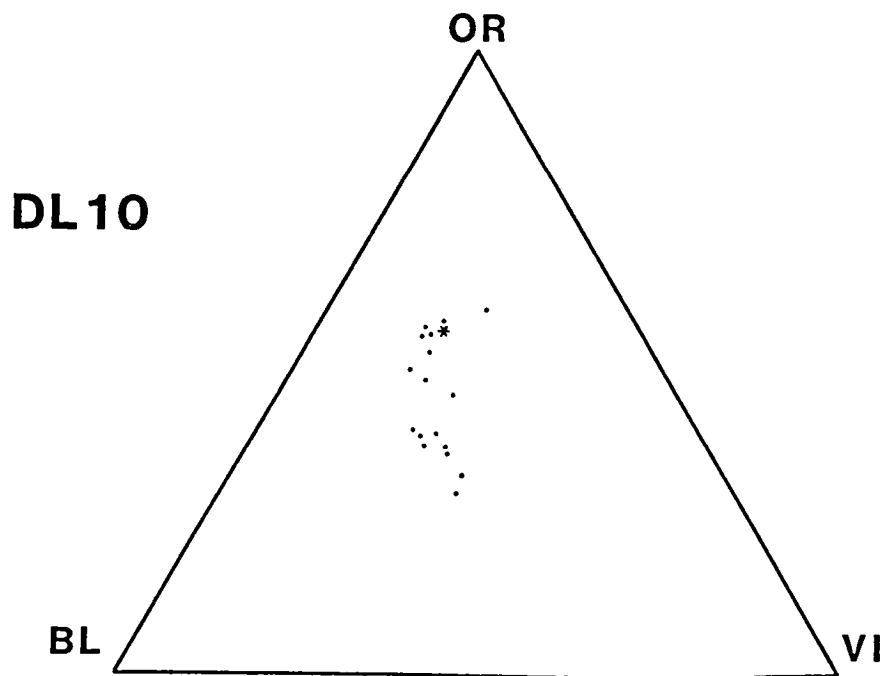
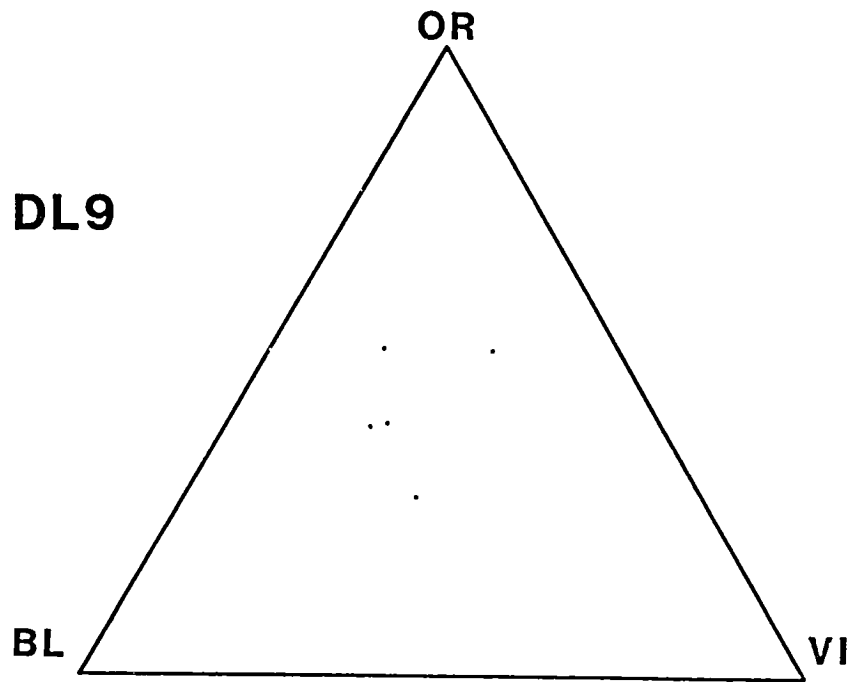
Relative spectral reflectance plots on reference ternary diagrams for the 193 dark lineation (DL) segments in the DL study area. In this appendix and appendices C, D, and E, an asterisk denotes locations where two or more data points have the same rel% coordinates or are too near each other to be plotted separately. Where more than two data points are in this situation, a number beside the asterisk indicates how many data points are at this location. There is no significance to the different sizes of asterisks used. Also, note that a few data points are plotted outside their reference ternary diagrams if they have less than 40 orange rel%, greater than 50 orange rel%, less than 20 violet rel%, etc.

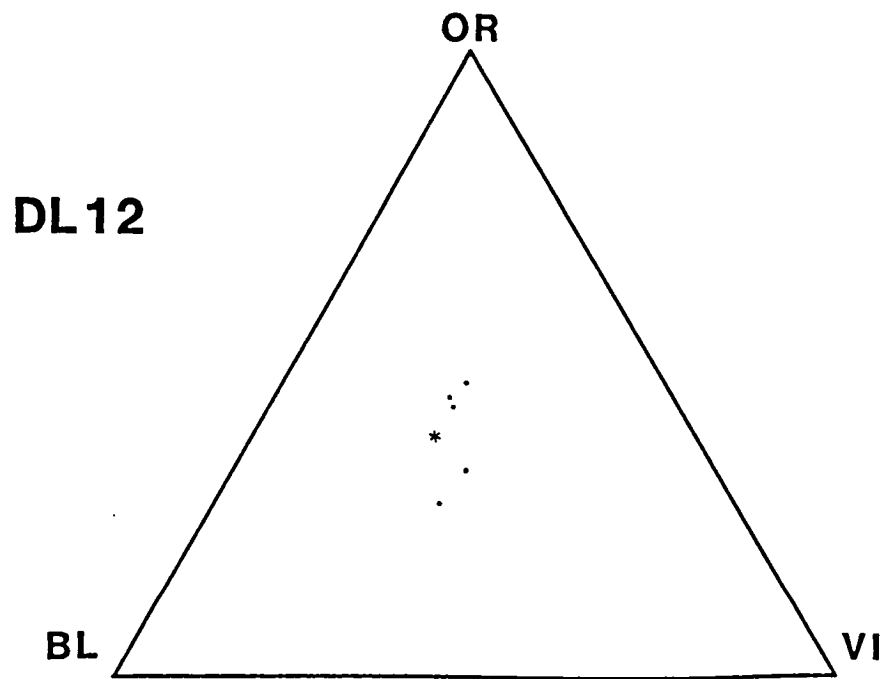
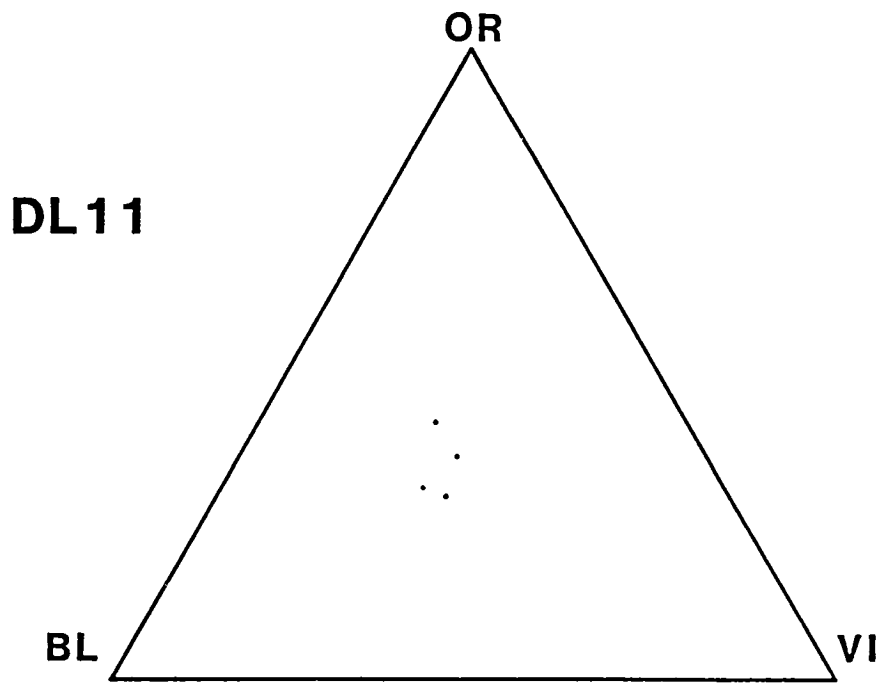


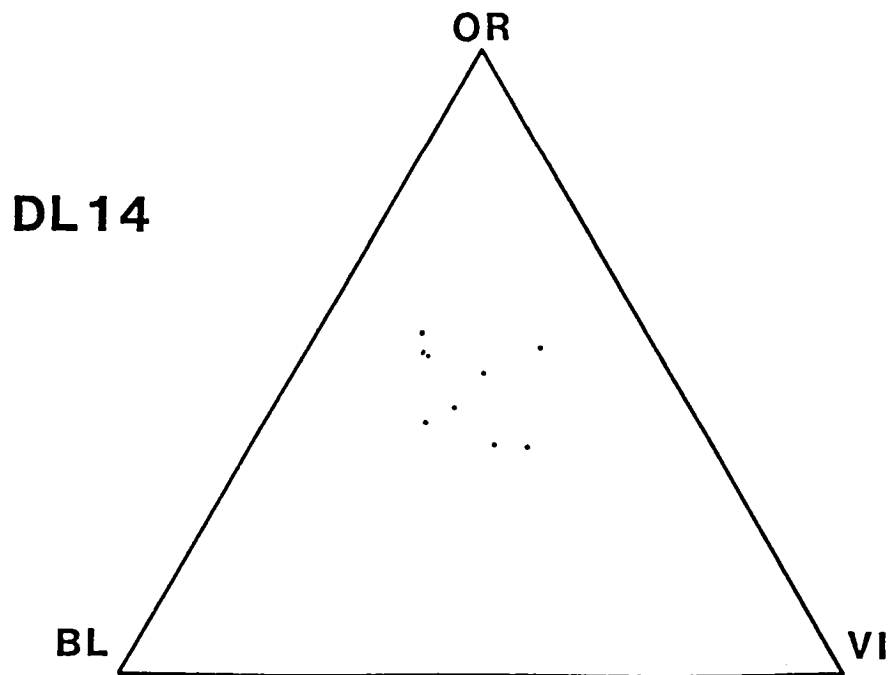
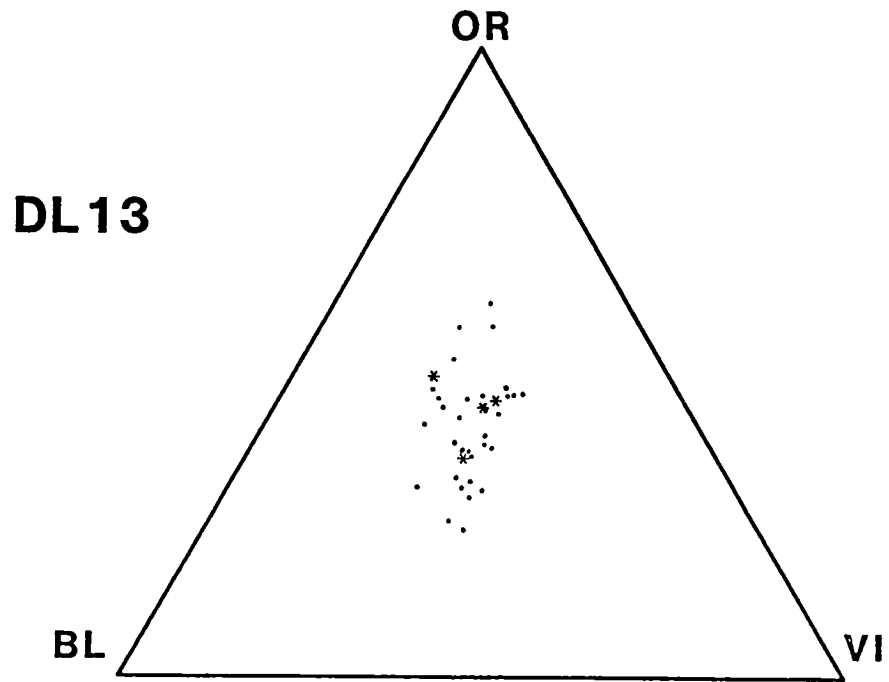


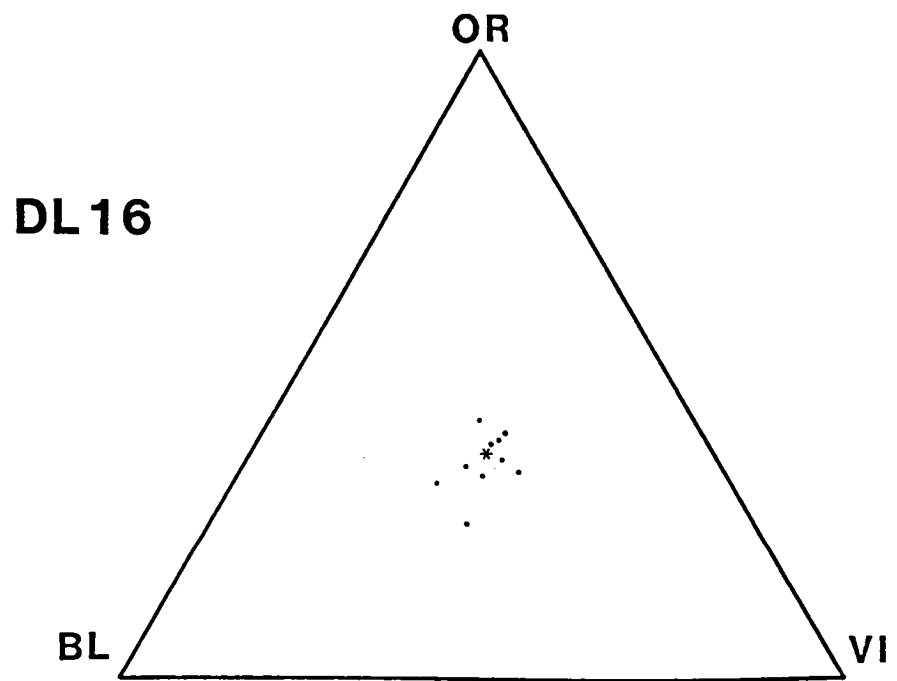
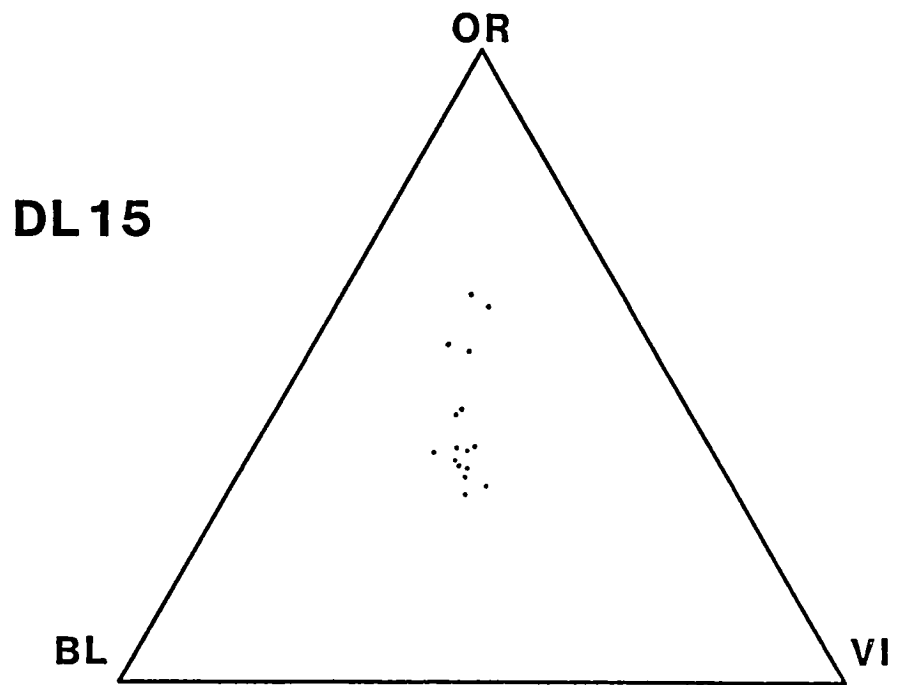


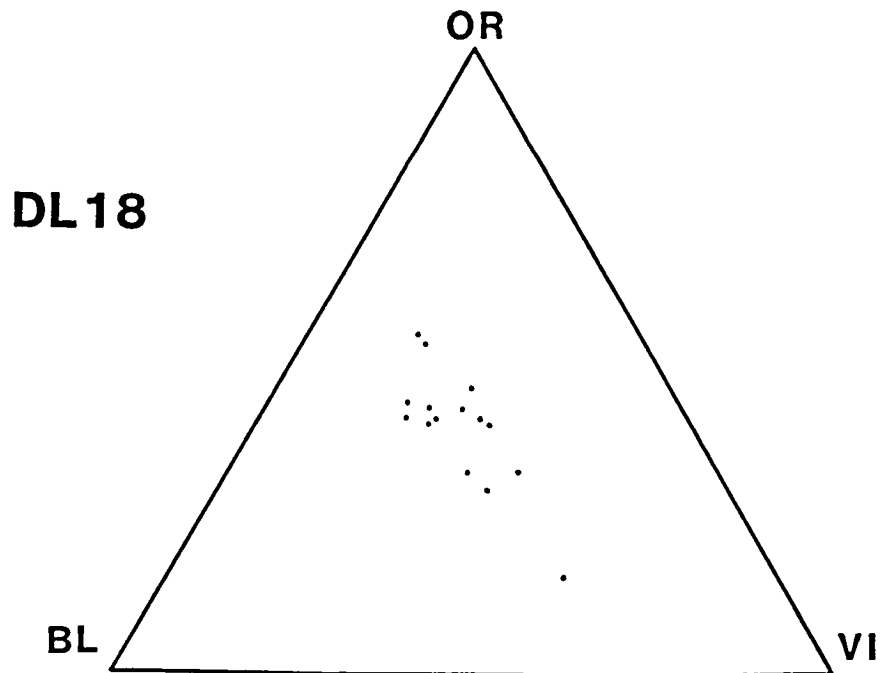
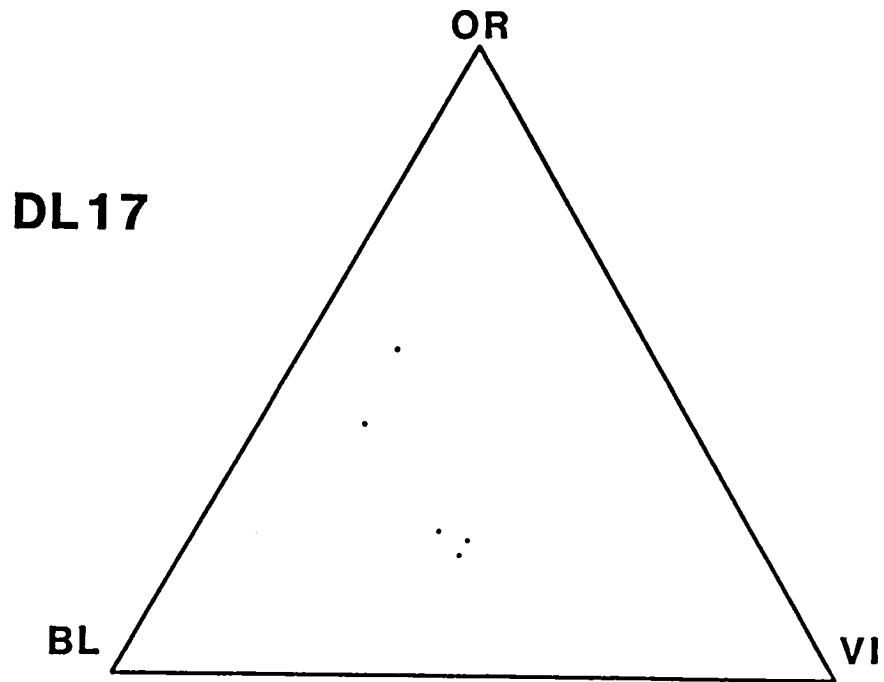


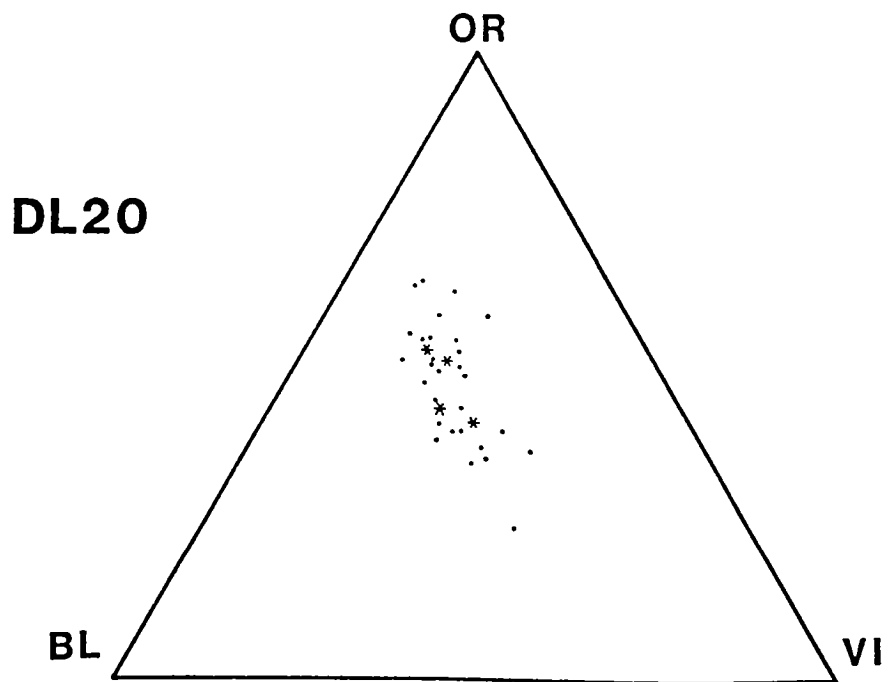
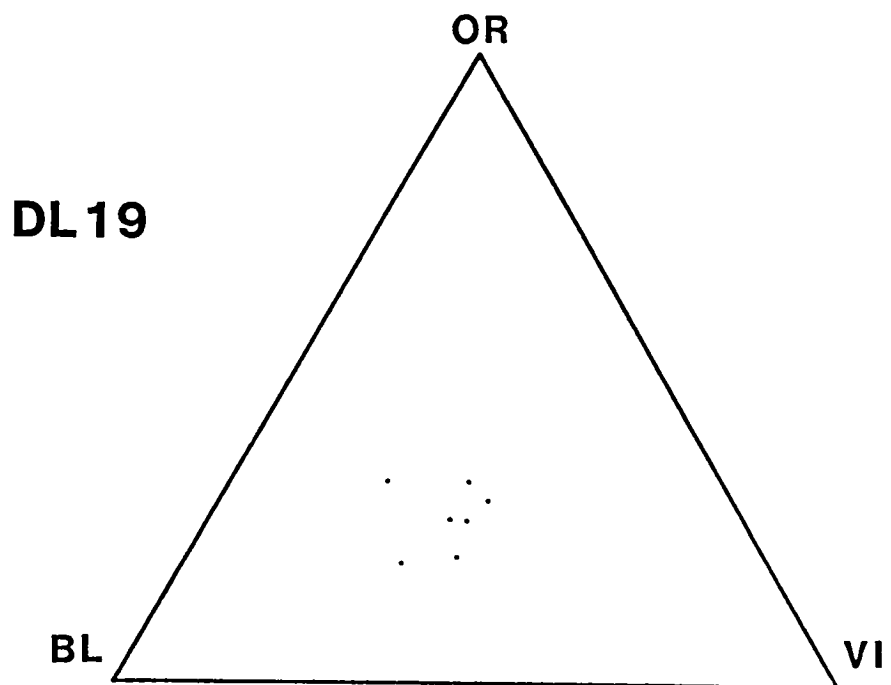


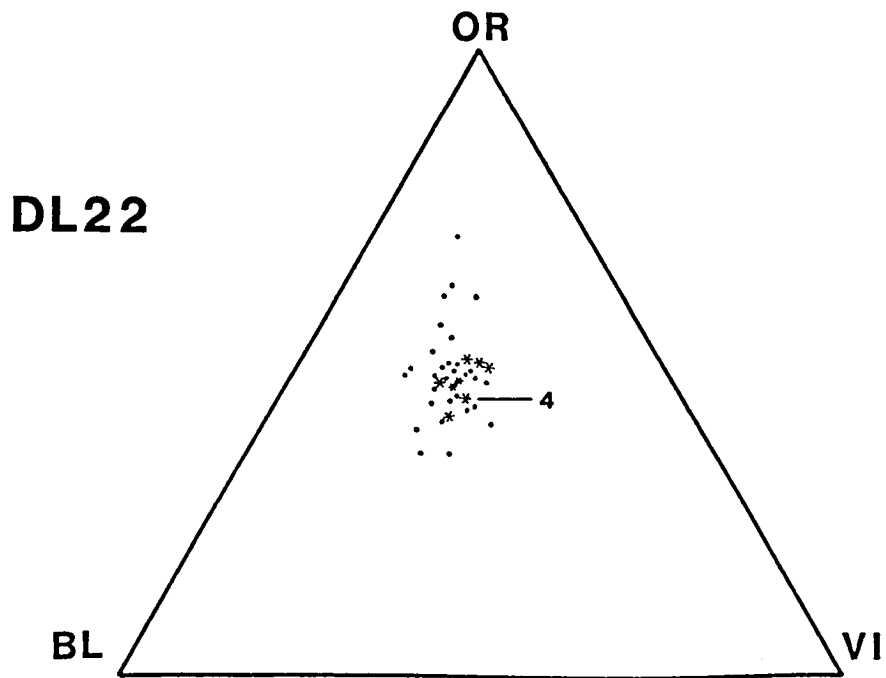
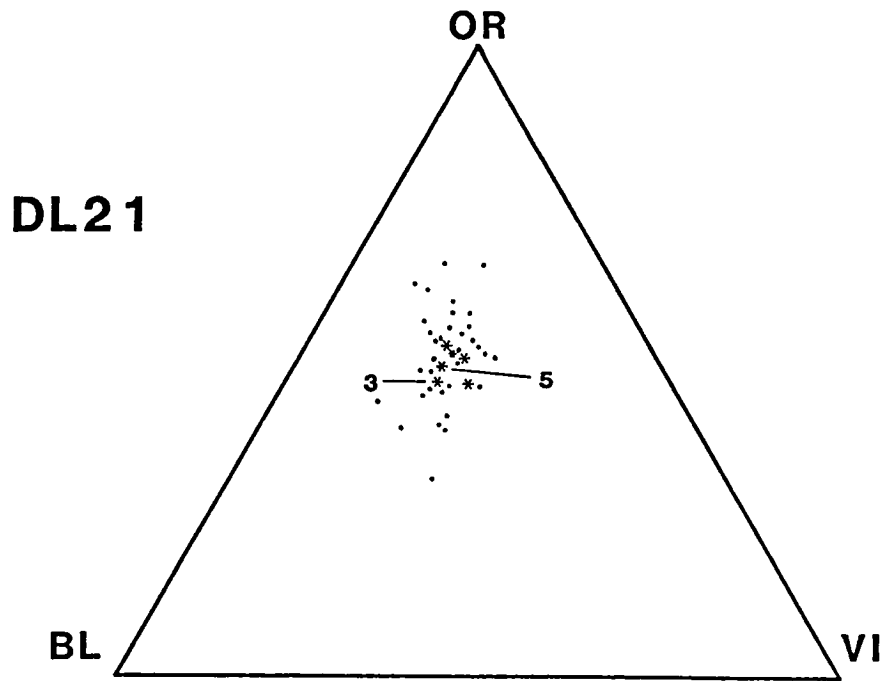


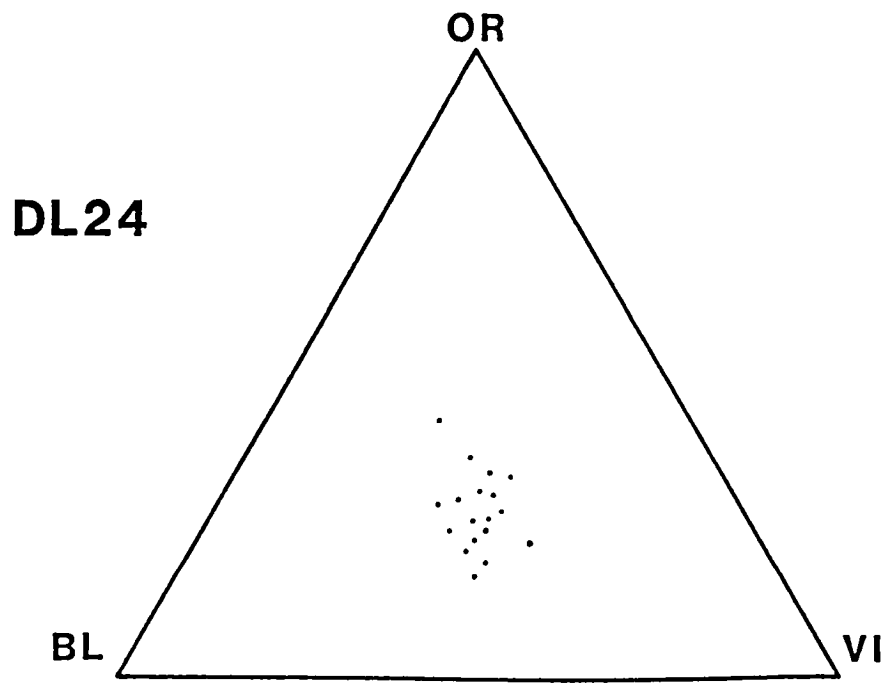
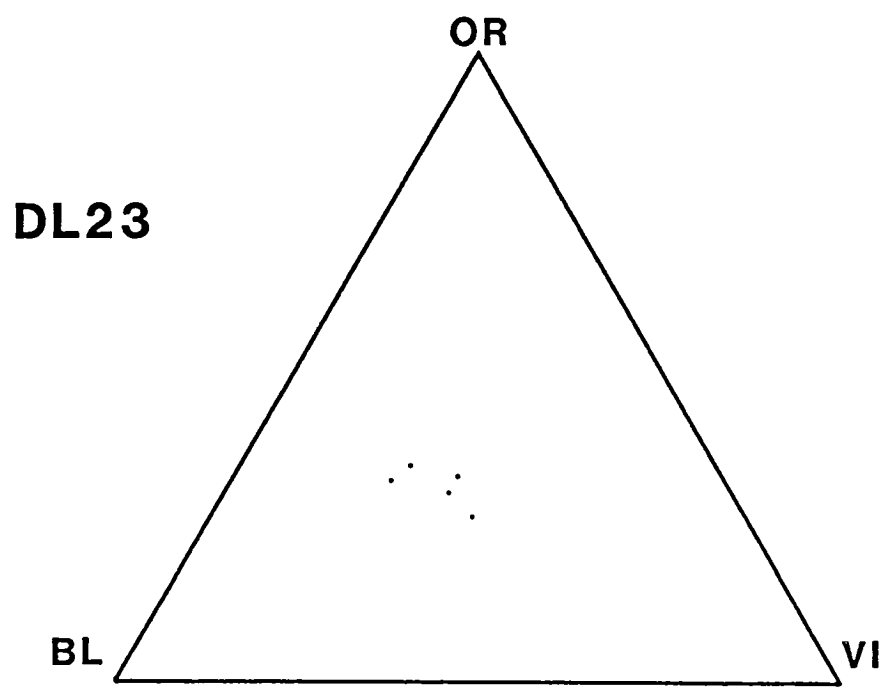


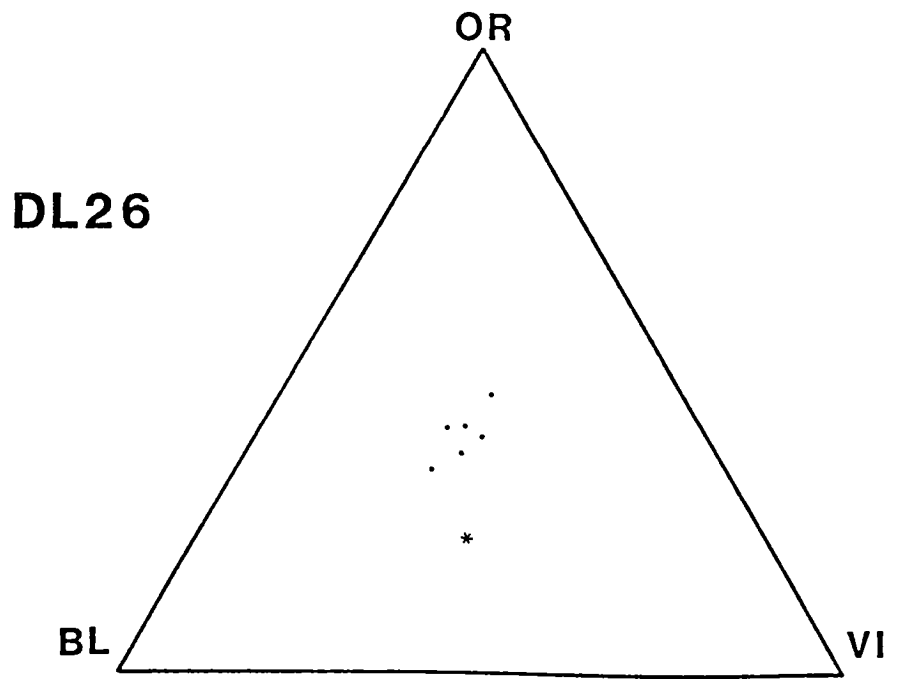
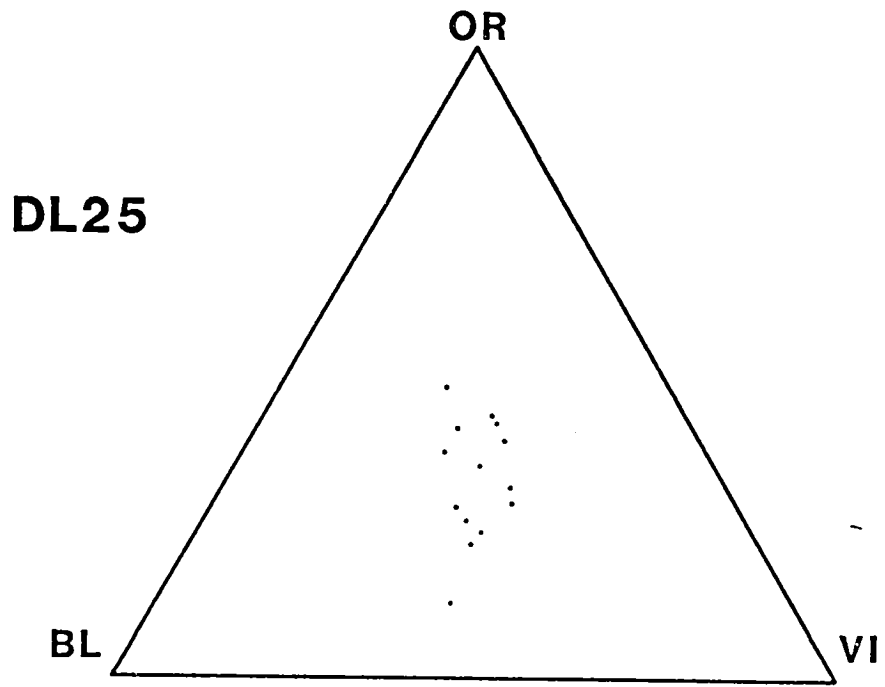


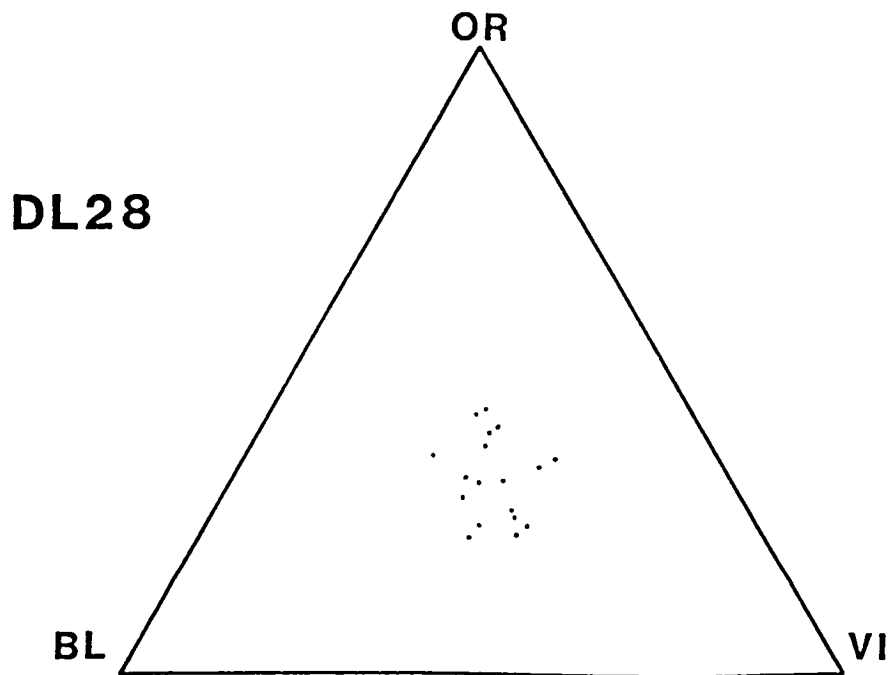
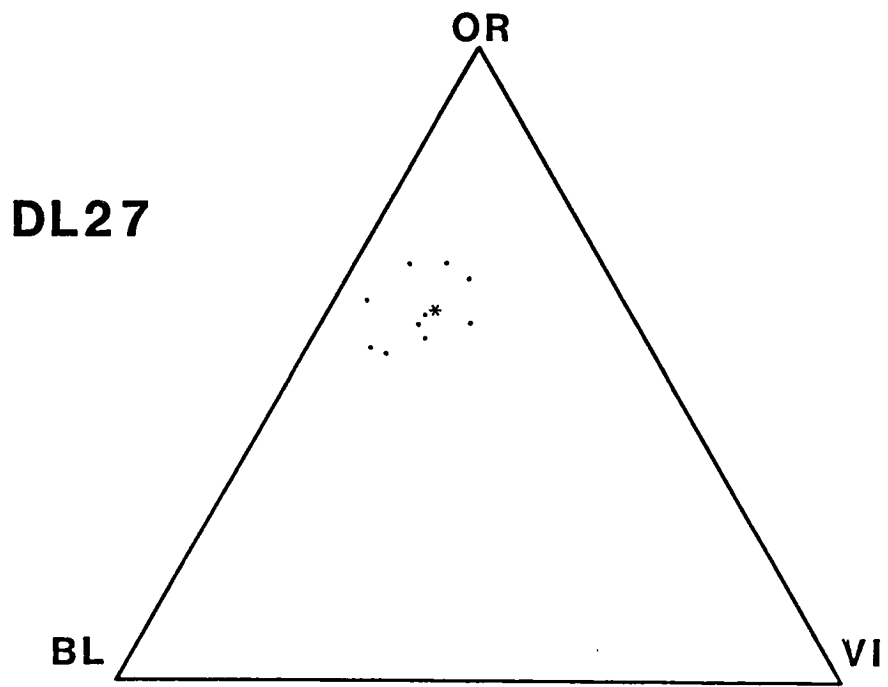


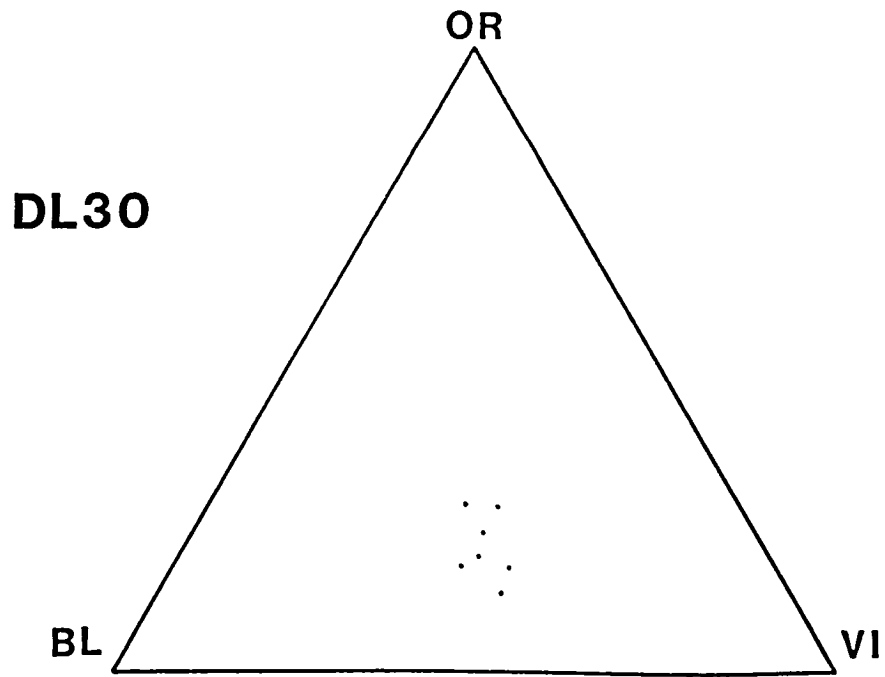
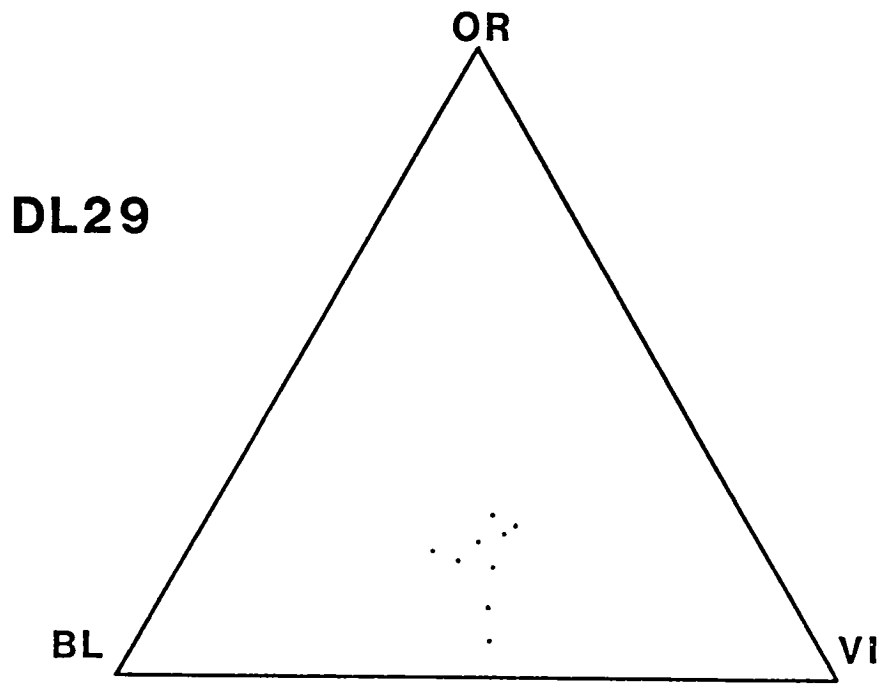


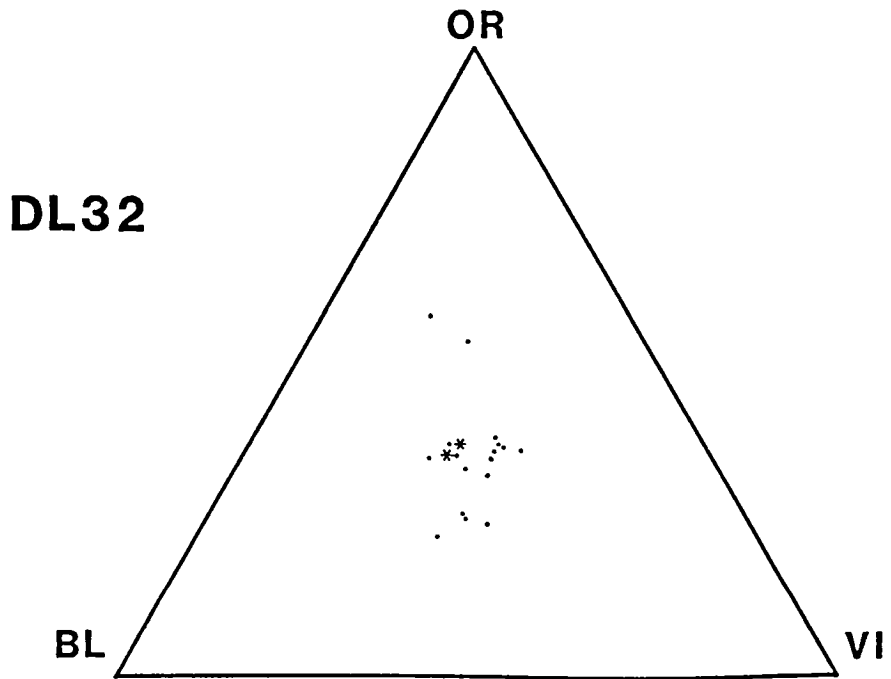
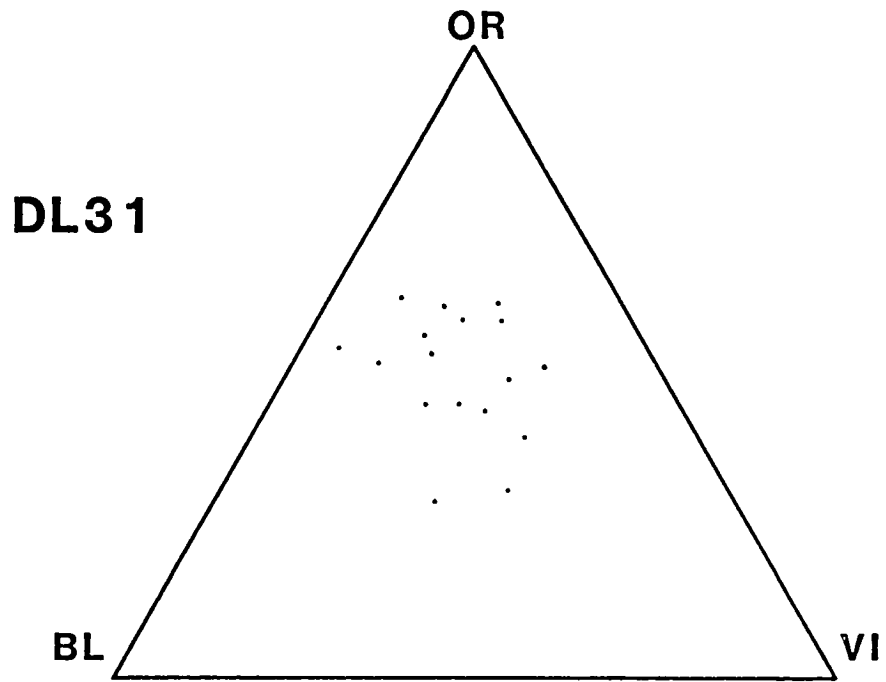


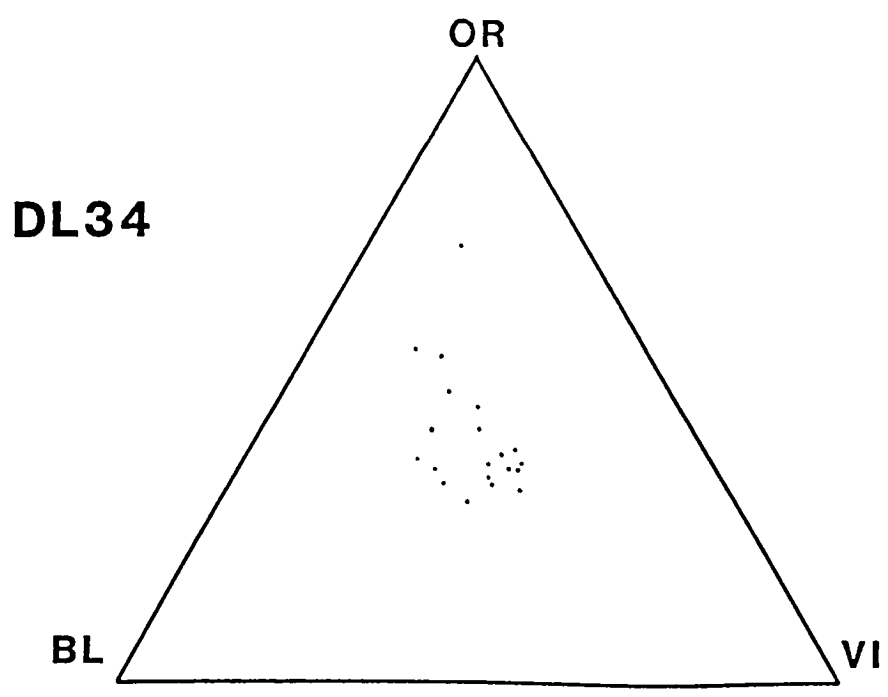
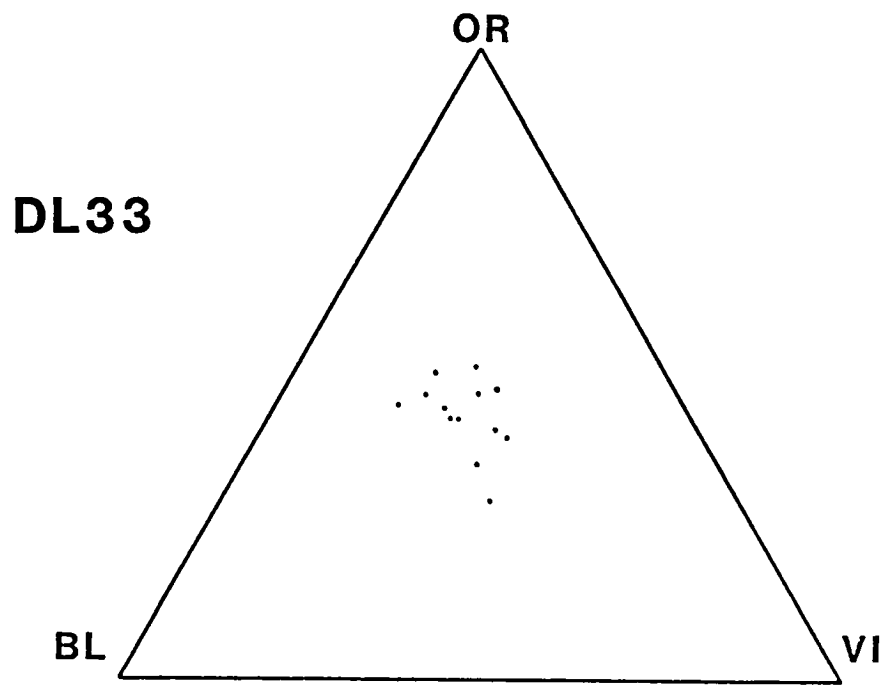


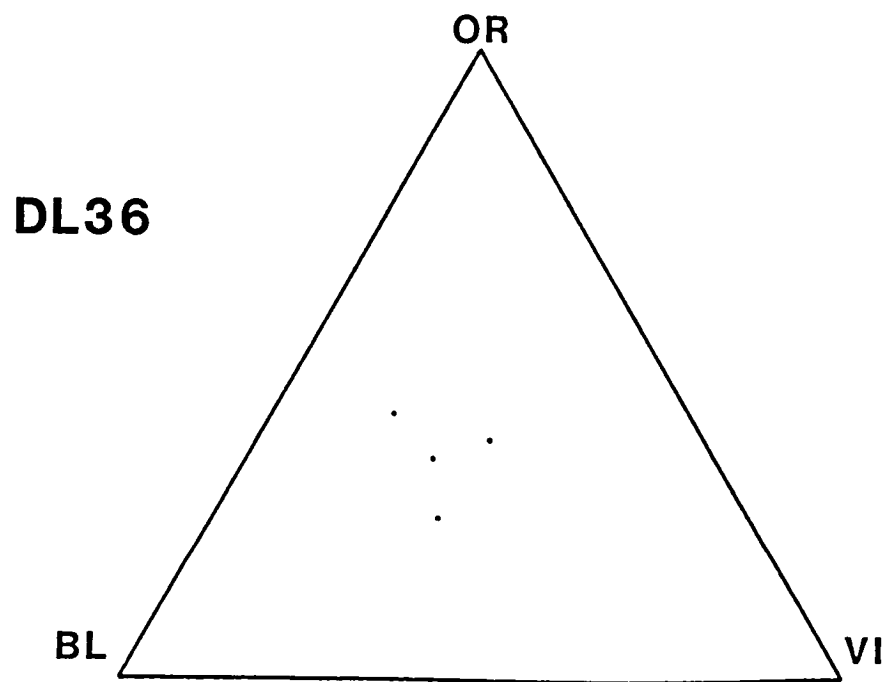
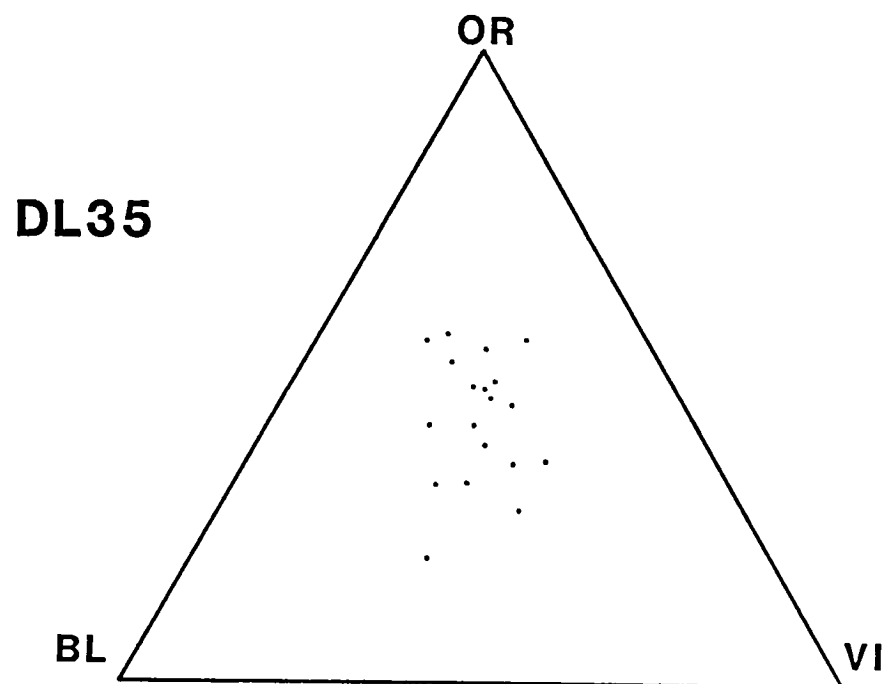


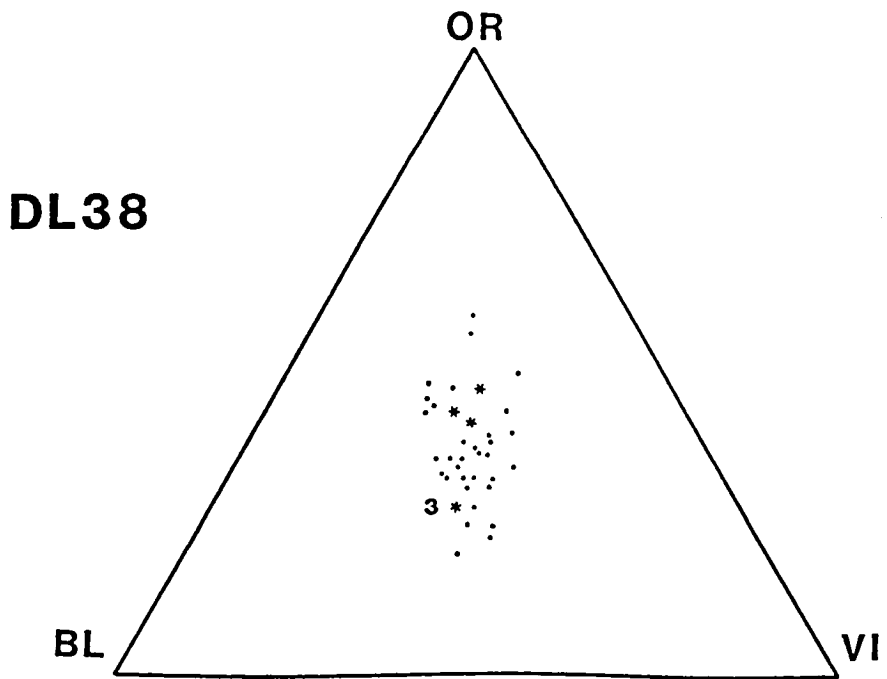
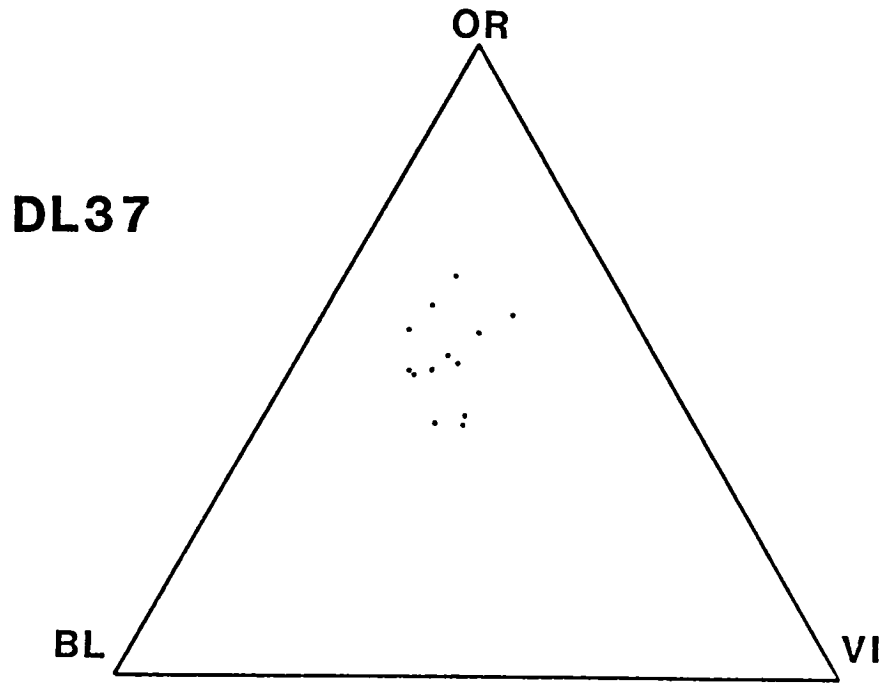


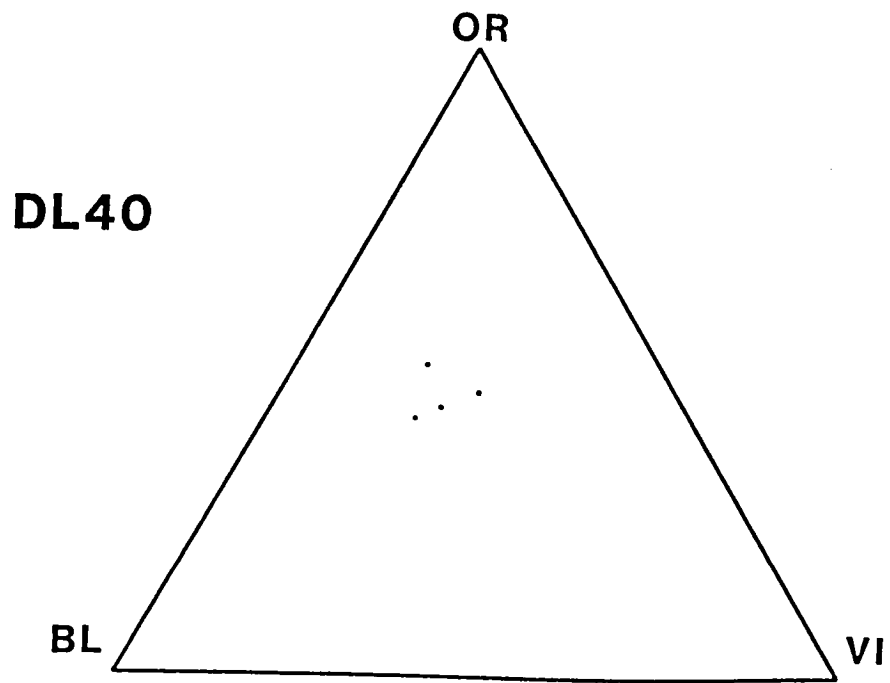
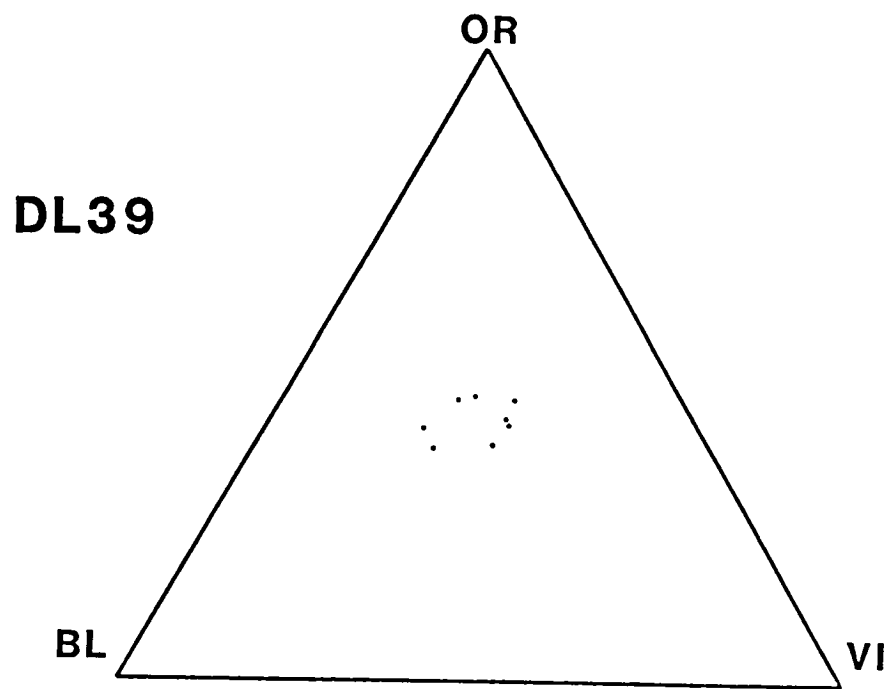


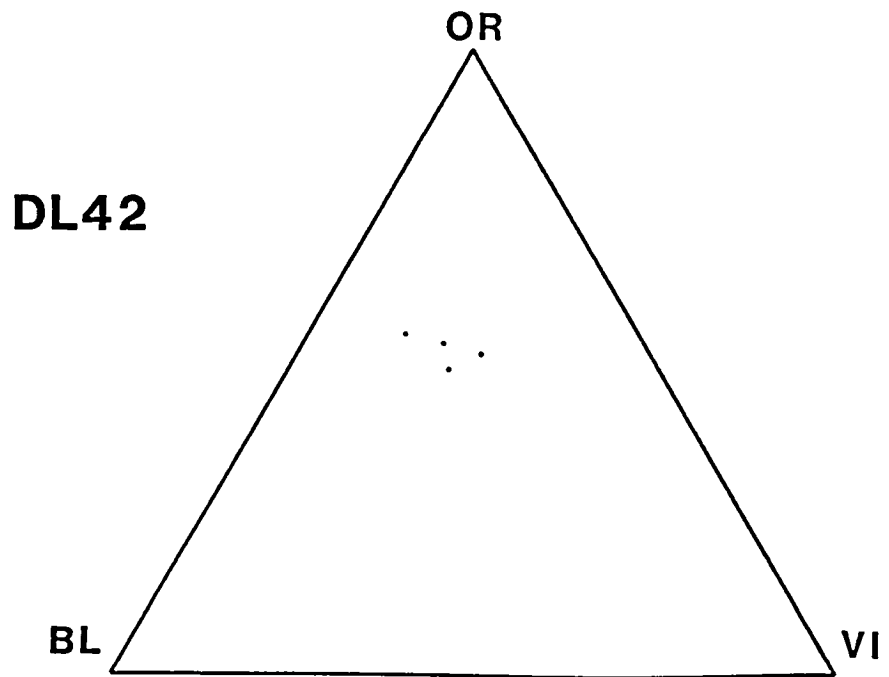
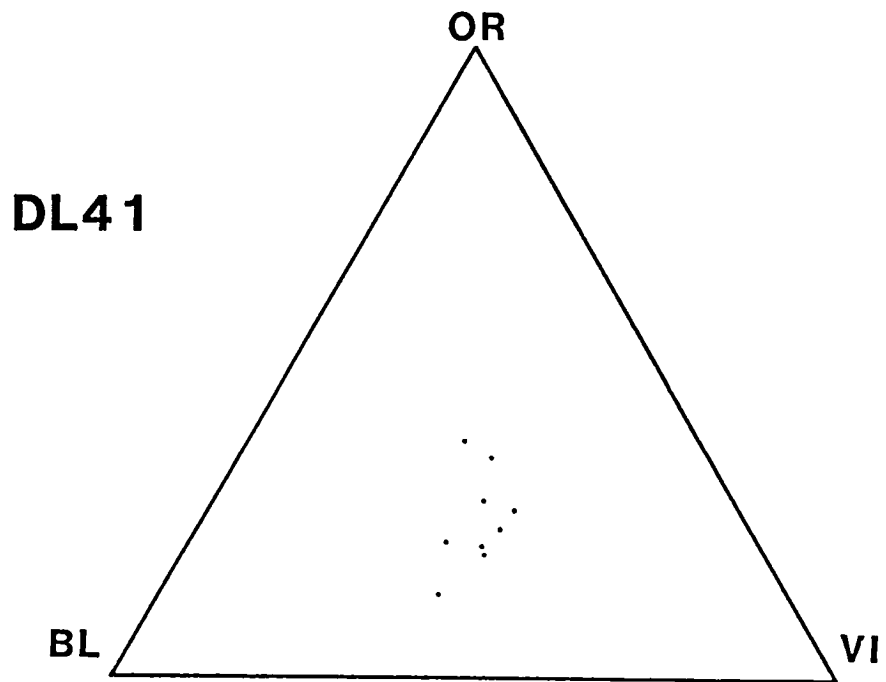


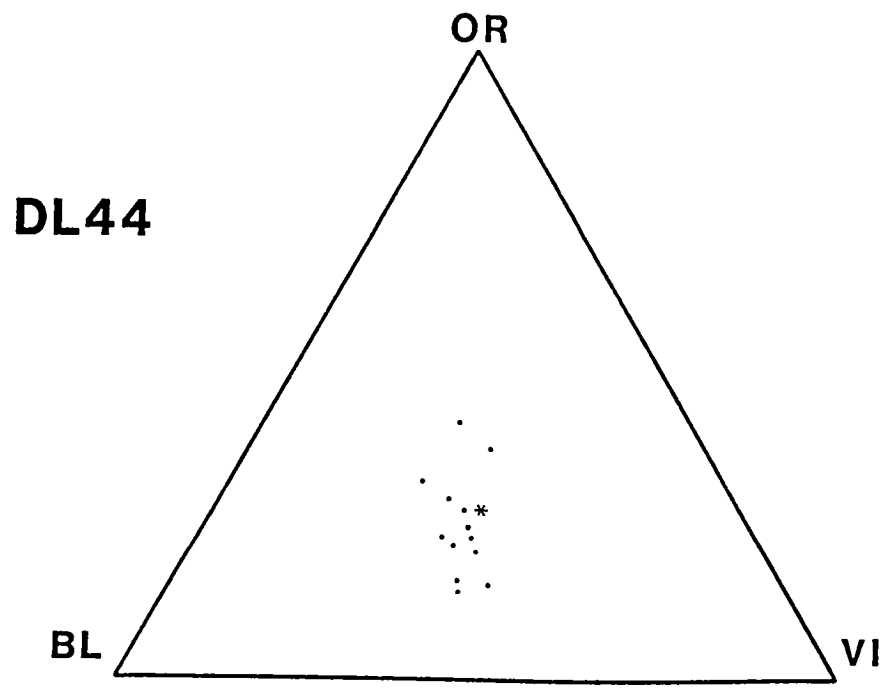
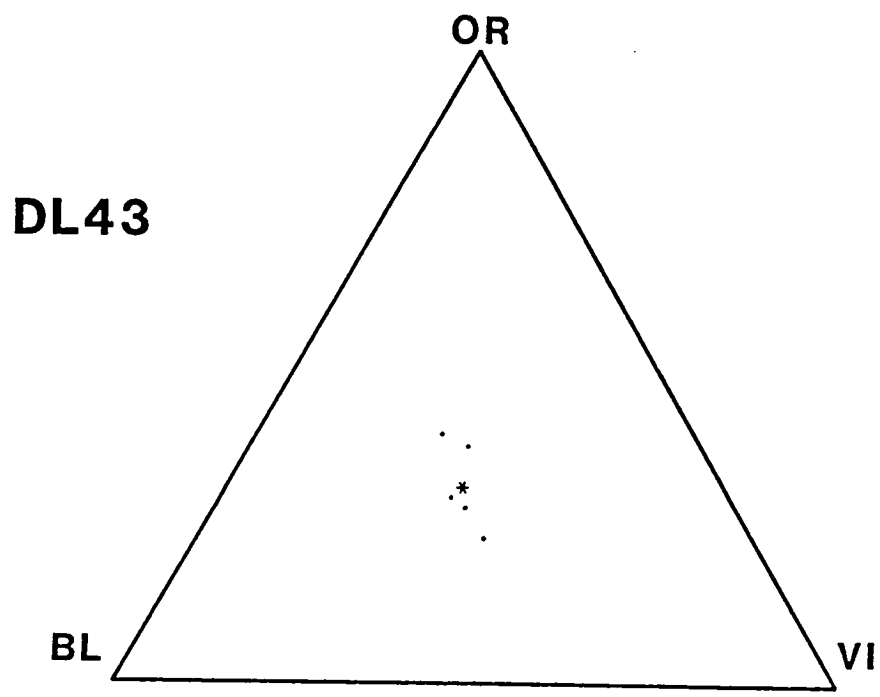


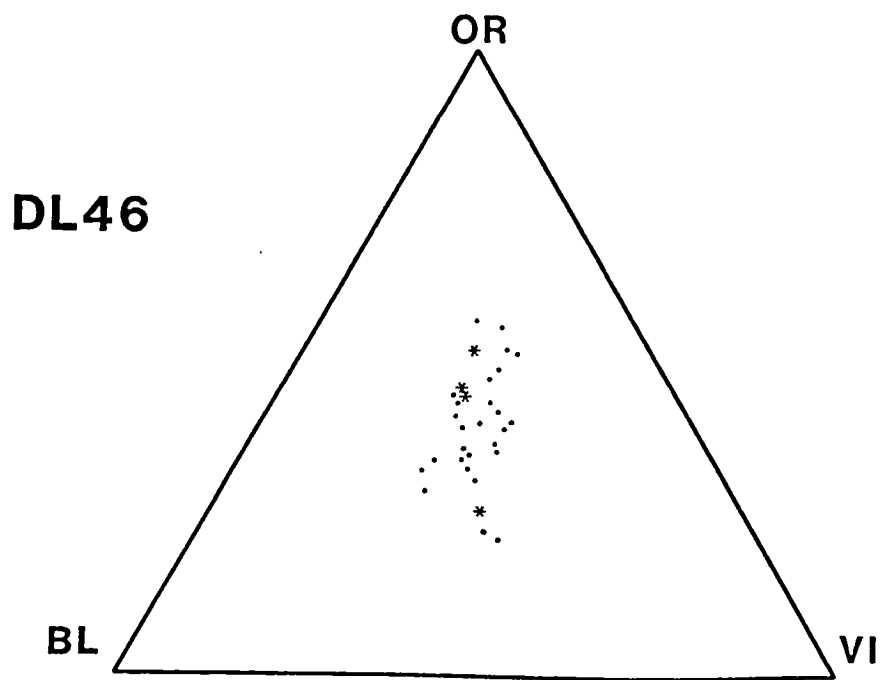
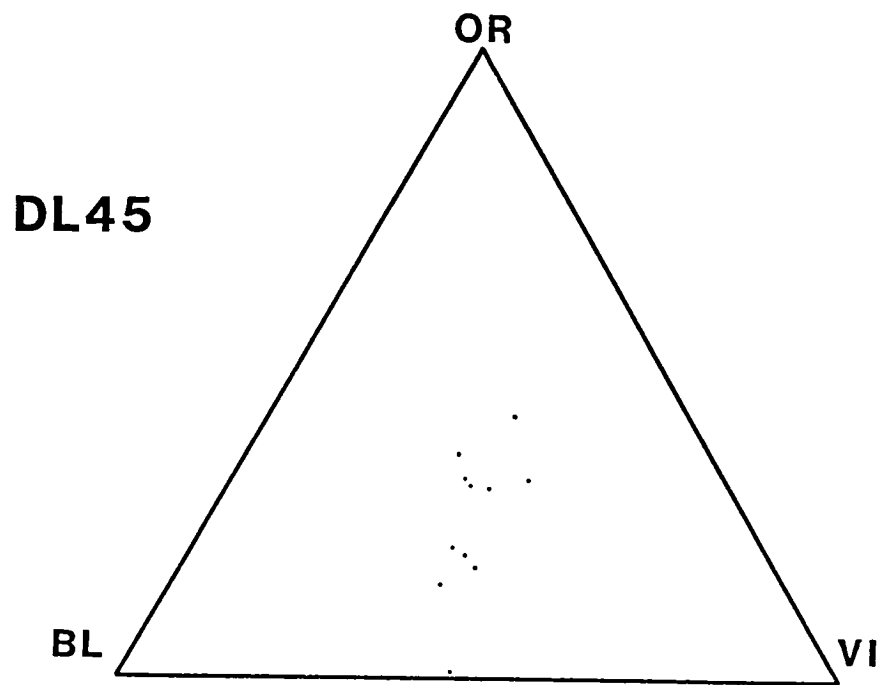


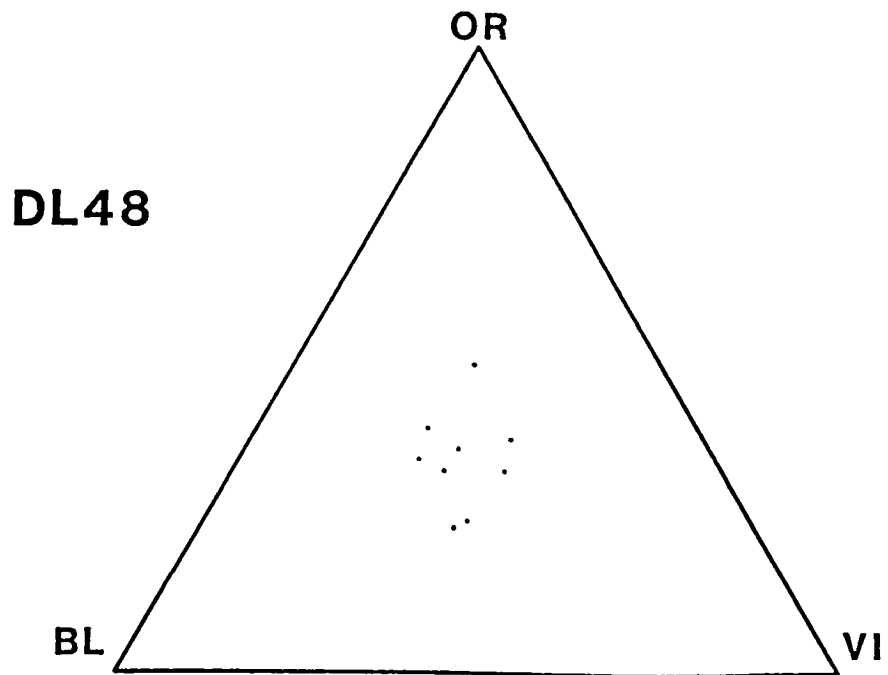
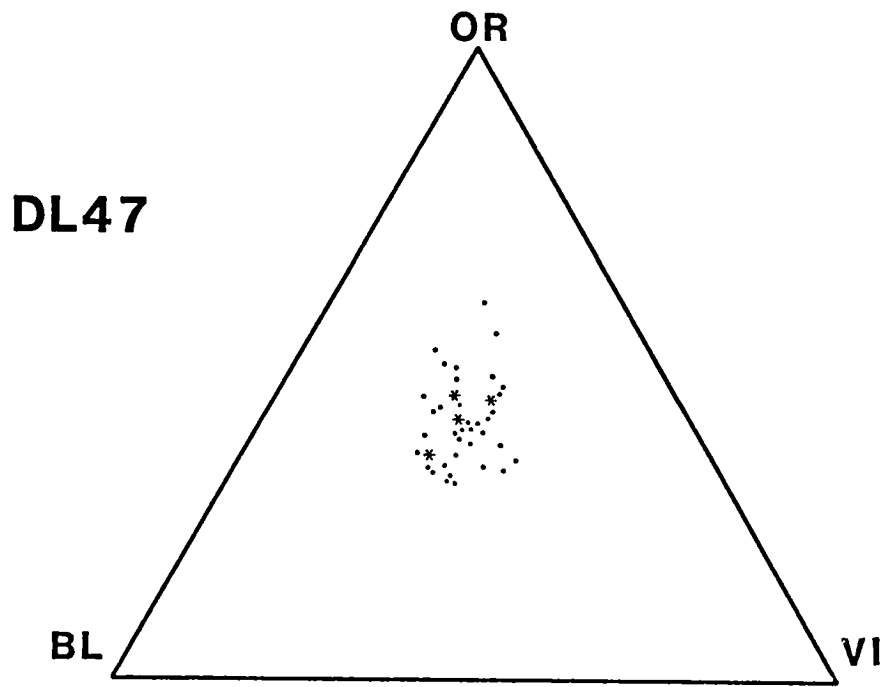


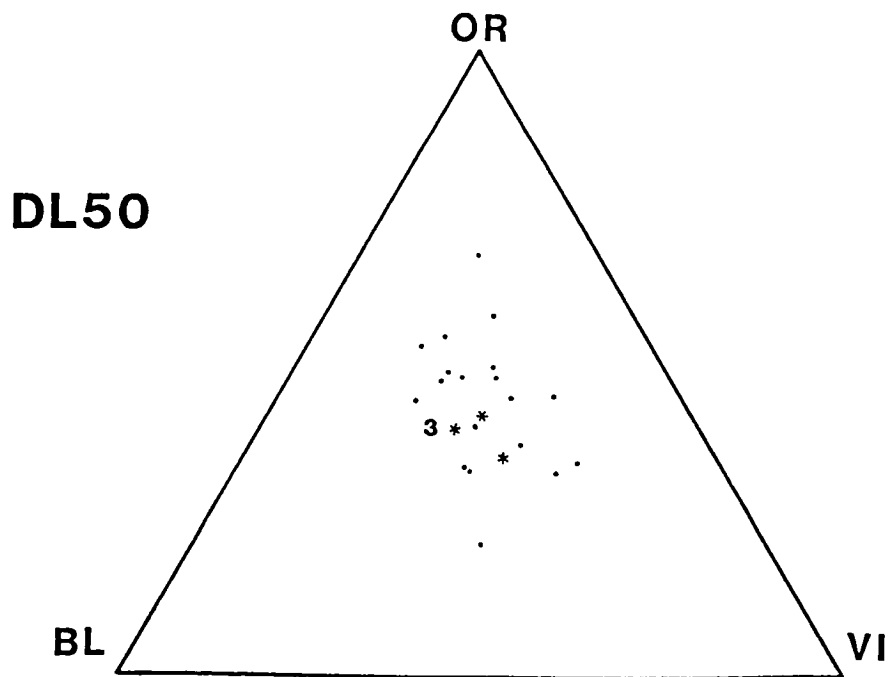
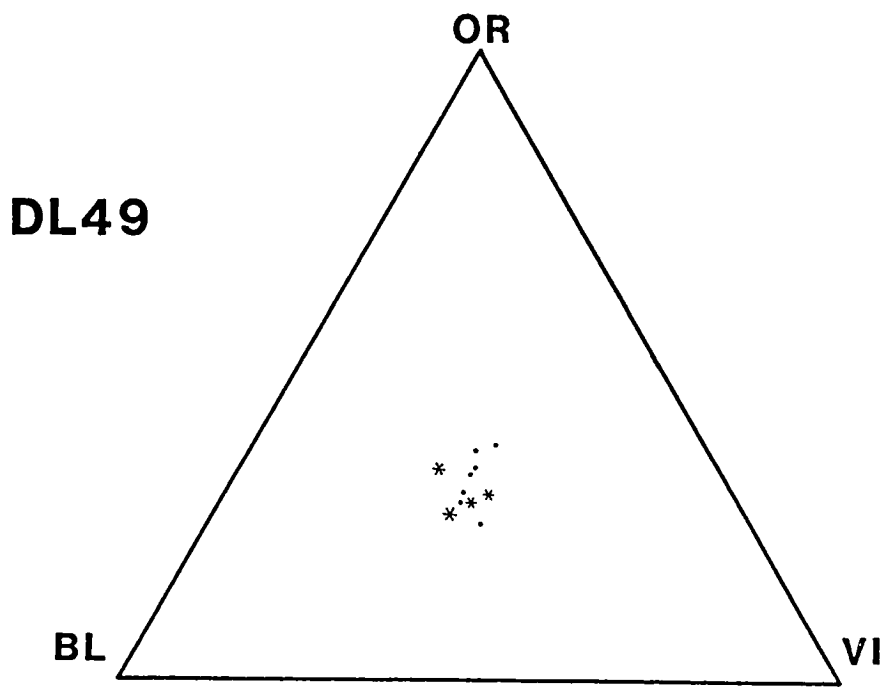


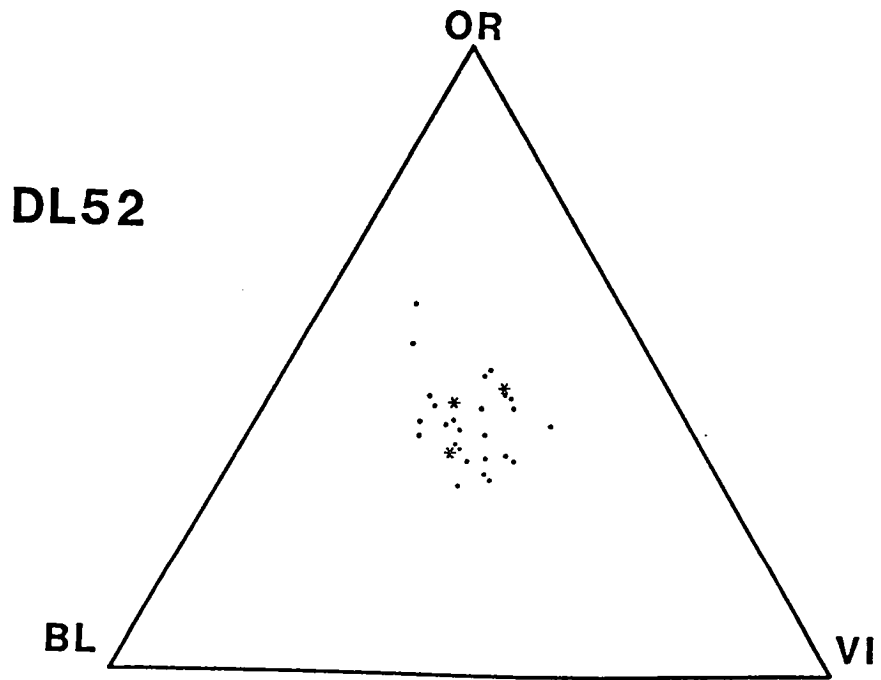
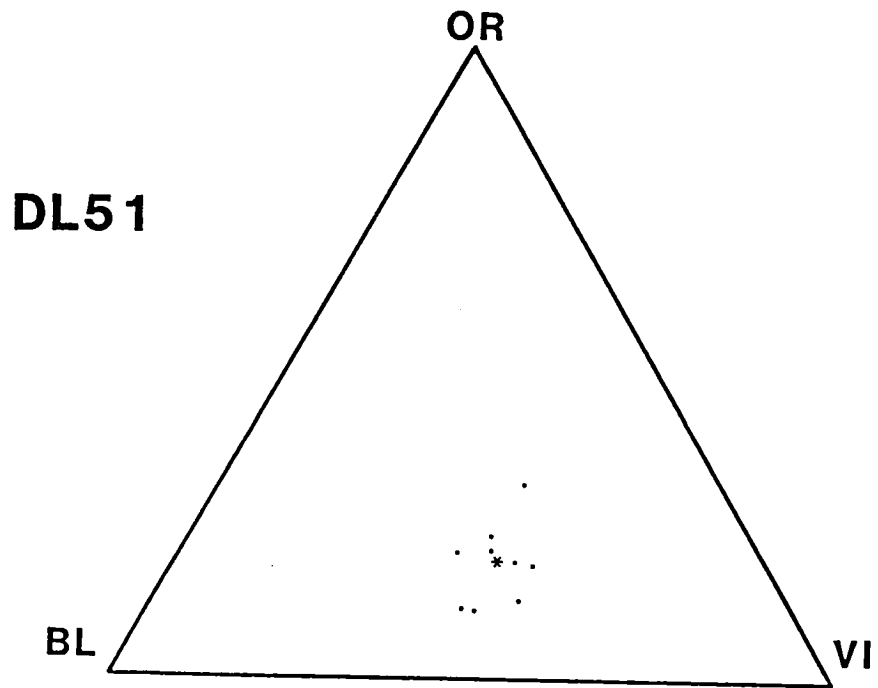


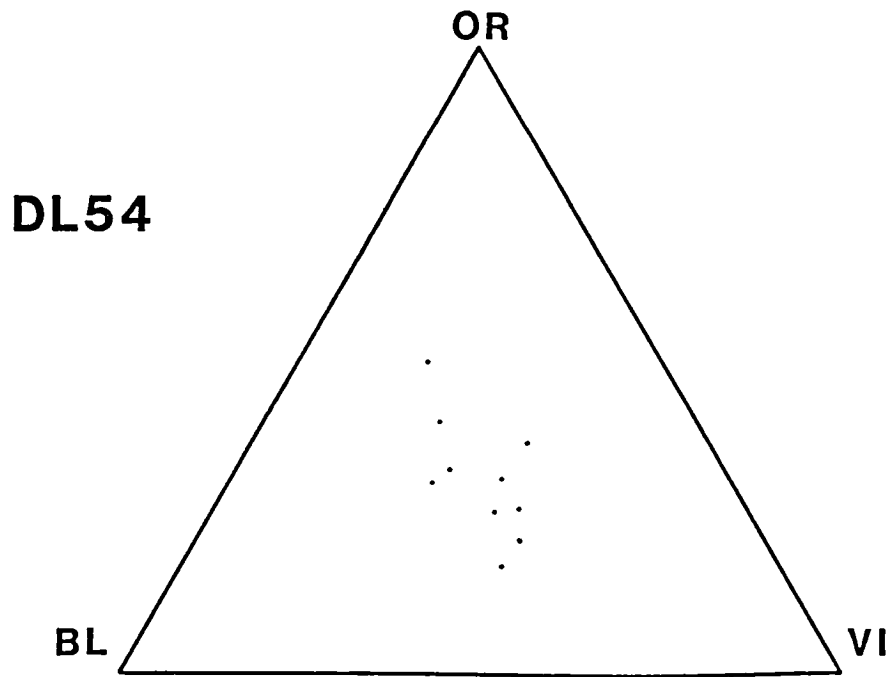
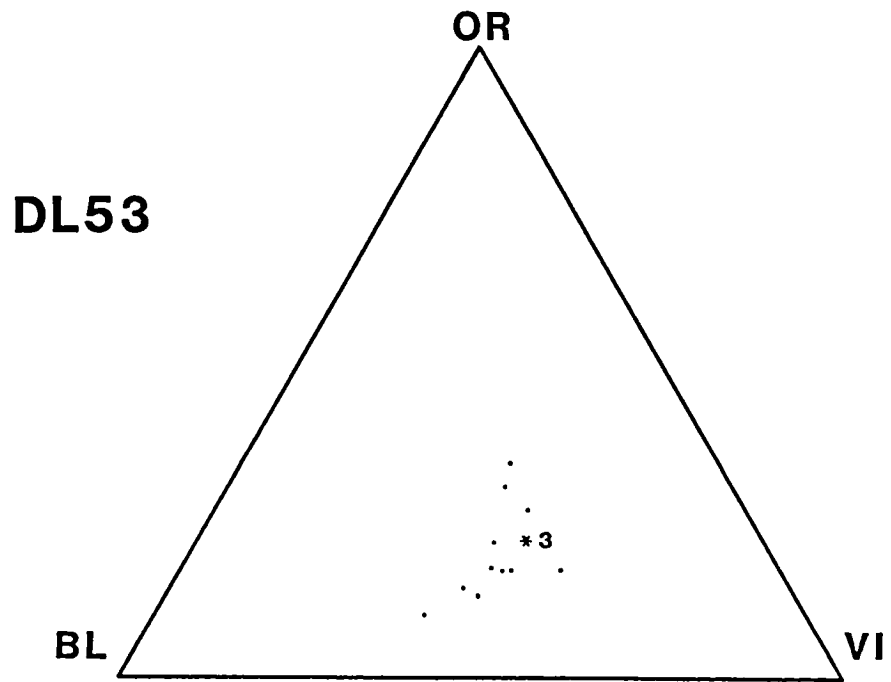


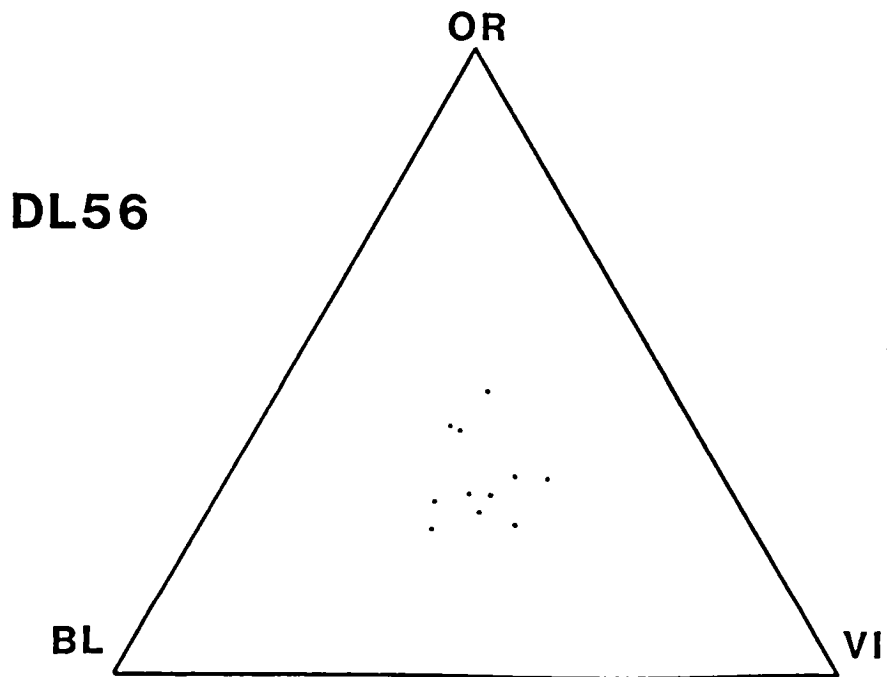
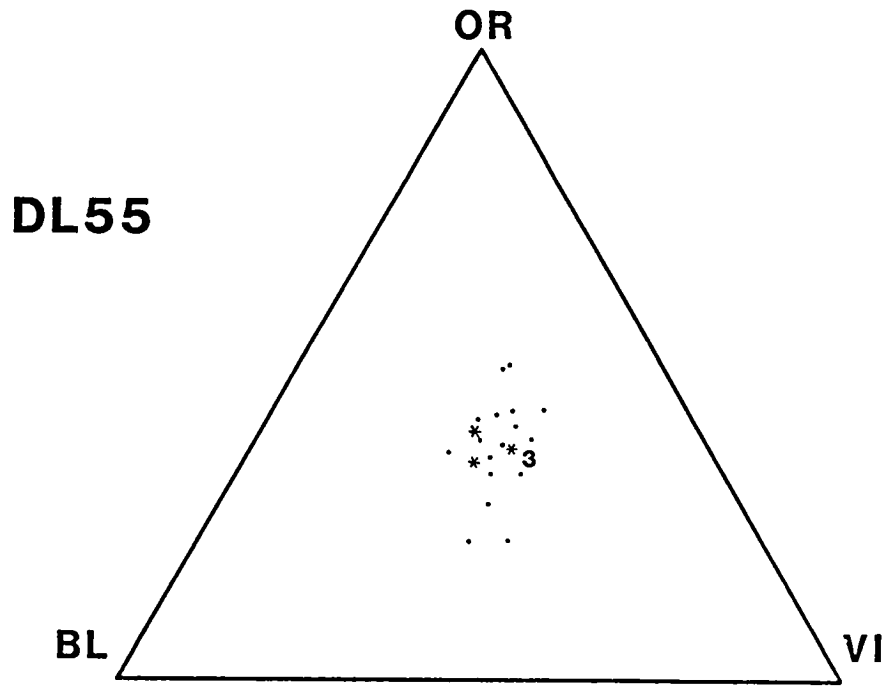


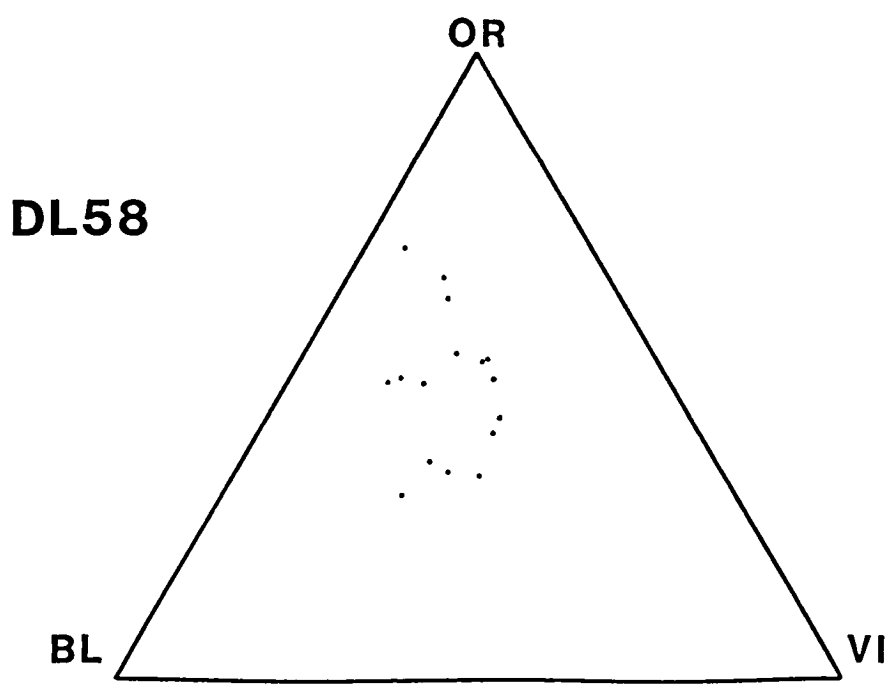
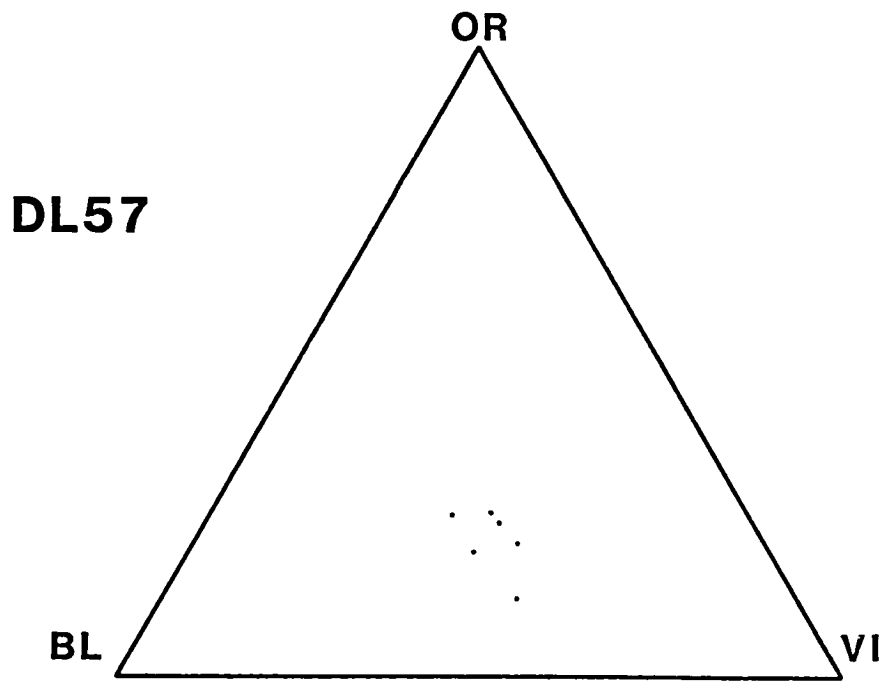


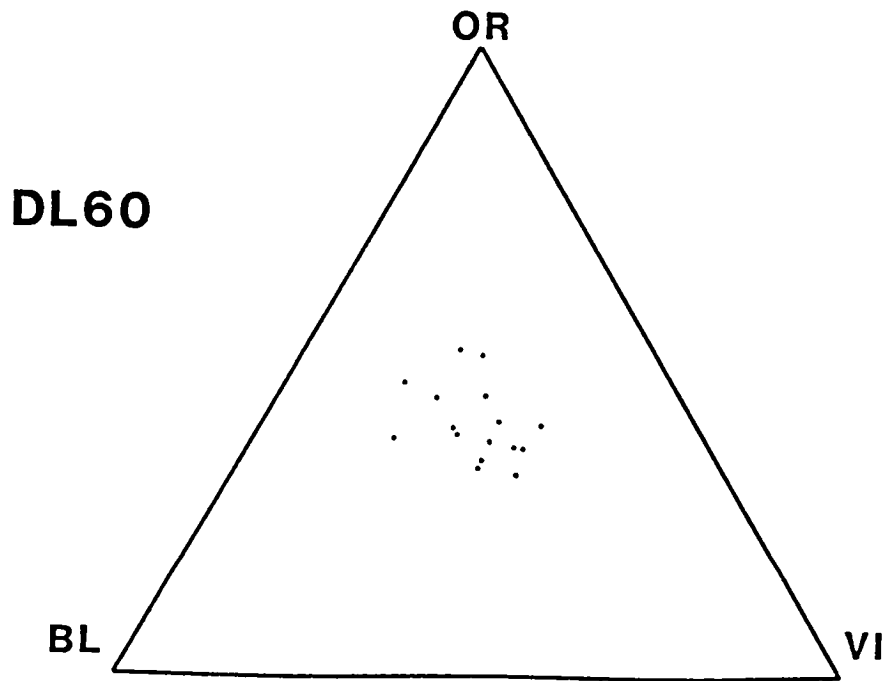
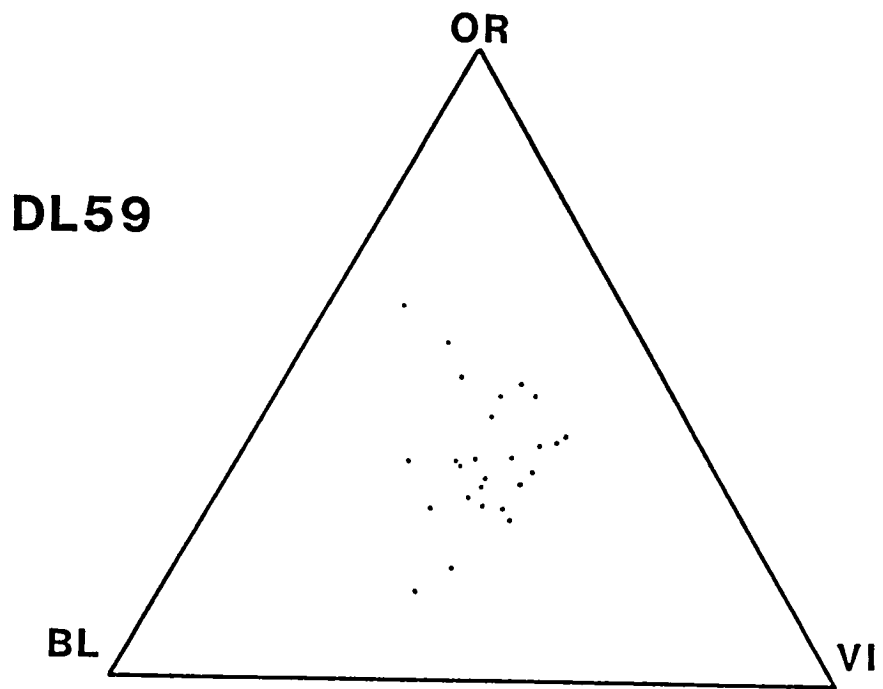


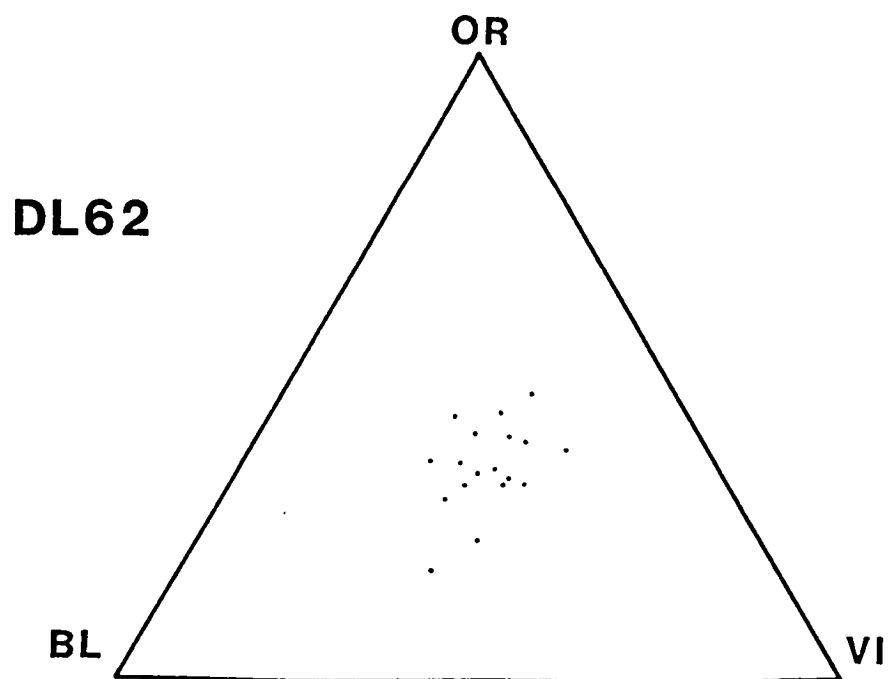
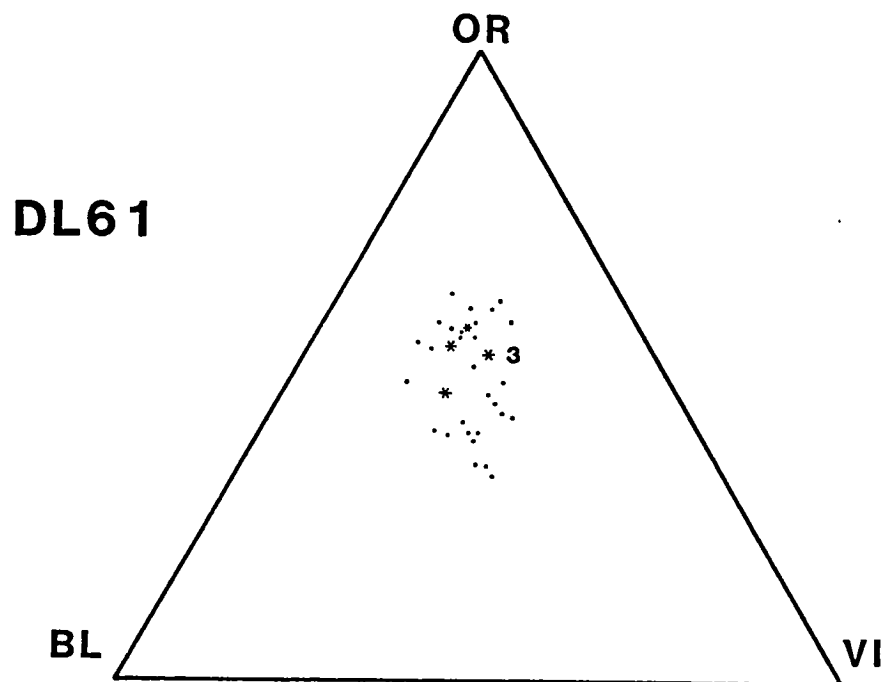


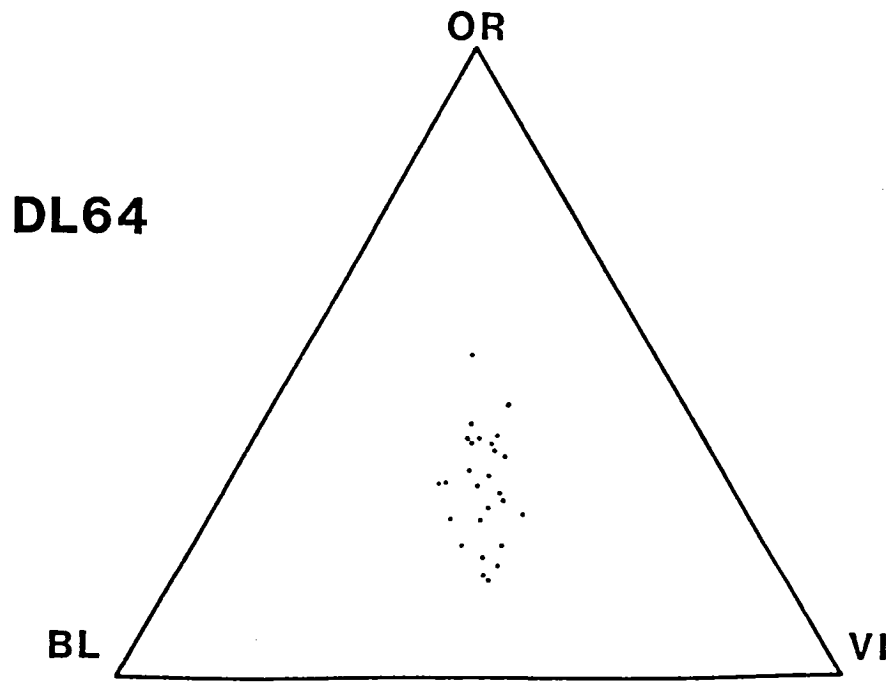
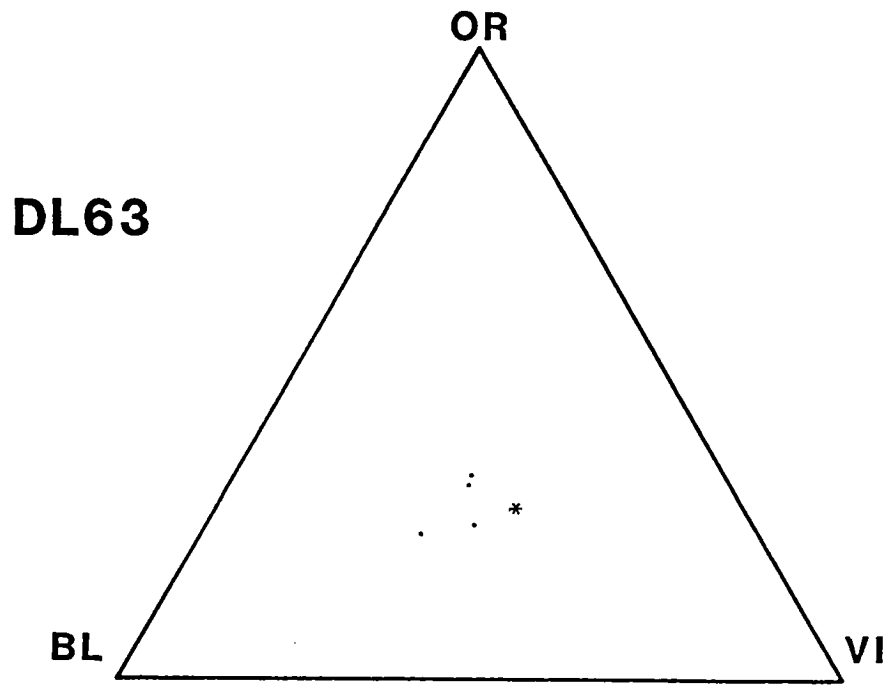


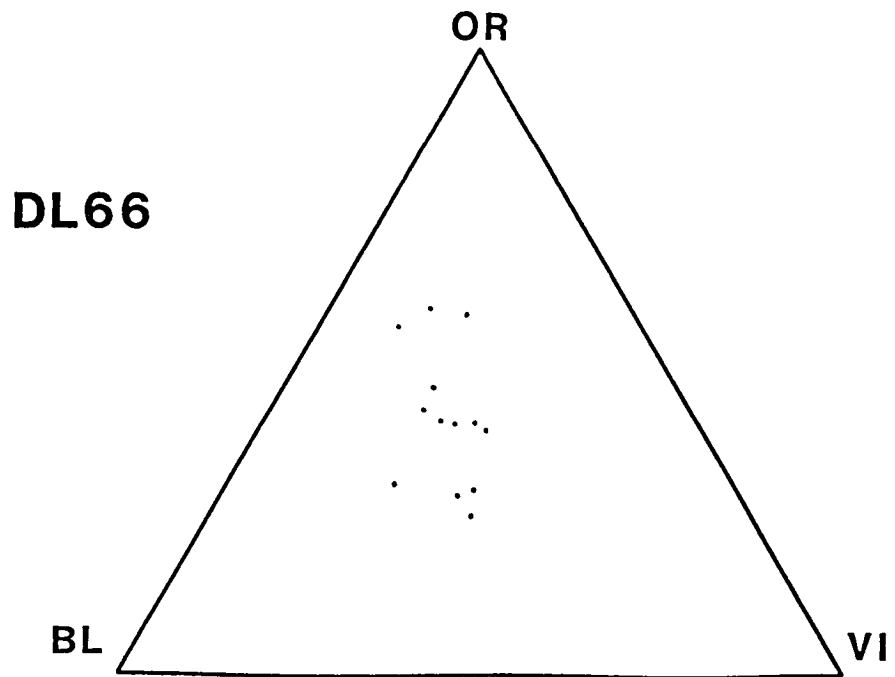
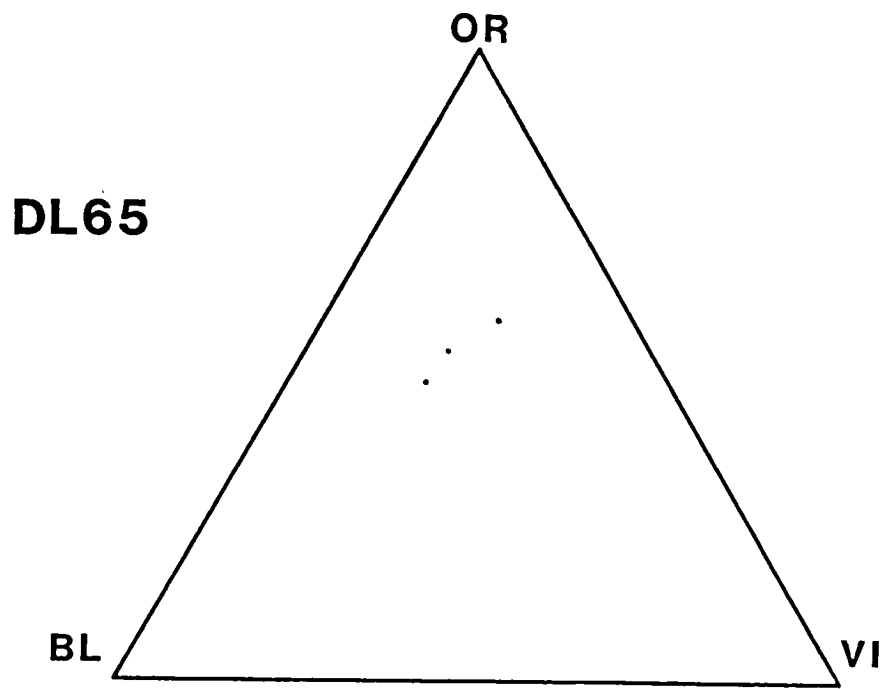


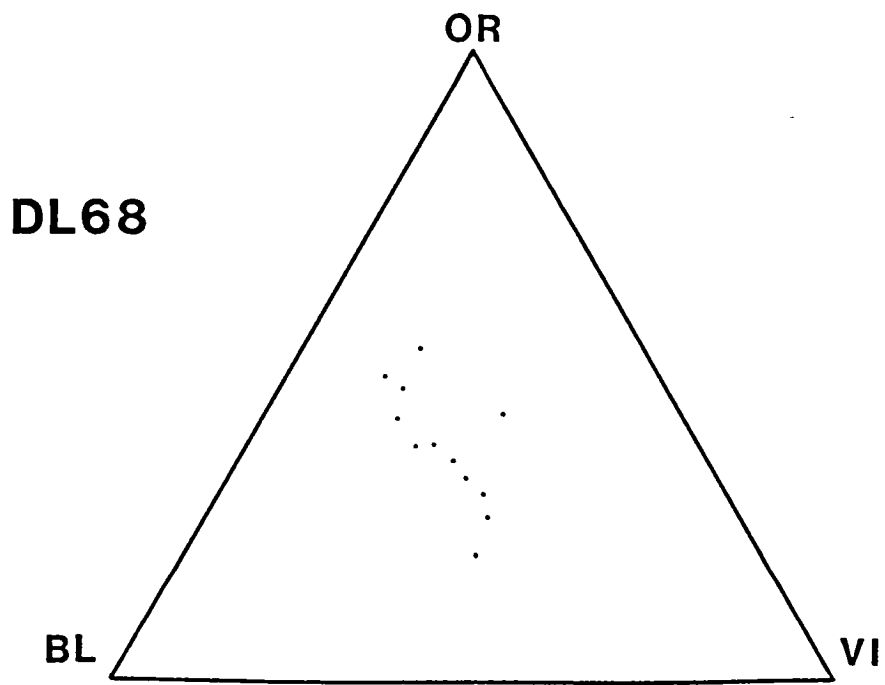
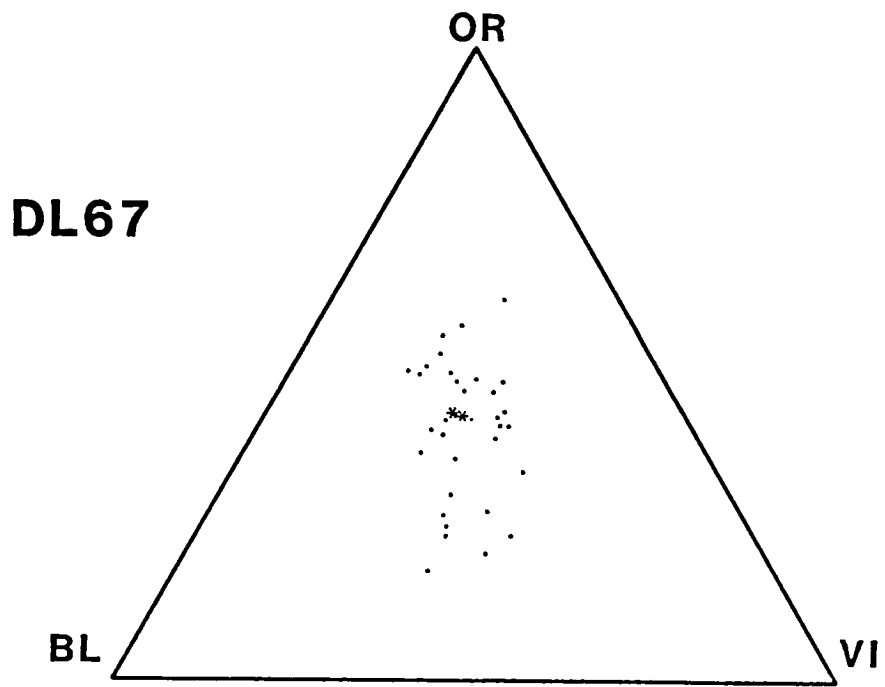


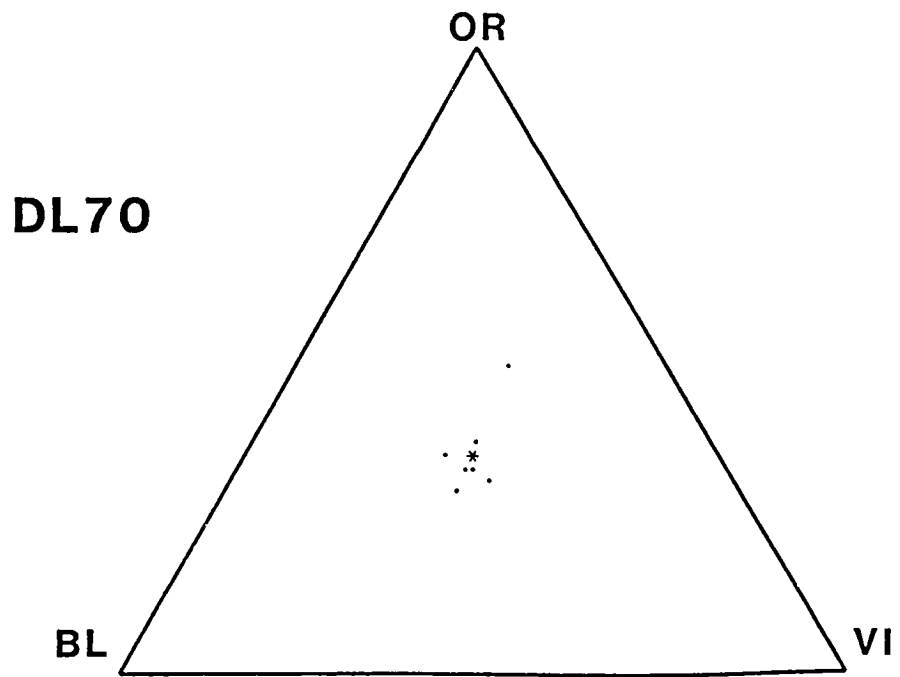
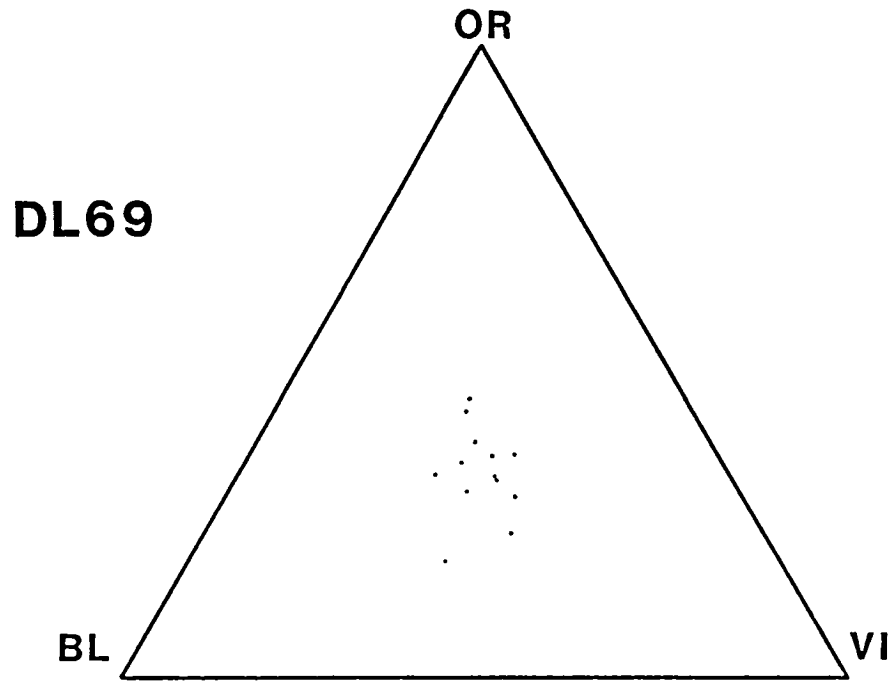


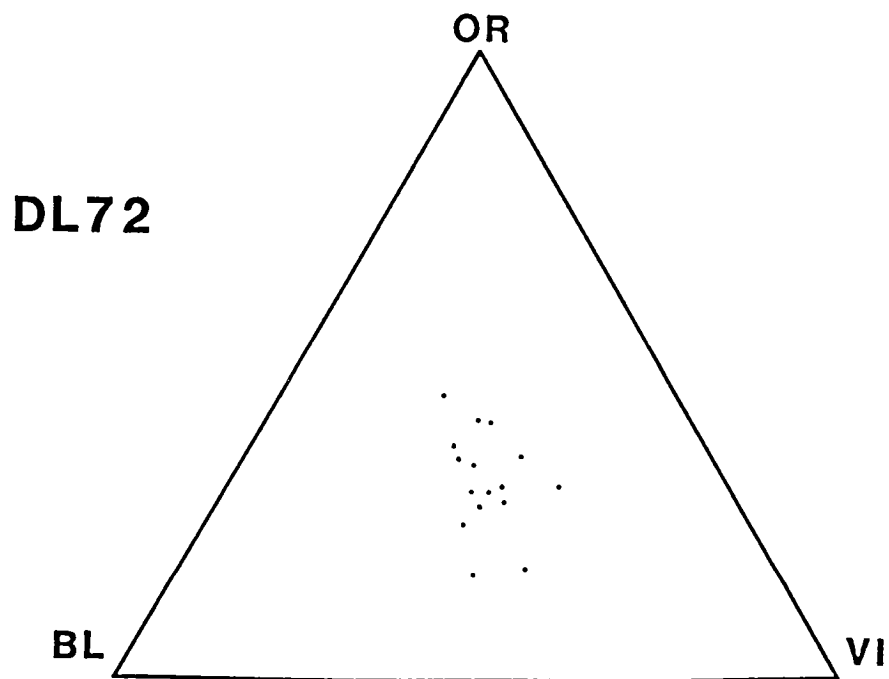
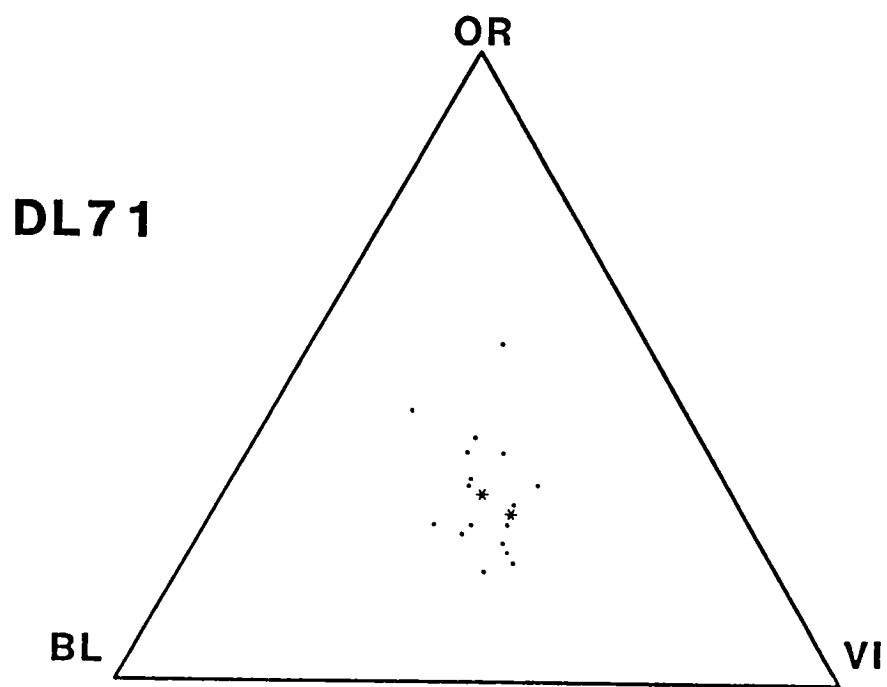


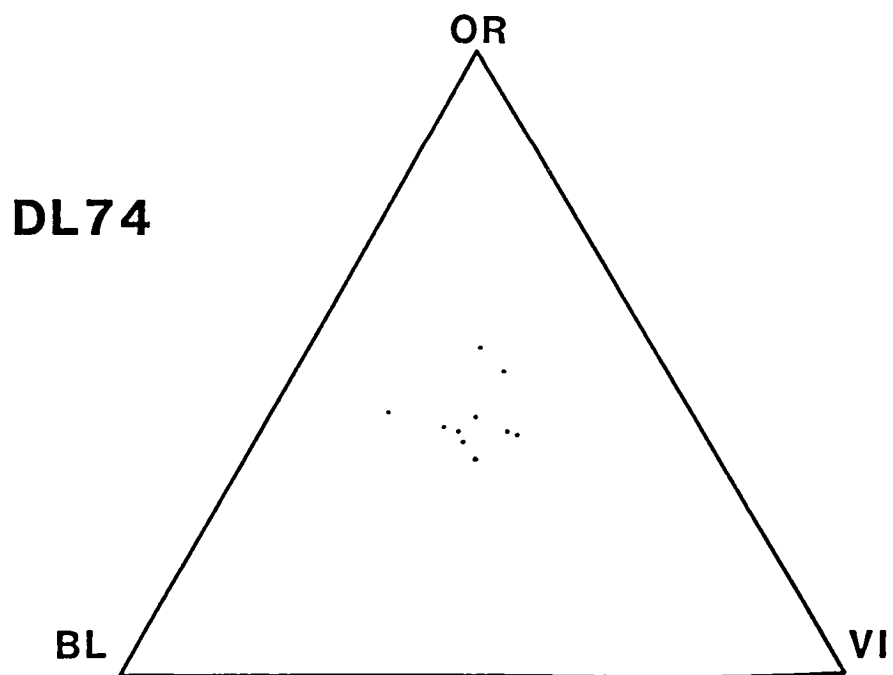
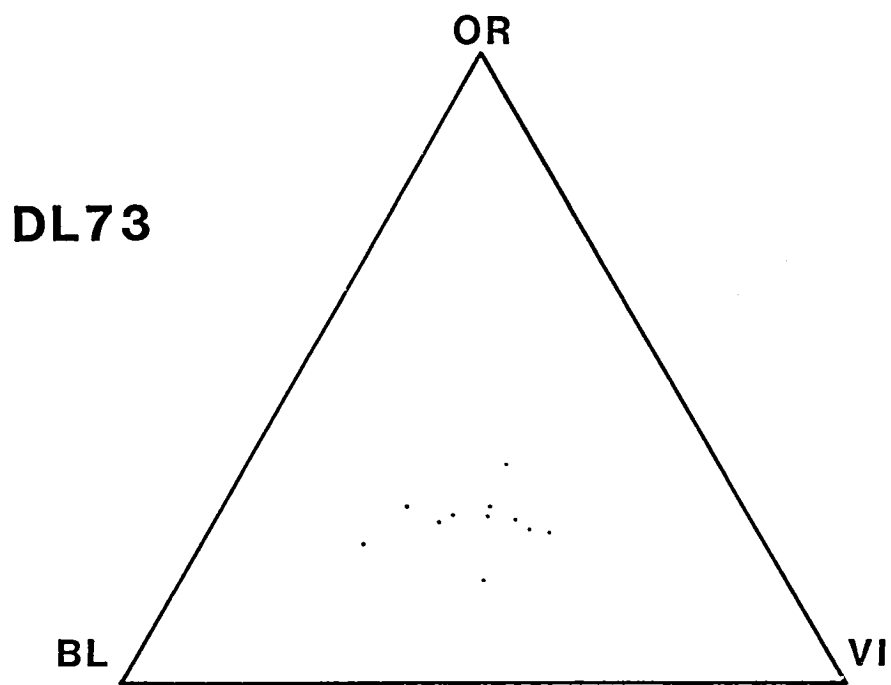


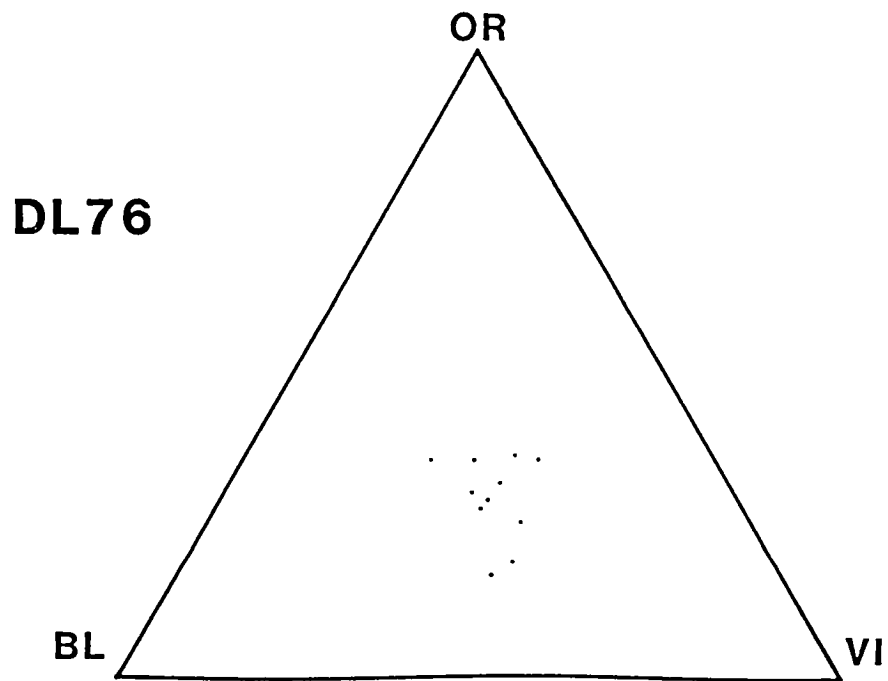
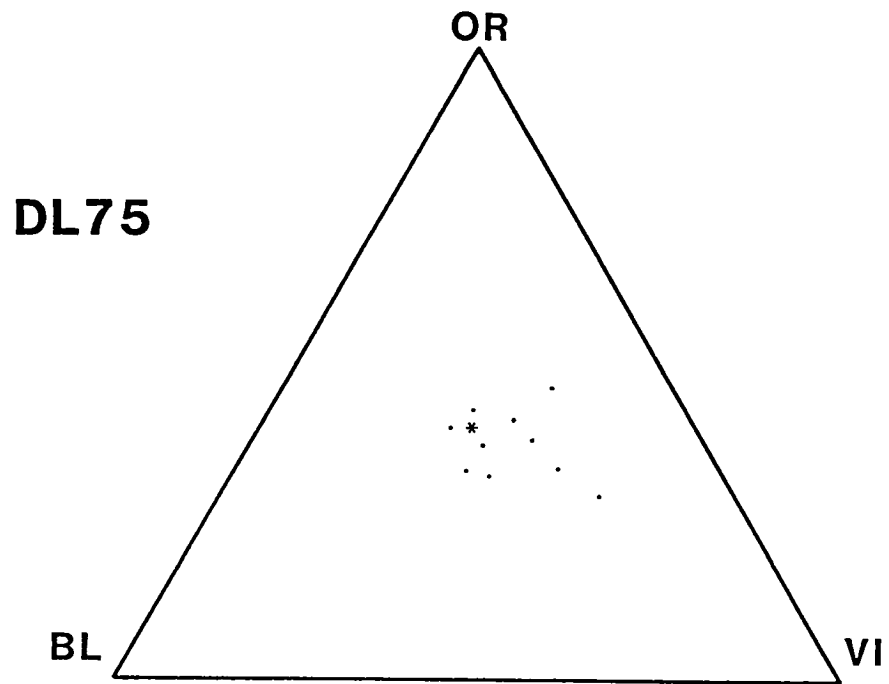


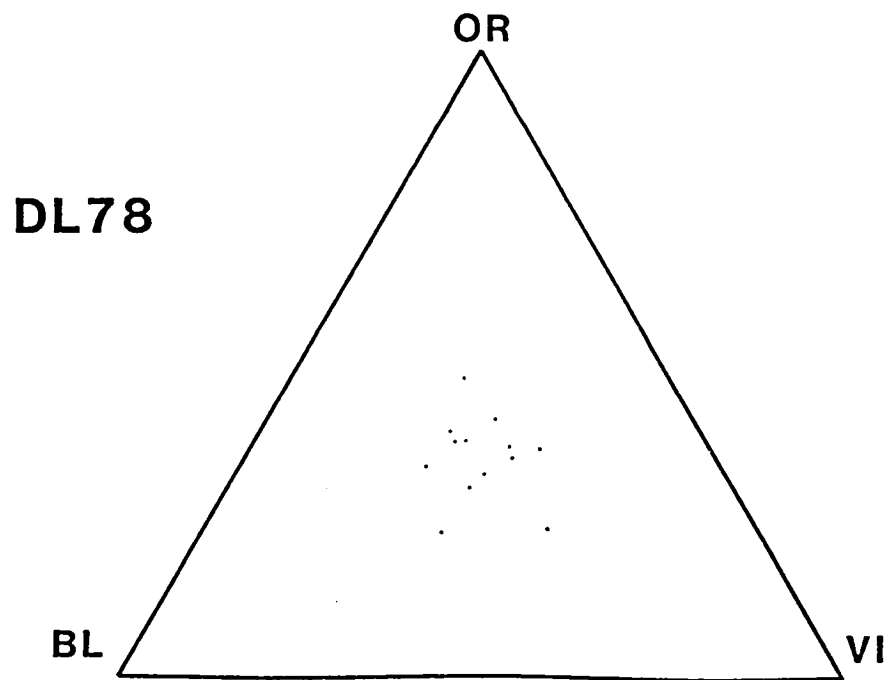
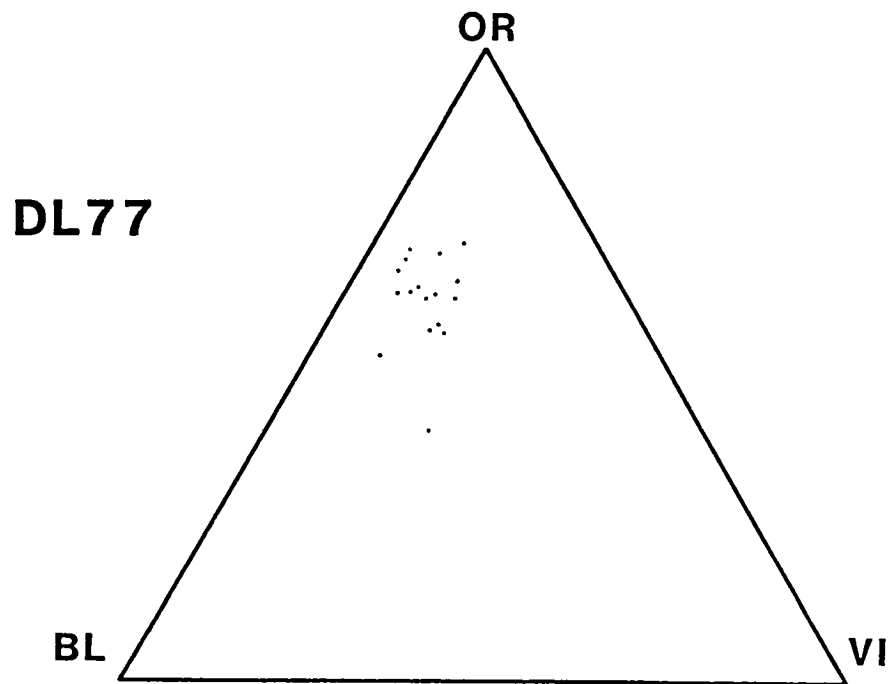


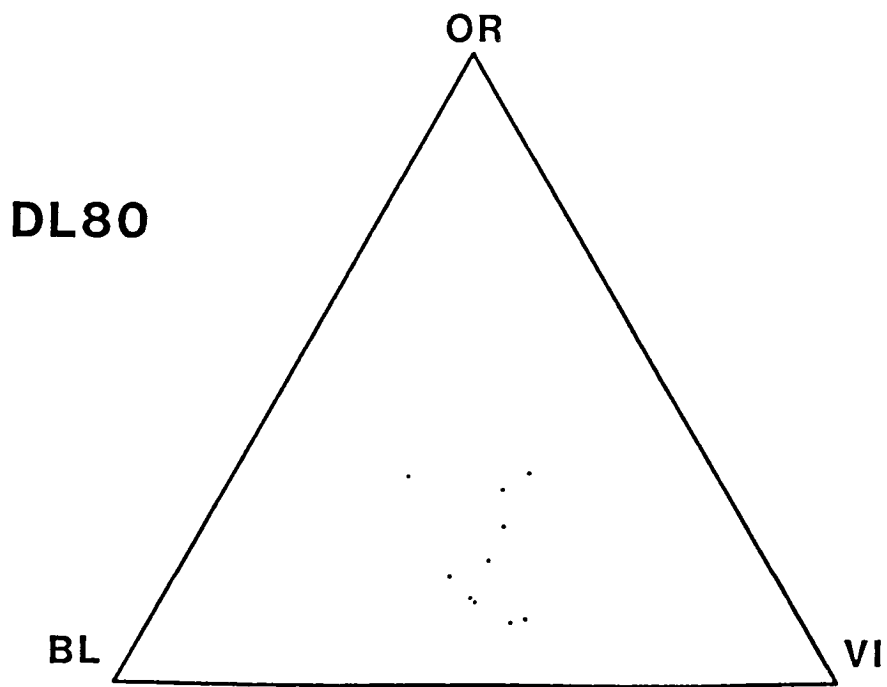
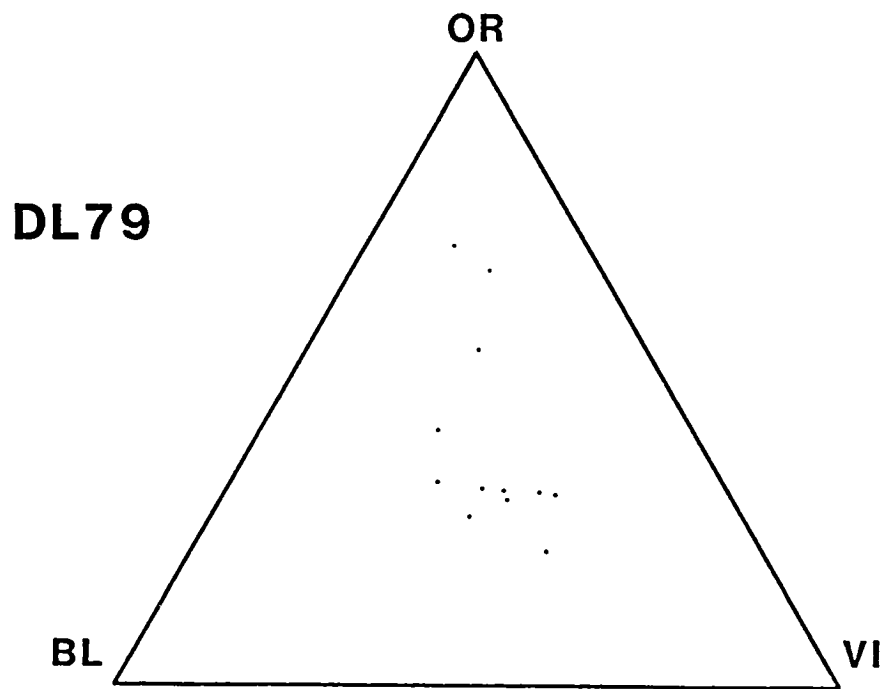


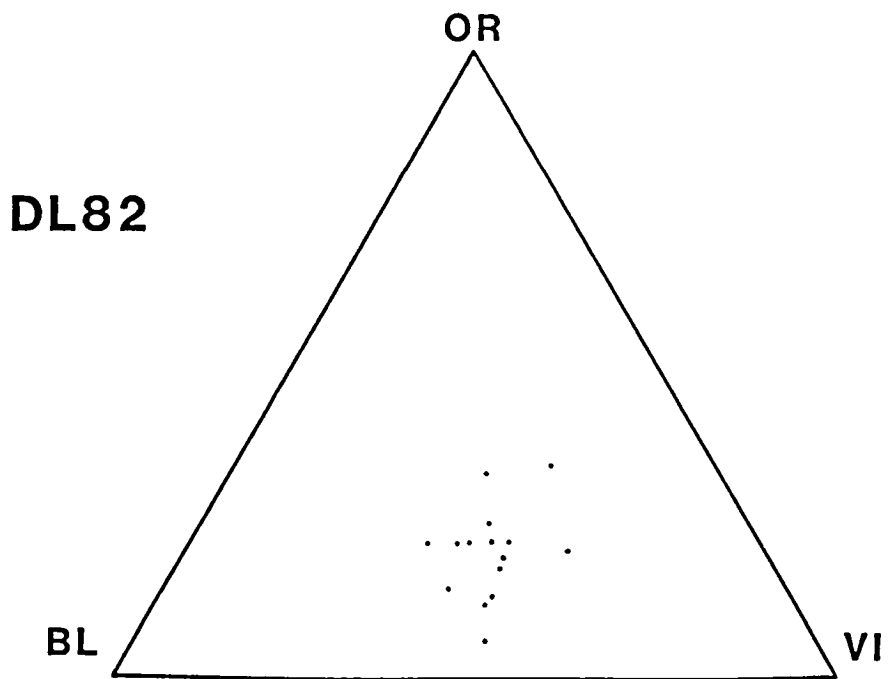
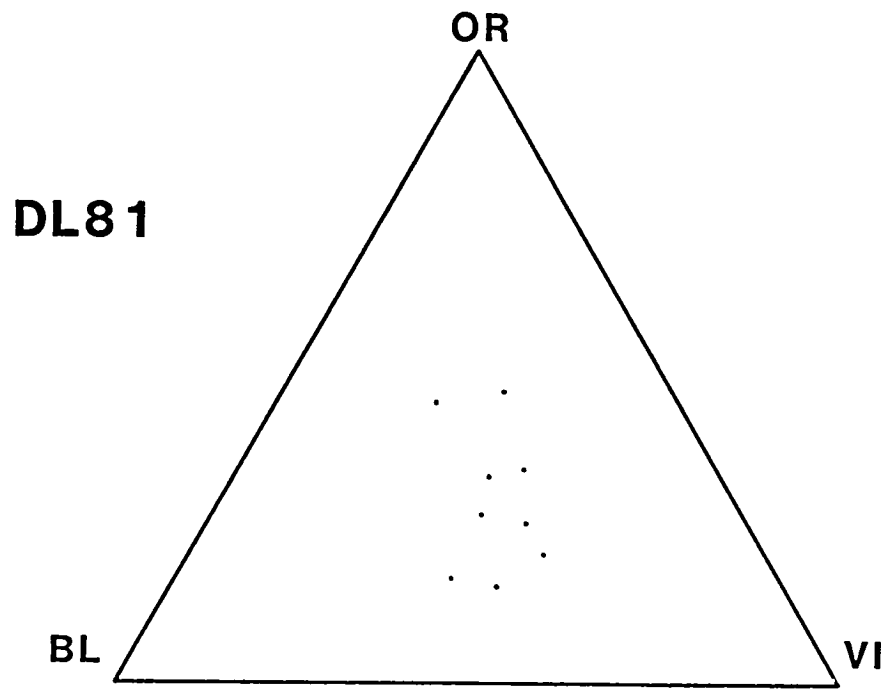


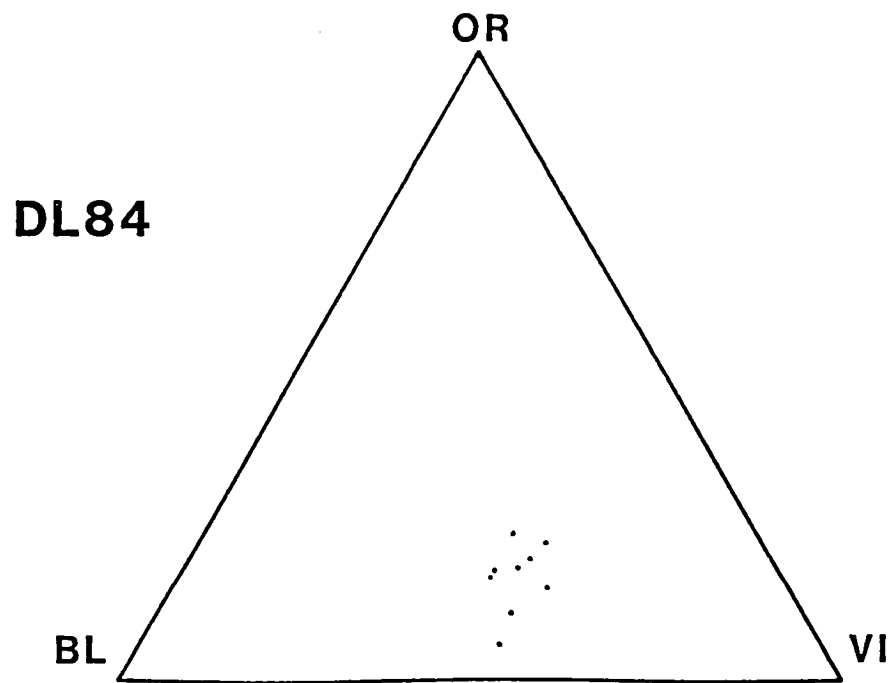
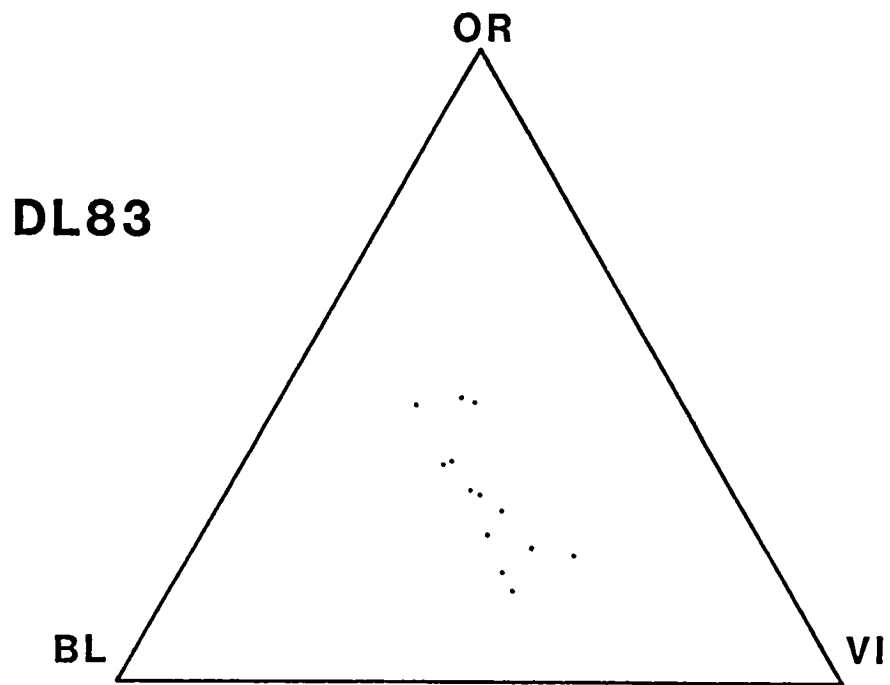


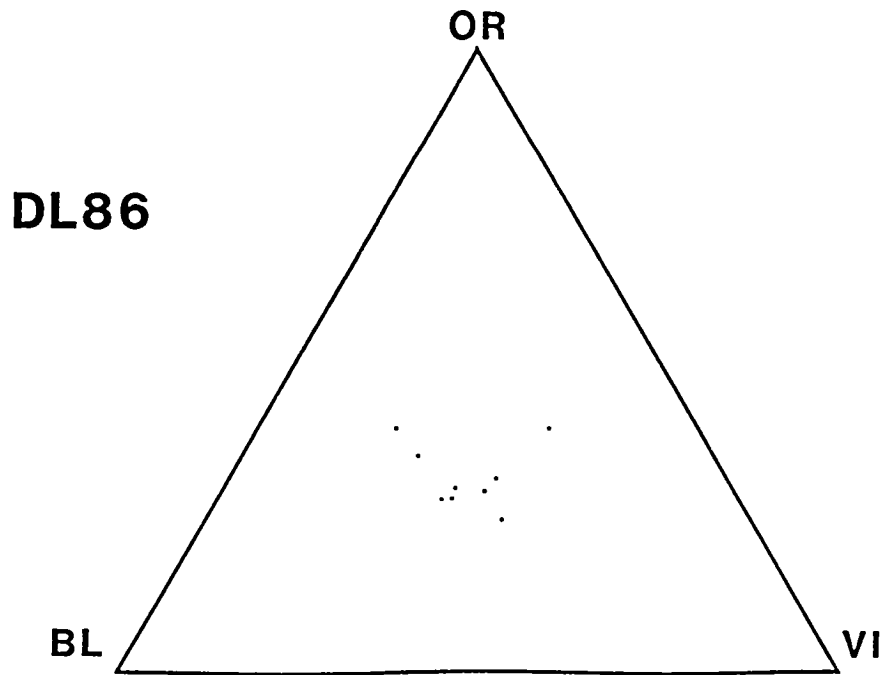
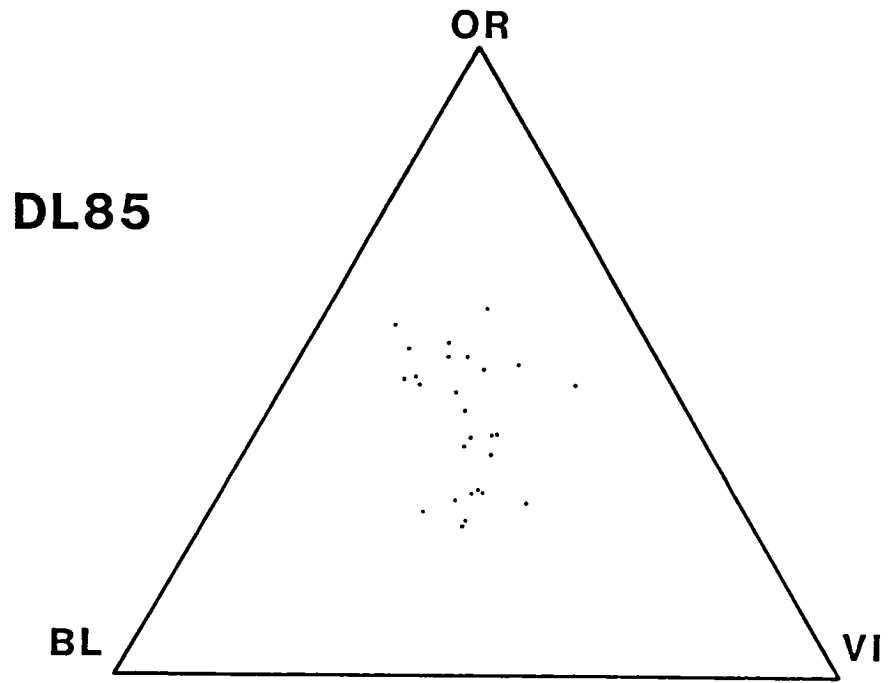


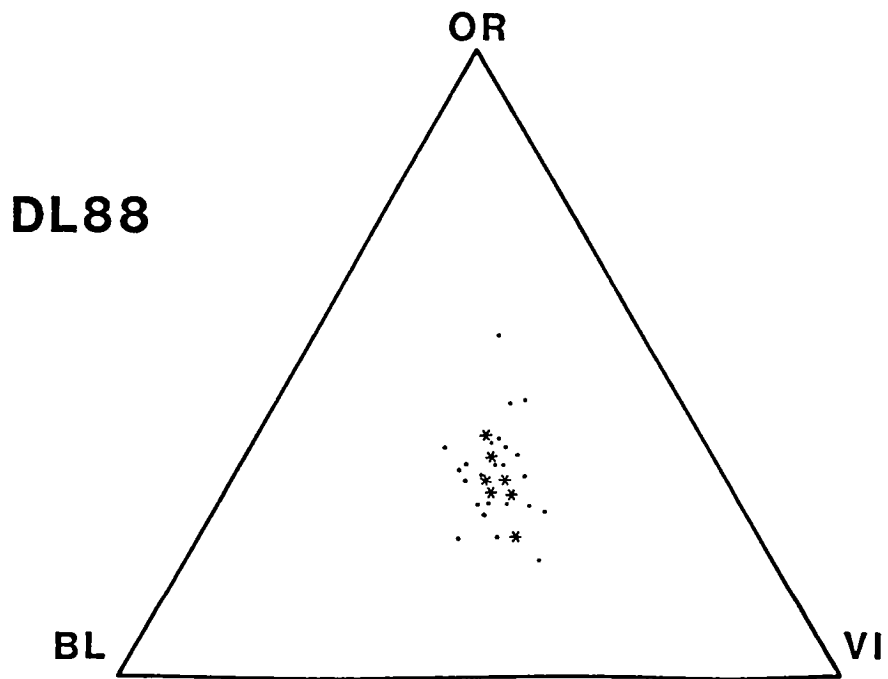
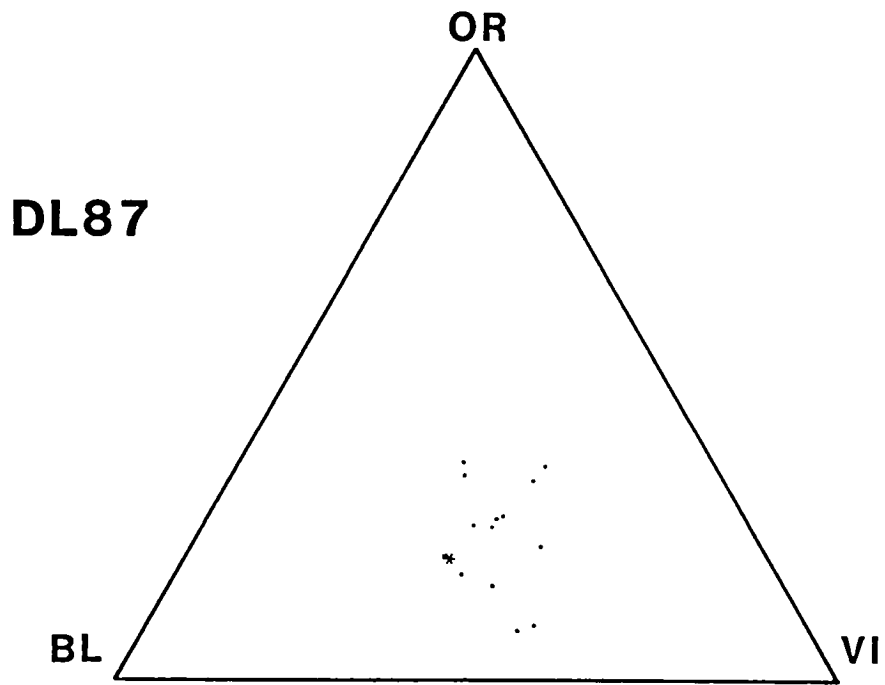


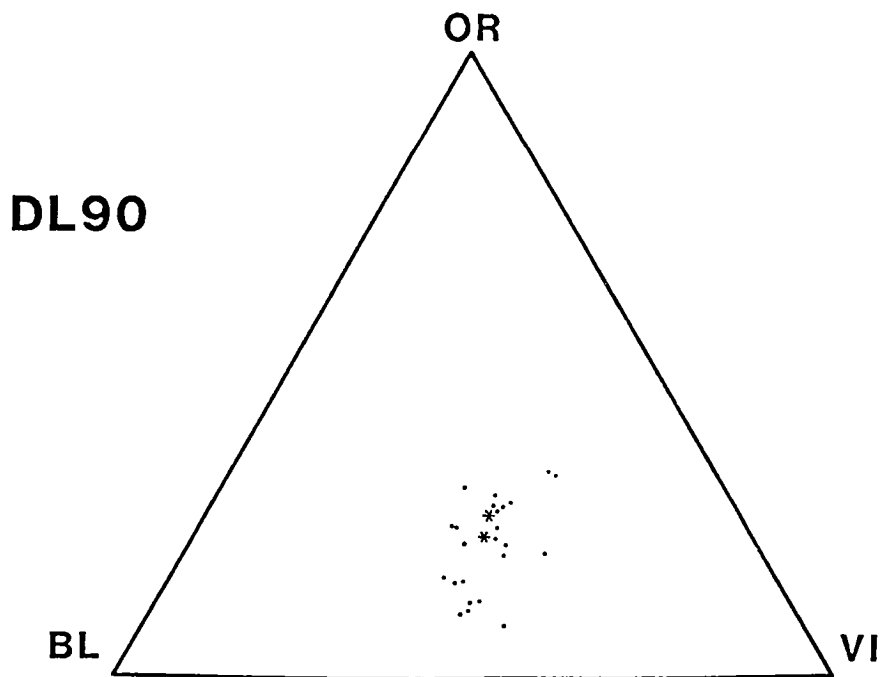
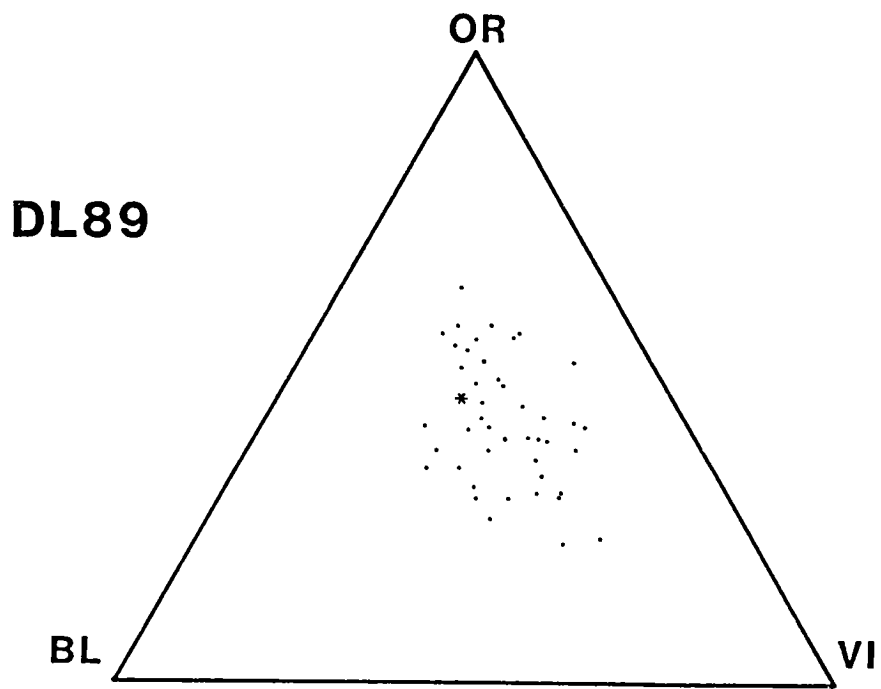


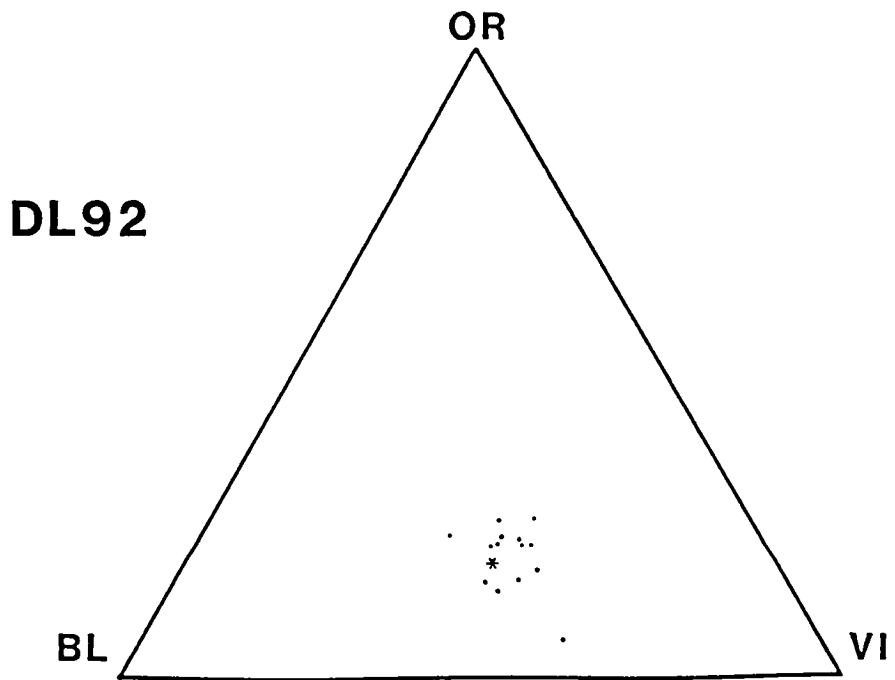
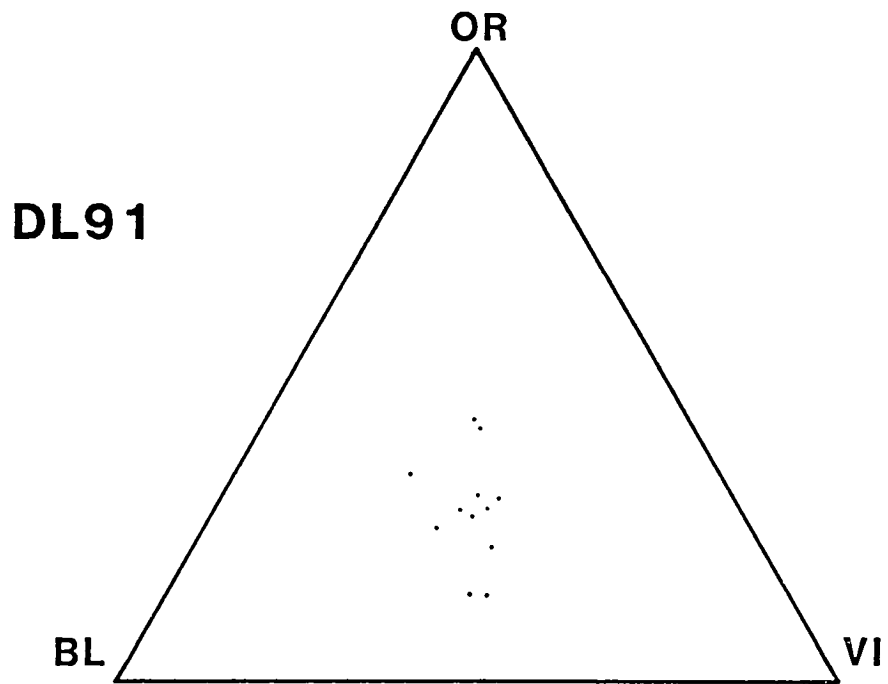


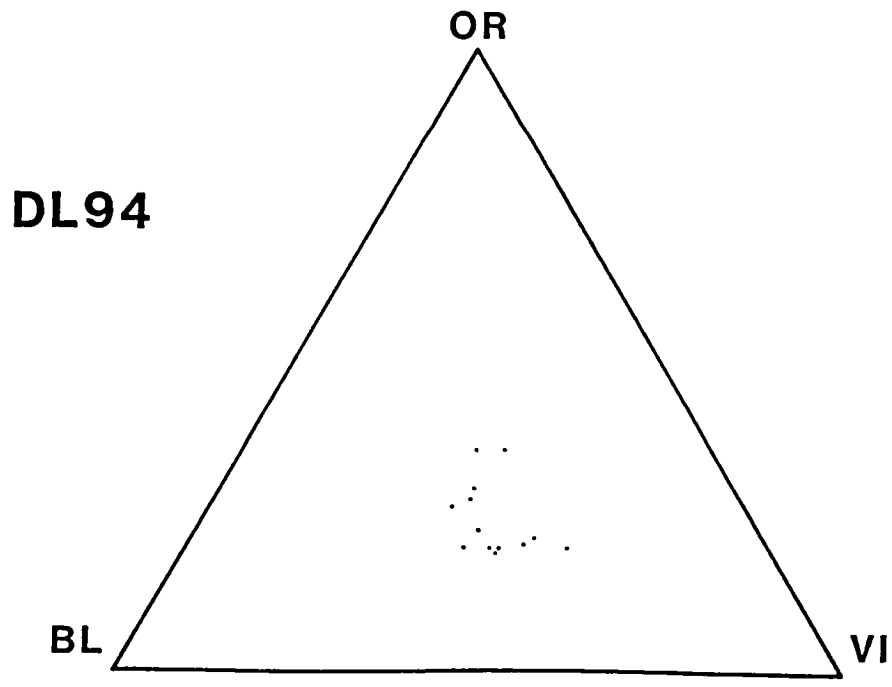
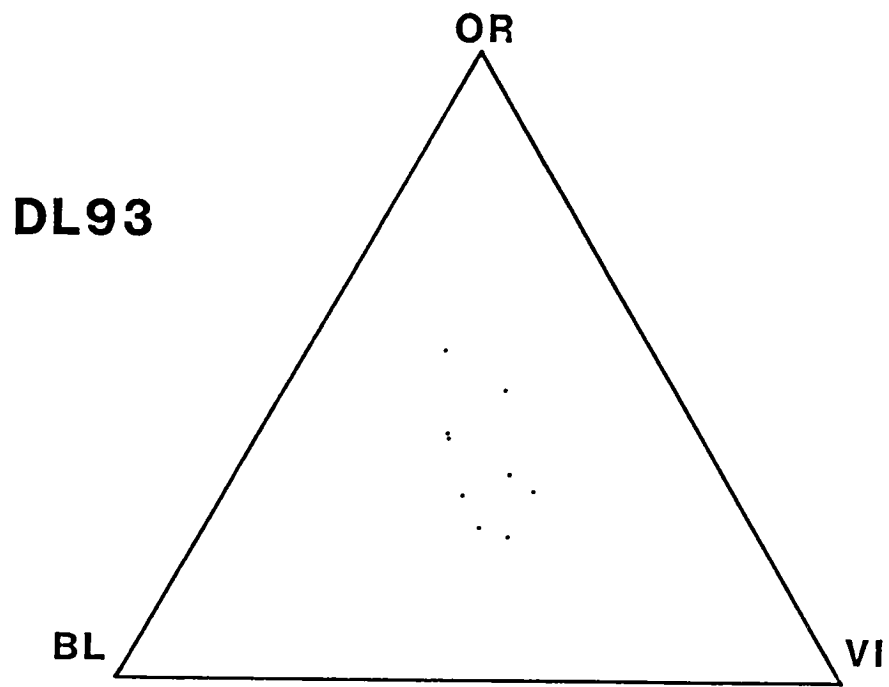


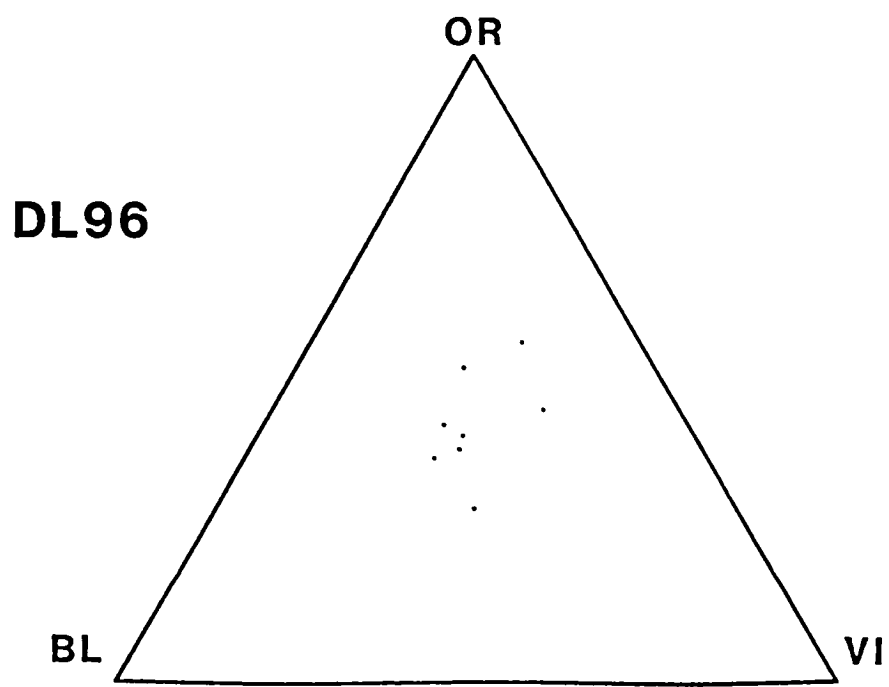
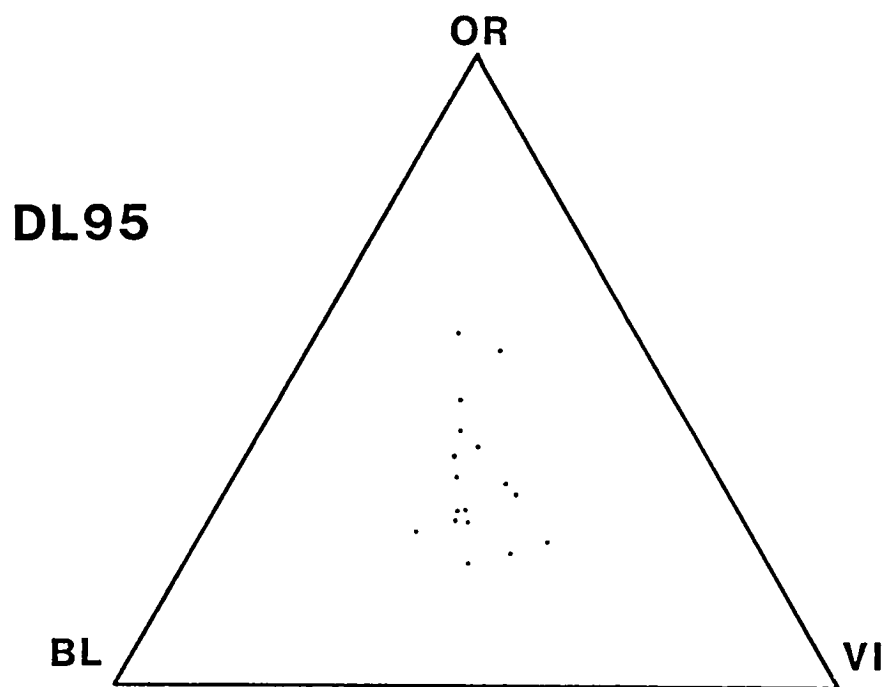


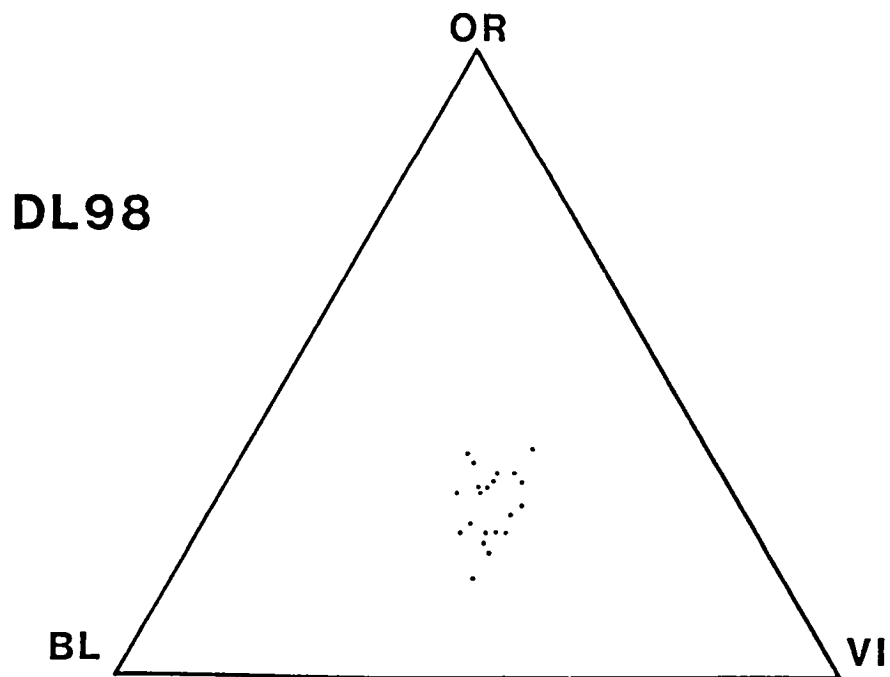
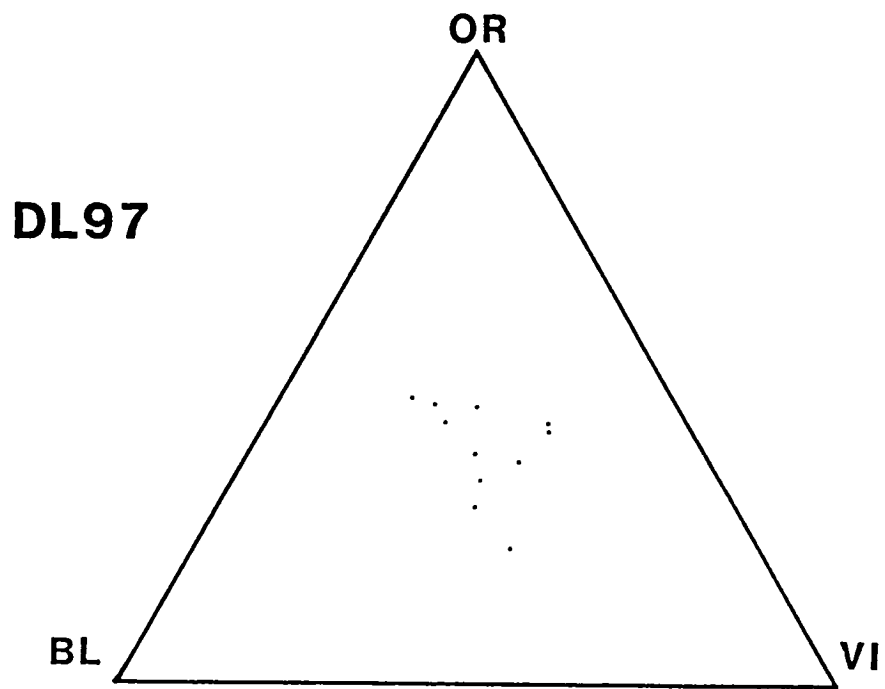


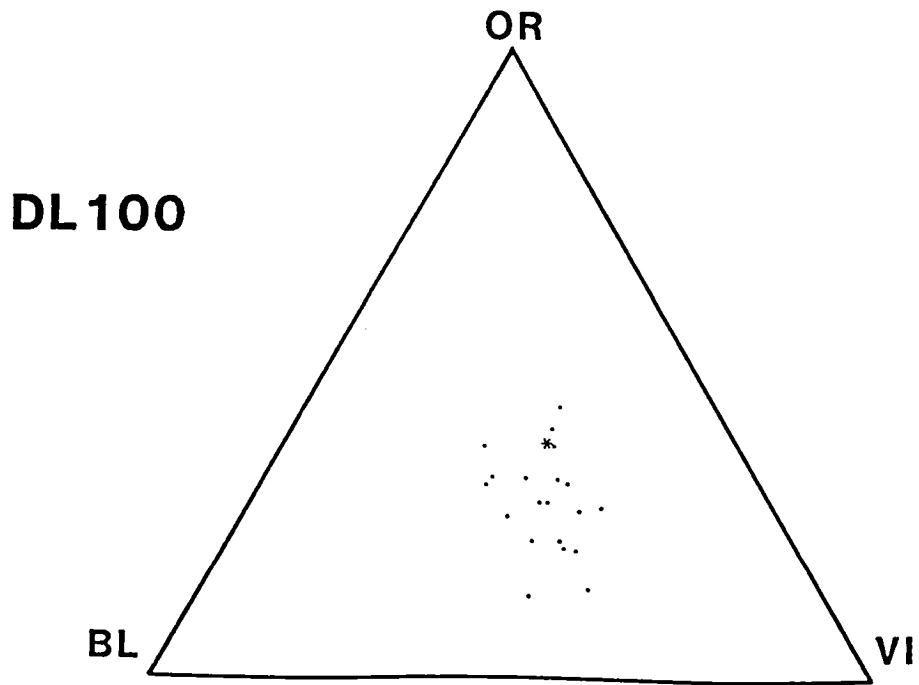
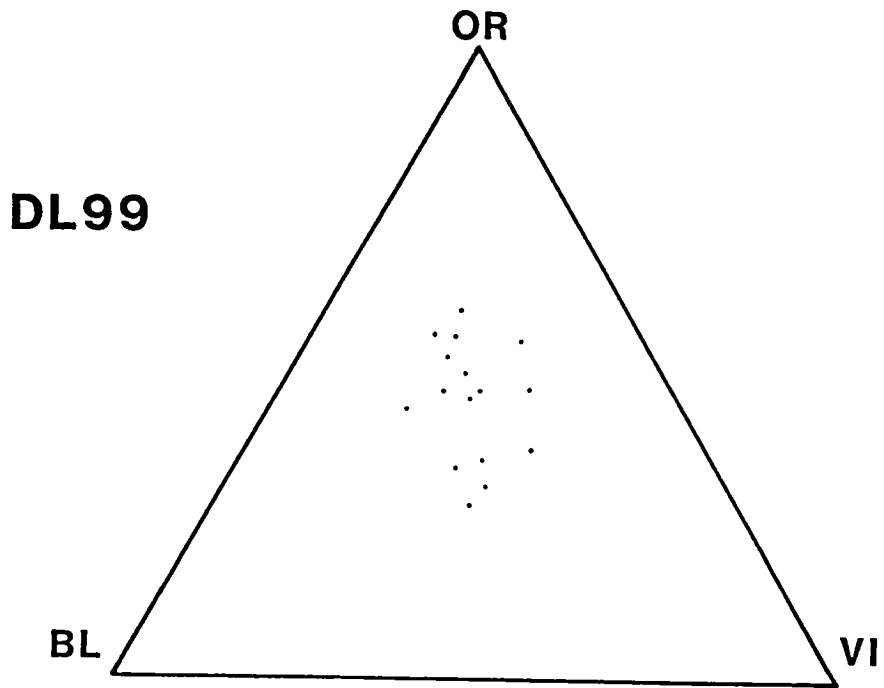


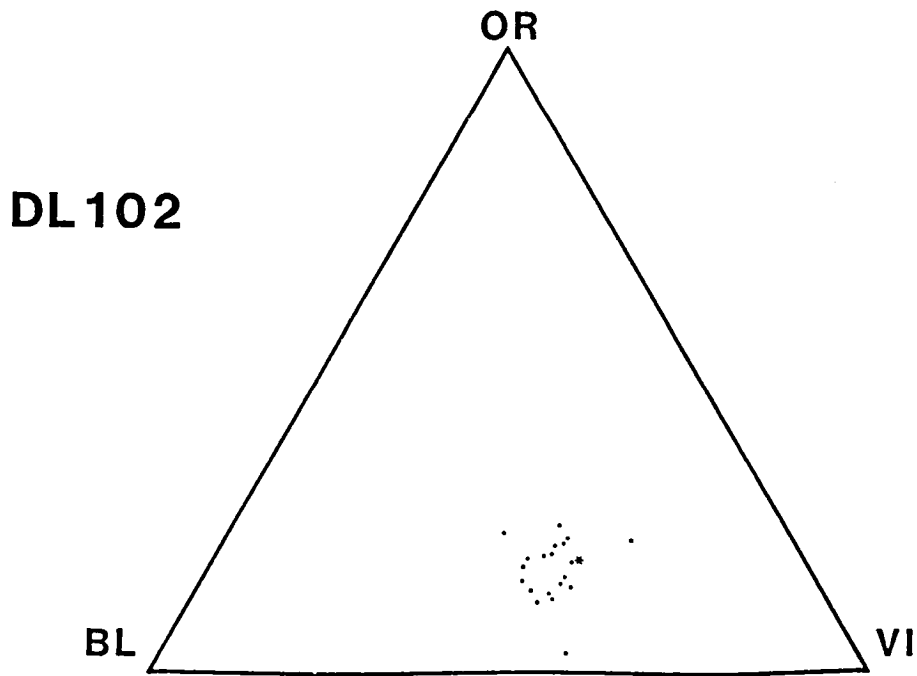
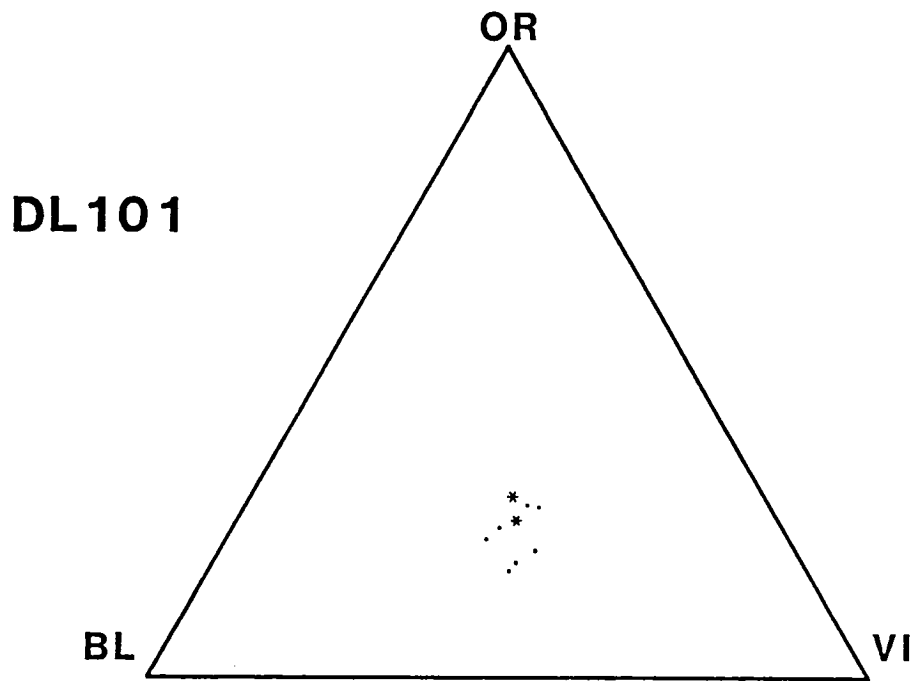


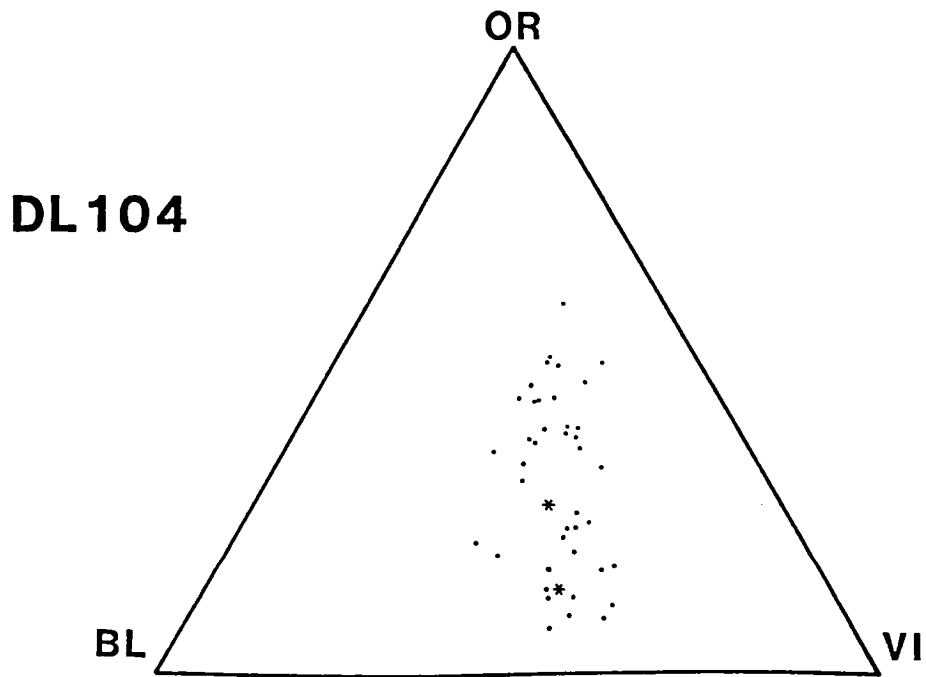
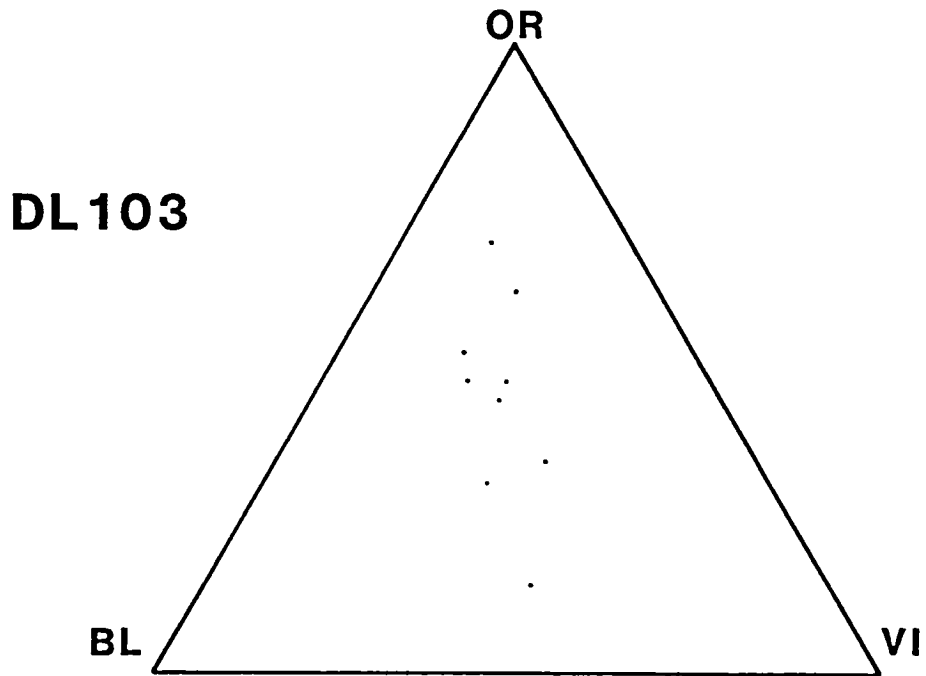


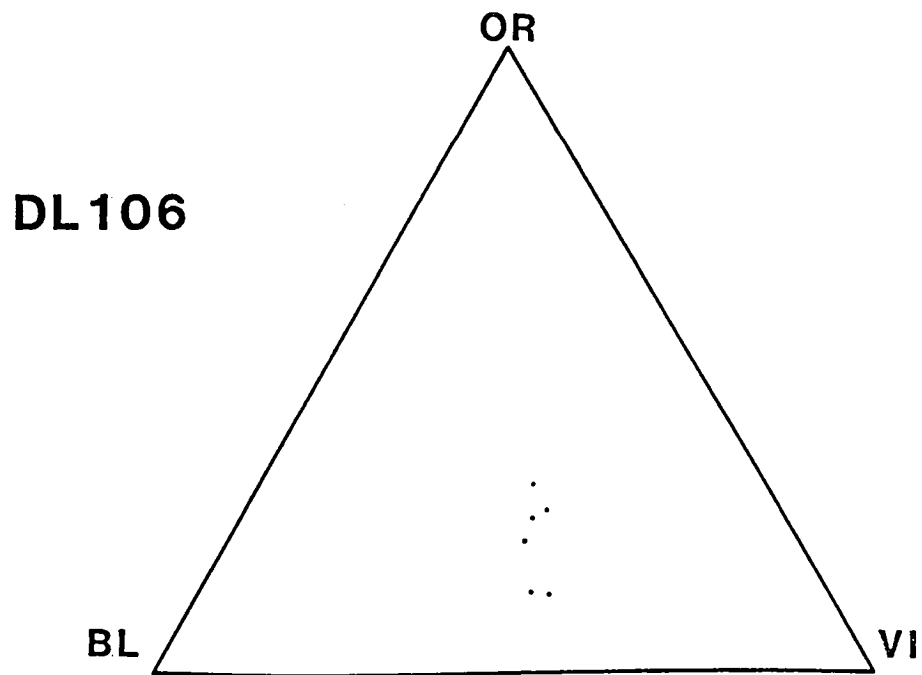
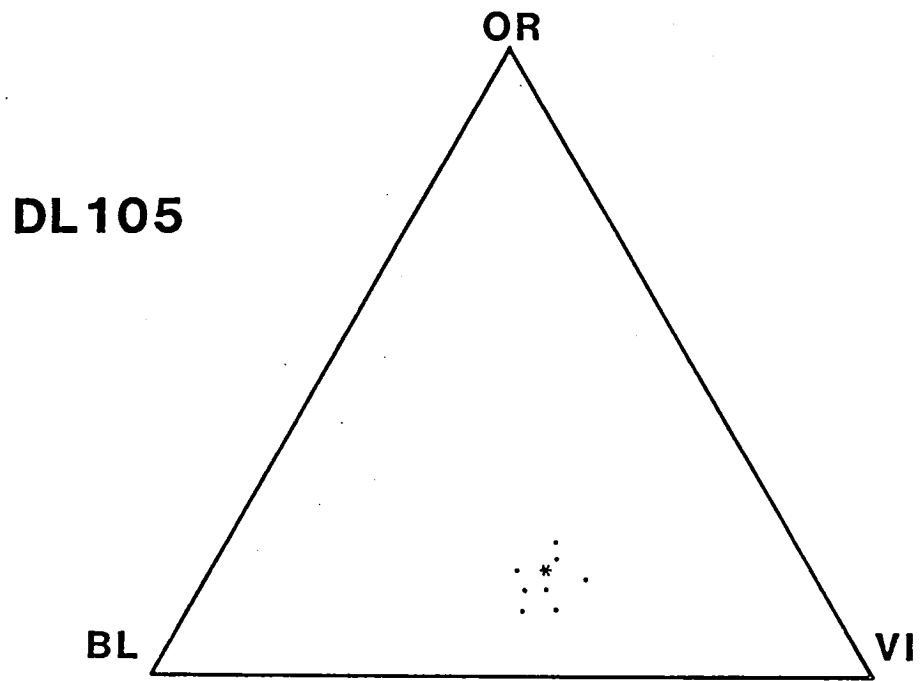


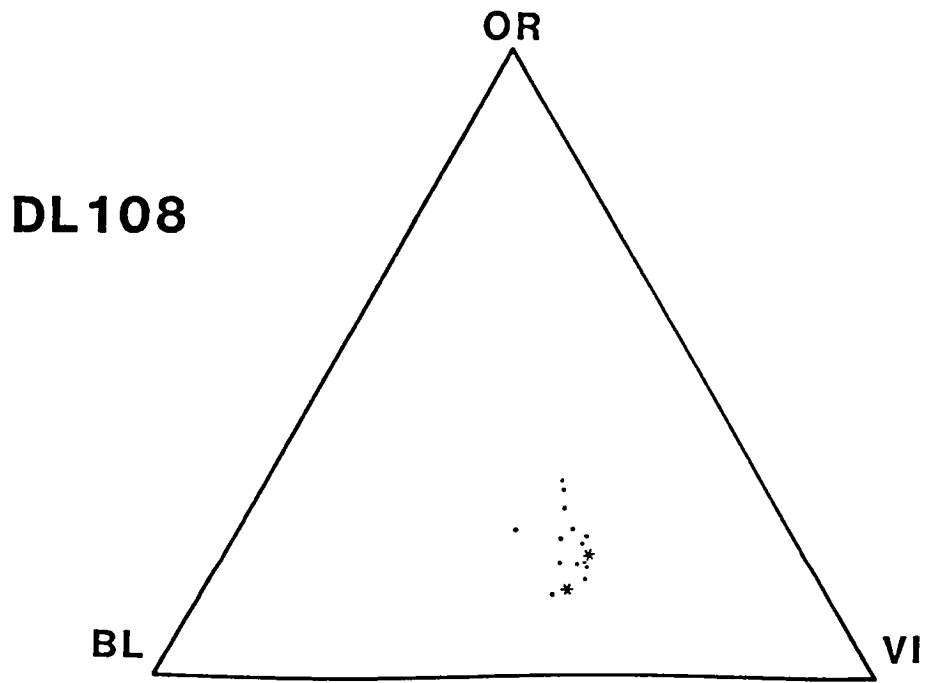
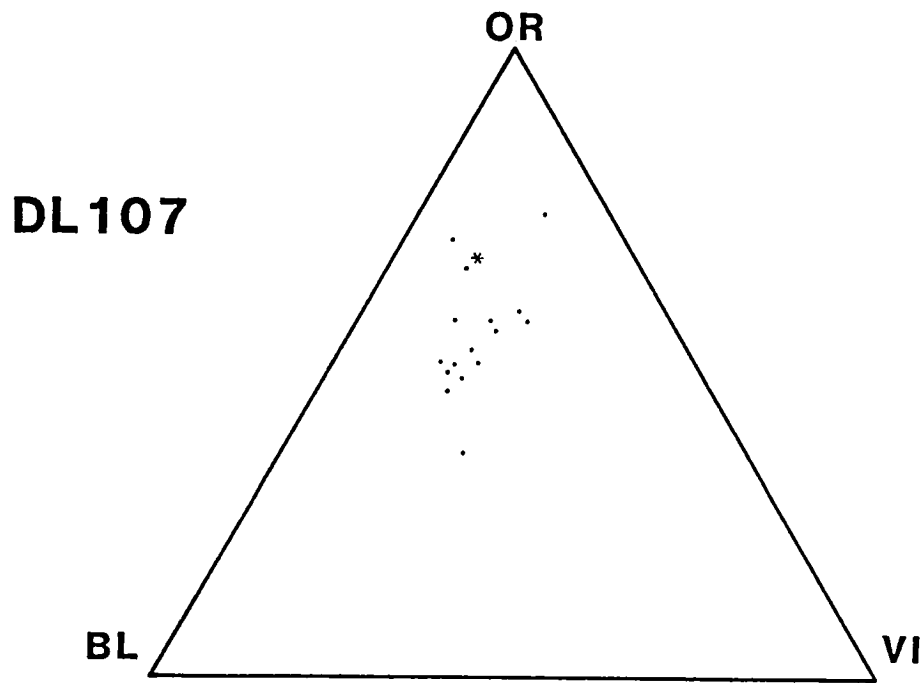


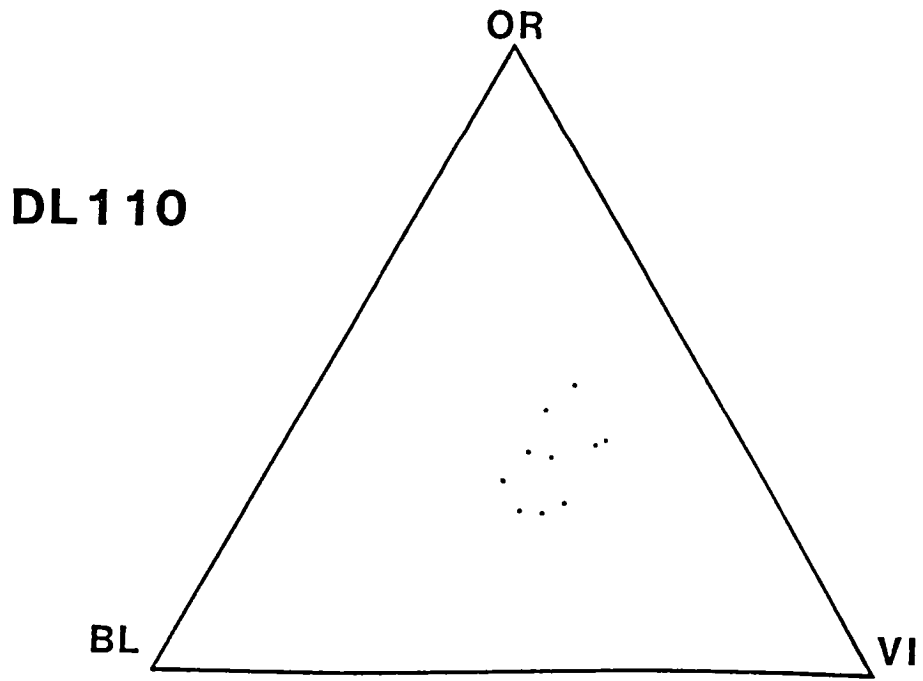
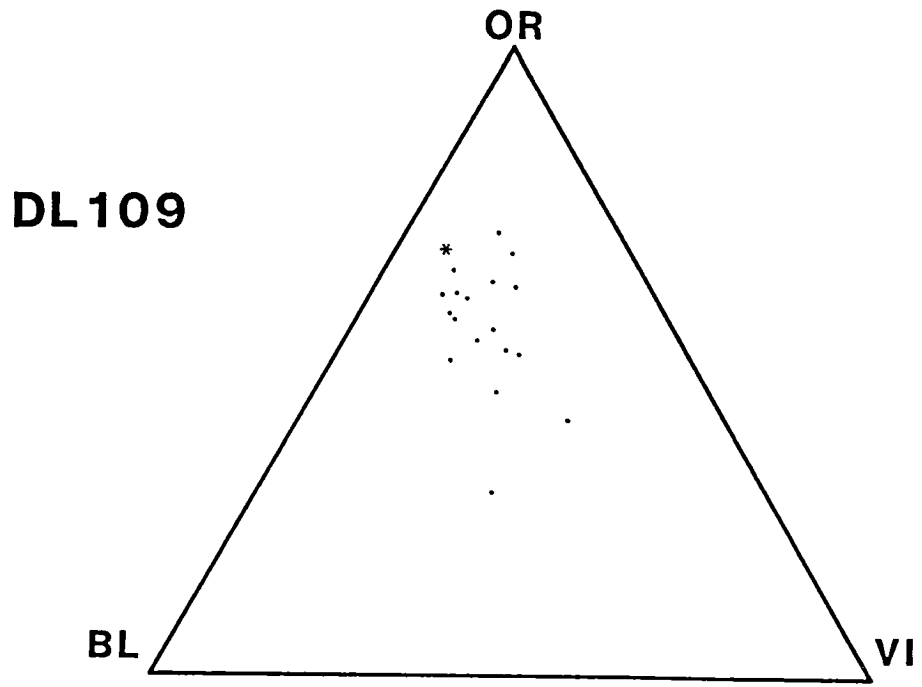


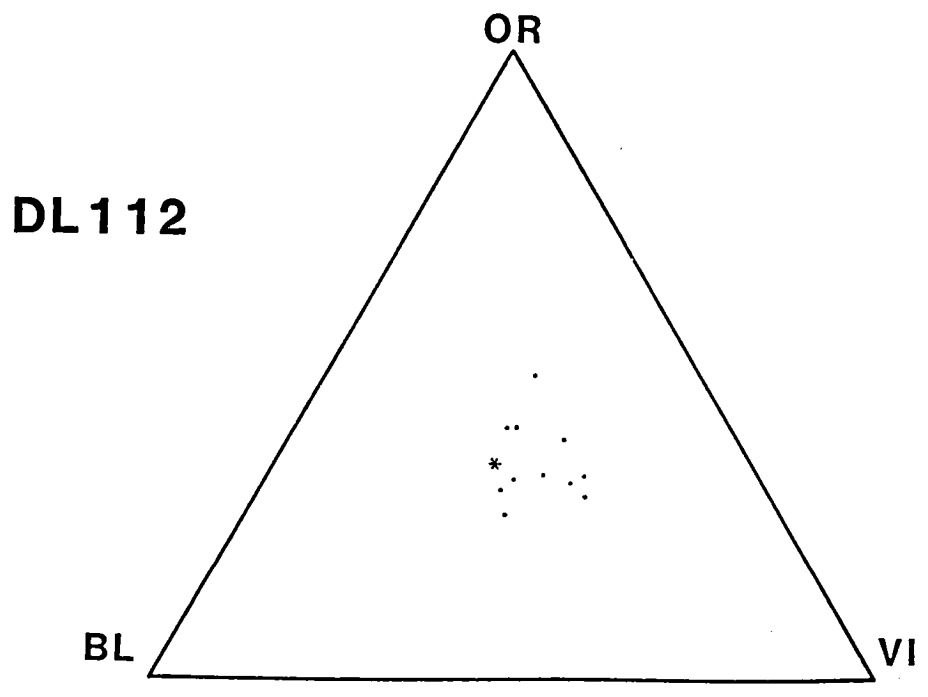
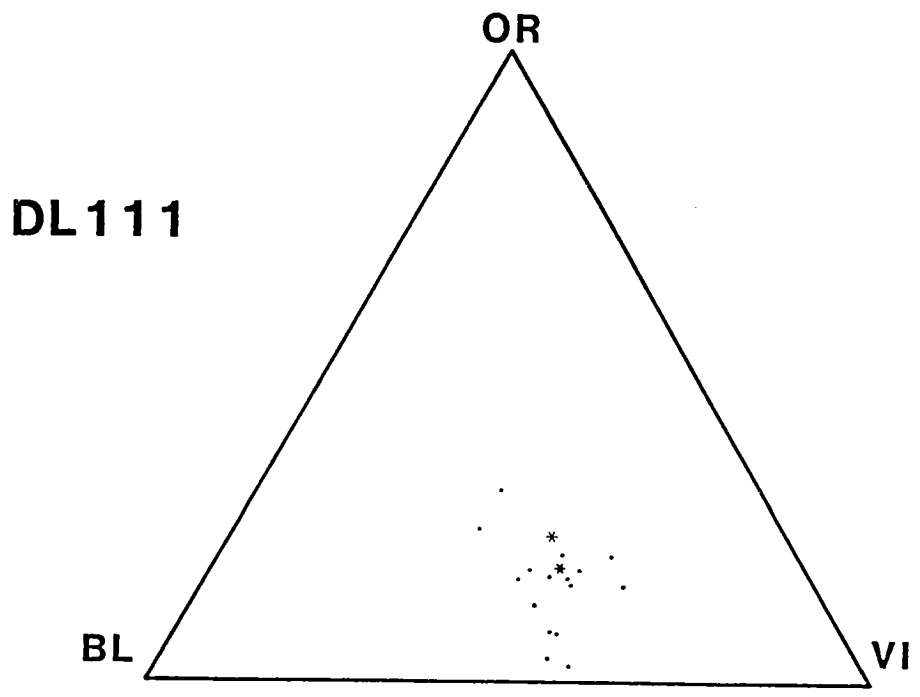


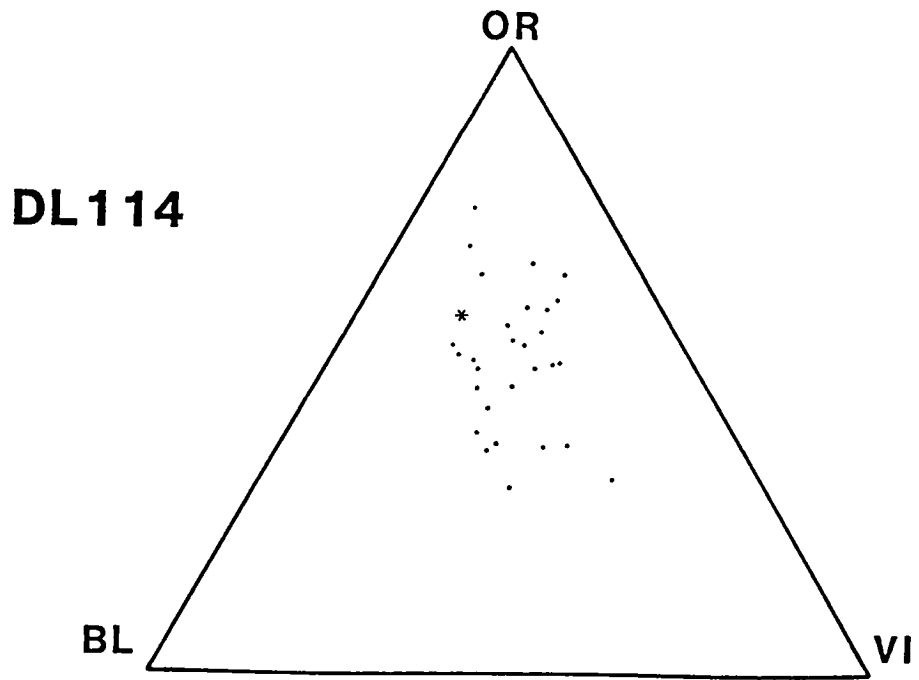
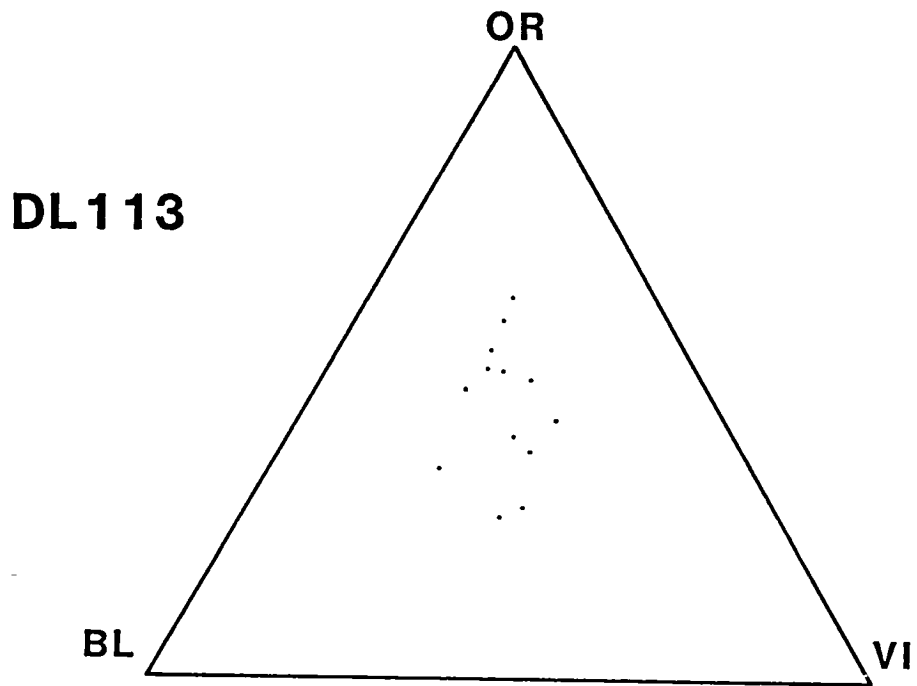


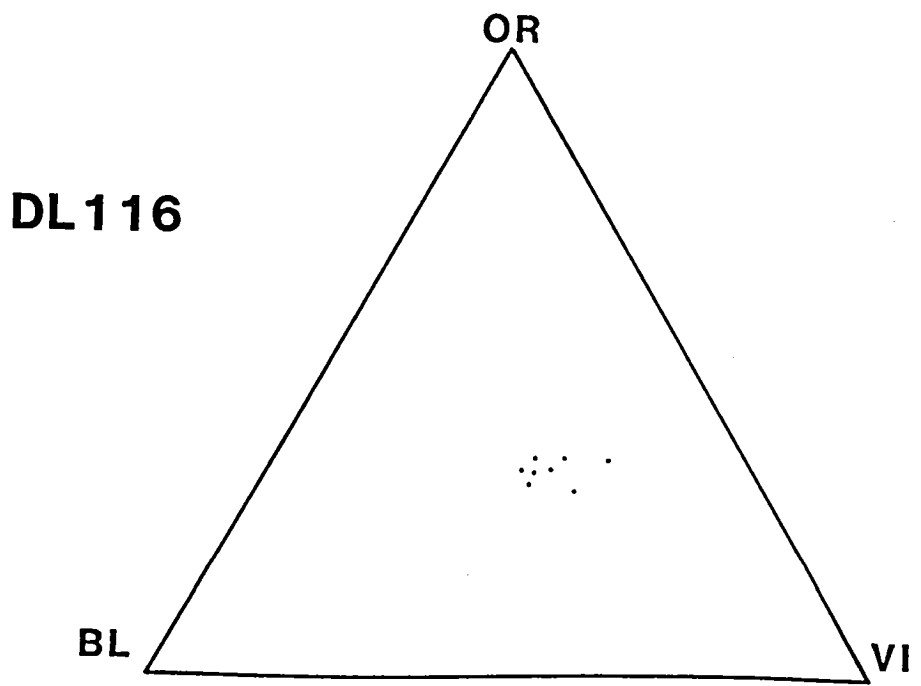
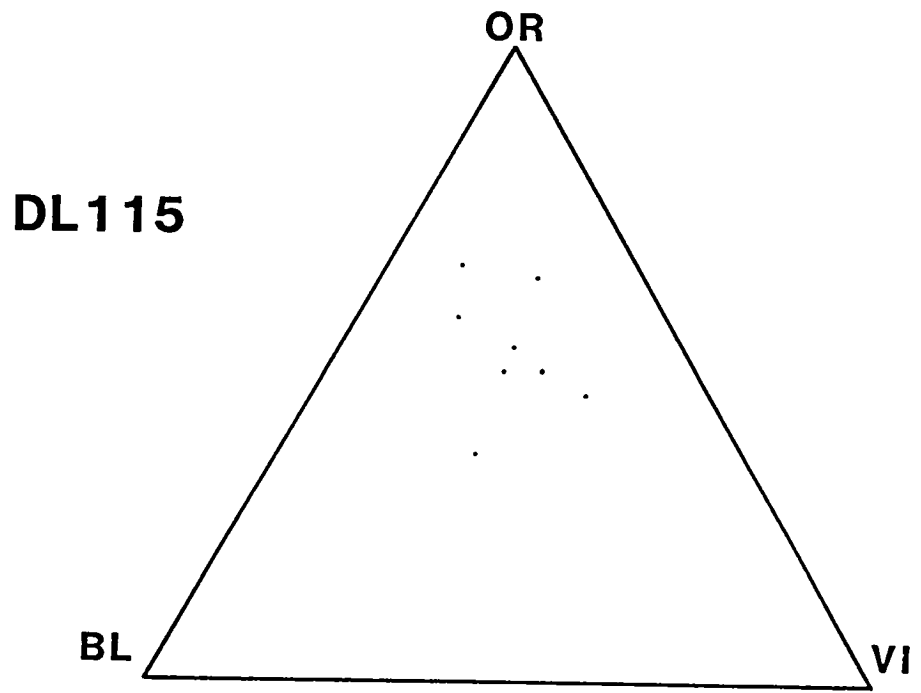


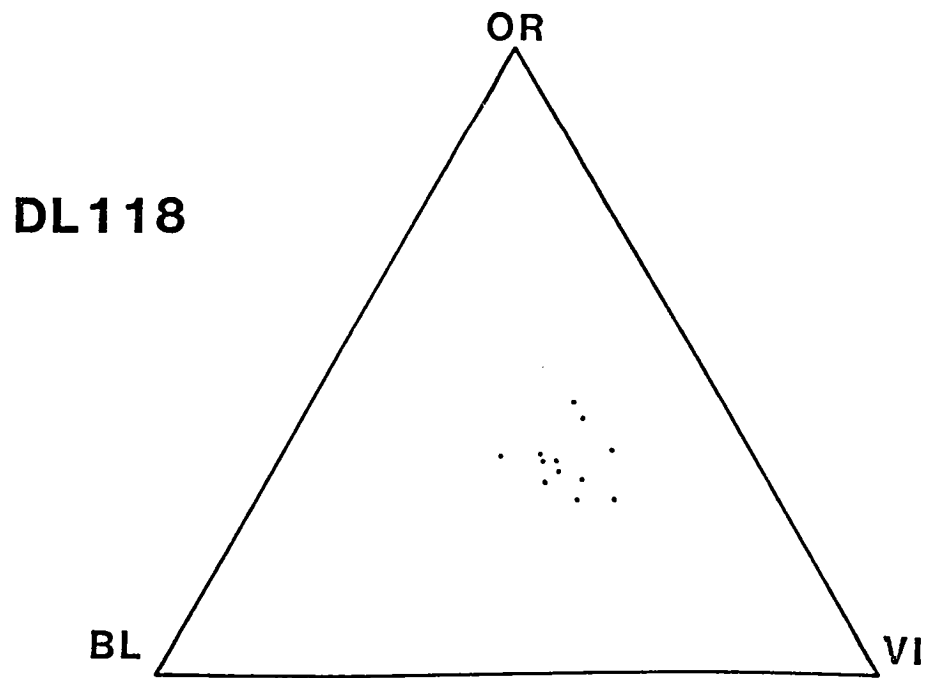
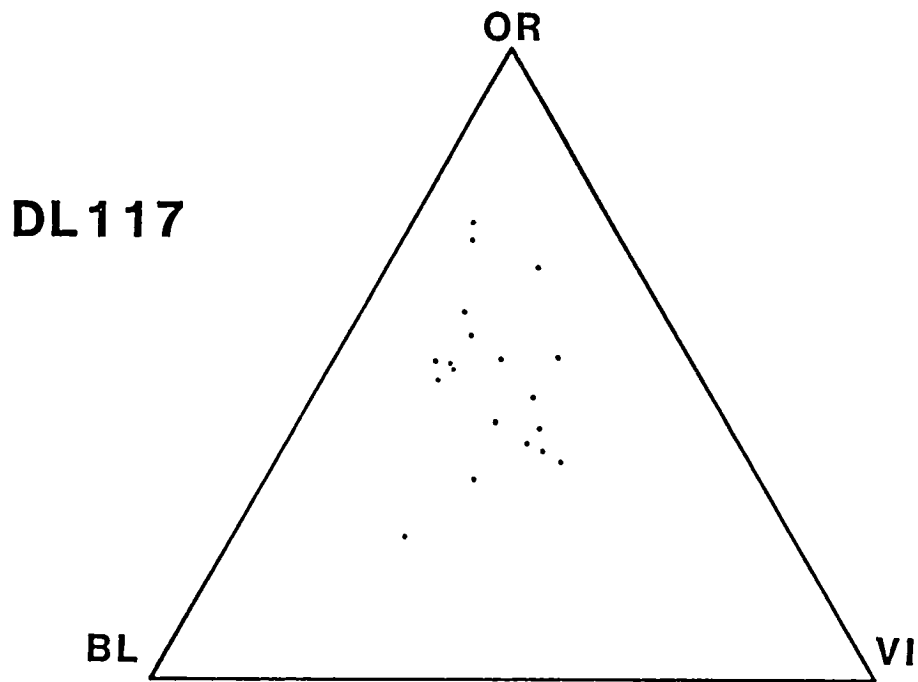


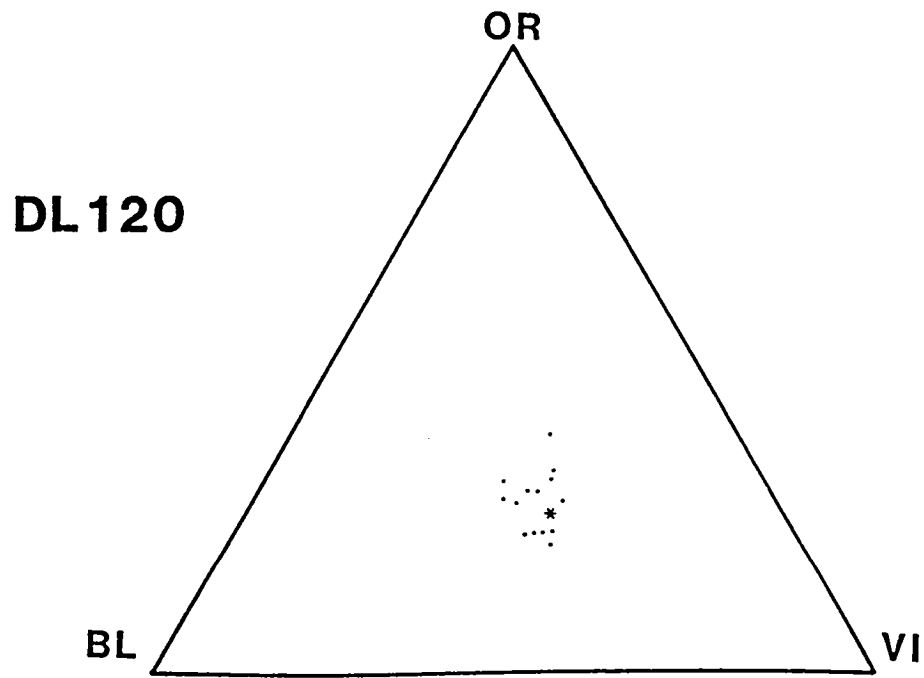
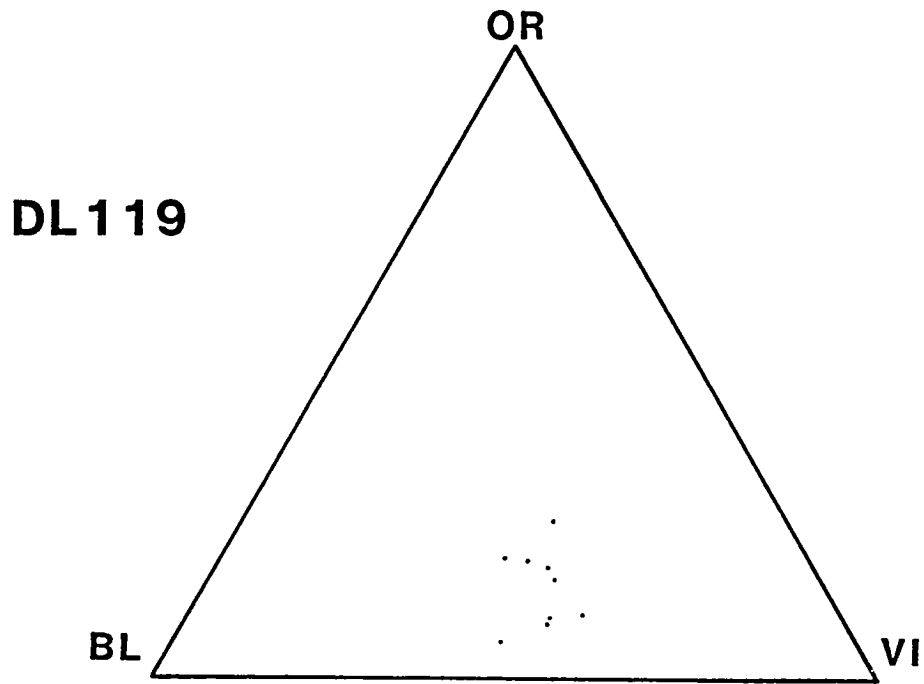


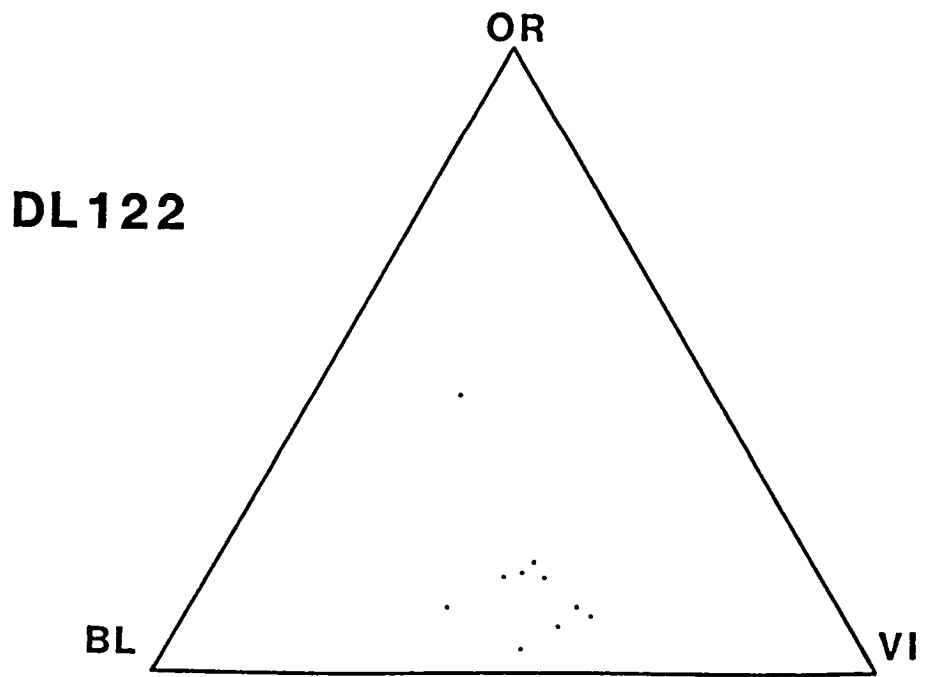
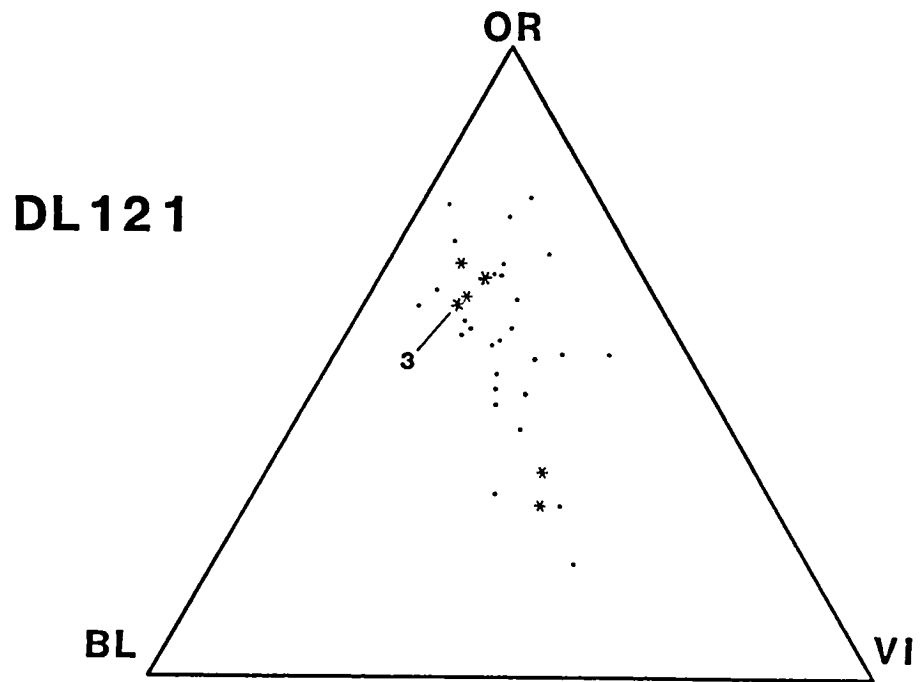


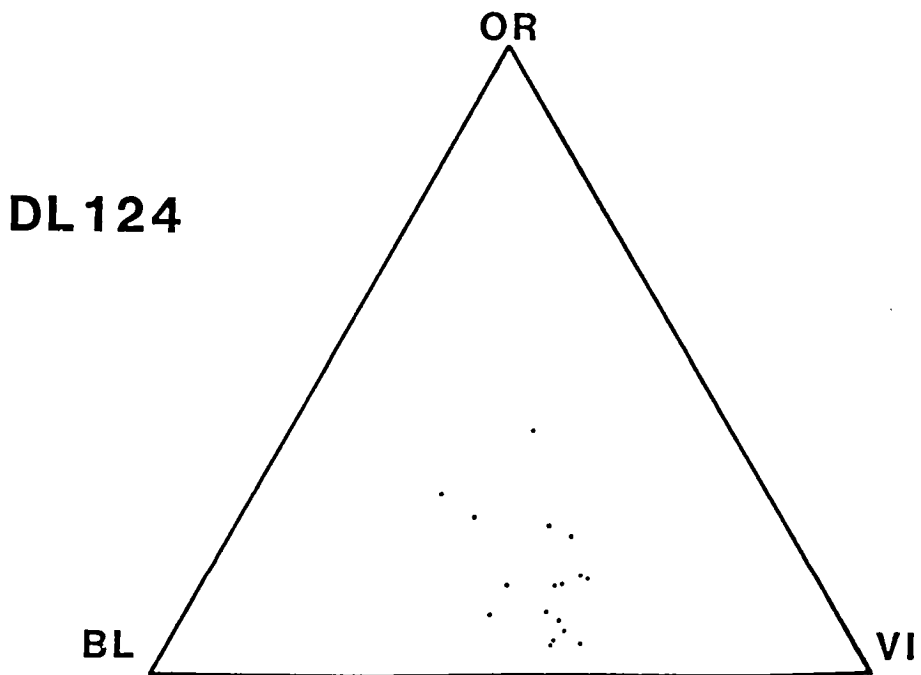
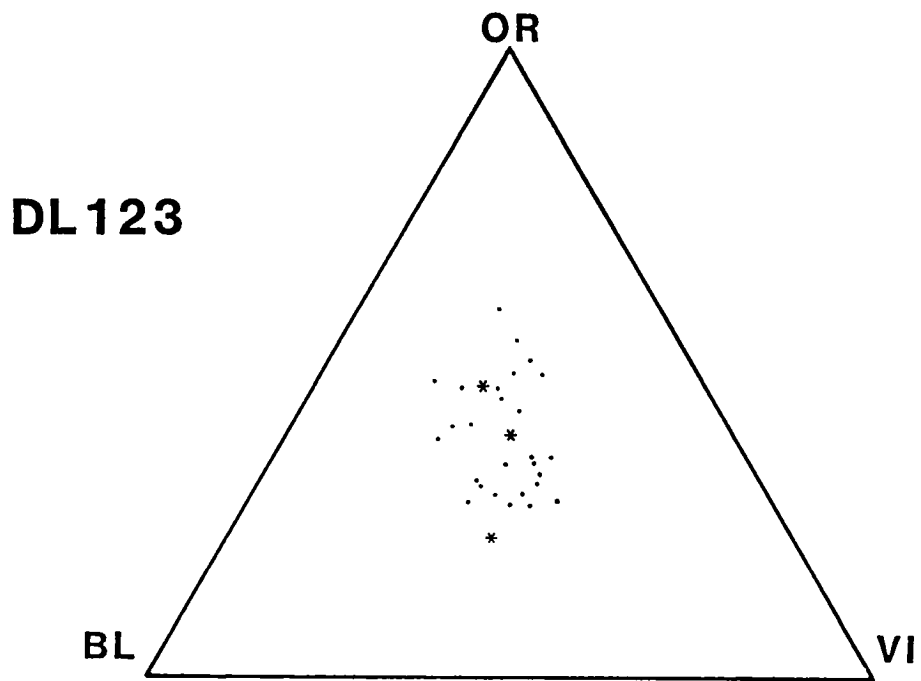


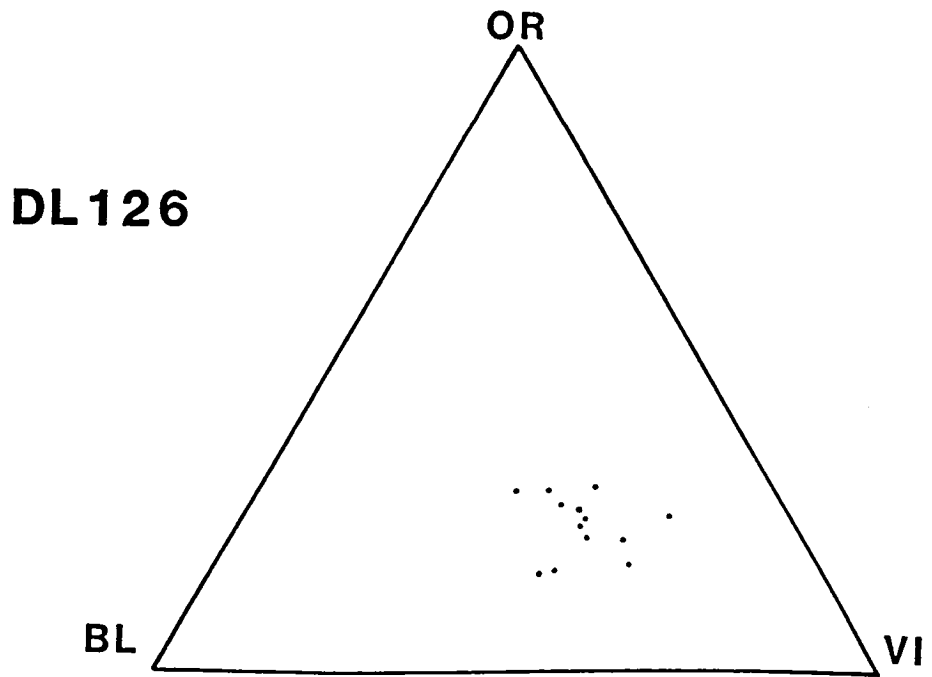
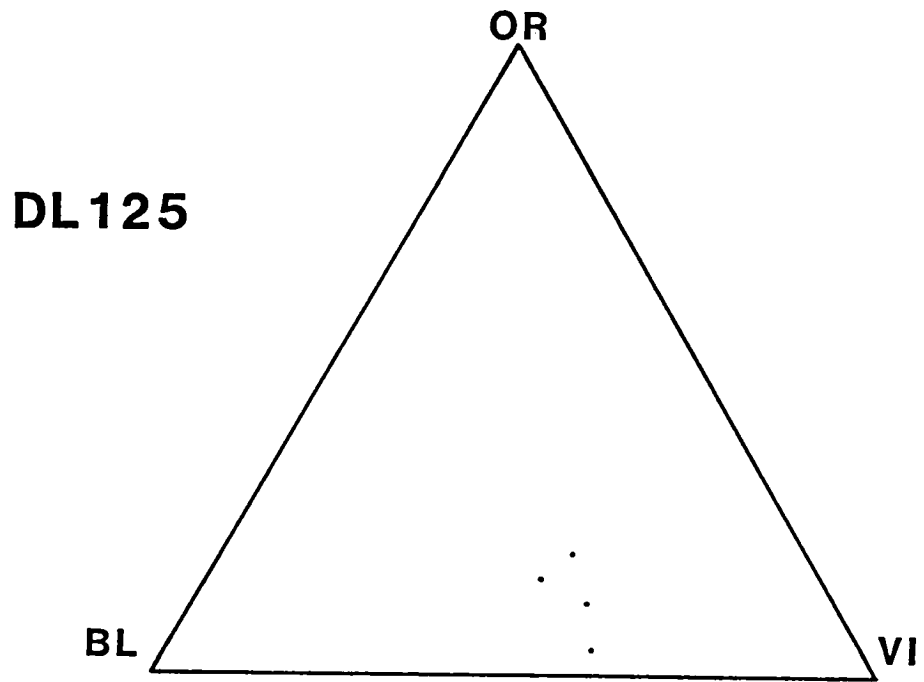


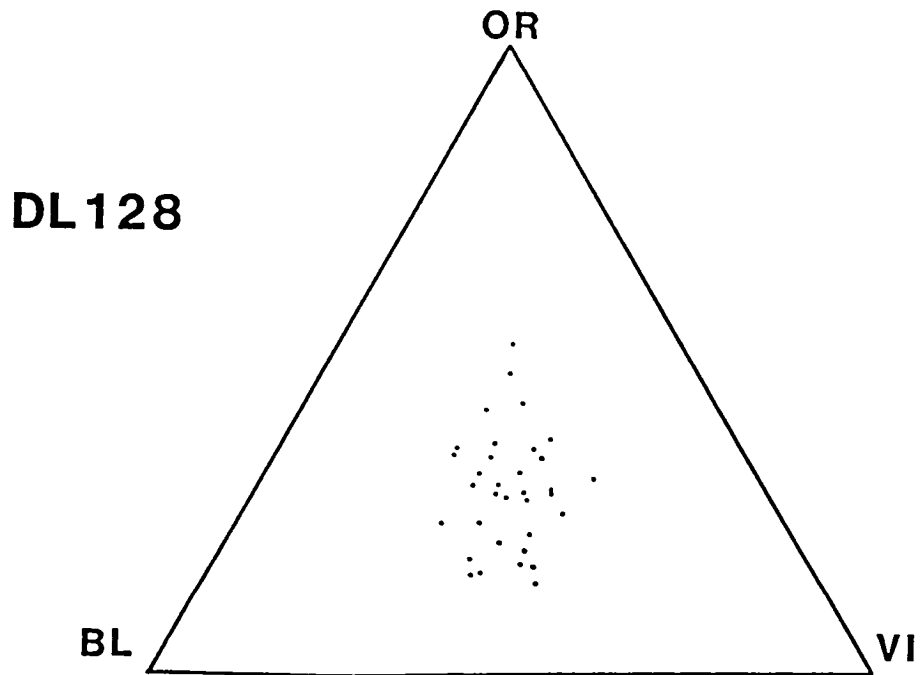
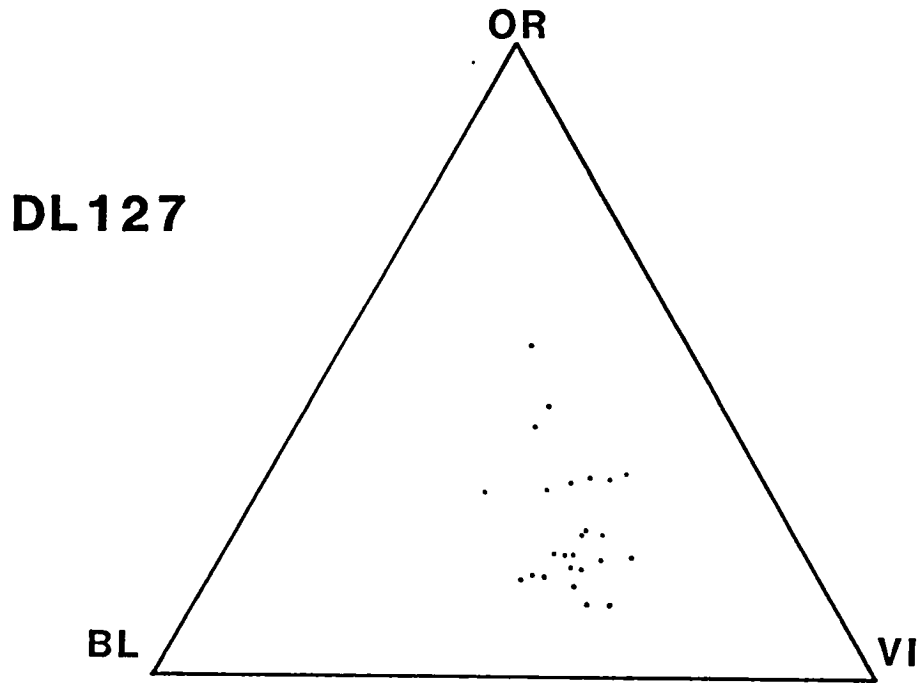


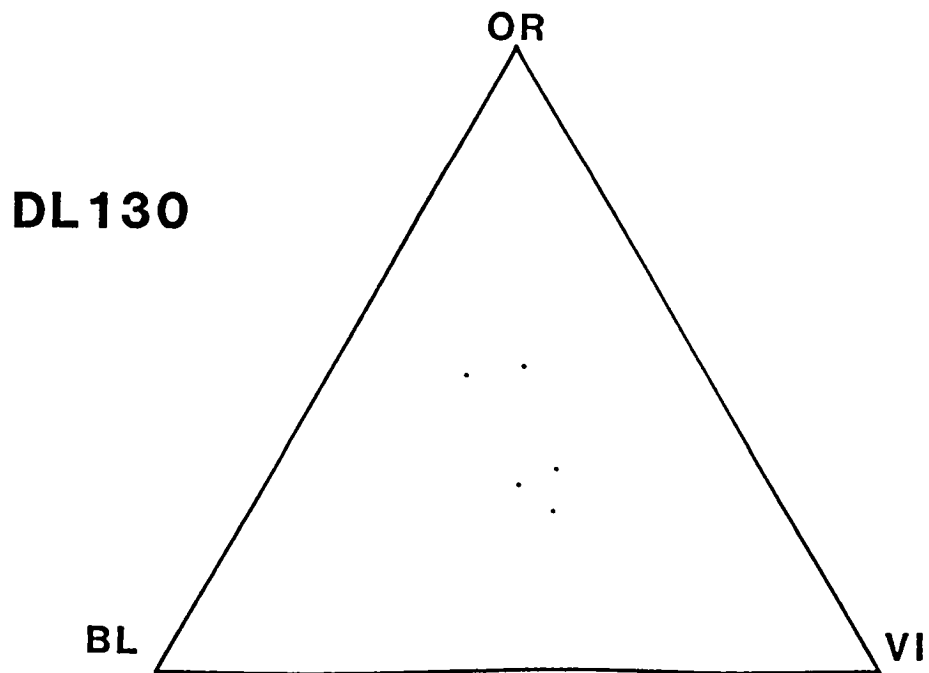
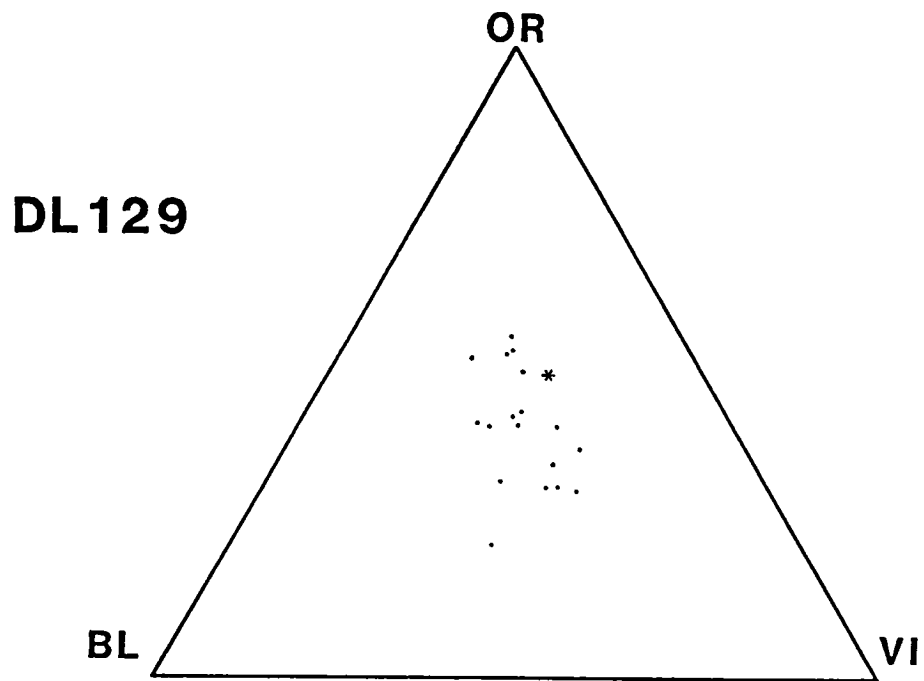


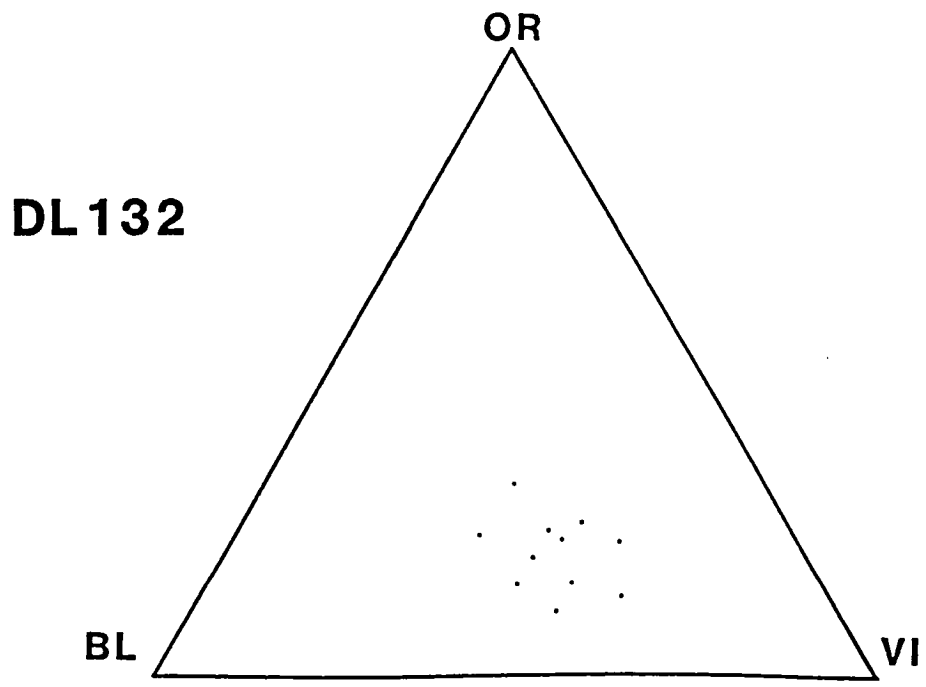
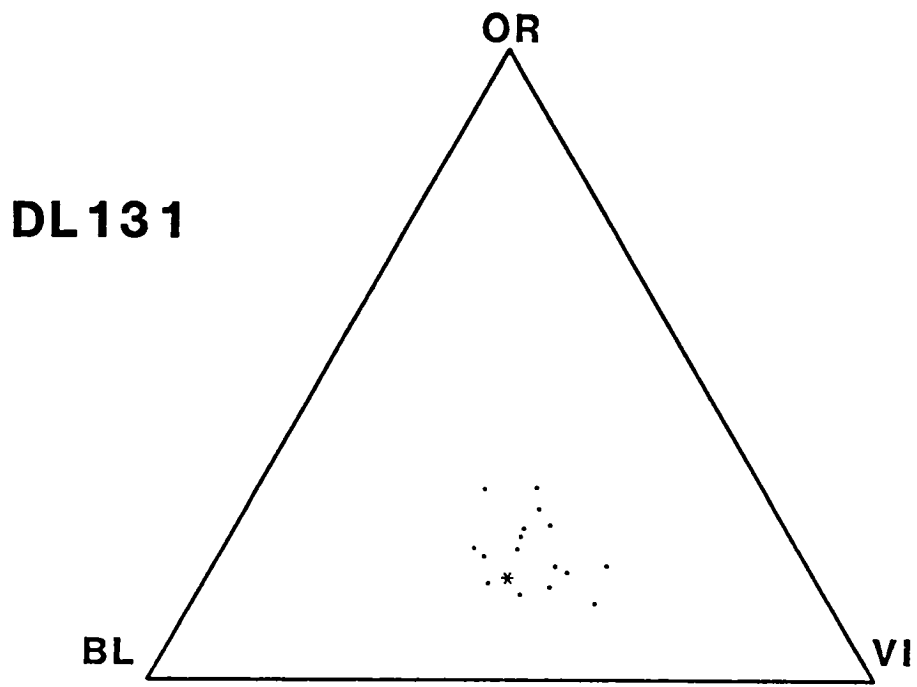


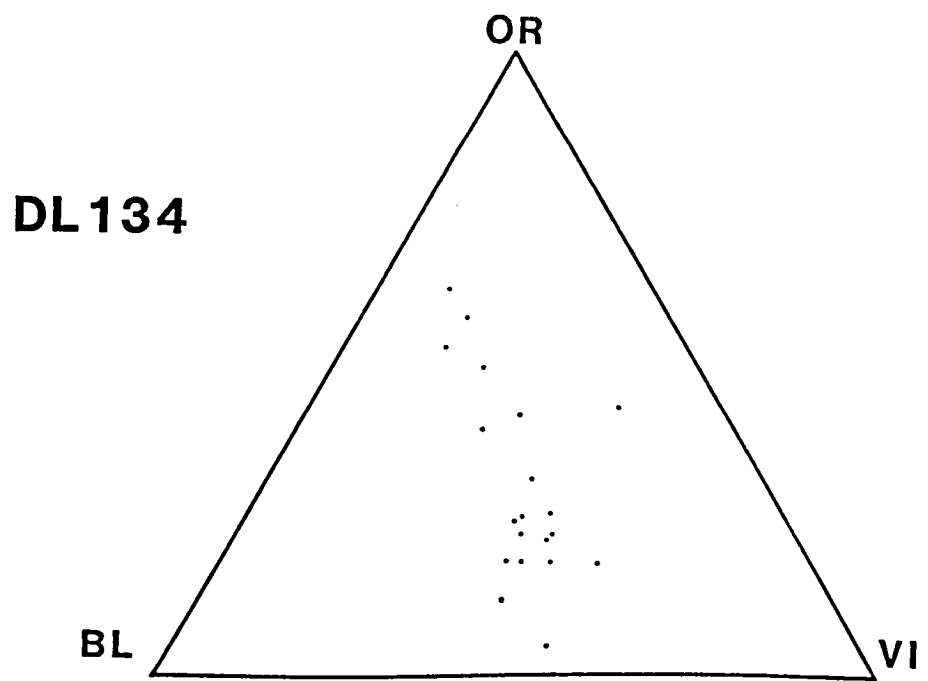
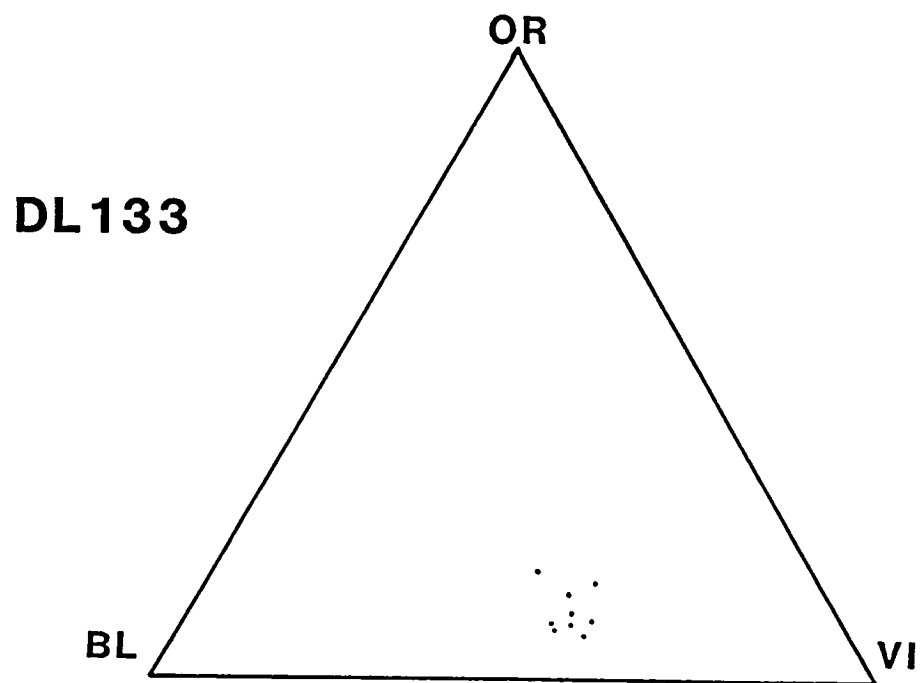


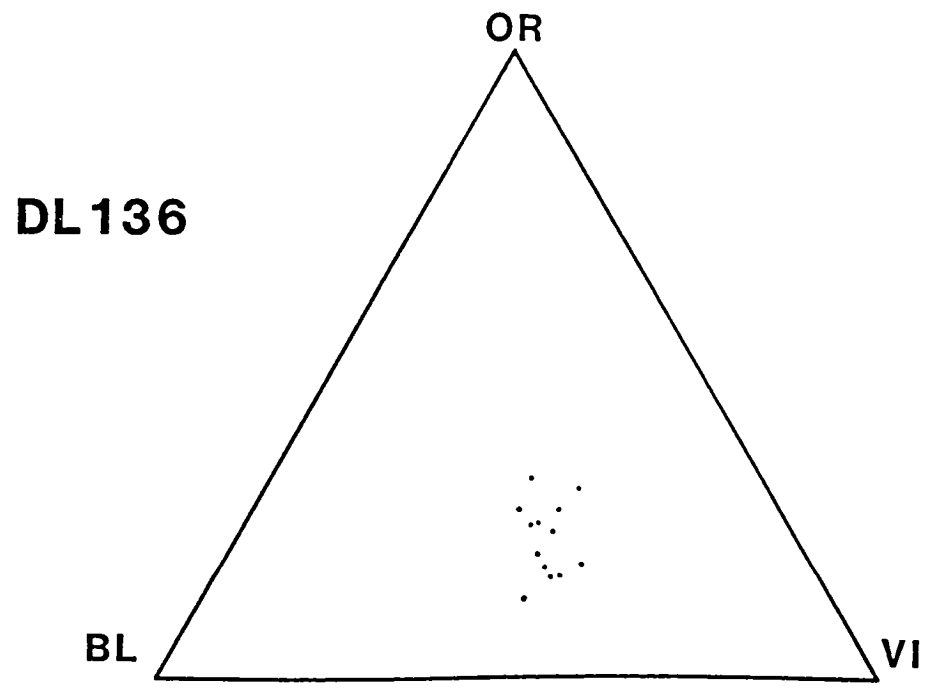
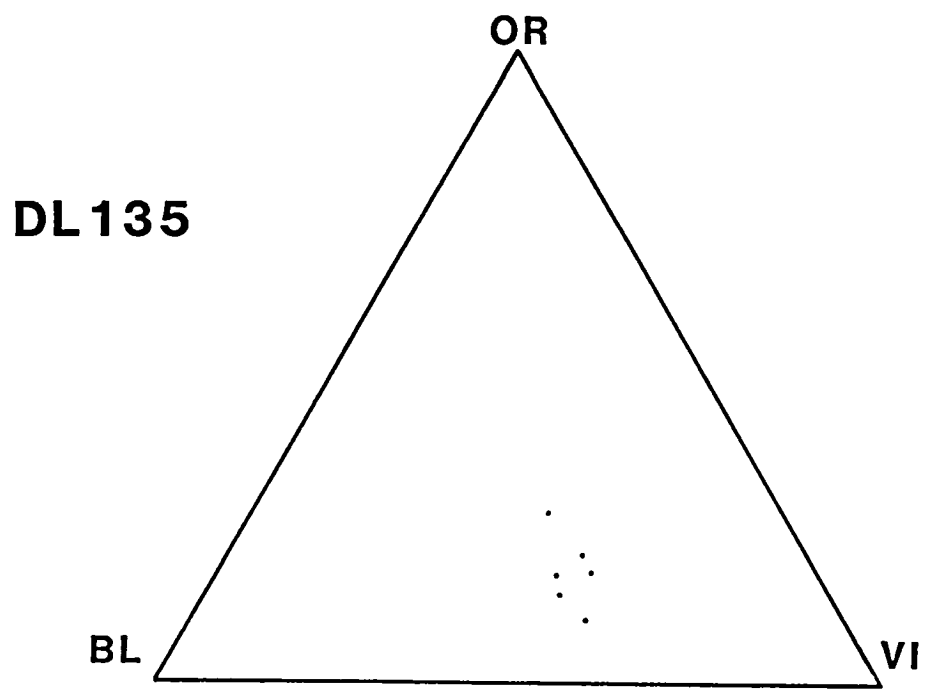


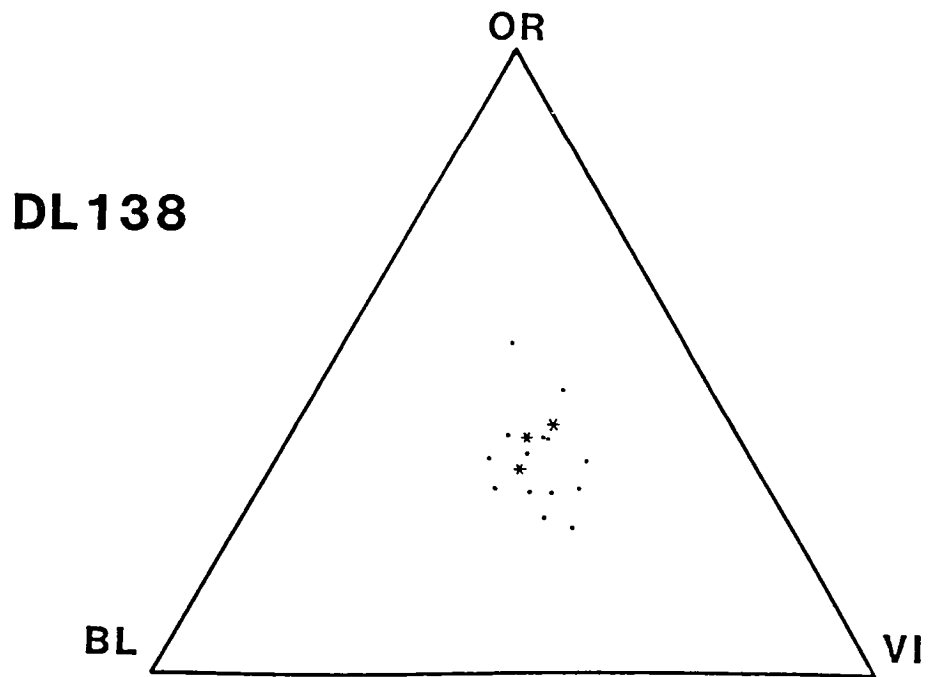
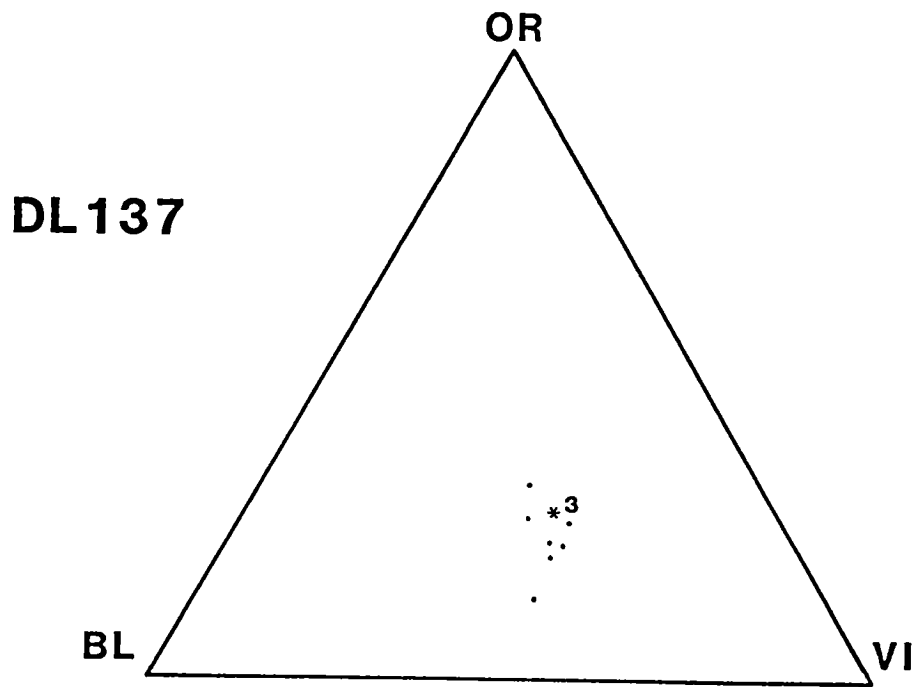


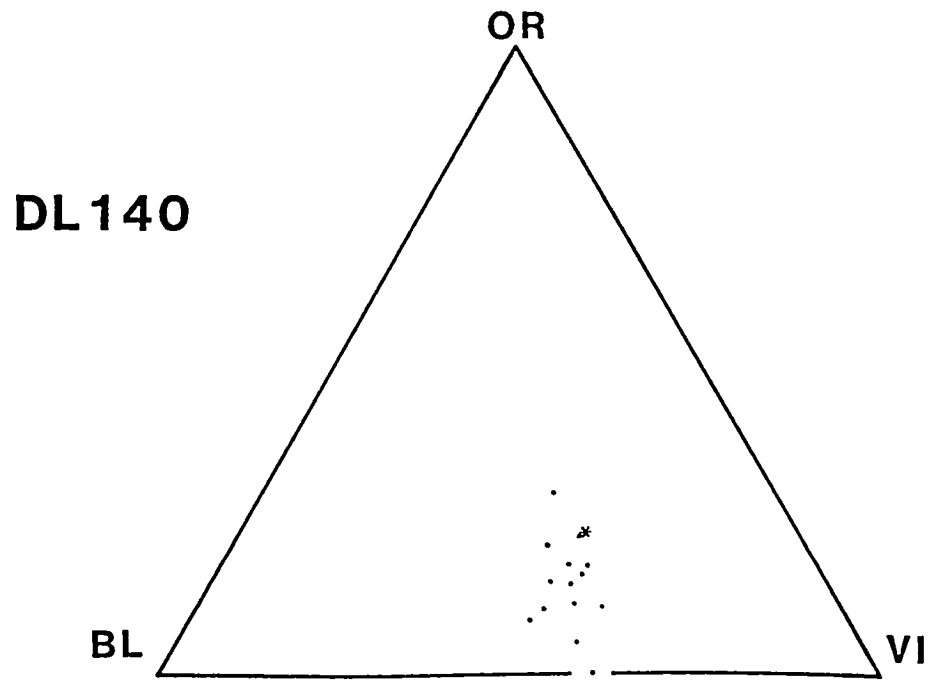
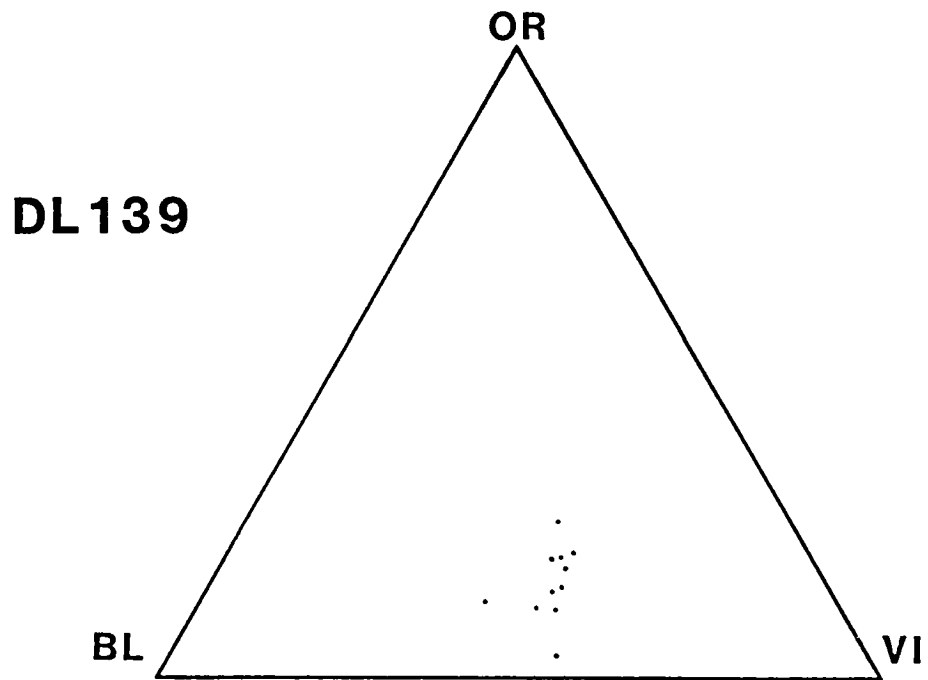


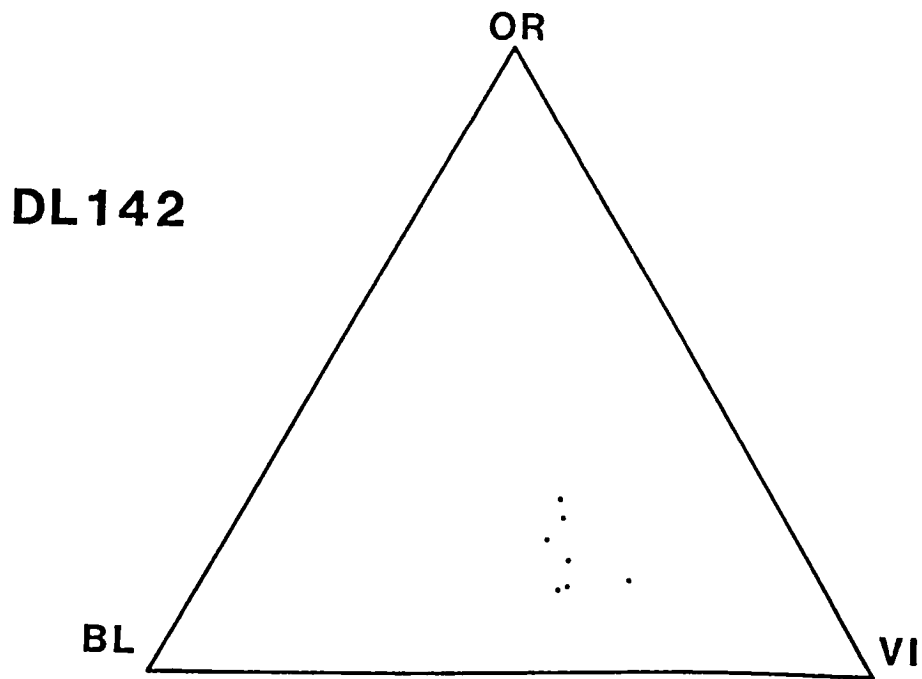
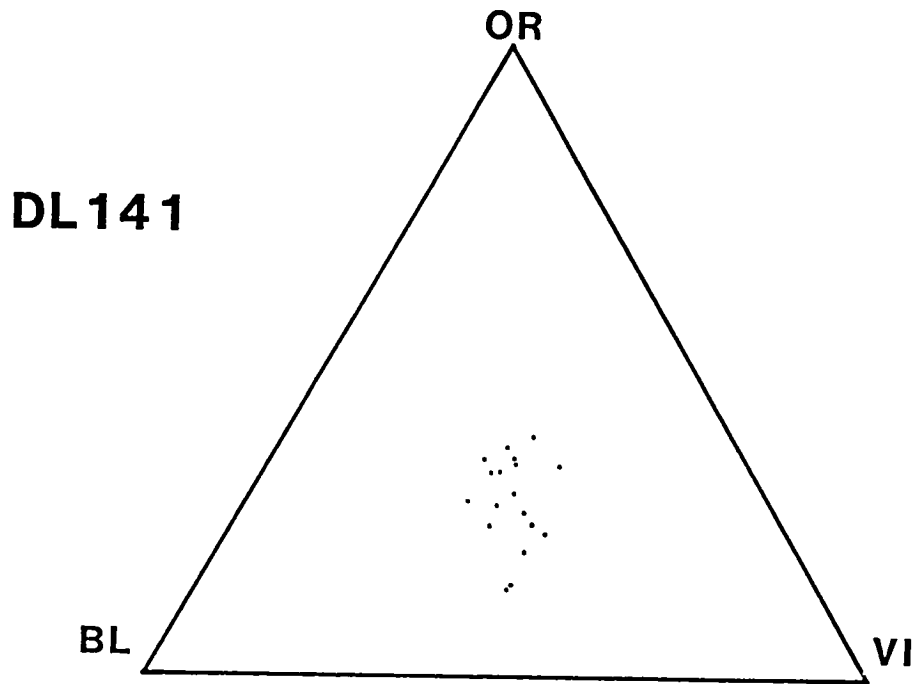


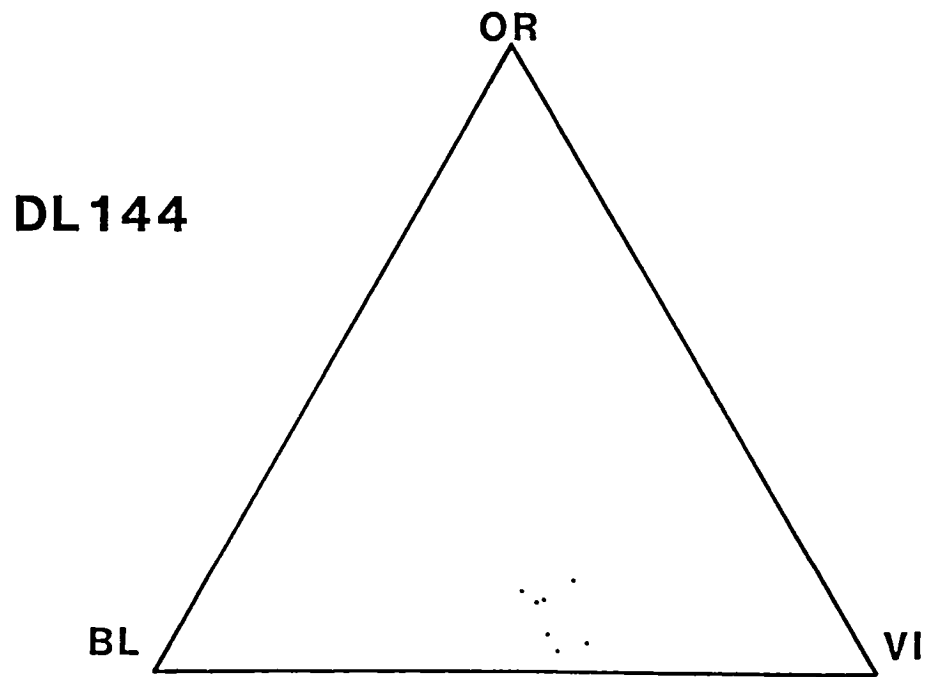
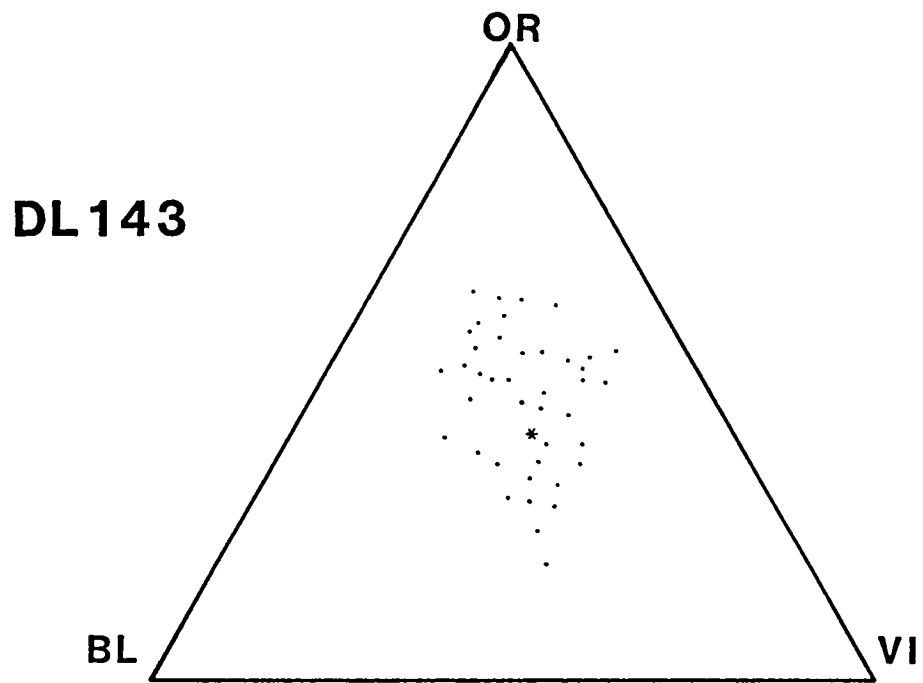


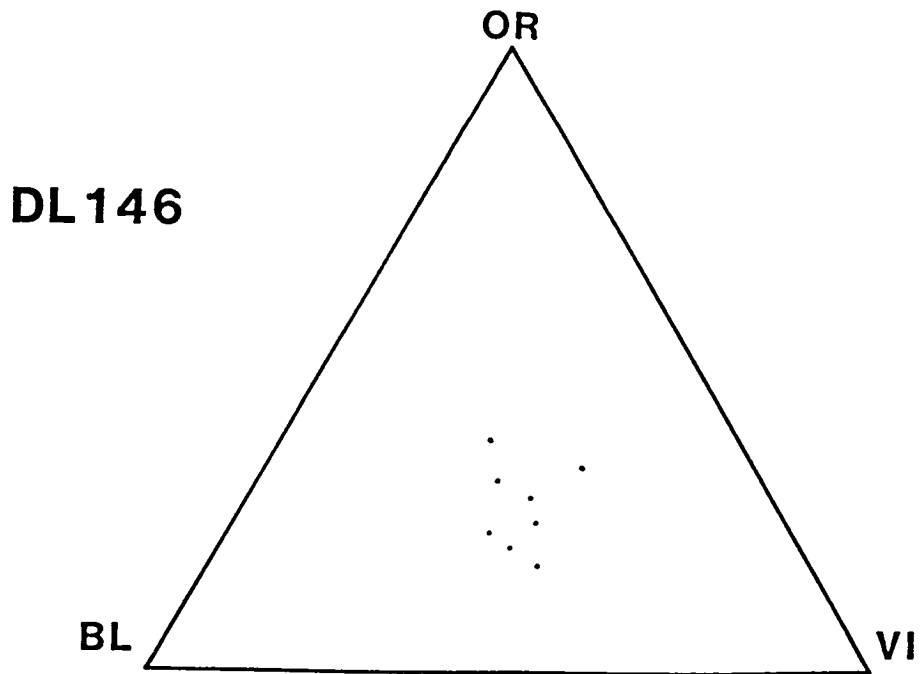
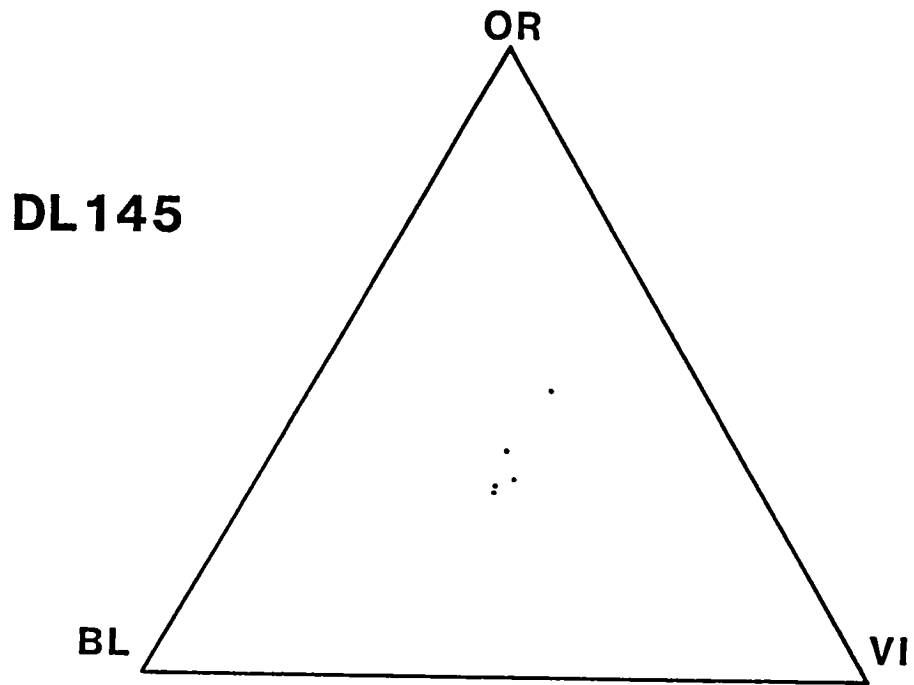


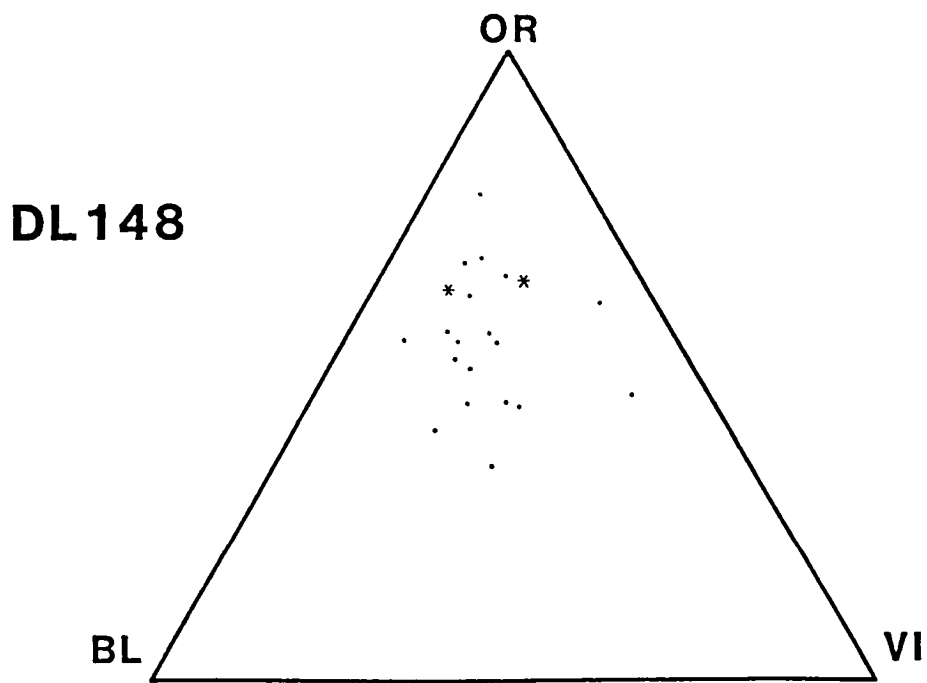
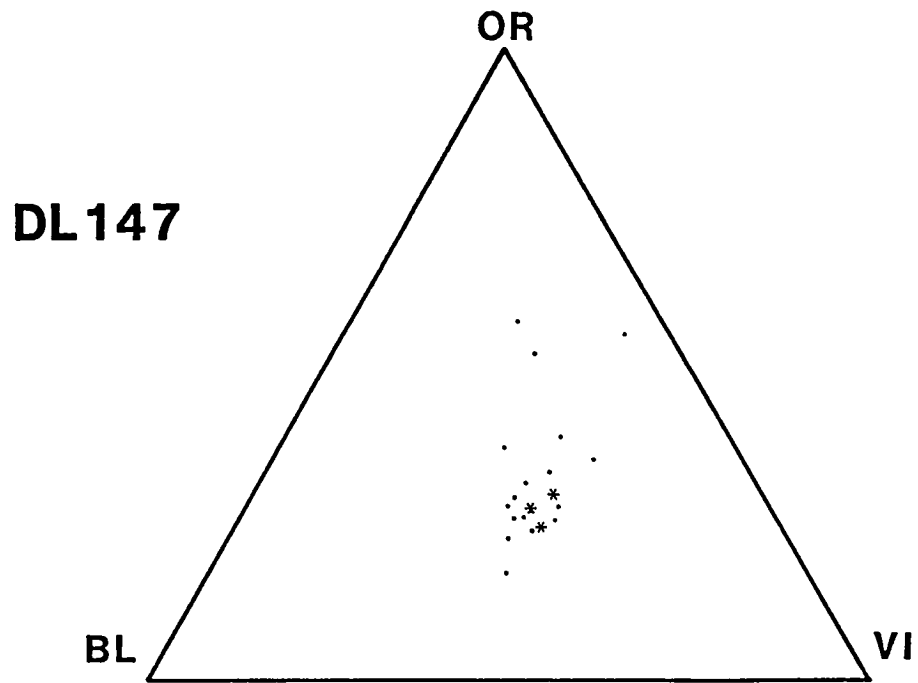


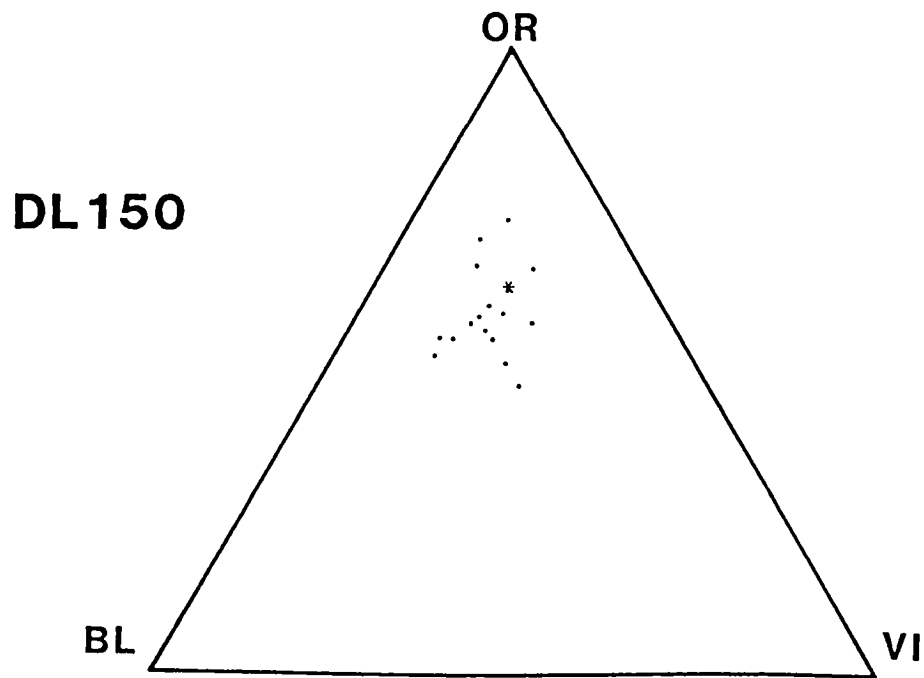
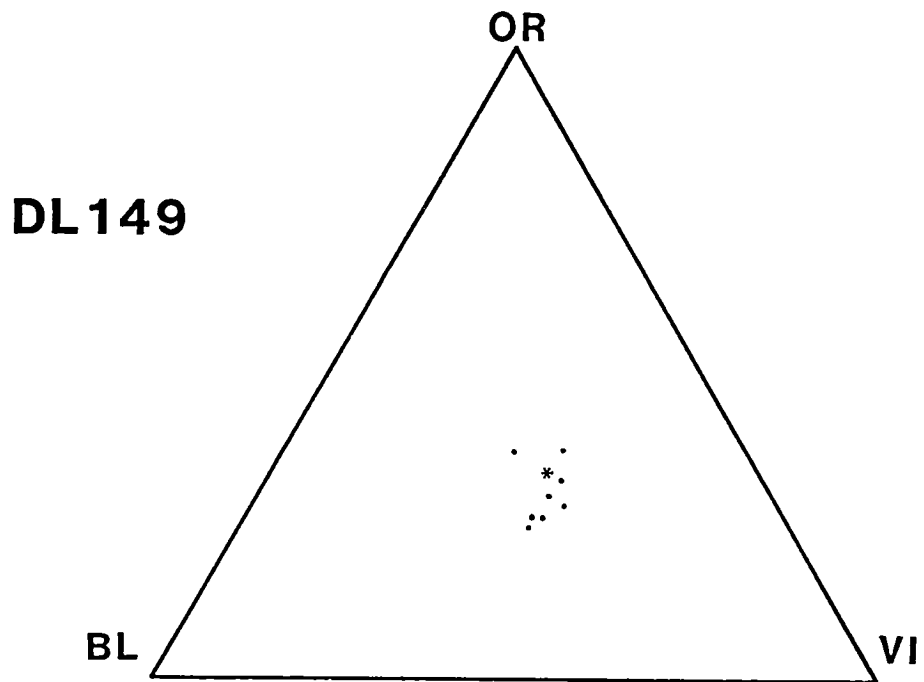


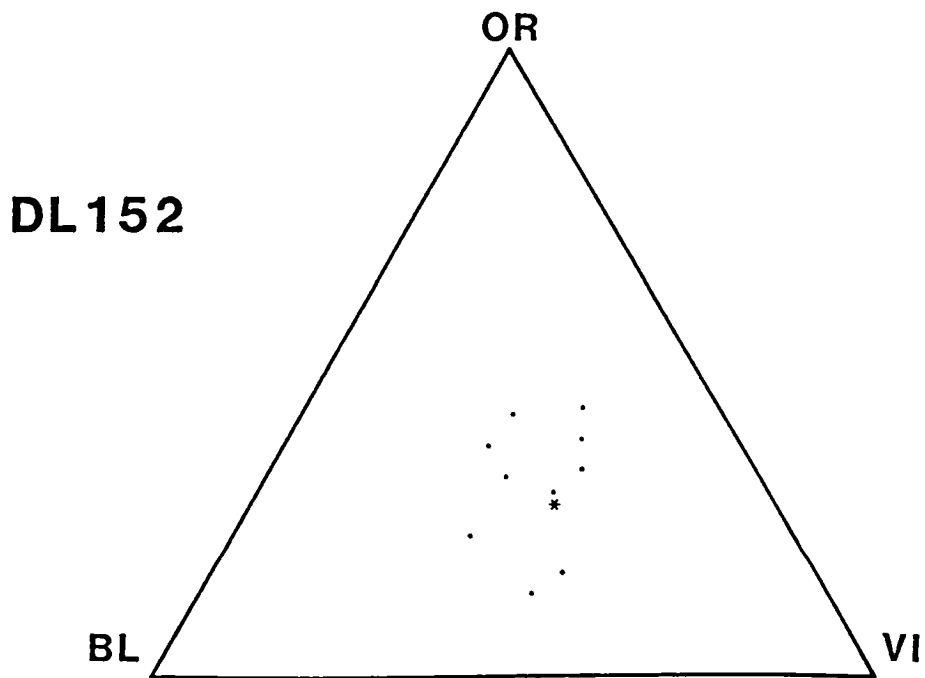
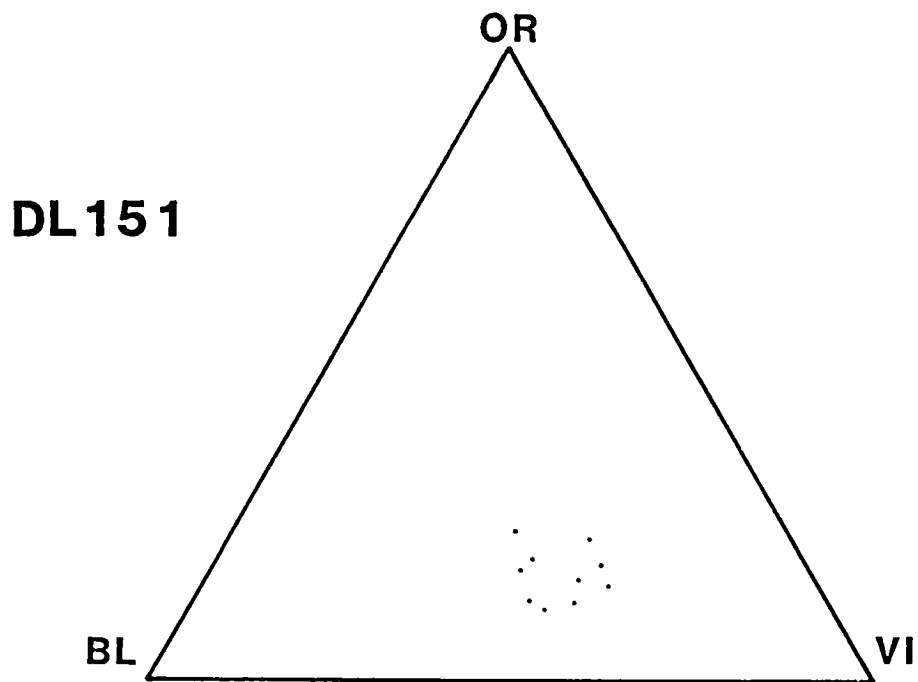


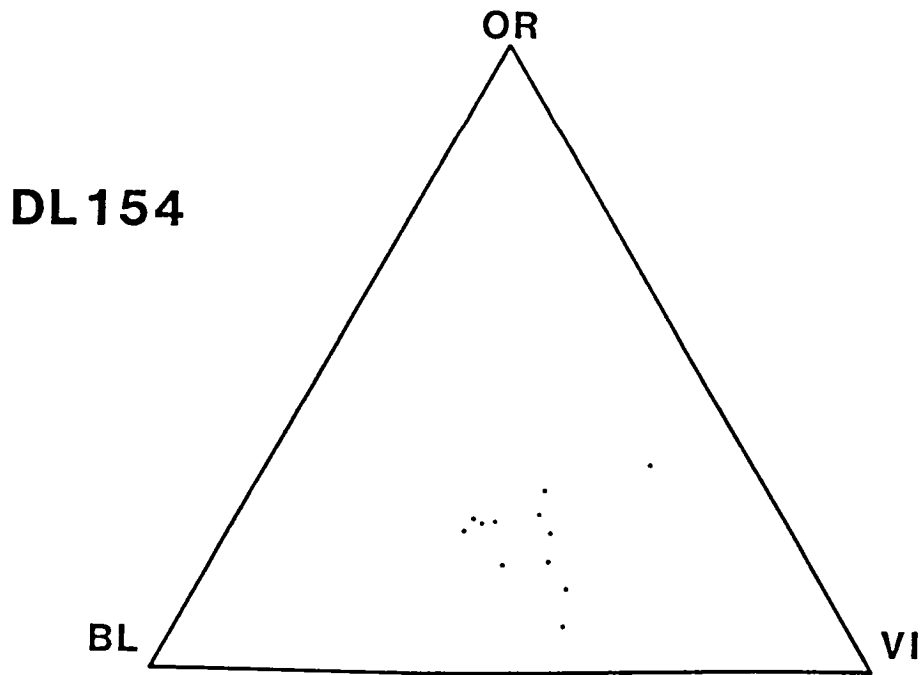
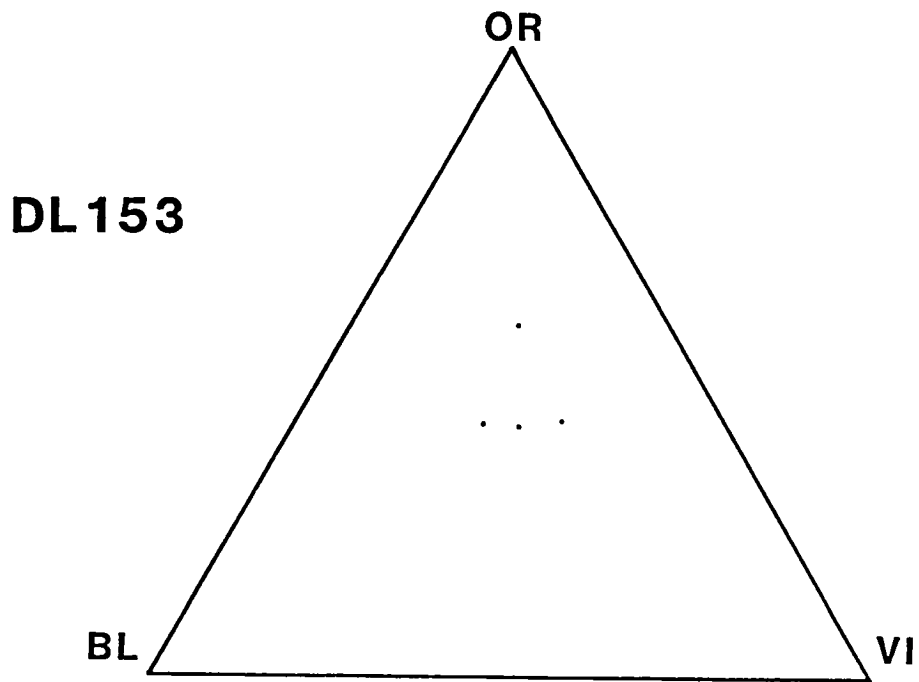


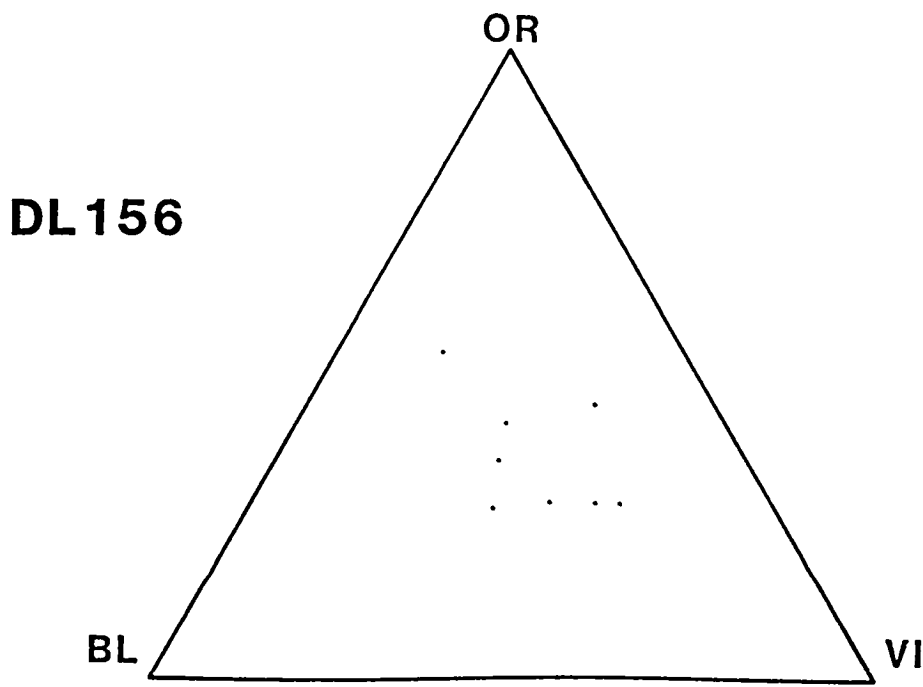
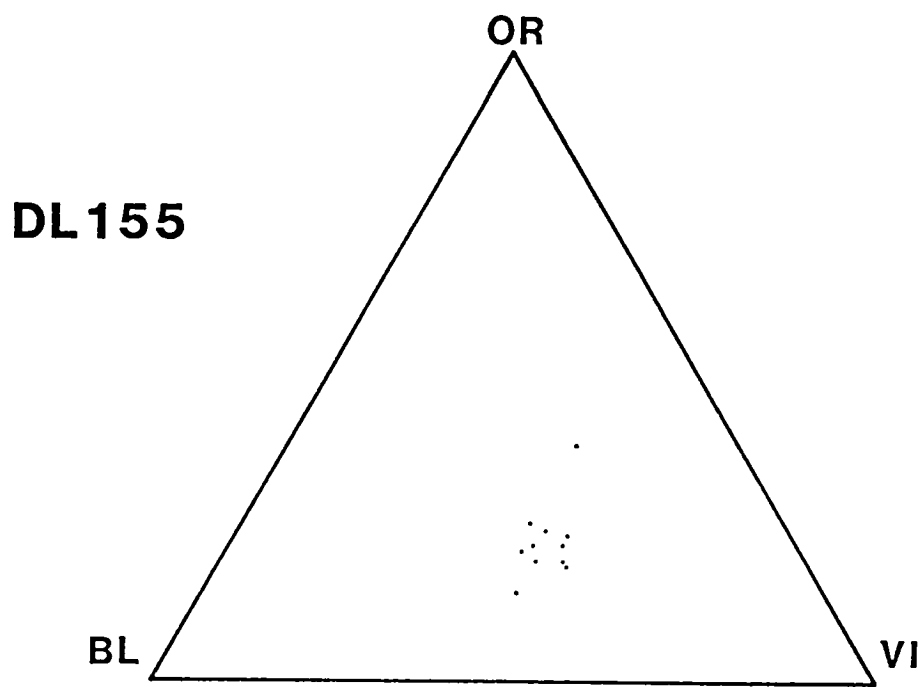


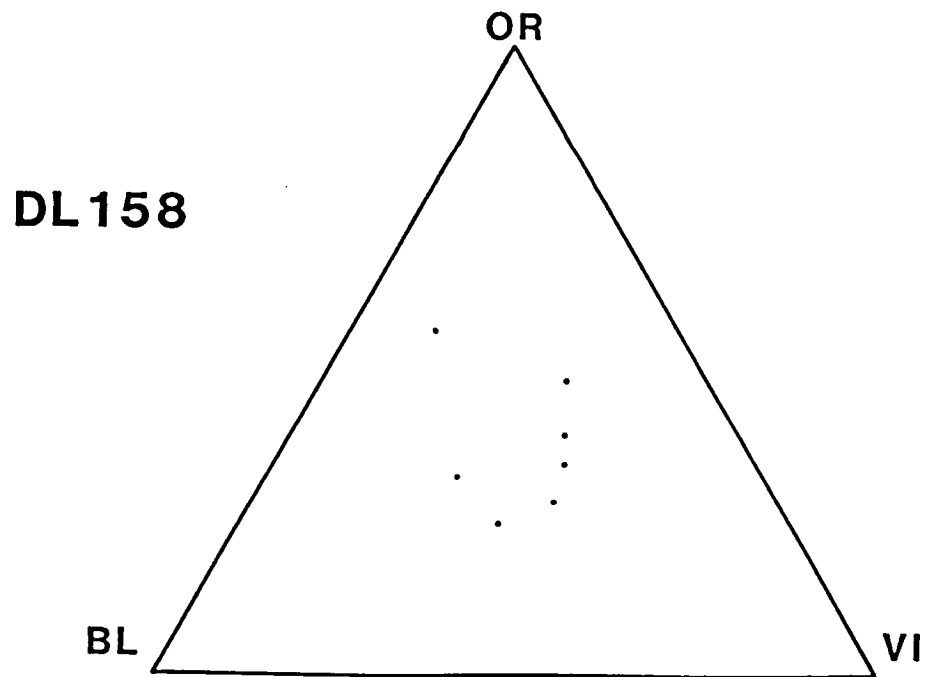
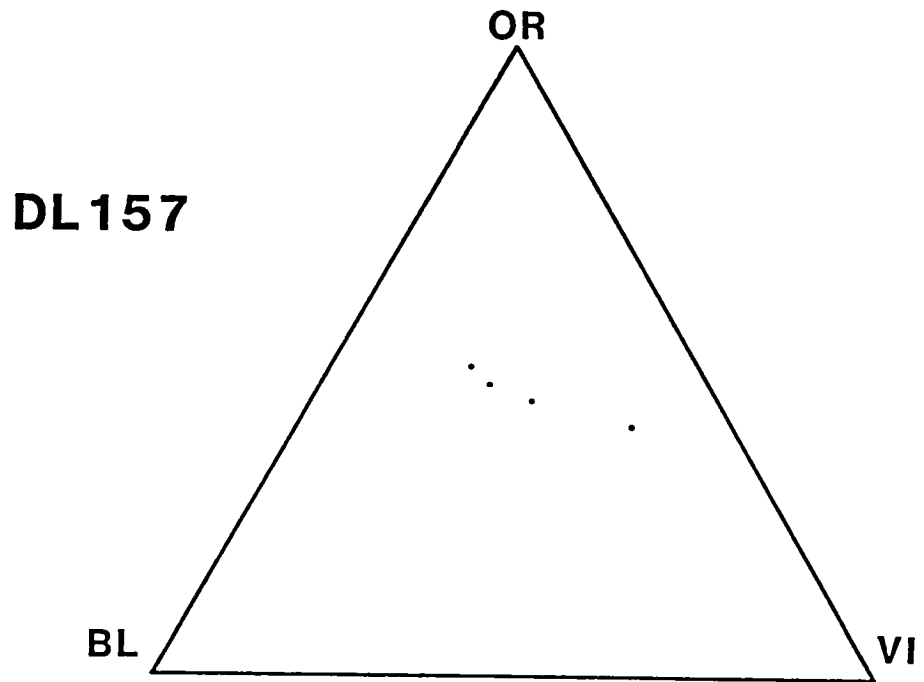


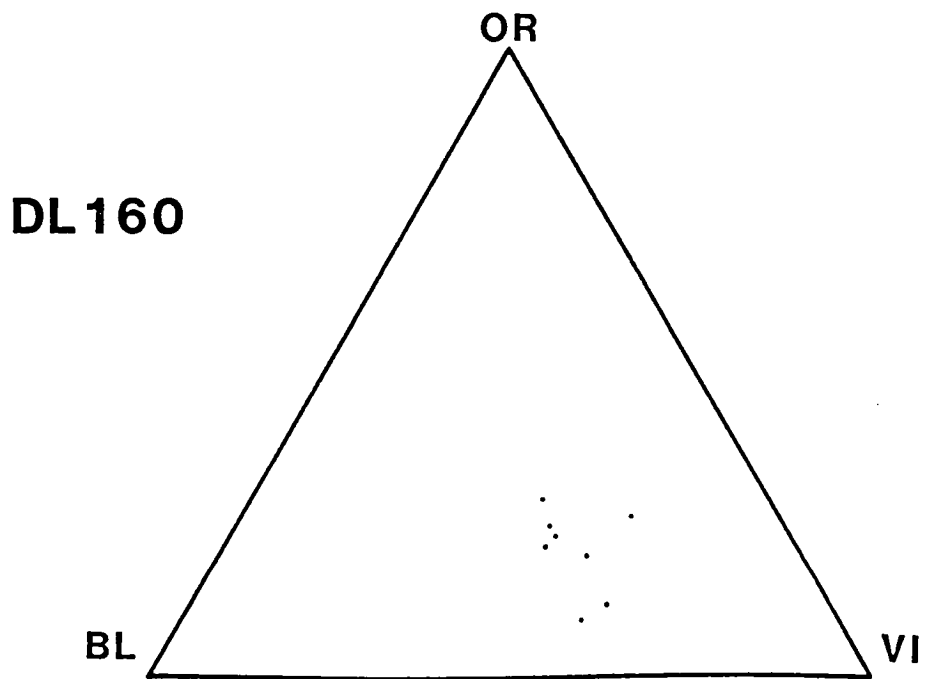
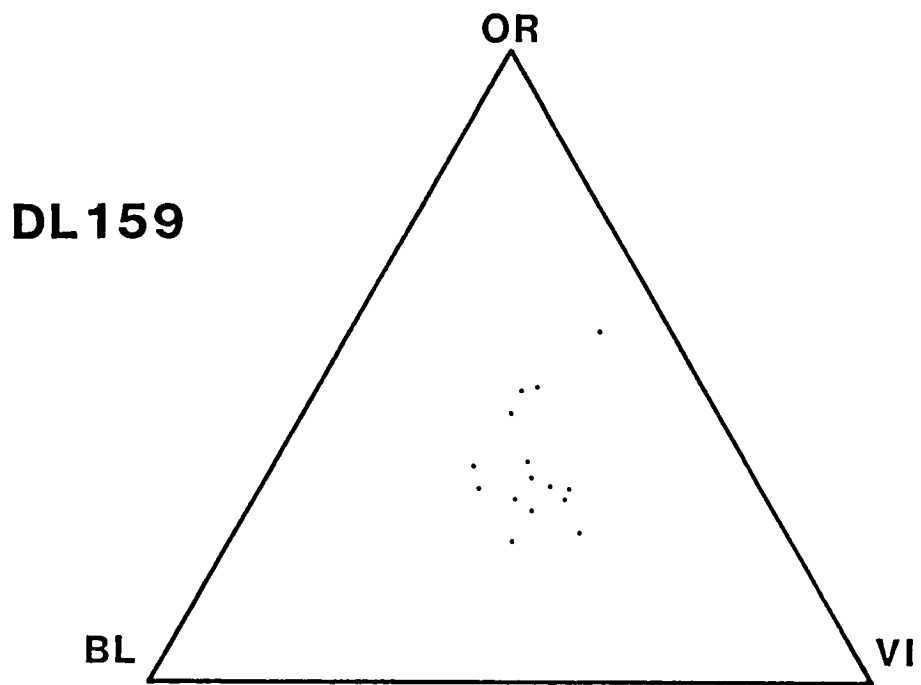


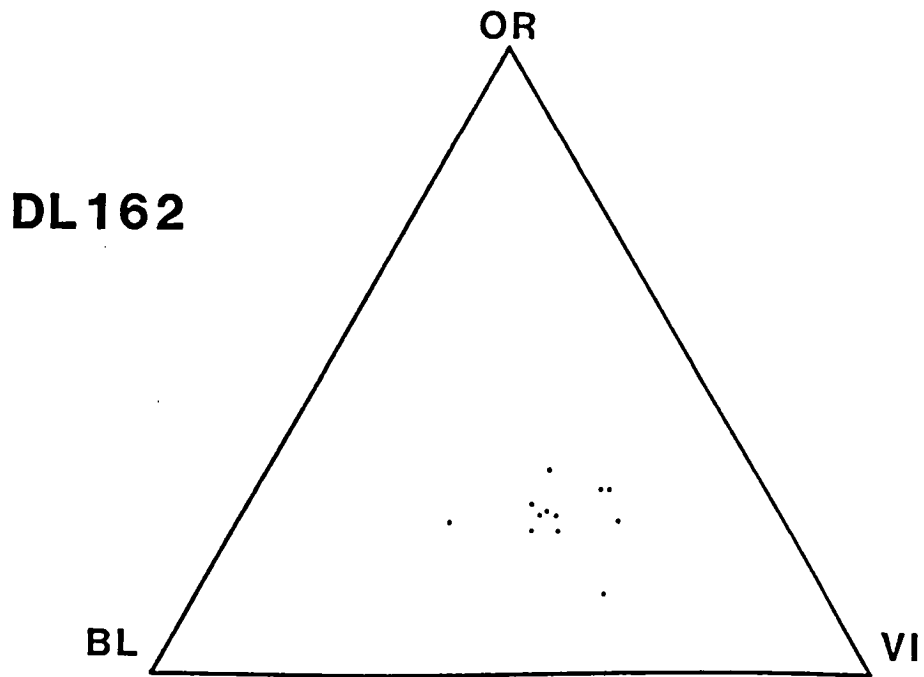
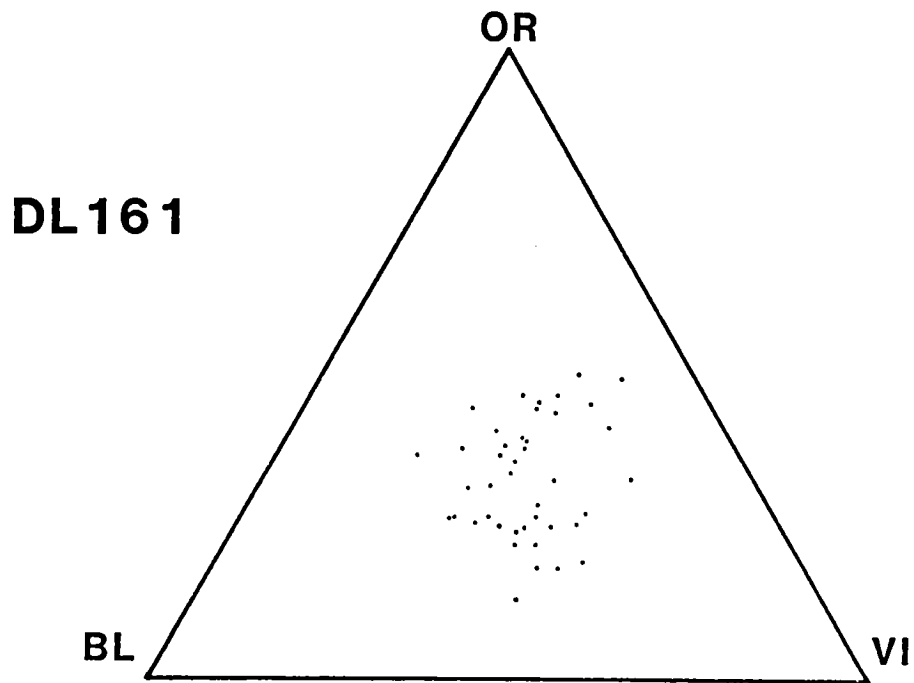


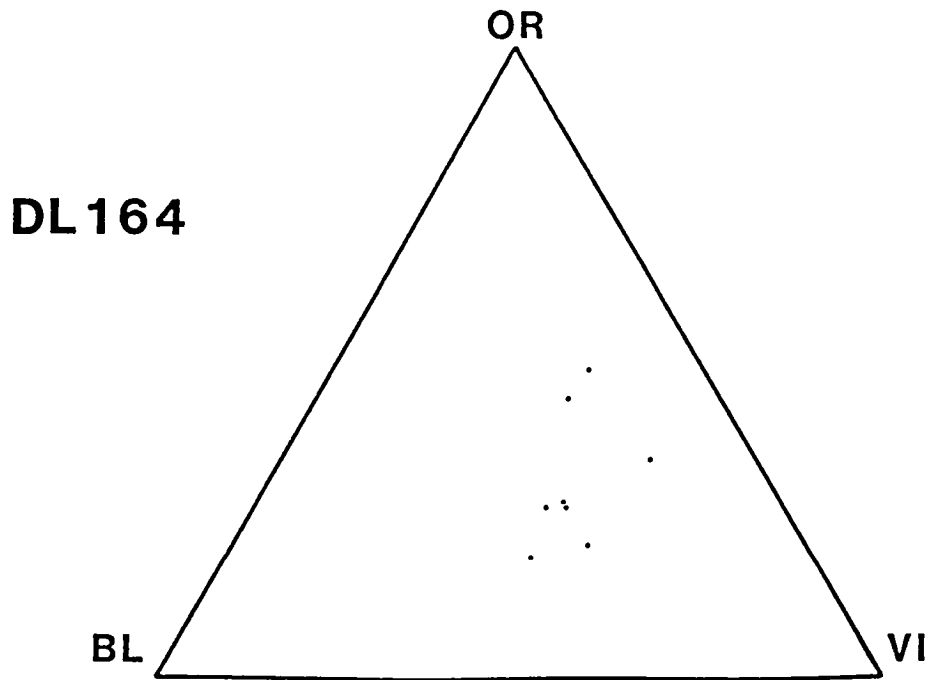
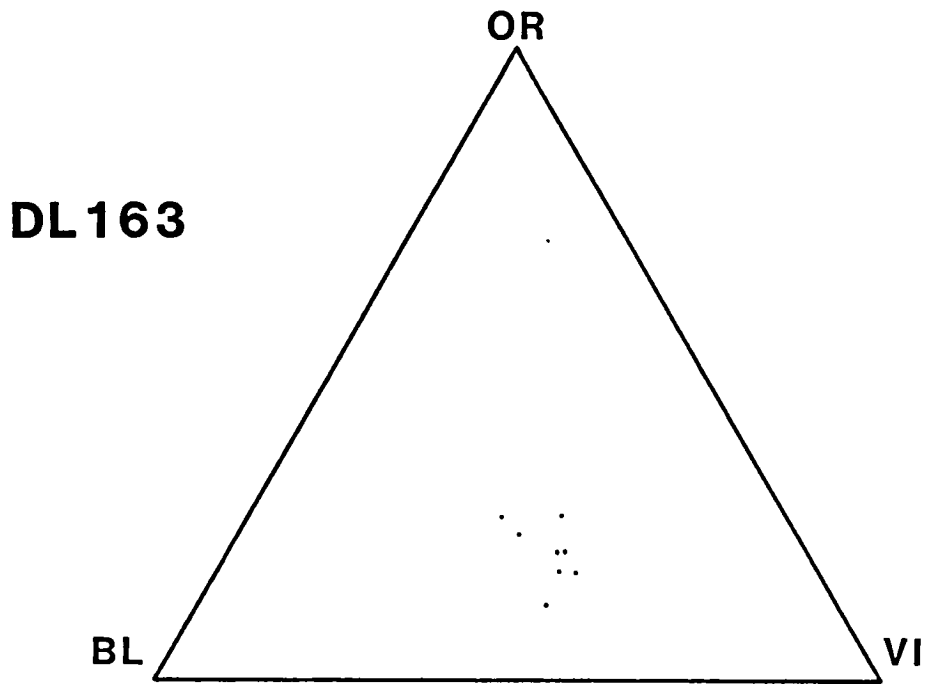


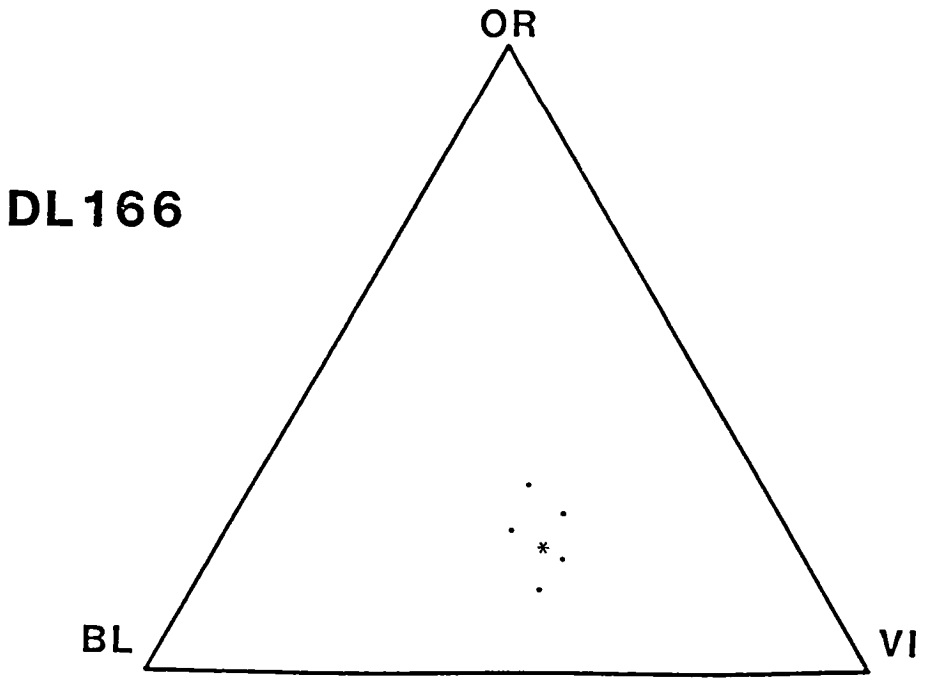
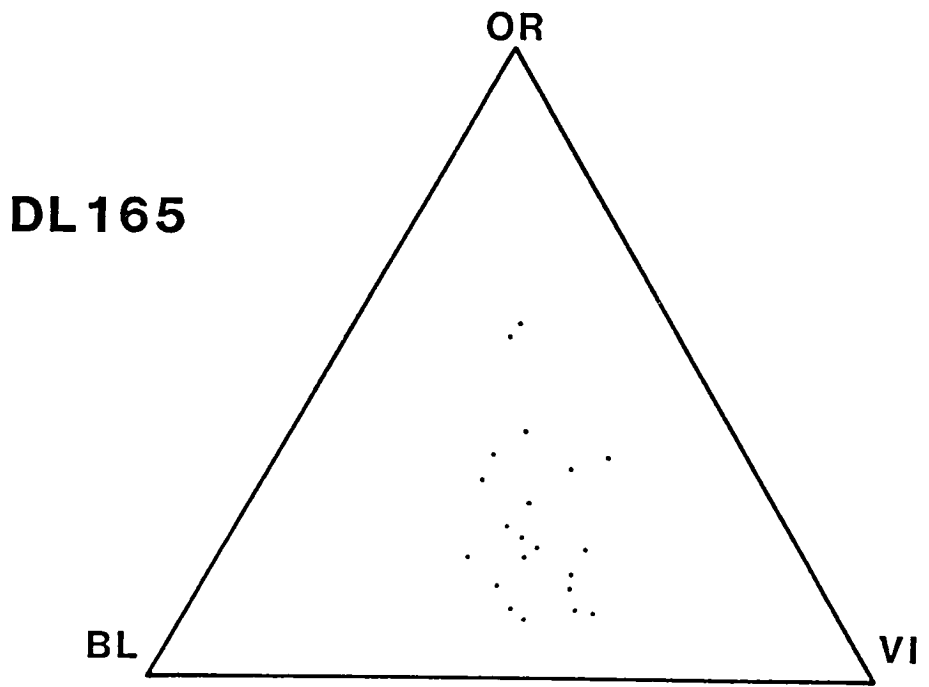


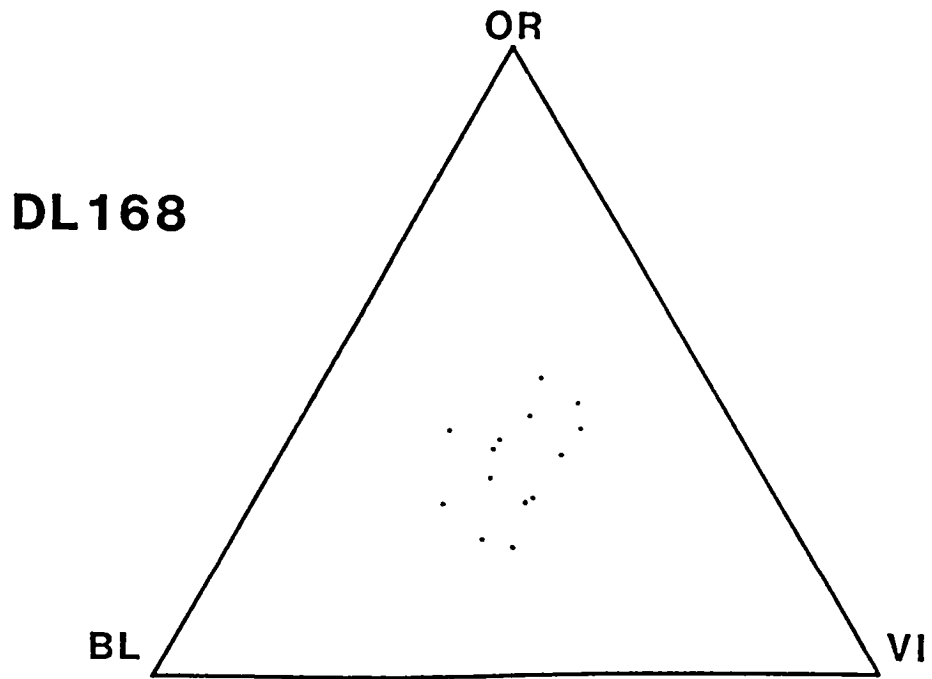
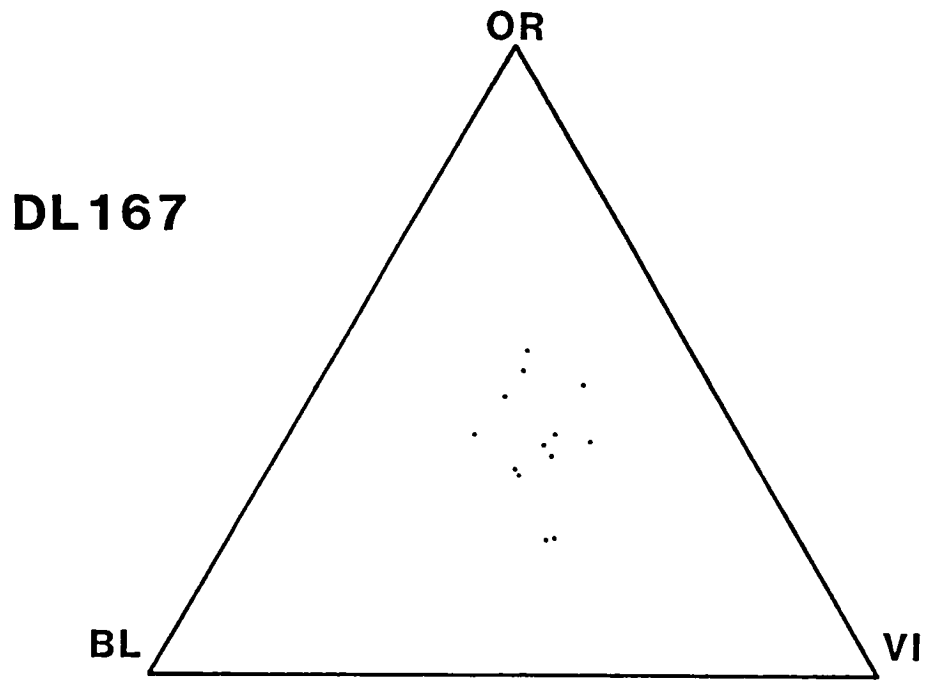


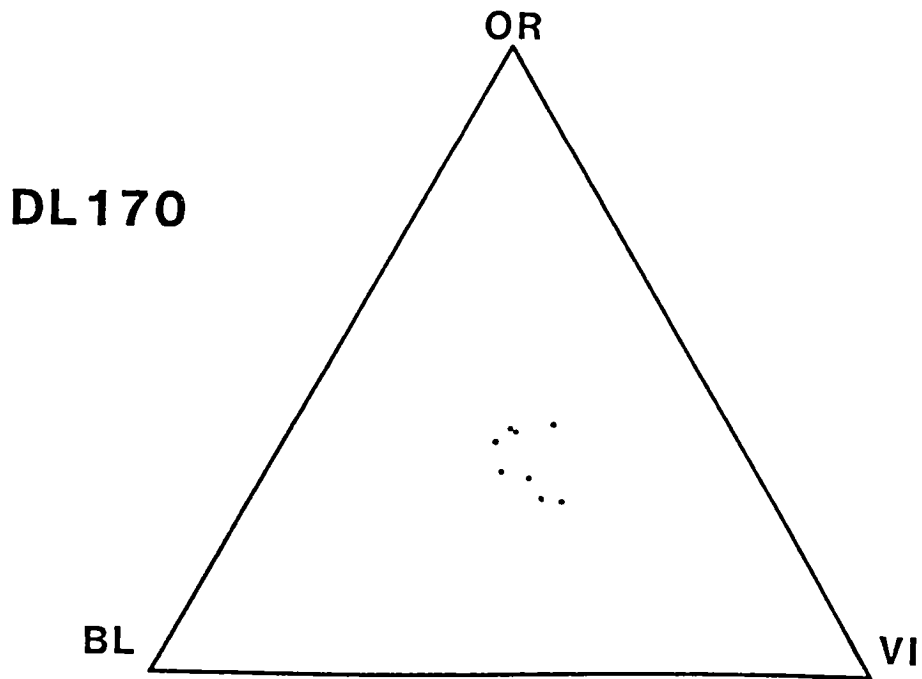
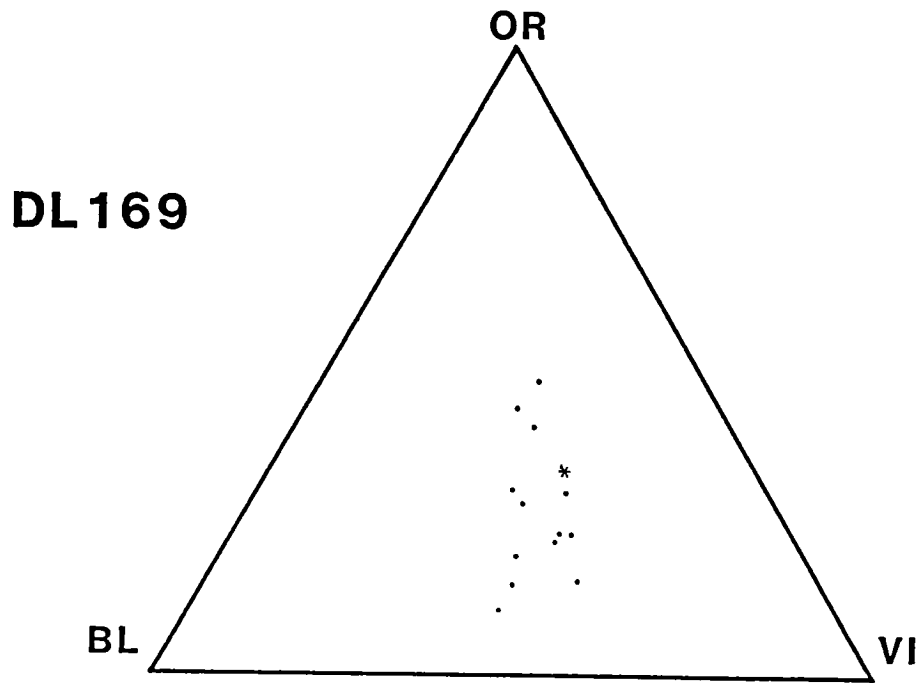


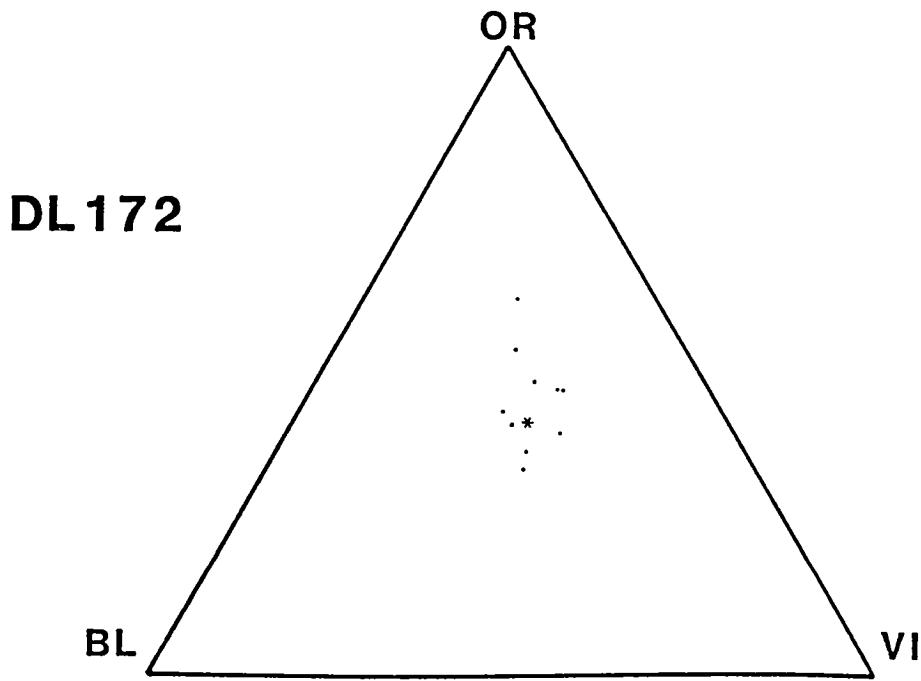
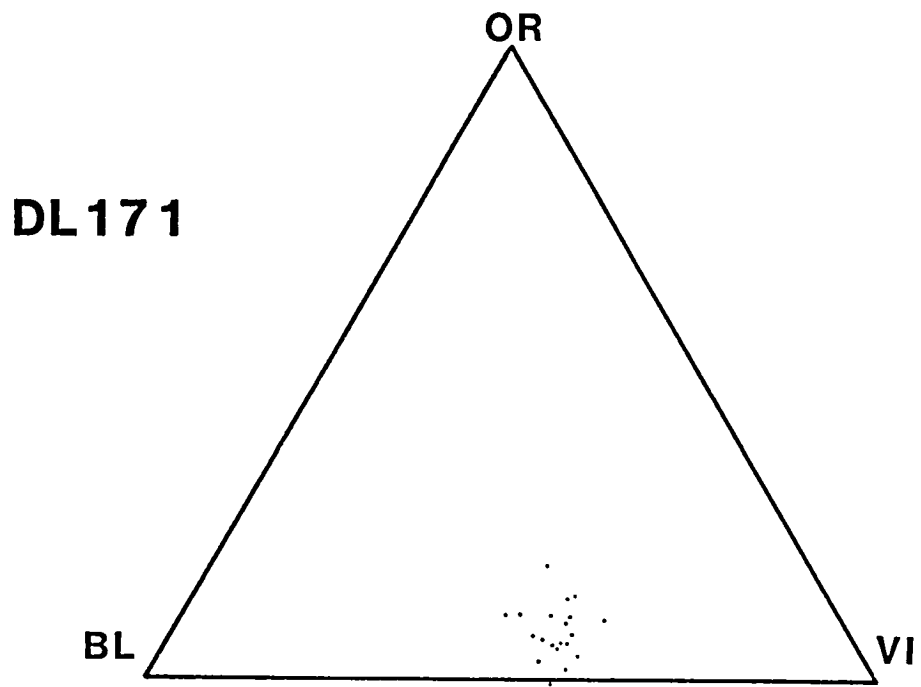


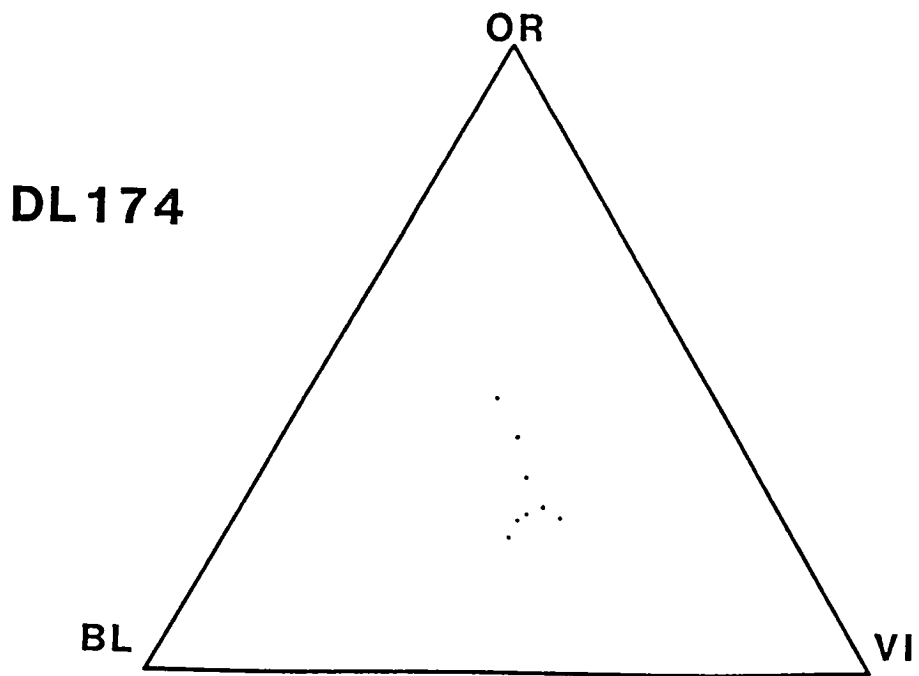
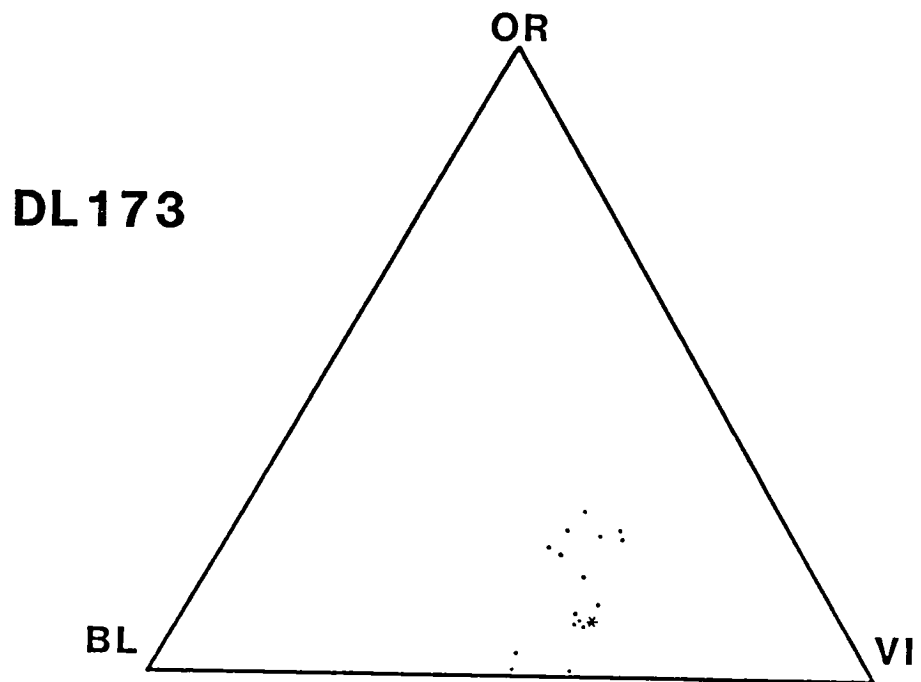




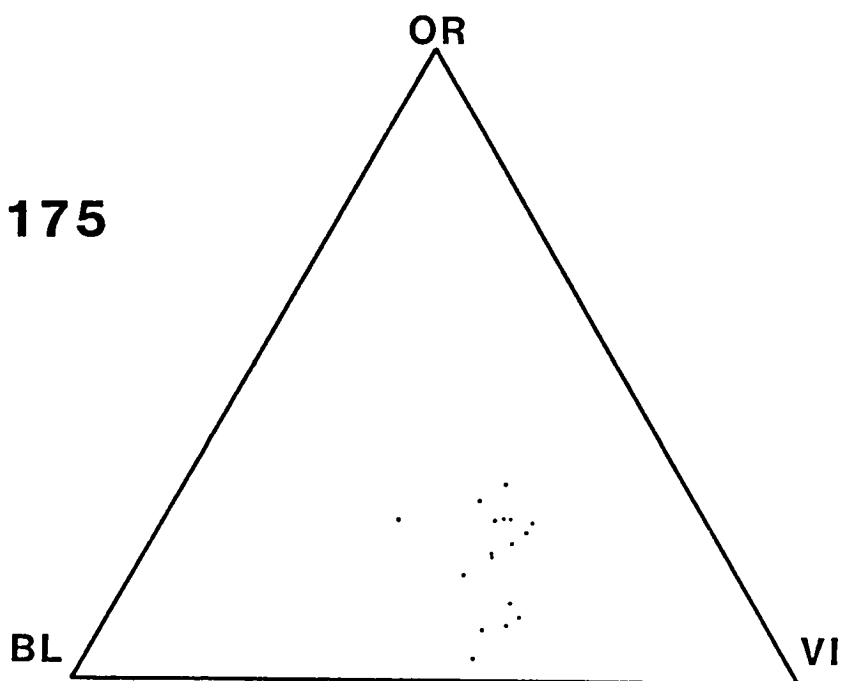




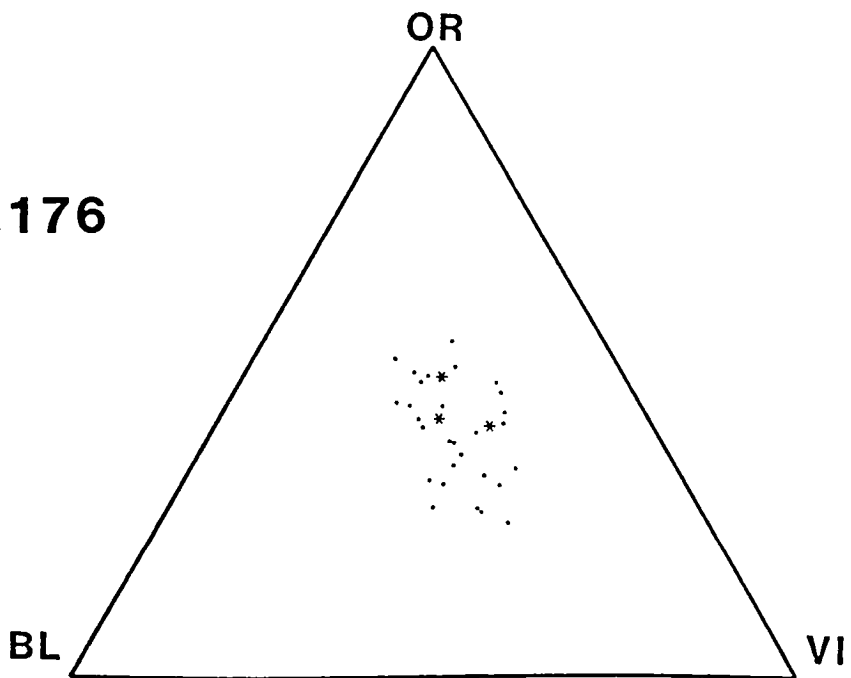


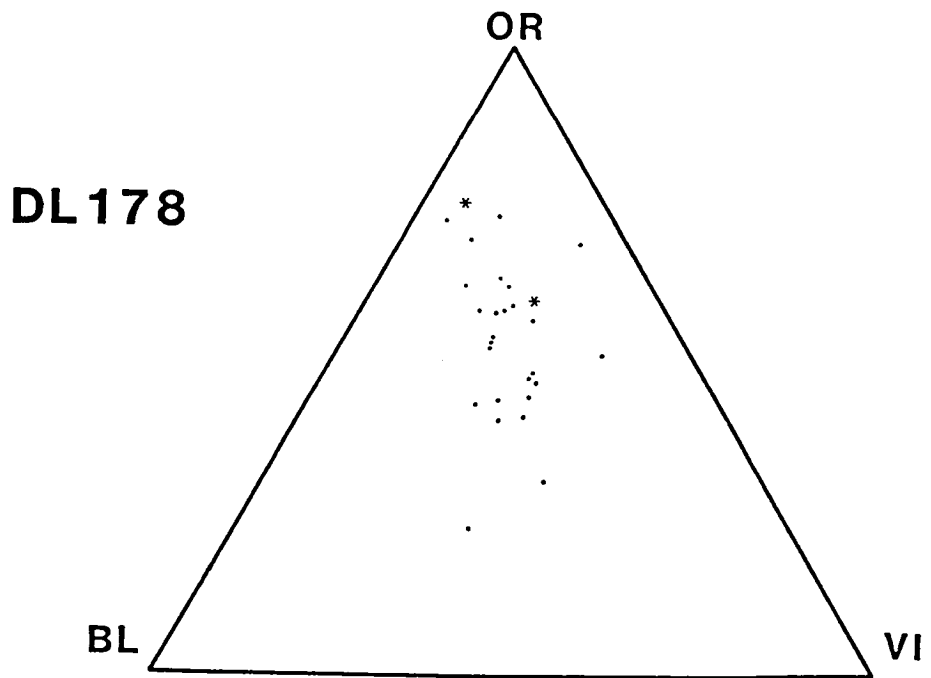
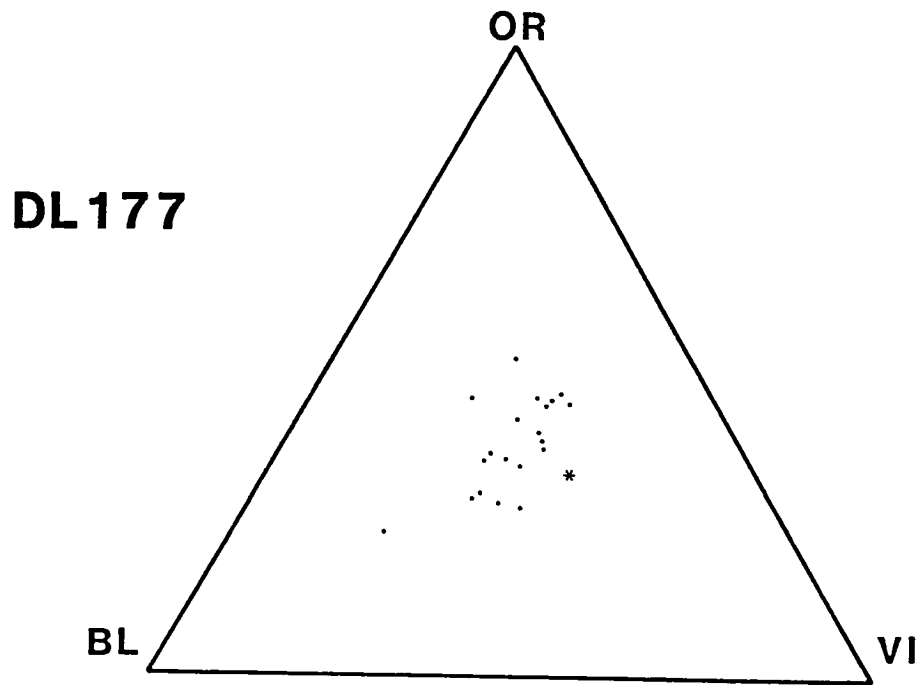


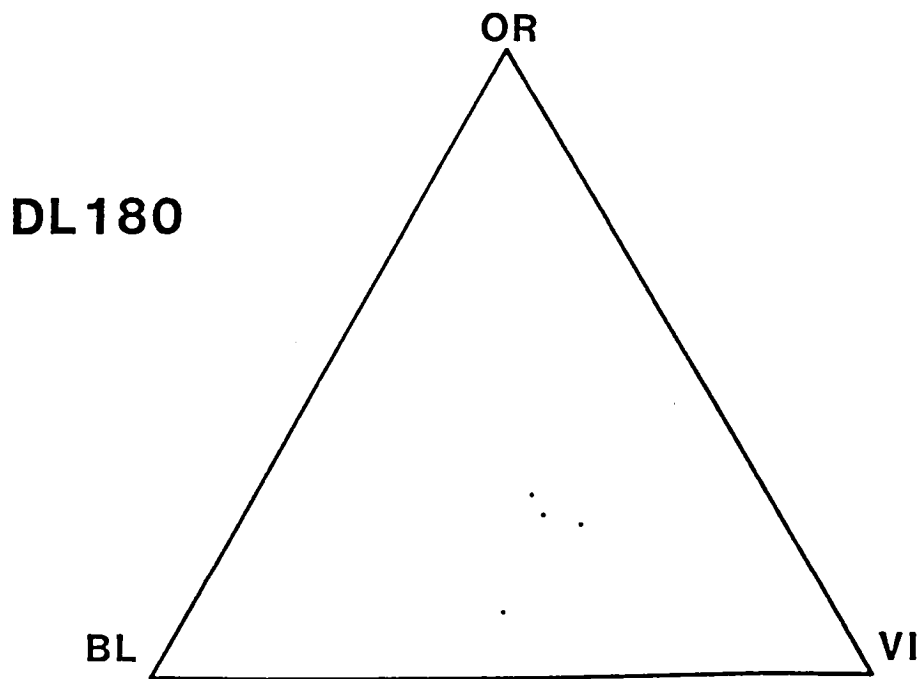
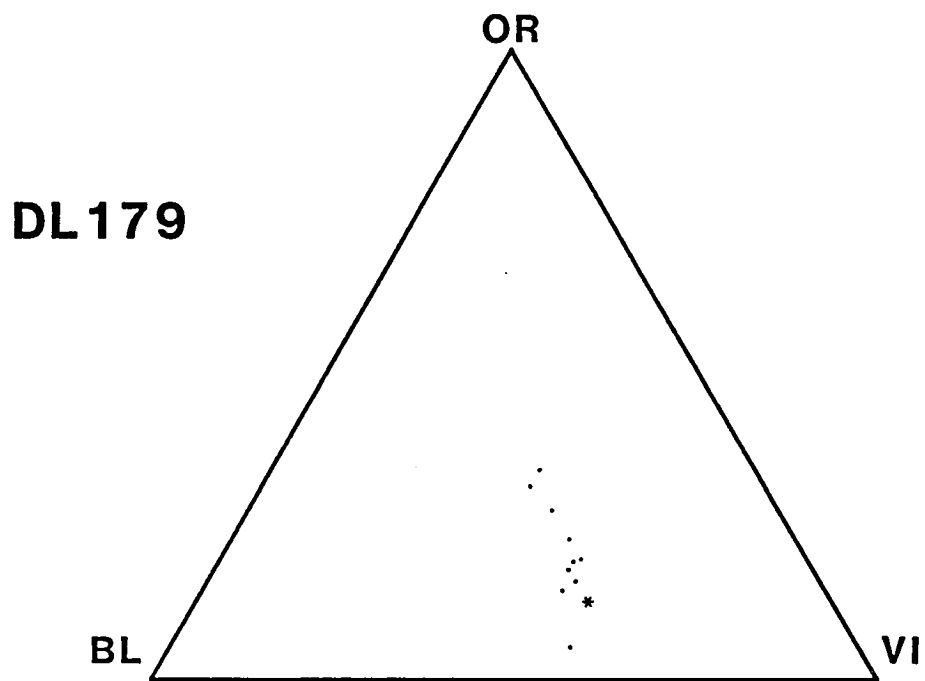
DL 175

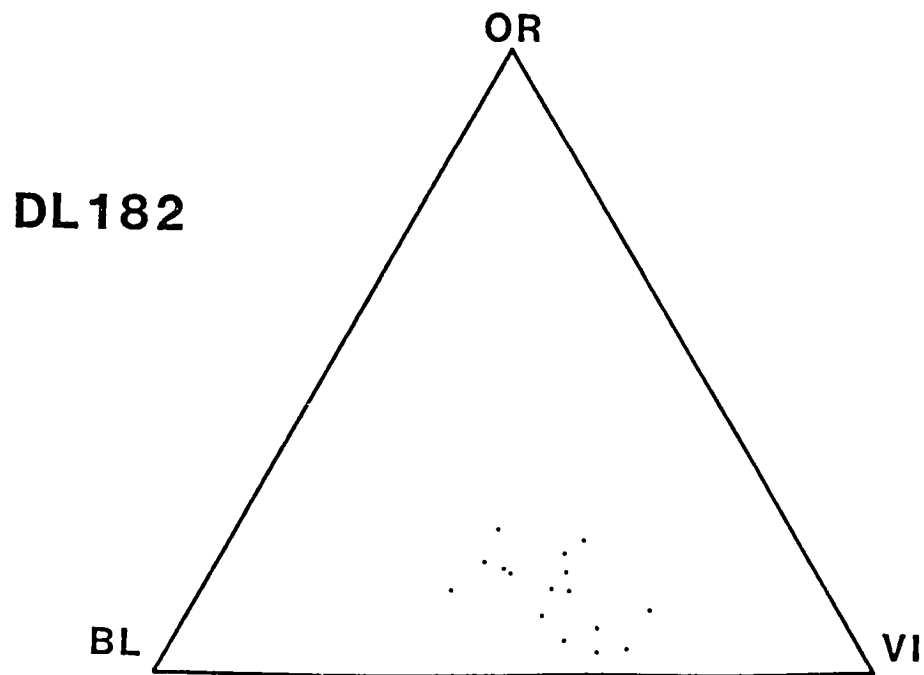
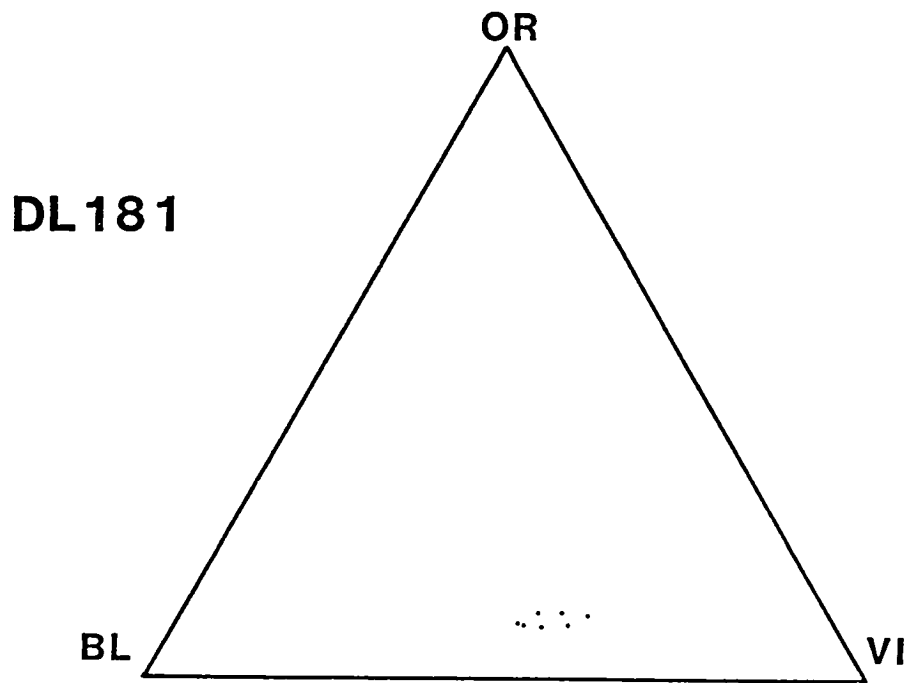


DL 176

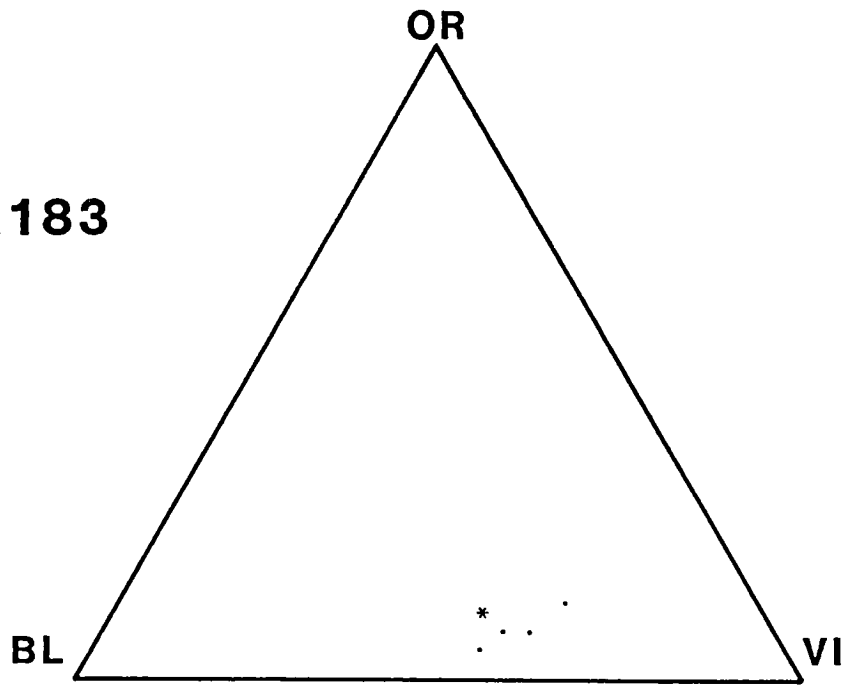




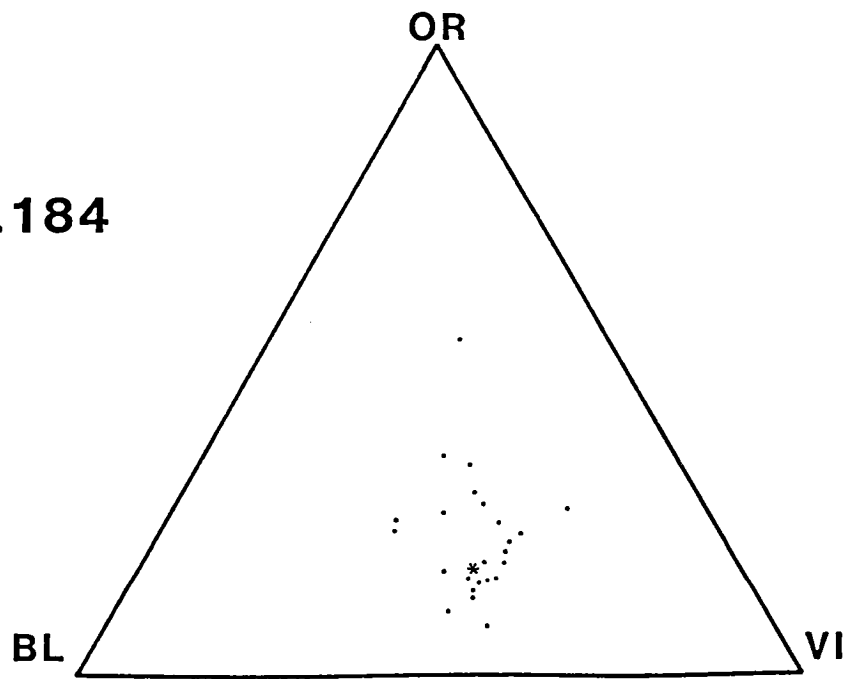


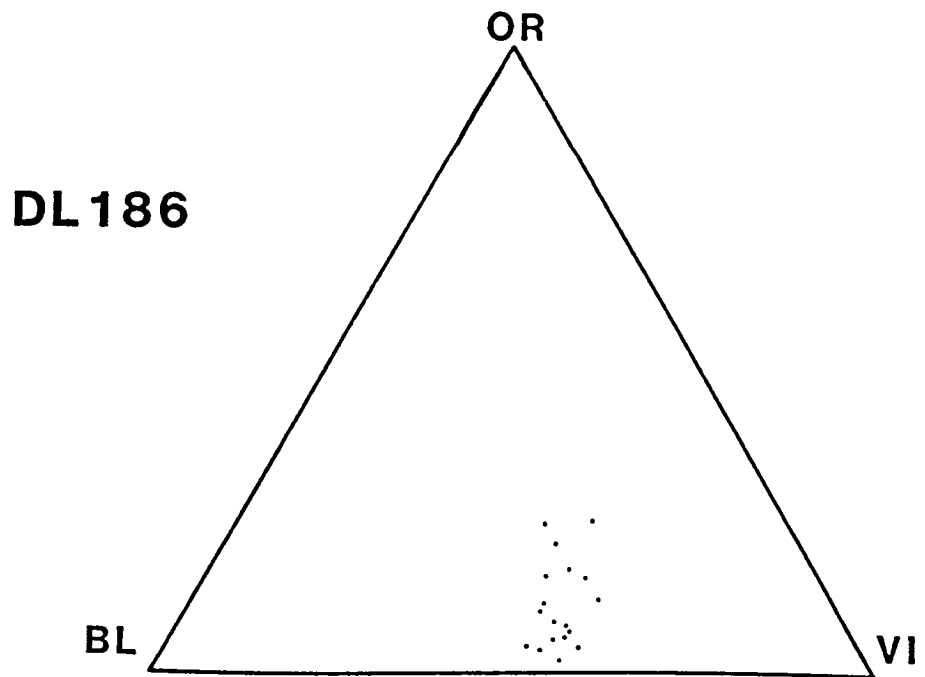
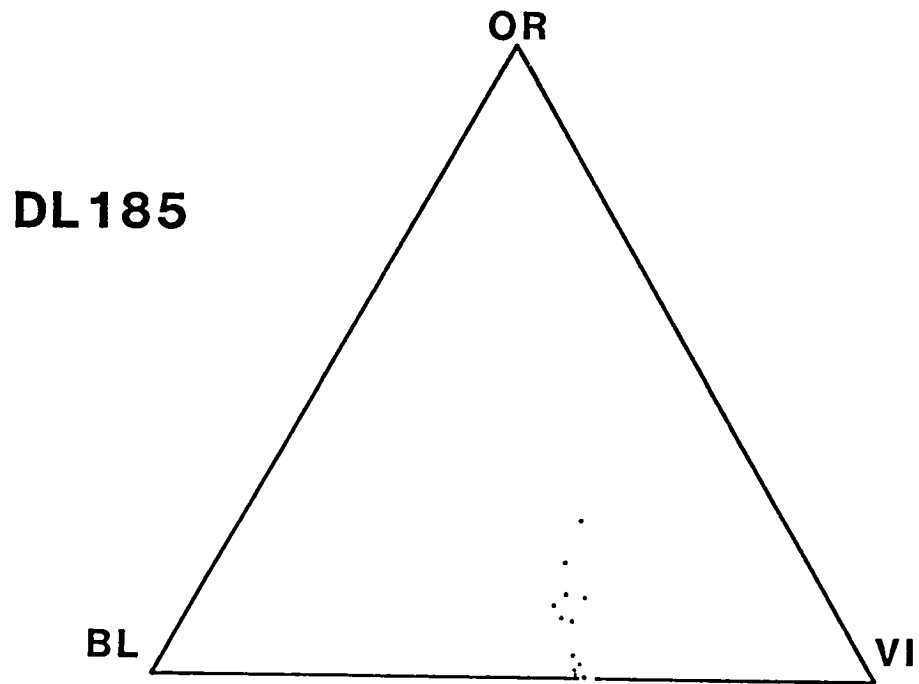


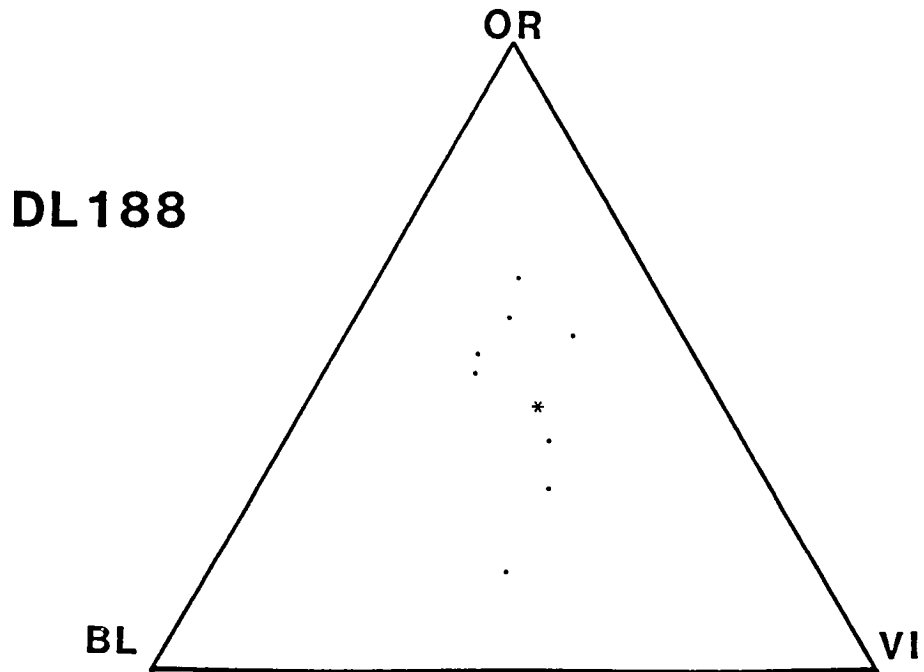
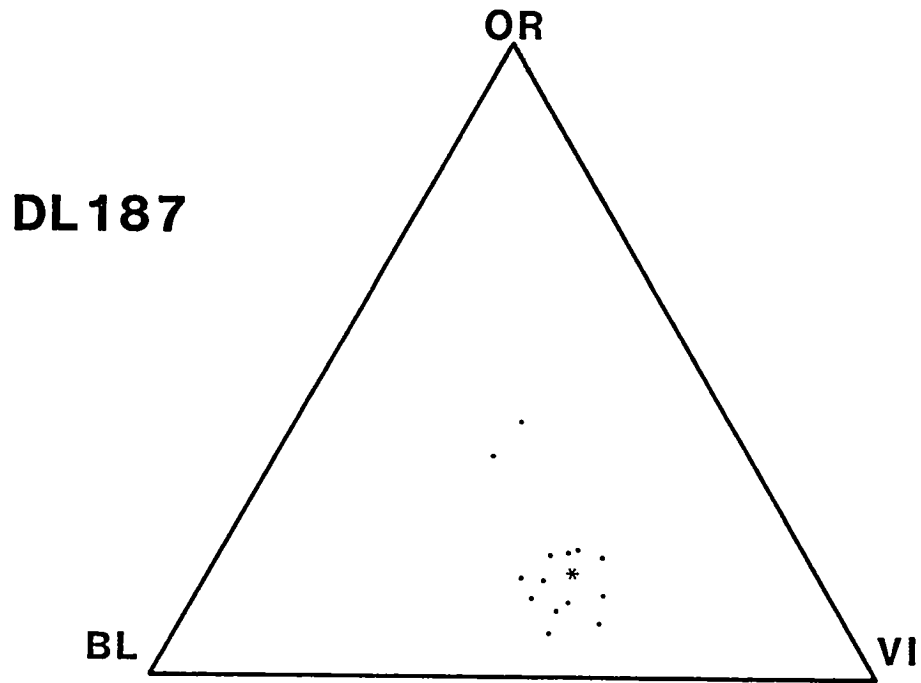
DL 183

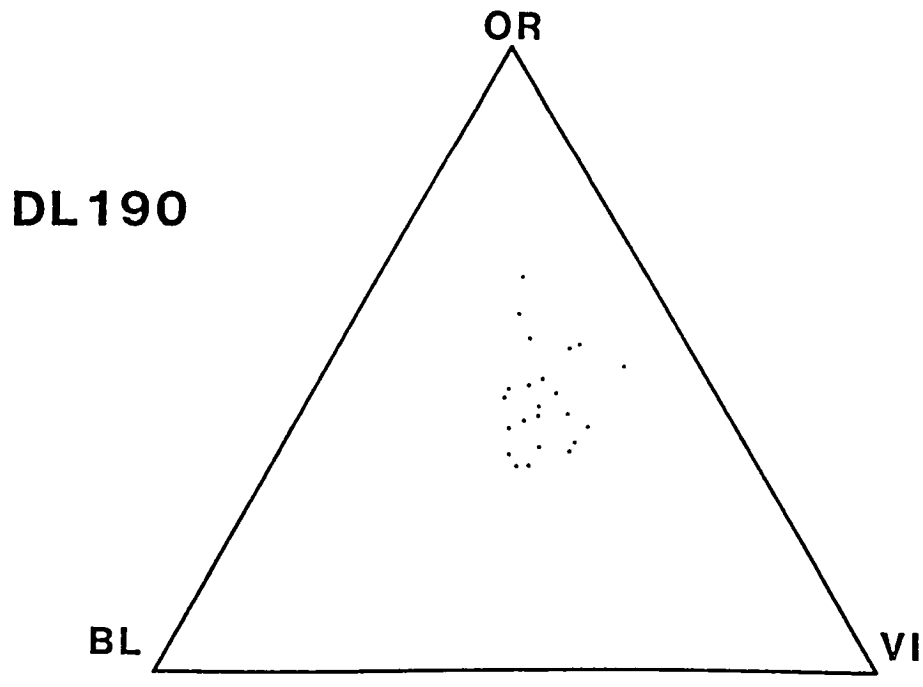
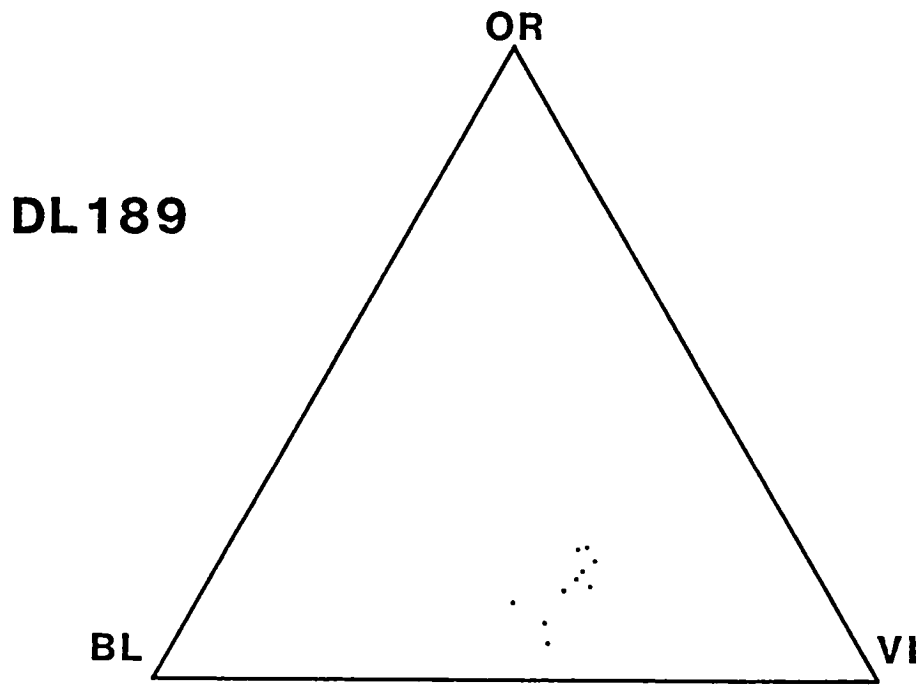


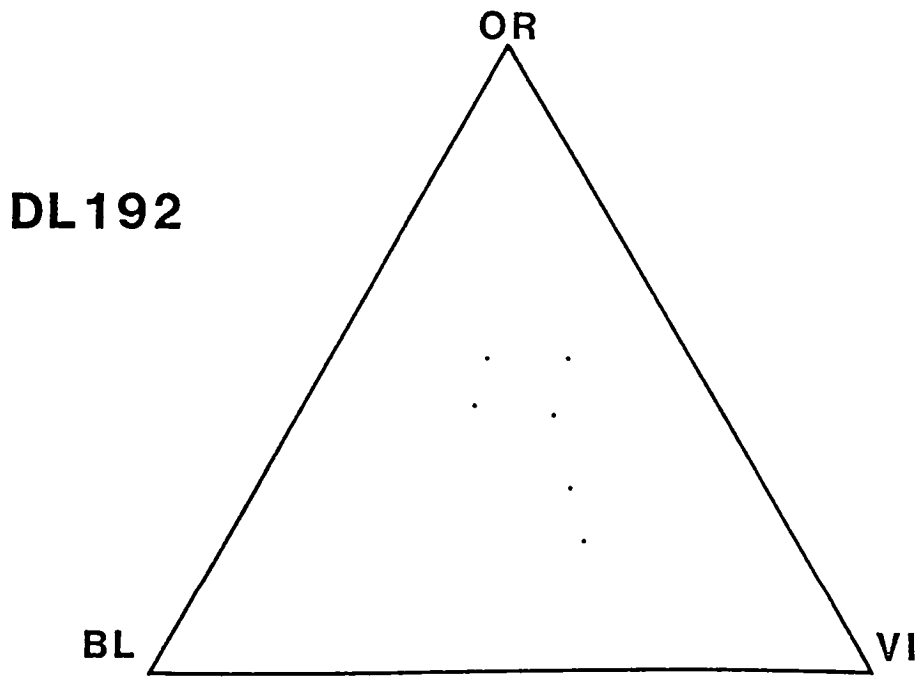
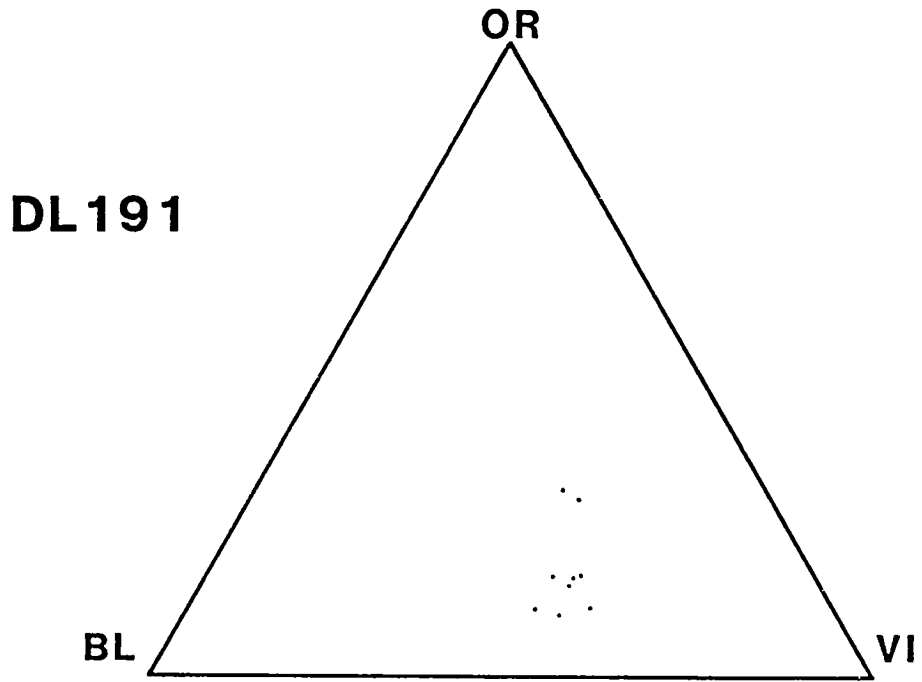
DL 184

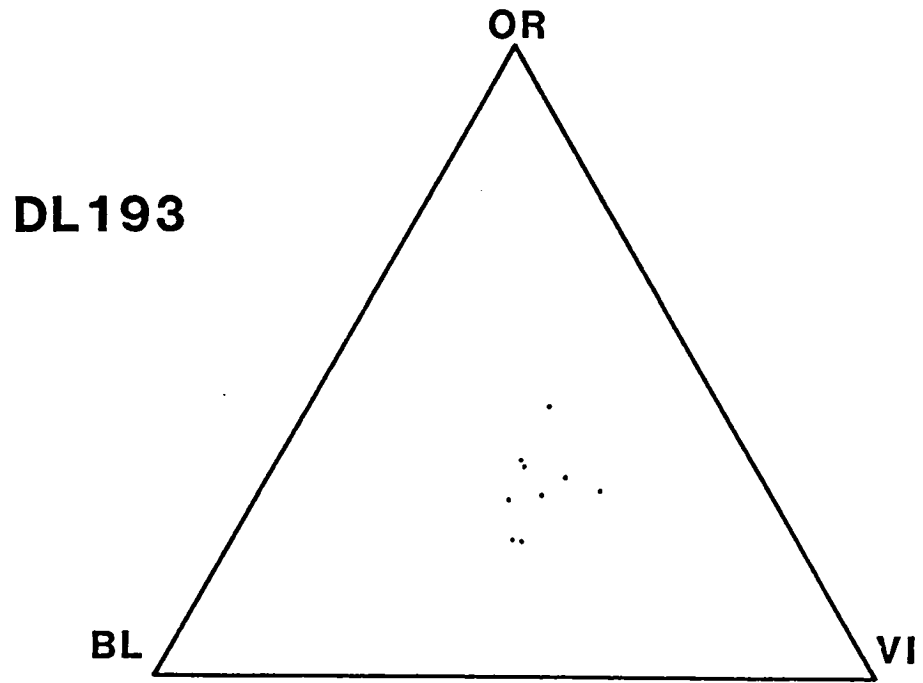






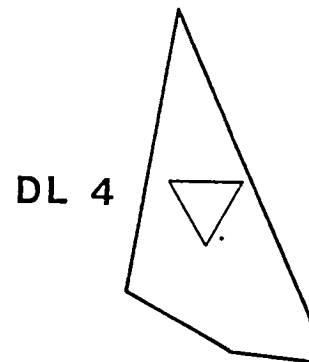
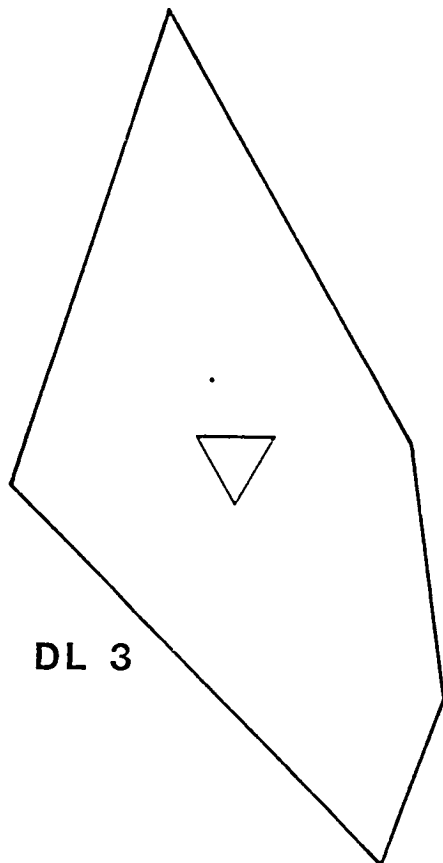
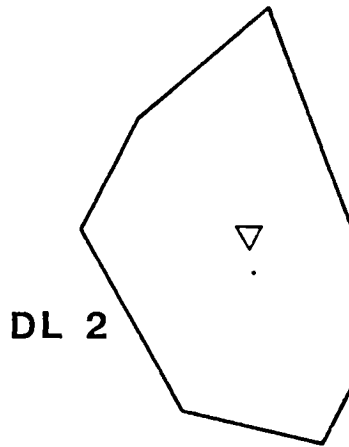
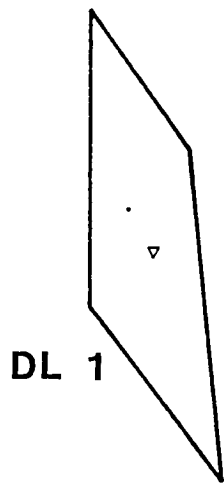


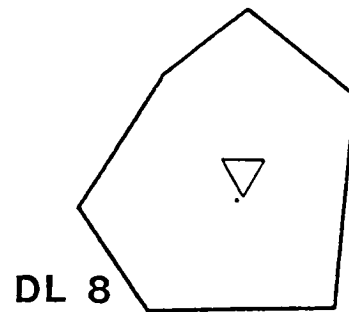
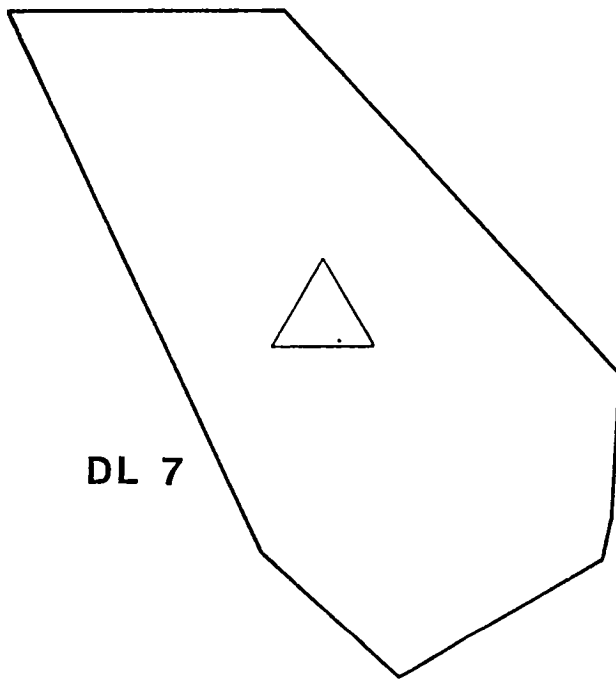
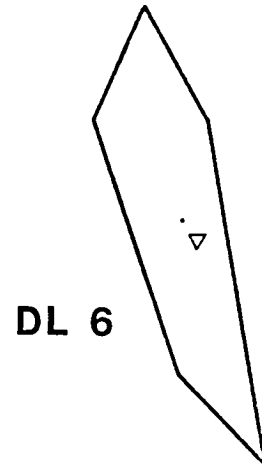
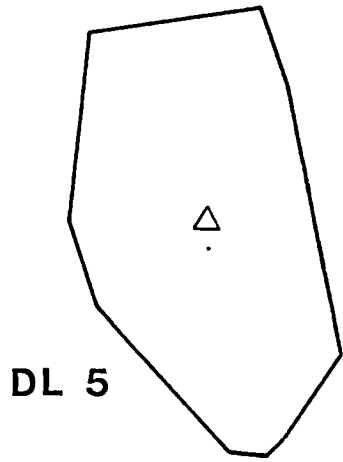


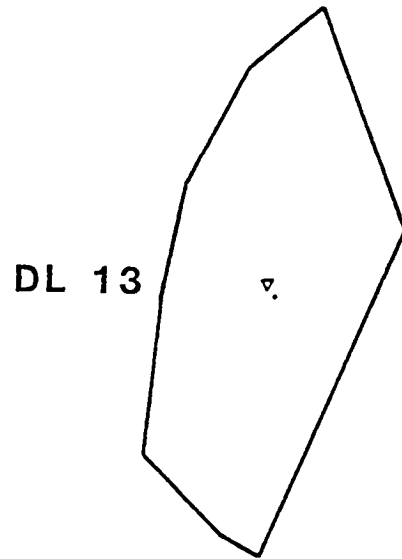
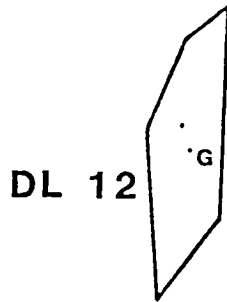
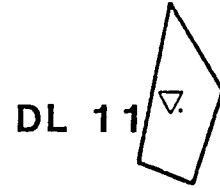
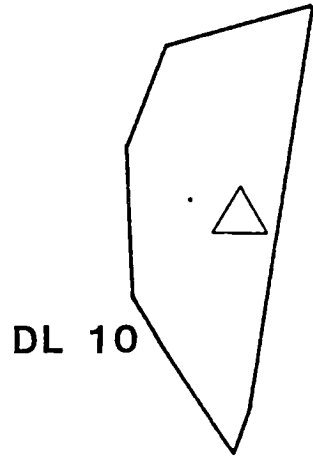
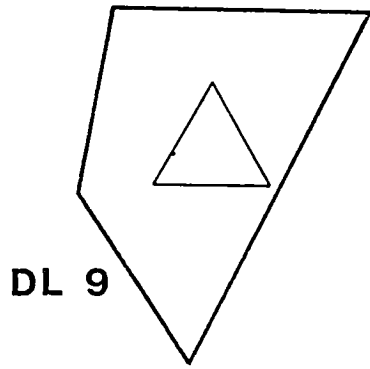


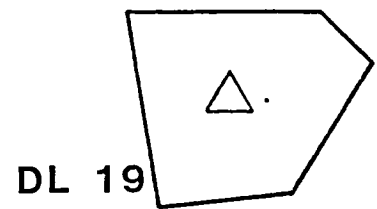
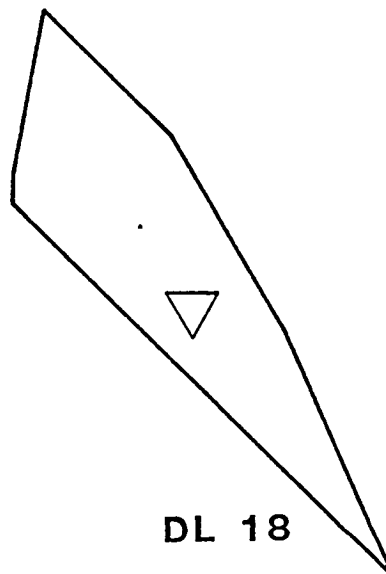
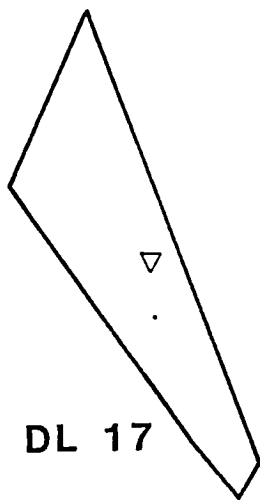
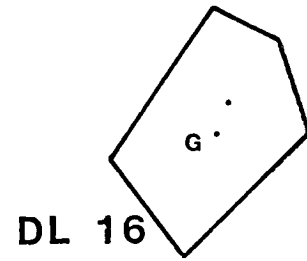
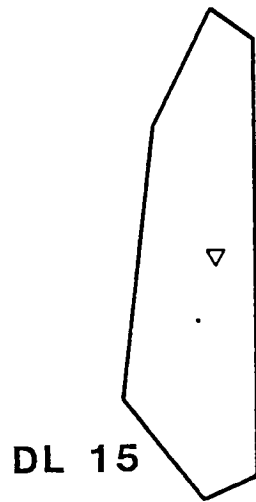
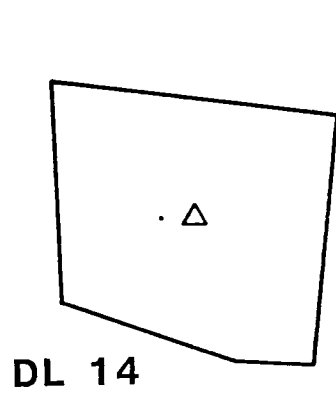
A P P E N D I X B

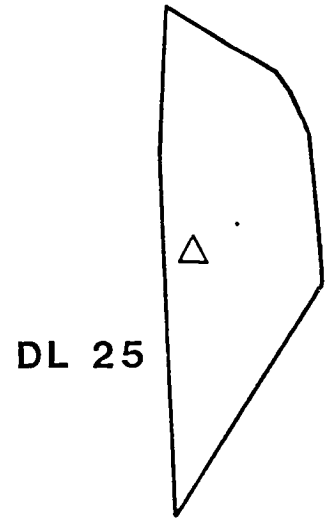
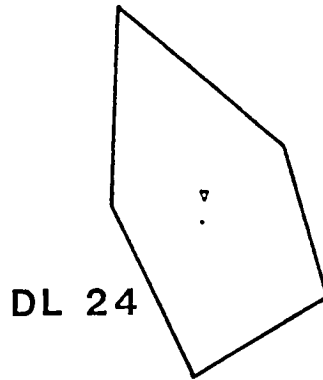
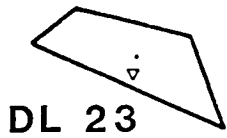
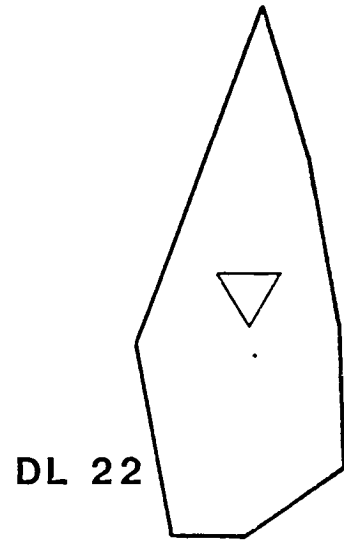
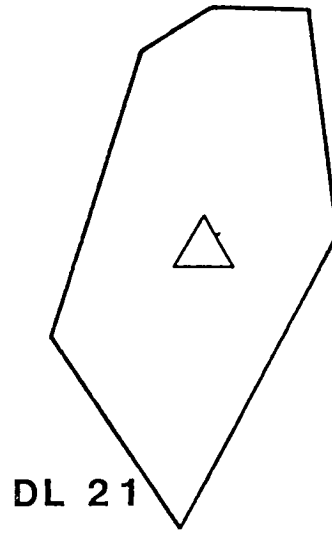
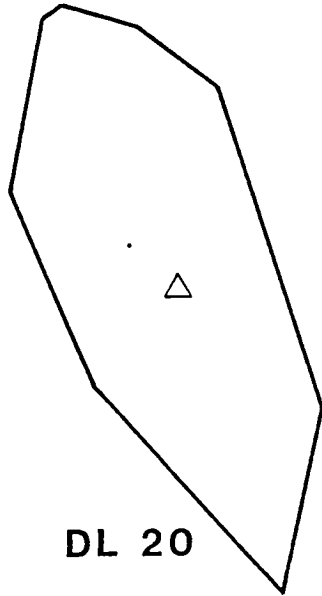
Color distribution field (CDF) polygons for all 193 dark lineation (DL) segments in the DL study area. Polygons were constructed from the rel% data point plots in Appendix A. Geometric centers are shown as triangles formed by the intersection of the center of the range of rel%'s for each of the three colors (i.e., orange, blue, and violet). Statistical centers are shown as points. Where geometric center triangles are so small that they plot as points, the points are labeled with "g"'s. All CDF polygons are drawn to the same scale to show the differences in CDF areas present in the DL suite.

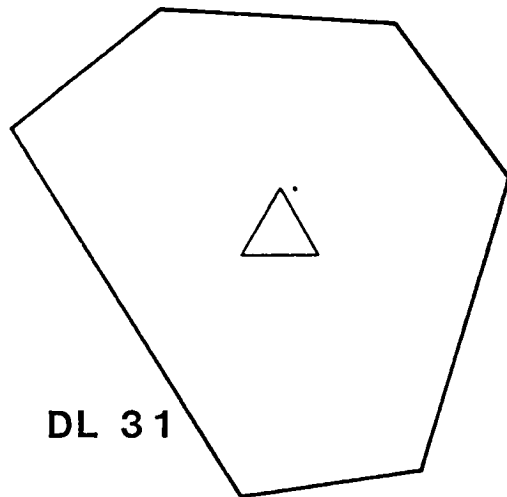
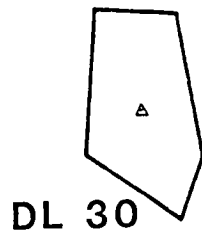
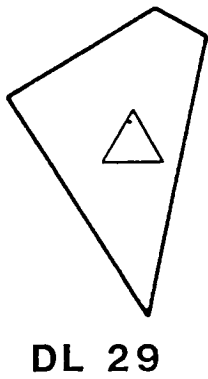
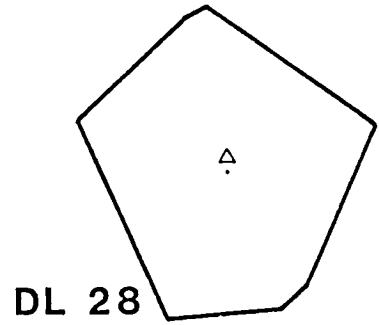
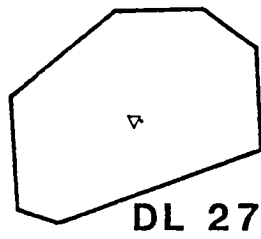
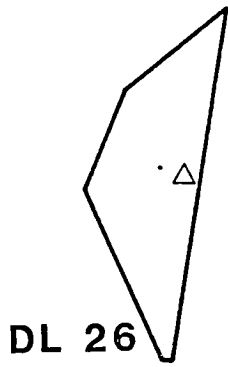


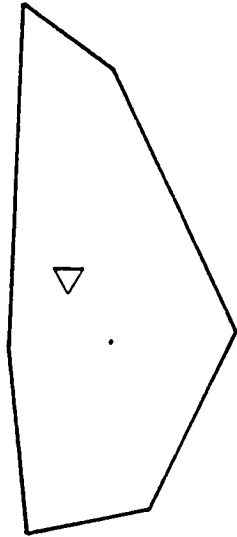




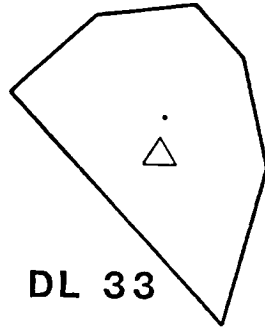




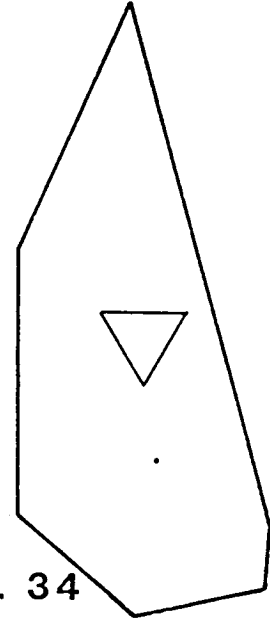




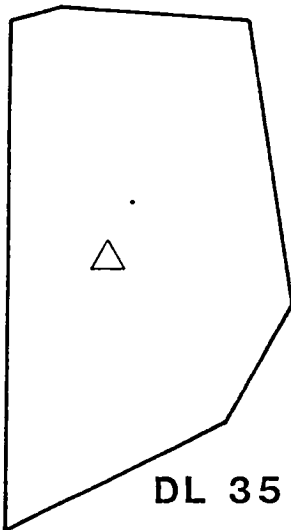
DL 32



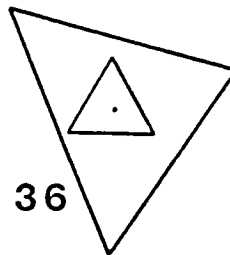
DL 33



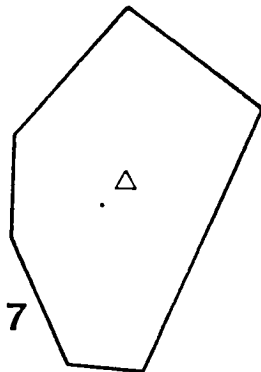
DL 34



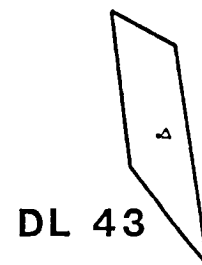
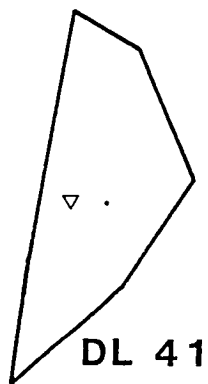
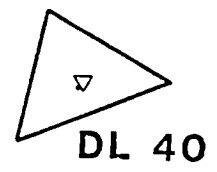
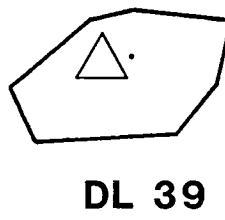
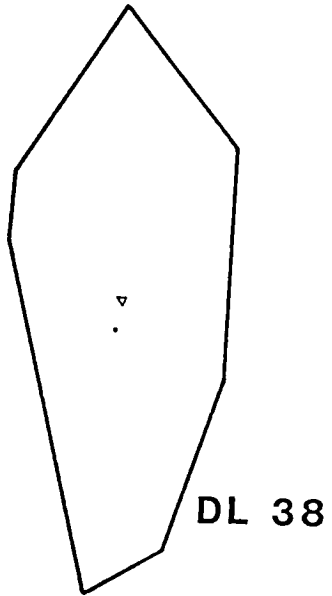
DL 35

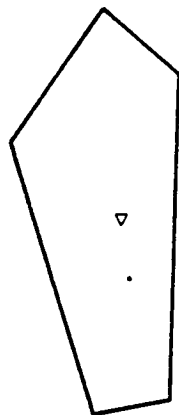


DL 36

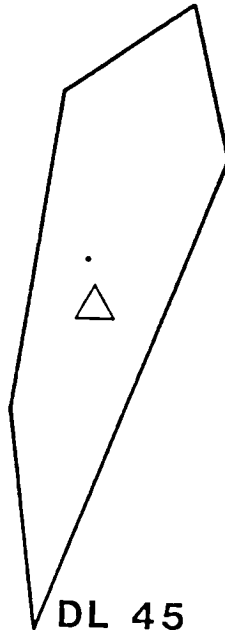


DL 37

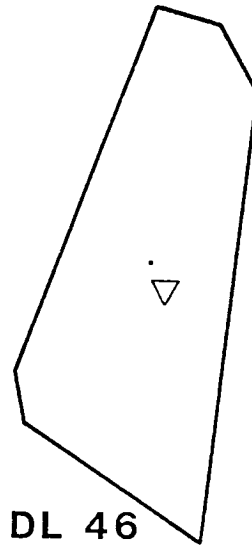




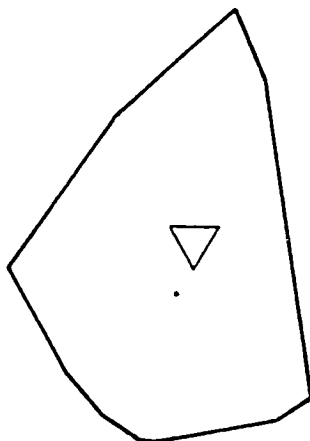
DL 44



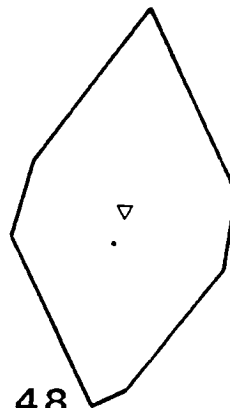
DL 45



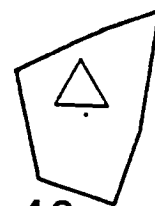
DL 46



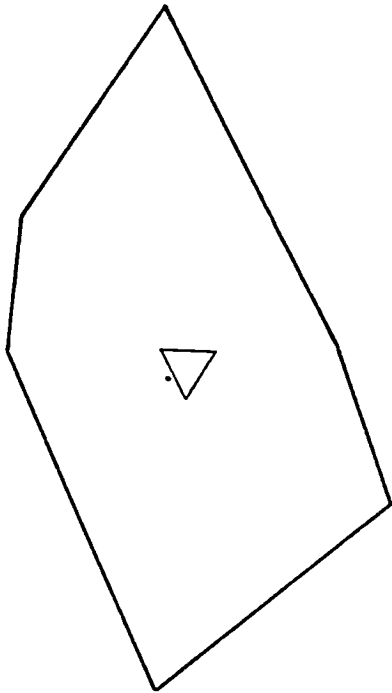
DL 47



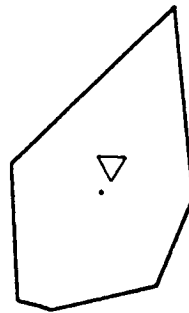
DL 48



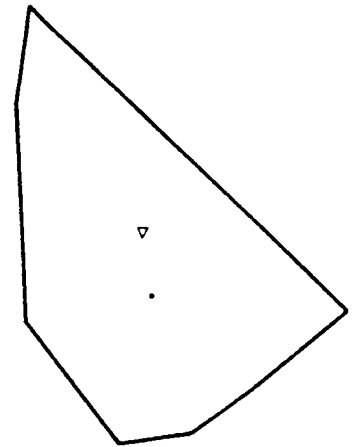
DL 49



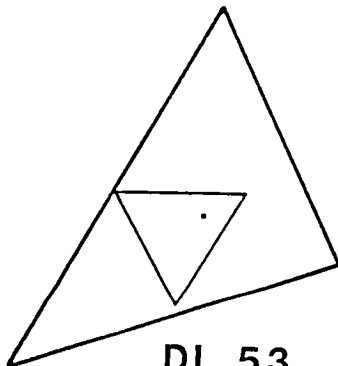
DL 50



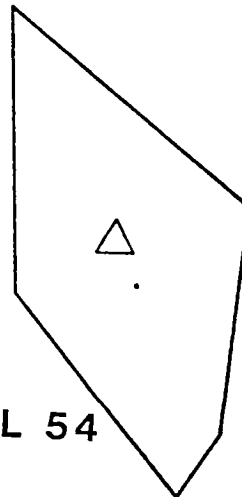
DL 51



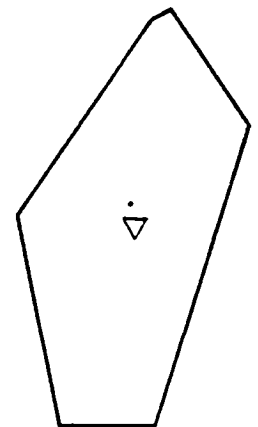
DL 52



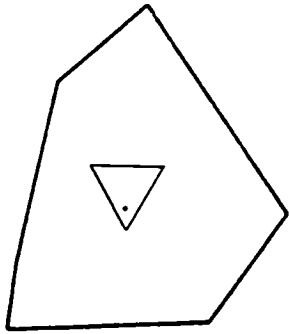
DL 53



DL 54



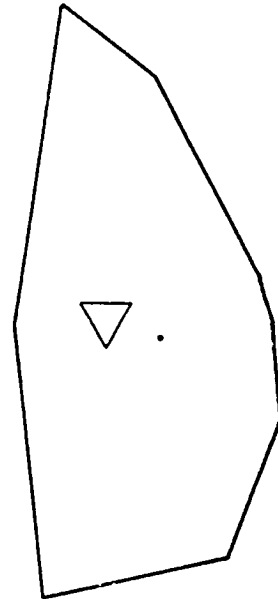
DL 55



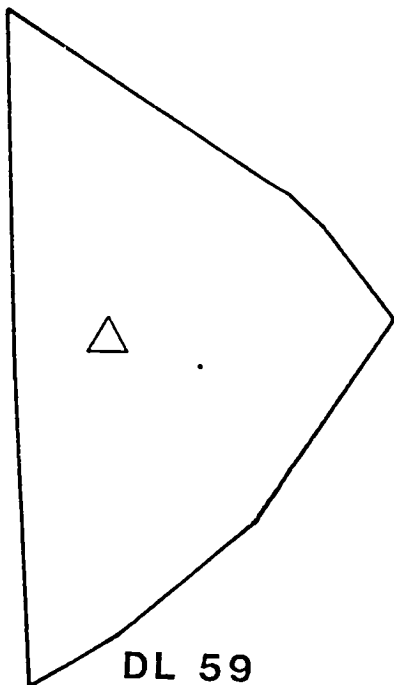
DL 56



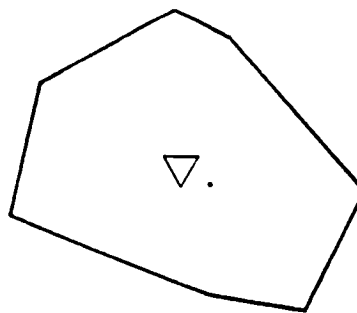
DL 57



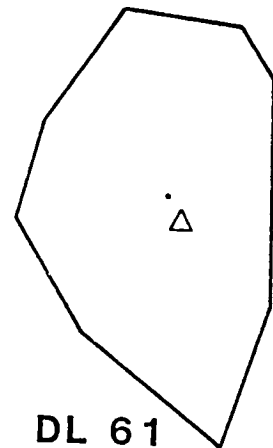
DL 58



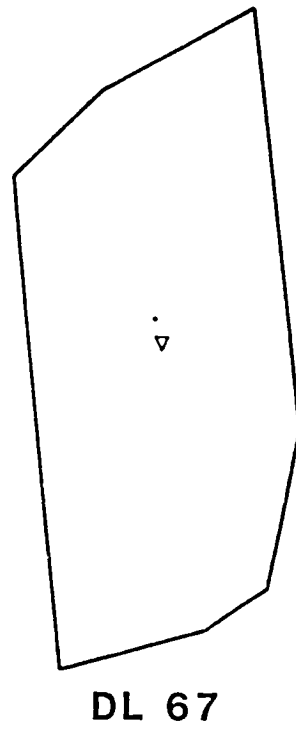
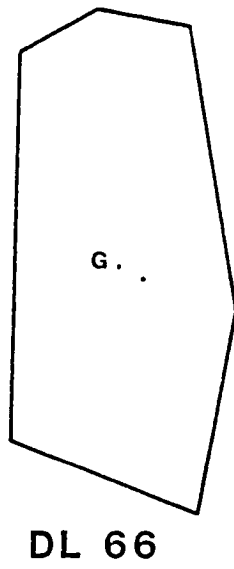
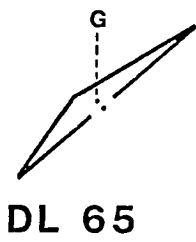
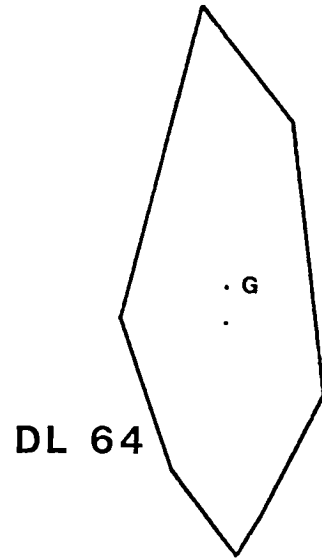
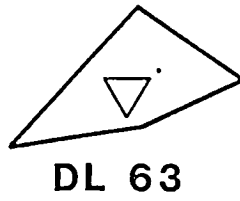
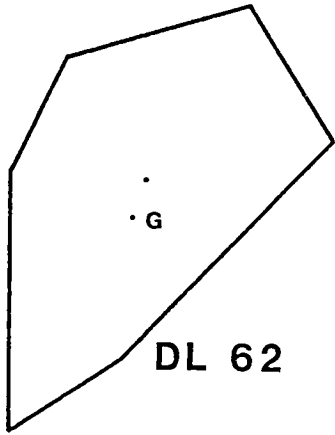
DL 59

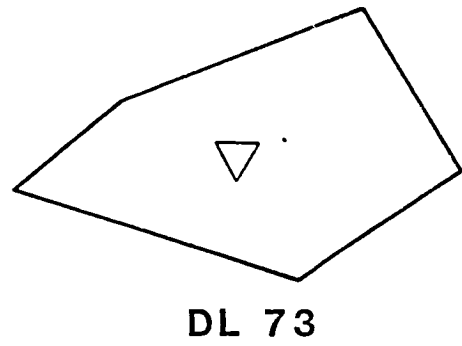
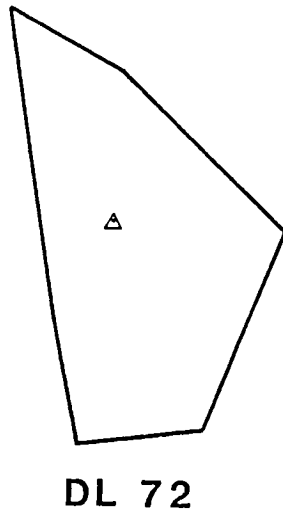
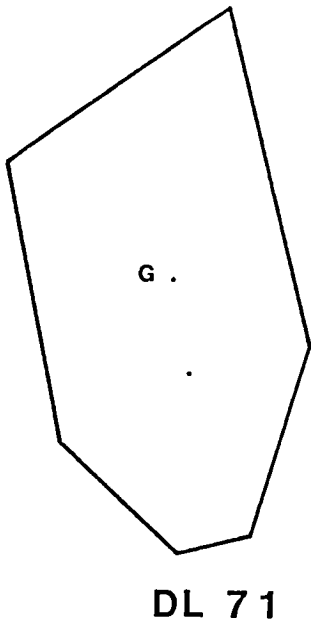
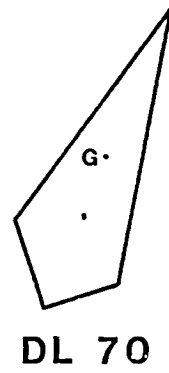
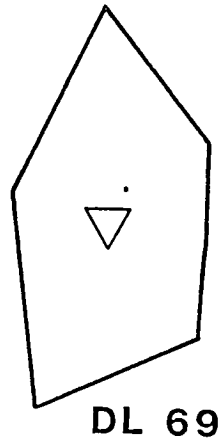
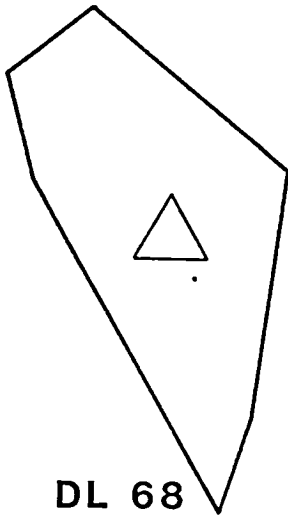


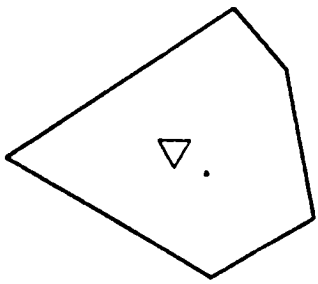
DL 60



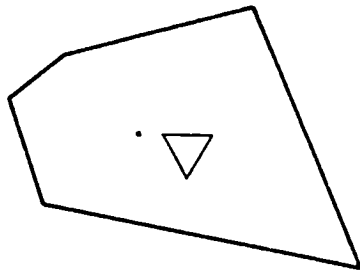
DL 61



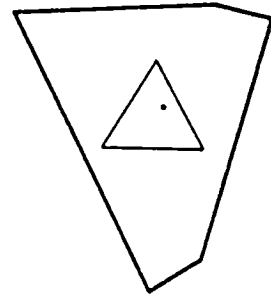




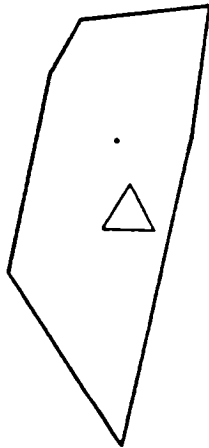
DL 74



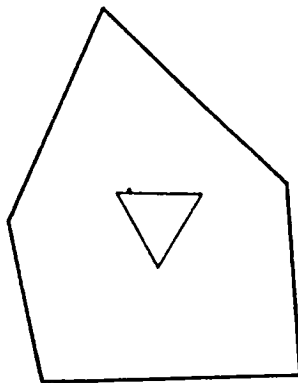
DL 75



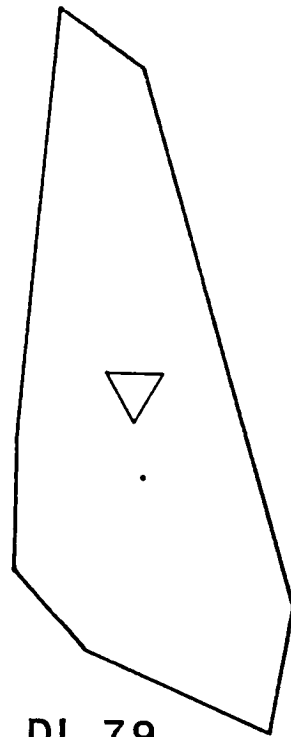
DL 76



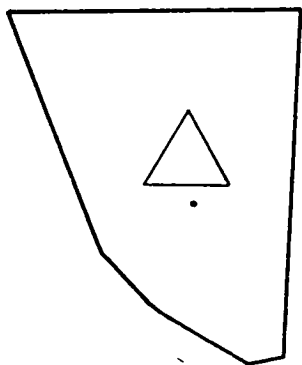
DL 77



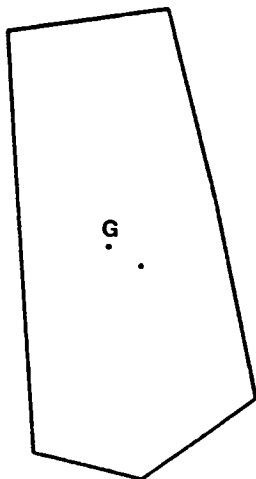
DL 78



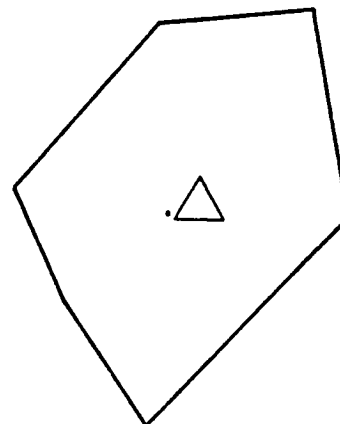
DL 79



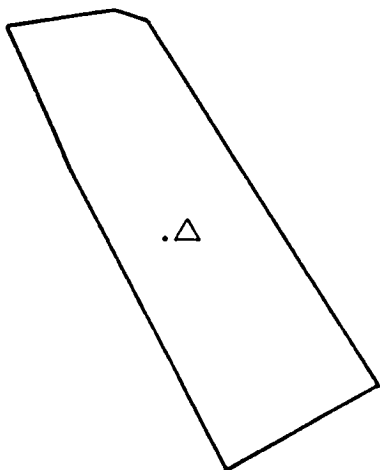
DL 80



DL 81



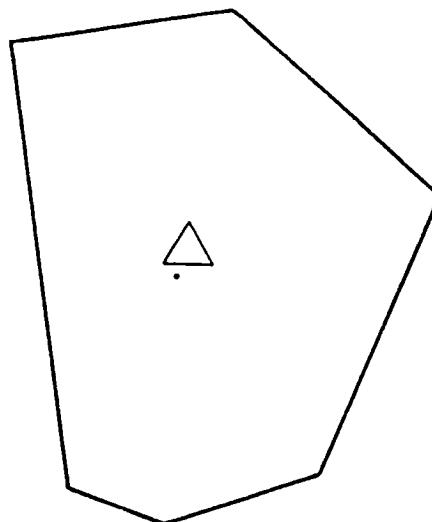
DL 82



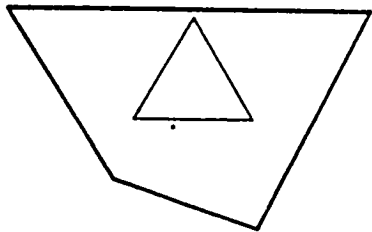
DL 83



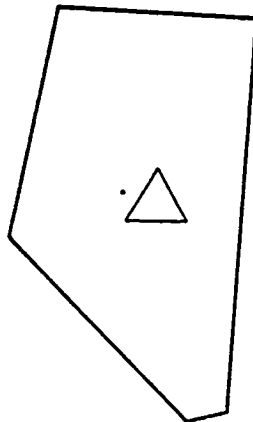
DL 84



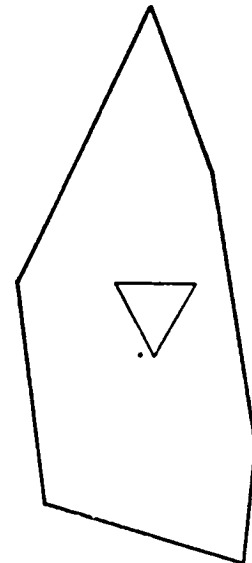
DL 85



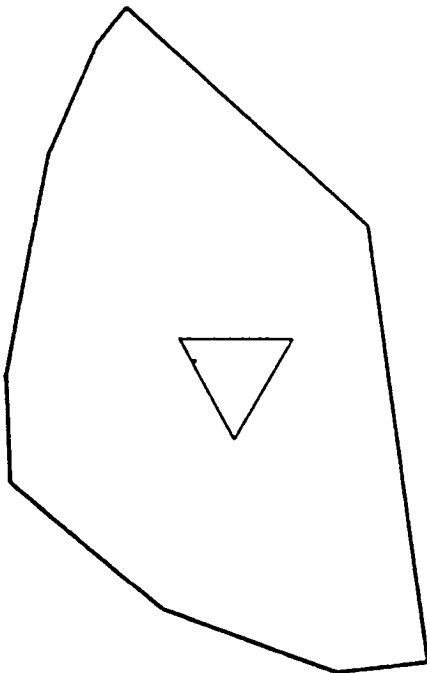
DL 86



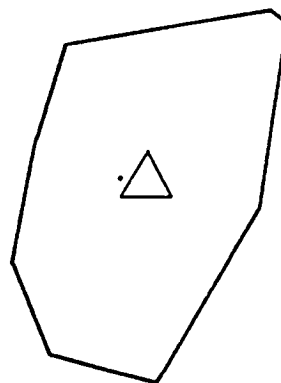
DL 87



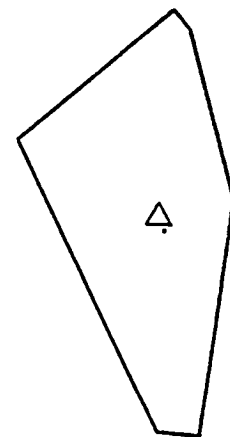
DL 88



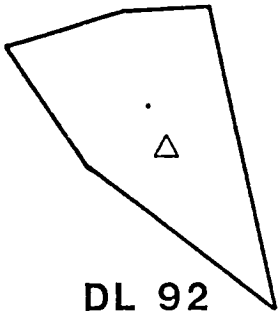
DL 89



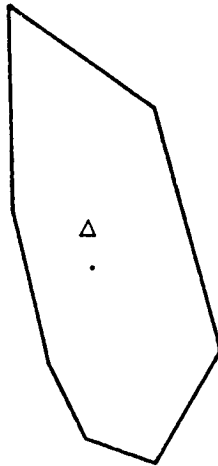
DL 90



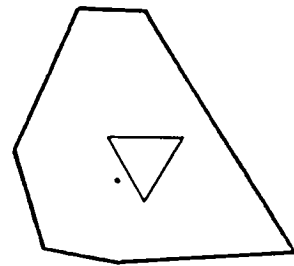
DL 91



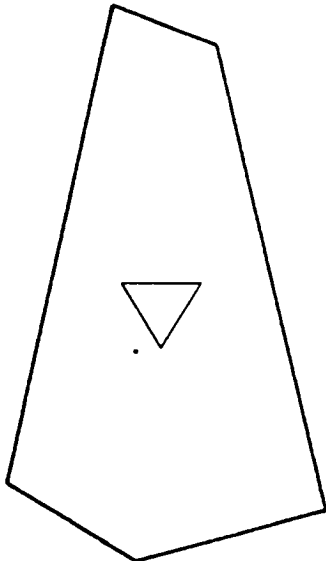
DL 92



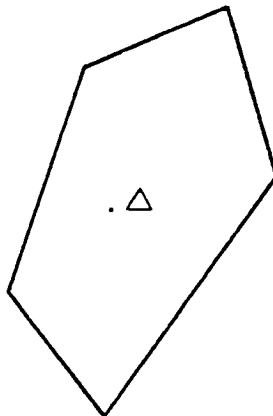
DL 93



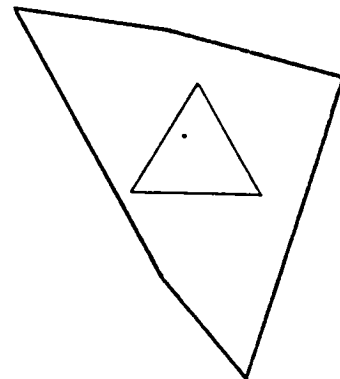
DL 94



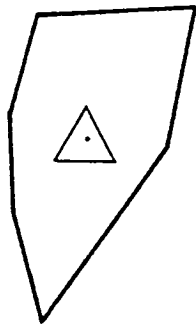
DL 95



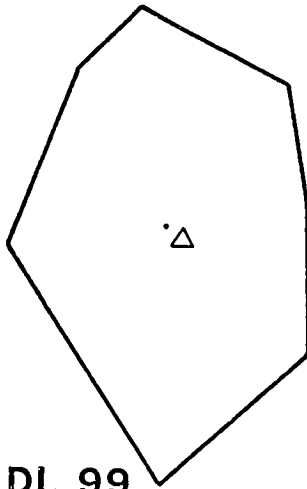
DL 96



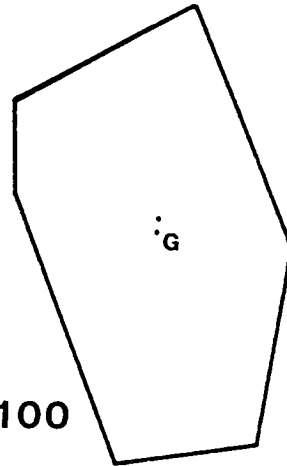
DL 97



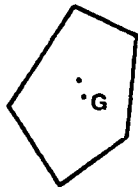
DL 98



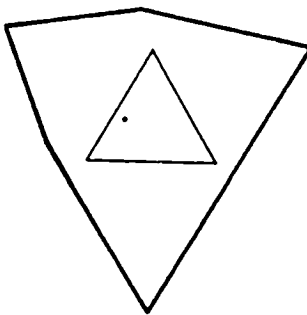
DL 99



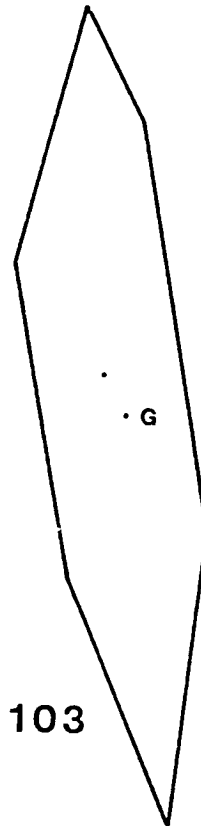
DL 100



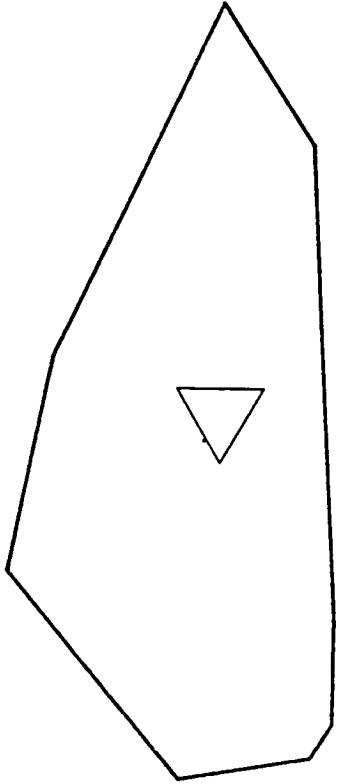
DL 101



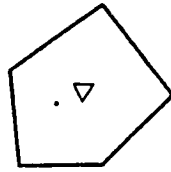
DL 102



DL 103



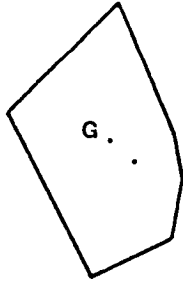
DL 104



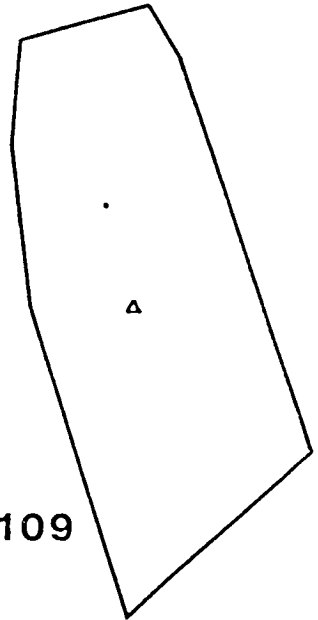
DL 105



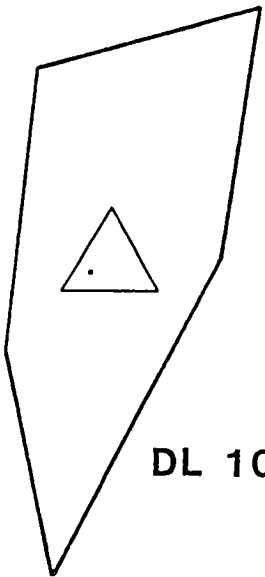
DL 106



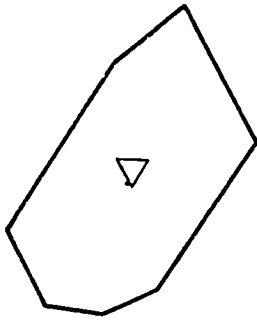
DL 108



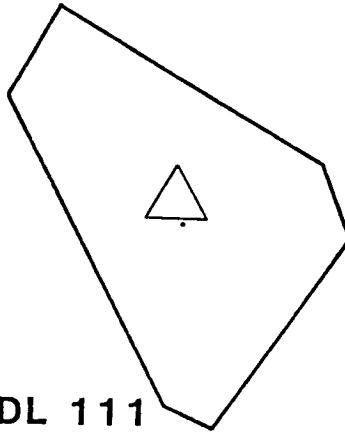
DL 109



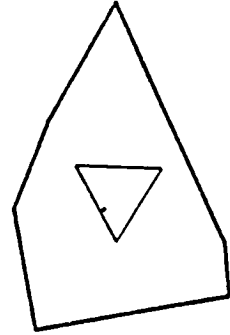
DL 107



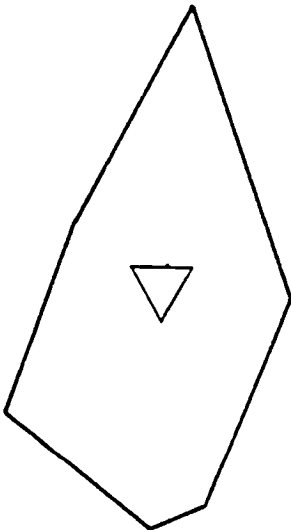
DL 110



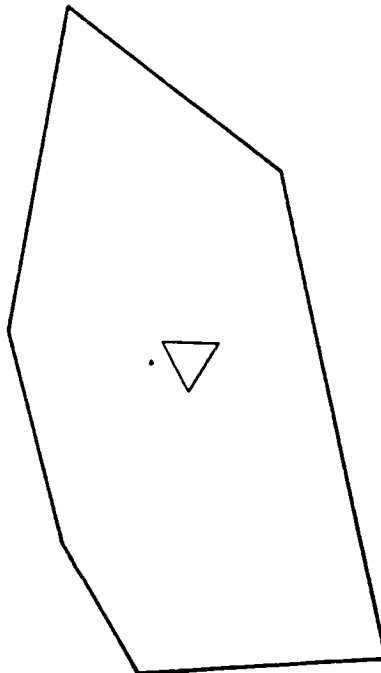
DL 111



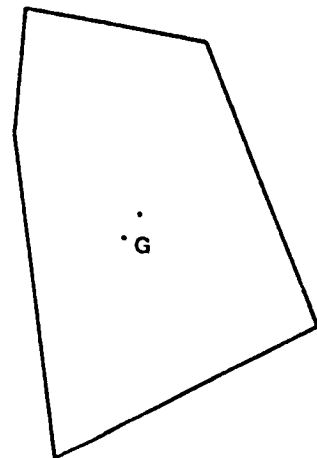
DL 112



DL 113



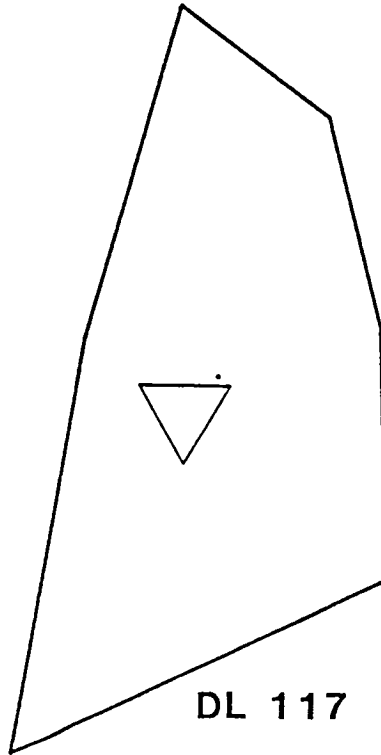
DL 114



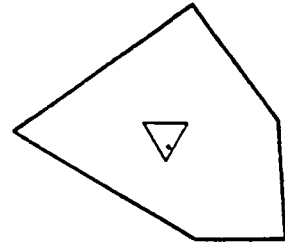
DL 115



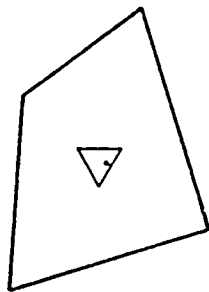
DL 116



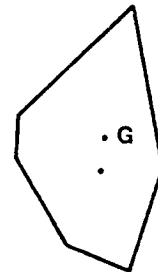
DL 117



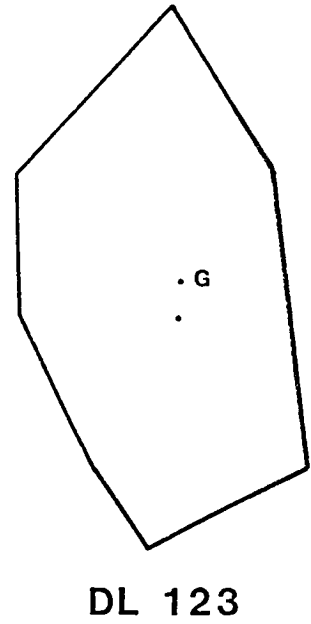
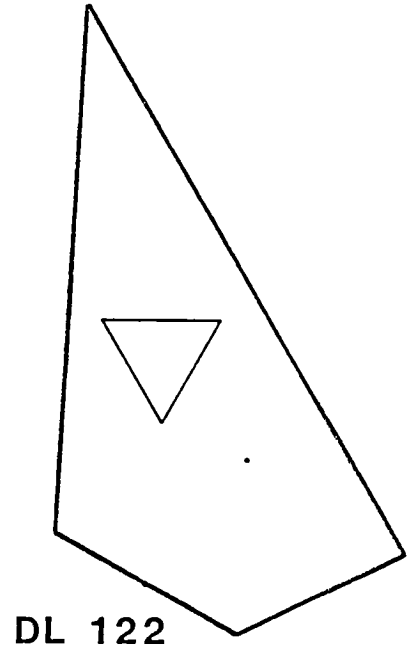
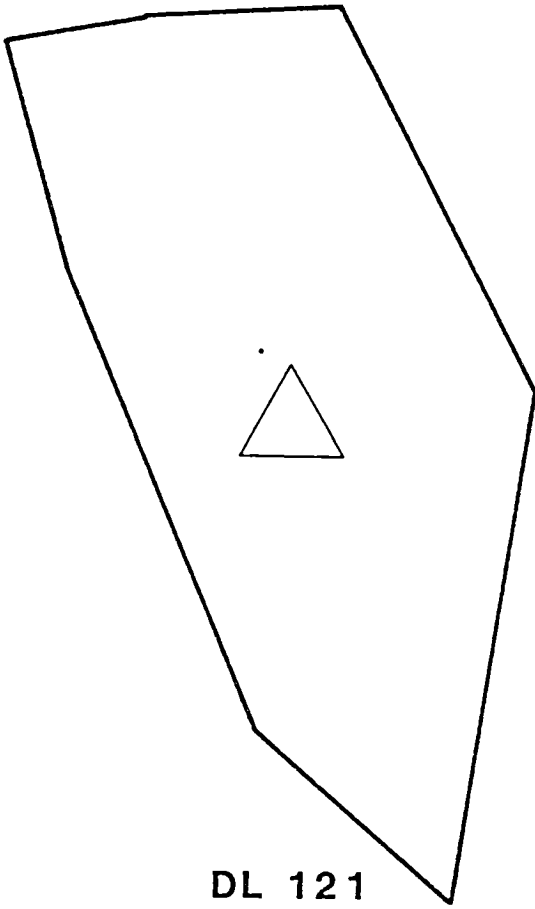
DL 118

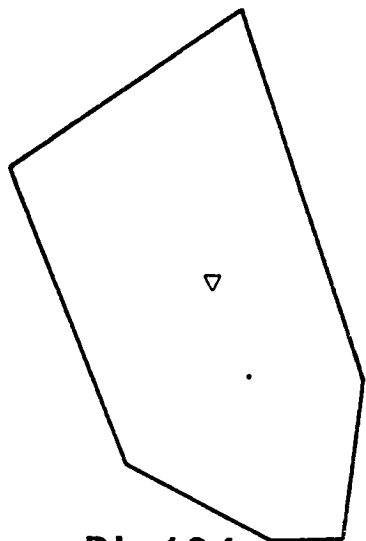


DL 119



DL 120

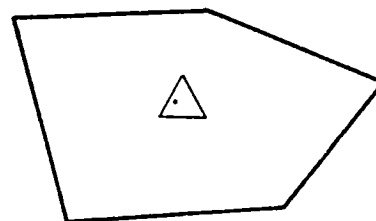




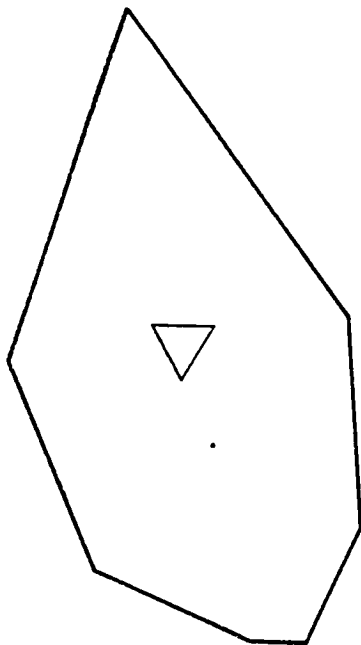
DL 124



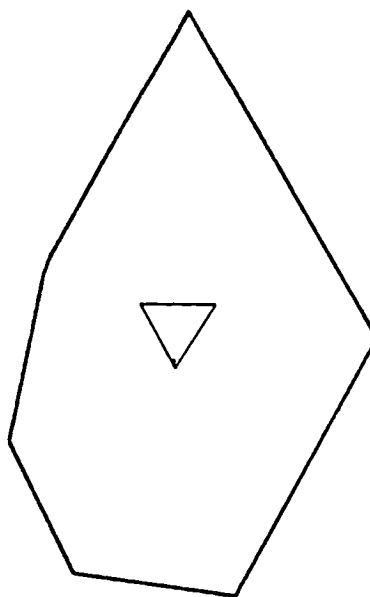
DL 125



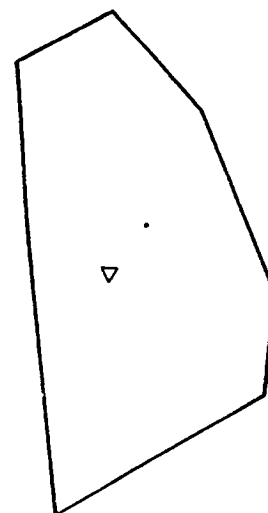
DL 126



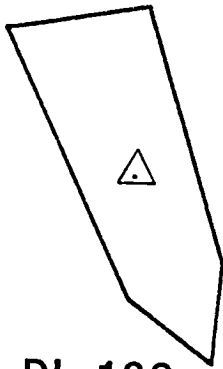
DL 127



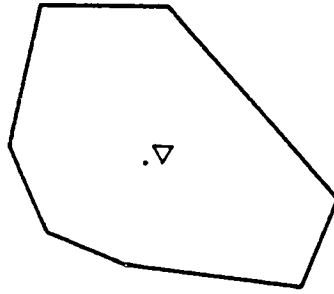
DL 128



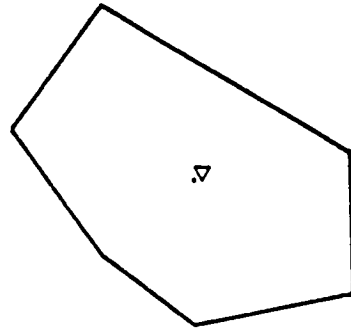
DL 129



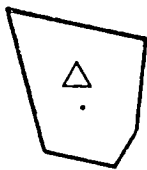
DL 130



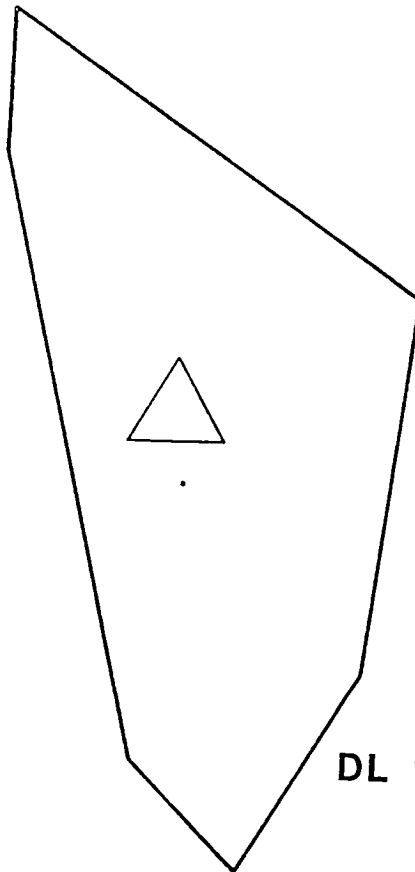
DL 131



DL 132



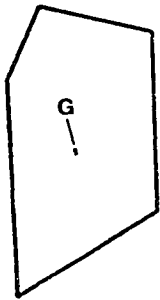
DL 133



DL 134



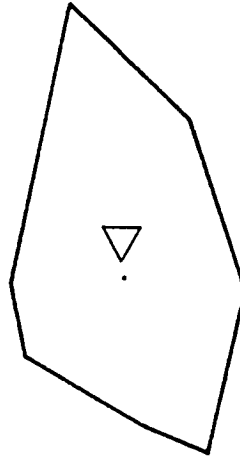
DL 135



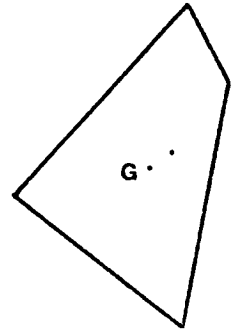
DL 136



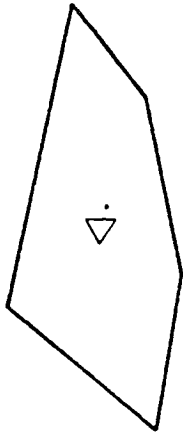
DL 137



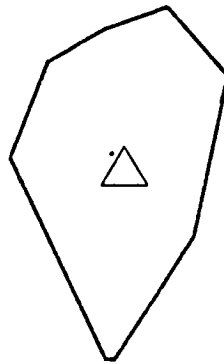
DL 138



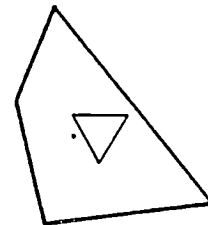
DL 139



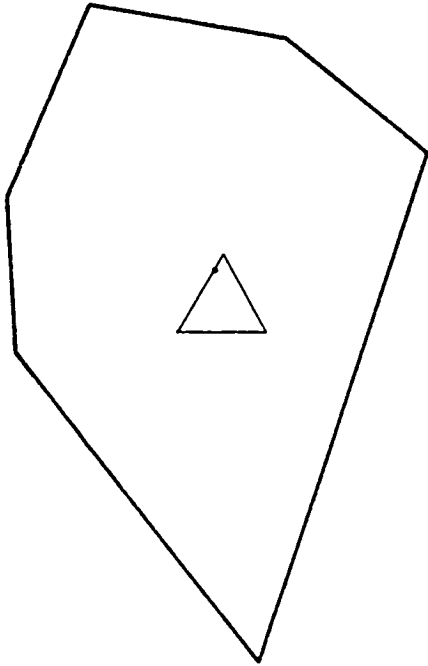
DL 140



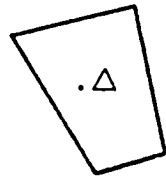
DL 141



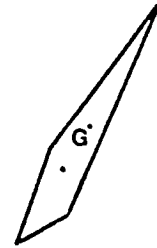
DL 142



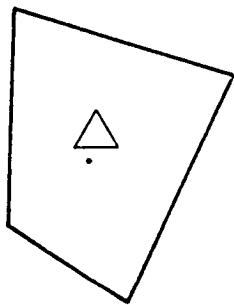
DL 143



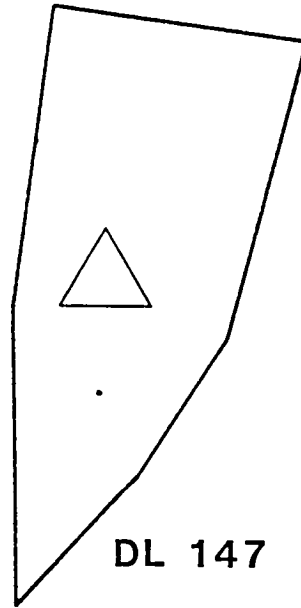
DL 144



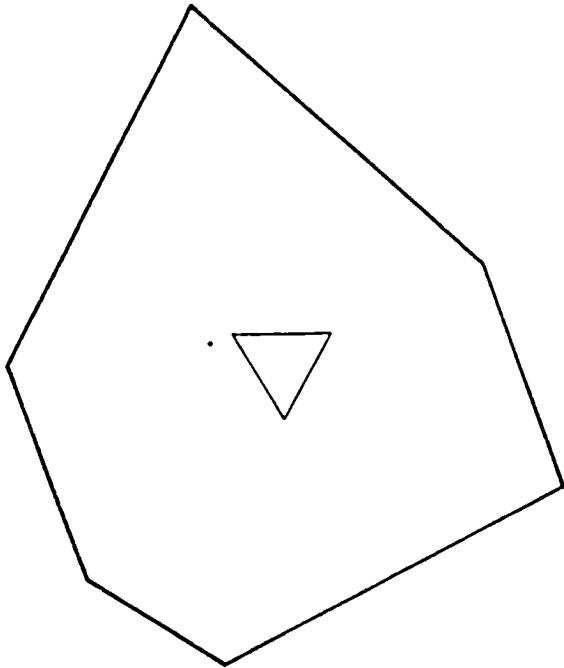
DL 145



DL 146



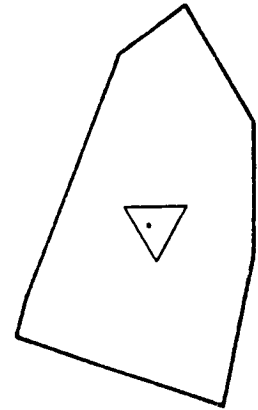
DL 147



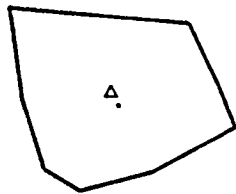
DL 148



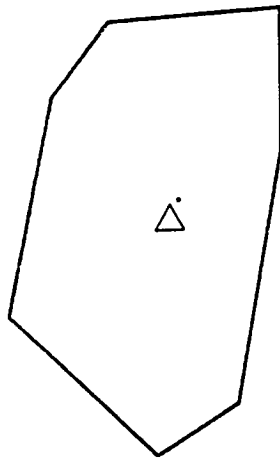
DL 149



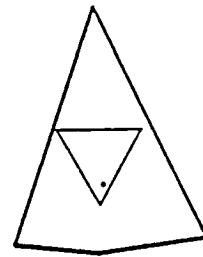
DL 150



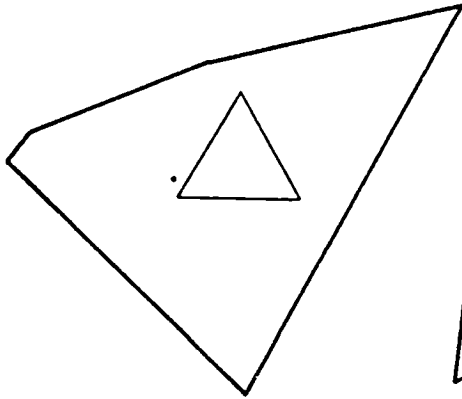
DL 151



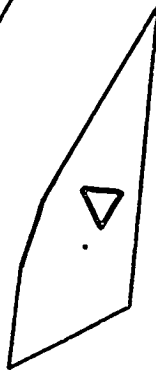
DL 152



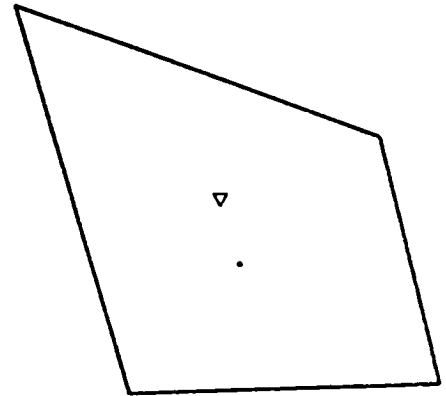
DL 153



DL 154



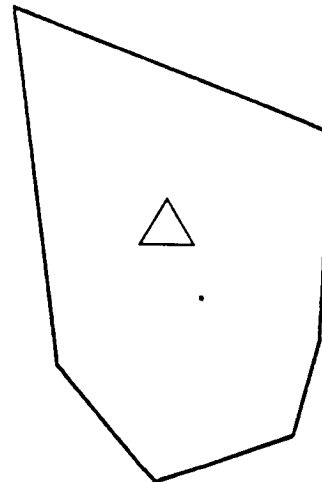
DL 155



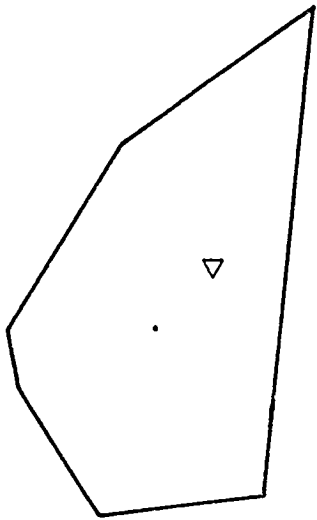
DL 156



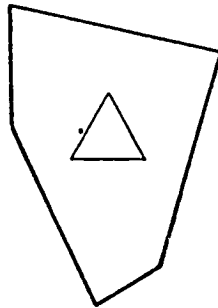
DL 157



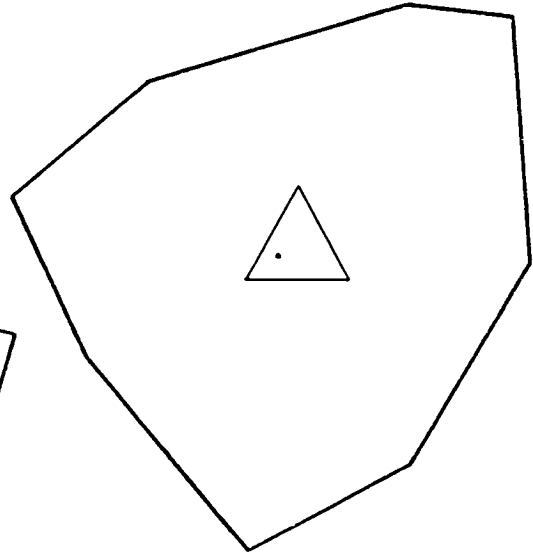
DL 158



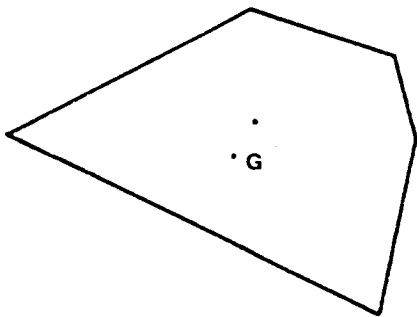
DL 159



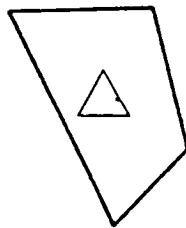
DL 160



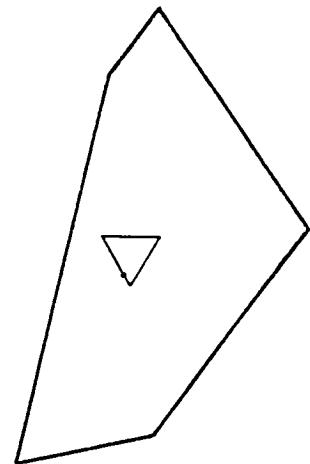
DL 161



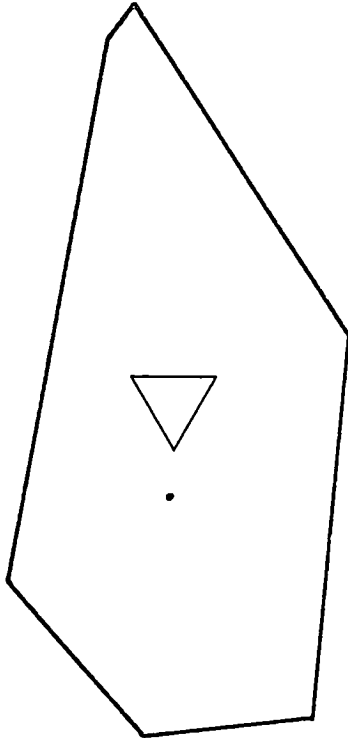
DL 162



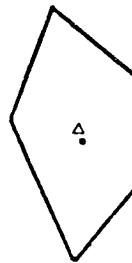
DL 163



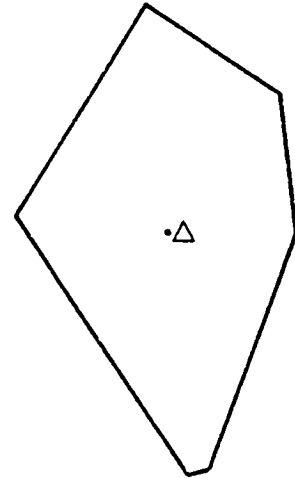
DL 164



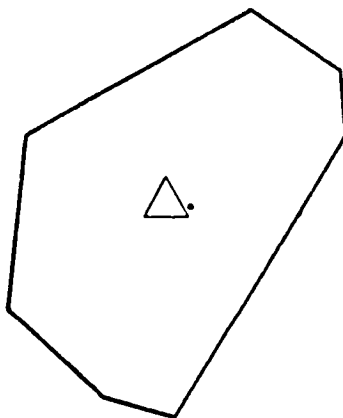
DL 165



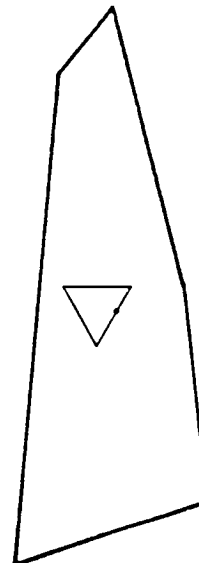
DL 166



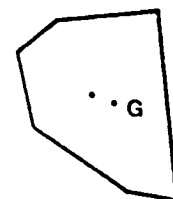
DL 167



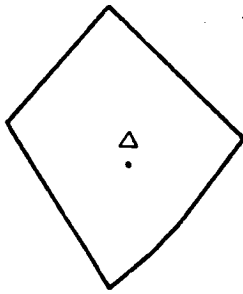
DL 168



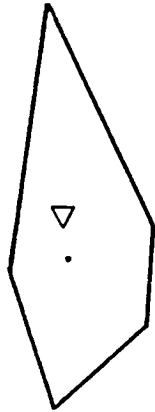
DL 169



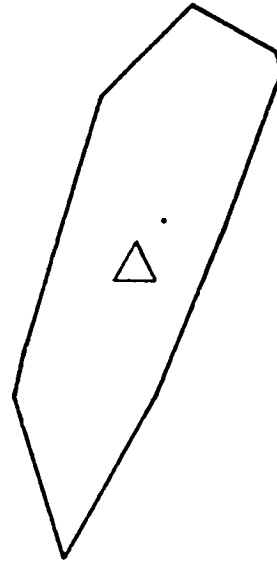
DL 170



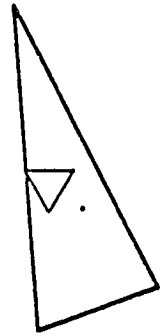
DL 171



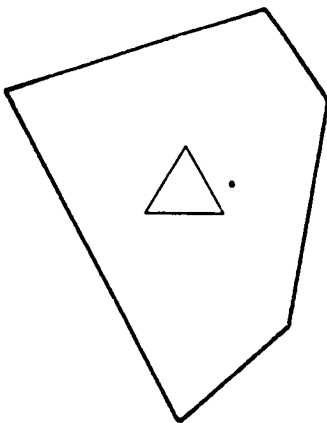
DL 172



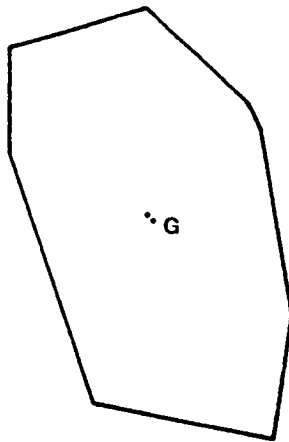
DL 173



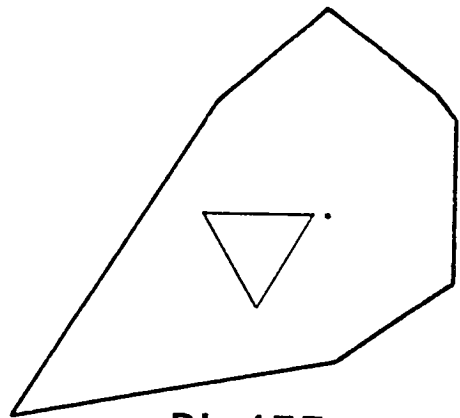
DL 174



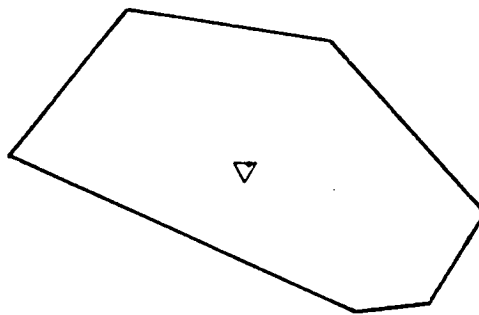
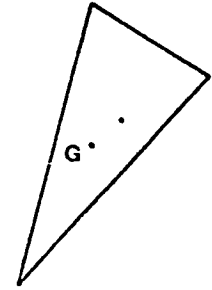
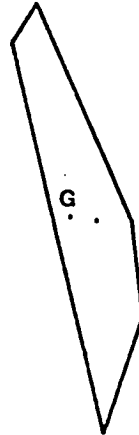
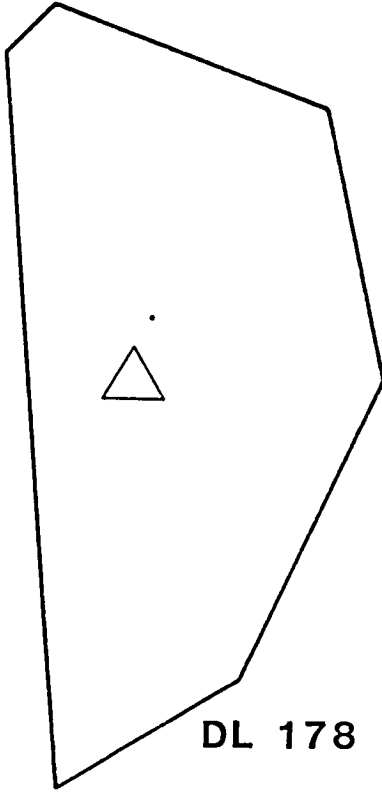
DL 175

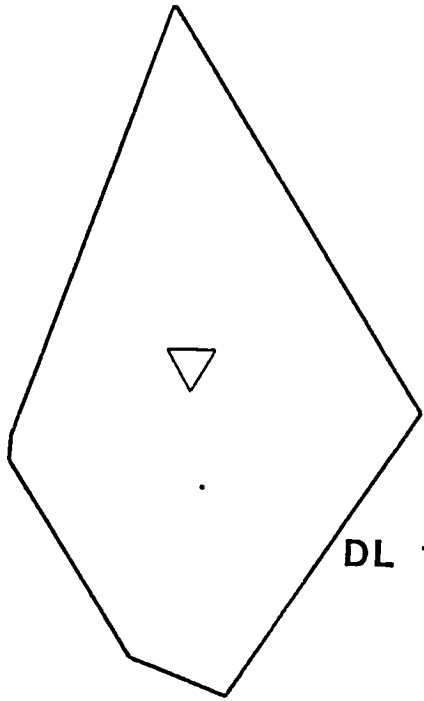


DL 176

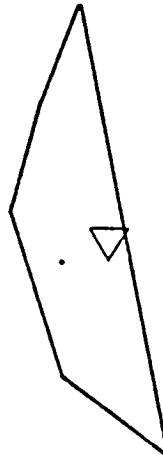


DL 177

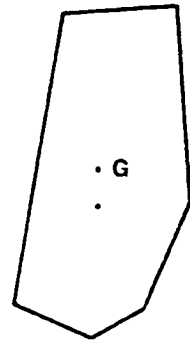




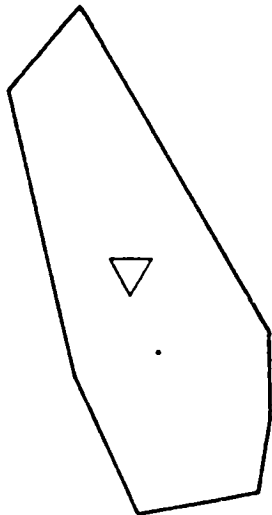
DL 184



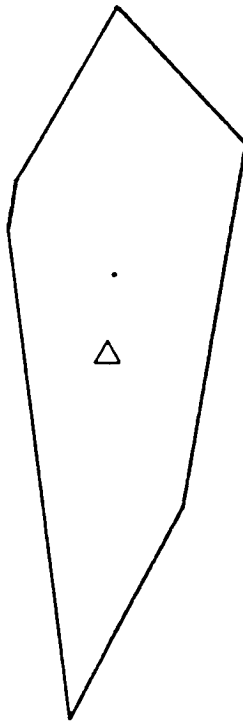
DL 185



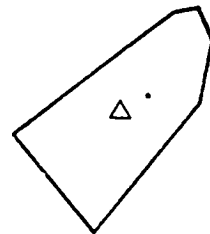
DL 186



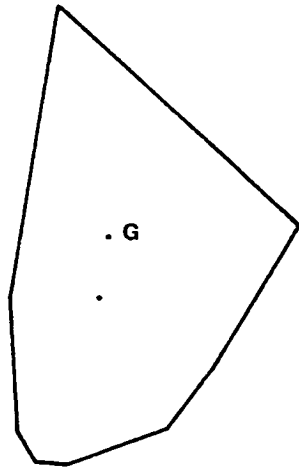
DL 187



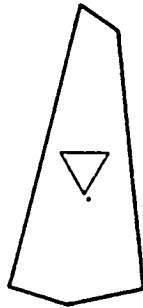
DL 188



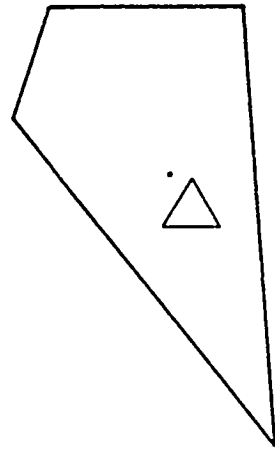
DL 189



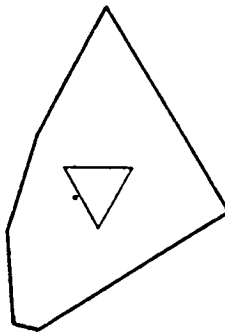
DL 190



DL 191



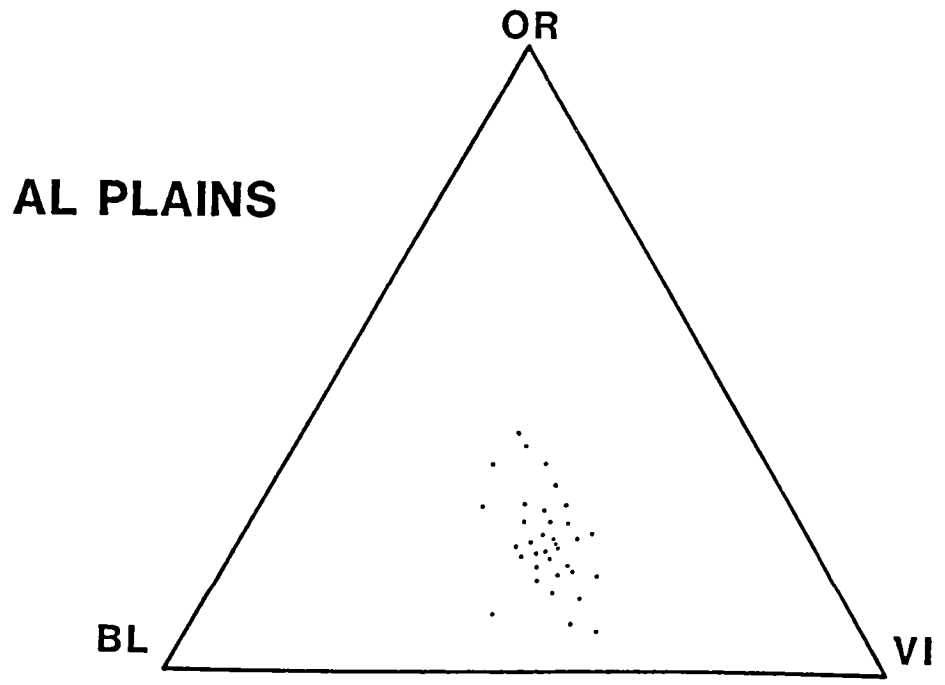
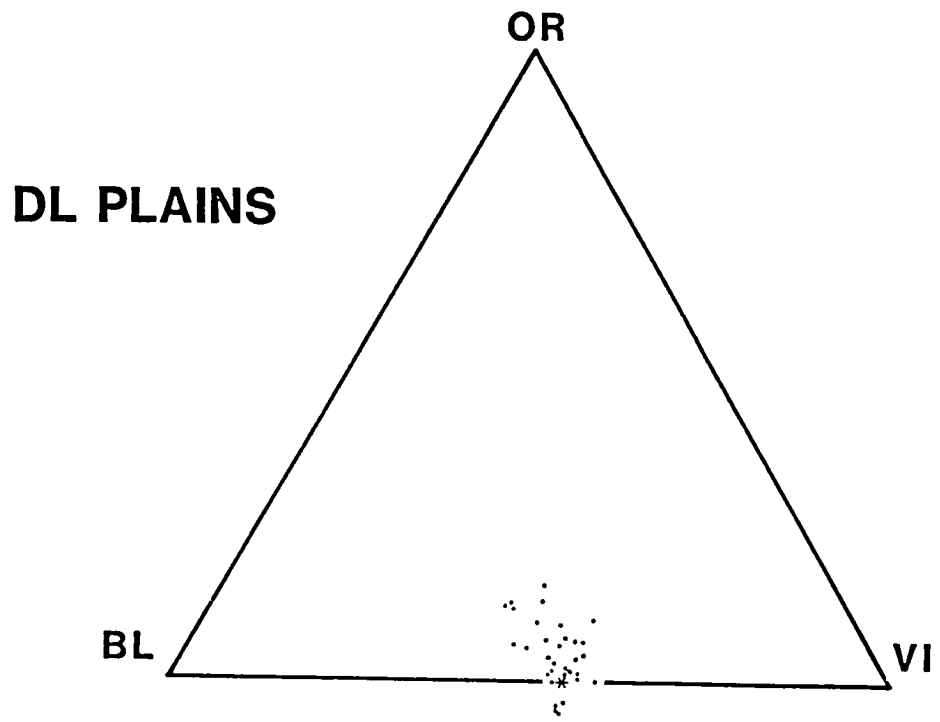
DL 192



DL 193

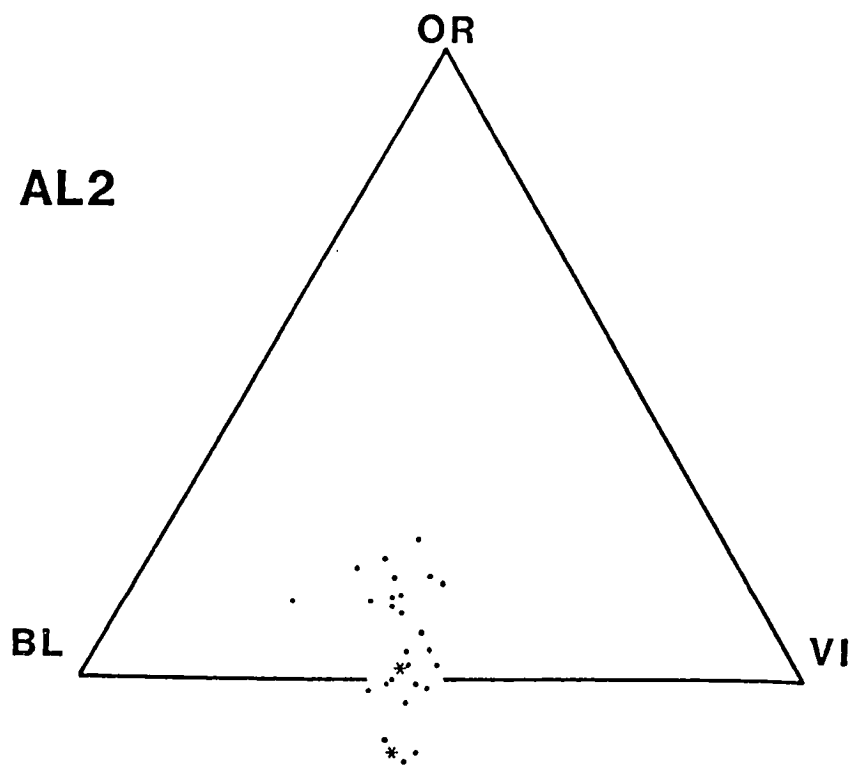
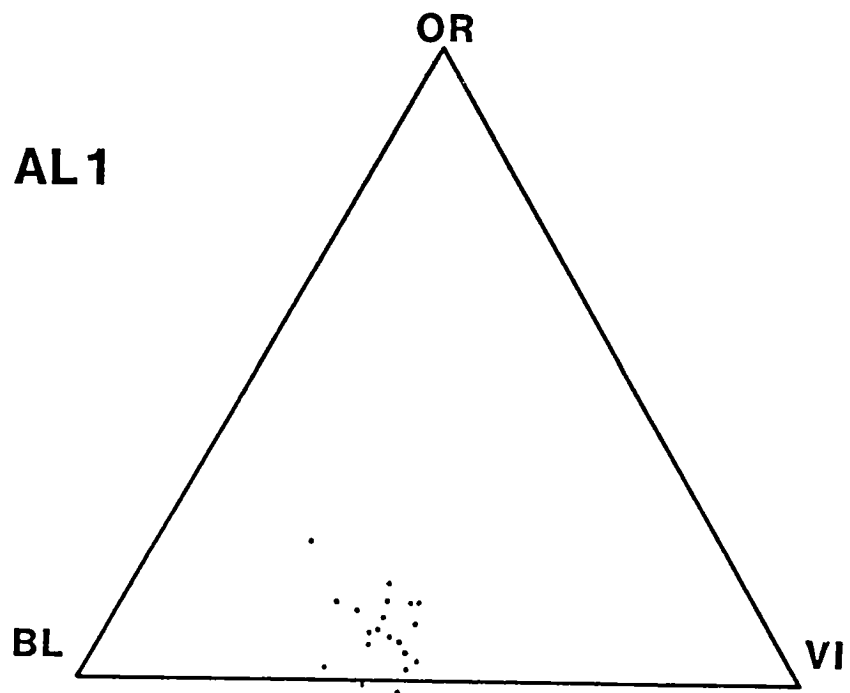
A P P E N D I X C

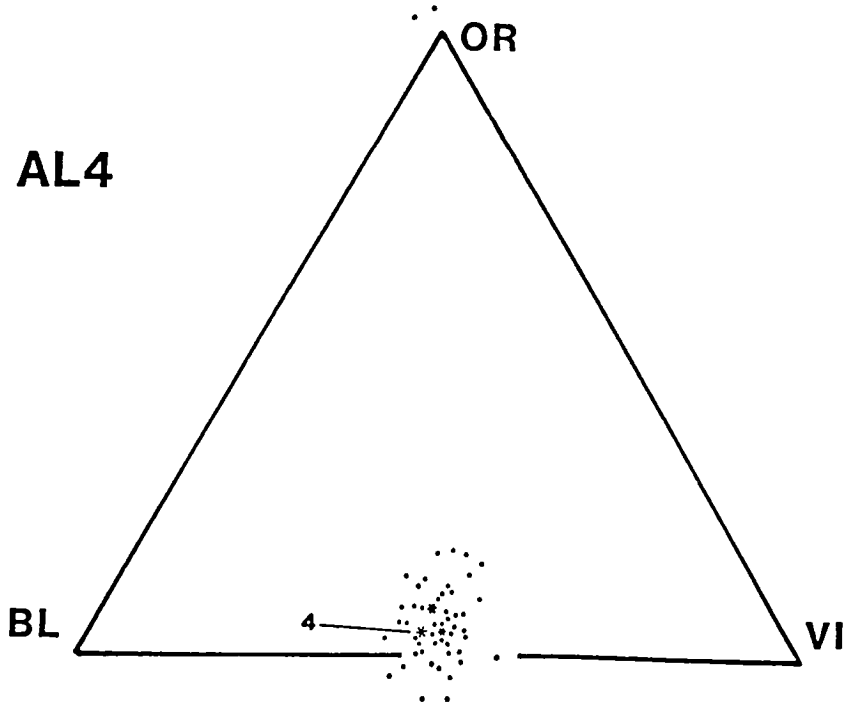
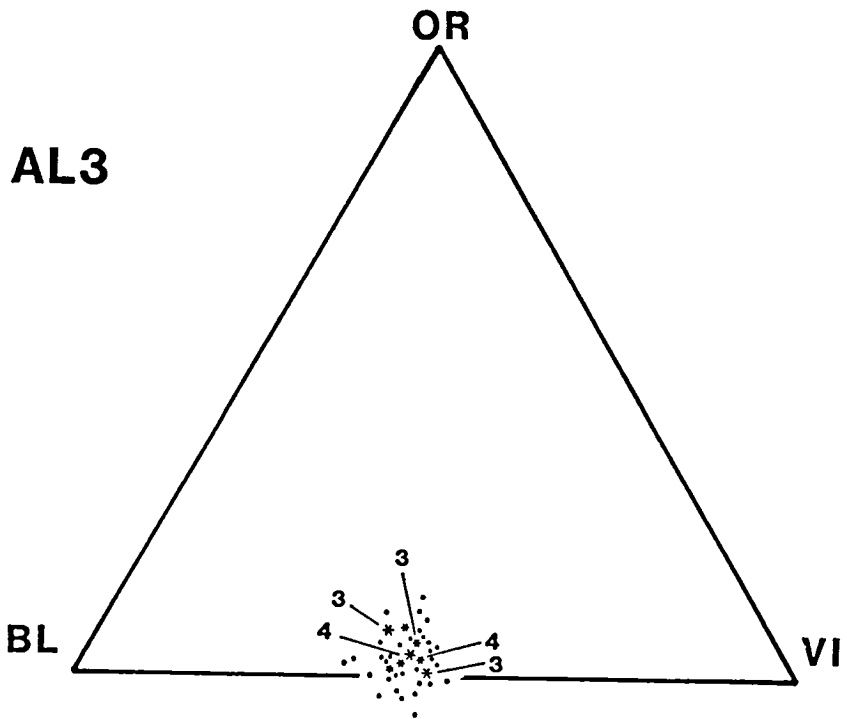
Relative spectral reflectance plots on the reference ternary diagram for Europa's plains unit in (A) the dark lineation study area, and (B) the Agenor Linea study area.



A P P E N D I X D

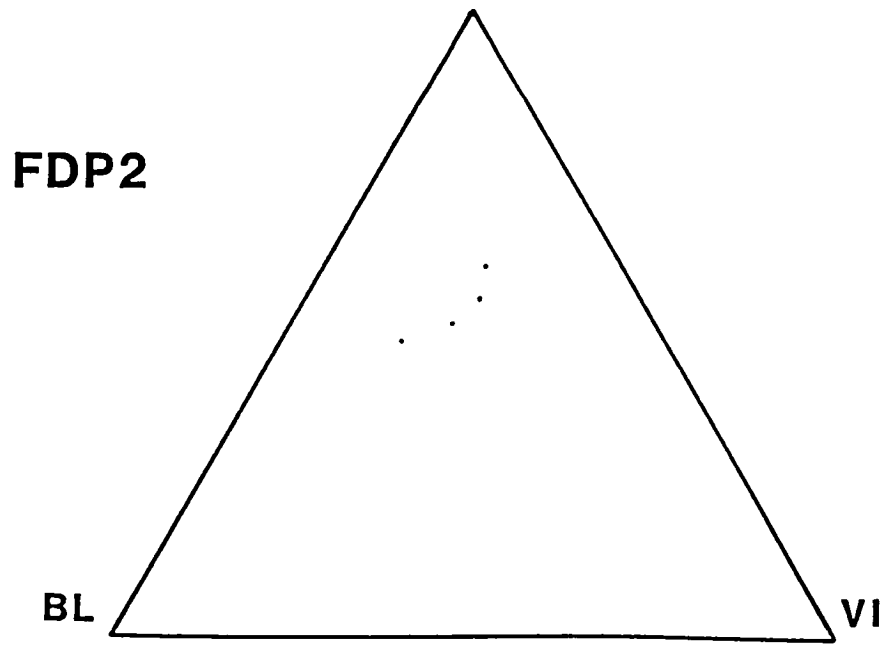
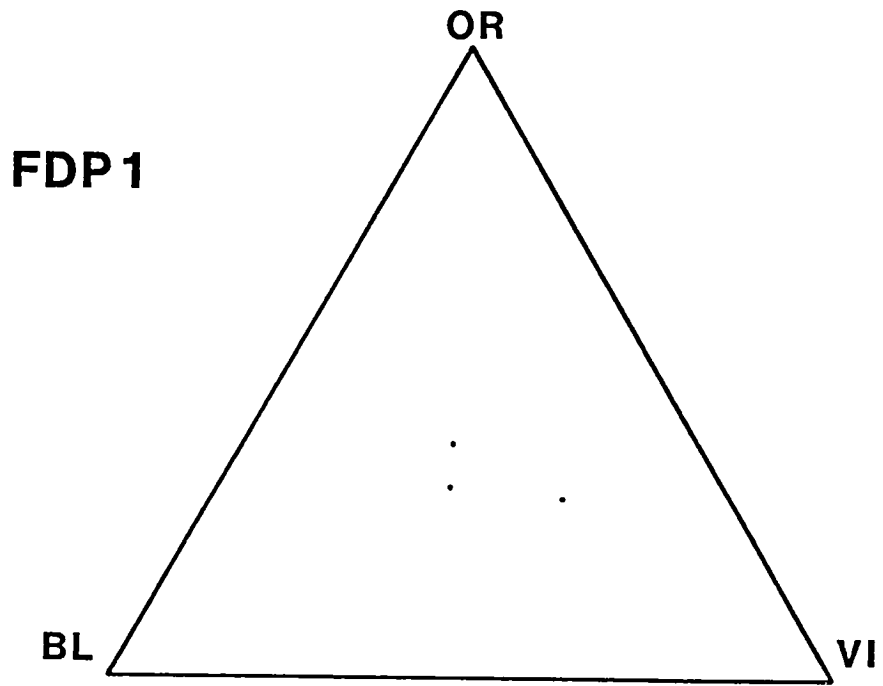
Relative spectral reflectance plots on reference ternary diagrams for profiled segments of Agenor Linea. Separate plots were used to reduce photometrically-induced errors in rel%'s over the large range of longitude covered by Agenor Linea. Profiled segments of Agenor Linea cover pixel sequences: (A) 1-20 (the southwesternmost portion of the feature), (B) 21-50, (C) 51-106, (D) 107-162 (the easternmost portion). These pixel numbers correspond to those in the lengthwise compositional variation map of Agenor Linea in Figure 20.

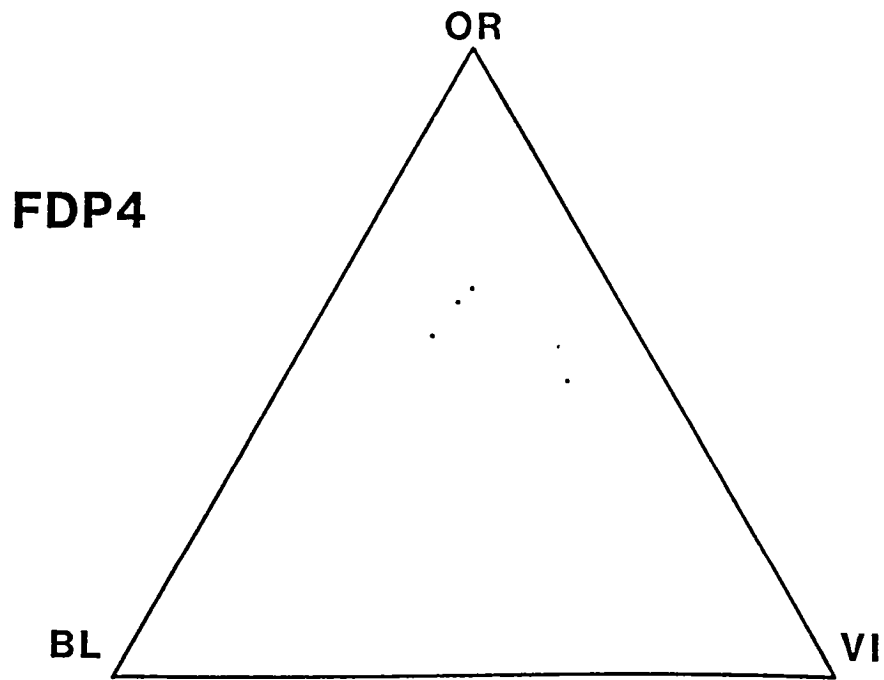
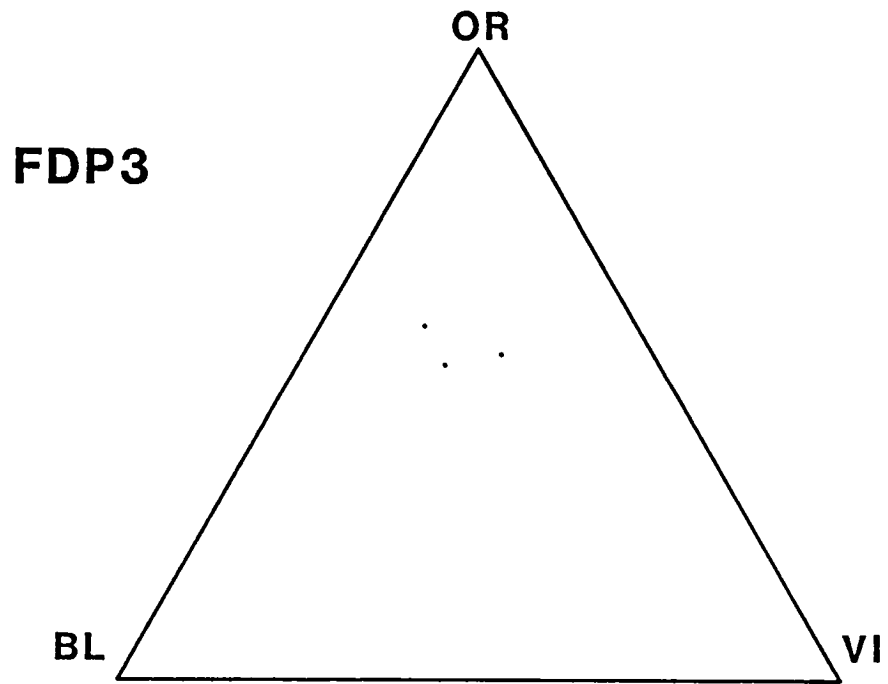


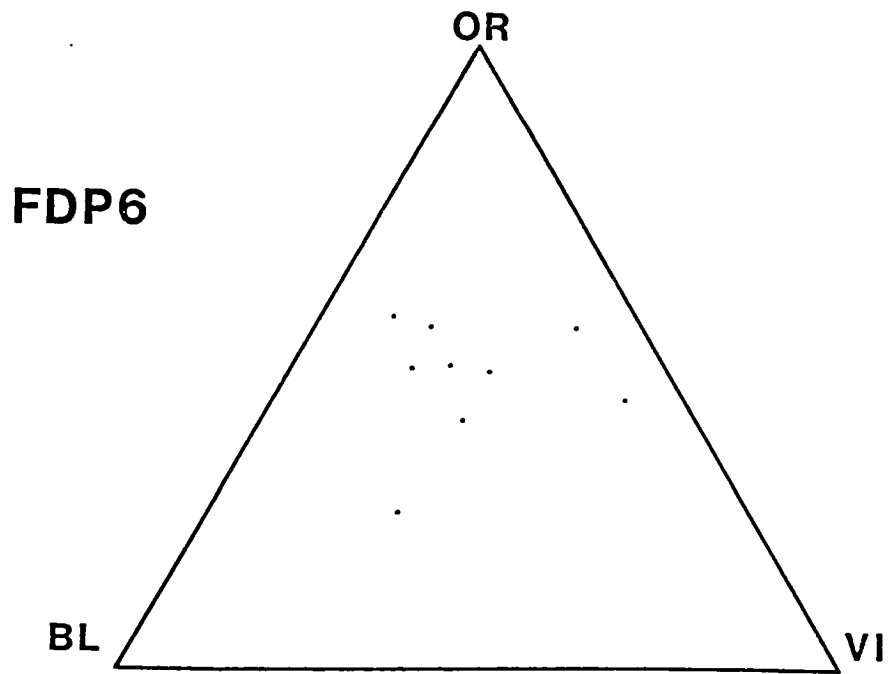
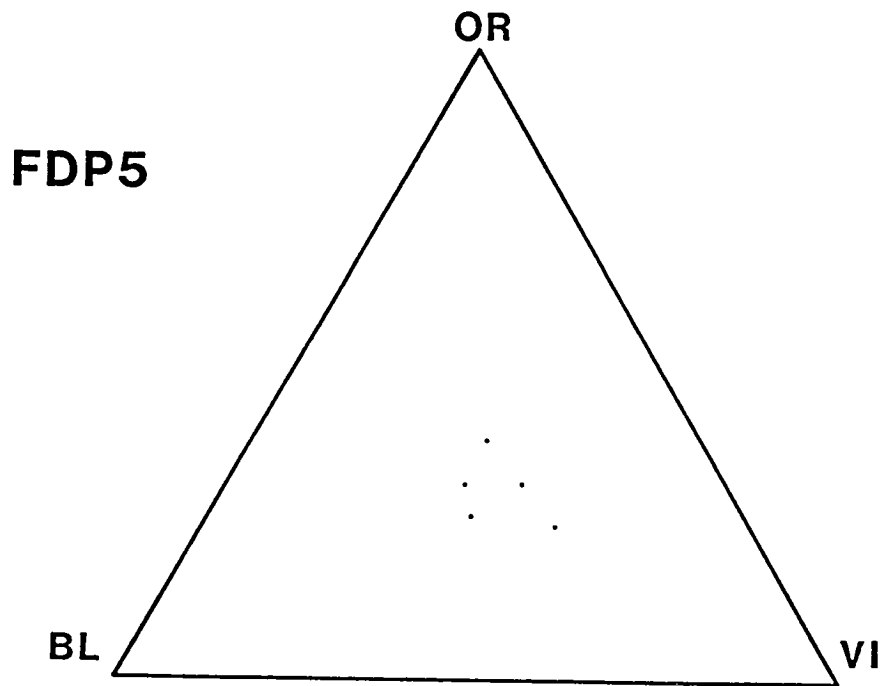


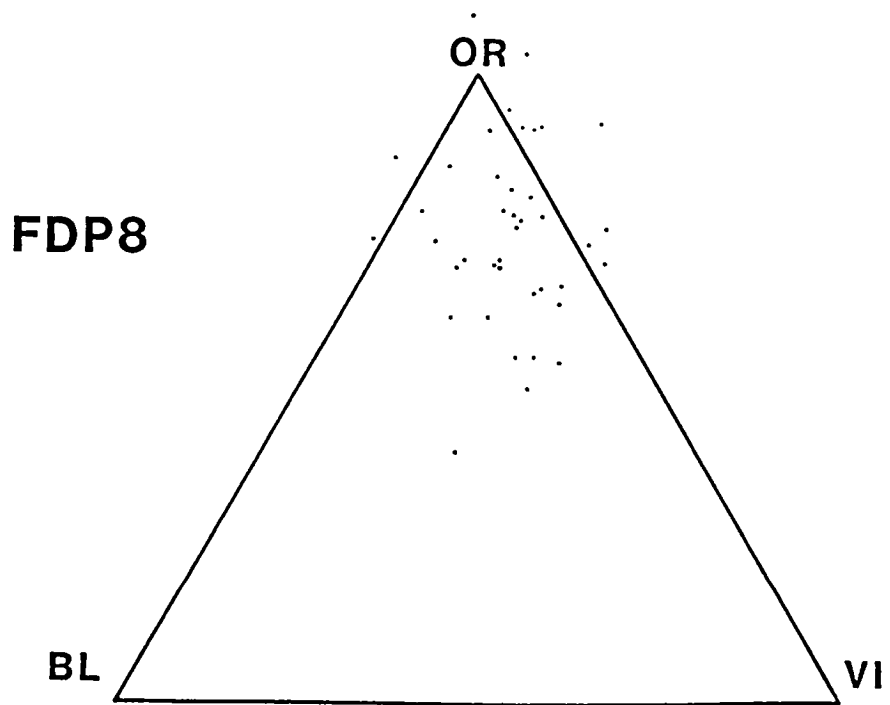
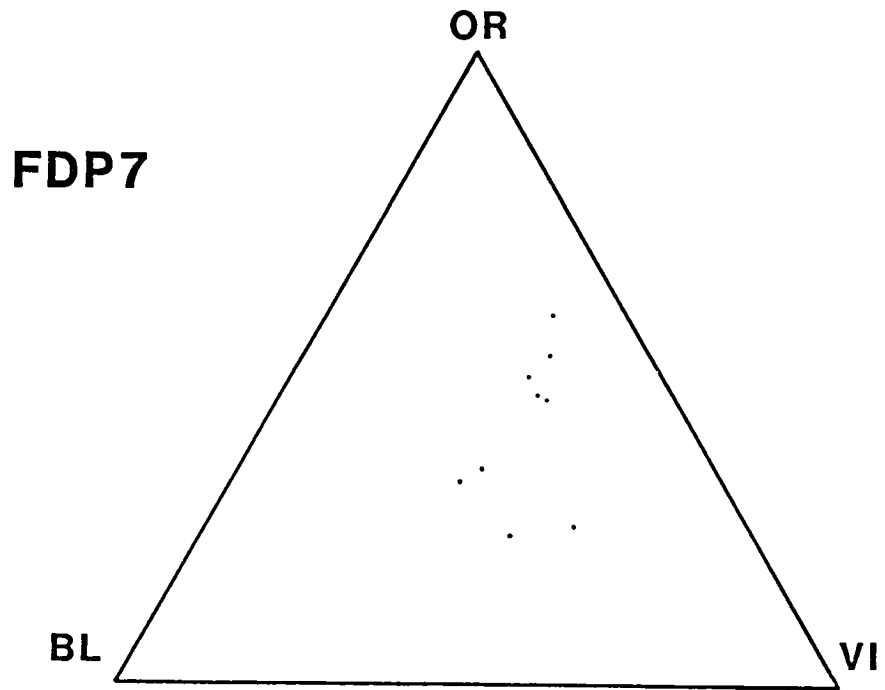
A P P E N D I X E

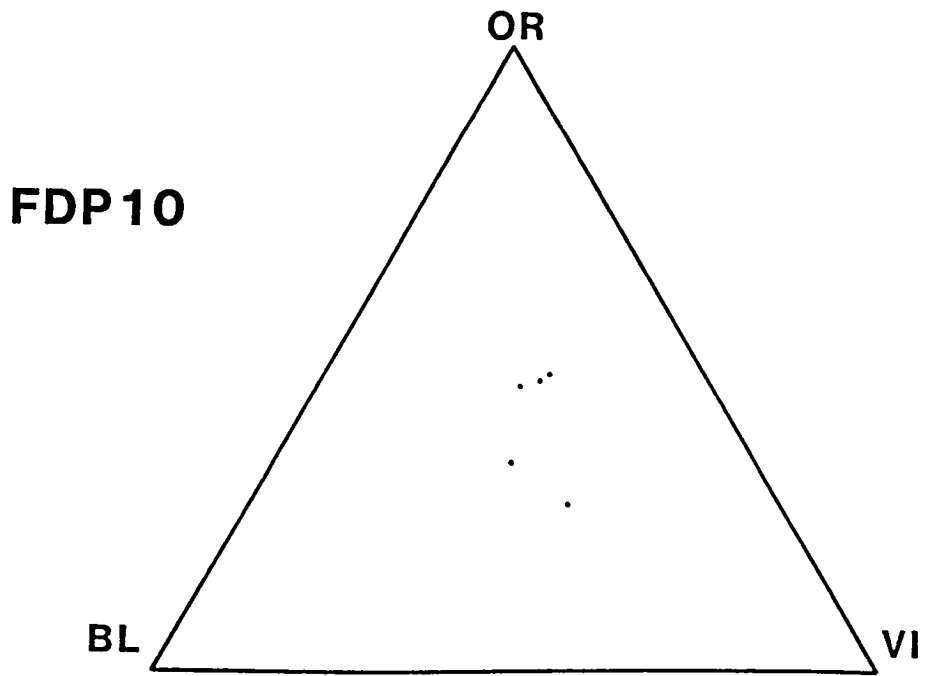
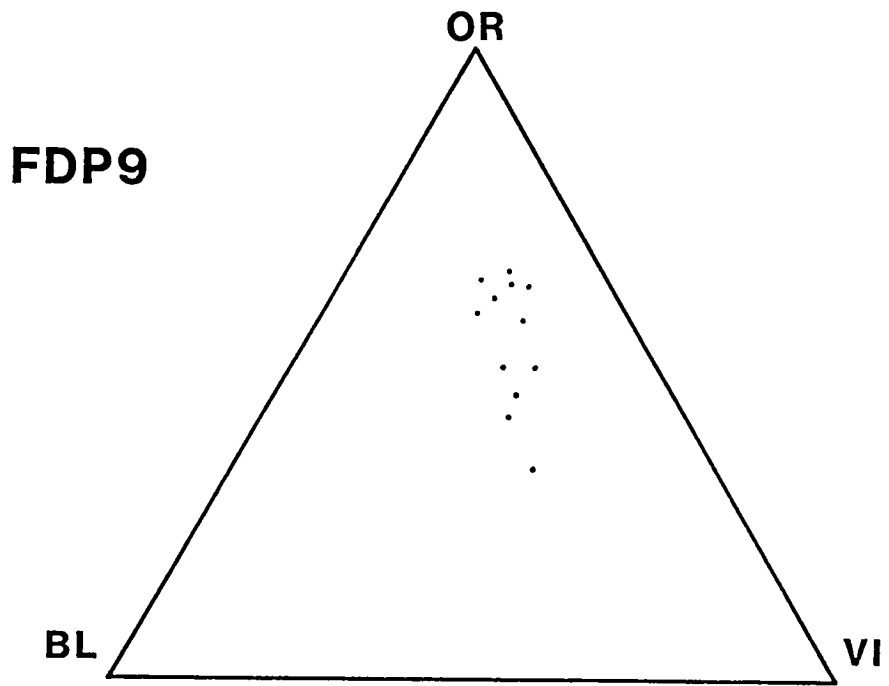
Relative spectral reflectance plots on reference ternary diagrams for profiled flanking dark patches (FDP's) of Agenor Linea. The location of each FDP can be found on the map of the Agenor Linea area in Figure 18.











STRUCTURAL CONTROL OF VALLEY NETWORKS ON MARS
Virginia Gulick, c/o V.R. Baker, Department of Geosciences
University of Arizona, Tucson, Arizona 85721

Groundwater sapping is one of the most widely accepted hypotheses proposed in order to explain valley network formation in the heavily cratered terrain on Mars. The most compelling evidence in favor of this process is the presence of blunt, theater-headed tributaries, which commonly exhibit strong structural control.

Schultz (1982) suggests that the morphology of the valley networks on Mars can be explained by the presence of deep-seated fracture zones of ancient multi-ring basins, which have long been concealed by basin ejecta. He concludes that the formation of the valley networks by sapping has since re-exposed these ancient fracture patterns.

The goals of this project are: (1) to study the structural control of the valley networks and to determine any implications that this control might have for Mars' early fluvial history; (2) to test on Schultz' hypothesis by relating his ancient multi-ring basins to the formation and control of valley network morphology; and (3) to determine if the structural control of valley networks is also related to the formation of the established basins listed in Croft (1979).

In order to evaluate the structural control of Valley networks, orientations of channel-segments and fractures were measured. On a planet-wide basis, azimuth frequency diagrams of channel-segment orientations reveal no major trends (figure 1). However, on a more local scale, azimuth-frequency diagrams seem to indicate well-defined structural control (figure 2 and 3).

In order to determine whether Schultz' basins and/or the basins listed in Croft are related to valley network morphology; structural trends and major flow directions of the valley networks were determined. The results were compared with possible fracture patterns which might have formed from these impact basins. Fracture patterns from impact basins normally are concentric and radial to the associated basin center.

Two of Schultz' basins, Chryse and Ladon, seem to strongly control the morphology of the surrounding valley networks. The valley networks located in quadrangle 10 of the U.S.G.S. photomosaic series (1:2M) suggest structural control by Chryse, while several in quadrangle 19 appear to be controlled by Ladon (figure 2). The valley networks in these two regions exhibit both radial and concentric major trends and flow directions.

In addition to the apparent control of valley network morphology by multi-ring basins, the established basins listed in Croft (1979) appear to have this same control. Two of these basins, Hellas and Isidis, seem to control the morphology of the valley networks within and near their main rims. Hellas, with a main rim diameter of approximately 3678 kilometers may also be controlling the major structural trends of the valley networks to the northwest of its main rim (figure 3). However,

the major flow direction of these valley networks is away from the basin and follows the regional slope of the planet. This suggests that the formation and control of the valley networks may be the result of more than one process which operated during Mars' early tectonic history.

The exact cause of the structural control of the valley networks is not known, but this study suggests that this control may be the result of deep-seated fracture zones of ancient impact basins which predate the Tharsis Uplift. Fracture patterns initiated by the formation of impact basins may have been modified by Tharsis. In addition, new fractures formed by Tharsis, further complicated existing fractures by initiating new ones, which may themselves have been preferentially controlled by ancient deep-seated multi-fracture zones.

References:

Croft, Steven K., Impact Craters from Centimeters to Megameters, University of California at Los Angeles Ph.D. dissertation, 1979.

Schultz, Peter et al, The Structure and Evolution of Ancient Impact Basins on Mars, JGR 87, 9803-9830, 1982.

Acknowledgements

I would like to thank Professor Robert Strom for all his helpful advice and support in this project and to thank him, Dr. Victor Baker and Nadine Barlow for reviewing this abstract. I would also like to thank Steven K. Croft for his conversation with me regarding his research on impact basins. Last but not least, I would like to thank the NASA Planetary Geology Undergraduate Research Program for giving me this fine opportunity to do planetary research.

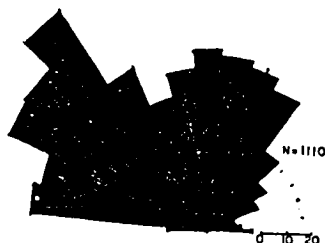


Figure 1. Orientations of channel segments for valley networks on Mars. Note the lack of planet-wide trends.

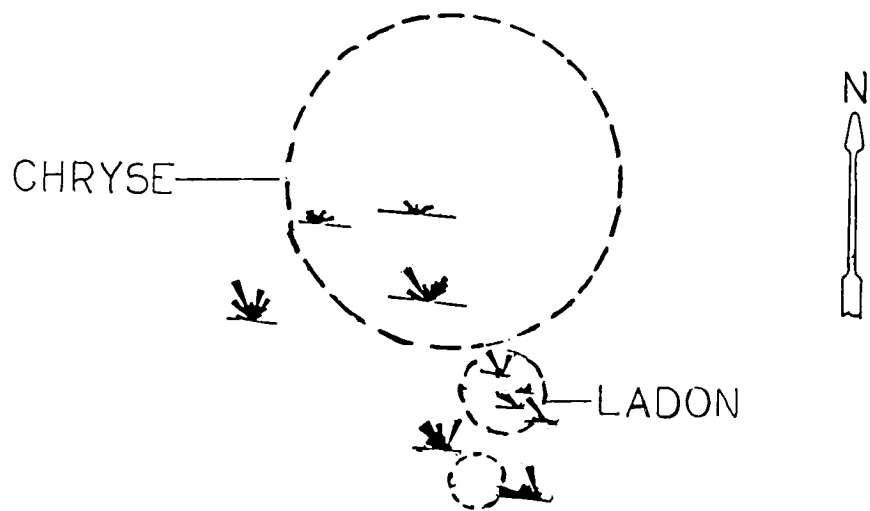


Figure 2. Chryse and Ladon basins (Schultz *et al.*, 1982) with locations and structural trends of nearby valley networks. The dotted lines show the approximate outer ring diameters of the basins (4300 km for Chryse; 975 km for Ladon).

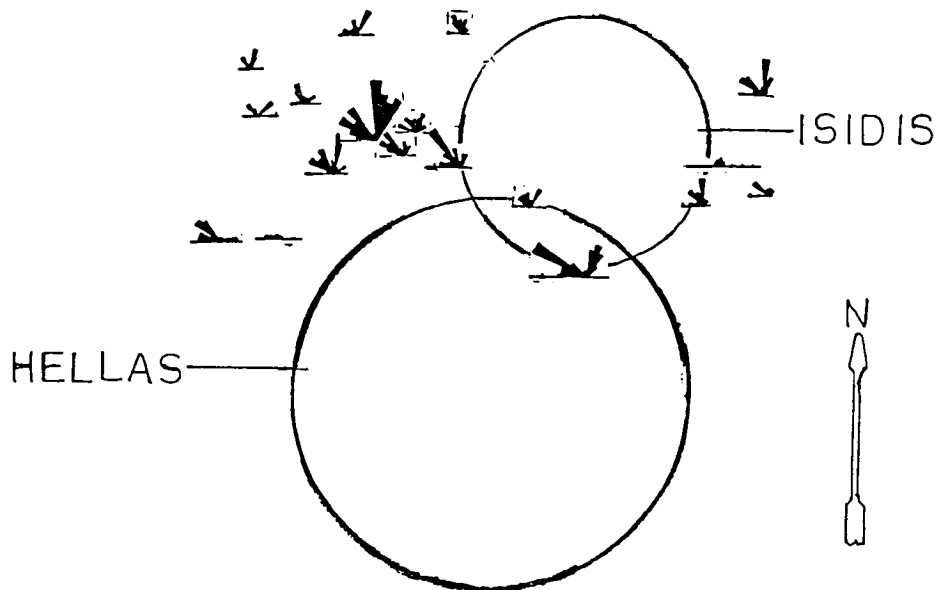


Figure 3. Isidis and Hellas basins (Croft, 1979) with locations and structural trends of nearby valley networks. The solid lines indicate the basin rim diameters (3678 ± 430 km for Hellas; 3000 ± 102 km for Isidis).

FLUX, RIPPLES, AND DUNES ON VENUS; S.J. Bougan, NASA-Ames Research Center, Moffett Field, California; PGGURP, Summer, 1983

Venus offers us the unique opportunity of studying the surface modifications of an entire planet by defining and simulating the aeolian processes presently operating on the surface. In such a study as this, one must first measure and define the process of flux (Q) across the surface of Venus: the mass moving past a point per unit time.

Flux measurements for Venus, for one particle size and wind speed, were divided into two types: Qa, saltation and traction loads, and Qb, the amount of material traveling in the bedforms. Qb is seven times Qa for Venus, in contrast to the Earth-like case where Qa and Qb are almost equal.

For the venusian case, Qb plots as a sinusoidal curve on a graph of total flux versus run time. This is a direct result of the bedforms moving off the plate and into the collector. Qa for Venus is also greatly affected by the bedforms - being extremely high upwind and falling to almost zero downwind of the crests, a characteristic highly suggestive of terrestrial dunes.

Bedform studies for one particle size and velocity led to the conclusion that dunes were forming under the venusian conditions. Ripples formed at earth-like conditions with a distinct region devoid of bedforms between the earth-like (2 bar) and venusian (30 bar) conditions. This region is most likely analogous to the region between ripple and dune formation on earth, a region of intermediate velocities.

INTRODUCTION

The surface of Venus, as seen through the instrumentation of the Soviet Venera landers, is a hot, dry desert with surface temperatures and pressures of $735^{\circ} \pm 3^{\circ} \text{K}$ and 90 ± 2 bar respectively. The only geological processes presently known to be operating on the surface are aeolian - deflation, abrasion, and deposition of and by sand of primarily basaltic composition. Defining and simulating the effects of this aeolian environment provides us with the unique opportunity of studying venusian surface modifications on a global scale.

Very little work has been done to study aeolian processes now active on Venus. The Venus Wind Tunnel (VWT), a facility at the NASA-Ames Research Center, is used to carry out research on aeolian processes under simulated venusian conditions. Threshold wind speeds have been determined for range of particle sizes and some preliminary flux measurements have been made.

Objectives of Study

The objectives of this study are:

- (1) to determine and compare the time and spatial dependence of the total flux (Q), the mass of material moving past a point during a specified time, of windblown particles for simulated venusian surface conditions and compare these to terrestrial conditions;
- (2) to separate the total flux (Q) into its distinct components: Qa = saltation and traction loads, and Qb = the material moving within the bedform.

- (3) to begin preliminary studies on the bedform morphology; and
- (4) to define the region between the 2 and 30 bar where no bedforms develop.

EXPERIMENTAL EQUIPMENT AND PROCEDURES

Venus Wind Tunnel - VWT

The conditions on the surface of Venus are CO₂ gas at 90 bar (1306 psi) and 480°C; conditions very difficult to duplicate or control in a laboratory. However, since density and velocity of a transporting medium determine the rate of sediment movement, both the temperature and pressure of the gas could be reduced, keeping the density constant. VWT was designed to operate at ambient temperature; the pressure could then be reduced to 30 bar (445 psi) and the CO₂ density would be the same as the atmospheric density on the surface of Venus. The only parameter not duplicated was the viscosity of the gas, which also affected the Reynolds number, the unit Reynolds number in the tunnel being approximately twice the unit number on Venus.

Collector

The collector used throughout the experiments consisted of a metal ring which fit inside the tunnel directly downwind from the test section, with a nylon bag filtering cloth, mesh size of 18 μm (nominal) and 23 μm (absolute). The collector was removed between experiments and the sand collected was weighed.

Sand

The sand used in the experiments was fine whole-grained silica sand. It was sifted and separated into the size range 61 μm to 88 μm . This size was used because it saltates at the lowest wind speed measured on Venus.

Procedure

The wind tunnel floor plate is 19.5 cm wide and 126 cm long and was taped securely inside the test section throughout the experiments. Two kilograms of sand were weighed out, placed on the plate, and smoothed to form a relatively flat surface. This procedure was repeated at the beginning of each separate set of runs.

Flux measurements: The tunnel was filled with CO₂ gas to approximately 30 bar (445 psi). The threshold freestream velocity (U_{ot}), defined as the velocity at which most grains were observed to be saltating, was determined for that density. Three sets of runs of varying time increments were then conducted at 1.2 x U_{ot} (threshold freestream velocity), and one set of runs at 1.6 x U_{ot} and 30 bar.

For the earth-like runs, the tunnel was filled with CO₂ gas at 17 bar and then the pressure was reduced to 2 bar. This insured an even mixture of approximately 95% CO₂ and 5% air. Two bar pressure was used for the earth-like experiments because the tunnel was unable to achieve threshold freestream velocity at 1 bar with the collector in place. Two sets of runs, of varying time increments, at 1.2 x U_{ot} were completed after U_{ot} was determined for the new density.

Bedforms: Following each run, the plate was photographed to illustrate any modification of the surface. Sketched of the plate were made for runs # 3, 4, and 5 at 30 bar and runs # 1 and 2 at two bar. The dimensions of the bedforms - wavelength and height - were also recorded.

Transition Zone: A series of runs was conducted to bracket the region between 2 bar and 30 bar which was devoid of bedforms. Tests were run for five minute intervals at 27, 23, 20, 17, 13, 10, 7, and 3.5 bar. Between each run the bed was photographed, the dimensions of the bedforms recorded, and the bed smoothed for the next run.

EXPERIMENTAL RESULTS

Flux

Particles at 2 and 30 bar were determined to travel by two separate modes: Qa includes saltation and traction loads and Qb includes the material moved in the bedforms. This was first suggested by early data deviation during the venusian runs and substantiated through further runs at smaller time intervals, varying densities, and comparison of bedform movement with the data deviations.

At 30 bar, Qb, at its peak, was approximately seven times Qa. The plot of total flux (Q) against total run time (at 30 bar) resembles a sine wave, with maximum (Qb) measurements defining the crests and minimum (Qa) measurements defining the troughs. The time interval between the crests of the wave corresponds with the velocity measurements recorded for the bedforms - crest to crest.

The amount of material carried in saltation and traction, Qa, was much more difficult to define. At 30 bar, the vast majority of moving sand travels in the bedforms. Qa is very small for Venus, in contrast to the 2 bar case where Qa and Qb are almost equal. This suggests that aeolian processes on Earth are more effective in transporting in material in saltation and traction than on Venus.

Not only does the magnitude of Qa differ between 30 and 2 bar, but also its spatial dependence. At 2 bar, Qa was constant over the bedforms - it was not observed to vary over the length of the plate. However, at 30 bar, Qa varied from one end of the bedform to the other. Qa was observed to be extremely high on the upwind end of the bedform and then fall to almost nothing as the particles dropped over the crest - a characteristic very similar to terrestrial dunes.

Bedforms

During the early runs at 30 bar, the bedforms were simply referred to as ripples. However, as the experiment progressed, it became apparent that the bedforms were not behaving as ripples. Erosion was high on the upwind surface and the particles rolled or bounced quickly up to the crest. Once there, they dropped over the slip face and came to rest. The Venus ripples were analogous to dunes on Earth.

At 2 bar, the bedforms were considered to be ripples. Erosion was high on the upwind surface and dropped in intensity on the downwind surface.

Bedform Variation with Changing Density

Between 2 and 30 bar there was a region devoid of bedforms. From 30 to 23 bar the bedform morphology remained constant - on large dune at the leading edge

of the plate and smaller dunes along the length of the plate. Between 20 and 17 bar was a region of mixed dunes and low relief wave forms, a transition zone. Then between 13 and 7 bar there was a region practically devoid of any recognizable bedforms. The large dune at the leading edge of the plate, so characteristic of the the higher density runs, disappeared below 13 bar.

Below 7 bar, ripples began to appear, and were the dominant bedform on down to 2 bar. The large dune was replaced by two low, parallel ridges.

It was also noted that wavelength and height of the bedforms varied directly with increasing pressure. The transition zone (between 20 and 17 bar) defined by varying wave height and constant wavelength over the range of densities.

CONCLUSIONS

A flux pattern was defined for simulated venusian conditions for one particle size range and one wind speed, and can be applied to the venusian surface (for those parameters) for first order approximations of flux rates. A flux range at 2 bar, using these same parameters, allows for some comparison. Observed total flux at 30 bar is approximately on half the total flux at 2 bar, suggesting that sediment movement by aeolian processes on Venus is about one half that observed on Earth.

Preliminary studies of bedform morphology under simulated venusian conditions were begun. Bedforms evolved at 30 bar resemble terrestrial dunes.

A region basically devoid of bedforms was identified between 7 and 13 bar. Increasing density produced dunes (up to 30 bar) and decreasing density produced ripples (down to 2 bar). This region could be analogous to that found on earth between ripples and dunes, a region of intermediate wind speeds where no bedforms develop.

Further work needs to be done on venusian flux measurements - for both different particle sizes and wind speeds. This study provides a basic starting point for additional research in this area. More detailed studies on the bedform morphology should be done, including the effects of density/pressure changes, again with varying particle size and velocity. This research could prove extremely helpful in understanding ripple and dune initiation, a process which has long puzzled geologists.

E. Ann Kirkpatrick

09/09/83

MORPHOLOGICAL FEATURES OF TERRESTRIAL AND MARTIAN LANDSLIDES

Introduction

The specific mode of failure of landslides and the morphological features of the resulting deposit will depend, among other things, upon the physical properties of the failed material, such as its lithology, degree of weathering, presence and location of joints and other discontinuities, and the amount of interstitial water present. Therefore, the morphological features of a landslide deposit should be able to be used to imply something about these properties. It is hoped that the morphology of the martian landslides as observed on the Viking Orbiter images can be used in such a way.

Terrestrial Landslides

In order to make useful observations and analyses of martian landslides, a knowledge of terrestrial landslides is essential. I undertook a review of the geologic literature on landslides in order to try to determine the relationships between mode of failure, geological material, and morphological features. A brief summary of the results of this literature search is given below.

Landslide modes of failure can generally be divided into three categories: falls and topples, slides (both rotational and translational) and flows (Varnes, 1958, 1978). Any one slide may involve just one mode of movement or a combination.

Falls and topples typically involve highly fractured rock or a newly detached mass that fails along a discontinuity parallel to the cliff face (Brunsden, 1979). They leave steep free faces at the head scarp, and talus slopes at the base of the face. The role of water is chiefly as a facilitator of weathering.

Rotational slides occur in thick, homogeneous, cohesive materials such as clays. The head scarp is steep and U-shaped, and the failed mass usually does not show much distortion. There may be transverse tension cracks at the foot, and bulging at the toe. The head area consists of large slump blocks that are tilted backwards (Brunsden, 1979; Rib and Liang, 1978).

Translational slide movements occur on discontinuities that parallel the slope surface, such as dipping bedding planes or the bedrock-slope debris interface. These slides are associated with high water tables, and debris slides may develop into debris avalanches if the water content is high enough and the slopes are steep enough. In this case, the initially sliding debris starts to flow with high velocity down stream channels and valleys. Mudslides are a type of translational slide that surge forth seasonally. They consist of an upper supply area, a central neck with discrete shear surfaces, and a bulbous, lobate toe with radial and transverse cracks (Brunsden, 1979).

Flows involve loose debris or weak, easily weathered rock, and can be either wet or dry. Debris flows begin as heavily laden streams of water that follow existing drainageways. More material is picked up in long neck areas, and is deposited downslope as long narrow lobes with lateral levees of coarser material (Varnes, 1978). Flow deposits are generally smoother than slide deposits, lacking transverse cracks and ridges; however, radial flow lines are usually present (Rib and Liang, 1978).

Complex landslides that begin as large rock falls or slides, and which then disintegrate and spread out at high speeds over long distances and cover large areas have been intensely studied. In spite of this, the mechanism that allows these "catastrophic rock-fall-avalanches" to travel a distance farther than that predicted by the energy generated during their fall, remains poorly understood. Shreve (1966, 1968) proposed that the slide or fall leaves the ground at a sudden steepening of slope, trapping and compressing a cushion of air beneath it. This provides a low friction surface that allows the debris sheet to travel the long distances.

Hsu (1975) postulated a mechanism of cohesionless grain flow, whereby kinetic energy is transmitted through contact of grains. The stress is not fluid transmitted; however, an interstitial fluid is necessary in this model to reduce normal stress and frictional resistance. Hsu suggests that dense dust may be a possibility for this fluid, as well as water, mud, or air.

Kent (1966) suggested fluidization with air, while more recently Melosh (1983) has suggested a process he calls "acoustic fluidization". Presumably acoustic energy builds up during the initial rockfall, resulting in pressure fluctuations due to sound waves that relieve the overburden pressure in places, allowing local failure to occur.

Some of these authors have described morphological features of these types of slide deposits, and their origins in terms of the mechanisms that they propose. Low lateral ridges are found on some of these slides. These may be analogous to levees at the edges of debris flows and lava flows (McSaveny, 1978; Voight and Pariseau, 1978); Shreve (1968) thinks that they reflect leakage of air at the edges of the slide. A low distal ridge is sometimes present; this is probably due to the sudden stop of the landslide, whether it be by sudden loss of air (Shreve, 1968), or a sudden change in

mechanical properties of the debris. Transverse ridges and folds dominate the entire surface of some deposits; these may be formed as the zone of impact travels back up the landslide (Shreve, 1968) or may reflect the arrival of successive waves of flowing debris (Hsu).

A lateral and distal scarp is almost always present. This indicates the sudden halt of the debris, and the cessation of fluid-type behavior. Transverse fissures have been observed, and longitudinal grooves were observed at several slides. The longitudinal grooves may indicate shear between substreams of debris or lateral tension as the debris settles (Shreve, 1968).

Martian Landslides

Eight areas of landslides were selected in Valles Marineris for preliminary mapping and study of their morphological features. A representative sample was aimed for; however, many areas of Valles Marineris are not covered by sufficiently good resolution images for this purpose. The images selected were assembled into mosaics, the maps were made, and the features noted. Four main types of morphological features of the deposits were identified. These are described below, in order of their usual appearance outward from the head scarp:

- 1) Large ridges in head area, transverse to direction of movement. Associated with large, wide horseshoe-shaped scarp. May be slump blocks or large pieces of the wall that fell or toppled. If these blocks are tilted backward, they would imply a rotational movement which occurs in homogeneous, cohesive materials.
- 2) Smaller ridges, convex towards distal edge of slide. Many have lobate pattern, and some may be step-like scarps rather than ridges. Are also found where a portion of the slide appears to have

flowed as a thick lobe down a narrow section of a canyon, as in the large, wide slides in western Ius Chasma.

- 3) Thin sheet-like debris cover; forms discrete fan shaped lobe with edge scarps where unconfined. Sheet reflects underlying topography, which in many cases appears to be edges of pre-existing flow lobes. Short transverse ridges and possibly fissures are sometimes present. Radial, longitudinal grooves, however, are very common.
- 4) Low, transverse, continuous ridges; may be folds. Found at distal edge of slides where the debris appears to be backed up against obstructions such as the opposing canyon wall, although not all such confined slides show this feature.

Any one landslide may possess from just one to all four of these features. Slides in Tithonium and Ius Chasmas, in western Valles Marineris, are usually more complex and show more of a variety of the features than do slides in more eastern sections of Valles Marineris, such as Coprates, Capri, and Gangis Chasmas. These differences may be related to the topographical and structural differences between these areas. Western Valles Marineris has greater relief of canyon walls (3-7 km), canyon walls are commonly highly ridged and gullied, and there are many shallow graben-like fractures paralleling the canyon on the plateau surface. Eastern Valles Marineris, probably due to its farther distance from the Tharsis bulge, has fewer graben on its surrounding plateau, and the relief of the canyon walls is lower, about 1-2 km. There is also less gully and ridge topography. Slides here usually lack head scarps and the large slump blocks, and the sheet-like debris lobes are the dominant feature. The deposits are also generally smaller in area and involve smaller volumes of material than landslides in western Valles Marineris.

Conclusion

It remains as a problem for future research to determine the significance of these features and their differences with different areas of Valles Marineris and with terrestrial landslides. This research may shed light into the properties of the material the slides are composed of and specifically its volatile content. As the proposed mechanisms for terrestrial long-run-out landslides currently stand, water is not a required element, although it may facilitate initial failure or subsequent flow. The flow lobes of the martian landslides and the flow-like morphology of the martian rampart craters may be of similar origin; this relationship also remains to be explored. The images and maps that I have assembled and prepared, and the research into the current state of thinking on terrestrial landslides will be a useful data base for further research.

References

- Brundson, D., 1979. Mass movements. In Embleton, C. and Thornes, J. B., Process in Geomorphology, pp. 130-186. Halsted Press.
- Hsu, K. J., 1975. Catastrophic debris streams (sturzstroms) generated by rockfalls. Geol. Soc. Amer. Bull. 86: 129-40.
- Kent, P. E., 1966. The transport mechanism in catastrophic rock falls. Jour. Geology 74:79-83.
- McSaveny, M. J., 1978. Sherman glacier rock avalanche, Alaska, U. S. A. In Rockslides and Avalanches (B. Voight, ed.), pp. 197-256. Elsevier, New York.
- Melosh, H. J., 1983. Acoustic fluidization. American Scientist 7:158-65.
- Rib, H. T. and Liang, Ta, 1978. Recognition and identification. In Landslides: Analysis and Control, pp. 34-80. Natl. Acad. Sci., Natl. Res. Council Spec. Rept. 176.
- Shreve, R. L., 1966. Sherman landslide, Alaska. Science 154:1639-43.
- Shreve, R. L., 1968. The Blackhawk Landslide. Geol. Soc. Amer. Spec. Paper 108, 47 pp.
- Varnes, D. J., 1958. Landslide types and processes. In Landslides and Engineering Practice (E. B. Eckel, ed.), pp. 20-47. Natl. Res. Council, Highway Research Board Spec. Rept. 29.
- Varnes, E. J., 1978. Slope movement types and processes. In Landslides: Analysis and Control, pp. 11-33. Transportation Research Board, Natl. Acad. Sci., Natl Res. Council Spec. Rept. 176.
- Voight, B. and Pariseau, W. G., 1978. Rockslides and avalanches: An introduction. In Rockslides and Avalanches (B. Voight, ed), pp. 1-63. Elsevier, New York.

LOCALIZED MEASUREMENTS OF GEOTHERMALLY ENHANCED
HEAT FLOW THROUGH REMOTE INFRARED IMAGING

by

Mark S. Marley
Division of Geological and Planetary Sciences
California Institute of Technology
Pasadena, California 91125

NASA Planetary Undergraduate Research Program Participant at

U.S. Geological Survey
Branch of Astrogeology
Flagstaff, Arizona 86001

August 31, 1983

Host: Dr. Elliot Morris
Advisor: Dr. Hugh Kieffer

LOCALIZED MEASUREMENTS OF GEOTHERMALLY ENHANCED HEAT FLOW THROUGH REMOTE INFRARED IMAGING

Information regarding a planetary surface's thermal characteristics can be obtained through remote infrared sensing of the surface. Infrared systems have been carried by Mariner, Viking, and Voyager spacecraft, while measurements of Earth are carried out by some meteorologic and Landsat satellites and scanners flown in aircraft, producing high resolution thermal images. One important result of infrared sensing is that information regarding anomalous geothermally enhanced localized heat flow can be produced which may provide valuable information about the volcanic activity of the region. Regardless of the surface being sensed, however, the problems, such as non-ideal surface emissivity, atmospheric absorption in the infrared spectrum, non-ideal viewing geometries, varying surface types, and varying seasonal characteristics, encountered in drawing quantitative conclusions based on data of this type are universal. A method for removing such complicating factors and quantifying excess thermal radiation produced by geothermal sources has been formulated and tested on thermal data acquired from digital infrared images of the Long Valley Caldera, California. If reliable, such a method would allow for periodic sensing to determine variations in heat flow from this geothermally active area.

Digital thermal images of the Long Valley area were produced by an infrared line scanner flown in an aircraft over the region in 1982. The line scanner sampled the surface below 738 times in each scan. A Mercury-Cadmium-Antimide detector which was sensitive to radiation in the 8-12 micrometer region was used in the scans. This region is selected since it is a natural "window" through the atmosphere which is generally opaque to infrared radiation. The scanner incorporated two black-bodies of known temperature

into each scan, thus allowing for temperature calibration to a resolution of about 0.1° C. Each sample, or pixel, is assigned a value between 0 and 255 with higher pixel values representing greater amounts of received infrared flux. The data is then recorded on magnetic tape for later retrieval. The motion of the aircraft, in a direction perpendicular to the scan plane of the detector, resulted in a two-dimensional data array which was built up one scan line at a time. An image which can be visually examined is then produced by assigning a specific shade of gray to each pixel value. The pixels are then printed on photographic film resulting in an image. The digital data can also be computer processed.

Before this data can be analyzed, however, certain inherent geometric distortions must be removed. Since the scanner obtains the samples at uniform increments in time, and therefore uniform increments in angle from the nadir, pixels away from the center of a scan represent increasingly larger areas on the ground. This is corrected for by a multiplicative factor which is based on the cross-track extent of any area of interest. If the area is not located on a level plane the observation is distorted further. Thus a topographic correction must be introduced. The angle between the normal to the surface of interest and the line of sight from the aircraft is used to determine and remove this source of distortion. When these corrections have been applied individual geothermal areas may be compared between differing flights and dates even if the observation geometries are significantly different.

With this corrected data, the excess radiation produced by local geothermal sources can be estimated. The general method is to compute the power produced in a core region which includes the geothermal area. From this power a reference power typical of the background is subtracted, leaving only the excess power produced by the geothermal feature. The background area used

for comparison is a border directly surrounding the core. It is assumed that the border material is thermally similar to the core material so that power comparisons may be made. Depending on which portions of the temperature distributions of the border and core are used in calculating power, maximum and minimum excess power estimates can be produced. These power estimates can then be compared between different viewing geometries and dates to determine the consistency of the estimates and to see if they exhibit any long term trends. The presence of long term trends is especially important in the Long Valley Caldera area which may be becoming volcanically active after a dormant period.

The method outlined above has certain advantages and disadvantages. Since the power of the core is compared to a surrounding border, seasonal variations which affect the overall temperature of the region are removed. Also since the core is compared with similar material nearby the difficulty of accounting for surface emissivity variations over a wide area is circumvented. The major difficulty with the excess power estimates is that, while they can be easily compared, they do not account for all of the energy released by the thermal area; energy from non-radiative loss is not accounted for. Examples are the latent heat of vaporization of water which is carried away by steam if fumaroles are present or the heating of the atmosphere which is removed by wind. These difficulties notwithstanding, the excess radiative power estimate is a measureable quantity which may be compared between measurements.

In this study 9 geothermal areas were analyzed based on data from 6 different flights in two separate months. Once geometric distortions had been removed and the data analyzed using the general technique outlined above, it was found that power estimates for the areas generally agreed within 15%. The

high degree of consistency indicates that thermal infrared surveys can yield repeatable and reliable estimates of excess power radiated by geothermal features. The method used is the analysis as well as the results from the Long Valley region will be published.

The techniques for geothermal infrared analysis which have been shown in this study to be reliable can be readily applied to infrared data returned both from Earth orbiting satellites and planetary probes where adequate spatial resolution is available. Because of the generally small area extent, sensitive radiometric analysis techniques such as these developed here will generally be required to even detect locally enhanced geothermal heat flow.

The author wishes to thank Dr. Hugh Kieffer for the great amount of assistance that he provided in his role as advisor and Dr. Elliot Morris for his assistance in obtaining housing.

NEW TECHNIQUES IN MORPHOMETRIC ANALYSIS
OF CRATERS

IRENE LLEWELLYN MEGLIS
BROWN UNIVERSITY
JULY 29, 1983

Introduction:

Previous studies of lunar craters have resulted in a variety of age and type classifications based on morphology (Pohn and Offield,1970;Wood and Andersson,1978). Few attempts have been made at systematic morphometric descriptions (Croft,1978). This project examined some techniques for quantifying crater descriptions in a systematic and reproducible way, with the intent that the resulting parameters would provide a basis for an objective approach to crater classification and detailed examinations of shape changes with size and degradation state. Preliminary analyses indicate that these techniques may provide such a basis.

Procedure:

The first parameter examined was crater volume. The method tested was a modification of the technique previously used for determining the volumes of central peaks (Hale and Grieve,1982). Volumes were determined from Lunar Topographic Orthophotomaps by digitizing successive contours from the crater rim to the crater floor. The area enclosed by a given contour was computed by summing the area of triangles formed by contiguous points on the contour line and the center of mass of the region. An estimate of the volume between the areas enclosed by two successive contours was determined from the equation for the volume of a cone frustrum:

$$V = 1/3h(B_1+B_2+\sqrt{B_1B_2})$$

where h is the contour interval and B_1 and B_2 are the areas enclosed by the upper and lower contour lines. The final volume of the crater was found by summing all the volume elements.

Two estimates of crater volume were made. The first was the volume from the crater rim to the crater floor, and the second was the volume from the highest closed contour to the crater floor. The two were rarely equivalent. In the cases where the highest contours were not closed, the rim was defined as the highest contour, and the volume from the rim to highest closed contour was estimated by digitizing the interior portions of the discontinuous contours and linearly extrapolating across the crater between the unconnected ends of the contour. This estimate takes into account irregularities in crater rim elevations.

The second parameter examined was a Fourier analysis of crater profiles.

Four traverses were digitized across each crater: E-W, N-S, NE-SW, and NW-SE (see Figure I.c and Figure II.c). The profile was then scaled to a length of two crater diameters with the crater centered, rotated to eliminate regional slope, averaged to zero, resampled to 2^{512} evenly spaced points, and finally subjected to a Fourier transformation routine. The Fourier transformation converts the shape of the crater profile into a series of harmonic numbers and associated amplitudes, with the harmonic number directly related to the frequency of the sine or cosine wave which is a component of the profile shape. The amplitude gives a relative measure of the importance of that harmonic. The transform data were plotted as harmonic number vs. amplitude (see Figure I.b and Figure II.b) so that graphic comparisons could be made, and then the amplitude values for the first fifteen harmonic numbers were normalized with respect to the total area under the spectrum for each profile (see Figure I.a and Figure II.a), so that the spectra could be subjected to later statistical analyses.

Restrictions on the Data Set:

The data set was limited by several factors. The most significant limitation was incomplete coverage of craters by Lunar Topographic Orthophotomaps. Time constraints were a major factor, and for this reason the data set was restricted to crater types ALC and BIO as listed in Wood and Andersson's catalog of lunar craters (in press). Type ALC craters are bowl-shaped, with diameters up to 20 km and no break in slope between crater walls and floor. Type BIO craters are similar to type ALC, but with a clear break in slope at the contact between crater walls and floor. The sample was further restricted to those craters on the mare. This constraint was imposed as Wood and Andersson have shown that terrain type has a measurable effect on crater morphology (Wood and Andersson, 1978). It was hoped that these restrictions would allow us to attribute variations in morphometry to variations in crater type and degradation state. Time limitations prevented analysis of the complete data set. Table I lists those craters examined.

Results:

Preliminary examination of the data shows promising results and numerous possibilities for future analyses. A least-squares regression of the rim-to-floor volume vs. diameter data for ALC and BIO craters as classed in Wood and Andersson's catalog showed significantly different trends. The data were

Crater Name	LTO#	Diam(km)	Type	Class	V_r (km ³)	V_c (km ³)	
Linda	39B2S2	1.44 a	ALC	I	.099	-----	d
Verne	40A4S1	1.54 a	ALC	I	.222	.190	
Samir	39B2S1	1.96 a	BIO	I	.463	.350	
Ruth	39A1S1	3.10 a	ALC	I	1.377	1.118	
Ching Te	42C3S3	3.99 a	BIO	I	3.283	2.589	
Rocco	39A1S1	4.56 a	ALC	I	5.815	5.028	
Borel	42C2	4.71	ALC	I	6.688	5.491	
Banting (Linne E)	42A3	5.00	BIO	I	11.120	-----	d
Taruntius K	62D4	5.23	BIO	I	11.918	9.141	
Picard Y	62B1	5.68	ALC	I	4.970	4.148	
Fahrenheit (Picard X)	62B1	5.68	ALC	I	15.848	13.390	
Hadley (Hadley C)	41B4S2	5.82	BIO	I	12.903	10.142	
Deseilligny	42C1	6.20	ALC	I	13.521	11.198	
Heinrich (Timocharis A)	40B4	6.95	BIO	I	23.849	20.474	
Taruntius B	61C3	7.10	BIO b	I	23.763	21.075	
Sarabhai (Bessel A)	42B4	7.56	BIO	I	25.265	22.814	
McDonald (Carlini B)	40A2	7.63	ALC	I	26.124	19.718	
Messier D	79B2	7.93	ALC c	I	27.695	22.754	
Ross D	60B1	8.50	ALC c	I	40.364	33.602	
Theophrastus (Maraldi M)	43D3	8.76	ALC c	I	28.349	24.791	
Swift (Peirce B)	44D4	10.48	BIO	I	71.006	63.850	
Franck	43D2	12.11	BIO	I	111.914	86.980	
Sulpicius Gallus	42D4	12.17	BIO	I	98.690	86.063	
Peek	63C3	12.70	BIO	I	122.632	95.228	
Greaves	62A1	13.75	BIO	I	174.006	132.368	
Carmichael (Macrobius A)	43C4	20.06	BIO	I	564.631	497.142	
Theophilus W	78B3	3.79	ALC	II	1.293	.354	
Torricelli P	78B3	3.81	BIO	II	1.260	.344	
Langrenus BA	80A2	4.97	BIO	II	3.431	-----	d
Maraldi N	43D3	5.28	BIO	II	3.350	2.603	

Table I: The data set

Diameter, crater type, and degradation class taken from Wood and Andersson's catalog of lunar craters (in press). V_r refers to the volume from crater rim to floor. V_c refers to the volume from the highest closed contour to crater floor.

a) Not listed in catalog of lunar craters. Diameters and degradation class taken from Croft (1978). Crater types were assigned.

b) Classed as ALC in catalog of lunar craters.

c) Classed as BIO in catalog of lunar craters.

d) Highest contour was closed.

regressed again after four craters classed in the catalog and two craters not listed were reclassified (see Table I, items b and c). The resulting trends are remarkably similar (see Figure III).

For type ALC craters:

$$V = 3.12D - 1.36 \quad R = .987$$

$$R^2 = .975$$

For type BIO craters:

$$V = 2.98D - 1.17 \quad R = .997$$

$$R^2 = .994$$

where V is crater volume (km³) and D is crater diameter (km).

Examination of the Fourier analyses indicates that harmonic number two may be related to differences between type ALC and BIO craters. BIO craters, with broad, flat floors, such as Greaves (see Figure I), show a small contribution from harmonic number two, whereas bowl-shaped ALC craters, such as Deseilligny (see Figure II), show a much larger contribution. Harmonic numbers three and four tend to be the largest, with three usually the larger. Amplitudes were calculated for 512 harmonic numbers, with only the first 16 being generally significant components.

The transform data, and further examination of crater profiles suggest that four of the craters examined were misclassified by Wood and Andersson on the basis of morphologic data only: three craters in our sample without noticeable flat floors were classed as BIO, and one crater with a flat floor was classed as ALC. The five smallest craters were not listed in the catalog, but they were easily assigned types based on our data. These results suggest that the profile and transform data may provide a more rigorous basis for classification of those craters covered by Lunar Topographic Orthophotomaps.

Conclusions:

The similarity between the variations in volumes of type ALC and BIO craters with diameter was an unexpected result. It is possible that such volume studies will not in themselves be useful in crater classification, but combined with the profile and transform data, they can provide important information about changes in crater morphometry which may help constrain models of crater formation.

The importance of harmonic number two is associated with a fairly noticeable morphological feature, the flat floor. It is hoped that with refinements of the techniques, including filtering of the spectra, and with continued analysis of the data gathered, completion of the data set, and additional testing with, for example, artificially constructed craters, the Fourier analysis technique will

be used to analyze finer features, such as rim crest shape. The ultimate goal is to apply these types of analysis to quantifying the nature of crater degradation, and to understanding crater degradation processes.

Acknowledgements:

I would like to thank Richard A. F. Grieve, whose presence was enlightening and reassuring, but never intimidating. Thanks also to Jim Garvin and Mike Ravine for their help and encouragement. Thanks especially to Ed Robinson, who was constantly taking time out to fix something for me.

References:

- Croft, S. (1978) Lunar crater volumes: interpretation by models of impact cratering and upper crustal structure. Proc. Lunar Planet. Sci. Conf., 9th, 3711-3733.
- Hale, W.S. and Grieve, R.A.F. (1982) Volumetric analysis of complex lunar craters: implications for basin ring formation. J. Geophys. Res., 87, A65-A76.
- Pohn, H.A. and Offield, T.W. (1970) Lunar crater morphology and relative age determination of lunar geologic units, Part 1, Classification. U.S. Geological Survey Prof. Paper 700-C, C153-162.
- Wood, C.A. and Andersson, L.E. (1978) The Lunar and Planetary Laboratory catalog of lunar crater: Part 1: Nearside. NASA TM 79328, in press.
- Wood, C.A. and Andersson, L.E. (1978) New morphometric data for fresh lunar craters. Proc. Lunar Planet. Sci. Conf., 9th, 3669-3689.

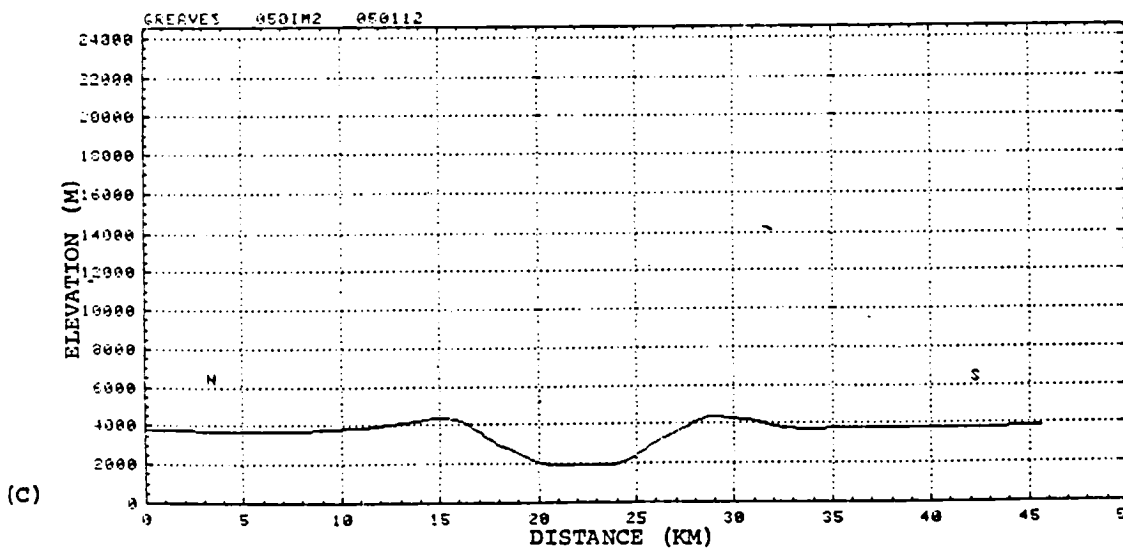
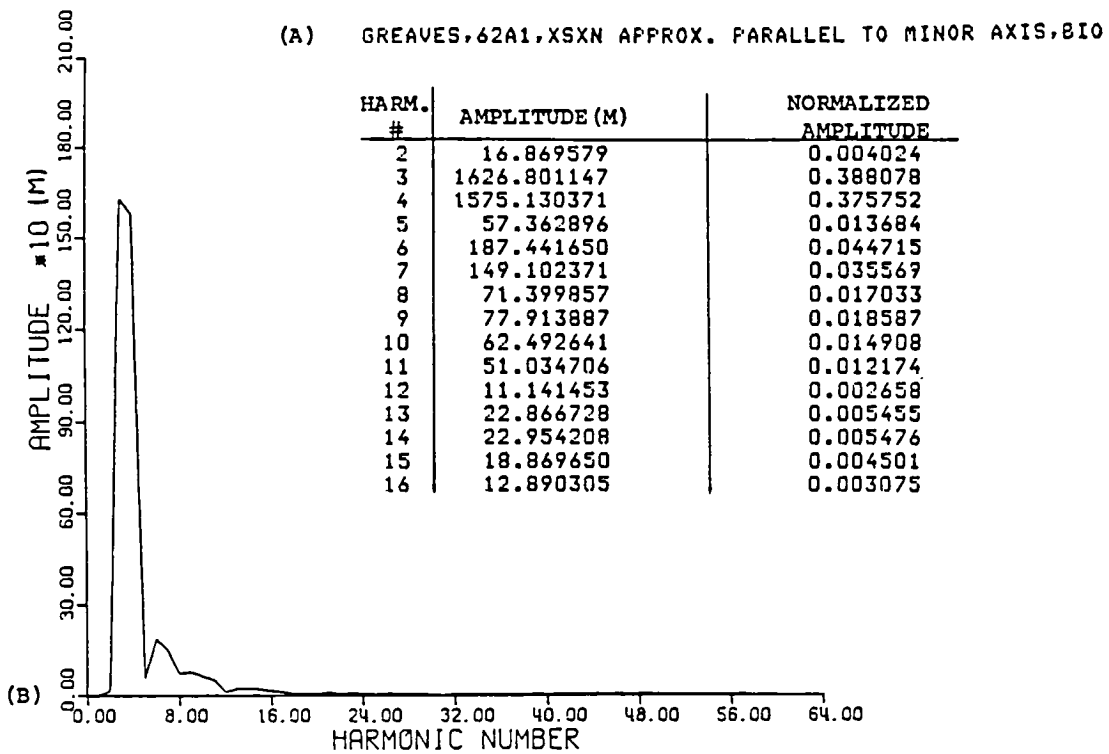


FIGURE I: DATA FOR GREAVES, BIO TYPE CRATER
 (A) TABLE OF TRANSFORM DATA, (B) PLOT OF TRANSFORM DATA,
 (C) CRATER PROFILE

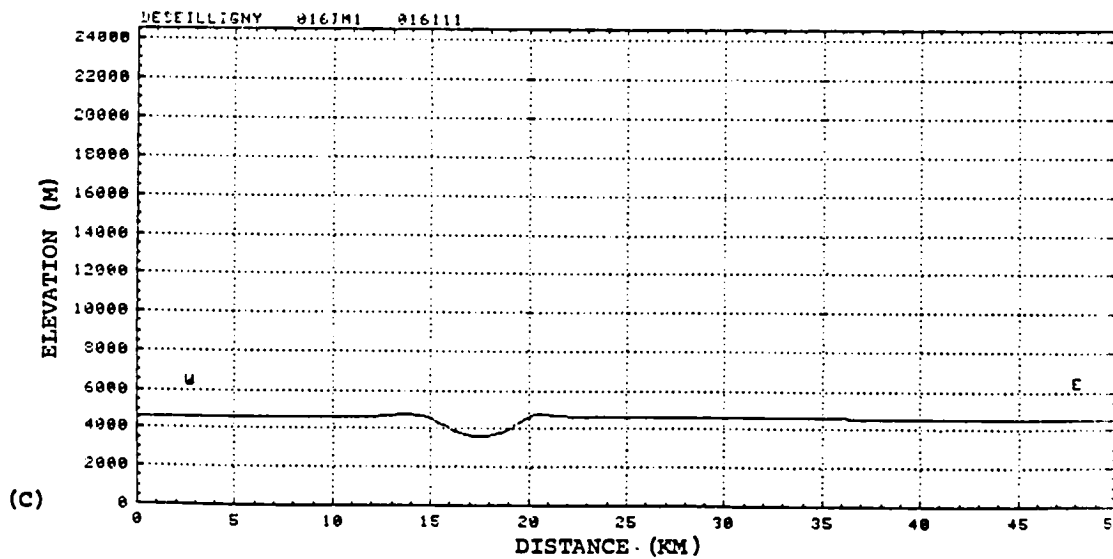
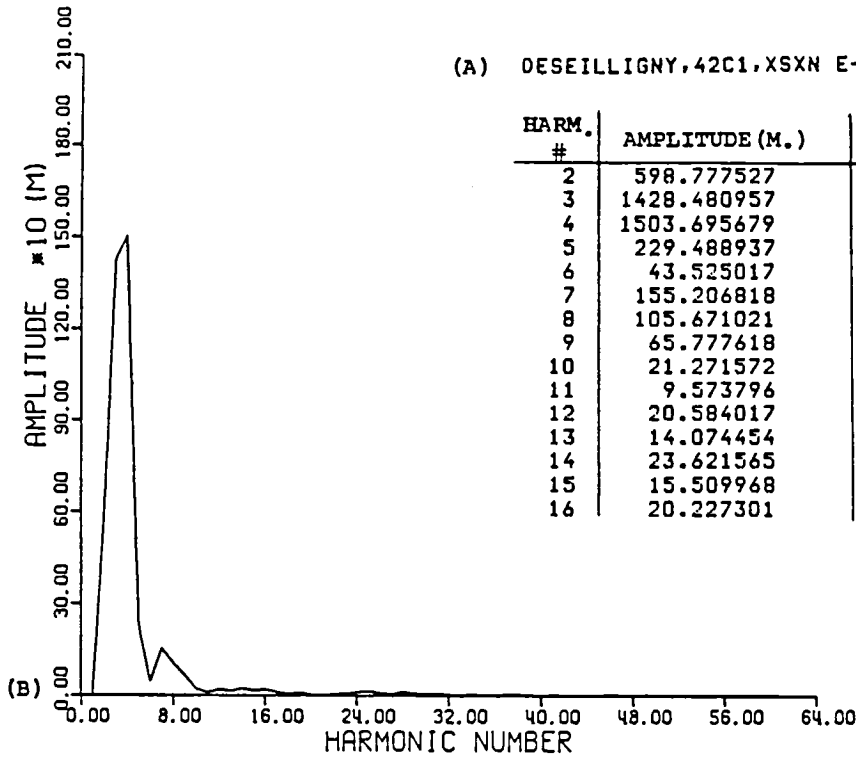


FIGURE II: DATA FOR DESEILLIGNY, ALC TYPE CRATER
 (A) TABLE OF TRANSFORM DATA, (B) PLOT OF TRANSFORM DATA,
 (C) CRATER PROFILE

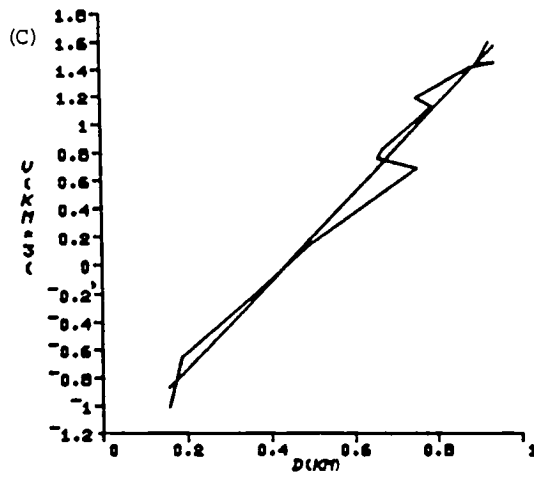
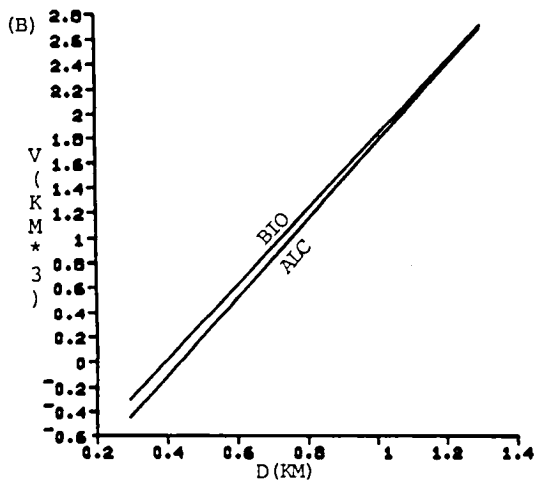
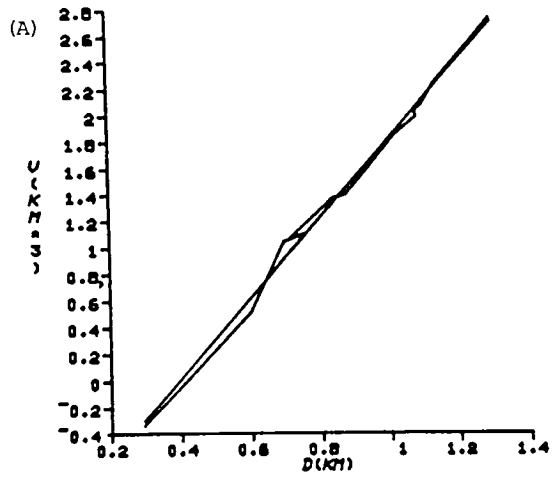


FIGURE III: LEAST-SQUARES FITS OF RIM-TO-FLOOR VOLUME VS. DIAMETER
 (A) FOR BIO CRATERS
 (B) BIO AND ALC CRATERS
 (C) FOR ALC CRATERS

SURVEY FOR BRIGHT MARS-CROSSING ASTEROIDS:
June 1983 Observations

Suzanne Smrekar
NASA Summer Intern,
Planetary Geology Research Program

U.S. Geological Survey
2255 North Gemini Drive
Flagstaff, Arizona 86001

Introduction:

The survey for bright Mars-crossing asteroids (ref. 1) was initiated by E. M. Shoemaker in 1980, and uses the Palmer Observatory 46-cm Schmidt camera. This survey developed out of the planet-crossing asteroid Survey (ref. 2) which began in 1973 and used the same telescope. The goal of the survey is to cover broad areas of the sky, allowing population estimates of various classes of asteroids. As bright Mars-crossing asteroids are accessible to a variety of techniques, such as U.B.V. photometry, polarimetry, radiometry and spectroscopy, it is also possible to assess the size, physical characteristics and compositional types of the various classes. Such data will ultimately provide information about the origin of asteroids. As perturbations can cause the orbits of Mars-crossing asteroids to intersect the orbits of terrestrial planets, asteroid population estimates also provide information on cratering rates (ref. 3). Additionally, such asteroids could conceivably be explored and mined in the future.

Methods:

IIa-D film exposed with the Palomer 46-cm Schmidt cameras have a blue magnitude limit of 17-18 and cover a field $8 \frac{3}{4}^{\circ}$ in diameter. Two 4-minute exposures of the field are taken per night with a 30 minute interval in between. This interval gives sufficient parallax from the asteroid's motion to allow detection by stereoscopy. Preliminary scans of the fields are done at the observatory during the run to ensure that interesting objects get as much coverage as possible.

A stereoscopic microscope, specially designed for scanning photographic films, allows the asteroids to be detected by stereopsis. The asteroid appears to float above the stationary stars. The positions of the unnumbered

asteroids on each film are measured relative to nearby Smithsonian Astrophysical Observatory (S.A.O.) catalogue stars using a Mann comparator, which has a precision of one arcsecond. The right ascension and declination of each asteroid is generated by a least squares fit of the measured positions of the stars and their precessed S.A.O. positions. The positions of the asteroids are submitted to the Minor Planet Center in Cambridge, Mass. for correlation with other observations. An asteroid receives a preliminary designation until it is observed on three separate apparitions, at which time it is numbered.

Results:

During the June 9-13 observing run, 51 fields were photographed. The fields ranged from 14 to 20 hours in right ascension (18 hours was approximately opposition) and from $+35^\circ$ to -30° in declination. June is usually a poor month for discovering asteroids, due to short nights and the position of the Milky Way in opposition fields. Three of these fields were follow-ups of specific, interesting objects. Most of the other 48 fields were photographed on 2 nights, while time allowed for only 1 photograph of some fields. Fields designated for measuring of all unnumbered asteroids, not merely planet-crossing asteroids, were photographed on 3 nights. Additionally, J. S. Bus observed many of these fields during the May lunation.

Of these 48 fields, I have only had time to work on 5 fields. The 5 fields contain 7 unnumbered asteroids bright enough to measure (16-18 in magnitude), and 3 which are detectable, but unmeasurable with these methods. They also contain 48 numbered asteroids, which were used to estimate magnitudes of unnumbered asteroids. So far, of the 7 unnumbered asteroids, only 3 asteroids have been located and measured on films from other nights during the June run. Carolyn Shoemaker reduced the data on 2 other fields,

obtaining 3 asteroids, 2 with inclinations of 10°-15°. These 3 asteroids, plus 3 of the ones I worked on, have received preliminary designs, and it is probable that the other 4 will also receive designations. It is hoped that the Minor Planet Center will eventually be able to correlate each of these asteroids with two other observations, that they may be numbered.

References

1. Shoemaker, E. M., Shoemaker, C. S., Helin, E. F., and Bus, J. S., Survey for Bright Mars-Crossing Asteroids, Reports of Planetary Geology Program, NASA Technical Memorandum 84211, 1981, p. 17-19.
2. Helin, E. F., and Shoemaker, E. M. (1979). The Palomar Planet-Crossing Asteroid Survey, 1973-1978. *Icarus* 40, p. 447-455.
3. Shoemaker, E. M., Williams, J. G., Helin, E. F., and Wolfe, R. F. (1979). Earth-Crossing Asteroids: Orbital Classes, Collision Rates with Earth, and Origin. In Asteroids, Gehrels, T., ed., Univ. of Arizona Press, Tucson.

PROPERTIES OF RESIDUES
FROM SUBLIMED DIRTY ICE

Stephen Sutton

Jet Propulsion Laboratory
California Institute of Technology
4800 Oak Grove Drive
Pasadena, CA 91109

19 August 1983

The properties of freeze-dried dilute dispersions of clay in water are of considerable interest in studies of comet nucleus mantles and the surface of Mars. In both environments the low pressure sublimation of water ice containing various amounts of clay may be an important process. As the water ice sublimates away a very open matrix of fine clay can develop on the surface. The properties of this clay mantle - its density, the size and shape of any aggregates, and the degree and type of cohesion between particles - are of importance in modelling Martian and cometary surfaces. To understand these properties I ran a series of low pressure/low temperature experiments during which the water sublimed out of $\sim 100 \mu\text{m}$ diameter particles of frozen clay-water mixtures. The properties of the resulting material - particularly the degree and dynamical nature of cohesion between particles - may explain some of the observations of Mars and the comets.

The sols were prepared by mixing water with air-classified monmorillonite clay (size $< 0.1 \mu\text{m}$) in weight ratios of 10:1, 100:1, and 1000:1. These mixtures were sprayed from a centrifugal paint sprayer into a bucket of liquid nitrogen. The individual drops froze very quickly upon contact with the LN_2 and generally sank below the surface, although many particles were suspended in the boiling liquid. The frozen mixture of water and clay was placed in a petri dish or beaker already containing LN_2 . Thus at no time after initial freezing could the temperature of the particles rise above that of the boiling point of LN_2 .

The experiments were run in a vacuum chamber capable of reaching pressures below 15 microtorr. A Dial Manometer gauge measured pressures between 20 and 0.1 torr. A thermocouple vacuum gauge measured pressures between 0.1 torr and 1 microtorr. A thermocouple was sandwiched between two layers of aluminum foil in the bottom of the dish; additionally, by making the assumptions that the pressure in the tank was equal to $P_{\text{H}_2\text{O}}$, and that the ice in the sample was in equilibrium or near-equilibrium with its vapor, either pressure gauge could function as a vapor-thermometer giving the maximum temperature of the ice.

Experimental runs lasted between 19 and 71 hours from the start of pumpdown to the beginning of repressurization. Pressures generally dropped below 1 torr within 1 hour of the start of a run. As long as solid or liquid nitrogen remained in the system, the temperature remained below 77 K and the pressure dropped rapidly. Once evaporation or sublimation of the nitrogen was complete the water ice was no longer cooled by that cryogen and the temperature rose quickly until stabilized by the sublimation of water ice. The temperature of the ice then dwelled at equilibrium for several hours as it slowly sublimed. During the equilibrium stage temperatures from -37° to -23°C and pressures from 0.30 to 0.10 torr were obtained. The thermocouple temperature sensor indicated a rising temperature primarily because it lost its thermal contact with the ice as the ice sublimed away. The pressure in the vacuum chamber indicated that the ice was at its lowest temperature at the very end of sublimation.

The results from several runs are shown in Table 1. The freeze-dried dirty snow (Runs 5, 8, and 11) forms light fluffy aggregates capable of supporting their own weight. The aggregates are dynamically cohesive; some are even elastic. The material in Run 11 (1000:1) behaved elastically even at 100 microtorr. The formation of blisters in the dried surface layer, several hours into Run 11, is further evidence that the bonds between clay particles are tough and flexible, even at pressures of 100 microtorr.

Optical and scanning electron microscopy show that the freeze-dried 10:1 and 100:1 water/clay mixtures consist of botryoidal aggregates of $10 \mu\text{m}$ to $200 \mu\text{m}$

diameter spheres; presumably this is the size and shape of the clay-water droplets from the paint sprayer. The presence of expansion cracks on the surfaces indicates that the outer layers of the droplets froze very quickly upon contact with the LN_2 and were ruptured by the subsequent expansion of the inner portions. Tube-like or petal-shaped structures are common in the relict spheres formed from the 100:1 sol. The material formed by freeze-drying the 1000:1 sol does not retain the original spherical shape of the droplets; instead it consists of a lacy network. Reconfiguration of the clay particles into a filamentary structure in this material is indicated both by the change in morphology (i.e., non-retention of spherical shapes) and by a substantial deviation from the decrease in bulk density which could be expected if the clay particles in the aggregate maintained their original positions in the frozen mud.

Three types of control experiments were made. Slurries of $75\ \mu\text{m}$ diameter SiO_2 glass beads were processed in a manner similar to the clay sols; but the resulting material was much less cohesive than the freeze-dried clays. In fact, the freeze-dried slurries of beads yielded material which was little different from unprocessed beads (Run 7A). Dry montmorillonite was mixed with LN_2 and placed in the vacuum chamber; the resulting material exhibited no change in cohesion and an only slightly lower density than unprocessed montmorillonite (Run 7C). Microscopically it is very similar to unprocessed montmorillonite. Finally, a 950:1 mixture of deionized water and montmorillonite was dried for 21 hours in an oven at atmospheric pressure and temperatures between 83° and 88°C . The dried clay formed a thin film over the surface of the dish; the material was not at all fluffy, but hard and brittle. The control experiments indicate that the production of a fluffy, dynamically cohesive aggregate is unique to the freeze-drying of a mixture of clay and ice.

The presence or absence of surface water might affect the properties of the aggregates of clay. However, aggregates from the 10:1 and 100:1 sols underwent no visible change after more than 16 hours in the 10^{-6} torr vacuum of the SEM. Heating at 181°C and ~ 10 torr for 80 hours had no noticeable effect on the sample from Run 8 (100:1 water/clay). Since temperatures from 120° to 200°C are sufficient to drive off the interlayer water from montmorillonite (Weaver and Flaggard, 1973), cohesion in the sample probably is not dependent on the presence of interlayer or surface water.

A 10 kW, 10,000X SEM electron beam rastered over a small area of the 10:1 freeze-dried material for 3 hours caused no observable change in conductivity, build-up of charge, or damage. Therefore the aggregate must be at least fairly conductive.

The dynamic (i.e., flexible and even elastic behavior) nature of the freeze-dried sols suggests that cementing between particles (i.e., deposits of salt on grain boundaries) is unlikely. The fact that little or no enhancement of cohesion between $75\ \mu\text{m}$ glass spheres occurred after a slurry was freeze-dried indicates further that cementing by salts was negligible.

The high conductivity indicated by the SEM experiment suggests that static charges might be difficult to maintain and that electrostatic forces between

particles might not be very important. Perhaps Van der Waals forces or forces related to minimizing surface energy could be responsible for binding particles together.

Comets probably form ^{from} ~~the~~ the aggregation of condensed refractory material, intermixed with and forming the nuclei of volatile phases (i.e., H₂O, CO₂) condensed on the initial particles. The product of this process is likely to be a set of tiny refractory particles separated but held together by ice - a "dirty snowball".

Unlike the case with material in the 100:1 and 10:1 mixtures, evidence based on bulk densities and SEM images suggests that the aggregate produced from the 1000:1 sol is collapsed - the structure and orientations assumed by the particles in the freeze-dried product are different from those existing when the particles were in the sol. The occurrence of collapsing strongly implies that most (perhaps almost all) of the particles in the frozen water/clay droplets were not in contact prior to sublimation; instead they were completely separated by ice, as probably the refractory particles in natural comets (and possibly the dust particles in Martian polar regions) are. Upon sublimation of the surrounding ice the individual particles are unsupported; some reconfiguration must occur. If attractive forces exist between particles, or if newly freed particles are dynamically unstable in a gravitational field, particles may come into contact. The spiderweb-like appearance of the aggregate produced in Run 11 (1000:1 water/clay) is an indication that whatever bonds formed upon initial contact were sufficiently strong to prevent much subsequent collapse. That these bonds are elastic, or at least flexible, is underlined by the formation of blisters during Run 11 and the apparent occurrence of blowholes, possibly formed by exhausting water vapor, in the 100:1 material.

Although there may be differences in exact temperature and pressure, the bonds that formed between particles in Run 11 developed in essentially the same environment as would occur on or near the surface of a comet or Mars: refractory particles that previously had been separated by ice were brought together in the presence of water at low vapor pressures (<0.2 torr) and temperatures (<25°C), in the absence of liquid water. Therefore, the properties of the freeze-dried 1000:1 mixture could be of relevance to the properties of cometary or Martian surfaces.

References

Weaver, C. E., and L. D. Pollard, 1973, The Chemistry of Clay Minerals (Developments in Sedimentology #15), Elsevier: New York, 213 p.

Acknowledgements

Jim Stephens and Eric Laue provided much advice and guidance, and Fraser Fanale, Stephen Saunders and Zdenek Sekanina made helpful comments during the project.

TABLE 1

EXPERIMENT		MATERIALS	H ₂ O CLAY RATIO	RECI-E	LENGTH OF RUN HRS: MIN	OBSERVABLES					COHESIVENESS	
NAME	DATE					DENSITY /g·cm ³	COMPRESSIVE STRENGTH: % /100 Agns.·m ²	SIZE OF CLUMPS AFTER TUNNELING mm	ANGLE OF REPOSE	MACRO STRUCTURE		HABIT
CLAY- RAW MATERIAL		CLAY	0	CLAY ONLY— UNPROCESSED	—	0.27±0.03	3±2	<0.5	~30°	VERY FINE, DUSTY	FINE GRANULAR	LOOSE—NOT VERY COHESIVE
RUN 7C	7-22-83	CLAY LN ₂	0	VACUUM-DRIED CLAY SPRINKLED INTO DISH OF LN ₂ —PUT IN VACUUM CHAMBER	18:30	0.22±0.04	—	<0.5	—	VERY FINE, DUSTY	FINE GRANULAR	LOOSE—NOT VERY COHESIVE
RUN 10	7-26-83	CLAY DI. WATER LN ₂	~35 (VOL)	DEIONIZED WATER WAS SPRAYED INTO LN ₂ . THE FROZEN ~100µm DROPLETS WERE PLACED IN A DISH WITH LN ₂ . CLAY SIFTED IN AND MIXTURE STIRRED.	45:33	0.16±0.03	—	0.5-1.0	—	SPONGY	GRANULAR, POROUS	WEAK DYNAMIC COHESION. FLEXIBLE BUT NOT ELASTIC. PIECES CAN BE BROKEN APART AND REATTACHED.
RUN 5	7-18-83	CLAY WATER LN ₂	10 (WT)	CLAY-WATER SOL SPRAYED INTO LN ₂	21:53	0.021 ±0.005	5±2	0.5-3	>70°	SPONGY TO FLUFFY-LIKE BROKEN UP STYROFOAM	BOTRYOIDAL (RELICT FROM WATER DROPS)	FAIRLY STRONG DYNAMIC COHESION. AGGREGATE IS QUITE FLEXIBLE BUT ONLY SLIGHTLY ELASTIC. ADHERES ON RECONTACT.
RUN 8	7-25-83	CLAY WATER LN ₂	100 (WT)	SOL SPRAYED INTO LN ₂	19:19	0.0031 ±0.0008	3±2	1-3	90°	FLUFFY	BOTRYOIDAL (RELICT FROM WATER DROPS)	STRONG DYNAMIC COHESION. FLEXIBLE AND ELASTIC. GOOD ADHESION ON RECONTACT.
RUN 11	7-29-83	CLAY WATER LN ₂	1000 (WT)	SOL SPRAYED INTO LN ₂	71:00	0.0022 ±0.0007	2±2	1-4	90°	VERY FLUFFY	WEBLIKE-VERY LACY	STRONG DYNAMIC COHESION. ELASTIC (LESS STIFF THAN 100:1 MATERIAL) AND FLEXIBLE. GOOD ADHESION ON RECONTACT.
RUN 7A	7-22-83	75µm SILICA GLASS BEADS • WATER • LN ₂	—	SLURRY SPRAYED INTO LN ₂	18:30	—	—	—	—	SIMILAR TO UNPROCESSED BEADS	—	LOOSE—PARTICLES SLIDE OVER EACH OTHER EASILY.
VARIATION EXPERIMENT	8-10-83	CLAY WATER	950 (WT)	SOL IN PETRI DISH—OVEN DRIED AT P=1 atm, T= 83° to 88°C	20:40	LOOKS FAIRLY COMPACT—TOO LITTLE TITRIL TO MEASURE	—	—	—	FINE—SMOOTH FILM ON SURFACE OF DISH	—	RIGID

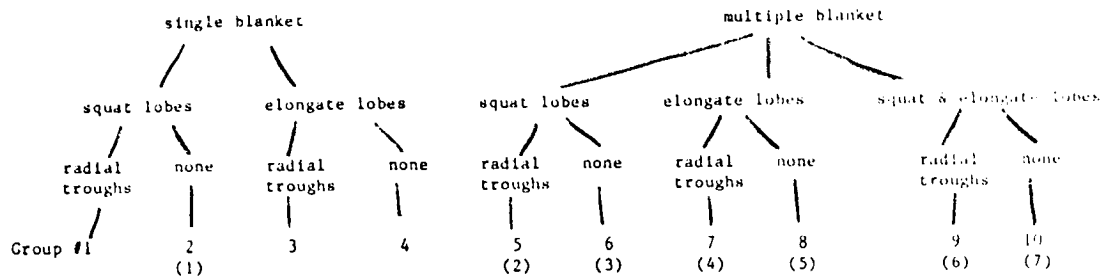
THE CLASSIFICATION OF MARTIAN RAMPART CRATERS

Mary Norris

Found only on Mars, rampart craters have a unique morphology which indicates a unique formation process. Their surrounding deposits extend much further than those around lunar and Mercurian craters which appear ballistically deposited, and their flowlike features suggest the presence of water on Mars. Currently, no physical model for the formation of these flow blankets exists although such a model could pinpoint the location of any possible water. Before someone can produce an accurate model, however, they must study the blankets in detail, choose their most important characteristics, and classify the craters accordingly. Although previous research (Johansen, 1979; Mougini-Mark, 1977) classified the craters, it did so by gross morphology. I attempted to incorporate their finer features into a classification system.

First, I studied the collection of literature on Martian rampart craters to build a general understanding of the situation. I then looked through the Viking photographs for visibly different craters attempting to find clear images at all latitudes. To unveil or amplify their less visible features, I had the pictures blown up and, from these blow-ups, made 16 morphologic and 4 stratigraphic unit maps. For more detailed interpretation, I assembled a set of stereo pairs and high/low resolution complements for the mapped craters. Finally, I classified the craters and listed their characteristics and how they may be used to model their formation.

Because I found certain traits very dependent on lighting I ignored them in my classification and divided the craters on the basis of single or multiple blankets, squat or elongate lobes, and the presence or absence of radial troughs. This division summarizes as follows:



Finding no craters in groups 1, 3, or 4, I abolished these groups and renumbered the rest as shown in parentheses.

The following traits are not dependable enough to use in crater classification, but can help define certain crater properties.

1. Extent of blanket - the radial distance from the crater rim to the farthest edge of the blanket measured in terms of the crater radius; best used to imply energy of flow.
2. Native terrain - morphology of surrounding land; may imply rock types involved in blanket formation and, consequently, physical properties of blanket material.

3. Thickness of blanket - could be a good clue to energy and general processes of blanket formation, but rarely definable.
4. Edge morphology - high resolution photographs only reliable indicators; divide into these categories:
 - a) rim - hill running around blanket edge;
 - b) scarp - sharp, cliff-like drop into underlying feature;
 - c) jumbled margin - wide zone of overlapping scarps and/or ridges;
 - d) worn - gradually grades down into underlying feature. Good indicator of energy dissipation during blanket formation and strength of blanket material.
5. Albedo - outermost, elongate, radial lobes with no relief, only color; indicates another stage of blanket formation.
6. Zone of ballistic ejecta - thin discontinuous blankets with no distinct edge; indicates another stage of blanket formation.

If well-defined categories based on these less dependable characteristics exist, only a much more extensive study will discover them. As it stands, the five groups I've proposed are valid and can be coupled with the other six characteristics for a thorough view of a crater. This material should prove useful to later studies. The maps provide the beginning of a source and the classification a method of interpretation.

References

- 1) Johansen, L. A., Martian Splosh Craters: A Relationship to Latitude Reveals the Distribution of Water on Mars, unpublished manuscript, August 10, 1979.
- 2) Mouginis-Mark, P. J., The Morphology and Mode of Formation of Martian Rampart Craters, thesis submitted for Doctor of Philosophy, University of Lancaster, England, November, 1977.

The Gravity Response of Impact Craters and
Volcanic Constructs on Mars: A Preliminary Study

Teresa F. McDonald
(University of Arizona, Tucson, Arizona)
Planetary Geology Undergraduate Research
Program 1983 Intern
U.S.G.S., Branch of Astrogeology
Flagstaff, Arizona 86001

Introduction

The highest resolution gravity data acquired from Mars were in the form of Doppler radio-tracking signals received from the Viking Orbiter 2 spacecraft during a period between October 1977 and March 1978. Many geometric factors were considered optimum for the collection of gravity data at that time: periapsis was lowered to just below 300 km, the Earth-Mars distance was relatively close, the Doppler signal path was further from the sun and its distorting effects than had previously been the case, the line of sight from Earth was less than 20° from Viking Orbiter 2 orbital plane which allowed an almost direct measure of the vertical gravity component, and the orbital inclination of 80° provided extensive latitudinal coverage (Sjogren, 1979). The Doppler residuals were reduced by Sjogren to obtain line of sight (LOS) acceleration values. These accelerations were plotted at 10 milligal intervals to develop the first detailed gravity map of Mars. Sjogren and others have used this data to analyze a few of the larger structures on Mars such as Olympus Mons, Tharsis Montes, Hellas Planitia Basin, Isidis Planitia, and others. Sjogren has concluded that the larger volcanoes in the Tharsis region are essentially isostatically uncompensated and that, in general, the larger craters are not associated with gravity minima as are many lunar craters.

This study is the beginning of a larger, on-going project (Scott, 1984 proposal) which will examine the gravity response of many craters, canyons, and volcanoes of various sizes and ages. Using new topographic and stratigraphic information for better model control, these investigations will provide relevant correlations between anomaly amplitudes and structural types, sizes, and relative ages. This study is an extension of Sjogren's work, but at a more detailed scale. It is, specifically, an examination of small- and intermediate-sized craters and volcanic constructs and associated anomalies observed on profiles from the Viking spacecraft orbital tracks. The individual profiles are used instead of Sjogren's gravity map as the observed anomalies are generally less than 10 mgals and require a more "in depth" look at the LOS accelerations. Some of the large volcanoes previously investigated were reexamined using more recent topographic data. This study substantiates Sjogren's previous findings as to the degree of compensation of Olympus Mons. The Bouguer anomaly calculated for Olympus Mons from new and more accurate topographic and volumetric data (Wu et al, 1981) was -10.5 mgal, indicating that very little, if any, compensation has occurred.

Procedure

The basic procedure used in this investigation was to:

1. Locate features that lie as close as possible beneath the Viking Orbiter 2 flight paths, that is, within 20° either side of periapsis since the highest resolution data and most accurate representation of anomaly magnitude are those values recorded closest to periapsis. Fifteen impact craters and ten volcanic structures were chosen for study. Among the more interesting features, 4 craters and 5 volcanic structures are discussed herein.
2. Plot the gravity data (milligals versus latitude) from portions of the profiles corresponding to selected feature locations.
3. Determine whether an anomaly existed that was correlative with the structure selected, and estimate the residual anomaly value by measuring its departure from the regional.

4. Model the features by using current topographic data, where available, to determine the volume and mass (or mass deficit) of each structure. Best estimates were made by comparison with other features for the smaller, more obscure structures for which there was no topographic information. Pike's formula ($R=1.044 D \exp 0.301$, where R is crater depth and D is rim-crest diameter, both in km) was used for determining the depth of several of the craters (Pike, 1977). This formula was derived for fresh lunar craters greater than 15 km in diameter and the depths obtained for martian modeling purposes should be considered maxima which will yield maximum theoretical anomaly values. A single, cylindrical, volume-equivalent disk was determined by fixing the radius and volume found from the topographic model. A series of stacked disks was used as a model for the larger volcanoes.
5. Compute theoretical anomaly values from the models using Nettleton's formula:

$$(\Delta g) \text{ THEORETICAL} = \gamma \sigma \omega t \quad (\text{see figure 1})$$

- γ = gravitational constant = 6.667×10^{-8} (cgs units)
 σ = density contrast (since there is no direct way to measure this parameter accurately, σ is assumed to be 3 g/cm^3 for all features)
 ω = solid angle in radians between spacecraft and model disk dependent upon z/r , (spacecraft altitude/radius of disk) and x/z (offset of location of disk center from orbital track/altitude)
 t = thickness of cylindrical model disk (cm)

6. Compare the observed anomaly and theoretical anomaly values to obtain the Bouguer anomaly (observed gravity - theoretical gravity = Bouguer Anomaly).
7. To eventually use the Bouguer anomalies to interpret possible correlations between gravity measurements and (a) degree of isostatic compensation, (b) relative age of features, (c) sizes and types of structures, (d) depth to zone of compensation and (e) composition or density of feature and/or surrounding material.

Table 1 shows the Bouguer anomalies obtained for the selected features. In general, it should be noted that the volcanic constructs induce a greater gravity response than do the impact craters, confirming Sjogren's findings.

Discussion of Selected Features

Uranus Tholus is a small- to moderate-size (60 km diameter) symmetric shield volcano with relatively steep flanks. It is located north of Ceraunius Tholus and west of Uranus Patera. It is probably similar in age to the large Tharsis volcanoes which are older than Olympus Mons and younger than the Elysium volcanic field (Scott and Carr, 1978). The base of Uranus Tholus is embayed by lava flows and the volcano may therefore be substantially larger than it appears. The slightly southeasterly offset of the caldera is considered too small to be of significance in the gravity calculations. Topographically, Uranus Tholus is considered cone-shaped, 2 km in height, and 60 km wide. A cylindrical disk of equivalent volume situated at the martian surface was found to be 0.667 km in height and 60 km in diameter. The observed anomaly over Uranus is +5.0 mgals compared to a theoretical value of +0.52 mgals. The Bouguer anomaly of +4.48 mgals indicates that an unknown portion of the flanks of Uranus Tholus may be buried by less dense material, or that there may be a plutonic body or subsurface feeder system present beneath the volcano.

Ulysses Patera is a minor Tharsis shield volcano located directly east of Biblis Patera and northwest of Pavonis Mons. It appears to be embayed by flows from Pavonis. Its large caldera is 55 km in diameter and is estimated to be 1.7 km deep (Pike, verbal communication). It is similar in age to Uranus Tholus. The volume for a 3 km high flat-topped cone of radius 47.5 km was calculated and the caldera volume was subtracted. The resulting cylindrical disk model developed was 95 km in diameter and .78 km high with a mass of 1.7×10^{19} g. From this model, a theoretical anomaly value of +1.6 mgals was calculated and compared to the observed value of +5.7 mgals. The Bouguer anomaly of +4.2 mgals is very similar to that of Uranus Tholus and similar implications may be made as to partially buried flanks and/or subsurface structures. Another model was constructed for a 5 km high structure with flanks continuing at a 3.6° slope beneath the surface to arrive at a basal diameter of 158.6 km. The theoretical anomaly obtained from this model was +7.7 mgals. Therefore, a 3-5 km high volcano buried in 1-2 km of less dense flows could possibly approximate the observed anomaly, indicating no isostatic compensation.

Hecates Tholus is the northernmost Elysium volcanic field construct with a low shield morphology. It is a relatively old structure, older than the Tharsis Montes. Recent studies have led Mouginis-Mark and co-workers (1982) to examine Hecates Tholus for evidence of explosive volcanism on Mars. They have found evidence of a possible young air fall to the west-northwest of the nested summit caldera. The apparent offset of the caldera is due to partial burial of the southern flanks by flows from Elysium Mons. There are numerous sinuous lava channels radial to the caldera and "unlike the large Tharsis shields which show ample evidence of lobate lava flows on their flanks, Hecates Tholus has no flow features of this kind" (Mouginis-Mark, et al., 1982), indicating possible differences in magma composition between Elysium and Tharsis volcanoes. The topographic model was a 6 km high cone-shaped mountain with a basal diameter of 167.5 km. The caldera volume was calculated from a disk model 0.47 km deep and 10 km wide and was subtracted from the volume of the topographic model. The cylindrical disk of equal volume was found to have a radius of 83.75 km and a height of 2 km. Using Nettleton's formula, the theoretical anomaly was calculated to be +9.8 mgals. The observed anomaly was only +2.8 mgals, leaving a Bouguer anomaly of -7.0 mgals. If Hecates is indeed more of a strato volcano composed of alternating pyroclastics, ash falls, and lava flows, the assumed density of 3 g/cm^3 may be too high an assumption compared to the density expected from the Tharsis shields which are probably composed of thick layers of basaltic lava. A relatively large negative Bouguer anomaly over a topographic high on Earth can indicate low density "roots". This may imply the partial isostatic compensation of Hecates Tholus.

Ascraeus Mons and Pavonis Mons are both large Tharsis shield volcanoes perched atop the Tharsis Plateau. They were both modeled as a series of disks stacked concentrically from the 10 km contour seen on topographic maps of the features (Wu et al., 1982). The Bouguer anomalies indicate that these volcanoes are uncompensated. It should be noted that the regional effect of the Tharsis Plateau has been removed from the LOS acceleration values and is not reflected in the observed anomalies for either volcano. The peak of the anomaly over Pavonis is offset 158 km southward of the center of the structure along the orbital track. This places it between Arsia Mons and Pavonis Mons. The flight path was west of Pavonis and east of Arsia which may mean that the combined gravitational responses of both volcanoes are influencing the position of the anomaly peak. It is a much broader anomaly than those

which appear directly over Ascreaus and Olympus Mons and may encompass both structures, thereby obliterating the true peak anomaly values of each (Sjogren, 1979).

Sharonov Crater is a medium-sized crater located directly north of Kasei Vallis in a heavily channeled region east of Chryse Planitia and north of Lunae Planum. It appears to be a relatively fresh crater, though it certainly predates Kasei since the channels cut through and have eroded much of the ejecta blanket, particularly to the south and southwest of Sharonov. It has central peaks and what appears to be a smooth, flat floor. Bright wind streaks from smaller craters within Sharonov indicate probable eolian action, deposition as well as erosion. The crater rim exhibits slumping which has increased the diameter of the original impact structure. The topographic data available shows Sharonov to be 2 km deep and 100 km across. A cylindrical disk with these dimensions was used to find the theoretical gravity anomaly value of -4.2 mgals. The observed value was -1.55 mgals. The Bouguer anomaly, +2.65 mgals, suggests partial isostatic compensation of Sharonov. However, the peak of the plotted anomaly occurs 126 km south of the center of Sharonov along the orbital track. The peak is centered exactly between Sharonov and Kasei Vallis which implies that the two structures, each of which would cause negative anomalies, may be represented by one gravity anomaly, similar to the Arsia Mons-Pavonis Mons combined anomalies. It's also possible that due to LOS location problems the anomaly may represent either structure. These possible influences and errors notwithstanding, the Bouguer anomaly supports the observation that Sharonov is partly filled or injected with relatively dense material compared with adjacent terrain.

Antoniadi is a very large, ancient crater 430 km in diameter located northwest of Syrtis Major Planitia. It is highly modified by erosion and is discernable by a vague rim escarpment that exhibits only a small amount of relief in most places. There are a few craters within Antoniadi that have been completely filled, presumably by volcanic flows from Syrtis Major, leaving only faint rim outlines. There is no recent topographic information on Antoniadi; a disk with a radius of 215 km and a depth of 200 meters was assumed as a model. The observed anomaly is -1.88 mgals and the theoretical value is -5.0 mgals. The Bouguer anomaly of +3.2 mgals again suggests that the density of the flows filling the crater may be compensating for the mass deficit of material lost by impact excavation and for the effect of the brecciated lens of unknown thickness that underlies the floor of Antoniadi. Part of the Bouguer anomaly may also be attributed to crustal compensation by uplift of mantle material beneath the floor of the crater.

Cassini is another old, nearly basin-sized crater, a bit smaller than Antoniadi, with a diameter of 391 km. There is evidence of an inner ring concentric to the highly eroded rim of Cassini. There seems to be a history of resurfacing in the area and Cassini has been filled by flows and possibly other deposits. Lobate scarps and wrinkle ridges are evident and craters on the floor of Cassini have been nearly obliterated by the fill. The rim scarp exhibits deeply incised furrows on the south and southeast and appears to be much steeper there. The model disk selected has a 200 meter depth and 391 km diameter. The depth is probably too shallow and should be considered a minimum. The observed anomaly, -2.2 mgals, is somewhat greater than that associated with Antoniadi, despite Cassini's smaller diameter. The theoretical anomaly value calculated from the minimum 200 m depth is -4.2 mgals which implies partial isostatic compensation.

Mie is a large crater located northwest of the Elysium Volcanic field and east of the Viking Lander 2 landing site. It has a central peak and dark,

eolian deposits on a smooth, flat floor. The rim crest apparently stands high above the surrounding low plains which, along with other apparent morphological characteristics, indicates a relatively young age. A cylindrical disk with a diameter of 100 km and a depth of 4.2 km (calculated from Pike's formula) was used to model Mie. The theoretical anomaly value determined was -4.6 mgals. There is no observed anomaly over Mie. A relatively high spacecraft altitude (385 km) may be a contributing factor as well as possible errors in LOS location of the flight path. Mie is offset from the path at least 72 km but possibly more if LOS location errors do exist. The profile shows a steeply sloping, negatively trending regional effect, probably representing the limb of the regional high associated with the Elysium Rise. It is possible that any anomaly associated with Mie could be attenuated by the high spacecraft altitude and may be further attenuated or masked by the steep, already negative regional gravity effect. As Mie lies in the lowland plains, it may have been more readily invaded by dikes than highland craters.

Many of the craters examined in this study are not associated with observable anomalies. This is also true of some volcanic structures. These ambiguous features will remain so until further work is done in determining sources of error and making corrections where possible or until more complete data is obtained.

Sources of error in this study include: (1) inherent error in original data, (2) error in reduction of data; Sjogren (1979) has warned that the mathematical and statistical manipulations of the Doppler residuals may reduce the anomaly amplitudes by 20-30%, (3) modelling errors due to lack of sufficient topographic and stratigraphic controls, density contrasts, etc., (4) LOS location errors from slight variations of the Viking spacecraft's orbital plane, and (5) variable spacecraft altitude that may significantly reduce anomaly values. Corrections should be made and observed anomaly values normalized before further relevant correlations and comparisons can be made between feature characteristics and their gravity responses.

Acknowledgements: I would like to sincerely thank Dr. D. H. Scott for his guidance and support throughout this study and Dr. E. C. Morris, my host during my stay at the USGS in Flagstaff. I am primarily indebted to the NASA PGURP Selection Committee for providing this tremendous opportunity to meet and work with the many outstanding and friendly people involved in planetary research in Flagstaff.

References

- Mouginis-Mark, P. J., Wilson, L., Head III, James W., (1982), Explosive volcanism on Hecates Tholus, Mars: Investigation of eruption conditions, J. Geophys. Res., 87, p. 9890-9904
- Nettleton, L. L., (1942) Gravity and Magnetic Calculations, Geophysics 7(3), p. 293-303.
- Pike, Richard J., (1977) Size dependence in the shape of fresh impact craters on the Moon, Impact and Explosion Cratering, Roddy, D. J., Pepin, R. O., Merrill, R. B., editors, p. 489-509.
- Scott, D. H., Carr, M. H., (1978) Geologic Map of Mars, U.S.G.S.
- Sjogren, W. L., (1979) Mars gravity: High resolution results from Viking Orbiter 2, Science 203, p. 1006-1010.
- Wu, S. S. C., Garcia, P.A., Jordan, R., Schafer, F. J., (1981) Topographic Map of Olympus Mons, U.S.G.S.

<u>NAME</u>	<u>LOCATION</u>	<u>(Δg) OBSERVED</u> (mgal)	<u>(Δg) THEORETICAL</u> (mgal)	<u>BOUGUER ANOMALY</u> (mgal)
A.				
Uranus Tholus	26.5N97.5W	+5.0	+0.52	+4.48
Ulysses Patera	2N122W	+5.7	+1.47	+4.23
Hecates Tholus	34N210W	+2.8	+9.8	-7.00
Ascræus Mons	11.5N104W	+61.6	+59.1	+2.50
Pavonis Mons	0.5N113W	+71.3	+63.2	+8.10
B.				
Sharonov	27N58.5W	-1.55	-4.2	+2.65
Antoniadi	23N298W	-1.8	-5.0	+3.20
Cassini	24N327.5W	-2.2	-4.2	+2.00
Mie	49N220W	0	-4.6*	+4.6

TABLE 1
A. Volcanic Structures
B. Impact Craters

* Maximum expected anomaly value

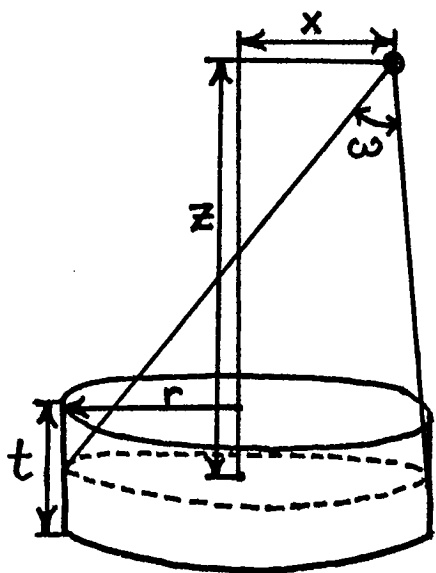


Figure 1. Diagram showing parameters used in calculating the theoretical gravity anomaly value (Bouguer correction) from a cylindrical disk model. (from Nettleton, 1942)

ORIGIN OF THE MOON: CONSTRAINTS FROM VOLATILE ELEMENTS*. Melanie E. Kreuzberger**, Michael J. Drake, John H. Jones, Lunar and Planetary Laboratory, University of Arizona, Tucson, AZ 85721. **Present address: University of Michigan.

Fission of the Moon from the Earth following core formation is a hypothesis for the origin of the Moon (Ringwood, 1979). Supporting arguments include the low density of the Moon corresponding to the density of the Earth's mantle and the low volatile content of the lunar rocks vs. those of terrestrial origin. Vapor pressures of the alkali elements and their oxides increase in the following order: Na, K, Rb and Cs. The Moon should, therefore, be more depleted in Cs relative to Rb, Rb relative to K, and K relative to Na than the Earth if the fission model is correct. Analyses of lunar mare basalts and terrestrial mid-ocean ridge and other young basalts indicate that this behavior is not observed; for example, the Moon shows a higher Cs/Rb ratio than the Earth--i.e., it lies between chondrites and the Earth.

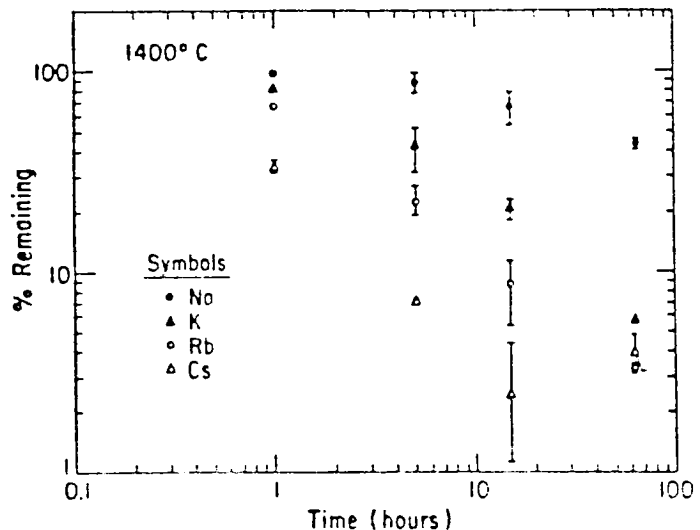
It is possible that monovalent alkali elements might be lost from silicate materials in a different order than that inferred from elemental and oxide vapor pressures, as a result of differences in the way they are bound in silicate materials. To test this hypothesis we conducted a series of experiments to investigate alkali loss at high temperatures. A synthetic basalt of composition $Di_{75}An_{25}$ containing approximately one wt.% each of Na, K, Rb, and Cs was prepared. The mixture was ground under acetone, fused twice at $1400^{\circ}C$, and quenched to form a homogeneous glass. The glass was used as our starting material. Experiments were conducted using the wire loop technique at 1 atmosphere and $1400^{\circ}C$ and $1050^{\circ}C$ in air, allowing volatile loss as a function of time to be determined. The resulting glass beads were then analyzed using the scanning electron microprobe.

Analyses indicate that the behavior of volatiles dissolved in a silicate melt is similar to that inferred from elemental and oxide vapor pressures. At $1400^{\circ}C$ (superliquidus), Cs is most readily volatilized, followed by Rb, K, and Na (see figure). The mass of the glass beads is not a major factor in the rate of volatile loss. At $1050^{\circ}C$, no significant loss of volatiles was detected after 1 week.

These results are consistent with previous experiments by Gibson and Hubbard (1972) on 12022. We conclude that alkali element ratios in the Earth and Moon are not readily interpreted in terms of the Fission hypothesis.

*Research conducted in conjunction with the Tucson Lunar Origin Consortium.

REFERENCES: GIBSON E.K. AND HUBBARD N.J. (1972) Proc. Lunar Sci Conf. 3rd, 2003-2014. RINGWOOD A.E. (1979) Origin of the Earth and Moon. Springer-Verlag.



INQUIRIES INTO THE NATURE OF THE MARTIAN HIGHLANDS-LOWLANDS BOUNDARY

Jeffrey D. Corrigan, Department of Geology, University of Notre Dame,
Notre Dame, IN. 46556

INTRODUCTION

The surface of Mars is characterized by two major geologic asymmetries. One is defined by the perimeter of the Tharsis province, the other by a boundary which divides the northern smooth plains from the topographically higher ancient cratered terrain of the southern hemisphere (Mutch *et al.*, 1976). In places, the boundary is sharply defined by a scarp which rises approximately 2-3 km above the northern smooth plains. In other places, the boundary is manifest as a broad transitional zone in which the change from highland terrains to lowland plains is gradual and imperceptible. The following is a brief description of two aspects of the highlands-lowlands boundary problem which were undertaken during the present authors internship at the Center for Earth and Planetary Studies in Washington D.C. in an attempt to gain a better understanding of the nature of this fundamental crustal asymmetry.

PHOTOGEOLOGIC CONSTRAINTS

A number of speculative theories have been forwarded in an attempt to account for the origin of the highlands-lowlands dichotomy. These include:

- 1) A large early impact in the north polar region (Wilhelms and Squyres, 1984)
- 2) Subcrustal erosion and foundering of ancient highlands terrain in the north due to mantle convection processes (Wise *et al.*, 1979)
- 3) Volumetric increase and break up of the northern crust due to a phase change in the mantle; lower elevations are the result of isostatic readjustment (Mutch and Saunders, 1976)

Although each of these hypotheses attempt to present a plausible explanation for the existence of the martian crustal asymmetry, little quantitative analysis has been done to test these theories. While any inferences concerning subcrustal processes are highly speculative, it should at least be possible to put forth some photogeologic constraints on the formation of the boundary. In an attempt to provide such constraints, structural features along and around the boundary have been classified and mapped for the Ismenius Lacus, Arabia, Syrtis Major and Amenthes quadrangles utilizing 1:2,000,000 Viking orthomosaics as base maps. The mapping of these features, primarily graben, ridges and escarpments, represent one stage of a long term project here at the Center for Earth and Planetary Studies to develop a digital data base containing the location, orientation and length of such features on Mars. A better

understanding of the genesis of the highlands-lowlands boundary may eventually be provided by transferring the digitized maps to image processing systems so that structural features can be overlaid with other Mars data (i.e. Mars consortium data). Preliminary results, based on the orientation of graben that are similar to the overall trend of the boundary zone, suggest that the evolution of the boundary has been dominated by structural control (Maxwell et al. 1984).

APPROACH COLOR DATA AND MAPPING

The second inquiry into the highlands-lowlands boundary problem consisted of utilizing Viking orbiter violet, green and red approach color data (Soderblom et al., 1978) in an attempt to delineate various terrain types in the Amenthes quadrangle. In order to reduce the magnitude of the correlations among the three spectral bands, a principal component analysis was performed on the data (Jacobberger et al., 1982). The resulting elongated, cigar shaped distribution of the data in three dimensional component space was then "stretched" along the three component directions into a spherical shape and rotated back into the original variable space. This particular transformation was employed in order to obtain an enhanced color image which provides maximum discrimination between various terrain types and surface units within the quadrangle (Jacobberger, personal communication). Similar techniques performed on the Mars consortium data have been successfully employed to aid the classification of surface units for other areas of Mars (Arvidson et al., 1981; Arvidson and Guinness, 1982).

Two techniques were employed to evaluate the utility and limitations of applying the approach color data to aid mapping of areas near the boundary. The first is qualitative and involved projecting the acquired color composite image directly onto a reconstruction of the entire Amenthes quadrangle (MC-14) made by fitting together the 1:2,000,000 photomosaics of the four subquadrangles (NW, SW, NE, SE). The second technique is semi-quantitative and involved using the 1:2,000,000 photomosaics as a base to construct a generalized map of the major terrain types within the quadrangle (Fig. 1). Basic statistics for specific areas (Fig. 2) within these mapped terrain types were then derived from the transformed approach color data and displayed in graphical form (Fig. 3).

The following is a brief summary of the more pertinent results that were derived from this investigation:

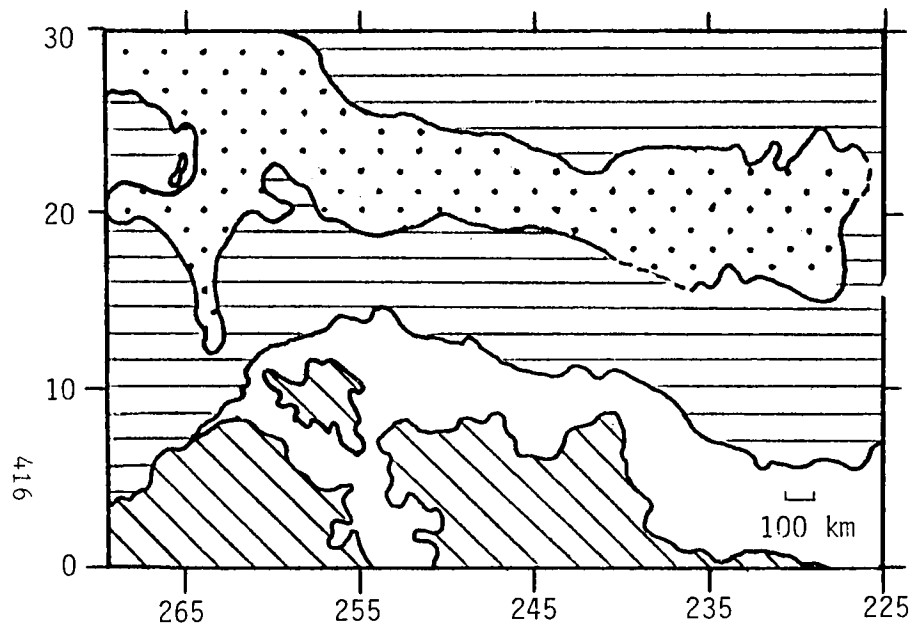
- 1) The mapped terrain types which consist of highlands materials (unit 1) and flat topped mesas and rounded to subangular hills (unit 2) are highly correlated (see Fig. 3) supporting the interpretation that these mesas and hills are remnants of plateau material produced by erosional retreat of the scarp (Hiller, 1979).
- 2) The highlands and disrupted highlands terrain (unit 1 and unit 2) are easily discriminated from the smooth plains terrain (unit 3) on the color composite.

- 3) Statistics derived from an area within the Isidis basin (see area 6, Fig. 3) differ markedly from those derived for other areas within the smooth plains unit, supporting the assertion that the two plains deposits may not represent the same geologic unit (Scott, 1978).
- 4) Projection of the color composite image for the Amenthes quadrangle onto the 1:2,000,000 photomosaic for this area revealed that where the scarp forms a sharp contact between the highlands and lowlands (southeastern section of quadrangle) a thin swath on the color composite parallels the boundary along the lowlands side of the scarp. This swath contrasts markedly with the surrounding areas and forms a sharp divide between the highlands terrain (unit 1) and the erosional remnants terrain (unit 2) which are poorly differentiated on the color composite. While there is no perceivable feature on the photomosaics which might account for this color variation, a conceivable explanation, although highly speculative, is that this variation may be due to a basement surface which underlies the highlands material and has been exposed by erosional retreat of the highlands (Scott, 1978; Guest, et al., 1977).
- 5) Unit 4 was mapped as a distinct terrain type on the basis of the numerous small knobby hills which are found in this region. Whether these features represent severely degraded highland remnants or are related to some other process is unknown. The approach color data provides little information concerning this terrain type due to the poor resolution of data in the northern sections of the quadrangle (Fig. 4).

While a large percentage of the approach color data for the Amenthes region is characterized by poor resolution data, the good quality data was found to provide information that was not otherwise obvious in spite of the 10 to 20 km per line pair spacial resolution (Soderblom et al., 1978). Although the approach color image data only covers latitudes 30 degree North to 63 degree South, this data could prove to be a useful tool for future studies of the highlands-lowlands boundary problem in areas where good quality data is available.

REFERENCES

- Arvidson, R. E., and Guinness, E. A. (1982). Classification of surface units in the equatorial region of Mars based on Viking Orbiter color, albedo, and thermal data. Reports of Planetary Geology program - 1982, NASA Tech. Mem. 85127, p. 320-321 (Exp. abstract.)
- Guest, J. E., P. S. Butterworth, and R. Greeley (1977). Geologic observations in the cydonia region of Mars from Viking, Jour. Geophys. Res., v. 82, p. 4111-4120.
- Guinness, E. A., R.E. Arvidson, and A. Zent (1981). Multivariate classification of surficial units on Mars from Viking Orbiter color and infrared data. Reports of Planetary Geology program - 1981, NASA Tech. Mem. 84211, p. 449. (Exp. abstract.)
- Hiller, K. H. (1970). Geologic map of the Amenthes quadrangle of Mars. U. S. Geol. Survey Misc. Geol. Inv. Map I-1110.
- Jacobberger, P. A., R. E. Arvidson, and D. L. Rashka (1983). Applications of Landsat multispectral scanner data and sediment Spectral reflectance measurements to mapping of the Meatiq Dome, Egypt, Geology, v. 11, p. 587-591.
- Maxwell, T. A., H. Frey, and A. M. Semeniuk (1984). Geomorphology and evolution of the ancient cratered terrain - smooth plains boundary of Mars, Geol. Soc. Am. Abstr. Programs, in press.
- Mutch, T. A., and R. S. Saunders (1976). The geologic development of Mars: A Review, Space Sci. Rev., v. 19, p. 3-57.
- Scott, D. H. (1978). Mars, highlands-lowlands: Viking contributions to Mariner relative age studies, Icarus, v. 34, p. 479-485.
- Soderblom, L. A., K. Edwards, E. M. Eliason, E. M. Sanchez, and M. P. Charette (1978). Global Color Variations on the Martian Surface, Icarus, v. 34, p. 446-464.
- Wilhelms, D. E., and S. W. Squyres (1984). The martian hemispheric dichotomy: caused by a giant impact?, Nature, in press.
- Wise, D. U., M. P. Golombek, and G. E. McGill (1979). Tectonic evolution of Mars, Jour. Geophys. Res., v. 84, p. 7934-7939.



- | | | | |
|---|--|---|--------------------------------|
|  | Unit 1 - Cratered highlands terrain |  | Unit 3 - Smooth plains terrain |
|  | Unit 2 - Disrupted highlands & remnant terrain |  | Unit 4 - Knobby hills terrain |

Fig. 1. Generalized map of designated terrain types within the Amenthes quadrangle.

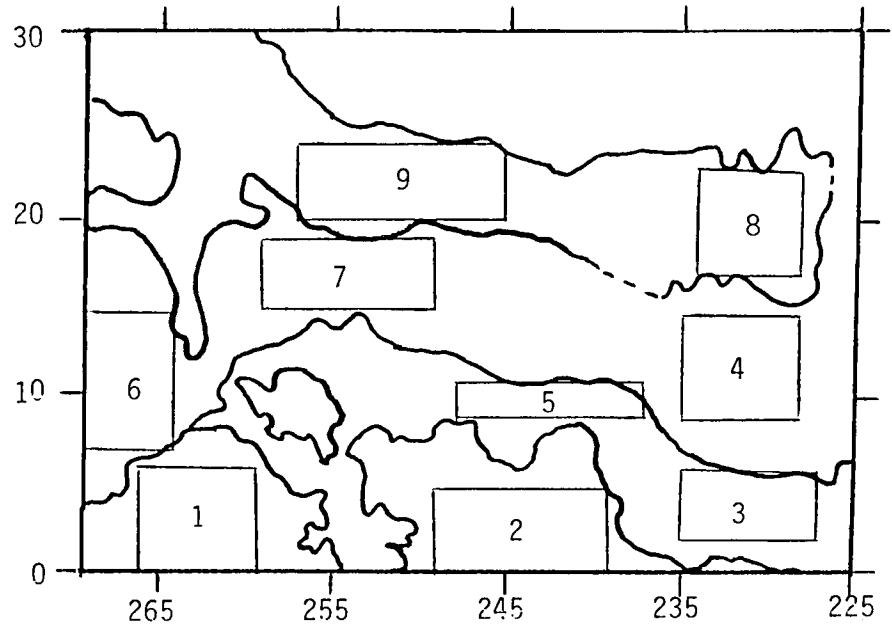


Fig. 2. Numbered rectangles represent areas for which means and standard deviations were derived. These numbers correspond with those below each bar in figure 3.

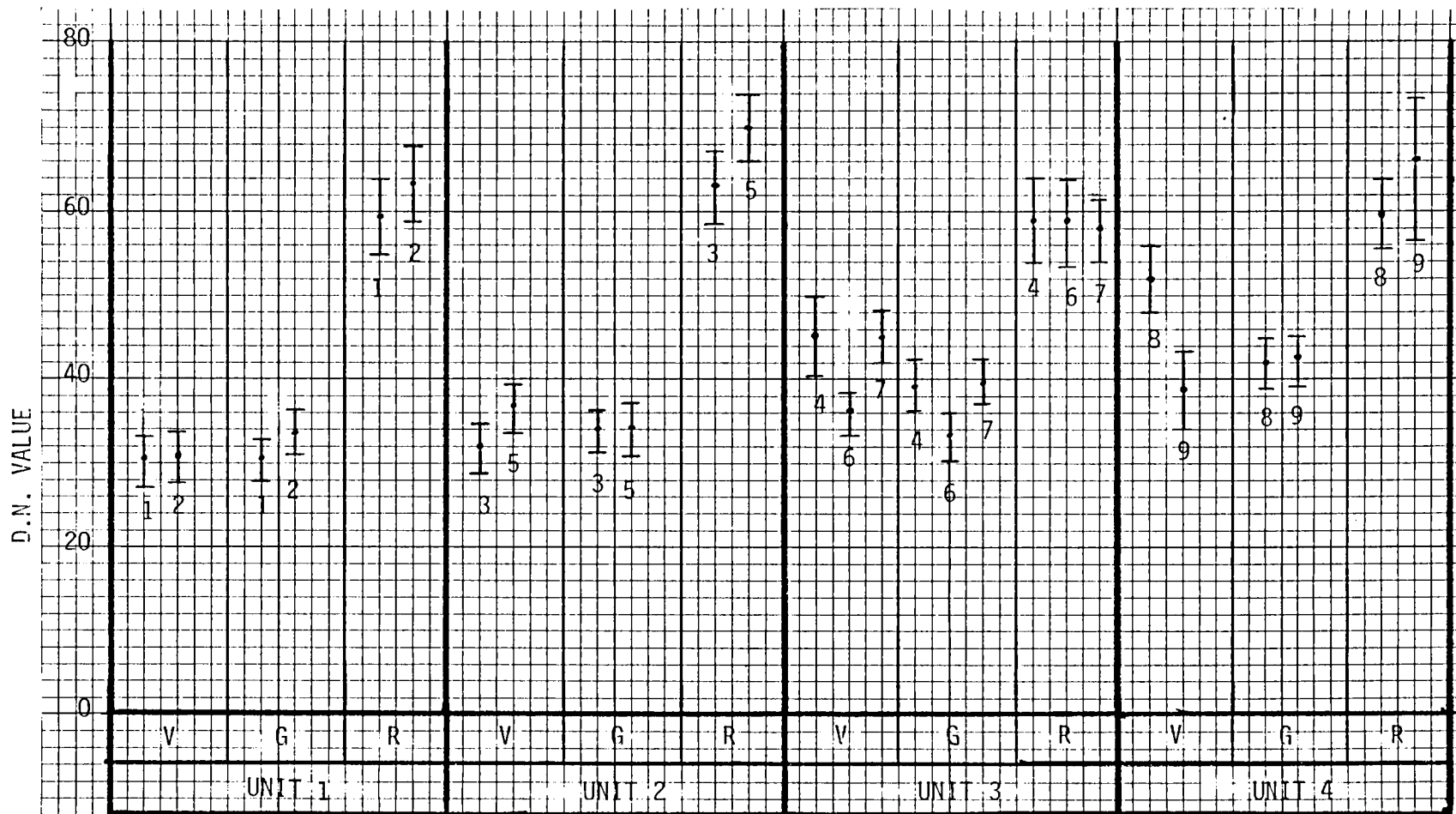


Fig. 3. Bar graph representing pixel value means and standard deviations within selected areas(fig. 2) for violet(V), green(G), and red(R) wavelength images which made up the derived color composite. Values are those derived after the multivariate analysis was performed on the original data.

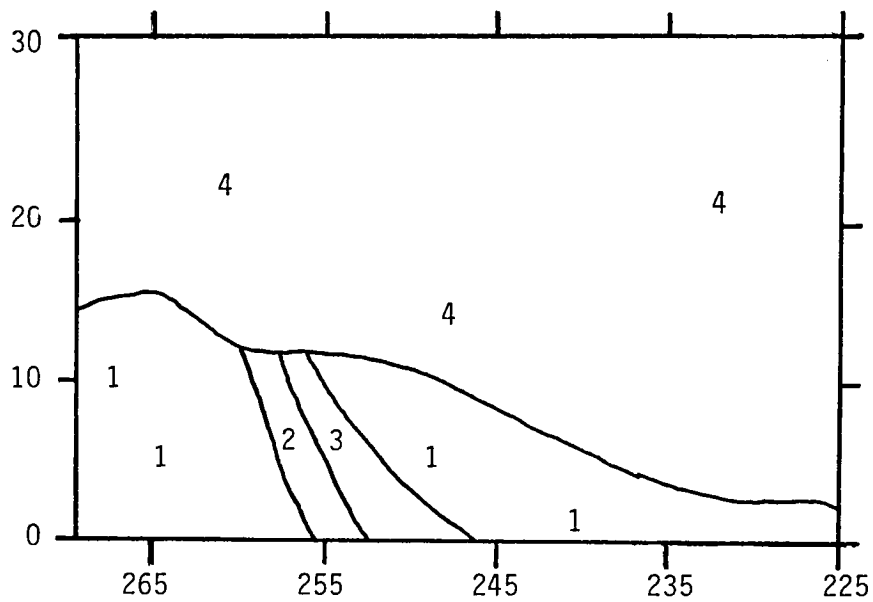


Fig. 4. Approach color quality data for Amenthes quadrangle.

- 1 - best coverage
- 2 - poor resolution
- 3 - near terminator
- 4 - clouds & poor resolution

SPECTRAL REFLECTANCE (0.4-0.7 μm) OF CARBON-SULFUR MIXTURES

April Clare*†
and
Jonathan Gradie

Center for Radiophysics
and Space Research
Cornell University
Ithaca, NY 14853

*Current Address:

Department of Geology
Lafayette College
Easton, Pennsylvania 18042

†Planetary Geology Undergraduate Research Intern

ABSTRACT

The spectral reflectances ($\lambda = 0.39$ to $0.70 \mu\text{m}$) of ultrapure sulfur contaminated with various quantities of a coal tar residue and charcoal were found to decrease with an increase in peak heating temperature. Contamination at the 10^{-4} (by weight) level produced detectable spectral changes relative to the pure sulfur under the same conditions. The coal tar residue was more effective than the charcoal at altering the spectral reflectances and about one hundred times more effective than basalt. The flux of carbonaceous material calculated to fall on Io is not sufficient to cause significant discoloration of sulfur if the suggested resurfacing rate (10^{-1} to 10^{-3} cm/yr) is correct.

INTRODUCTION

The surface composition of Io has been the topic of study for some time, the main question being whether it is covered by elemental sulfur or sulfur compounds. Sulfur was first suggested by Wamsteker (1972) due to the similarity between the disk-integrated spectral reflectance of Io and the spectral reflectance of pure sulfur. Various compositions have been suggested for the surface since, almost all involving ~~any~~^e sulfur, altered sulfur or sulfur compounds. For example, Nelson and Hapke (1978) suggested that Io's surface was due to hot, elemental sulfur emitted from volcanic fumaroles that was subsequently quenched on the cold surface. This theory was further expanded by Sagan (1979) and others to include quenched sulfur flows after the discovery of active volcanism on Io. However, the relevance of quenching of the surface of Io has been brought into question (cf. Young, 1984; Gradie et al., 1972; Gradie and Moses, 1983) since pure sulfur flows would be too thick to cool fast enough to allow the S_3 and/or S_4 allotropes formed in the liquid to remain stable.

It appears that sulfur must either occur in a state other than the elemental form, i.e. either in compounds or mixtures. Fink et al. (1983) have proposed that as the flows on Io appear similar to terrestrial flows of silicate composition, the peculiar spectral properties may apply only to the upper few millimeters of the surface. If this is indeed the case then sulfur could be mixed with basalt to form basalt-sulfur mixtures that have the spectral properties peculiar to Io. Gradie and Moses (1984) have examined the spectral properties of basalt and sulfur mixtures. Indeed, some basalt-sulfur mixtures

have spectral properties that match volcanic regions on Io. However, many material can alter the spectral properties of elemental sulfur. Contamination by carbon from carbonaceous meteorites is one possibility since as much as 2.4×10^{-2} gm/cm³ of carbon from carbonaceous meteorites is delivered to the lunar regolith in 10^7 years (Taylor, 1982).

Here we examine the effects that carbon contamination has on the spectral properties of pure sulfur heated to temperatures that may be typical of those in the volcanic regions of Io. The temperature of 433°K was chosen since it is near the temperature where sulfur has a minimum viscosity and would become most mobile. The temperature of 717°K was chosen since it is near the temperature that sulfur would attain in close proximity to silicate magmas. The spectral range ($\lambda = 0.39$ to $0.70 \mu\text{m}$) was chosen as ^{it is} the region where sulfur appears to be most optically active and matches the wavelength region of the Voyager spacecraft images.

EXPERIMENTAL

Five different compositional mixtures of ultrapure sulfur (99.99% Aldrich Chem. Gold Label) and coal tar residue (Gradie and Veverka, 1980) (CTR) were prepared: 100 wt% S, 99.99% S + 0.01% CTR, 99.9% S + 0.1% CTR, 99% S + 1% CTR, and 90% S + 10% CTR. The coal tar residue is thought to be an analogue of the carbonaceous component of some asteroids. Between 15 to 20 g of sample were prepared, weighing the components on a Mettler balance reaching to 1 part in 10^5 . To insure as thorough mixing as possible, the coal tar was ground into a fine

powder to allow for better dispersion among the powdered sulfur upon shaking of the sample vial. 99.9 % sulfur and 0.01 % charcoal and

99.9 % sulfur and 0.1 % charcoal samples were prepared also and the charcoal mixture were

Each of the first four compositions listed above ~~was~~ heated to 160°C and a second set to 430°C. These temperatures were chosen as they are the temperature of minimum viscosity and temperatures of boiling at 1 atmosphere. Sulfur on Io would be expected to be most mobile at 160°C. Contact with silicate magmas could bring the temperature of the sulfur to its boiling point. A 15 × 125 mm test tube was filled about 2/3 full with the sample under consideration. For the 160°C samples, the open tube was heated slowly over an open flame, removing it from the flame several times in the process. No attempt was made to exclude air. When the mixture had melted to a viscosity like that of water, with the color a shade of orange, it was removed from the flame and allowed to cool in the air. The 430°C samples were heated beyond this stage, the color getting darker and the viscosity increasing with temperature until the boiling point was approached, where the viscosity began to lessen. The sample was allowed to boil for a few seconds before being placed to one side and allowed to cool. After the samples had cooled, the surrounding test tubes were carefully broken and removed from the solid sample, with as little sample loss as possible. The sample particles were ground and sieved to approximately < 150 μm diameter. The samples were measured at room temperature at an incidence angle of -4° and an emission angle of 0°.

RESULTS

It is well known that mechanically mixing small amounts of opaque material can substantially darken a highly reflective material. Clark (1981) demonstrated that parts per thousand of soot (carbon) could noticeably reduce the reflectance of water ice. The addition of charcoal and our CTR to sulfur is no exception. As illustrated in Fig. 1, the spectral reflectance of pure sulfur is seen to decrease as increasing amounts of coal tar residue (CTR) are added to the sulfur. Charcoal has the same effect, but is more effective due to the smaller particle sizes in our sample as discussed below.

The interaction between our organic material (CTR) and sulfur in the molten state is not well understood. However, it is sufficient to say that organic materials and sulfur can combine to form thiolated organic compounds. In fact, one common test for the presence of organic material (oil) in sulfur is to heat the sulfur to its boiling point and then to note any dark spots that form from the interaction of the organics with the sulfur.

Our experiments were designed to test and quantify the relative ability of the coal tar residue and the charcoal to alter the spectral properties of molten sulfur.

In Fig. 2 we compare the spectral reflectance of pure sulfur and a mixture of sulfur with 10^{-3} parts of CTR that have been mechanically mixed, heated to 160°C and cooled or heated to 433°C and cooled. Pure sulfur heated to the low viscosity point (160°C) returns to nearly its original spectral state upon cooling. However, the addition of the CTR causes a marked change in the spectrum; the reflectance from 0.40

to 0.45 μm is increased relative to the unheated mixture, the reflectance from 0.5 to 0.7 μm decreased, and the spectral reflectance from 0.5 to 0.7 μm is no longer neutral but is reddened.

The sample heated to the boiling point showed similar changes in overall reflectance. However, whereas the pure sulfur heated to 433°C and then cooled is highly reddened spectrally from 0.5 to 0.7 μm , the contaminated sample is more spectrally neutral. A similar effect has been noted by Gradie and Moses (1984) for mixtures of basalt and sulfur. In those experiments, the addition of 10% by weight of basalt to sulfur lowered the reflectance at $\lambda = 0.70 \mu\text{m}$ by a factor of two while not affecting the reflectance shortward of $\lambda = 0.45 \mu\text{m}$ (see Fig. 3b).

We can compare the ability of CTR in affecting spectral changes by comparing the ratio of the reflectivity at several wavelengths or the colors. These values are tabulated in Table 1. In Fig. 3a we compare the reflectivity at 0.50 μm (green) with that at 0.40 μm (blue) as a function of temperature and the amount of contaminant.

The decreasing ratio with increased peak heating and increased contaminant level implies a weakening of the strong ultraviolet sulfur absorption either by the reduction in S_8 molecules or the masking of the S_8 absorption by materials produced by the interaction between the contaminant and the sulfur during the heating process. Because pure sulfur shows a similar trend, we suspect that the reduction in the abundance of S_8 relative to other sulfur allotropes is the primary cause and the production of thiolated hydrocarbons is secondary.

In Fig. 3b we compare the red (0.70 μm) and blue (0.40 μm) reflectances as a function of temperature and the amount of contaminant. The same trends are apparent. Included in this figure is the color ratio for the 9:1 sulfur:basalt mixture heated to 430°C measured by Gradie and Moses. It is immediately apparent that basalt is about 100 times less effective in the alteration of the spectral reflectance.

In Fig. 4 we compare the reflectance in the red ($\lambda = 0.70 \mu\text{m}$) with that in the green ($\lambda = 0.50 \mu\text{m}$). This index gives a measure of how the spectrally neutral reflectance region of pure sulfur changes with temperature and level of contaminant. Here we see some important trends. Pure sulfur becomes more spectrally reddened as the peak heating temperature is increased, whereas the contaminated sulfur, which is more spectrally reddened than the pure sulfur when heated to 160°C, becomes less spectrally reddened than the pure sulfur when heated to a peak temperature of 430°C. In fact, at the highest levels of contamination (10^{-2}), the mixture heated to 430°C is more spectrally neutral than the same mixture heated to 160°C.

Finally we compare in Figs. 5 and 5b the effectiveness in producing spectral changes in the heated sulfurs by two levels of contamination of CTR and charcoal. For both the 10^{-3} to 10^{-4} levels of contamination the charcoal is the more efficient darkening agent. This result is probably due to the smaller particle sizes of the charcoal grains ($< 44 \mu\text{m}$) relative to the CTR grains ($< 150 \mu\text{m}$). However, for the molten sulfur the situation is reversed. The CTR is the more effective darkening agent. [It is also apparent in Figs. 5 and 5b that the wavelength position of the shoulder of the 0.35 μm S_8

absorption shifts to shorter wavelengths as the samples are heated.] Apparently, the CTR which is composed of aromatic and aliphatic hydrocarbons is more effective than simple carbon in producing discoloration and darkening in molten sulfur.

DISCUSSION

Considerable controversy still exists over the nature of the "colored" surface of Io. Sagan (1979), Smith et al. (1979) and others have argued that quenched sulfur could easily explain the colorful surface. However, Gradie and Moses (1983) and Young (1984) point out that due to sulfur's physical producing quench sulfur on Io may be difficult in spite of the low ambient temperature.

Gradie and Moses (1984) have shown that certain heated sulfur and basalt mixtures have spectral reflectances that match certain volcanic regions on Io and may provide an analog for these materials. It is apparent from our experiments here that the addition of a carbonaceous component to sulfur can significantly alter the spectral properties of the melted sulfur also.

We ask then, is carbonaceous contamination an important factor on Io? Taylor (1982) notes that the carbon component (~ 115 ppm) of the lunar regolith is almost totally meteoritic in origin. If we take into account the gardening rate of the moon for the first few centimeter depth (10^7 yr/cm) and account for the variation in the flux rate of meteorites on Io relative to the moon (10^{-9} g/cm²/yr) we find that the carbon in the lunar regolith is probably placed at the level

of 10^{-4} in a few times 10^7 years. However, the calculated resurfacing rates on Io are as high as estimated (10^{-1} to 10^{-3} cm/yrs) (Johnson et al., 1982), then the carbon content on Io's surface due to meteoritic sources is probably no more than 1 part in 10^{-7} !

Therefore, it seems unlikely that carbon contamination from meteoritic sources is important for altering the spectral properties of molten sulfur on Io. Carbon contamination may become important if any thiolated hydrocarbons are recycled through the postulated sulfur and sulfur dioxide aquifers and not removed from the system.

ACKNOWLEDGMENTS

This research was supported by NASA Grant NSG 7606 and the Planetary Geology Undergraduate Research Program.

REFERENCES

- Clark, R. N. (1981). The spectral reflectance of water-mineral mixtures at low temperatures. J. Geophys. Res. 86, 3074-3096.
- Fink, J. H., S. O. Park, and R. Greeley (1983). Cooling and deformation of sulfur flows. Icarus 56, 38-50.
- Gradie, J., and J. Moses (1983). Spectral reflectance of unquenched sulfur. Lunar Planet. Sci. XIV, 255-256.
- Gradie, J., and J. Veverka (1980). The composition of the Trojan asteroids. Nature 283, 840-842.
- Gradie, J., and J. Veverka (1984). Photometric properties of powdered sulfur. Icarus 58, 227-245.
- Johnson, T. V., and L. A. Soderblom (1982). Volcanic eruptions on Io: Implications for surface evolution and mass loss. In Satellites of Jupiter (T. Gehrels, ed.), U. of Arizona Press, Tucson, pp. 634-646.
- Nelson, R. M., and B. W. Hapke (1978). Spectral reflectivities of the Galilean satellites and Titan, 0.32 to 0.86 micrometers. Icarus 36, 304-329.
- Sagan, C. (1979). Sulfur flows on Io. Nature 280, 750-753.
- Smith, B. A., and the Voyager Imaging Team (1979). The Jupiter system through the eyes of Voyager 1. Science 204, 951-971.
- Taylor, S. R. (1982). Planetary Science: A Lunar Perspective. Lunar and Planetary Institute, Houston, TX, 481 pp.
- Wamsteker, W. (1972). Narrow-band photometry of the Galilean satellites. Comm. Lunar Planet. Lab. 9, 171-177.
- Young, A. (1984). No sulfur flows on Io. Icarus 58, 197-226.

TABLE 1.

Sample	Room temp. (22°C)			T = 160°C			T = 430°C		
	Color 1 ¹	Color 2 ²	Color 3 ³	Color 1	Color 2	Color 3	Color 1	Color 2	Color 3
Pure sulfur	16.58	16.63	15.87	8.89	8.92	8.00	6.75	5.24	3.85
Sulfur 99.99% + 0.01% CTR	16.25	16.79	15.72	8.69	8.37	7.46	5.29	4.55	3.61
Sulfur 99.9% + 0.1% CTR	15.00	14.83	14.75	7.19	6.60	5.90	4.03	3.52	2.96
Sulfur 99% + 1% CTR	16.02	15.95	15.39	4.12	3.78	3.11	2.15	1.86	1.72
Sulfur 90% + 10% CTR	10.10	9.95	9.98						
Sulfur 99.99% + 0.01% charcoal	15.43	15.45	15.38	9.33	9.35	8.97	7.25	6.04	4.67
Sulfur 99.9 + 0.1% charcoal	12.24	12.31	12.41	6.54	6.64	6.52	6.41	5.89	4.73

¹R($\lambda = 0.70$)/R($\lambda = 0.40$)

²R($\lambda = 0.60$)/R($\lambda = 0.40$)

³R($\lambda = 0.50$)/R($\lambda = 0.40$)

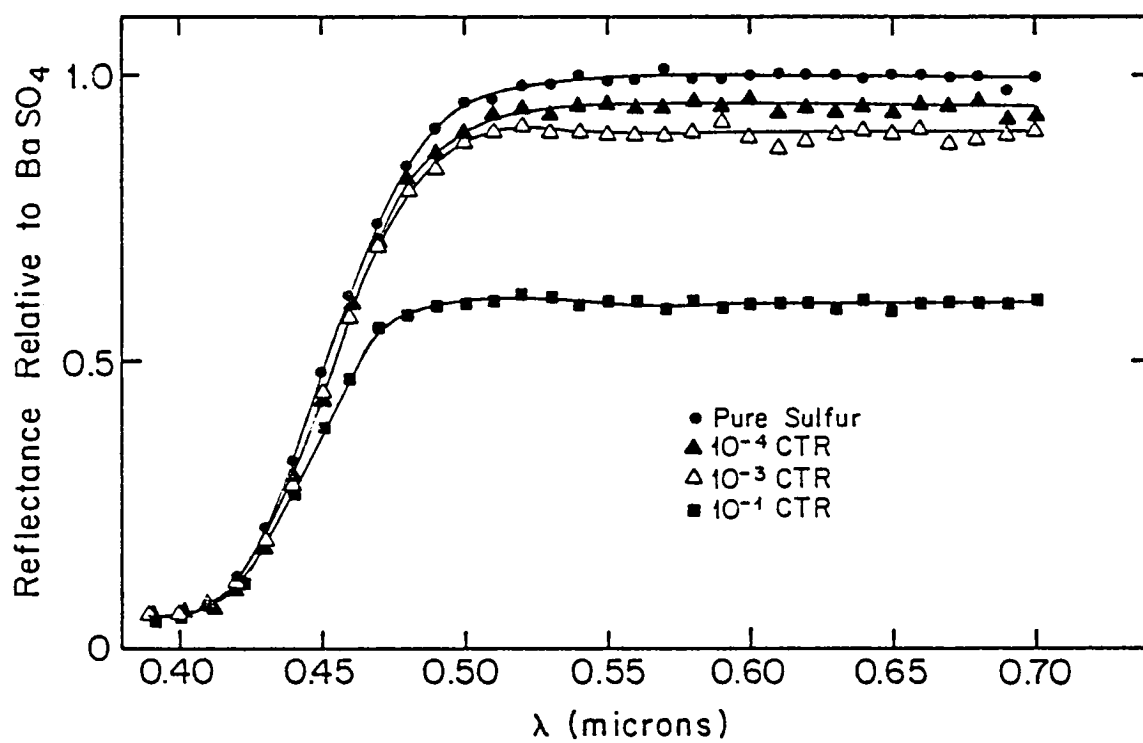


Fig. 1. The spectral reflectance ($\lambda = 0.39$ to $0.70 \mu\text{m}$) relative to a BaSO_4 standard of pure sulfur and sulfur contaminated with various concentrations (by weight) of a complex hydrocarbon residue (CTR) made from coal tar (see text).

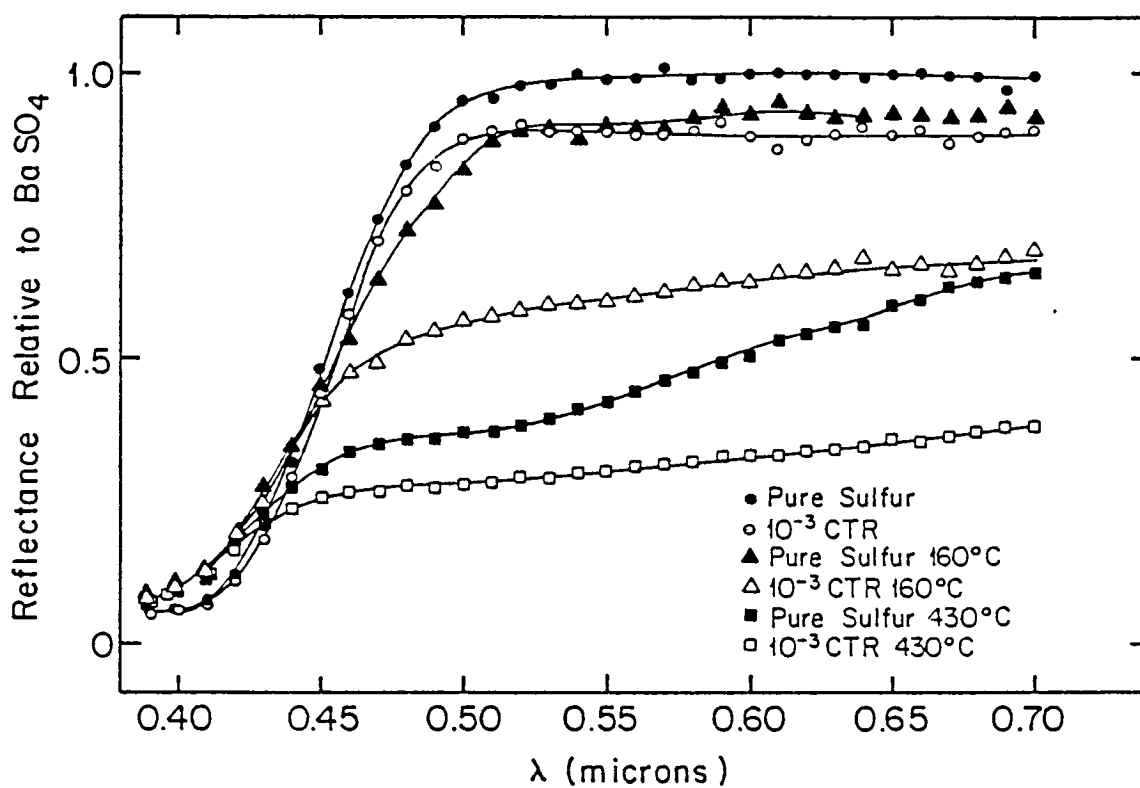


Fig. 2. The spectral reflectance ($\lambda = 0.39$ to $0.70 \mu\text{m}$) relative to a BaSO₄ standard of pure sulfur and sulfur contaminated with 10^{-3} parts (by weight) of the CTR that have undergone different thermal histories: unheated, mechanical mixtures, heated to 160°C and then cooled to room temperature, and heated to 430°C and then cooled to room temperature.

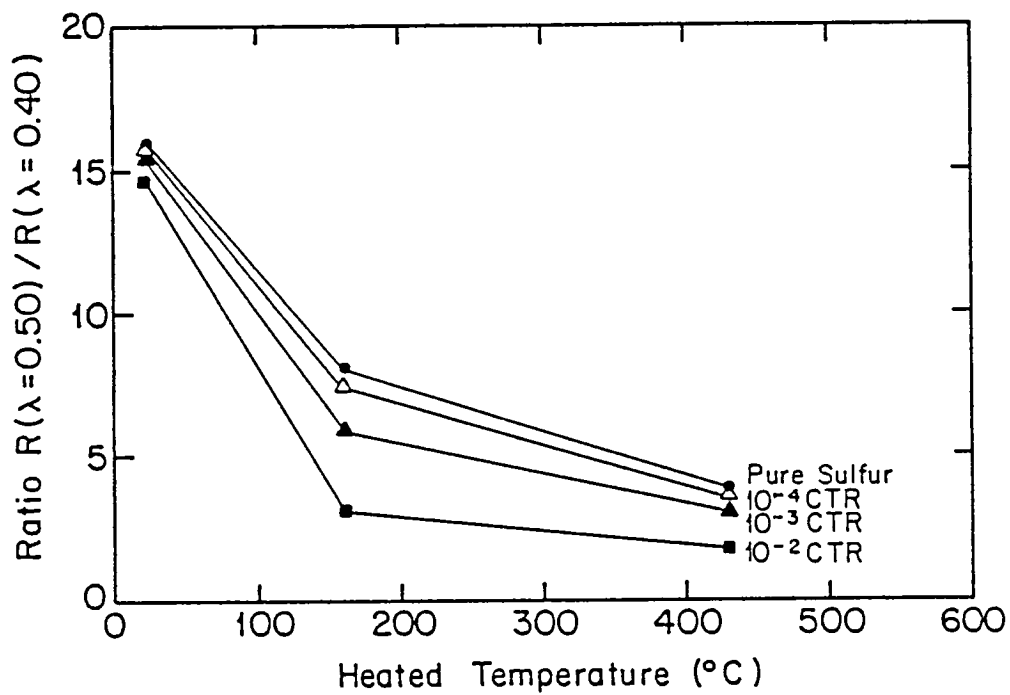


Fig. 3a. The change in the ratio of reflectance in the green ($\lambda = 0.50 \mu\text{m}$) and blue ($\lambda = 0.40 \mu\text{m}$) as a function of peak heating temperature and concentration of CTR contaminant.

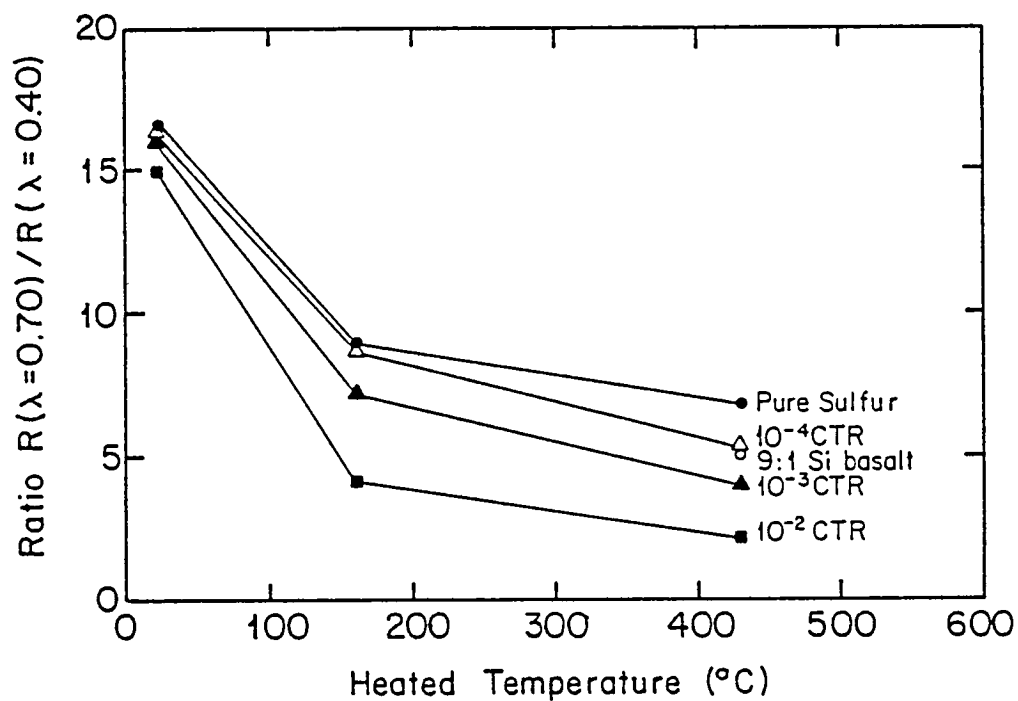


Fig. 3b. The change in the ratio of reflectances in the red ($\lambda = 0.70 \mu\text{m}$) and blue ($\lambda = 0.40 \mu\text{m}$) as a function of peak heating temperature and concentration of CTR contaminant. The 9:1 sulfur:basalt mixture is from Gradie and Moses (1984).

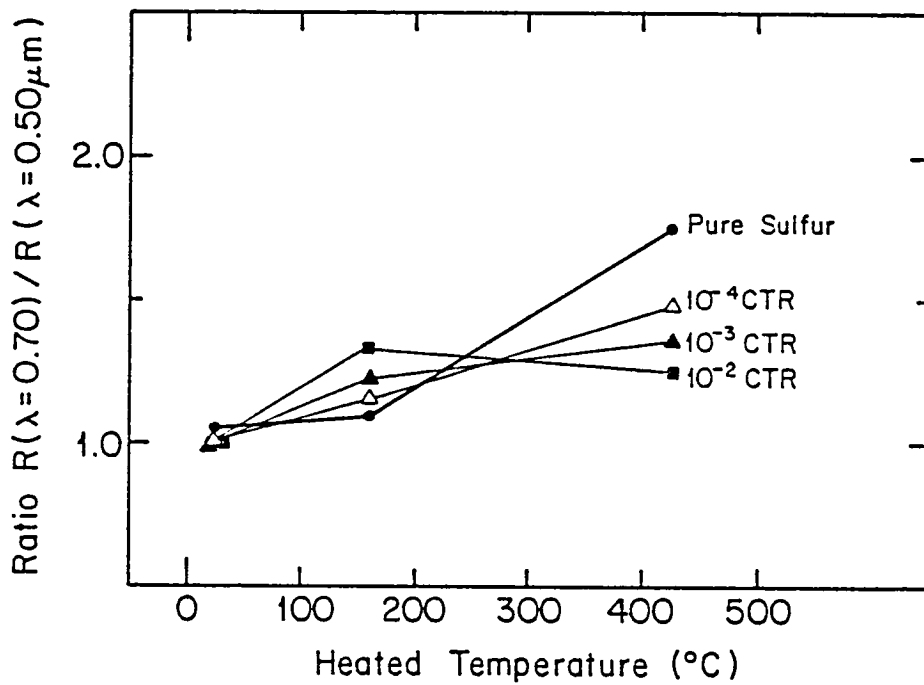


Fig. 4. The change in the ratio of the reflectances in the red ($\lambda = 0.70 \mu\text{m}$) relative to the green ($\lambda = 0.50 \mu\text{m}$) as a function of peak heating temperature and concentration of CTR contaminant.

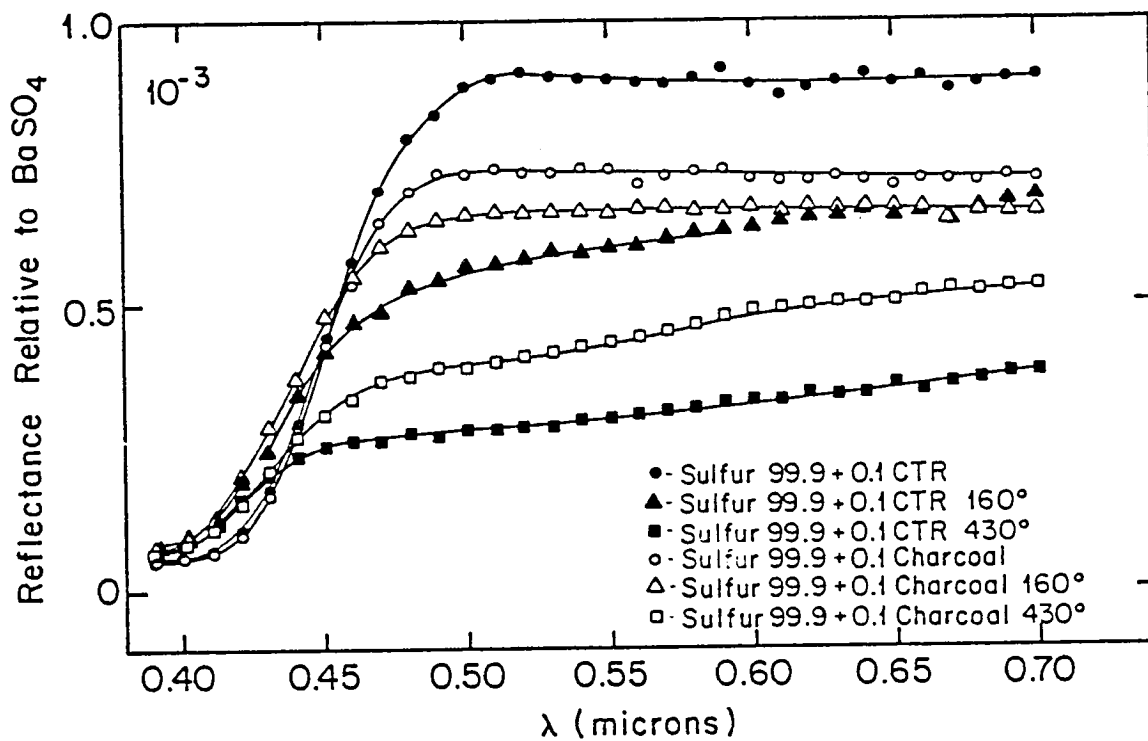


Fig. 5a. A comparison of the heating induced spectral reflectances of CTR-sulfur mixtures and charcoal-sulfur mixtures for contaminant concentrations at the 10^{-3} (by weight) level.

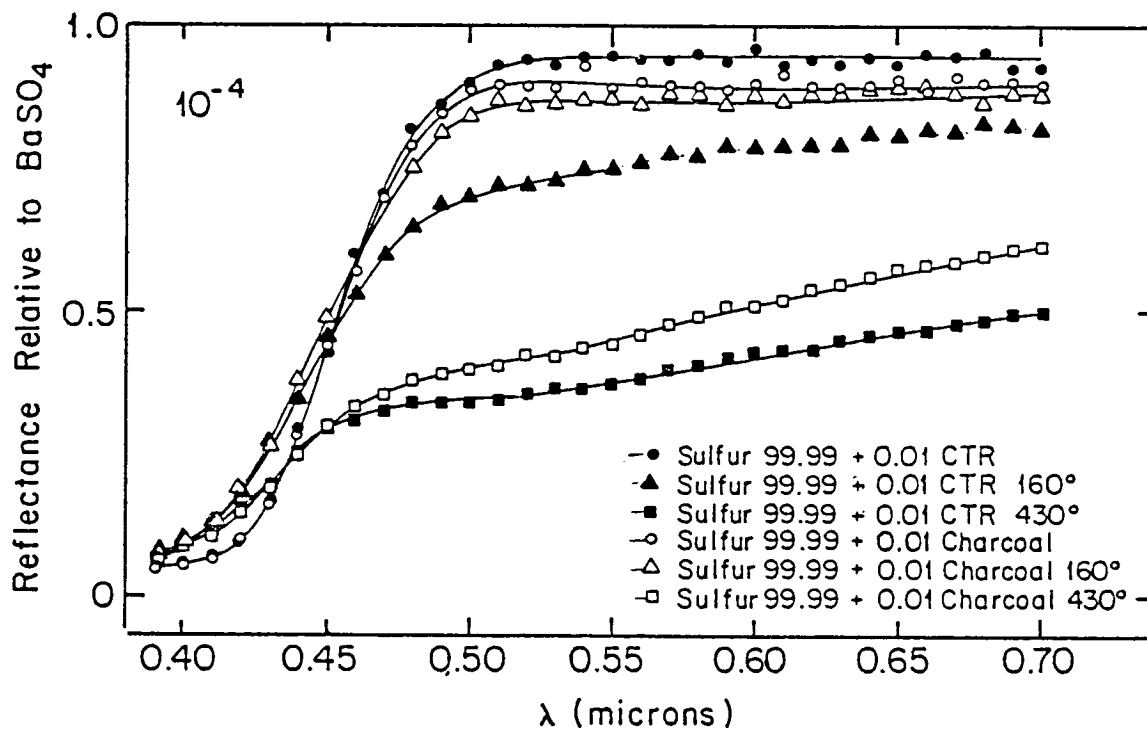


Fig. 5b. A comparison of the heating induced spectral reflectances of CTR-sulfur mixtures and charcoal-sulfur mixtures for contaminant concentrations at the 10^{-4} (by weight) level.

LAB EXPERIMENTS ON UV SPECTRA OF GASEOUS AND ADSORBED
SULFUR DIOXIDE AND APPLICATIONS TO IO

By:

Julianne I. Moses
Cornell University
Ithaca, NY 14850
NASA Planetary Geology Intern at
Jet Propulsion Laboratory

Advisor:

Douglas B. Nash
Jet Propulsion Laboratory
4800 Oak Grove Drive
Pasadena, CA 91109

24 August 1984

Introduction

Jupiter's satellite, Io, has proven to be one of the most interesting and confusing planetary bodies in our solar system. From ground-based aircraft and spacecraft spectral data, investigators have, for years, been trying to determine the surface composition of the satellite. In the past few decades, the search for the surface composition of Io has concentrated on studies of silicate rocks and surface frosts. Silicates were studied because Io has a mean bulk density similar to that of the Earth's moon, and frosts were studied because Io has a high visible albedo and cold surface. Early on, however, it was clear that Io was different from the other Galilean satellites in having no water absorption bands in its near infrared ground-based spectra, and hence probably no water ice on its surface (Bridge, et al., 1979). In addition, the spectral reflectance of the satellite as a whole is unlike that of common silicate rocks. The compositional search later concentrated on sulfur and sulfur compounds after Wamsteker (1972) noted that the strong ultraviolet absorption shoulder and overall reflectance spectrum of Io resembled that of ordinary sulfur, S₈. Other clues pertaining to Io's surface composition were revealed when Io was believed to be the source both for the sulfur and oxygen ions observed in Jupiter's magnetosphere and for the neutral sodium and potassium atoms in Io's plasma torus (Brown, 1974; and others).

Sulfur dioxide is the only molecule that has been positively identified on Io. The thermal infrared spectrum of Io measured by Voyager IR spectrometer indicates the presence of gaseous sulfur dioxide near a volcanic plume, Loki (Pearl et al., 1979). Pearl et al. estimate an abundance of 0.2 cm-atm with an estimated probable error of a factor of 2. This number corresponds to an SO₂ surface pressure of about 10⁻⁷ bar which could indicate that the atmosphere is in equilibrium with solid SO₂ at the local surface equilibrium temperature of 130°K. The discovery of SO₂ in the atmosphere has led investigators to identify the strong 4 micron absorption feature in Io's infrared spectrum as belonging to the $\nu_1 + \nu_3$ combination band of sulfur dioxide (Fanale et al., 1979; Nash and Nelson, 1979; Smythe et al., 1979). There has been disagreement, however, as to the phase of the SO₂. Is it present as a solid (ice or frost) or is it present as gas adsorbed on the particles that make up the satellite's surface?

Frost vs. Adsorbate

If the atmosphere on Io were as "thick" as Pearl et al. (1979) and others claim, then SO₂ frost deposits should be widespread on the surface. The SO₂-saturated atmosphere would be buffered locally by SO₂ frost. Since sulfur dioxide condenses at 200°K and since (as Soderblom et al., 1980 point out) there are physical-chemical reasons for SO₂ frost to occur along with S₈, it would seem that SO₂ frost is a likely surface constituent. In addition, SO₂ frost has an absorption shoulder at about 0.32 microns--a feature which is also present in IUE data of Io (Nelson et al., 1980; Nash et al., 1980).

There are problems, however, with the suggestion that frost is widespread on the surface of Io. In studying the surface texture of the satellite, Pang et al. (1981) have estimated that the bulk density of the topmost surface layer is about 0.7-0.8 g/cm³ and conclude that SO₂ frost is not present in an optically thick layer. Nash (1983) points out that the 10⁻⁸-10⁻⁷ bar equilibrium pressure required to sustain SO₂ frost is much higher than the

predicted subsolar SO₂ pressure on Io. Pearl and Sinton (1982) claim that the poles of Io should act as cold traps for SO₂ just as the Martian poles act as coldtraps for CO₂. However, no large deposits of the white material associated with SO₂ frost are observed. In addition, Matson and Nash (1983) point out that the lack of regular night-time frost and the lack of post-eclipse brightening place severe restrictions on the amount of stable SO₂ frost in equilibrium with an SO₂ atmosphere. Matson and Nash also claim that the "fluffy" volcanic ash thought to cover much of Io's surface would be a perfect substrate for adsorbed gas. The material would be heated in the volcanoes and so have clean particulate surfaces allowing for gas to adhere. Hence, subsurface coldtrapping would result in a "thin" atmosphere of only 10⁻¹² bars and permafrost formation would play the dominant role in the control of Io's equilibrium atmospheric pressure. Nash (1983) argued that the theory of adsorbed SO₂ rather than SO₂ frost is supported by high resolution Fourier transform spectroscopy data by Fink *et al.* (1980) which place the center of the 4 micron absorption band of Io at 4.054 μm. Adsorbed sulfur dioxide has a band at 4.05 μm while SO₂ frost has a band closer to 4.08 μm. However, more recent data of Howell *et al.* (1984) places Io's band minimum at 4.07 μm, the same as laboratory frost, not adsorbate.

It is very likely that both SO₂ frost and adsorbed SO₂ are present on Io's surface. Since the sulfur dioxide is probably released through the plumes and other volcanic mechanisms, the SO₂ distribution would be subject to much spatial and temporal variation. Local deposits of SO₂ frost may be scattered over the surface at any one time, but its entire coverage must be limited. Adsorbed SO₂ gas seems a prime candidate for explaining some of the observed spectral features on Io.

Laboratory Experiments

Laboratory data concerning the effects of adsorbed sulfur dioxide on the spectral reflectance of various substrates are practically nonexistent. There are many questions that have not been answered concerning adsorbed SO₂. For instance, since SO₂ has a strong UV band, does the presence of an SO₂ adsorbate affect the spectral reflectance of the sample in the UV region? What samples will accept the adsorbed gas? What are some of the temperature effects? Where exactly is the ultraviolet absorption band? What effects does SO₂ gas pressure have on the adsorbate? We have performed preliminary experiments in an attempt to answer some of these questions.

To accomplish this we have made low resolution measurements of the spectral reflectance from 0.25 to 0.40 μm of three different substrates. Each measurement was a three-step process: 1) intensity measurement under vacuum; 2) intensity measurement at varying pressure of SO₂; and 3) intensity measurement after the gas has been pumped out again. Dividing the latter two intensities by the first one (for each sample) will give a relative reflectance of either the SO₂ gas (2) or adsorbate (3). In addition, we examined the effect of heating one of the samples to over 100°C to drive away any previously adsorbed water vapor to see if this process had any effect on the results.

The spectra were measured with a grating spectrometer and S-20 photomultiplier detector in the ultraviolet region from 0.25 to 0.40 μm. Wavelength calibration was achieved with an Hg-vapor lamp. The illumination was

produced by a Xenon lamp with a liquid Nickel-sulfate filter behind the lamp exit port to reduce the intensity of the visible light. From here, the filtered light enters the vacuum chamber through a sapphire window and variable diaphragm which is adjusted to produce a beam with a one centimeter radius. Then, the beam is reflected off a planar, front surface aluminum mirror onto a sample container. The sample scatters light in all directions. A sapphire window is placed at a 45° to the sample surface to permit the resulting spectral reflectance intensity to be recorded. A variable slit on the spectrometer, and an electronic amplifier allows the necessary adjustment of the signal so that the intensity is plotted against wavelength on a pen recorder. All measurements reported here were taken at room temperature. An accurate error analysis has not been conducted, so the following results are meant to be more qualitative than quantitative. Because of the age of the optics in the system and because of the relatively large slit width needed (0.2-0.6 mm) to receive the signal, we estimate that the error in the reflectance measurement is as much as 10%.

The three substrates we chose were Cab-O-Sil™ (amorphous fumed silica) because of its high specific surface area and high reflectance in the ultraviolet region; MgO because of its high reflectance in the UV region and widespread use as a standard; and sulfur because of its obvious applications to Io's surface. The Cab-O-Sil, from Cabot Corporation, had a particle size of 0.018 μm . We packed the Cab-O-Sil moderately in an aluminum cup 3mm deep. The MgO was freshly smoked onto a 1mm deep aluminum cup. The sulfur (sublimed) from Mallinckrodt Chemical Work, was ground to a powder ($<100 \mu\text{m}$) in and was lightly packed into a 1mm aluminum cup. We took care to make sure the samples were homogeneous throughout their depth and as identical to each other in texture as we could make them. In one experiment, we heated a Cab-O-Sil sample to over 373°K for one hour in the vacuum chamber. We allowed it to cool to room temperature, still under vacuum, before we introduced SO₂ gas to see if the heating had any effect on the amount of adsorbed gas. All spectral measurements were taken after the Xenon lamp was allowed to warm up for five minutes.

We introduced anhydrous sulfur dioxide gas (Matheson lecture bottle) into the chamber at pressures ranging from 100 mtorr of Hg to 1000 mtorr. This range of pressure was used for two important reasons. First, the pressure gauge we used is only accurate to just over 1000 mtorr on the high end. Secondly, we were trying to achieve roughly the same number of SO₂ molecules in our beam as Voyager and ground-based observers "see" in measuring the spectral reflectance of Io assuming Io has an equilibrium atmosphere. Our beam is about 40 cm in length. Estimates previously set Io's column density at 0.2 cm-atm or about 10^{18} molecules in a 1 cm² column. Thus we would want 3.14×10^{18} molecules in our beam of area 3.14 cm² or a number density of 2.5×10^{16} molecules/cm³. Using the ideal gas law, we determine that the pressure required in our chamber to achieve that number density is 765 mtorr. Of course, this is not an attempt to match the effect of Io's atmosphere on spectral reflectance measurements of Io because we do not take gravity or more complicated atmospheric effects into account, but it gives us a rough indication of the pressures that will be relevant to a comparison with Io.

Conclusions

We have shown two experimental results that bear on problems relating to understanding the nature of SO₂ on Io:

1. Measuring the UV spectral reflectance of a surface over which there is an SO₂ gas component (atmosphere) with column abundance equivalent to 0.2 cm-atm of SO₂ gas over Io's surface will yield a distinct UV band due to the gas component. Thus if Io has an equilibrium atmosphere of 0.2 cm-atm then the presence of this SO₂ atmosphere should contribute a UV absorption feature in Io's global reflectance spectrum.
2. Exposure of finely particulate material to SO₂ gas, followed by removal of the gas phase, produces enough adsorbed SO₂ on the particles to yield a detectable spectral absorption band centered near 0.29 μm in the material's UV reflectance spectrum. The strength of the adsorbate band in the UV depends on substrate composition, gas exposure time, and cleanliness of the substrate particles. If particles making up Io's surface regolith come in contact with SO₂ gas they may retain an adsorbed SO₂ component that could contribute structure to Io's global UV reflectance spectrum.

produced by a Xenon lamp with a liquid Nickel-sulfate filter behind the lamp exit port to reduce the intensity of the visible light. From here, the filtered light enters the vacuum chamber through a sapphire window and variable diaphragm which is adjusted to produce a beam with a one centimeter radius. Then, the beam is reflected off a planar, front surface aluminum mirror onto a sample container. The sample scatters light in all directions. A sapphire window is placed at a 45° to the sample surface to permit the resulting spectral reflectance intensity to be recorded. A variable slit on the spectrometer, and an electronic amplifier allows the necessary adjustment of the signal so that the intensity is plotted against wavelength on a pen recorder. All measurements reported here were taken at room temperature. An accurate error analysis has not been conducted, so the following results are meant to be more qualitative than quantitative. Because of the age of the optics in the system and because of the relatively large slit width needed (0.2-0.6 mm) to receive the signal, we estimate that the error in the reflectance measurement is as much as 10%.

The three substrates we chose were Cab-O-Sil™ (amorphous fumed silica) because of its high specific surface area and high reflectance in the ultraviolet region; MgO because of its high reflectance in the UV region and widespread use as a standard; and sulfur because of its obvious applications to Io's surface. The Cab-O-Sil, from Cabot Corporation, had a particle size of 0.018 μm . We packed the Cab-O-Sil moderately in an aluminum cup 3mm deep. The MgO was freshly smoked onto a 1mm deep aluminum cup. The sulfur (sublimed) from Mallinckrodt Chemical Work, was ground to a powder (<100 μm) in and was lightly packed into a 1mm aluminum cup. We took care to make sure the samples were homogeneous throughout their depth and as identical to each other in texture as we could make them. In one experiment, we heated a Cab-O-Sil sample to over 373°K for one hour in the vacuum chamber. We allowed it to cool to room temperature, still under vacuum, before we introduced SO₂ gas to see if the heating had any effect on the amount of adsorbed gas. All spectral measurements were taken after the Xenon lamp was allowed to warm up for five minutes.

We introduced anhydrous sulfur dioxide gas (Matheson lecture bottle) into the chamber at pressures ranging from 100 mtorr of Hg to 1000 mtorr. This range of pressure was used for two important reasons. First, the pressure gauge we used is only accurate to just over 1000 mtorr on the high end. Secondly, we were trying to achieve roughly the same number of SO₂ molecules in our beam as Voyager and ground-based observers "see" in measuring the spectral reflectance of Io assuming Io has an equilibrium atmosphere. Our beam is about 40 cm in length. Estimates previously set Io's column density at 0.2 cm-atm or about 10^{18} molecules in a 1 cm² column. Thus we would want 3.14×10^{18} molecules in our beam of area 3.14 cm² or a number density of 2.5×10^{16} molecules/cm³. Using the ideal gas law, we determine that the pressure required in our chamber to achieve that number density is 765 mtorr. Of course, this is not an attempt to match the effect of Io's atmosphere on spectral reflectance measurements of Io because we do not take gravity or more complicated atmospheric effects into account, but it gives us a rough indication of the pressures that will be relevant to a comparison with Io.

Results and Discussion

MgO

The results of dividing the intensity of the light reflecting off freshly smoked MgO with SO₂ gas present in the chamber by the intensity of the light reflecting off MgO in vacuum are shown in Figure 1A. This is effectively the relative absorption spectrum of the gas. The most obvious thing to note from the figure is that the absorption band deepens with increasing pressure. We used a spectral increment of 0.0025 μm to determine this spectrum. The true absorption spectrum of sulfur dioxide gas in the ultraviolet has much structure at even finer wavelength division. This fact combined with the low resolution of the instrument mode we were using prevented us from actually resolving this finer structure. Therefore, the smooth curves shown average this finer structure in the spectrum, but the location of the band minima should be fairly accurate (within our ~10% error). Notice that the location of the band minima seems to shift to higher wavelengths as the pressure of the SO₂ gas is increased. The band minima change from ~0.289 μm at low pressures (less than 500 mtorr) to ~0.292 μm at 730 mtorr to 0.293 μm at 980 mtorr. This becomes even more obvious at high pressures of a few psi where the band minimum can be as high as 0.31 μm. These results show that an SO₂ atmosphere of column density ~10¹⁸ molecules cm⁻² above a surface that is bright in the UV will result in a distinct UV absorption band in the observed reflectance spectrum of that surface.

The reflectance spectra of the MgO samples after the SO₂ gas has been pumped out are shown in Figure 1B. We only included the spectra of two of the samples so as to not clutter the diagram. The only sample which seemed to be unaffected by the SO₂ after the gas has been pumped out was the sample which had been exposed to 100 mtorr SO₂. All the other samples exhibited some residual sulfur dioxide effects. In addition, the higher the pressure the sample had been exposed to, the deeper the absorption effect. Although the wiggles and structure do not seem to be "real" effects, we did not try to smooth out the curves, but connected the various points by straight lines. Clearly, an analysis of the band minimum position would be difficult and probably inaccurate, so we just note that there seems to be some adsorbate effect on MgO that causes a slight spectral absorption feature in its spectrum from 0.25 to 0.34 μm.

Cab-O-Sil

Figure 2A shows the ratios of intensities of the Cab-O-Sil samples both with and without SO₂ gas present in the chamber. The trends follow those for SO₂ in Figures 1A. Increasing the amount of SO₂ gas increases the depth of the absorption band. In addition, the band minima seems to shift to slightly higher wavelengths with increasing pressure, and the reflectance drops slightly from 0.38 to 0.39 μm.

Figure 2B shows the reflectances of two of the samples after the SO₂ gas has been pumped out. Note that the sample which had been exposed to 480 mtorr of SO₂ shows a deeper absorption in general than the sample that was exposed to 1000 mtorr. This is contrary to the results with MgO in Figure 1B. The spectrum of Cab-O-Sil pumped out from 250 mtorr is generally located in between that of the 1000 mtorr and 480 mtorr spectra, and the 730 mtorr

spectrum is similar to that of the 1000 mtorr spectrum. Hence, there seems to be no correlation between the original SO₂ pressure and the adsorbate. This lack of correlation may be due to the samples themselves. Cab-O-Sil is difficult to pack uniformly and inhomogeneities in the samples may allow for more or less SO₂ gas to be adsorbed than usual.

Figure 2C shows the effect of heating under vacuum on a Cab-O-Sil sample which was exposed to 530 mtorr SO₂ before the gas was pumped out. There seems to be a dramatic effect. The heating process (desorbing the H₂O contaminant) seems to have allowed more SO₂ gas to adsorb and thus decrease the reflectance of the Cab-O-Sil sample at low wavelengths.

Sulfur

Figure 3A shows the relative reflectance of the sulfur samples that were exposed to SO₂ gas inside the chamber. Sulfur follows the same trends as both the MgO and Cab-O-Sil. The depth of the absorption band increases with increasing pressure, and the band minima seem to shift even more noticeably towards higher wavelengths with increasing pressure.

Figure 3B shows the reflectance of two sulfur samples after the gas has been pumped out. The results are significantly different from that of MgO and Cab-O-Sil. The overall relative reflectances are similar no matter what the peak pressure was. In addition, the band minima seem to be centered at higher wavelengths than the minima were for the adsorbed gas on the MgO and Cab-O-Sil. Apparently the sulfur has changed chemically either due to the SO₂ or to the UV light or both. The sulfur samples appeared bleached white after removal from the chamber (for discussion of this see Nash and Moses, 1984).

Beer's Law

One thing noticed about the SO₂ gas present in the chamber with all three sample substrate was that the gas absorption did not obey Beer's Law. Beer's Law is the "fundamental law governing all types of electromagnetic radiation" (Skoog and West, 1971). If I₀ is the intensity incident upon a solution (solid, liquid, or gas) and I the intensity of the light after it is transmitted through the solution, then Beer's Law states that

$$\log_{10} \frac{I_0}{I} = \epsilon C l$$

where C is the concentration in moles/liter, l the length of the path of the light through the solution, and ϵ a constant called the molar extinction coefficient. The molar extinction coefficient is unique to a particular species and should not vary with concentration until very high concentrations are used. The molar extinction coefficient of SO₂ gas over MgO and Cab-O-Sil seems to be approximately constant with pressure until it jumps to ~300 liters/mole cm at pressure near 1000 mtorr (see Tables 1 and 2). Rao (1967) claims that SO₂ has two absorption bands at 0.360 μ m ($\epsilon=0.05$) and 0.290 μ m ($\epsilon=342$) due to singlet-triplet and singlet-singlet $n \rightarrow \pi^*$ transitions. An $\epsilon=342$ seems to be consistent with the higher pressure data with sulfur, however, ϵ seems to increase and may eventually reach 342 or so.

Probably the main reason that our samples did not obey Beer's Law is that the light was reflected from the samples as well as transmitted through the gas. In addition, chemical or physical interactions between the gas molecules and the substrates could be responsible for the apparent non-linearity in Beer's Law.

Conclusions

We have shown two experimental results that bear on problems relating to understanding the nature of SO₂ on Io:

1. Measuring the UV spectral reflectance of a surface over which there is an SO₂ gas component (atmosphere) with column abundance equivalent to 0.2 cm-atm of SO₂ gas over Io's surface will yield a distinct UV band due to the gas component. Thus if Io has an equilibrium atmosphere of 0.2 cm-atm then the presence of this SO₂ atmosphere should contribute a UV absorption feature in Io's global reflectance spectrum.
2. Exposure of finely particulate material to SO₂ gas, followed by removal of the gas phase, produces enough adsorbed SO₂ on the particles to yield a detectable spectral absorption band centered near 0.29 μm in the material's UV reflectance spectrum. The strength of the adsorbate band in the UV depends on substrate composition, gas exposure time, and cleanliness of the substrate particles. If particles making up Io's surface regolith come in contact with SO₂ gas they may retain an adsorbed SO₂ component that could contribute structure to Io's global UV reflectance spectrum.

REFERENCES

- Brown, R. H. (1974) "Optical line emission from Io." In Exploration of the Planetary System. (A. Wozczyk and C. Iwaniszweka, eds.) pp 527-531. D. Reidel, Dordrecht, Holland.
- Fanale, F. P., Brown, R. H., Cruikshank, D. P. and Clarke, R. N., "Significance of absorption features on Io's IR reflectance spectrum." Nature 280, pp 761-763.
- Fanale, F. P., Banerdt, W. B., Elson, L. S., Johnson, T. V., and Zurek, R.W. (1982) Io's surface: Its phase composition and influence on Io's atmosphere and Jupiter's magnetosphere" in Satellites of Jupiter, D. Morrison, ed., Tucson: University of Arizona Press, pp 756-781.
- Fink, U., Larson, H. P., Lebofsky, L. A., Frierberg, M., and Smith, H. (1980) "The 2-4 μ m spectrum of Io" Bull. Am. Astron. Soc. 10, p. 580.
- Howell, R., Cruikshank, D., and Fanale, F. (1984) Sulfur dioxide on Io: Spatial distribution and physical state. Icarus 57, in press.
- Matson, D. L., and Nash, D. B. (1983) "Io's atmospheric pressure control by regolith coldtrapping and surface venting." Journal Geophys. Res. 88, pp 4771-4783.
- Nash, D. B. and Moses, J. I. (1984). Surface photolysis of SO₂ and photophysical changes in sulfur may affect Io's surface UV-VIS reflectance. Bull. Am. Astron. Soc. 16 (in press).
- Nash, D.B., and Nelson, R. M. (1979) "Spectral evidence for sublimates and adsorbates on Io." Nature 280, pp 763-766.
- Nash, D. B., Fanale, F. P., and Nelson, R. M. (1980) "SO₂ frost: UV-visible reflectivity and limits on Io surface coverage." Geophys. Res. Letters 7, pp 665-668.
- Nash, D. B. (1983) "Io's 4 μ m band and the role of adsorbed SO₂" Icarus 54, pp 511-523.
- Nelson, R. M., and the JPL International Ultraviolet Explorer Team (1980) "Io longitudinal distribution of sulfur dioxide frost" Science 210, pp 784-786.
- Pang, K. D., Lumme, K., and Bowell, E. (1981) "Microstructure and particulate properties of Io and Ganymede: Comparison with other solar system bodies." Proc. Lunar Planet. Sci., Vol. 12B, pp 1543-1553.
- Pearl, J., Hanel, R., Kunde, V., Maguire, W., Fox, D., Gupta, S., Ponnaperuma, C., and Raulin, F. (1979) "Identification of gaseous SO₂ and new upper limits for other gases on Io." Nature 280, pp 755-758.
- Rao, C. N. R. (1967) Ultra-violet and visible spectroscopy: Chemical applications, London: Butterworths.

- Skoog, D. A., and West, D. M. (1971) Principles of Instrument Analysis, New York: Holt, Rinehart and Winston, Inc.
- Smythe, W. D., Nelson, R. M., and Nash, D. B. (1979) "Spectral evidence for SO₂ frost or adsorbate on Io's surface." Nature 280, p. 766.
- Soderblom, L. and the Voyager Imaging Team (1980) "Spectrophotometry of Io: Preliminary Voyager I results." Geophys. Res. Letters 7, pp 963-966.
- Wamsteker, W. (1972) "Narrow-band photometry of the Galilean Satellites". Comm. Lunar Planet. Lab 9, pp 171-177.

Table 1: SO₂ gas over MgO substrate

<u>pressure</u> (<u>mtorr</u>)	<u>wavelength</u> (<u>μm</u>)	<u>molar ext. coeff.</u> (<u>Lit/mole cm</u>)
100	.2900	159.6
250	.2875	194.6
480	.2875	177.2
730	.2925	170.8
980	.2925	343.5

Table 2: SO₂ gas over Cab-O-Sil substrate

<u>pressure</u> (<u>mtorr</u>)	<u>Wavelength</u> (<u>μm</u>)	<u>Molar Ext. Coeff.</u> (<u>Lit/mole cm</u>)
230 μm	.2925	125.9
480 μm	.2900	171.3
730 μm	.2900	189.9
1000 μm	.2950	376.3

Table 3: SO₂ gas over sulfur substrate

<u>pressure</u> (<u>mtorr</u>)	<u>Wavelength</u> (<u>μm</u>)	<u>Molar ext. coeff.</u> (<u>Lit/mole cm</u>)
260	.3025	46.24
500	.2950	70.00
750	.2975	77.15
910	.3000	134.8
1050	.3075	162.9

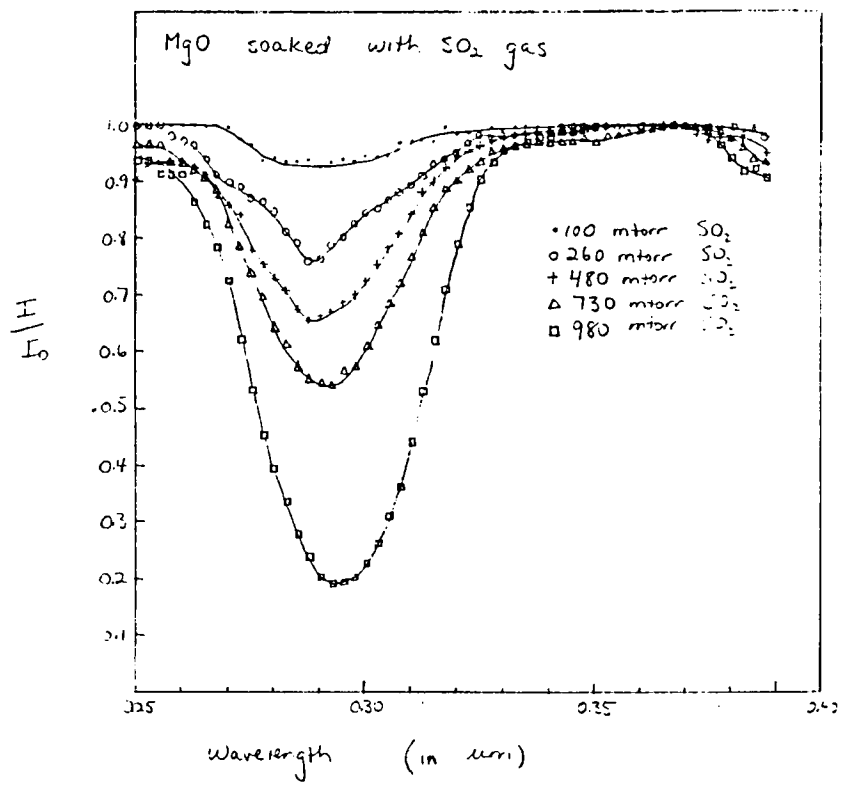


Figure 1A

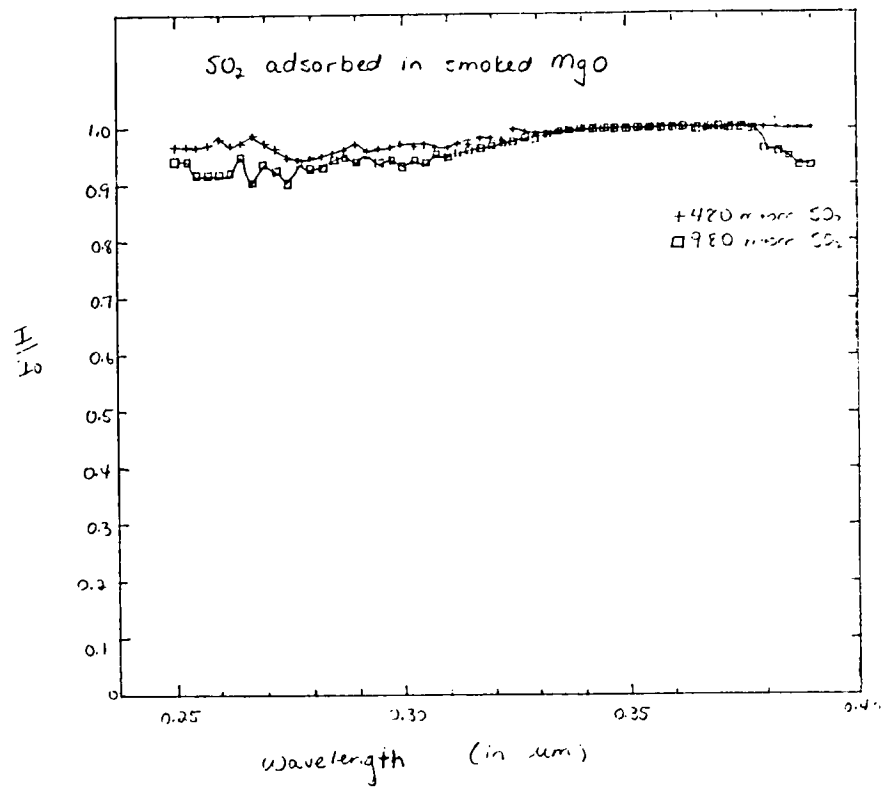


Figure 1B

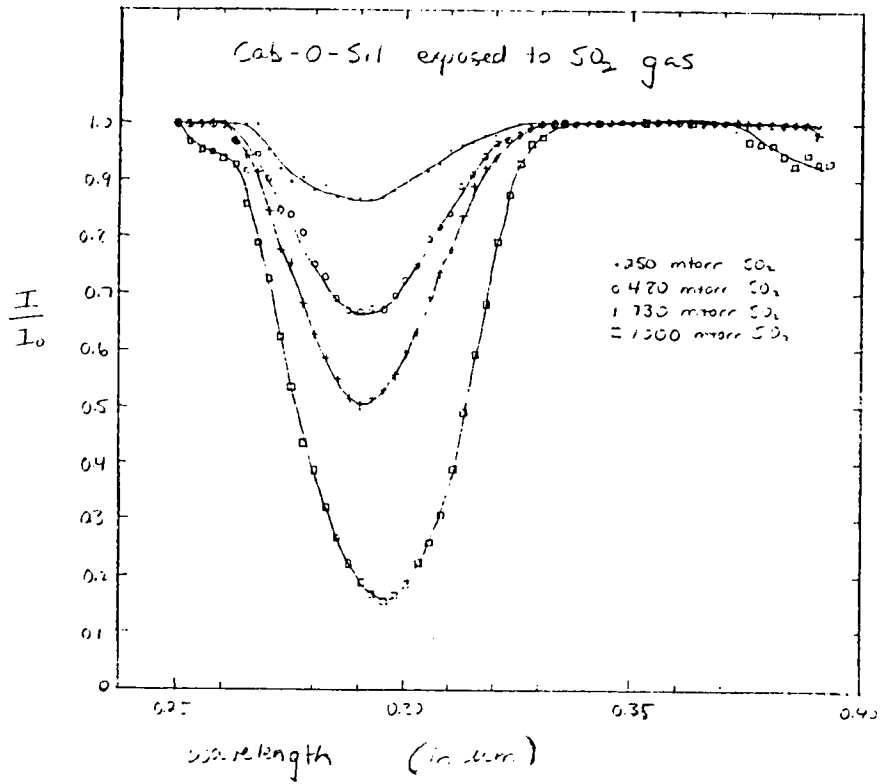


Figure 2A

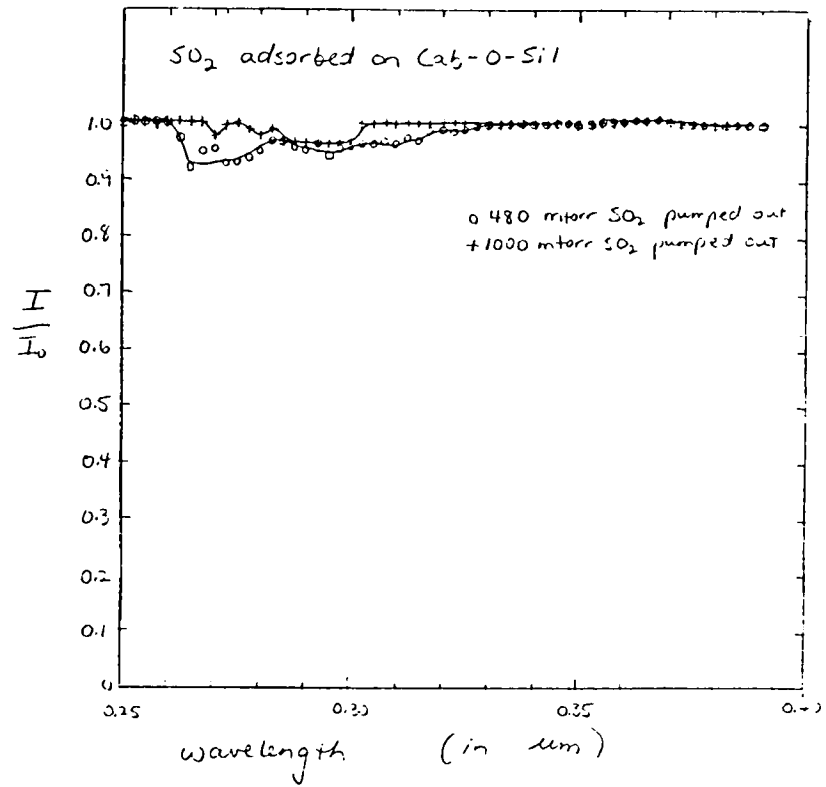


Figure 2B

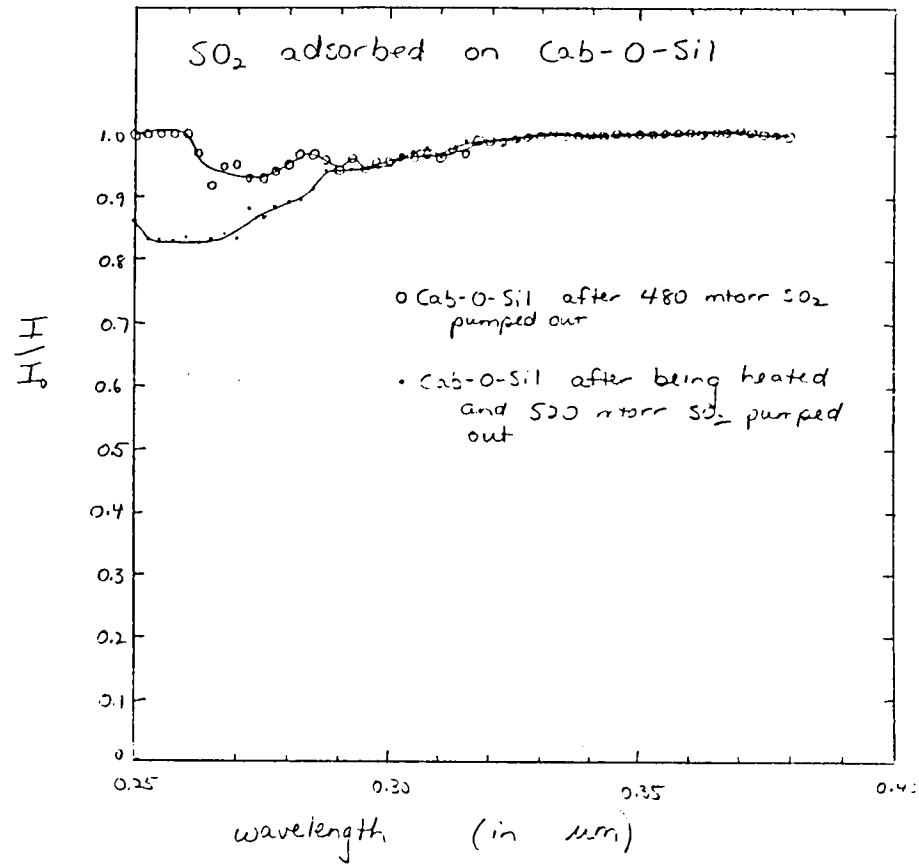


Figure 2C

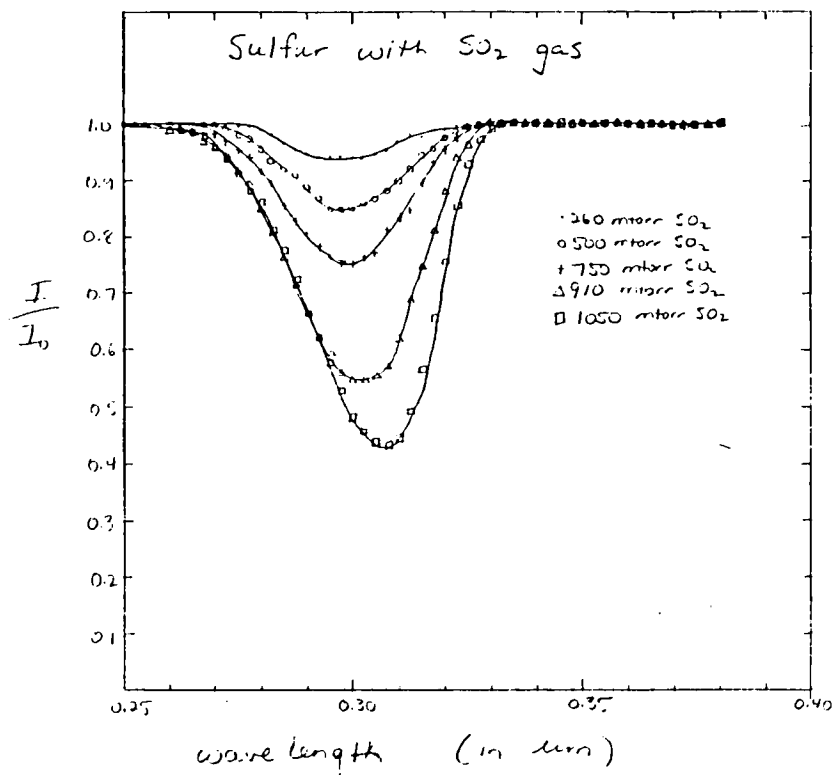


Figure 3A

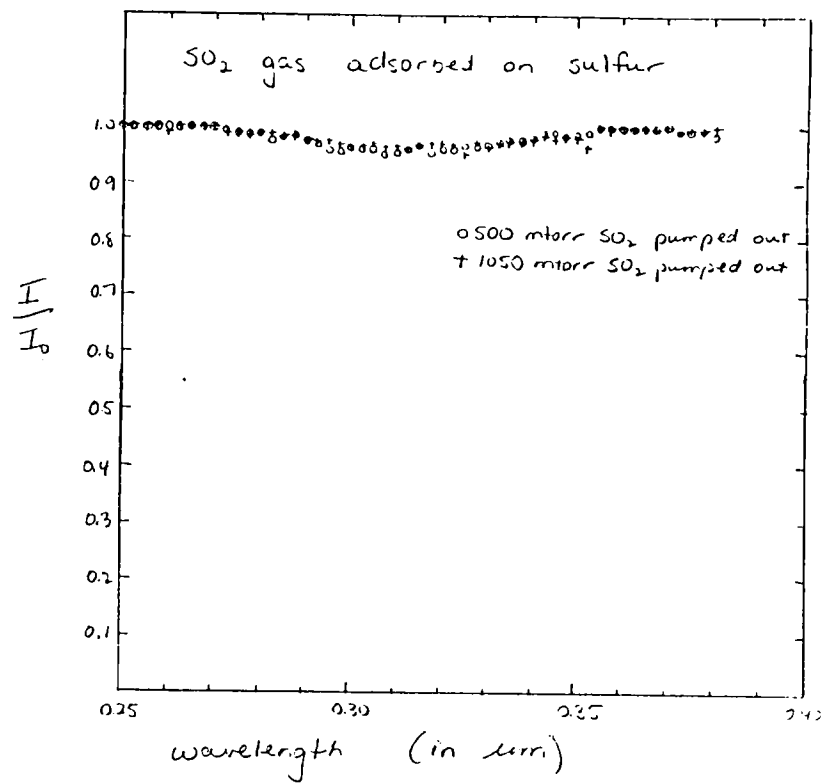


Figure 3B

Topographic slope of lunar maria and highlands
at resolutions of 2.5, 5, 10, 20, 40, and 80 km

Bruce A. Minturn
1984 Summer Intern
Planetary Geology Undergraduate Research Program
Dr. J. W. Head
Brown University

INTRODUCTION

The topography of a planetary surface reflects its geologic character and history. On earth, the relationship between a topographic feature and its underlying causes can be derived by considering independent evidence, such as lithology and age. Such relationships, however, may not necessarily apply to other planets, which appear to have evolved quite differently from earth. Seemingly familiar topographic features, such as a mountain chain, may have formed under completely different circumstances than their terrestrial counterparts. It is desirable, therefore, to broaden our understanding of the geologic nature of topography to those bodies for which there is both topographic data and sufficient geologic control. These conditions are met at the present time by the moon. Telescopic and orbital observations have been used to construct detailed geologic maps while manned and unmanned landers have returned samples for analysis. Topographic data has been obtained for large areas by Apollo mission photogrammetry and by earth-based radar observations.

It is the purpose of this study to begin to construct a data base of lunar topography that may later be used to establish the relationships between topography and geology on the moon.

CHARACTERIZATION OF TOPOGRAPHY: SLOPE

The most easily defined characteristic of topography is the slope of the surface. The magnitude of the slope is an indicator of the constructional and destructional forces at work on a topographic feature. Slopes can be measured directly on earth but must be determined indirectly for other planetary bodies.

In this study, slopes are calculated trigonometrically along topographic profiles constructed from Lunar Topographic Orthophotos (LTO). Analogous to digital topographic data, the calculated slopes are a function of the horizontal resolution ie. the horizontal separation of the two points between which the slope is determined. The effect that baseline length has on the characterization of a topographic feature will be examined here by calculating slope at several baselines along the same profiles.

PROFILES OF LUNAR TOPOGRAPHIC PROVINCES

The lunar surface can be divided into two major topographic provinces: mare and highlands. Highlands are composed of primitive crustal material that has been intensely modified by impact cratering. The maria are very large impact basins that were filled with volcanic deposits. For this work, profiles of representative traces of these two provinces were constructed, including three radial profiles each of Mare Crisium and Mare Serenitatis and their adjacent highlands, and one long profile of the farside lunar highlands (Figures 1, 2, and 3).

RESULTS

The results of the slope calculations are presented in tables 1, 2, and 3. The minimum, maximum, and mean slope are shown for each profile at resolutions of 2.5, 5, 10, 20, 40, and 80 kilometers.

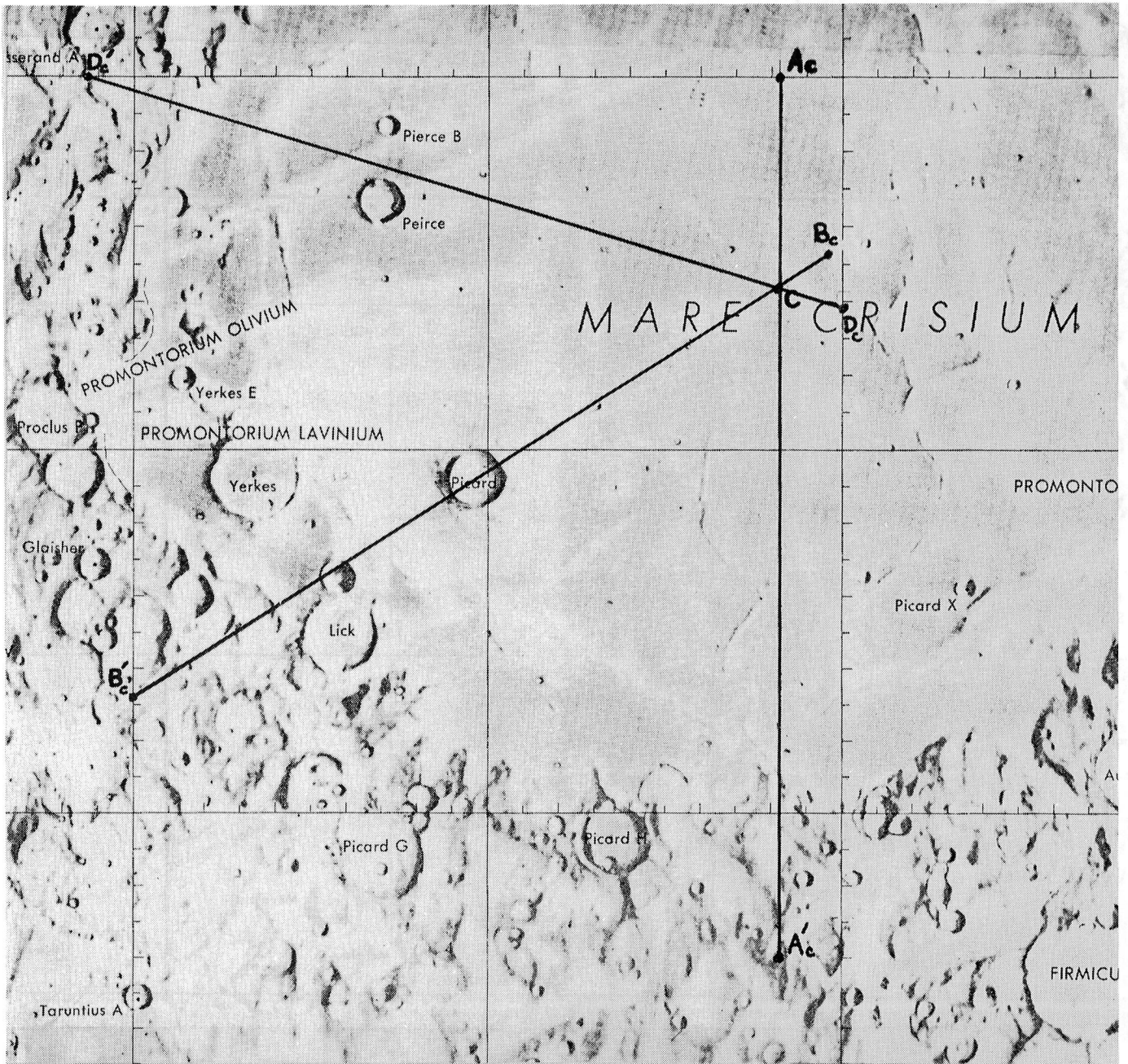


FIGURE 1: Mare Crisium profiles

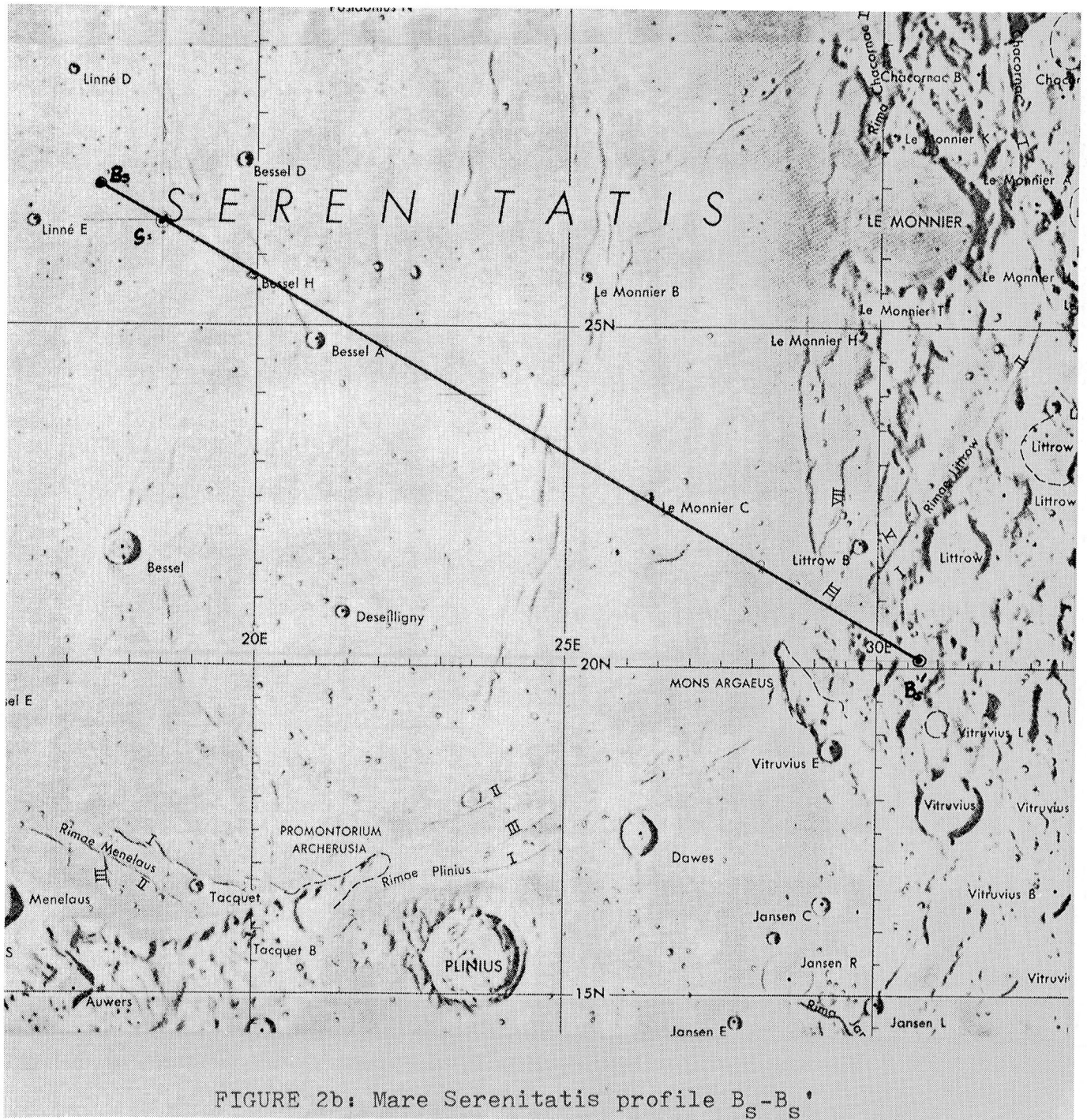


FIGURE 2b: Mare Serenitatis profile $B_S-B'_S$

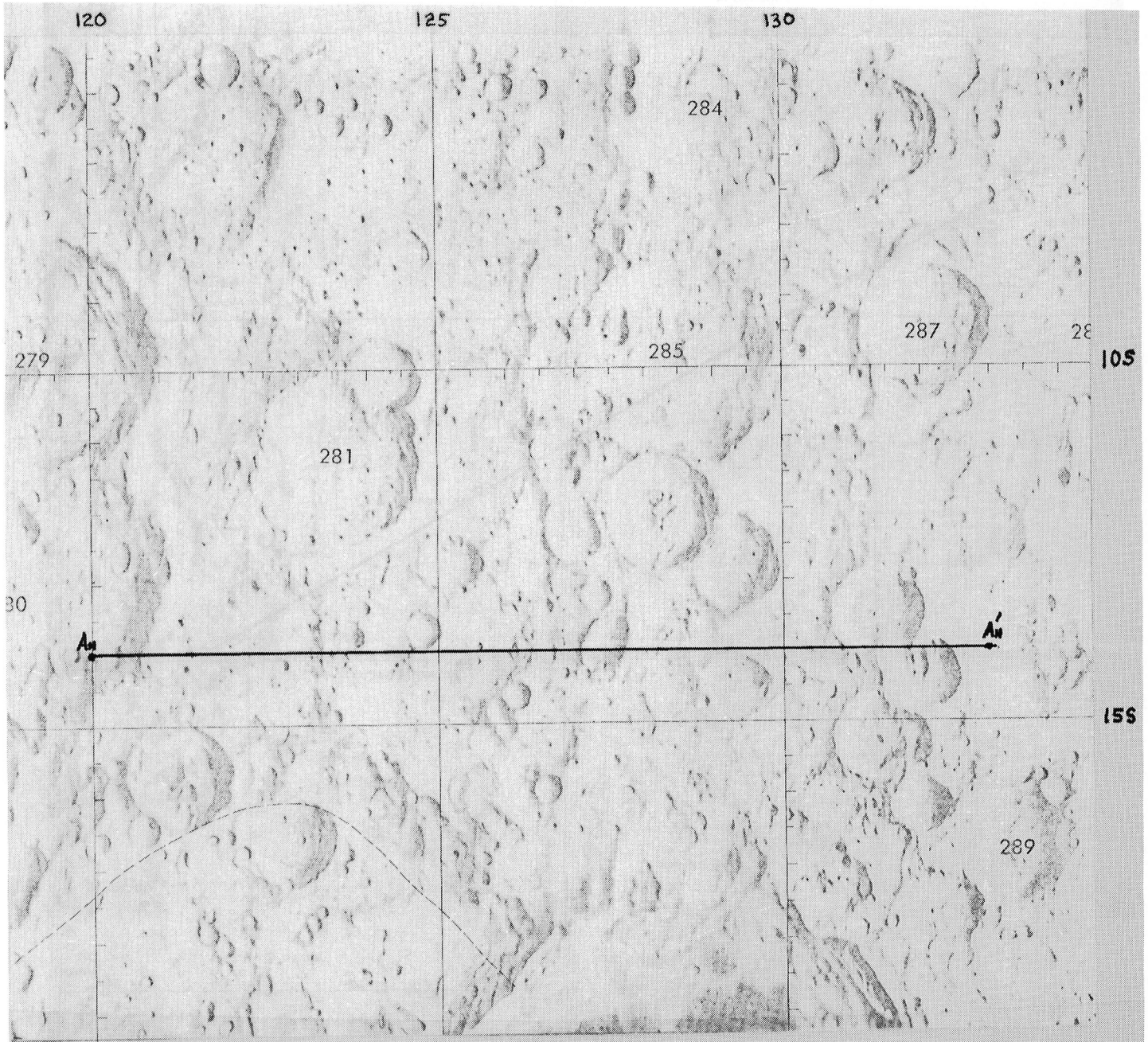


FIGURE 3: Farside lunar highland profile A_h-A_h'

TABLE 1: Mare slopes (in degrees)

profile	2.5 km			5 km			10 km			20 km			40 km			80 km		
	min	max	mean	min	max	mean	min	max	mean	min	max	mean	min	max	mean	min	max	mean
A _C -C	0.00	0.80	0.14	0.00	0.52	0.13	0.00	0.29	0.12	0.00	0.25	0.10	0.00	0.16	0.09	-	-	0.09
B _C -C	0.00	0.96	0.31	0.00	0.57	0.21	0.04	0.57	0.44	0.44	0.25	0.24	0.05	0.11	0.12	-	-	-
D _C -C	0.00	4.35	0.29	0.00	2.23	0.27	0.02	1.15	0.26	0.01	0.65	0.20	0.01	0.32	0.16	0.01	0.09	0.08
Crisium profiles	0.00	4.35	0.25	0.00	2.23	0.20	0.00	1.15	0.27	0.00	0.65	0.18	0.00	0.32	0.12	0.01	0.09	0.08
A _S -S	0.00	2.70	0.32	0.00	1.92	0.29	0.00	1.59	0.24	0.01	0.53	0.19	0.01	0.29	0.10	0.01	0.11	0.07
B _S -S	0.00	17.1	0.70	0.00	2.77	0.31	0.00	1.09	0.24	0.02	0.37	0.16	0.00	0.31	0.13	0.08	0.16	0.12
C _S -S	0.00	0.92	0.37	0.00	0.80	0.26	0.00	0.63	0.25	0.00	0.42	0.25	0.00	0.23	0.08	-	-	0.06
Seren. profiles	0.00	17.1	0.46	0.00	2.77	0.29	0.00	1.59	0.24	0.00	0.53	0.20	0.00	0.31	0.10	0.01	0.16	0.08
Mare	0.00	17.1	0.36	0.00	2.77	0.29	0.00	1.59	0.24	0.00	0.53	0.20	0.00	0.31	0.10	0.01	0.16	0.08

TABLE 2: Highland slopes (in degrees)

profile	2.5 km			5 km			10 km			20 km			40 km			80 km		
	min	max	mean	min	max	mean	min	max	mean	min	max	mean	min	max	mean	min	max	mean
A _c -C	0.23	8.87	3.47	0.00	8.08	1.88	0.03	3.55	1.24	0.27	1.89	1.24	-	-	1.76	-	-	-
B _c -C	0.18	21.4	8.92	0.00	18.1	7.50	5.16	7.33	6.60	1.10	6.96	4.58	-	-	2.54	-	-	-
D _c -C	0.11	25.4	11.1	0.06	21.9	10.9	3.49	17.2	7.69	5.03	7.10	6.06	-	-	1.05	-	-	-
Crisium profiles	0.11	25.4	7.84	0.00	21.9	6.76	0.03	17.2	5.18	0.27	7.10	3.96	-	-	1.92	-	-	-
A _s -S	0.16	6.50	2.26	0.02	3.43	1.52	0.83	2.83	1.83	-	-	1.32	-	-	-	-	-	-
B _s -S	0.11	11.9	2.79	0.63	6.73	2.50	0.72	2.18	1.01	-	-	0.72	-	-	-	-	-	-
C _s -S	0.00	13.4	4.93	0.00	8.98	2.86	0.17	4.74	2.27	1.95	2.55	2.26	0.10	2.08	1.09	-	-	0.99
Seren. profiles	0.00	13.4	3.33	0.00	8.98	2.29	0.17	4.74	1.70	1.95	2.55	1.43	0.10	2.08	1.09	-	-	0.99
A _h -A _h	0.00	24.9	4.85	0.00	22.4	4.37	0.26	11.9	3.69	0.09	5.82	2.57	0.04	4.67	1.67	0.06	1.42	0.70
Highlands	0.00	25.4	5.34	0.00	22.4	4.47	0.03	17.2	3.52	0.09	7.10	2.65	0.04	4.67	1.56	0.06	1.42	0.85

TABLE 3: Basin perimeter slopes (in degrees)

profile	2.5 km			5 km			10 km			20 km			40 km			80 km		
	min	max	mean	min	max	mean	min	max	mean	min	max	mean	min	max	mean	min	max	mean
A _c -C	0.00	14.2	3.52	0.03	13.4	3.18	0.72	7.97	3.20	0.90	5.51	3.20	0.90	5.51	3.02	-	-	1.70
B _c -C	0.18	23.0	6.99	0.45	19.4	7.40	0.27	14.0	7.22	1.60	12.8	7.22	-	-	1.29	-	-	-
D _c -C	0.00	21.5	4.05	0.00	14.3	4.08	0.06	10.8	4.01	0.87	7.13	4.00	-	-	4.01	-	-	2.01
Crisium profiles	0.00	23.0	4.85	0.00	19.4	4.89	0.06	14.0	4.81	0.87	12.8	4.81	-	-	2.77	-	-	1.86
A _s -S	13.6	20.1	16.9	-	-	16.9	-	-	8.75	-	-	5.79	-	-	2.69	-	-	-
B _s -S	0.11	9.43	1.99	0.23	7.01	2.00	1.08	1.26	1.16	-	-	1.11	-	-	0.91	-	-	-
C _s -S	0.00	12.8	3.32	0.06	7.91	2.39	0.14	6.65	2.34	-	-	3.26	-	-	1.75	-	-	1.53
Seren. profiles	0.00	20.1	7.35	0.06	7.91	7.10	0.14	6.65	4.08	-	-	3.37	-	-	1.78	-	-	1.53
Basin perims.	0.00	23.0	6.10	0.00	19.4	6.00	0.06	14.0	4.45	0.87	12.8	4.09	-	-	2.28	-	-	1.70

DISCUSSION

The mare surfaces are broadly dome-shaped and, in general, possess very low apparent slopes, averaging less than 0.5° at 2.5 km resolution. Perturbations of this trend occur at mare ridges (slopes up to 2°) and post-emplacement craters (slopes up to 25°). A comparison of Mare Serenitatis and Mare Crisium reveals that Serenitatis has steeper slopes at high resolution but that the two maria are very similar at longer baselines. This is due to the greater population of mare ridges and small craters (diameter less than 5 km) in the Serenitatis profiles. The topographic signature of such small objects is usually diminished or removed at longer baselines.

Horizontal surfaces are found at all baseline lengths in both maria.

Slopes increase abruptly as the basin rims are crossed, in some cases exceeding 20° at 2.5 km resolution.

Highland slopes are quite high compared to the maria, even at baselines of 40 and 80 km. At 2.5 km, apparent slopes range from horizontal to over 25° , with a mean of 5.34° . Mean slopes decrease approximately 0.9° for every doubling of the baseline length. At 80 km, the mean highland slope is 0.85° compared to 0.08° in the maria.

CONCLUSION

The values presented in tables 1, 2, and 3 represent a very small sample of apparent slopes on the lunar surface. Major lunar provinces, the mare and the highlands, can be seen to possess unique slope characteristics which will aid in the further interpretation of geologic features, both on the moon and other planetary bodies.

EVAPORATION OF VOLATILE ICES DURING ICY SATELLITE ACCRETION

Zoran Spasojevic

Planetary Geology Intern

California Institute of Technology

It is generally believed that the Sun and the planets condensed from a cloud of interstellar matter about 4.6 billion years ago. The composition of the cloud is thought to be similar to the composition of Jupiter's atmosphere at the present time.

In this paper I will try to understand the evaporation of volatile ices during the first period of icy satellite accretion.

Many people have analyzed the stability of volatiles in the solar system (Watson 1961, Watson 1963, Delsemme 1971) and the escape mechanism of (light) gases is rather well understood. Consider an accreting satellite of instantaneous mass M and radius R in a very sparse gas environment of temperature T_0 . A rough estimate for the surface temperature T_s during accretion can be obtained from the energy balance (Stevenson 1984).

$$\sigma(T_s^4 - T_0^4) 4\pi R^2 + LmZ4\pi R^2 = \frac{dM}{dt} [GM/R - C(T_s - T_0)] \quad (1)$$

Where σ is the Stefan-Boltzmann constant, L is the heat per molecule lost in sublimation (which can be calculated from Clapeyron's equation), m is the molecular mass, C is the specific heat of the accreted material, Z is the net number of molecules that leave the surface per square meter per second, and G

is the gravitational constant. If τ is the characteristic accretion time then $dM/dt \approx M/\tau$.

When the forming satellite is small such that $V_{esc} < U$ and $l = 1/nQ$ (where V_{esc} is the escape velocity of a satellite, U is the thermal velocity of molecules, l is the mean free path, n is the number density, and $Q \approx 3.3 \times 10^{-19} \text{m}^2$) is the collision cross section) then the expression for the evaporation rate Z_0 is (Delsemme 1971):

$$Z_0 = P(2\pi m kT_s)^{-1/2} \quad (2)$$

Where P is the vapor pressure and k is the Boltzmann's constant.

As more of the accretion material falls in, the gravitational pull on the escaping molecules increases, and only those molecules with velocities greater than the escape velocity of the satellite leave the satellite. Provided that $l \gg R$, the equation for the evaporation rate becomes:

$$Z = Z_0 \frac{\int_{V_{esc}}^{\infty} v^2 e^{-(v/u)^2} dv}{\int_0^{\infty} v^2 e^{-(v/u)^2} dv} \quad (3)$$

With more accretion material falling in the surface temperature of the satellite increases which in turn makes the evaporation rate higher and the collisions between molecules become important in the escape mechanism. The temperature at which this happens can be calculated from equation 4 (Chamberlain 1978):

$$\int_{r_c}^{\infty} n(r) Q dr \approx n(r_c) Q \Delta = 1 \quad (4)$$

Where $\Delta = R$ if $H > R$ and H otherwise, $H [= kT/mg(r)]$ is the density scale height, $g(r)$ is the acceleration of gravity and r_c denotes the distance from the center of the satellite to the critical level (where equation 4 holds). And the new equation for the evaporation rate when the collisions become important is:

$$\phi_J = n \frac{U}{2(\pi)^{-1/2}} (1 + \lambda_c) e^{-\lambda} \quad (5)$$

This is the equation for Jeans or hydrodynamic escape (Hunten 1973) which can be evaluated at any level with the same temperature as the critical level. Here λ_c is equal to $\lambda(=v_{esc}/U)^2$ at the critical level.

It is very hard to evaluate λ_c but the error in equation 5 due to the uncertainty in λ_c is not large since ϕ_J is only linearly dependent on λ_c .

Figures 1(a,b) and 2(a,b) show the solution of Equation 1 (using equation 5) for T_s as a function of R , for methane and carbon dioxide respectively, and for $\tau = 10^4$ years, $C = 1000$ J/Kg, and T_0 is shown on each figure. Since I am primarily interested in the evolution of satellites like Encelidus, Tethys, Rhea and Miranda for mass density I used $\rho = 1300$ Kg/m³.

It can be seen from figures 1(b) and 2(b) that when T_0 is high enough the evaporation rate is so high that the surface temperature is lower than T_0 for relatively small radii. At that point the theory breaks down since the accretion material loses most of its gas before it reaches the surface of a satellite.

The total number of molecules of a gas that escape from a satellite during the characteristic accretion time can be calculated using equation 6:

$$N = \int_0^{t_c} 4\pi R^2 Z dt + \int_{t_c}^{\tau} 4\pi R^2 \phi_J dt \quad (6)$$

Where t_c denotes the time when the escape becomes collisional.

For cases when N is comparable to the total number of molecules in a satellite ($t_c \rightarrow 0$) the first integral becomes negligibly small compared to the second integral. Figure 3 shows the fraction of mass that is lost during the characteristic accretion time as a function of radius for four different gases.

It can be seen from figure 3 that a satellite with the size of Rhea would lose 18% of its present mass by the evaporation of methane during time τ . Therefore most, if not all, of its methane would be lost.

Equation 6 only sets the upper bound since the total number of molecules of some gas that escape from a forming satellite is largely determined by the amount of that gas present in the accretion material, and by the presence of other less volatile gases.

It is very hard to check these results since Earth based observations can determine the composition of a layer of the surface only to a depth of one micron, such results are not very conclusive for the overall satellite composition.

Acknowledgment

I wish to extend my gratitude to Dr. D.J. Stevenson without whose help the writing of this paper would have been impossible. Also I would like to thank Mrs Christine Gibbons for conducting this NASA program, and Kay Campbell for typing this paper.

References

Chamberlain, J.W. (1978). Theory of Planetary Atmospheres, Academic press: Chap. 7.

Delsemme, A.H. and Miller, D.C. (1971). Physico-chemical Phenomena in Comets III. Planet. Space Sci. 19, 1229-1257.

Hunten, M.D. (1973). The Escape of Light Gases from Planetary Atmospheres. J. of Atmos. Sci 30, 1481-1494.

Space Program Summary 3:37-64 J.P.L.

Stevenson, D.J. (1984). Composition, Structure and Evolution of Uranian and Neptunian Satellites. Proceedings of a workshop held in Pasadena, CA, February 6-8, 1984.

Timmerhous and Snyder, ed., Advances in Cryogenic Engineering, 25:662-670.

Watson, K., Murray, B.C. and Brown, H. (1961). The Behavior of Volatiles on the Lunar Surface. J. Geophys. Res. 66, 3033-3045.

_____ (1963). The Stability of Volatiles in the Solar System. Icarus 1, 317-327.

FIGURE 1

a $\rightarrow T_0 = 30$
b $\rightarrow T_0 = 40$

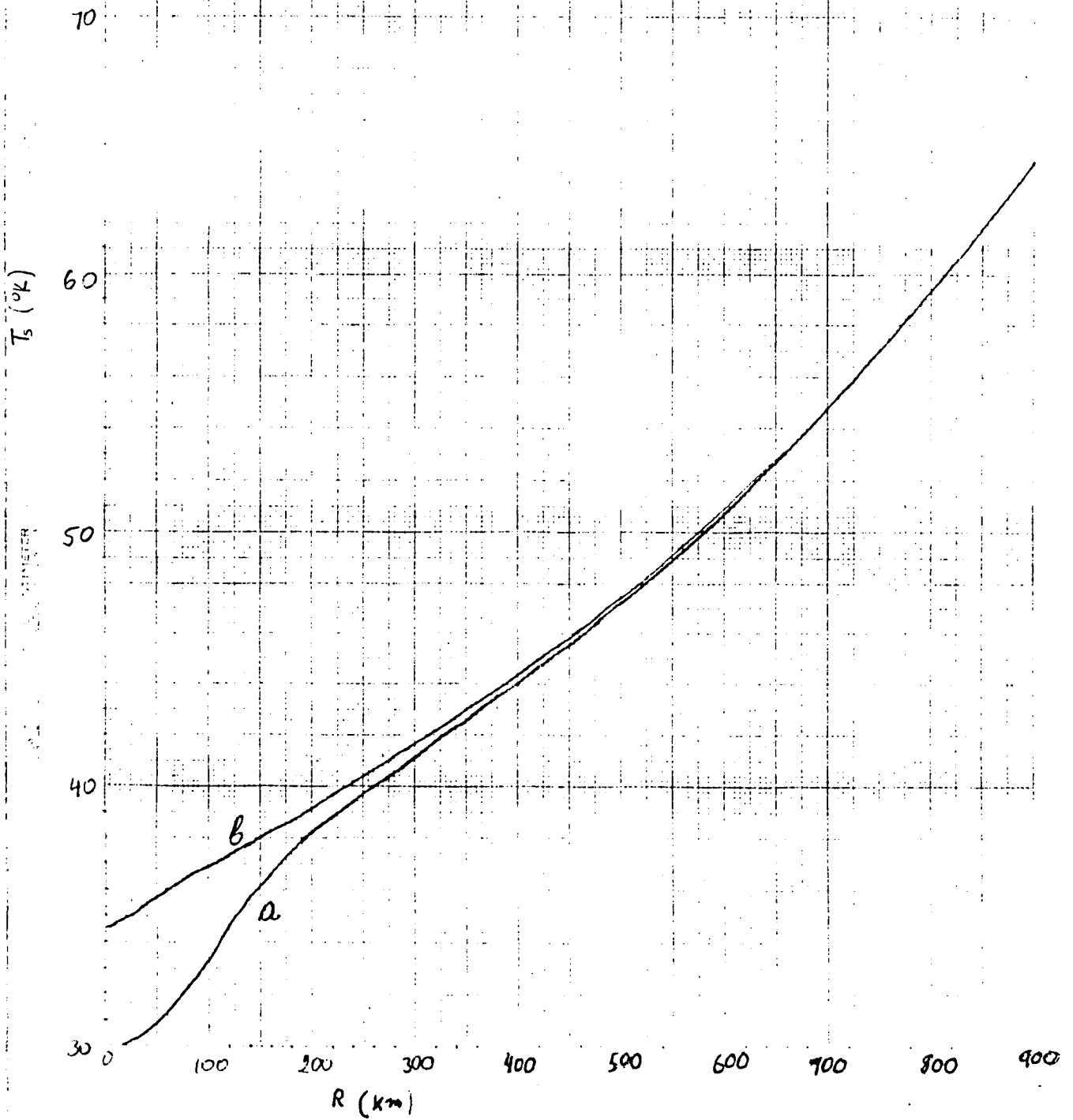


FIGURE 2

a \rightarrow $T_0 = 78$
b \rightarrow $T_0 = 88$

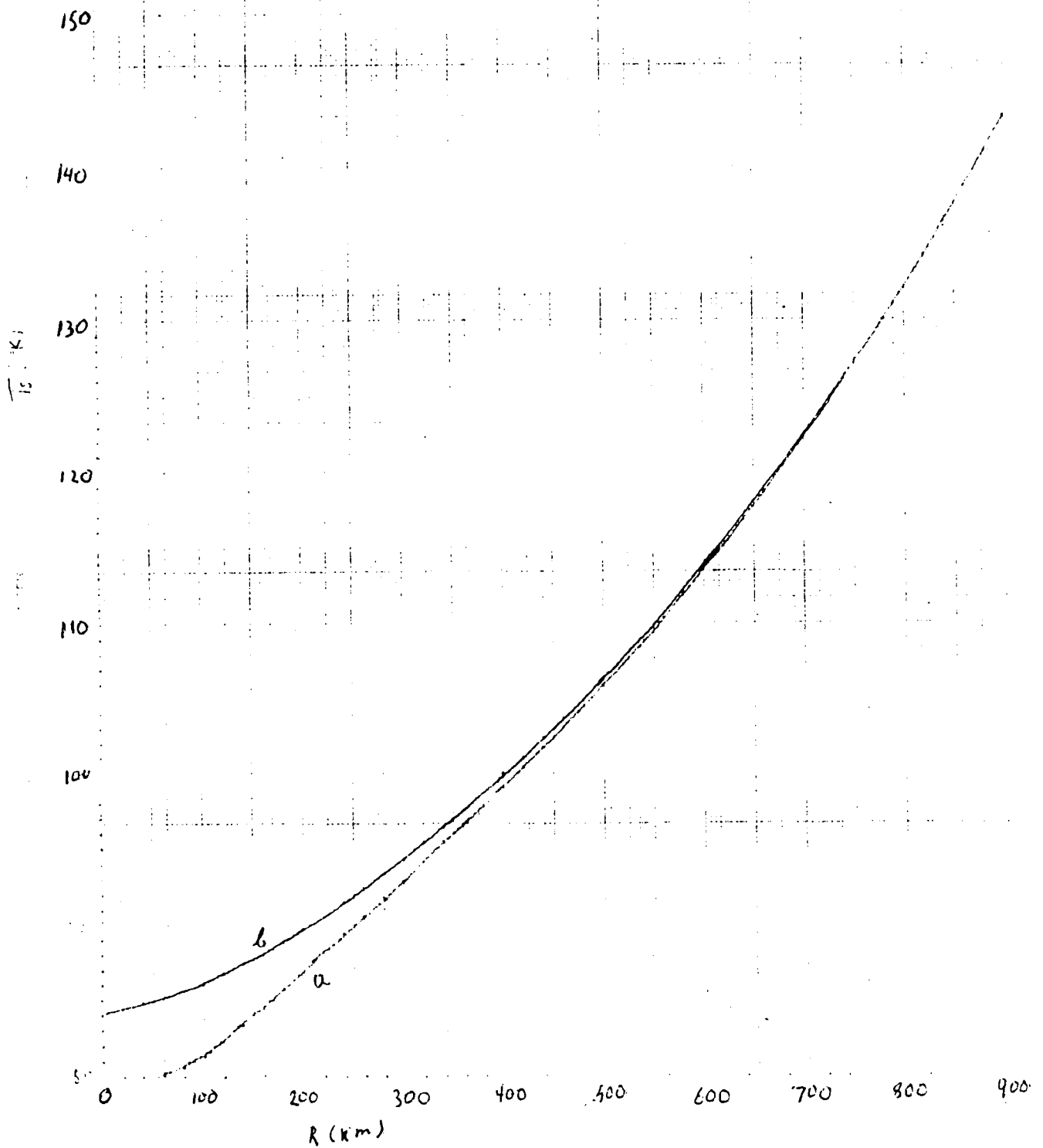
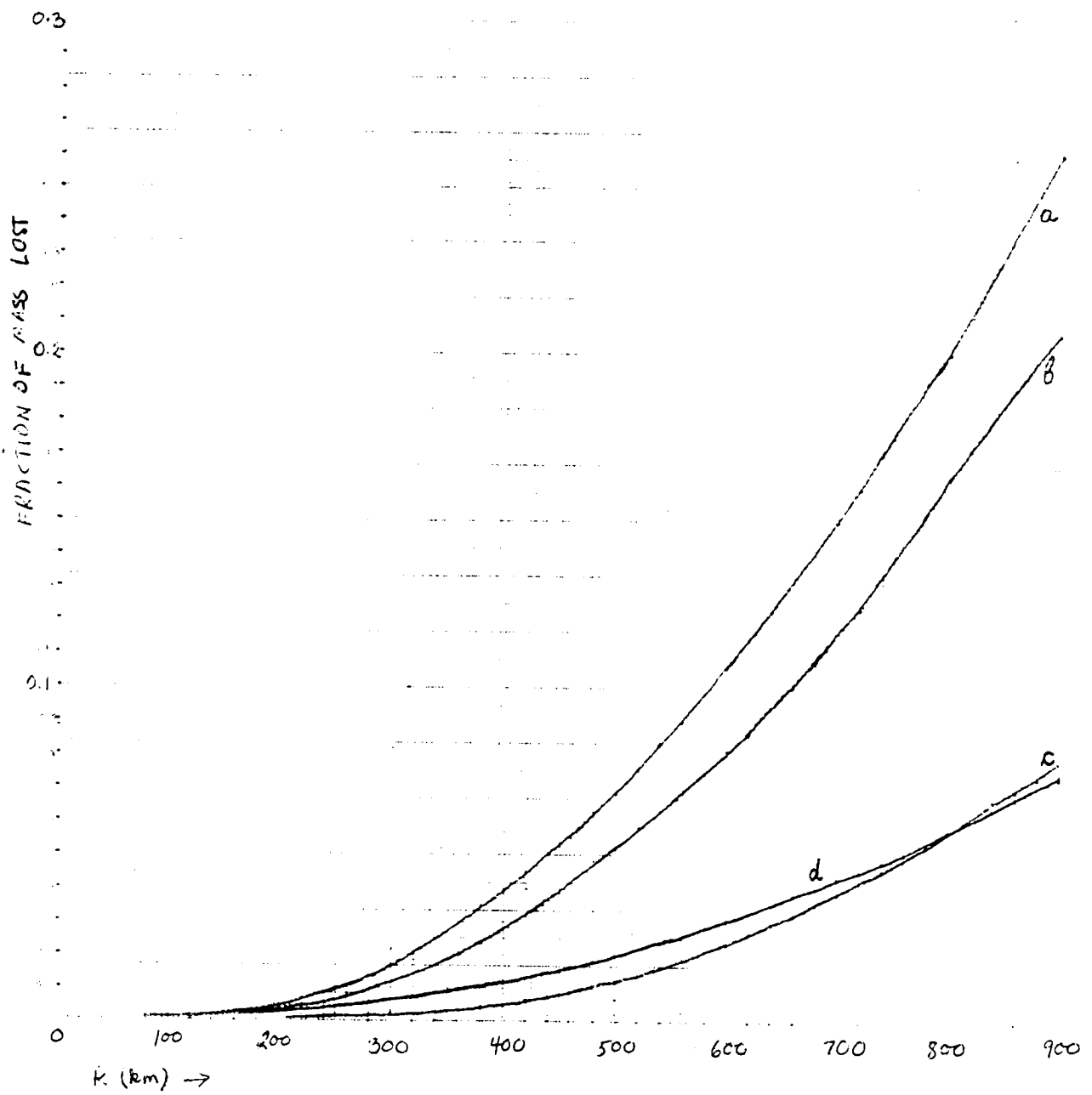


FIGURE 3

- a \rightarrow CH₄; T₀ = 30 °K
- b \rightarrow CO₂; T₀ = 80 °K
- c \rightarrow NH₃·H₂O; T₀ = 130 °K
- d \rightarrow NH₃; T₀ = 100 °K

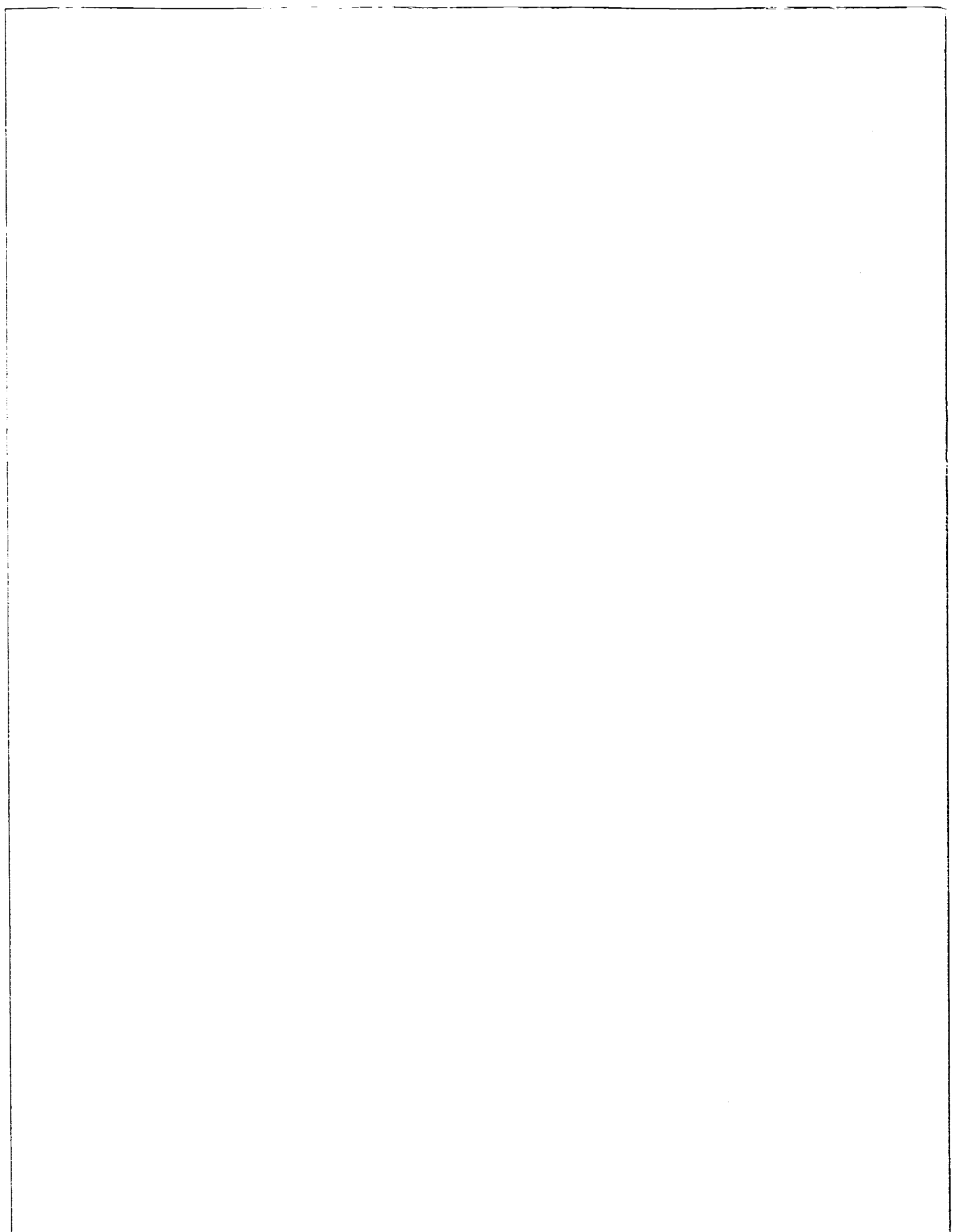








1. Report No. NASA TM-88784 volume 2		2. Government Accession No.		3. Recipient's Catalog No.	
4. Title and Subtitle Advances in Planetary Geology - Volume 2				5. Report Date July 1986	
				6. Performing Organization Code EL	
7. Author(s)				8. Performing Organization Report No.	
9. Performing Organization Name and Address Office of Space Science and Applications Solar System Exploration Division Planetary Geology and Geophysics Program				10. Work Unit No.	
				11. Contract or Grant No.	
				13. Type of Report and Period Covered Technical Memorandum	
12. Sponsoring Agency Name and Address National Aeronautics and Space Administration Washington, DC 20546				14. Sponsoring Agency Code	
15. Supplementary Notes					
16. Abstract This publication is a continuation of volume 1; it is a compilation of reports focusing on research into the origin and evolution of the solar system with emphasis on planetary geology. Specific reports include a multispectral and geomorphic investigation of the surface of Europa and a geologic interpretation of remote sensing data for the martian volcano Ascreaus Mons.					
17. Key Words (Suggested by Author(s)) planetary geology planetology			18. Distribution Statement Unclassified - Unlimited Subject Category 91		
19. Security Classif. (of this report) Unclassified		20. Security Classif. (of this page) Unclassified		21. No. of Pages 472	22. Price A20



**National Aeronautics and
Space Administration
Code NIT-4**

**Washington, D.C.
20546-0001**

**Official Business
Penalty for Private Use, \$300**

**SPECIAL FOURTH-CLASS RATE
POSTAGE & FEES PAID
NASA
Permit No. G-27**

NASA

**POSTMASTER: If Undeliverable (Section 158
Postal Manual) Do Not Return**
